Transactions of the ASME®

Journal of Heat Transfer

Published Quarterly by The American Society of Mechanical Engineers

VOLUME 120 • NUMBER 2 • MAY 1998

Transactions of the ASME, Journal of Heat Transfer (ISSN 0022-1481) is published quarterly (Feb., May, Aug., Nov.) for $220.00 per year by The American Society of Mechanical Engineers, 345 East 47th Street, New York, NY 10017. Periodicals postage paid at New York, NY and additional mailing offices. POSTMASTER: Send address changes to Transactions of the ASME, Journal of Heat Transfer, c/o THE AMERICAN SOCIETY OF MECHANICAL ENGINEERS, 22 Law Drive, Box 2300, Fairfield, NJ 07007-2300.
CHANGES OF ADDRESS must be received at Society headquarters seven weeks before they are to be effective. Please send old label and new address. **PRICES:** To members, $40.00, annually: to nonmembers, $220.00. Add $40.00 for postage to countries outside the United States and Canada.

TECHNICAL PAPERS

(Contents continued on Outside Back Cover)

This journal is printed on acid-free paper, which exceeds the ANSI Z39.48-1992 specification for permanence of paper and library materials. ♾™

♻ 85% recycled content, including 10% post-consumer fibers.

(Contents continued)

TECHNICAL NOTES

(Contents continued on Inside Back Cover)

(Contents continued)

ANNOUNCEMENTS

Nanoscale Temperature Distributions Measured by Scanning Joule Expansion Microscopy

A. Majumdar[1]
Department of Mechanical Engineering,
University of California,
Berkeley, CA 94720
majumdar@me.berkeley.edu

J. Varesi[2]
Department of Mechanical and
Environmental Engineering,
University of California,
Santa Barbara, CA 93106

This paper introduces scanning Joule expansion microscopy (SJEM), which is a new thermal imaging technique with lateral resolution in the range of 10–50 nm. Based on the atomic force microscope (AFM), SJEM measures the thermal expansion of Joule-heated elements with a vertical resolution of 1 pm, and provides an expansion map of the scanned sample. Submicron metal interconnect lines as well as 50-nm-sized single grains of an indium tin oxide resistor were imaged using SJEM. Since the local expansion signal is a convolution of local material properties, sample height, and as temperature rise, extraction of the thermal image requires deconvolution. This was experimentally achieved by coating the sample with a uniformly thick polymer film, resulting in direct measurement of the sample temperature distribution. A detailed thermal analysis of the metal wire and the substrate showed that the predicted temperature distribution was in good agreement with the measurements of the polymer-coated sample. However, the frequency response of the expansion signal agreed with theoretical predictions only below 30 kHz, suggesting that cantilever dynamics may play a significant role at higher frequencies. The major advantage of SJEM over previously developed submicron thermal imaging techniques is that it eliminates the need to nanofabricate specialized probes and requires only a standard AFM and simple electronics.

1 Introduction

The inventions of the scanning tunneling microscope (STM) (Binnig et al., 1982) and the atomic force microscope (AFM) (Binnig et al., 1986) have led to the development of a new class of microscopes known as scanning probe microscopes (SPMs). A common factor among all of the numerous SPMs in use today is that they utilize a sharp probe tip in close proximity to a sample surface to measure its topography as well as other physical quantities with nanometer scale spatial resolution. Scanning thermal microscopy (SThM) was first developed by fabricating a thermocouple at the end of an STM tip (Williams and Wickramasinghe, 1986a, b). The primary purpose of the original system was not to measure surface temperature, but to use tip-sample heat conduction as a means to image the surface topography of insulating surfaces. This setup was subsequently used for photothermal measurements with approximately 100 nm spatial resolution (Williams and Wickramasinghe, 1988a, b). Later development of SThMs (Nonnenmacher and Wickramasinghe, 1992; Majumdar et al., 1993) have been based on the AFM system since the feedback control required for topographical imaging is force based and, hence, decoupled from tip-sample heat conduction.

SThMs in the past have mostly used a proximal sharp probe with a temperature sensor fabricated on the very tip of the probe. Majumdar et al. (1993, 1995) originally constructed a thermocouple with an approximate diameter of 25 mm using an electrochemical etching process. Pylkii et al. (1994) used a resistance thermometer made of a 5-mm-dia Wollaston wire that was bent into the shape of a sharp probe. This size was improved upon by Fish et al. (1995), who used a micropipette drawn to a sharp tip. The spatial resolution of the measured temperature distribution by such probes was generally found to be on the order of 300–500 nm. Most recently, Luo et al. (1995) devised a fabrication process that resulted in tip thermocouples ranging from 100–300 nm in diameter, which increased the resolution to about 25 nm. It was found that the dominant mechanism of tip-sample heat conduction for such probes was through a water film that bridged the tip-sample junction due to surface tension forces (Luo et al., 1997a, b). Consequently, both the spatial resolution and the measured temperature strongly depended on the size of the water bridge, which was influenced by tip geometry, relative humidity, and the chemistry of the tip and sample surfaces. These parameters are often difficult to control and standardize, which makes quantitative measurements by such probes time consuming and difficult. In addition, further increase in spatial resolution by this approach requires fabrication of sharper tips and smaller thermocouples, which is at present extremely difficult. Goodson and Asheghi (1997) have developed a near-field optical thermometry (NFOT) technique, which measures the light reflected from a sample after it is squeezed through a sub-wavelength aperture formed at the end of a metal-coated tapered optical fiber. They quote a resolution of about 50 nm, which is approximately the aperture size. In addition to the resolution being limited by the aperture size, the degree of fabrication difficulty increases as the aperture size is reduced. Reduction in aperture size also decreases transmission efficiency, which heats the tip and its neighboring sample, making it difficult to measure the temperature of sample surfaces.

In response to these difficulties with previous techniques, we propose a new approach, which circumvents these problems of

[1] Corresponding author.
[2] Current Address: Santa Barbara Research Center, Loc. SB, Bldg. B3, MS 54, 75 Coromar Drive, Goleta, CA 93117.

Contributed by the Heat Transfer Division and presented at the International Mechanical Engineering Congress & Exposition, Dallas, Texas, November 16–21, 1997. Manuscript received by the Heat Transfer Division August 18, 1997; revision received February 2, 1998. Keywords: Measurement Techniques, Microscale, Microstructures, Nanoscale, Temperature. Associate Technical Editor: T. L. Bergman.

temperature measurement at nanometer scales. The new technique is called scanning Joule expansion microscopy (SJEM) (Varesi and Majumdar, 1998), which eliminates the need to fabricate a temperature sensor on the probe tip. Hence, it does not rely on tip-sample heat conduction, making it an apertureless method, in contrast to the traditional SThM and NFOT systems. Instead, SJEM takes advantage of the astounding vertical resolution of the AFM ($\cong 10^{-12}$ m) to measure the thermal expansion of a Joule-heated sample with lateral or spatial resolution on the order of 10 nm. SJEM was first proposed under the title of Joule displacement microscopy by Martin and Wickramasinghe (1987). They used optical interferometry to measure small displacements of a thin-film conductor subjected to an AC current. Based on far-field optics, this technique's spatial resolution was diffraction-limited to a size on the order of the wavelength. Material expansion was also addressed by Weaver et al. (1989), who examined optical absorption microscopy using an STM. They predicted that the smallest feature that could be resolved through expansion using their technique was on the order of 100 nm, based on a thermal expansion coefficient, α, of 10^{-5} K^{-1}. Although they observed an expansion signal, they did not present any images since the spatial resolution of 100 nm was not sufficient for their purpose.

This paper presents a detailed description of the SJEM technique as well as the experimental evidence and theoretical background for temperature measurement using SJEM. Section 2 describes the technique and section 3 shows the expansion images and discusses the experiments performed to identify the source of the signals. Section 4 develops a simple model to estimate the temperature rise and expansion signals. An experimental technique to measure temperature distributions directly using SJEM is introduced in section 5.

2 Technique and System Description

2.1 Scanning Joule Expansion Microscope. Figure 1 shows a schematic diagram of SJEM, which is based on the AFM system. A sample is placed on top of a piezoelectric scanner, which is capable of motion along the three orthogonal axes. A sharp tip mounted on a cantilever is brought into contact with the sample surface. Off the back of the cantilever, a diode laser beam reflects into a two-segmented (segments A and B) or split photodiode, which provides a normalized differential signal, $(A - B)/(A + B)$, that is proportional to the cantilever deflection. A feedback system uses this signal to control the z-motion of the sample in order to maintain a constant cantilever deflection, while raster scanning the sample in the x and y directions. Hence, any topographical feature will result in the corresponding motion of the sample that forms the basis of topographical imaging. The spring constants, g, of the cantilevers are typically about 0.01–0.1 N/m and the bandwidth of the feedback control system is 0–20 kHz, although the usable bandwidth during imaging is usually 256 or 512 Hz. The vertical resolution, δ, of an AFM is typically about 0.5 Å over this measurement bandwidth. Thus the vertical or normal force resolution, $F = g\delta$, is approximately 5 pN. Such high force resolution allows control of single-atom contact and, hence, the AFM can image surfaces close to atomic scales.

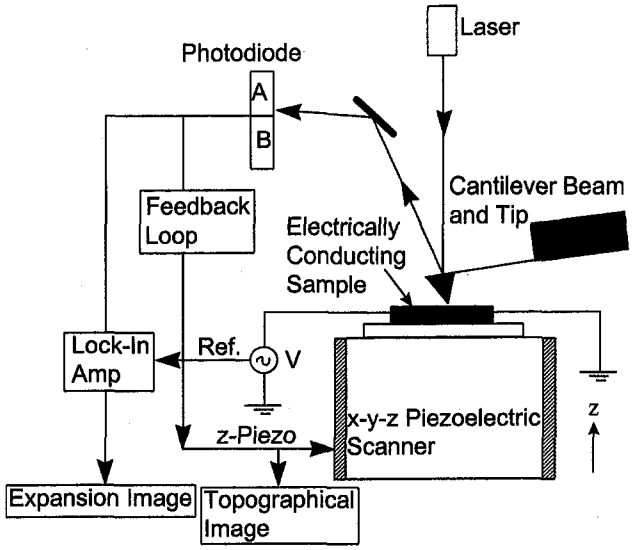

Fig. 1 Schematic diagram of an atomic force microscope (AFM) and scanning Joule expansion microscope (SJEM)

To use the SJEM system, a sinusoidal voltage signal is applied to an electrically conducting sample. This generates sample Joule heating and, therefore, a temperature rise resulting in thermal expansion of the sample. This deflects the AFM cantilever probe in contact with the expanding sample. The frequency, f, chosen for sample heating is kept higher than the feedback bandwidth of the AFM system (20 kHz) so that the expansion signal does not affect the topographical image. The heating frequency, f, is kept less than the natural frequency of the AFM cantilever in contact with the sample. The AFM photodiode detects the expansion-induced deflection of the cantilever as well as deflection due to sample topography. A lock-in amplifier, tuned to the Joule heating frequency, filters the photodiode signal and measures only the sample expansion signal. Thus, the topographical and Joule expansion signals are contained

Nomenclature

b = metal line thickness, m
C = capacitance, F
C_p = specific heat, J/kg-K
F = force, N
f = frequency, Hz
g = spring constant, N/m
h = interface thermal conductance, W/m^2-K
H = heat flux, W/m^2
J = electrical current density, A/m^2
k = thermal conductivity, W/m-K
k_B = Boltzmann constant, J/K
K_o = modified Bessel function of zeroth order
l = thermal expansion, m
L = length, m
N = number of data points
q = reciprocal of thermal wavelength, m^{-1}
Q = quality factor of resonance
T = temperature, K
V = voltage, V
w = half-width of metal line, m
α = thermal expansion coefficient, K^{-1}
δ = cantilever deflection, m
η = oscillatory temperature on substrate surface, K
ϕ = oscillatory temperature in metal wire, K
θ = integral of Bessel function K_o
ρ = density, kg/m^3
σ = electrical conductivity, $1/\Omega - m$
τ = time constant, s
ω = angular frequency, rad/s
ψ = nondimensional interface resistance = k_m/hb
Ψ = thermal vibrational noise density, m/$\sqrt{\text{Hz}}$
ξ = thermal diffusivity, m^2/s

Subscripts

AFM = atomic force microscope
i = internal
LI = lock-in amplifier
m = metal
s = substrate
rms = root-mean-square
x = external

in different spectral regions and provide simultaneous images. Instead of using a sinusoidal signal, a pulsed signal can also be used, where the pulse repetition rate should be higher than the feedback bandwidth. Finally, SJEM below 20 kHz can be achieved if the feedback circuit is disconnected.

2.2 Cantilever Dynamics and System Noise. Since the cantilever probe comes into contact with the sample and responds to a modulated signal, its dynamic behavior is critical. This study used commercially available silicon nitride (SiN_x) samples, which were 0.6 μm thick and 20–40 μm wide, and either 120 μm or 200 μm long. A pyramidal tip that was 5 mm at the base with a tip radius of 10–30 nm was fabricated at the end of each cantilever. The two different cantilever lengths led to different values of spring constant and natural frequency. Figure 2 (top) shows a power spectrum of a free-standing 200-μm-long SiN_x cantilever. The peak in the spectrum at approximately 20 kHz indicates the natural frequency of the cantilever when not in contact with the sample. When the cantilever contacts the sample surface, the end of the free-standing cantilever is pinned, which increases the spring constant. Given the natural frequency of a free-standing cantilever, that of a pinned cantilever can be calculated by beam theory. The predicted value of the natural frequency of the in-contact cantilever is approximately 88 kHz. Figure 2 (middle) shows the spectrum of the cantilever in contact, which shows a highly damped resonance at around 80 kHz. The damping is suspected to be due to the presence of a water film on the surface. The high damping may be responsible for the shift in the natural frequency from the predicted value.

Figure 2 (bottom) shows the spectrum of the cantilever vibration when the tip is in contact with a metal interconnect line (described later) to which a pulsed bias is applied with 100 ns pulses that were repeated at 36 kHz. Note the peak at 36 kHz and the next higher harmonic at 72 kHz, both of which were lower than the natural frequency at 80 kHz. One can use the lock-in amplifier to tune to either of the peaks and provide the expansion signal. It is possible to raise the frequency such that one of the expansion peaks is tuned to cantilever resonance. Although this amplifies the signal, it also amplifies noise and hence may not be desirable. In addition, it was found that the variability of the surface water layer thickness changes the resonance frequency and, hence, the amplification of the signal at a fixed frequency. Thus, changes in signal amplification near resonance result in image artifacts. Therefore, it was more reliable to create an expansion signal off resonance. It must noted that although the bandwidth of 80 kHz is seemingly incompatible with modern microprocessor speeds, the quadratic dependence of Joule heating with current can be used to mix two signals of high frequencies such that the frequency difference between them is kept below 80 kHz. In a separate study, Varesi et al. (1998) have demonstrated that this difference frequency can be used for SJEM to study thermal behavior of a device operating at 1 GHz. Although the signals in Fig. 2 (bottom) are well above the noise floor, it is important to determine the noise in the system in order to estimate the resolution of SJEM.

It is well known (Sarid, 1994) that the dominant noise in AFMs arises from the thermal vibrations of the cantilever. These have white-noise spectral characteristics, as observed in Fig. 2. The off-resonance spectral density of thermal vibrational noise of a cantilever can be estimated from a single-mode analysis to be (Sarid, 1994)

$$\Psi = \sqrt{\frac{4k_BT}{g\omega_o Q}}, \tag{1}$$

where k_B is the Boltzmann constant, T is the absolute temperature, g the cantilever stiffness, ω_o the resonant frequency of the cantilever, and Q is the experimentally determined quality factor. From Fig. 2, the quality factor can be estimated to be about

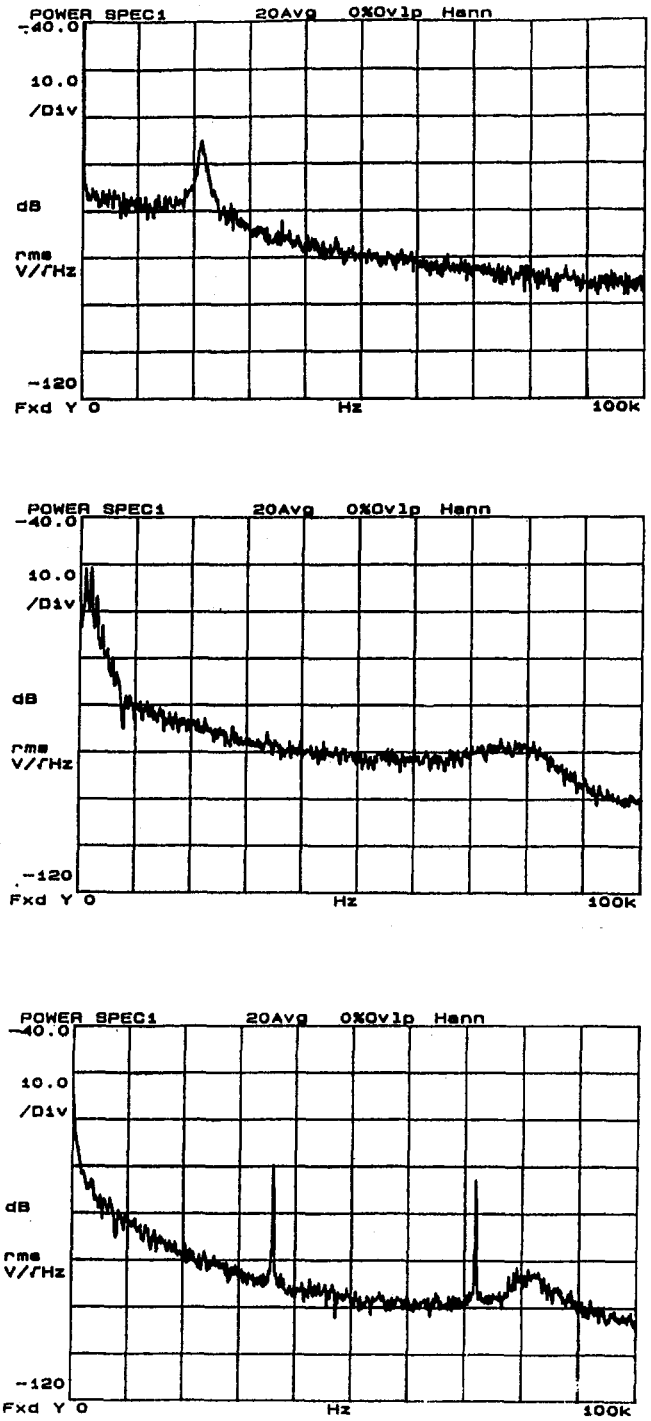

Fig. 2-Vibrational spectra of a 200-μm-long, 0.6-μm-thick, and 40-μm-wide SiN_x cantilever, (top) out of contact (free standing); (middle) in contact with a gold interconnect; (bottom) in contact with a gold interconnect under pulsed heating using 100 ns pulses repeated at 36 kHz

10 for a free-standing cantilever. For this cantilever probe, the thermal noise density can be estimated to be 1 pm/$\sqrt{\text{Hz}}$. Hence, the root-mean-square vibrational noise, δ_n, in the system can be estimated to be

$$\delta_n = \Psi\sqrt{\Delta f}. \tag{2}$$

The lock-in amplifier measures the signal within a user-specified narrow bandwidth, Δf, centered at the heating frequency, f. Although a smaller Δf results in lower noise, the resulting larger time constant results in slower data acquisition and,

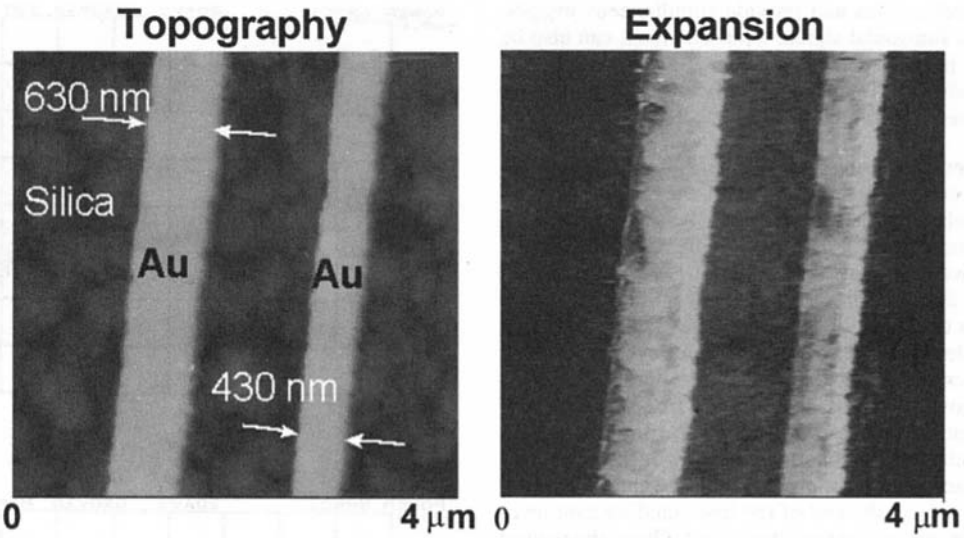

Fig. 3 4 μm $\times$ 4 μm topographical and Joule expansion images of two 160-nm-thick gold interconnects under a bias of 1.4 V, at a bias frequency of 30 kHz and current density of 5.9×10^{10} A/m^2. The expansion image was obtained using a lock-in bandwidth of 26 Hz.

hence, a slower imaging speed. For compatibility between the lock-in bandwidth and the AFM scan rate, f_{AFM} (lines/second), the following relation can be used:

$$\Delta f = \frac{N f_{\text{AFM}}}{2\pi} \tag{3}$$

where N is the number of data points per line. Hence, for a scan rate of $f_{\text{AFM}} = 0.2$ Hz with each line containing 256 points, a bandwidth of about 8 Hz was used. For this bandwidth, the vibrational noise, δ_n, can be estimated to be 2.8 pm. Note that when the tip comes into contact, the effective spring constant increases, which reduces the noise density even further. In addition, the quality factor reduces due to increased damping as shown in Fig. 2.

3 Experimental Results of SJEM

3.1 Joule Expansion Images. Figure 3 shows images of two parallel gold lines fabricated by electron beam lithography on a SiO_2 substrate. The gray scale indicates relative magnitudes with bright as high and dark as low. A voltage of 1.4 V at 30 kHz was applied to the sample, and the expansion image was obtained with $\Delta f = 26$ Hz. The lines had full-width–half-maximum values of 630 and 430 nm, and were both 160 nm thick. The expansion signal was about 1.6 V after a 66 dB gain. A 1.6 V signal corresponds to approximately a 0.8 mV signal generated in the photodiode. Using a photodiode sensitivity of 30 nm/V, the expansion measured in this case was 24 pm. Figure 2 shows the noise floor to be approximately -100 dB or 1×10^{-5} V/$\sqrt{\text{Hz}}$ in the range of 60–80 kHz. With a photodiode sensitivity of 30 nm/V, the expansion signal due to noise was 1.53 pm for $\Delta f = 26$ Hz, which was more than an order of magnitude smaller than the expansion signals. For expansion, a measurement of 24 pm with an uncertainty of 1.53 pm gave a relative uncertainty of 6.4 percent. Note that since the noise depends only on the cantilever, whereas the expansion signal depends on the sample and the heating conditions, the relative uncertainty can change.

Figure 3 clearly shows the sub-micrometer spatial resolution of SJEM. Note that although the narrower line was 430 nm wide, the sharpness of the expansion image suggests the resolution to be sub-100 nm. To confirm this, Fig. 4 shows topographical and expansion images of an indium tin oxide (ITO) resistor. The ITO sample contains grains typically ranging from 50–100 nm in lateral size. It is evident from the topography image that some grains are higher than the others. The expansion image shows that individual grains can be resolved and that higher grains result in larger expansion signals, as indicated in the cross section. It is interesting to note that the expansion occurs over the entire grain, suggesting that significant shear exists at the grain boundaries. Although the smallest grains in this sample are about 50 nm in lateral size, there does not seem to be a loss of spatial resolution between the topographical and expansion images. This observation is certainly promising and warrants further study.

3.2 Signal Characteristics. The deflection of the cantilever in response to an AC bias of the sample could be due to several reasons. The possible sources for the signal are: (1) sample expansion resulting from Joule heating of the sample; (2) thermally induced cantilever bending that can result from a bimaterial effect due to the presence of the metal coating evaporated onto the backside of the cantilever, or residual stresses in a pure SiN_x cantilever; (3) an acoustic wave in the gas resulting from heating of the surrounding gas; (4) piezoelectric deformation of the sample; and (5) electrostatic forces between the tip and the sample.

Since the AFM cantilevers typically have a reflective metal film on top of the SiN_x, the possibility of a bimaterial effect existed in this study. To remove this effect, the cantilevers were stripped of all metal coatings using a solution of concentrated hydrochloric and nitric acids. The removal of the metal film was not entirely necessary to eliminate the bimaterial effect, since its characteristic response time was calculated and measured to be in the range of 0.17–0.33 ms for these cantilevers (Lai et al., 1997). This time corresponds to a frequency of about 5 kHz — an order of magnitude lower than the frequencies used in this study. Thermally induced cantilever bending has also been observed in pure SiN_x cantilevers by Radmacher et al. (1995). The deflections result from residual stresses that develop during the cantilever fabrication process. Just as with the bimaterial effect, these effects are much too slow to be responsible for the observed signal.

A second possible signal source is cantilever deflection resulting from a thermal pressure wave rising from the sample. This source was discounted by several tests. First, assuming a sound propagation speed of 350 m/s, a sinusoidal heating at 50 kHz corresponds to a wavelength of 7 mm. This is much larger than the cantilever size and, hence, will not deflect the cantile-

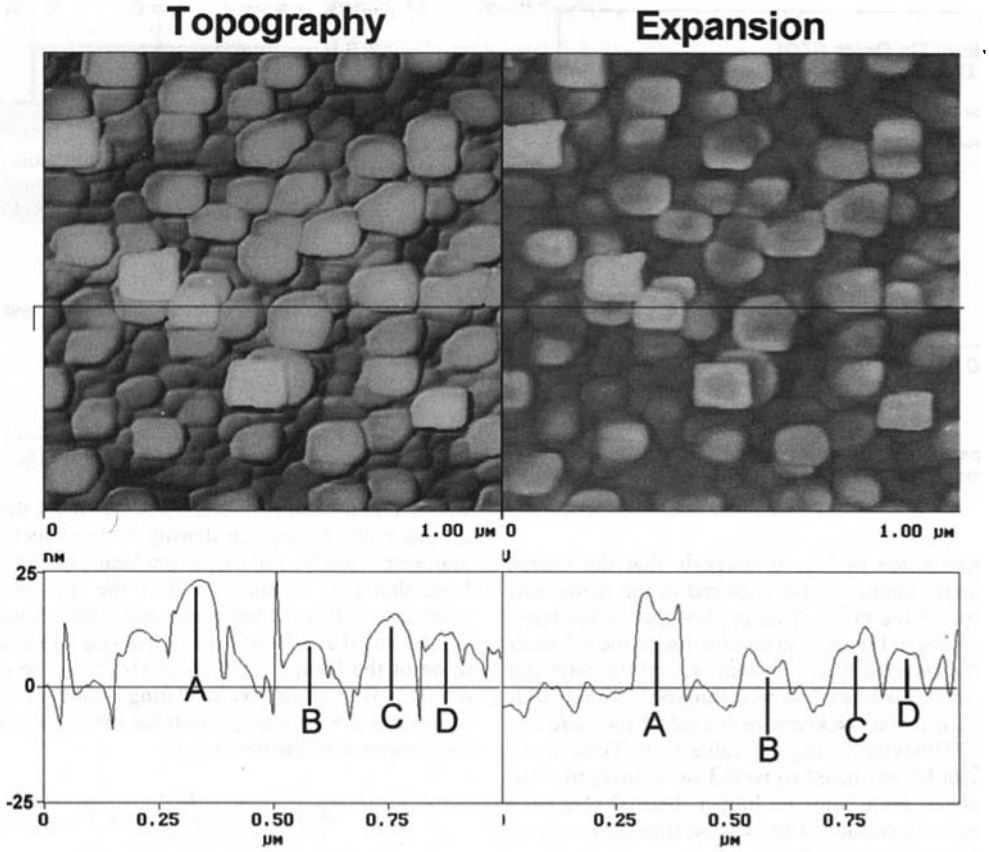

Fig. 4 1 μm × 1 μm topographical and Joule expansion images of an indium tin oxide resistor. Note that grains and grain boundaries that are in the range of 10–50 nm in size can be observed in both the images.

ver, due to a lack of pressure differential across the cantilever. It was found, however, that under pulsed heating of the sample, gas acoustics can produce cantilever deflection only if the cantilever was out of contact. To rule out the possibility of acoustic effects with the cantilever in contact, the system was tested in a vacuum of 10^{-5} Torr. With the cantilever out of contact, the system detected no signal, whereas in contact, a signal was detected of the same magnitude as that in air. This clearly indicated that the expansion signal was due to solid expansion and not from gas acoustics. Further evidence discounting the pressure-wave effect is the observed resolution of the SJEM. Since the sub-50 nm resolution observed in Fig. 4 is much less than the mean free path of gas molecules at atmospheric pressure (approximately 300 nm), any pressure wave effect could not possibly reveal this level of detail.

The arguments given above clearly suggest that the observed signal was due to sample expansion, which may result from piezoelectric or thermal effects. To rule out piezoelectricity, the simplest method is to choose a non-piezoelectric sample such as gold (see Fig. 3) or other metals. A stronger evidence to rule out piezoelectricity is shown in Fig. 5, which plots the expansion signal as a function of applied voltage. Since piezoelectric expansion depends on electric field, it should vary linearly with voltage. The V^2 dependence in Fig. 5 clearly eliminates piezoelectric effects.

Another source of cantilever deflections is due to electrostatic forces between the tip and the sample, which follow the relation

$$F = \frac{1}{2}\frac{dC}{dx}V^2, \tag{4}$$

where C is the tip–sample capacitance and V is the voltage between the tip and the sample. It is clear that the V^2 dependence can be confused with the thermal expansion signal. However, when examined in vacuum with the cantilever stripped off metal films, no out-of-contact cantilever deflection was detected.

A second verification that the signal was due to sample thermal expansion and not to electrostatic interactions is shown in Fig. 6. Here, the expansion signal is plotted as a function of the width of voltage pulses applied across the sample. The linear dependence suggests that the signal depends on the energy within each pulse. An electrostatic signal would be independent of the pulse width and would depend only on the pulse height. Hence, it is quite clear that the measured signal is from thermal expansion of the sample.

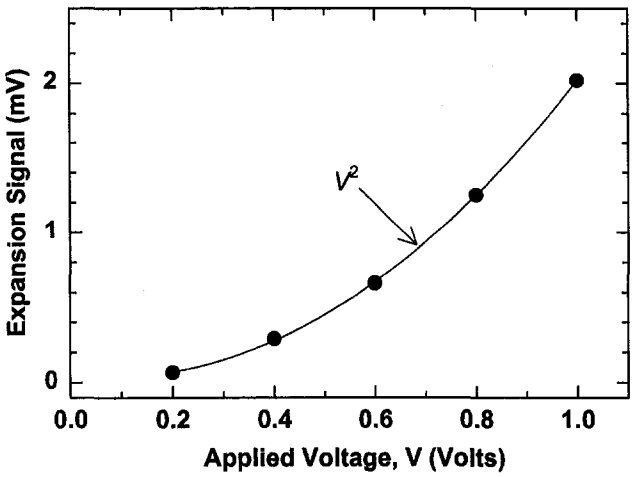

Fig. 5 Plot of expansion signal as a function of applied voltage across gold interconnect

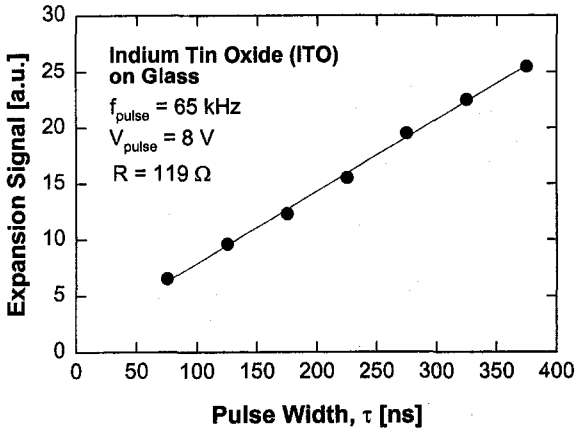

Fig. 6 Plot of expansion signal as a function of the width of voltage pulses applied across gold interconnect

The linear dependence in Fig. 6 suggests that the energy dissipated in a single voltage pulse is stored in the metal wire within the duration of the pulse. This implies that in the range of pulse widths shown in Fig. 6, heat conduction to the substrate did not occur. The internal time constant, τ_i, of the wire due to its internal thermal resistance can be estimated by the relation $\tau_i = b^2/\xi_m$ where b is the thickness or height of the wire and ξ_m is its thermal diffusivity. Using the value from Table 1 and $b = 0.2$ μm, τ_i can be estimated to be 0.3 ns. Hence, the data in Fig. 6 suggest that there must be higher thermal resistance at the metal–substrate interface. The external time constant, τ_x, can be estimated from the relation

$$\tau_x = \frac{(\rho C_p)_m b}{h} \tag{5}$$

where h is the interface conductance. Given the fact there was no heat loss to the substrate for 375 ns pulses, one can estimate $h < 1.3 \times 10^6$ W/m^2-K. It is now important to predict the role of the substrate since it may be useful for determining the properties of the substrate material.

4 Analysis

4.1 Model. To determine the temperature distribution in the metal wire and the substrate, one should ideally perform a two-dimensional analysis for both media and match the temperature and heat flux at the interface. However, that requires numerical solution to the heat conduction equation, which has not been employed in this study. Instead, a simpler analysis is proposed here. It is assumed that the temperature distribution in the metal line is uniform in the lateral or x direction and that the only gradients occur across the thickness or in the z direction due to heat conduction to the substrate. Two-dimensional heat conduction analysis is considered for the substrate where an integral formulation is used.

Consider a metal line fabricated on a substrate as illustrated in Fig. 7. The heat conduction equation in the metal line is

Table 1 Thermophysical properties of gold and glass

	ρC_p [10^6 J/m^3-K]	k [W/m-K]	ξ [10^{-4} m^2/s]	α [10^{-6} K^{-1}]
Gold	2.49	317	127	14.2
Glass	1.88	1.38	0.75	0.5

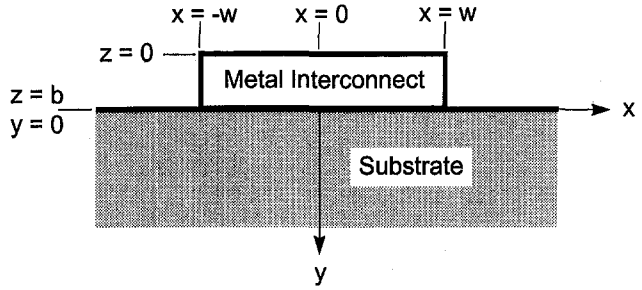

Fig. 7 Coordinate system of metal interconnect and substrate used for theoretical analysis

$$\text{Metal Line: } \frac{\partial T}{\partial t} = \xi_m \frac{\partial^2 T}{\partial z^2} + \frac{J_o^2}{2\sigma(\rho C_p)_m}(1 + e^{i2\omega t}) \tag{6}$$

where T is the temperature, ξ_m is the metal thermal diffusivity, J_o and σ are the current density and conductivity of the metal line, respectively, and ρC_p is the heat capacity per unit volume. Note that $z = b$ and $y = 0$ is the line–substrate interface, whereas $z = 0$ is the top of the metal line. Since the heat source is modulated at a frequency of 2ω, one can assume the solution to be of the form $T(z, t) = \phi(z)e^{i2\omega t}$ in the metal line. Using $\phi'(0) = 0$ to ensure an insulating boundary on the top surface of the metal wire, the solution for the oscillatory component of the temperature distribution is

$$\phi(z) = \frac{J_o^2}{4i\omega\sigma(\rho C_p)_m} + B\cosh(qz) \tag{7}$$

where $q = \sqrt{2i\omega/\xi_m}$ is the reciprocal of the thermal wavelength and B is an unknown constant. The heat flux, H, to the substrate is given by the relation, $H = -k_m qB \sinh(qb)$.

The temperature distribution, $T(s, y, t)$, in a semi-infinite medium due to an infinitely narrow periodic line source of strength, Hdx', is given by the relation (Carslaw and Jaeger, 1959)

$$T(x, y, t) = \frac{Hdx'}{\pi k_s} K_o(q_s\sqrt{(x - x')^2 + (y - y')^2})\exp(2i\omega t) \tag{8}$$

where x' and y' are the coordinates of the source, k_s is the substrate thermal conductivity, $q_s = \sqrt{2i\omega/\xi_s}$ is the reciprocal of the thermal wavelength in the substrate, and K_o is the modified Bessel function. Since the metal line extends from $-w \leq x' \leq w$ at $y' = 0$, the amplitude of the periodic component of the temperature distribution on the top surface ($y = 0$) can be obtained as

$$\eta(x) = -\frac{k_m qB\sinh(qb)}{\pi k_s}\int_{-w}^{w} K_o(q_s|x - x'|)dx' \tag{9}$$

Here, the relation for H has been used to ensure heat flux continuity at the metal–substrate interface. The temperature at the origin ($x = 0$) is

$$\eta(0) = -\frac{2B\gamma\sinh(qb)}{\pi}[\theta(q_s w) - \theta(0)] \tag{10}$$

where θ is the integral of the modified Bessel function and $\gamma = \sqrt{(k\rho C_p)_m/(k\rho C_p)_s}$. Integrals of K_o were numerically computed using polynomial expansions of the Bessel functions (Abramowitz and Stegun, 1972). The unknown constant, B, is determined by the interface relation $H = h[\phi(b) - \eta(0)]$. The

temperature distribution in the metal wire is then determined to be

$$\phi(z) = \frac{J_o^2}{4i\omega\sigma(\rho C_p)_m} \times \left[1 - \frac{\cosh(qz)}{\cosh(qb) + \psi qb \sinh(qb) + 2\gamma \sinh(qb)\Delta\theta/\pi}\right] \tag{11}$$

where $\psi = k_m/hb$ is the nondimensional interface resistance and $\Delta\theta = \theta(q_s w) - \theta(0)$.

Assuming that the substrate expansion is negligible, the thermal expansion of the metal wire can be found by the relation

$$l = \int_0^b \alpha_m \phi(z) dz \tag{12}$$

Using Eq. (11), the expansion signal can be calculated to be

$$l = \frac{J_o^2 \alpha_m b}{4i\omega\sigma(\rho C_p)_m}\left[\frac{\cosh(qb) - \sinh(qb)/qb + \psi qb \sinh(qb) + 2\gamma \sinh(qb)\Delta\theta/\pi}{\cosh(qb) + \psi qb \sinh(qb) + 2\gamma \sinh(qb)\Delta\theta/\pi}\right] \tag{13}$$

Since $b \cong 0.2$ μm and $|1/q| \cong 18$ μm for the frequencies used, $|qb| \approx 0.01$ such that the hyperbolic functions can be expanded, keeping only the lowest order terms. Note, however, that $\psi = 10^3$, $\gamma = 17.4$ for the gold-glass combination, and $|q_s w| \cong 0.2$, resulting in $\Delta\theta \cong 0.6$. Keeping only the first-order terms, Eq. (13) can be simplified to

$$l = \frac{J_o^2 \alpha_m b}{4i\omega\sigma(\rho C_p)_m}\left[\frac{\psi(qb)^2 + 2\gamma qb\Delta\theta/\pi}{1 + \psi(qb)^2 + 2\gamma qb\Delta\theta/\pi}\right] \tag{14}$$

Since $2\gamma qb\Delta\theta/\pi \cong 0.06$, three cases arise with different relations for the expansion signal:

$$\text{Case 1:}\quad l = \frac{J_o^2 \alpha_m b^2 \Delta\theta}{\pi\sigma\sqrt{2i\omega(k\rho C_p)_s}}; \quad \text{for} \quad \psi qb \ll 2\gamma\Delta\theta/\pi$$

$$\text{Case 2:}\quad l = \frac{J_o^2 \alpha_m b}{4i\omega\sigma(\rho C_p)_m}; \quad \text{for} \quad \psi(qb)^2 \gg 1$$

$$\text{Case 3:}\quad l = \frac{J_o^2 \alpha_m b^2}{2\sigma h}; \quad \text{for} \quad \psi(qb)^2 \approx 1 \tag{15}$$

Note that the frequency dependences for these three cases are all different.

Figure 8 plots the expansion signal of a metal line as a function of frequency. It is clear that in the low-frequency region (below 30 kHz), the expansion signal varies as $l \propto 1/f$, which suggests that the conditions of case 2 best represent the experiments. This also confirms that the metal–substrate interface resistance is very high. The conditions of case 2 suggest that $h < 10^5$ W/m^2–K. What remains unexplained is the high-frequency regime where Fig. 8 exhibits a $l \propto 1/f^{1.8}$ behavior. It is possible that since the resonant frequency of a free-standing cantilever is on the order of 20 kHz, the high-frequency behavior is governed by a coupling between sample expansion and cantilever dynamics. This has not yet been thoroughly studied.

4.2 Comparison With Experiments. For the expansion image shown in Fig. 3, the applied voltage was 1.4 V and total resistance of the two parallel gold lines was 140.7 Ω. Assuming the same properties for both lines, the current density was $J = 5.9 \times 10^{10}$ A/m^2. Using $\sigma = 4.9 \times 10^7(\Omega - m)^{-1}$ for gold, applied bias frequency of 30 kHz, $b = 160$ nm, and the material properties from Table 1, the relation for case 2 in Eq. (15) gives the magnitude of $l_{rms} = l/\sqrt{2} = 60$ pm. Although within the same order of magnitude of the measured value of 24 pm, the predicted one is 2.5 times larger. Note that the heating frequency of 60 kHz falls in the regime where the frequency response follows the relation $l \propto 1/f^{1.8}$ with values lower than that predicted from the $l \propto 1/f$ behavior. Hence, it is not surprising that the measured value is lower. This also suggests that for proper understanding of SJEM, cantilever dynamics at high frequency must be well understood.

5 Measurement of Surface Temperature Distribution

It clear from the discussion so far that SJEM measures local thermal expansion of an electrically heated sample. The local expansion signal, $l(\mathbf{r}, f)$, at vector position, $\mathbf{r}$, on the sample surface and frequency, f, can be written as $l(\mathbf{r}, f) = \alpha(\mathbf{r})L(\mathbf{r})\Delta T(\mathbf{r}, f)$, where $\alpha(\mathbf{r})$ is the local thermal expansion coefficient, $L(\mathbf{r})$ is the local sample height, and $\Delta T(\mathbf{r}, f)$ is the local temperature rise at frequency f. The sample temperature can be obtained only indirectly through calculations, as discussed in section 4. But the measurements do not provide the temperature distribution in the substrate since the expansion of silicon dioxide is much smaller than that of gold for the same temperature rise. For the purpose of thermometry, it is important to develop a technique to deconvolute $l(\mathbf{r}, f)$ and directly obtain $\Delta T(\mathbf{r}, f)$. Such a technique is now described.

To obtain $\Delta T(\mathbf{r}, f)$, nonuniformities of $\alpha(\mathbf{r})$ and $L(\mathbf{r})$ must be eliminated. This is achieved by uniformly coating the sample with a thin layer of a polymer. The thermal expansion coefficient of polymers is typically about 10^{-4} K^{-1}, which is an order of magnitude higher than that of metals and two orders of magnitude larger than that of most ceramics. Hence, if the polymer film thickness is on the same order as the metal film thickness, the expansion signal of the polymer film will dominate. In the present experiments, polymethylmethacrylate (PMMA) was spin coated on top of the samples containing the gold metal lines. Figure 9 shows a typical expansion image of a 870-nm-wide and 200-nm-thick gold wire on SiO_2 substrate with a 230-nm-thick PMMA film covering the whole sample. Spin coating ensures thickness uniformity of about 0.3 percent (Madou, 1997), which in this case is about 1 nm. The image was obtained

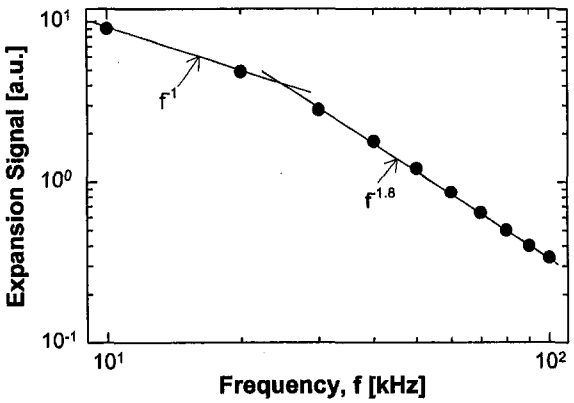

Fig. 8 Plot of expansion signal as a function of heating frequency (twice bias frequency) of gold interconnect. Data were obtained after turning off the feedback circuit.

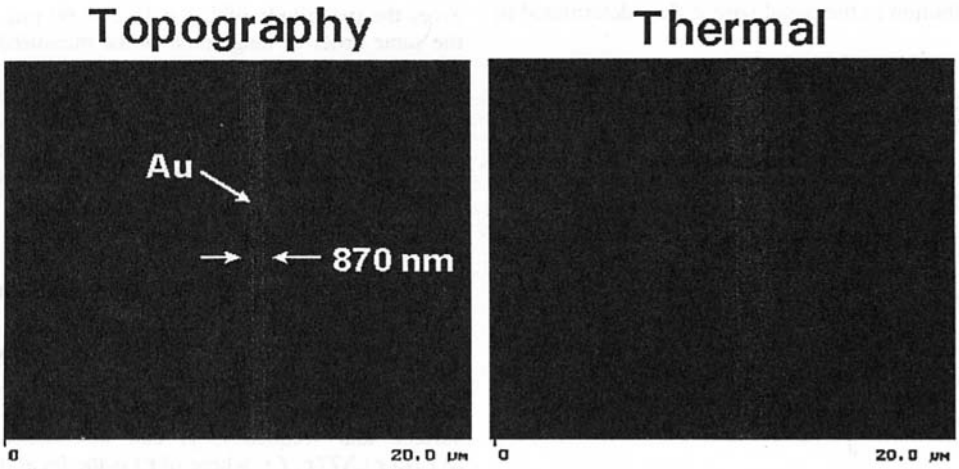

Fig. 9 Topographical and Joule expansion images of an 870-nm-wide and 200-nm-thick gold interconnect on an SiO_2 substrate covered with a 230-nm-thick uniform coating of polymethyl methacrylate (PMMA). Voltage was applied at 20 kHz.

for an applied bias frequency of 20 kHz. The images shows the spread of the temperature distribution as one may expect. Since the expansion coefficient of the polymer was not precisely known, no attempt was made to compare the experimental data with theoretical predictions. Instead, comparison was made with the normalized distribution as follows.

The temperature distribution can be obtained from Eq. (9) and normalized by the value at $x = 0$. The normalized distribution follows the relation

$$\frac{\eta(x/w)}{\eta(0)} = \frac{\theta[q_s w(1 + x/w)] + \theta[q_s w(1 - x/w)] - 2\theta[0]}{2\{\theta[q_s w] - \theta[0]\}}; \quad \text{for } \frac{x}{w} \le 1$$

$$= \frac{\theta[q_s w(x/w + 1)] - \theta[q_s w(x/w - 1)]}{2\{\theta[q_s w] - \theta[0]\}}; \quad \text{for } \frac{x}{w} \ge 1 \quad (16)$$

Figure 10 shows a comparison between the predictions of Eq. (16) and the experimental data. The good agreement between them justifies the use of polymer films for deconvolution of the expansion signal to measure the temperature distribution of a sample directly. Also shown is the normalized experimental data for expansion of the metal line in the absence of the polymer film, such as that measured in Fig. 3. It is clear that in the absence of the polymer film, there is large disagreement between the theoretical predictions and the measurements. The polymer film shows a significant difference in the measured temperature distribution and the agreement with the theoretical predictions is promising.

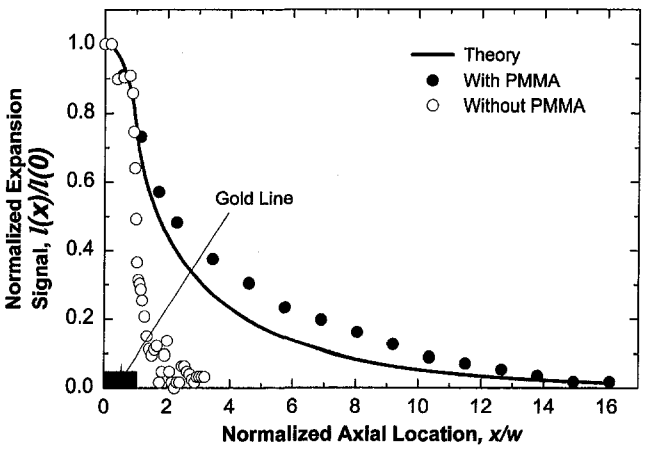

Fig. 10 Comparison between theoretical predictions and experimental measurements of temperature distribution of PMMA-coated gold interconnect and uncoated gold interconnect

6 Summary and Conclusions

This paper proposes a new technique called scanning Joule expansion microscopy (SJEM) by which thermal expansion of Joule-heated samples can be measured with 1 pm vertical resolution and lateral resolution in the range of 10–50 nm. In contrast with previous scanning thermal and near-field optical microscopes, the SJEM technique eliminates the need to fabricate specialized probes and only requires a standard atomic force microscope for its operation.

The SJEM was used in this study to measure the thermal expansion of sub-micrometer metal interconnect lines. The paper presents a heat conduction analysis of a metal line in contact with a semi-infinite substrate. The frequency response as well as the response to pulsed bias suggests that there was considerable thermal resistance at the metal–substrate interface. Although the frequency response followed the predicted behavior in the low-frequency range (below 30 kHz), the high-frequency behavior could not be explained. It is possible that cantilever dynamics may be responsible for the discrepancy.

The local expansion signal was found to depend on the local sample height, expansion coefficient, and temperature rise. To measure the temperature distribution of a Joule-heated resistor as well as its surrounding substrate directly, material and height nonuniformities were eliminated by uniformly coating the sample with a polymer film. Since thermal expansion coefficients of polymers are about ten times higher than those of metals, the expansion of the polymer dominates over those of metals and substrates for the same thickness. The measured expansion distribution of the polymer film agreed well with the temperature distribution predicted from theoretical calculations.

Acknowledgments

This work was supported by the National Science Foundation through the Young Investigator Award to AM and through grant No. CTS-9796166. We would like to thank Ernie Caine of UCSB for electron beam lithography. Our deep appreciation

goes to the late Prof. Kunio Hijikata of Tokyo Institute of Technology.

References

Abramowitz, M., and Stegun, I. A., 1972, *Handbook of Mathematical Functions*, Dover, New York, pp. 378–379.

Binnig, G., Rohrer, H., Gerber, C., and Weibel, E., 1982, "Surface Studies by Scanning Tunneling Microscopy," *Physical Review Letters*, Vol. 49, pp. 57–61.

Binnig, G., Quate, C. F., and Gerber, Ch., 1986, "Atomic Force Microscope," *Physical Review Letters*, Vol. 56, pp. 930–933.

Carslaw, H. S., and Jaeger, J. C., 1959, *Conduction of Heat in Solids*, Clarendon Press, Oxford, p. 263.

Fish, G., Bouevitch, O., Kokotov, S., and Lieberman, K., 1995, "Ultrafast Response Micropipette Based Thermocouple Sensors," *Review of Scientific Instruments*, Vol. 66, pp. 3300–3306.

Goodson, K. E., and Asheghi, M., 1997, "Near-Field Optical Thermometry," *Microscale Thermophysical Engineering*, in press.

Lai, J., Perazzo, T., Shi, Z., and Majumdar, A., 1997, "Optimization and Performance of High-Resolution Micro-optomechanical Thermal Sensors," *Sensors and Actuators*, Vol. 58, pp. 113–119.

Luo, K., Shi, Z., Lai, J., and Majumdar, A., 1996, "Nanofabrication of Sensors on Cantilever Probe Tips for Scanning Multiprobe Microscopy," *Applied Physics Letters*, Vol. 68, pp. 325–327.

Luo, K., Shi, Z., Varesi, J., and Majumdar, A., 1997a, "Sensor Nanofabrication, Performance, and Conduction Mechanisms in Scanning Thermal Microscopy," *Journal of Vacuum Science and Technology B*, Vol. 15, pp. 349–360.

Luo, K., Lederman, M., and Majumdar, A., 1997b, "Liquid-Film Mediated Scanning Thermal Microscopy of a Magnetoresistive Head," *Microscale Thermophysical Engineering*, in press.

Majumdar, A., Carrejo, J. P., and Lai, J., 1993, "Thermal Imaging Using the Atomic Force Microscope," *Applied Physics Letters*, Vol. 62, pp. 2501–2503.

Majumdar, A., Lai, J., Chandrachood, M., Nakabeppu, O., Wu, Y., and Shi, Z., 1995, "Thermal Imaging by Atomic Force Microscopy Using Thermocouple Cantilever Probes," *Review of Scientific Instruments*, Vol. 66, pp. 3584–3592.

Martin, Y., and Wickramasinghe, H. K., 1987, "Study of Dynamic Current Distribution in Logic Circuits by Joule Displacement Microscopy," *Applied Physics Letters*, Vol. 50, pp. 167–168.

Madou, M., 1997, *Fundamentals of Microfabrication*, CRC Press, Boca Raton, p. 3.

Nonnenmacher, M., and Wickramasinghe, H. K., 1992, "Scanning Probe Microscopy of Thermal Conductivity and Sub-surface Properties," *Applied Physics Letters*, Vol. 61, pp. 168–170.

Pylkki, R. J., Moyer, P. J., and West, P. E., 1994, "Scanning Near-Field Optical and Scanning Thermal Microscopy," *Japanese J. Appl. Phys.:* Part 1, Vol. 33, pp. 3785–3790.

Radmacher, M., Cleveland, J. P., and Hansma, P. K., 1995, "Improvement of Thermally Induced Bending of Cantilevers Used for Atomic Force Microscopy," *Scanning*, Vol. 17, pp. 117–121.

Sarid, D., 1994, *Scanning Force Microscopy: With Applications to Electric, Magnetic, and Atomic Forces,* Oxford Univ. Press, New York.

Varesi, J., and Majumdar, A., 1998, "Scanning Joule Expansion Microscopy at Nanometer Scales," *Applied Physics Letters*, Vol. 72, pp. 37–39.

Varesi, J., Muenster, S., and Majumdar, A., 1998, "High-Resolution Current and Temperature Mapping of Electronic Devices Using Scanning Joule Expansion Microscopy," presented at the IEEE International Reliability Physics Symposium, Reno, Mar. 30–Apr. 2.

Weaver, J. M. R., Walpita, L. M., and Wickramasinghe, H. K., 1989, "Optical Absorption Microscopy and Spectroscopy With Nanometer Resolution," *Nature*, Vol. 342, pp. 783–785.

Williams, C. C., and Wickramasinghe, H. K., 1986a, "Scanning Thermal Profiler," *Applied Physics Letters*, Vol. 49, pp. 1587–1589.

Williams, C. C., and Wickramasinghe, H. K., 1986b, "High Resolution Thermal Microscopy," *Ultrasonics Symposium Proc.*, B. R. McAvoy, ed., IEEE, New York, pp. 393–397.

Williams, C. C., and Wickramasinghe, H. K., 1988a, "Photothermal Imaging With Sub-100 nm Spatial Resolution," in: *Optical Sciences*, A. L. Schawlow, ed., Springer Series, pp. 364–369.

Williams, C. C., and Wickramasinghe, H. K., 1988b, "Thermal and Photothermal Imaging on a Sub-100 Nanometer Scale," *Proc. SPIE*, Vol. 897, pp. 129–134.

Short-Time-Scale Thermal Mapping of Microdevices Using a Scanning Thermoreflectance Technique

Y. S. Ju
Graduate Student Researcher.
Student Mem. ASME

K. E. Goodson
Assistant Professor.
Assoc. Mem. ASME
e-mail: goodson@vk.stanford.edu

Department of Mechanical Engineering,
Stanford University, CA 94305-3030

The performance and reliability of microdevices can be strongly influenced by the peak temperature rise and spatial temperature distribution during brief electrical overstress (EOS) phenomena, which can occur at sub-microsecond time scales. The present study investigates short-time-scale laser reflectance thermometry of microdevices by examining the impact of passivation overlayers on the thermoreflectance signal and by demonstrating a calibration method suitable for metallization. This manuscript also describes a scanning laser thermometry facility that captures temperature fields in microdevices with 10 ns temporal resolution and 1 μm spatial resolution. The facility combines scanning laser optics with electrical stressing capability to allow simultaneous interrogation of the thermal and electrical behavior of devices. Data show the transient temperature distribution along the drift region of silicon-on-insulator (SOI) power transistors and along metal interconnects subjected to brief electrical stresses. The theory and experimental capability developed in this study are useful for studying short-time-scale thermal phenomena in microdevices and verifying models employed for their simulation.

1 Introduction

Many figures of merit of microdevices are influenced by transient thermal phenomena. Changes in the electrical behavior of semiconductor devices can result from self-heating, which occurs as a by-product of normal device operations. Transient self-heating is especially important for devices made from silicon-on-insulator substrates due to the large thermal resistance of the buried silicon dioxide layer, whose impact is most pronounced for rapid heating (Arnold, 1994). Semiconductor devices and interconnects can fail due to the temperature rise occurring on a time scale less than 1 μs during electrostatic discharge (ESD) (Amerasekera and Duvvury, 1995). Microdevices subjected to brief electrical stresses can experience large spatial temperature variations, which can vary with the duration of the stress and can induce highly localized failures (e.g., Ju and Goodson, 1997; Salome et al., 1997). In many microsensors and actuators, short-time-scale heating is required for proper functionality of the devices (Murguia and Bernstein, 1993; Chui et al., 1996). Thermometry techniques with high temporal and spatial resolution are needed to study the operation and failure of microdevices subjected to short-time-scale heating and to verify models used in device simulations.

Electrical thermometry methods use either electrically passive or active elements in an integrated circuit to obtain spatially averaged operating temperatures in devices. Temperature rises in interconnect structures subjected to sub-microsecond pulses have been obtained by measuring the temperature-dependent electrical resistance (e.g., Maloney and Khurana, 1985; Banerjee et al., 1996). Other investigators monitored temperature-sensitive electrical parameters (TSEPs), such as the emitter-base voltage of bipolar devices, to measure device temperatures (e.g., Arnold et al., 1994; Zweidinger et al., 1996). However, the spatial temperature distribution and the maximum temperature rise are often very difficult to obtain using the electrical methods (e.g., Leung et al., 1997). Another problem is that the achievable temporal resolution is limited by electrical transients in the case of TSEP-based thermometry and by electrical capacitive coupling between thermometers and devices in the case of the electrical-resistance thermometry.

Other thermometry techniques can obtain spatial temperature distributions in microdevices. Some optical techniques, such as liquid-crystal and fluorescence thermometry (Kolodner and Tyson, 1982), rely on a foreign film deposited on device surfaces. In these techniques, the characteristic time required for the changes in optical properties of the films restricts the achievable temporal resolution. The characteristic time for cholesteric liquid crystals is a few milliseconds (Fergason, 1968) and that for the EuTTA film used in fluorescence thermometry is around 100 μs as estimated from its fluorescence decay time (Kolodner and Tyson, 1983). The temporal resolution is ultimately limited by the thermal diffusion time across passivation layers present in many microdevices to the order of a few microseconds. Thermometry techniques based on scanning atomic force microscopy (AFM) can map temperature distributions with potential spatial resolution below 100 nm. This technique has been particularly successful at mapping steady-state temperature distributions in field-effect transistors and in semiconductor lasers (e.g., Majumdar et al., 1995). The temporal resolution of AFM-based techniques is diminished by the time lag resulting from thermal diffusion across passivation and into the probe tip as well as that associated with electrical capacitive and inductive coupling.

Infrared thermography has been used for failure studies of integrated circuit elements (e.g., Bennett and Briles, 1989; Kondo and Hinode, 1995). This technique requires careful calibration of the emissivity, which depends strongly on the surface topography and the wavelength. The optical interferometry technique (Martin and Wickramasinghe, 1987; Claeys et al., 1993) probes surface displacements due to thermal expansion to obtain temperature fields. This technique requires accurate knowledge of the relationship between local surface displace-

Contributed by the Heat Transfer Division and presented at the National Heat Transfer Conference, Houston, Texas, August 3–5, 1996. Manuscript received by the Heat Transfer Division April 21, 1997; revision received January 23, 1998. Keywords: Conduction, Measurement Techniques, Transient and Unsteady Heat Transfer. Associate Technical Editor: M. F. Modest.

ments and the temperature field, and is thus difficult to apply to semiconductor devices made of composite structures of materials with very different thermal expansion coefficients. Micro-Raman spectroscopy has been used for thermometry (Ostermeir et al., 1992). This approach is time-consuming and an application to transient measurements has not been reported.

The thermoreflectance technique is based on the temperature dependence of the optical reflectance (e.g., Cardona, 1969; Rosei and Lynch, 1972). This technique is promising for rapid thermal mapping of microdevices due to the temporal resolution better than 1 ns that has already been demonstrated on flat metal surfaces. Also promising is the opportunity to use radiation wavelengths for which most passivation layers are transparent. Several researchers employed the thermoreflectance thermometry technique to map the steady-state temperature distributions in semiconductor lasers (Epperlein, 1993; Mansanares et al., 1994) and the temperature distributions in interconnects and resistors (Claeys et al., 1993; Quintard et al., 1996). The short-time-scale thermometry of transistors and interconnects in integrated circuits subjected to brief electrical stresses, however, has received little attention. Another problem is that the development of calibration methods suitable for microdevices has not been properly addressed. The importance of accurate calibration grows with the application to integrated circuits, whose surfaces have optical properties that are not well characterized and can vary depending on the processing details.

In the present manuscript, we provide several results important for thermoreflectance thermometry of microdevices, including a theoretical study of the impact of passivation layers and a new calibration method. The passivation layers can strongly influence thermoreflectance signals due to the interference among multiply reflected beams, which is investigated here using thin film optics. The calibration method developed in this study uses electrical heating and thermometry in microstructures fabricated under the same processing conditions as the devices of interest. This work also develops a thermoreflectance thermometry facility that combines scanning laser optics with electrical stressing capability, which allows simultaneous investigation of thermal as well as electrical characteristics of microdevices. The facility achieves temporal resolution near 10 ns, which is limited by the bandwidth of the electrical measurement system, and spatial resolution near 1 μm, which is limited by the diffraction of a probe laser beam. The theory and experimental facility are used to obtain and interpret data for SOI power transistors and for interconnect structures.

2 Thermoreflectance Thermometry of Microdevices

A parameter characterizing the thermoreflectance phenomenon is denoted by C_{TR}, which is defined as the relative change in the reflectance per unit change in temperature. In this section we discuss various issues related to the thermoreflectance thermometry of microdevices, including the theoretical and experimental determination of thermoreflectance coefficients. The theoretical understanding and the calibration technique developed here are used in the design of subsequent experiments and the interpretation of experimental results.

2.1 Thermoreflectance Coefficient and Its Calibration. The previous thermoreflectance thermometry studies used C_{TR} from either theoretical predictions or existing experimental data on bulk samples or films, whose fabrication processes did not necessarily match those of actual samples tested. This is not appropriate for integrated circuits, whose surface materials, including passivation materials and various metal alloys, have optical properties that can vary with the processing conditions (e.g., Pliskin, 1977). Additional complications can arise for the case of semiconductors when they are part of an electrically active region of microdevices due to optoelectric effects. However, this issue will not be pursued further in this study, which performs thermometry using light–metal interactions.

Most films found in integrated circuits have relatively smooth surfaces with roughness smaller than the typical wavelength of the probe beam used in the thermoreflectance thermometry. The reflectance, in this case, can be expressed as a product of a surface-dependent quantity and a material-dependent quantity (Stagg and Charalampoulos, 1991). The thermoreflectance coefficient, defined in terms of the relative change in the reflectance, can therefore be modeled to first order as independent of the surface roughness.

Two different calibration methods for thermoreflectance coefficients can be used, one using an external temperature controller and the other employing microfabricated structures. In the first method, the temperature of a sample is controlled externally while variations in its reflectance are measured (e.g., Qiu et al., 1993). This approach has the advantage of a relatively simple experimental setup and is employed in the calibration of the power transistor structures studied in Section 3.2. Detailed discussion of the method is provided in that section. This method is difficult to apply when a sample or a film of interest has a small surface area. Thermal expansion of a sample–heater assembly can lead to systematic errors for an optical system with a high numerical aperture and a shallow focal depth. This problem can be remedied by localizing the heating, which strongly diminishes the thermally induced deflection of the surface. An example of this approach is to use a microstructure made of a film of interest both as a heater and as a thermometer.

Ju and Goodson (1997) performed calibration studies on long microfabricated metal lines, which are very nearly isothermal when subjected to electrical heating pulses. The temperature

Nomenclature

C = heat capacity per unit volume, J m^{-3} K^{-1}
C_{TR} = thermoreflectance coefficient, K^{-1}
d = thickness of a layer, m
k = thermal conductivity, W m^{-1} K^{-1}
k_{base} = imaginary part of the complex index of refraction of base material
$k_{T,Al}$ = temperature derivative of the imaginary part of index of refraction of aluminum, K^{-1}
L = overlayer thickness, m
n_{air} = index of refraction of air
$\tilde{n}_{\text{base}}$ = complex index of refraction of base material = $n_{\text{base}} - ik_{\text{base}}$
n_{base} = real part of the complex index of refraction of base material
n_{over} = index of refraction of an overlayer material
$n_{T,Al}$ = temperature derivative of the real part of the index of refraction of aluminum, K^{-1}
$n_{T,\text{SiO2}}$ = temperature derivative of the index of refraction of a silicon dioxide overlayer, K^{-1}
R = reflectance
r, r_1, r_2 = reflection amplitude coefficients
t = time after pulse initiation, s
x = coordinate along interconnect structures, m
y = coordinate along drift regions of power transistors, m
λ = wavelength in vacuum of probe laser, m

Subscripts

base = property of base material
BO = dimension of the buried silicon-dioxide layer in SOI power transistors
over = property or dimension of overlayer
s = dimension of silicon device layer in SOI power transistors

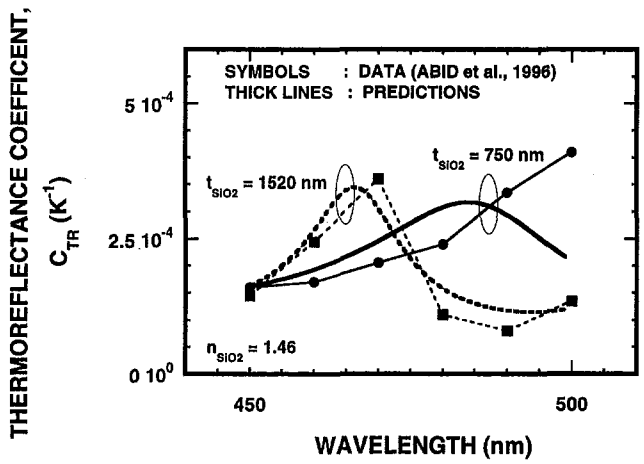

Fig. 1 Wavelength dependence of the thermoreflectance coefficient of silicon with silicon-dioxide overlayers. The predictions take into account the interference among multiply reflected beams.

derivative of the electrical resistance of the metal line was calibrated using a temperature-controlled wafer holder. The thermoreflectance coefficient was obtained by comparing the changes in the surface reflectance with those in the electrical resistance while subjecting the lines to electrical heating pulses. This method is ideally suited for the thermometry of interconnects and can also be applied to the thermometry of metallized portions of microdevices and doped semiconducting regions by microfabricating lines with the same material composition and fabrication techniques. This calibration method is employed in the thermal mapping of interconnect structures in the present study.

2.2 Impact of Overlying Passivation on the Thermoreflectance Signal. For a sample film with an overlying dielectric layer, whose thickness is typically of the order of the wavelength of a probe beam, the impact of the overlayer on the thermoreflectance signal must be considered. Interference among multiply reflected beams alters the optical reflectance and also influences the thermoreflectance signal in a manner that is sensitive to its thickness, the wavelength of a probe beam, and the optical properties of both the overlayer and the underlying base material. The presence of a silicon dioxide layer has been observed to alter the surface reflectance of silicon and its temperature dependence (e.g., Friedrich et al., 1991; Quintard et al., 1996).

The present study uses the theory of thin-film optics (Siegel and Howell, 1992) to predict the impact of passivation layers and to draw conclusions about the resulting uncertainty in thermoreflectance thermometry of underlying opaque layers. For normal incidence, the surface reflectance, R, is related to the indices of refraction, $\tilde{n}_{\text{base}}$ and n_{over}, and the thickness of the overlayer, L,

$$R = \left| \frac{r_1 + r_2 \exp(-i4\pi n_{\text{over}} L/\lambda)}{1 + r_1 r_2 \exp(-i4\pi n_{\text{over}} L/\lambda)} \right|^2 \tag{1}$$

The amplitude reflection coefficients r_1 and r_2 are

$$r_1 = \frac{n_{\text{air}} - n_{\text{over}}}{n_{\text{air}} + n_{\text{over}}} \tag{2}$$

$$r_2 = \frac{n_{\text{over}} - \tilde{n}_{\text{base}}}{n_{\text{over}} + \tilde{n}_{\text{base}}} \tag{3}$$

The dielectric overlayer is assumed to be transparent at the probe beam wavelength and its absorption coefficient is neglected. The thermoreflectance coefficient, C_{TR}, is given by

$$C_{TR} = \frac{1}{R}\frac{dR}{dT} \tag{4}$$

and can be calculated if the temperature dependence of the indices of refraction of a given material is known.

Equations (1) – (3) are applied to passivated silicon samples, whose thermoreflectance coefficients were measured by Abid et al. (1996) for several different probe beam wavelengths. Silicon is chosen since its optical properties are very well characterized over large temperature and wavelength ranges and hence the comparison of the prediction with the data is most meaningful. The experimental data of Jellison and Modine (1982a, b) and Jellison and Burke (1986) are used in the present calculations. The index of refraction of silicon dioxide is assumed to be constant at the value of 1.46 unless otherwise specified. Figure 1 compares the experimental data with the predictions for two different thicknesses of the silicon dioxide layers. Although the thermoreflectance coefficient of silicon is nearly constant over the wavelength range examined, large variations in C_{TR} result from the interference effects. The predictions agree reasonably well with the data except for the 750 nm oxide case near the wavelength of 500 nm. The discrepancy can result from several different sources, including the uncertainties in the indices of refraction of silicon and silicon dioxide as well as those in the thickness of the overlayer.

Another source of error, which has been neglected in the previous studies, is associated with the temperature dependence of the index of refraction of silicon dioxide. The magnitude of the temperature derivative of the index of refraction, $n_{T,\text{SiO2}}$, is comparable to 10^{-5} K^{-1} (van der Meulen and Hien, 1974; Guidotti and Wilman, 1992). However, this temperature dependence can have a significant influence on the thermoreflectance signal. If n_{over} is assumed to be independent of temperature, both the reflectance, R, and its temperature derivative are periodic functions of the overlayer thickness L. If, in contrast, $n_{T,\text{over}}$ is nonzero, phase differences between the oscillations of R and dR/dT exist as illustrated in Fig. 2 for the case of a silicon-dioxide passivated silicon sample. The variations in dR/dT are not periodic and the thermoreflectance coefficient oscillates with growing amplitude as L increases. The thermal expansion of the silicon dioxide layer is not considered explicitly but, since the thickness of the overlayer appears only as a product with n_{over}, its influence is contained in $n_{T,\text{over}}$.

The influence of the temperature dependence of n_{over} on the thermoreflectance signal has an additional implication for the transient thermometry of passivated microdevices. When the thermal diffusion time across the passivation overlayer is larger

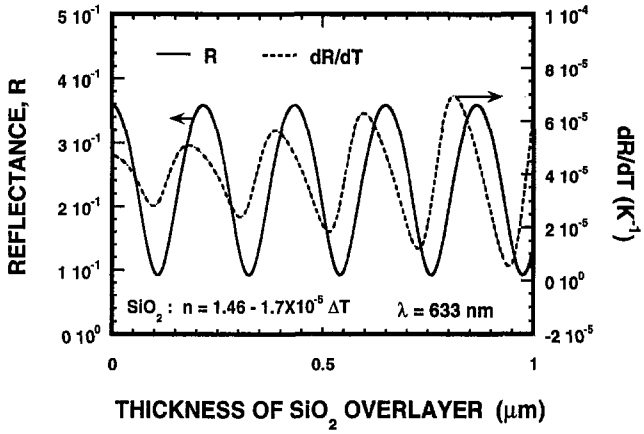

Fig. 2 The reflectance and its temperature derivative as functions of the thickness of an overlying silicon-dioxide layer for the case of silicon base material. The temperature derivative of the index of refraction of silicon dioxide, $n_{T,\text{SiO2}}$, is taken from previous research.

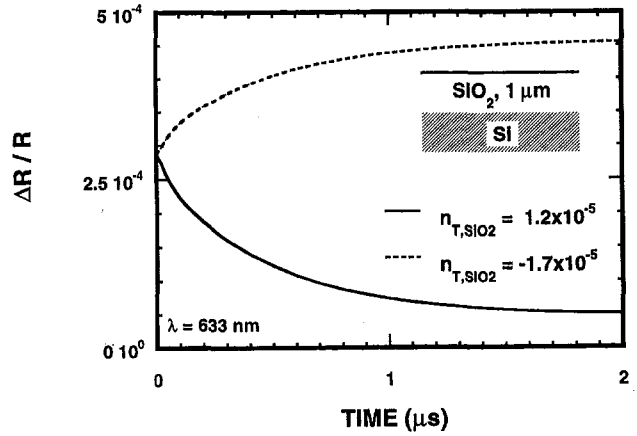

Fig. 3 Time evolution of thermoreflectance signals of a silicon sample covered with a 1-μm-thick silicon-dioxide layer, which results from the time variation of temperature fields within the overlayer. The temperature of the silicon sample undergoes a step change at time $t = 0$ and remains constant thereafter.

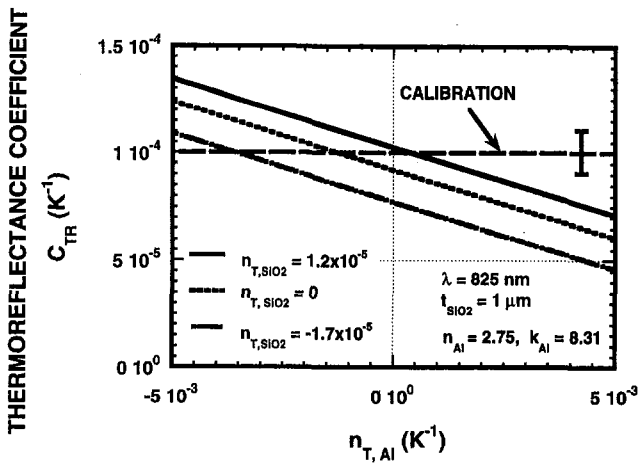

Fig. 4 Impact of uncertainties in the temperature dependence of the index of refraction of aluminum on the thermoreflectance coefficient of an aluminum layer with a 1-μm-thick silicon-dioxide overlayer. The calibration result, shown as a horizontal line, is a guide for comparison with the calculations. The vertical bar represents the experimental uncertainty limit and its horizontal location is immaterial.

than or comparable to the measurement time scale, the variation of the thermoreflectance signal resulting from the temperature distribution within the overlayer must be taken into account. To illustrate this point, the time evolution of a thermoreflectance signal is calculated for a silicon sample that experiences a step change in temperature. The silicon sample is covered with a silicon dioxide layer of thickness 1 μm, which is modeled optically as consisting of parallel sublayers of uniform thickness. For the optical analysis, each sublayer is assumed to be isothermal and its temperature is obtained by solving the transient one-dimensional heat conduction equation. An adiabatic boundary condition is applied to the outer surface of the oxide layer. The temperature of the silicon sample is increased by a step function at time $t = 0$.

The reflectance of a stratified multilayer can be calculated using the transmission matrix method (Knittl, 1976). Figure 3 shows the calculated results of the relative change in the surface reflectance as a function of time for two different values of $n_{T,SiO2}$ taken from the previously cited references. The thermoreflectance signal tends toward the values corresponding to the case where the entire overlayer is at the substrate temperature. The difference between the two steady-state values is large for the particular case shown here and depends on L and $n_{T,over}$ as well as the optical properties of the base material. The error resulting from this time-varying thermoreflectance signal would be less severe since the assumed step change in the substrate temperature tends to exaggerate its impact. When the thermoreflectance coefficient is very sensitive to $n_{T,over}$ and the time scale of interest is less than the thermal diffusion time across an overlayer, however, much care is required to interpret the thermoreflectance signal properly. Careful selection of the probe beam wavelength can help overcome difficulties related to the high sensitivity of thermoreflectance signals to the overlayer (e.g., Epperlein, 1993; Abid et al., 1996).

Similar calculations can be performed for a metal base material. Aluminum is chosen as a base material here and is used for the transistor structures studied in Section 3.2. The wavelength of the probe beam is chosen to be 825 nm, at which the previously measured thermoreflectance coefficient is maximum within the visible and near-infrared wavelength range (Decker and Hodgkin, 1981). The present calculation uses a complex refractive index of the form (Smith et al., 1985)

$$n_{\text{base}} = (2.75 + n_{T,Al}\Delta T) - i(8.31 + k_{T,Al}\Delta T). \quad (5)$$

The two parameters, $n_{T,Al}$ and $k_{T,Al}$, are not available in the literature to the best of our knowledge and cannot be determined uniquely from the index of refraction and the thermoreflectance coefficient of bare aluminum at a single temperature (e.g., Miklós and Lörincz, 1988). A parametric study is performed, where C_{TR} of a passivated aluminum film is calculated as a function of $n_{T,Al}$ and is shown in Fig. 4. For each value of $n_{T,Al}$, the corresponding value of $k_{T,Al}$ is first obtained by requiring the resulting C_{TR} in the absence of an overlayer to be the experimentally measured value. The thickness of the silicon-dioxide layer is fixed at 1 μm in the calculations, which is the thickness used in the later experiments. The results indicate that the thermoreflectance coefficient is much less sensitive to $n_{T,SiO2}$ than is the case for passivated silicon samples. The calibration result of the present study is also shown in Fig. 4 for comparison. Further discussion on the thermoreflectance coefficient of a passivated aluminum layer and its calibration are provided in Section 3.2 in connection with the thermometry of transistor structures.

3 Measurement Examples

This section describes the experimental apparatus developed in this study for high temporal and spatial resolution thermometry of microdevices and presents calibration results and data for SOI power transistors and metal interconnect structures.

3.1 Experimental Apparatus. The present study develops the experimental facility shown in Fig. 5, which integrates scanning laser diagnostics and electrical probing and thus allows

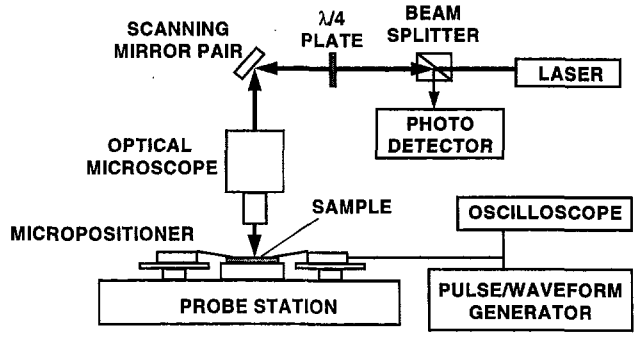

Fig. 5 Schematic of the scanning laser-reflectance thermometry facility developed in the present study. A probe laser beam is focused down to the diffraction limit by an optical microscope and scanned over a sample surface using a pair of scanning mirrors.

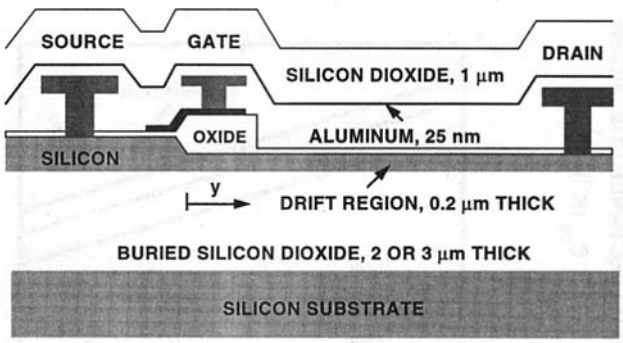

Fig. 6 Cross section of the silicon-on-insulator (SOI) high-voltage transistor structure studied in the present work. A thin aluminum layer of thickness 25 nm is deposited between silicon-dioxide passivation layers for measurement purposes. Temperature distributions along the drift region are measured using the facility shown in Fig. 5.

simultaneous investigation of thermal and electrical behavior of microdevices. A laser diode system with a single-element glass aspheric focusing lens and astigmatic correction optics is used. The output beam from the diode laser system has a Gaussian intensity profile with the beam divergence angle of 0.14 mrad. Radiation from the laser diode system is coupled into an optical microscope and focused to a diameter near the wavelength using microscope objective lenses with numerical aperture as high as 0.9. The wavelength of the laser diode used in the present study is 825 nm. The probe laser focus is scanned over the wafer surface using a pair of galvanometrically actuated mirrors that rotate about orthogonal axes while the semiconductor device and the electrical probes remain stationary. This feature allows the use of standard microprobes, facilitating wafer-level device characterization. A polarization cube and a quarter-wave plate separate the incident and reflected probe beam paths. Laser power fluctuations are subtracted using a reference beam drawn by a beam splitter. The radiation powers are captured using photodiodes with 500 MHz bandwidth and a digital oscilloscope with 1 GHz sampling frequency. The temporal resolution achievable in this setup is near 10 ns and the spatial resolution is limited by the diffraction of a probe beam to the order of its wavelength. The current setup allows the direct observation of sample surfaces during the measurements either through an eyepiece or a CCD camera. Using a calibration structure, the size and location of the focused beam spot can be measured and monitored during the scan process.

3.2 Thermometry of SOI High-Voltage Transistors. The thermoreflectance thermometry technique is applied to silicon-on-insulator (SOI) power transistors, which are designed to block high-voltages in power circuitry (Ju et al., 1997). A schematic of the transistor structure used in the experiments is shown in Fig. 6. To assist with the thermometry, an aluminum layer is sputtered within the surface oxide. The thickness of the aluminum layer is 25 nm, which is larger than the optical penetration depth of 8 nm at the probe beam wavelength. It therefore strongly reduces interaction between the radiation and the transistor and precisely defines the vertical location at which temperature is measured. The length of the drift region, over which the aluminum layer is deposited, is 40 μm.

The numerical aperture of the microscope objective lens used for the measurements is 0.5. The probe beam power is less than 1 mW. The temperature rise due to laser heating is estimated to be small since the conduction cooling through the substrate, which is augmented by the lateral spreading of heat in the metal film, is substantial. For values on the absorbed laser power as high as 0.1 mW, the estimated laser-induced temperature rise in the 25-nm-thick aluminum layer is less than 10 K. Since the present technique measures changes in temperature rather than its absolute magnitude, the steady-state temperature field does not directly influence the measurements. When the laser-induced heating is significant, however, it can alter device characteristics and thereby indirectly affect the results. The impact of laser heating on the measurements is examined experimentally by varying the incident probe beam power and also the focused beam spot size. There are no observable variations either in the measured temperature rises or in the electrical characteristics of the devices.

The calibration for the transistor structures is performed using the transistor structures themselves. The silicon wafer containing the transistors is fixed to a temperature-controllable hot-chuck, which is made of copper, by means of air suction. The changes in the surface reflectance are monitored while inducing periodic variations in the wafer temperature. The area of the transistor region, over which the aluminum layer is deposited, is large enough to allow the use of an optical system with a large depth of focus. This avoids error resulting from the thermal expansion of the calibration system. To verify the calibration, a control wafer is prepared using micro-fabrication processes identical to those for the transistor structures, but with the aluminum layer over the entire wafer. By removing the need for focusing optics, the impact of the thermal expansion of the calibration system can be eliminated. The two calibration results agree well within the uncertainty limit.

The area of a focused Gaussian beam varies as the beam travels through a medium in a manner that depends on the wavelength and the waist size of the beam. The spatial regions occupied by the multiply reflected beams do not exactly coincide with each other, which can influence interference among them and ultimately the thermoreflectance coefficient. The impact of the beam area variation, however, is not expected to be significant for the present measurements, where the reflected beam is collected through the lens used to focus the beam. Most of the collected light come from those portions of the multiply reflected beams that spatially overlap the beam waist. The small reflectance at the interface between the oxide layer and the ambient air, together with the fact that the Rayleigh range is over 5 μm for the present case, further reduces the impact. The insignificance of the beam area variation is verified experimentally using a transistor structure similar to the one shown in Fig. 6. The electrical resistivity and hence the local heat generation rate are made to be uniform along the drift region for this structure, which results in a temperature field that is uniform over a large portion of the drift region. Temperature measurements are performed using microscope objective lenses with numerical apertures of 0.1, 0.2, and 0.5, while subjecting the device to identical electrical stressing conditions. The results for the three lenses with very different beam waist sizes vary by less than 5 percent.

In Section 2.2, it is noted that the thermoreflectance coefficient can vary with time due to the temperature dependence of the index of refraction of the dielectric passivation layer. Parametric study performed on the aluminum layer indicates that for a reasonable range of values of the parameters involved, the resulting error is not significant. For times greater than the thermal diffusion time across the overlying oxide layer, which is near 1 μs in this case, the temperature variation within the passivation overlayer and its influence on the thermoreflectance signal can be neglected.

During the thermometry, periodic voltage pulses of duration near 30 μs and magnitude near 30 V are applied to the drain. The duration of the pulse is chosen such that the influence of the buried oxide layer on the temperature rise can be examined over a large duration. The duty cycle of the periodic pulses is less than 0.01 to ensure complete cooling of the devices between successive heating pulses. The gate of the transistor is positively biased at 12 V and the source is grounded. At each scan point, the periodic temperature rise is acquired as a function of time after pulse initiation. Once these data are obtained for the entire

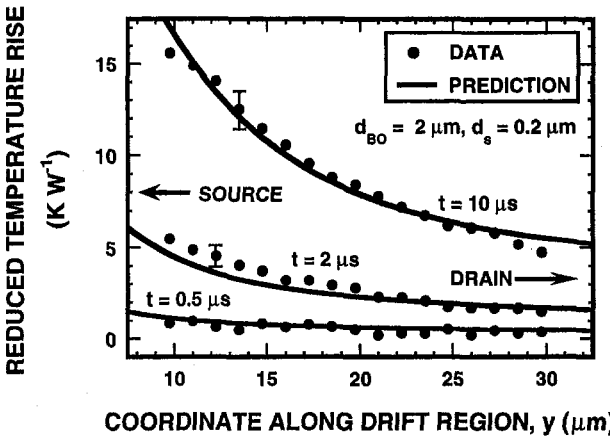

Fig. 7 Temperature distributions along the drift region of the transistors subjected to current pulses of duration 30 μs. The reduced temperature rise is the temperature rise per unit power dissipated in the device. Spatial variations in the impurity concentration lead to nonuniform temperature distributions.

sample surface, the spatial temperature-rise map can be extracted at any time.

A major source of noise in the current setup is the diode laser, which is sensitive to the back reflection and the environmental conditions. The photo-detector and signal amplifier contribute additional noise. The temperature resolution of 0.1 K is achieved by averaging signals 256 times. The relative uncertainty in the absolute value of the measured temperature rise is dominated by that in the calibration coefficient, C_{TR}, which is estimated to be 10 percent. Being independent of the calibration coefficient, the uncertainty in the ratio of temperature rises at different locations or at different times is much smaller, estimated to be 5 percent.

Practical limitations on the actual temporal and spatial resolution are imposed by the measurement structure due to the heat conduction within the aluminum and the passivation layers. Spatial resolution limit of 1 μm, which is not more restrictive than that due to the diffraction of the incident probe laser beam, and temporal resolution of 0.5 μs are estimated (Ju et al., 1997). These practical limitations on the resolution can be removed for the thermometry of interconnects and metallized regions of microdevices, which do not require any structure modifications.

Figure 7 shows the temperature distribution measured along the drift region of the SOI transistor for varying times after the initiation of the heating pulse. Since the thermal diffusion time normal to the buried silicon dioxide is comparable to 5 μs, the data actually describe transient heat diffusion *within* the silicon dioxide surrounding the active region. The temperature rise increases with decreasing coordinate y due to the spatial variation of the phosphorous impurity concentration, which is used to improve voltage-blocking capability (Leung et al., 1997). Since the current density does not vary significantly within the drift region, the rate of heat generation is proportional to the local electrical resistivity, which decreases with increasing impurity concentration. Figure 7 includes the predictions based on numerical solutions to the transient, two-dimensional heat equation in the drift region and surrounding silicon dioxide. The simulation uses bulk resistivity data for phosphorus-doped silicon with concentration distribution that is consistent with the fabrication process. The thermal conductivity and heat capacity used for the calculations are 100 W m^{-1} K^{-1} and 1.66 × 10^6 J m^{-3} K^{-1} for silicon and 1.4 W m^{-1} K^{-1} and 1.65 × 10^6 J m^{-3} K^{-1} for silicon dioxide, respectively (Goodson et al., 1996). The thermal conductivity of the silicon device layers used, which is lower than the bulk value, takes into account the reduction in the thermal conductivity due to phonon-boundary scattering. The simulation assumes that the top boundary condition for the passivation is adiabatic, and the bottom boundary condition for the buried silicon dioxide is isothermal. These assumptions are justified by the extremely low convection and radiation heat losses to the ambient air and by the short time scale of the heating pulse, respectively. The shape and time dependence of the calculated temperature rise agree well with the data.

3.3 Interconnect Thermometry. The interconnect structures examined in this study are shown in Fig. 8. The metal lines are 4 μm wide and 0.5 μm thick and are deposited on the composite passivation layers consisting of silicon-dioxide and polymer layers. The interconnects are made of Al-Cu-Ti alloy with the electrical resistivity of 3.37 × 10^{-8} Ω m. The thermoreflectance coefficient of 5.5 × 10^{-4} K^{-1} is obtained using a nearby 2000-μm-long metal line both as a heater and an electrical resistance thermometer according to the method described in Section 2.4. The uncertainty in the absolute magnitude of temperature rises is again dominated by that in the calibration coefficient, which is estimated to be 10 percent. The numerical aperture of the lens is 0.9 and the incident probe beam power is less than 1 mW. The influence of the laser-induced heating is examined by varying the laser power and is found not to be significant. Due to the increased detector noise at short time scales and the small thermoreflectance coefficient, achieving resolution better than 1 K requires averaging of signals by more than 1024 times. This number could be reduced by employing a more stable laser, such as a gas laser, as a light source, by prefiltering high frequency noise components, and by performing post-processing of data.

Figure 9 compares the normalized shapes of the spatial temperature distributions along interconnects subjected to electrical heating pulses of duration 200 ns and 2 μs. The temperature distributions become more rounded with increasing time after the pulse initiation. This is because the interconnect ends are anchored near the initial temperature due to their proximity to the metal regions with larger width. At a given time t, the influence of the lower temperature end conditions propagates inward over a distance comparable to the heat diffusion length in metal. For the largest value of t, the data are relatively independent of x only within a small portion of the interior of the line. Shown also are the predicted spatial temperature profiles, which are obtained from a numerical heat conduction analysis in the metal. The cross-sectional temperature distribution of the metal at each location along the interconnect is assumed to be uniform and all the boundaries are assumed to be adiabatic. The influence of the underlying passivation layer on the lengthwise temperature profile is neglected, since its thermal conductivity is two orders of magnitude smaller than that of the metal.

For the pulse of duration 200 ns, the temperature rise at the middle portion of the interconnect can be simulated by solving

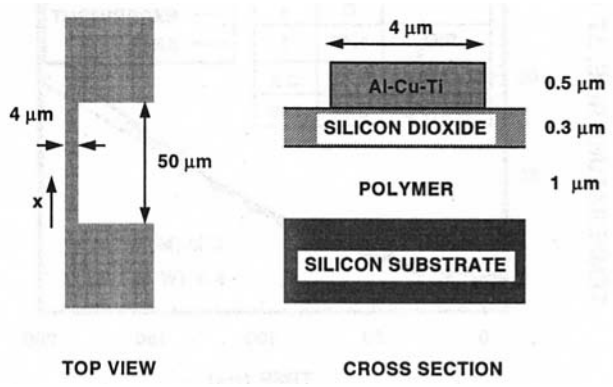

Fig. 8 Schematic of interconnect structures studied here. The interconnects are made of Al/Cu alloy and are separated from the silicon substrate by an underlying passivation layer. Electrical connections are made through two large area contact pads.

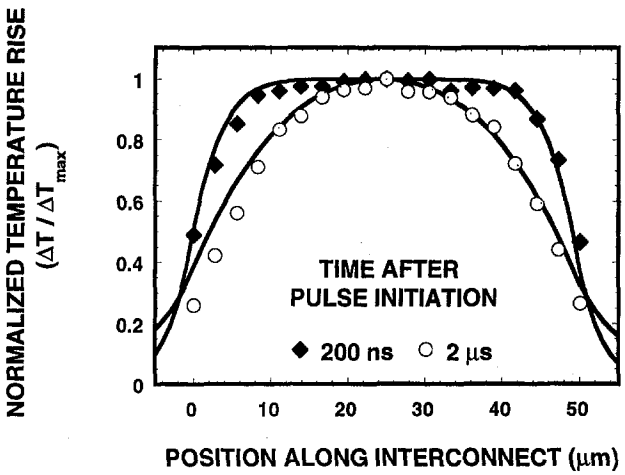

Fig. 9 Normalized temperature profiles along the interconnect structures subjected to brief electrical pulses of duration 200 ns and 2.5 μs. Solid lines are the predictions from the heat conduction analysis within the metals.

the transient two-dimensional heat conduction equation. Figure 10 plots the experimentally measured temperature rise and the predictions, which show good agreement up to the time after pulse initiation of 150 ns. The thermal boundary resistance resulting from the poor interface quality between the silicon dioxide and the polymer layer (Ju and Goodson, 1997) is believed to enhance temperature rises at later times. Numerical values of the thermal properties used for the simulations are shown in the figure. The time derivative of the temperature rise is small for short times after the pulse initiation due to the pulse rise time of 50 ns.

4 Summary and Conclusions

The performance and reliability of microdevices subjected to brief electrical stresses are strongly influenced by the presence of localized hot spots and regions with high temperature gradients, whose locations can vary with the time scales of electrical stresses. Concurrent electrical and thermal design are necessary to assure the optimal performance and reliability of these devices. Transient thermal mapping techniques can aid the design process by locating problematic regions and by providing quantitative information on temperature fields in microdevices.

The present work studies a scanning thermoreflectance technique, which is promising for transient thermal mapping of microdevices. The impact of passivation layers on the thermoreflectance coefficient is examined and a calibration technique suitable for integrated circuit elements is developed. This work shows that the proper interpretation of the thermoreflectance signal is necessary for the transient thermometry of passivated microdevices. A thermoreflectance thermometry facility combining scanning laser optics with electrical stressing capability is built and spatial resolution of 1 μm and temporal resolution near 10 ns are demonstrated.

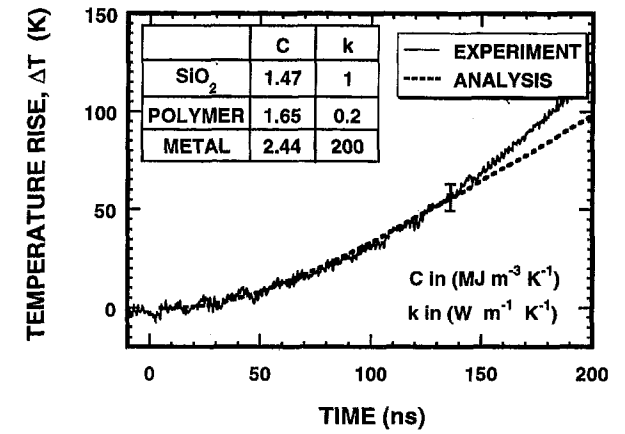

Fig. 10 Comparison of the experimentally measured time evolution of the temperature rise in the interconnect and the predictions based on the transient heat conduction equation

Acknowledgments

Y. S. J. acknowledges support from the member companies of the Center for Integrated Systems at Stanford University and Texas Instruments, Inc. K. E. G. acknowledges the ONR Young Investigator Award and support of the Semiconductor Research Corporation through contract No. 97-SJ-461. The SOI transistors were fabricated by Dr. Y.-K. Leung and Prof. S. S. Wong of Department of Electrical Engineering at Stanford University and the interconnect samples were provided by Intel Corporation. Y. S. J. appreciates the aid of Dr. O. W. Käding, W. Sabala, and L. Johal in building the experimental setup.

References

Abid, R., Miserey, F., and Mezroua, F.-Z., 1996, "Effet de la Température sur la Réflectivité du Silicium Oxydé: Détermination Expérimentale de la Sensibilité Relative; Application à la Mesure sans Contact de la Température à la Surface d'un Thyristor GTO en Commutation," *J. de Phys. III,* Vol. 6, pp. 279–300.

Amerasekera, A., and Duvvury, C., 1995, *ESD in Silicon Integrated Circuits,* Wiley, Chichester.

Arnold, E., 1994, "Silicon-on-Insulator Devices for High Voltage and Power IC Applications," *J. Electrochem. Soc.,* Vol. 141, pp. 1983–1988.

Arnold, E., Pein, H., and Herko, S. P., 1994, "Comparison of Self-Heating Effects in Bulk-Silicon and SOI High-Voltage Devices," *IEDM Technical Digest,* pp. 813–816.

Banerjee, K., Amerasekera, A., and Hu, C., 1996, "Characterization of VLSI Interconnect Heating and Failure under ESD Conditions," *Proc. Int. Reliab. Phys. Symp.,* pp. 237–245.

Bennett, G. A., and Briles, S. D., 1989, "Calibration Procedure Developed for IR Surface-Temperature Measurements," *IEEE Trans. Components, Hybrids and Manufacturing Technol.,* Vol. 12, pp. 690–695.

Cardona, M., 1969, "Modulation Spectroscopy," in: *Solid State Physics,* Suppl. 11, Seitz, F., Turnbull, D., and Ehrenreich, H., eds., Academic Press, New York.

Chui, B. W., Stowe, T. D., Ju, Y. S., Goodson, K. E., Kenny, T. W., Mamin, H. J., Terris, B. D., Ried, R. P., and Rugar, D., 1998, "Low-Stiffness Silicon Cantilevers With Integrated Heaters and Piezoresistive Sensors for High-Density AFM Thermomechanism Data Storage," *J. MEMS,* Vol. 7, pp. 69–78.

Claeys, W., Dilhaire, S., Quintard, V., Dom, J. P., and Danto, Y., 1993, "Thermoreflectance Optical Test Probe for the Measurement of Current-Induced Temperature Changes in Microelectronic Components," *Reliability Eng. Int.,* Vol. 9, pp. 303–308.

Decker, D. L., and Hodgkin, V. A., 1981, "Wavelength and Temperature Dependence of the Absolute Reflectance of Metals at Visible and Infrared Wavelengths," in: *National Bureau of Standards Special Publication,* NBS-SP-620, Washington, DC.

Eeseley, G. L., 1986, "Generation of Nonequilibrium Electron and Lattice Temperatures in Copper by Picosecond Laser Pulses," *Phys. Rev. B,* Vol. 33, pp. 2144–2151.

Epperlein, P.-W., 1993, "Micro-Temperature Measurements on Semiconductor Laser Mirrors by Reflectance Modulation: A Newly Developed Technique for Laser Characterization," *Jpn. J. Appl. Phys.,* Vol. 32, pp. 5514–5522.

Fergason, J. L., 1968, "Liquid Crystals in Nondestructive Testing," *Applied Optics,* Vol. 7, pp. 1729–1737.

Friedrich, K., Walther, H. G., and von Geisau, O. H., 1991, "A Method to Increase the Sensitivity of Temperature Measurements of Current-Carrying Microelectronic Components," *Rev. Sci. Instrum.,* Vol. 62, pp. 805–809.

Goodson, K. E., Flik, M. I., Su, L. T., and Antoniadis, D. A., 1995, "Prediction and Measurement of Temperature Fields in Silicon-on-Insulator Electronic Circuits," ASME JOURNAL OF HEAT TRANSFER, Vol. 117, pp. 574–581.

Goodson, K. E., Ju, Y. S., Asheghi, M., Käding, O. W., Touzelbaev, M. N., Leung, Y.-K., and Wong, S. S., 1996, "Microscale Thermal Characterization of High-Power Silicon-on-Insulator Transistors," *Proc. 31st ASME National Heat Transfer Conference,* Vol. 5, pp. 1–9.

Guidotti, D., and Wilman, J. G., 1992, "Nulling Optical Bridge for Nonintrusive Temperature Measurements," *J. Vac. Sci. Technol. A,* Vol. 10, pp. 3184–3192.

Jellison, G. E., Jr., and Modine, F. A., 1982a, "Optical Absorption of Silicon Between 1.6 and 4.7 eV at Elevated Temperatures," *Appl. Phys. Lett.,* Vol. 41, pp. 180–182.

Jellison, G. E., Jr., and Modine, F. A., 1982b, "Optical Constants for Silicon at 300 and 10 K Determined from 1.64 to 4.73 eV by Ellipsometry," *J. Appl. Phys.*, Vol. 53, pp. 3745–3753.

Jellison, G. E., Jr., and Burke, H. H., 1986, "The Temperature Dependence of the Refractive Index of Silicon at Elevated Temperatures at Several Laser Wavelengths," *J. Appl. Phys.*, Vol. 60, pp. 841–843.

Ju, Y. S., Käding, O. W., Leung, Y. K., Wong, S. S., and Goodson, K. E., 1997, "Short-Timescale Thermal Mapping of Semiconductor Devices," *IEEE Electron Device Lett.*, Vol. 18, pp. 169–171.

Ju, Y. S., and Goodson, K. E., 1997, "Short-Timescale Thermal Mapping of Interconnects," *IEEE Proc. Int. Reliab. Phys. Symp.*, Denver, CO, pp. 320–324.

Knittl, Z., 1976, *Optics of Thin Films*, Wiley, London.

Kolodner, P., and Tyson, J. A., 1982, "Microscopic Fluorescent Imaging of Surface Temperature Profiles With 0.01 C Resolution," *Appl. Phys. Lett.*, Vol. 40, pp. 782–784.

Kolodner, P., and Tyson, J. A., 1983, "Remote Thermal Imaging With 0.7-μm Spatial Resolution Using Temperature-Dependent Fluorescent Thin Films," *Appl. Phys. Lett.*, Vol. 42, pp. 117–119.

Kondo, S., and Hinode, K., 1995, "High-Resolution Temperature Measurement of Void Dynamics Induced by Electromigration in Aluminum Metallization," *Appl. Phys. Lett.*, Vol. 67, pp. 1606–1608.

Leung, Y.-K., Kuehne, S. C., Huang, V. S. K., Nguyen, C. T., Paul, A. K., Plummer, J. D., and Wong, S. S., 1997, "Spatial Temperature Profiles Due to Nonuniform Self-Heating in LDMOS's in Thin SOI," *IEEE Electron Device Lett.*, Vol. 18, pp. 13–15.

Maloney, T. J., and Khurana, N., 1985, "Transmission Line Pulsing Techniques for Circuit Modeling of ESD Phenomena," *Proc. EOS/ESD Symp.*, pp. 49–54.

Mansanares, A. M., Roger, J. P., Fournier, D., and Boccara, A. C., 1994, "Temperature Field Determination of InGaAsP/InP Lasers by Photothermal Microscopy: Evidence for Weak Nonradiative Processes at the Facets," *Appl. Phys. Lett.*, Vol. 64, pp. 4–6.

Majumdar, A., Lai, J., Chandrachood, M., Nakabeppu, O., Wu, Y., and Shi, Z., 1995, "Thermal Imaging by Atomic Force Microscopy Using Thermocouple Cantilever Probes," *Rev. Sci. Instrum.*, Vol. 66, pp. 3584–3592.

Martin, Y., and Wickramasinghe, H. K., 1987, "Study of Dynamic Current Distribution in Logic Circuits by Joule Displacement Microscopy," *Appl. Phys. Lett.*, Vol. 50, pp. 167–168.

Miklós, A., and Lörincz, A., 1988, "Transient Thermoreflectance of Thin Metal Films in the Picosecond Regime," *J. Appl. Phys.*, Vol. 63, pp. 2391–2395.

Murguia, J. E., and Bernstein, J. B., 1993, "Short-time Failure of Metal Interconnect Caused by Current Pulses," *IEEE Electron Device Lett.*, Vol. 14, pp. 481–483.

Ostermeir, R., Brunner, K., Abstreiter, G., and Weber, W., 1992, "Temperature Distribution in Si-MOSFET's Studied by Micro Raman Spectroscopy," *IEEE Trans. Electron Devices*, Vol. 39, pp. 858–863.

Pliskin, W. A., 1977, "Comparison of Properties of Dielectric Films Deposited by Various Methods," *J. Vac. Sci. Technol.*, Vol. 14, pp. 1064–1081.

Quintard, V., Deboy, G., Dilhaire, S., Lewis, D., Phan, T., and Claeys, W., 1996, "Laser Beam Thermography of Circuits in the Particular Case of Passivated Semiconductors," *Microelectronic Engineering*, Vol. 31, pp. 291–298.

Qiu, T. Q., Grigoropoulos, C. P., and Tien, C. L., 1993, "Novel Technique for Noncontact and Microscale Temperature Measurements," *Experimental Heat Transfer*, Vol. 6, pp. 231–241.

Rosei, R., and Lynch, D. W., 1972, "Thermomodulation Spectra of Al, Au, and Cu," *Phys. Rev. B*, Vol. 5, pp. 3883–3893.

Salome, P., Leroux, C., Chante, J. P., Crevel, P., and Reimbold, G., 1997, "Study of the 3D Phenomenon During ESD Stresses in Deep Submicron CMOS Technologies Using a Photon Emission Tool," *IEEE Proc. Int. Reliab. Phys. Symp.*, Denver, CO, pp. 325–332.

Shirley, C. G., 1985, "Steady-State Temperature Profiles in Narrow Thin-Film Conductors," *J. Appl. Phys.*, Vol. 57, pp. 777–784.

Siegel, R., and Howell, J. R., 1992, *Thermal Radiation Heat Transfer*, Hemisphere Publishing Co., Washington, DC.

Smith, D. Y., Shiles, E., and Inokuti, M., 1985, "The Optical Properties of Metallic Aluminum," in: *Handbook of Optical Constants of Solids*, Palik, E. D., ed., Academic Press, Orlando, FL.

Stagg, B. J., and Charalampopoulos, 1991, "Surface Roughness Effects on the Determination of Optical Properties of Materials by the Reflection Method," *Appl. Opt.*, Vol. 30, pp. 4113–4118.

van der Meulen, Y. J., and Hien, N. C., 1974, "Design and Operation of an Automated High Temperature Ellipsometer," *J. Opt. Soc. Amer.*, Vol. 64, pp. 804–811.

Zweidinger, D. T., Fox, R. M., Brodsky, J. S., Jung, T., and Lee, S., 1996, "Thermal Impedance Extraction for Bipolar Transistors," *IEEE Trans. Electron Devices*, Vol. 43, pp. 342–346.

A Data Reduction Procedure for Transient Heat Transfer Measurements in Long Internal Cooling Channels

J. von Wolfersdorf

R. Hoecker

C. Hirsch

ABB—Corporate Research Center, 5405—Baden, Switzerland

The effect of streamwise fluid temperature variation on the local heat transfer coefficient measurements in transient heat transfer tests in long channels is addressed. Previous methods are shown to result in considerable errors. A simplified model is proposed to characterize the local fluid temperature, which drives the heat transfer. With it, analytical solutions for the local wall temperature history are derived, which involve two unknowns, the local heat transfer coefficient and a lumped upstream heat transfer parameter. Using these solutions in the data reduction, these two parameters are determined from surface temperature measurements. Numerical experiments that simulate the physical experiment show the applicability and robustness of the proposed method. The method is finally demonstrated experimentally by investigating heat transfer in a smooth, square duct.

Introduction

The transient technique using Thermochromic Liquid Crystals (TLC), melting point coatings, or surface thermocouples is a well-established method for heat transfer measurements in internal cooling ducts of gas turbine blades (Clifford et al., 1983; Ireland and Jones, 1985; Metzger and Larson, 1986). For high heat transfer efficiency (i.e., large St L/d), these channels are often formed into multipass serpentine passages and are equipped with turbulence promoters (Clifford, 1985; Saabas et al., 1987). A further increase in heat transfer may be caused by rotation of the gas turbine rotor channels (Wagner et al., 1991; Blair et al., 1991).

Most design systems use heat transfer coefficients defined in terms of the wall temperature and the local fluid bulk temperature computed from a one-dimensional energy balance. In transient tests, however, the fluid temperature driving the heat transfer is a function of streamwise position and time and is usually unknown. Therefore, models are used to describe the local fluid bulk temperature. In some experiments, the entrance and exit fluid temperatures are measured and the local fluid temperature is determined by linear interpolation (Blair et al., 1991; Besserman and Tanrikut, 1992). Also, a series of thermocouples along the flowpath measuring the local time–temperature history of the flow is utilized and assuming some ratio between the measured temperature and the bulk temperature the latter is computed. One of the most frequently used methods applies an energy balance (Metzger and Larson, 1986; Baughn and Yan, 1992; Wang et al., 1994), which assumes isothermal walls. In this method, a preliminary evaluation of the heat transfer coefficient is made from the TLC temperatures and the inlet temperature employing a one-dimensional solution for heat conduction in a semi-infinite medium with a convective boundary condition:

$$\Theta_W = \frac{T_W - T_0}{T_E - T_0} = 1 - \exp\left(\frac{h_E^2 t}{k}\right) \operatorname{erfc}\left(\frac{h_E\sqrt{t}}{\sqrt{k}}\right). \quad (1)$$

where h_E is the heat transfer coefficient based on the inlet temperature. With this information and a steady-state energy balance, Metzger and Larson (1986) evaluated the heat transfer coefficient based on the local bulk temperature assuming isothermal walls:

$$h(x) = h_E(x) \Big/ \left(1 - \frac{1}{\dot{m}c_p} \sum_{i=1}^{x-1} \overline{h_{E_i}} F_i\right) \quad (2)$$

where the subscript i denotes measuring locations in the streamwise direction and $\overline{h_{E_i}}$ is the averaged heat transfer coefficient over the respective area F_i.

This method is straightforward and easy to implement in a data reduction procedure. However, the application of this method requires heat transfer information on all heat transfering walls. Otherwise further assumptions are necessary. Furthermore, this method may lead to erronous results for channels with high St (L/d). This may in particular be problematic in some tests, where a long entrance length is needed to achieve well-defined fluid boundary conditions (Wang et al., 1998).

In a transient experiment with large St (L/d), the local fluid time–temperature history varies considerably from that measured at the channel entrance, such that the heat transfer coefficient based on inlet temperature becomes a strong function of time. This problem is illustrated in Fig. 1, using a transient temperature data set for a one-dimensional channel flow that was numerically generated prescribing heat transfer coefficients (details given later in the paper). In the figure, the ratio of the heat transfer coefficients re-evaluated using the method of Metzger and Larson (1986) to the prescribed ones is shown. Large deviations from the exact result (ratio = 1) occur at different streamwise positions depending on the chosen wall indication temperature. These deviations grow in the streamwise direction, leading to increasingly overpredicted h values. An investigation of this effect with laminar boundary layers on a flat plate was recently presented by Butler and Baughn (1996).

An alternative model, which may be seen as a transient extension of the Metzger and Larson technique, is presented. Using multiple wall temperature indications (i.e., local information only) the local heat transfer coefficient can be determined. The paper has the following structure. After presenting the basic concept, the detailed derivation of the modeling leads to a solution for the local wall temperature history, which allows one

Contributed by the Heat Transfer Division for publication in the JOURNAL OF HEAT TRANSFER. Manuscript received by the Heat Transfer Division January 24, 1997; revision received January 30, 1998. Keywords: Conjugate Heat Transfer, Forced Convection, Measurement Techniques. Associate Technical Editor: M. K. Kelleher.

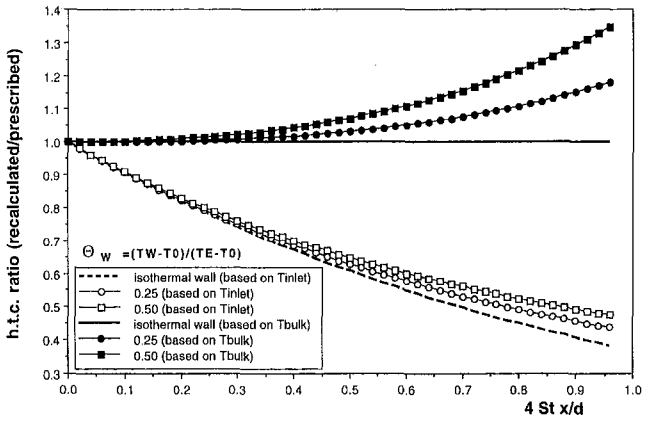

Fig. 1 Ratio of re-evaluated and prescribed heat transfer coefficient based on inlet temperature and on bulk temperature using the method of Metzger and Larson (1986)

to determine the local heat transfer coefficient using two wall temperature indications only. Then the robustness of this procedure is demonstrated using ideal reference data provided from a numerical experiment. Finally, the results of an investigation of heat transfer in a smooth, square duct underline the method's experimental applicability.

Conceptual Model

The experimental techniques addressed here rely on the following assumptions. All property values are independent of temperature (and thus time). The time-independent flow field is assumed to be established instantaneously at time zero. Under these assumptions the local heat transfer coefficient h depends on the flow field only and is therefore a constant with time. Beyond these prerequisites the experiment shall be conducted such that the local fluid temperature is a monotonic function of time. This is the case for transient experiments in long channels with a constant inlet temperature as considered here. With these conditions the locally measured wall temperature history uniquely (though not proven here) reflects the fluid temperature, which drives the local heat transfer. For instance, given the classical step change in the a priori unknown fluid temperature, two indications of wall temperature suffice to determine both the local heat transfer coefficient and the constant driving fluid temperature, as demonstrated by Vedula and Metzger (1991). All other choices for the driving temperature will lead to a time-dependent h, violating the basic assumptions. These observations are the basis for the method proposed in this paper.

In general, an arbitrarily varying local fluid temperature history and the local heat transfer coefficient cannot be determined directly, because the problem is ill-posed. However, if the fluid temperature history can be modeled accurately enough with a

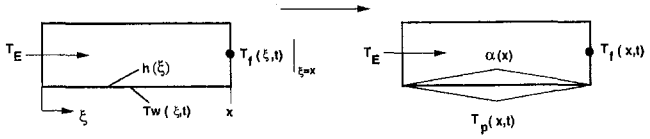

Fig. 2 Description of simplified model

n-parametric function of time, $n + 1$ wall temperature measurements are sufficient to obtain both, as evident in the example $n = 1$, i.e., the step change. The current approach minimizes the number of necessary parameters for a class of problems, e.g., turbulent flow and heat transfer in long channels. By introducing simplified modeling of the heat exchange between the fluid and the wall occurring upstream of a position considered, an approximation for the local driving fluid temperature history is derived.

The first step in the modeling approach is the description of the heat loss of the fluid to the upstream channel walls linking the fluid temperature at the considered location to the channel entrance temperature. This is achieved by representing the upstream wall heat transfer using a single, time-dependent surface temperature, the channel entrance temperature, and an upstream heat transfer parameter. Here the surface temperature history is assumed to follow the transient of the semi-infinite wall solution. Then the local fluid temperature is obtained at every instant by integrating a simplified energy equation for an isothermal surface, which is at the current upstream surface temperature. Like this the local fluid temperature becomes a function of the channel entrance temperature and the upstream heat transfer parameter.

Given this approximation of the local fluid temperature, the local wall temperature history solution is obtained, which is finally used for data reduction.

In the following sections the detailed derivation of this conceptual model is presented.

Fluid Temperature Model

To determine the time variation of the fluid temperature at a given position x, the following simplified one-dimensional model is proposed. The fluid enters the channel with the average velocity w and a constant temperature T_E. The initial temperature of the wall is T_0 (Fig. 2). The heat lost by the fluid to the walls from the channel entrance to the position x where the local heat transfer coefficient shall be determined is for constant perimeter U given by:

$$Q(x, t) = U \int_0^x h(\xi)(T_f(\xi, t) - T_W(\xi, t))d\xi \qquad (3)$$

This upstream heat loss is approximated by a single heat transfer parameter $\alpha(x)$ and a single time-dependent surface temperature $T_p(x, t)$, both of which are characteristic for the

Nomenclature

c_p = specific heat
d = diameter
F = area
h = heat transfer coefficient
$k = \lambda\varrho c_p$ material constant
L = length
$\dot{m}$ = mass flow
Nu = Nusselt number
Pr = Prandtl number
Q = heat loss
q_w = heat flow per unit length
Re = Reynolds number
St = Stanton number
t = time
T = temperature
U = perimeter
w = velocity
x = streamwise position
y = vertical coordinate
α = heat transfer parameter
ξ = streamwise coordinate
λ = thermal conductivity
ϱ = density
Θ = dimensionless temperature

Subscripts

b = bulk
cl = centerline
E = inlet or entrance
f = fluid
p = surface
s = solid
W = wall
0 = initial

measurement location x. With this approximation Eq. (3) simplifies to:

$$Q(x, t) = \alpha(x)U \int_0^x (T_f(\xi, t) - T_p(x, t))d\xi. \quad (4)$$

A similar approach was published very recently by Chyu et al. (1997) and shown there to work for a complex flow and heat transfer problem.

It should be noted that neither is $\alpha(x)$ the spatially averaged upstream heat transfer coefficient nor is $T_p(x, t)$ the spatially averaged upstream wall temperature. If we compare Eqs. (3) and (4), these parameters are defined by:

$$\alpha(x) = \frac{\int_0^x h(\xi)T_f(\xi, t)d\xi}{\int_0^x T_f(\xi, t)d\xi} \quad (5)$$

and

$$T_p(x, t) = \frac{\int_0^x h(\xi)T_W(\xi, t)d\xi}{\alpha(x)x}. \quad (6)$$

Only for the special case of constant heat transfer coefficient h will these parameters be equal to the spatially average upstream values. The upstream heat transfer parameter $\alpha(x)$ is taken to be independent of time, which is valid if the fluid temperature distribution $T_f(\xi, t)$ can be separated by $T_f(\xi, t) = T_{f1}(\xi)T_{f2}(t)$, which is usually the case.

With this concept a simplified energy equation for the fluid is given by:

$$\frac{\partial T_f}{\partial t} + w\frac{\partial T_f}{\partial \xi} = w\frac{\alpha U}{\dot{m}c_p}(T_p(x, t) - T_f(\xi, t)). \quad (7)$$

Using the following transformation (Schumann, 1929):

$$\tau = t - \frac{\xi}{w} \quad (8)$$

we obtain:

$$\frac{\partial T_f}{\partial \xi} = \frac{\alpha U}{\dot{m}c_p}\left(T_p\left(x, \tau + \frac{\xi}{w}\right) - T_f\left(\xi, \tau + \frac{\xi}{w}\right)\right). \quad (9)$$

Since the term ξ/w is usually small (in the order of 0.025 s) compared to the measurement time (on the order of 40 s) in the present applications, we neglect the difference in the time scales τ and t. For a discussion of the effect of the different time domains the reader is referred to Sucec (1981). Thus a quasi-steady energy balance results taking into account the time history of the single upstream surface temperature:

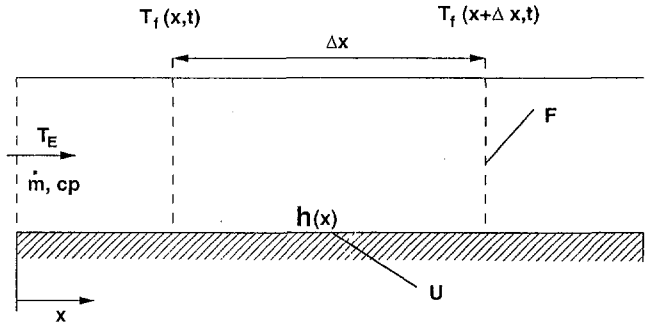

Fig. 3 Schematic for numerical model

$$\frac{\partial T_f}{\partial \xi} = \frac{\alpha U}{\dot{m}c_p}(T_p(x, t) - T_f(\xi, t)). \quad (10)$$

It has the boundary condition:

$$T_f(\xi = 0, t) = T_E. \quad (11)$$

Integrating Eq. (10) up to a location x formally gives the fluid temperature for an isothermal (yet time-dependent) wall at T_p with a constant (lumped) heat transfer coefficient α at every instant in time.

T_p is assumed to follow the semi-infinite wall temperature response to a step change of the inlet temperature T_E given an average heat transfer coefficient $\overline{h_E}$.

$$\frac{T_p - T_0}{T_E - T_0} = 1 - \exp\left(\frac{\overline{h_E}^2 t}{k}\right)\operatorname{erfc}\left(\frac{\overline{h_E}\sqrt{t}}{\sqrt{k}}\right) \quad (12)$$

This average heat transfer coefficient is defined as:

$$\overline{h_E} = \frac{1}{x}\int_0^x h_E(\xi)d\xi. \quad (13)$$

For an isothermal surface at temperature $T_p(x, t)$ and a constant $\alpha(x)$ as implied by Eq. (10), the following relationship exists between $h_E(\xi)$ and α:

$$h_E = \alpha \cdot \exp\left(-\frac{\alpha U}{\dot{m}c_p}\xi\right) \quad (14)$$

Substituting Eq. (14) into Eq. (13) we obtain:

$$\frac{\overline{h_E}}{\alpha} = \frac{1 - \exp\left(-\frac{\alpha U}{\dot{m}c_p}x\right)}{\frac{\alpha U}{\dot{m}c_p}x} = A. \quad (15)$$

Integrating Eq. (10) from 0 to x by taking into account Eqs. (12) and (11) yields the fluid temperature at the position x (using A as defined in Eq. (15) for brevity):

$$\frac{T_f - T_0}{T_E - T_0} = 1 - \left(1 - \exp\left(-\frac{\alpha U}{\dot{m}c_p}x\right)\right) \cdot \exp\left(\frac{\alpha^2 t}{k}A^2\right)\operatorname{erfc}\left(\frac{\alpha\sqrt{t}}{\sqrt{k}}A\right) \quad (16)$$

Equation (16) describes the local fluid temperature as a function of the entrance temperature, the initial temperature, and the upstream heat transfer parameter for a given geometry and flow rate.

Solutions for Wall Temperature History

Equation (16) for the fluid temperature is used as a boundary condition for the wall temperature at the location of interest. The local heat transfer coefficient at this location is h. The local wall temperature history will be obtained by solving the heat conduction equation:

$$\varrho_s c_{ps}\frac{\partial T_s}{\partial t} = \lambda_s\frac{\partial^2 T_s}{\partial y^2} \quad 0 < y < \infty \quad (17)$$

with the initial condition:

$$T_s(y, t = 0) = T_0 \quad (18)$$

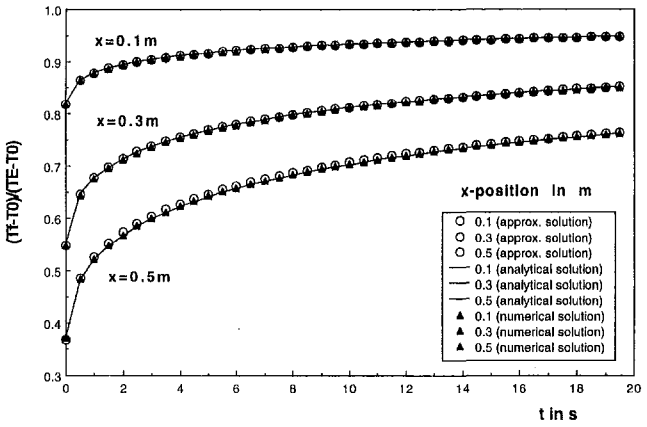

Fig. 4 Comparison of approximative solution with analytical and numerical solutions (uniform heat transfer coefficient distribution)

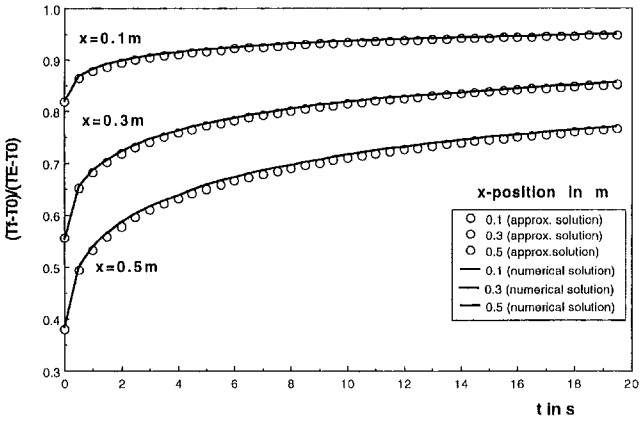

Fig. 5 Comparison of approximative solution with numerical solution (random heat transfer coefficient distribution)

and the boundary condition:

$$-\lambda_s \frac{\partial T_s}{\partial y}(y = 0, t) = h(T_f - T_s(y = 0, t)) = h(T_f - T_W) \quad (19)$$

with T_f from Eq. (16).

Using Laplace Transforms, we obtain for the wall temperature in the general case of $\alpha \cdot A \neq h$:

$$\Theta_W = \frac{T_W - T_0}{T_E - T_0} = 1 - \exp\left(\frac{h^2 t}{k}\right) \operatorname{erfc}\left(\frac{h\sqrt{t}}{\sqrt{k}}\right) + \left\{1 - \exp\left(-\frac{\alpha U}{\dot{m} c_p} x\right)\right\} \cdot \left\{\frac{1}{A\frac{\alpha}{h} - 1}\right\} \left\{\exp\left(\frac{\alpha^2 t}{k} A^2\right) \times \operatorname{erfc}\left(\frac{\alpha\sqrt{t}}{\sqrt{k}} A\right) - \exp\left(\frac{h^2 t}{k}\right) \operatorname{erfc}\left(\frac{h\sqrt{t}}{\sqrt{k}}\right)\right\}. \quad (20)$$

In the special case $\alpha \cdot A = h$ the solution is given by:

$$\Theta_W = \frac{T_W - T_0}{T_E - T_0} = 1 - \exp\left(\frac{h^2 t}{k}\right) \operatorname{erfc}\left(\frac{h\sqrt{t}}{\sqrt{k}}\right) - 2\frac{hUx}{\dot{m} c_p} \times \left\{\frac{h\sqrt{t}}{\sqrt{k}} \frac{1}{\sqrt{\Pi}} - \frac{h^2 t}{k} \exp\left(\frac{h^2 t}{k}\right) \operatorname{erfc}\left(\frac{h\sqrt{t}}{\sqrt{k}}\right)\right\}. \quad (21)$$

These equations involve the two unknowns h and α, which have to be determined from the local wall temperature indications.

Numerical Investigation

A numerical simulation of a transient test in a long channel was set up to provide "perfect" datasets of wall and fluid temperature for prescribed distributions of heat transfer coefficients. Taking wall temperature indications from this data set, the data reduction procedure can be qualified and the sensitivity of the method to imposed perturbations becomes measurable. The data were generated by integrating the one-dimensional thermal energy equation for an incompressible, constant-property fluid as a function of space and time with convective heat transfer to a semi-infinite solid (Fig. 3):

$$\varrho c_p F \frac{\partial T_f}{\partial t} + \dot{m} c_p \frac{\partial T_f}{\partial x} - \dot{q}_w = 0 \quad (22)$$

where $\dot{q}_w$ is the heat flow per unit length (Grigull and Sandner, 1990):

$$\dot{q}_w = hU \int_0^t \left\{-\exp\left(\frac{h^2(t-\tau)}{k}\right) \times \operatorname{erfc}\left(\frac{h\sqrt{t-\tau}}{\sqrt{k}}\right)\right\} \frac{\partial T_f(\tau)}{\partial \tau} d\tau \quad (23)$$

To check the model of the fluid temperature given by Eq. (16), the following data set is chosen. The one-dimensional numerical representation of a 500-mm-long square channel with a hydraulic diameter of 20 mm and an initial temperature of 293 K was computed. A mass flow rate of 0.01 kg/s of air enters the channel with a temperature of 353 K. The wall material is assumed to be perspex (plexiglass) ($\sqrt{k}$ = 569 (W/m^2 K) $\sqrt{s}$). This data set is similar to the test conditions of Wagner et al. (1991), Blair et al. (1991), and Besserman and Tanrikut (1992). Two different heat transfer distributions were prescribed. For the case of a uniform heat transfer coefficient, a value of 250 W/m^2 K is used, which is about 2.5 times the fully developed pipe flow value, leading to 4 St (L/d) of about 1. A second set of heat transfer coefficients is randomly generated with values between 100 W/m^2 K and 400 W/m^2 K.

Figure 4 shows the time history results for the fluid temperature with uniform heat transfer coefficients at various streamwise positions as given by the above numerical solution and an analytical solution for this case (derived in the appendix). These solutions are compared with the model as given in Eq. (16). For the case of the variable heat transfer distribution, the model and the numerical solutions are shown in Fig. 5. In both cases the agreement is excellent for all streamwise positions, which justifies the assumptions made in the derivation of the fluid temperature model.

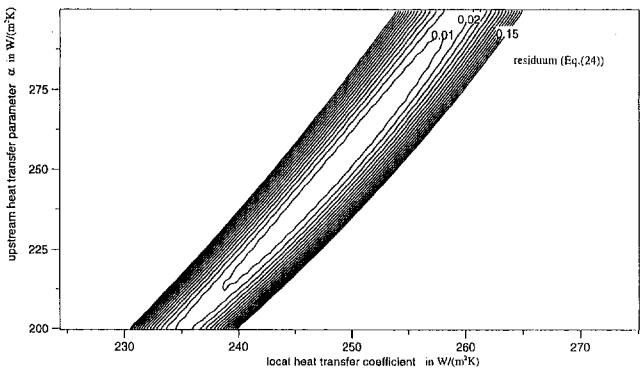

Fig. 6 Minimization function

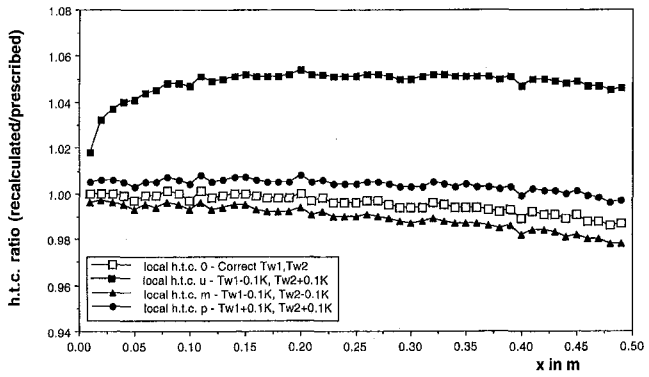

Fig. 7 Re-evaluated local heat transfer coefficients for uniform heat transfer coefficient distribution

The wall temperature indications were taken from the numerical experiments. Since the numerical model applies the same assumptions as the measurement technique, "perfect" indications are obtained. After the computation of the local wall temperature histories, two different wall temperatures (T_{W1} and T_{W2}) were chosen as indication temperatures and the times of their occurrence for all streamwise positions were determined using linear interpolation between the discrete time steps. To evaluate the local heat transfer coefficient and the lumped upstream heat transfer parameter, these times are inserted into Eqs. (20) and (21) and the sum

$$\sum_{i=1}^{2} (\Theta_W(t_i) - \Theta_{Wi})^2 = f(h, \alpha) \qquad (24)$$

with Θ_W from Eqs. (20) and (21) is minimized at each position. A downhill simplex method given by Press et al. (1989) is used for this minimization. A typical residual function of the minimization (Eq. (24)) is plotted in Fig. 6 versus the local heat transfer coefficient and the upstream heat transfer parameter. It can be seen that the sensitivity of the local heat transfer coefficient h with respect to the minimization is much smaller than for the upstream heat transfer parameter α.

To check the robustness of the method the indication temperatures were perturbed with values that are typical for experimental uncertainty. In the following comparison the correct (index 0) indication temperatures are perturbed simultaneously with +0.1 K (index p) and −0.1 K (index m) for both T_{Wi}. Furthermore a perturbation of −0.1 K for T_{W1} and +0.1 K for T_{W2} (index u) was applied. The comparison of the re-evaluated heat transfer coefficients with the known prescribed values for the uniform heat transfer distribution is given in Fig. 7. For the random distribution the results are given in Fig. 8.

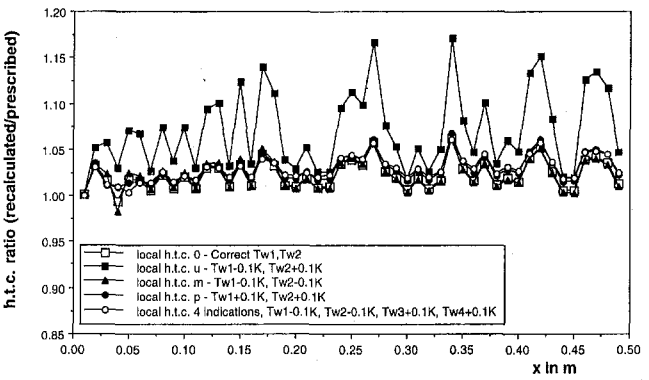

Fig. 8 Re-evaluated local heat transfer coefficients for random heat transfer coefficient distribution

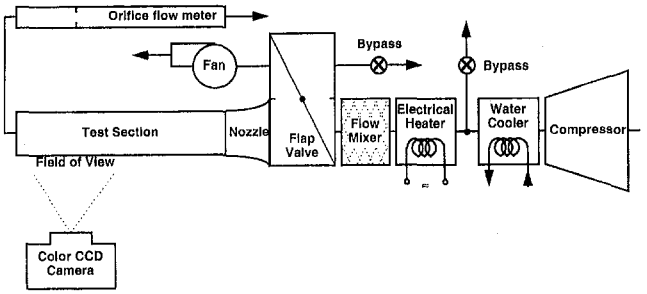

Fig. 9 Experimental arrangement

Using this method, all cases give good results. For the cases of disturbed data in different directions (index u), which is the worst case for the presented method, the deviations are about 5 percent for the uniform heat transfer distribution case and up to 17 percent for the random case.

The accuracy of the method might be increased by using a sophisticated image processing system (Wang et al., 1994b) which is able to determine a more detailed history of the surface temperatures, therefore using more indications in the data reduction. This is demonstrated in the fourth curve of Fig. 8, where using four perturbed indications (−0.1 K for T_{W1}, T_{W2} and +0.1 K for T_{W3}, T_{W4}) the error level is brought down to about 6 percent from 17.

Experiments and Results

Figure 9 shows a schematic of the test apparatus. Air is supplied to an electrical heater section followed by a valve. In operation the heated flow is diverted away from the test section prior to the test. Ambient air is sucked into the test section by a second pump to achieve uniform initial temperatures. The test section consists of a 1400-mm-long, straight, smooth, 50 mm × 50 mm square duct. The entire channel is constructed of perspex with a wall thickness of 10 mm for all walls. The walls are covered with three different small band TLC and black paint. Along the channel centerline 10 thermocouples are installed to measure the fluid temperature. A thermal transient is initiated using the valve to route the heated air flow suddenly through the test section. Experiments for different Reynolds numbers were made and the TLC pattern at one wall between the streamwise positions x = 1.115 m and x = 1.285 m were monitored by a CCD camera and evaluated by an image system. The three indications of one color of the different TLC at each location were used to determine the local heat transfer coefficient and the upstream heat transfer parameter applying the minimization procedure described above. A typical heat transfer distribution on one channel wall is shown in Fig. 10.

Figure 11 gives the determined heat transfer parameter distribution over the test surface. This distribution shows two long valleys of smaller α close to the sidewalls. Since lower α means higher fluid driving temperature this pattern might be attributed to the secondary flow in the channel. Hot fluid from the center is driven by the secondary flow toward the corners leading to higher fluid driving temperature there. The fluid cools down at

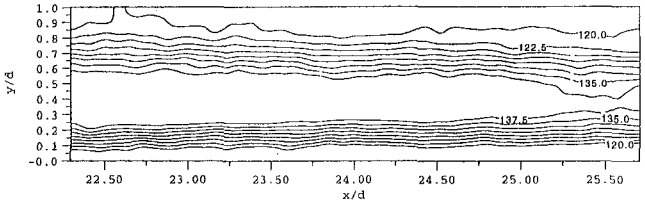

Fig. 10 Local heat transfer coefficient distribution in W/m² K (Re = 116,600)

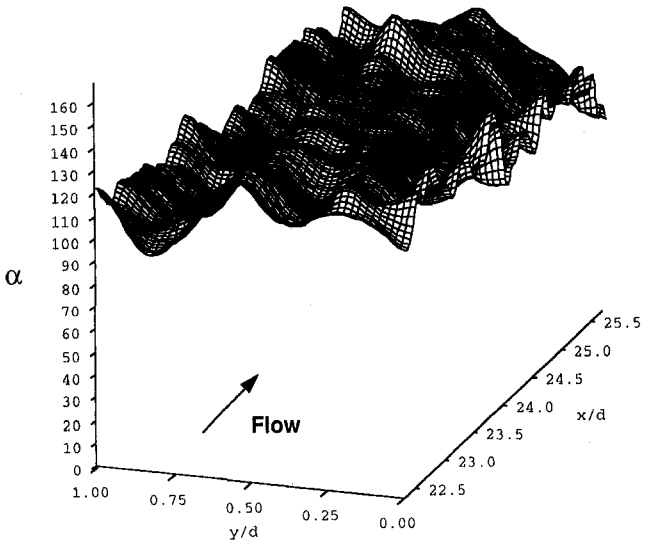

Fig. 11 Distribution of heat transfer parameter in W/m² K (Re = 116,600)

the wall and flows back close to the channel centerline, therefore creating a lower driving temperature there (higher α).

The method determines the heat transfer coefficient for the three-dimensional experimental situation based on local fluid driving temperature (adiabatic wall temperature, which is in the one-dimensional case the fluid bulk temperature) rather than on mixed bulk temperature. The distribution of the heat transfer parameter α is therefore a measure of the unmixness of the fluid.

Using the determined α distribution and Eq. (16) for the fluid driving temperature and averaging over the span at one streamwise location, the average fluid driving temperature $\overline{T_f}(t)$ at this location is determined. For a well-mixed flow as typical for, e.g., gas turbine blade cooling passages, this temperature should be close to the fluid bulk temperature, although the relationship between both is not given by this method.

The average fluid driving temperature $\overline{T_f}(t)$ and the upstream surface temperature $T_p(t)$ from the model have been calculated at the axial position of the measured centerline temperature $T_{cl}(t)$. The ratio of these temperatures, i.e., the profile factor γ was evaluated according to:

$$\gamma = \frac{\overline{T_f}(t) - T_p(t)}{T_{cl}(t) - T_p(t)} \tag{25}$$

For all tests, as well as for all times within one test, the determined value of γ shows only small variations (± 0.015)

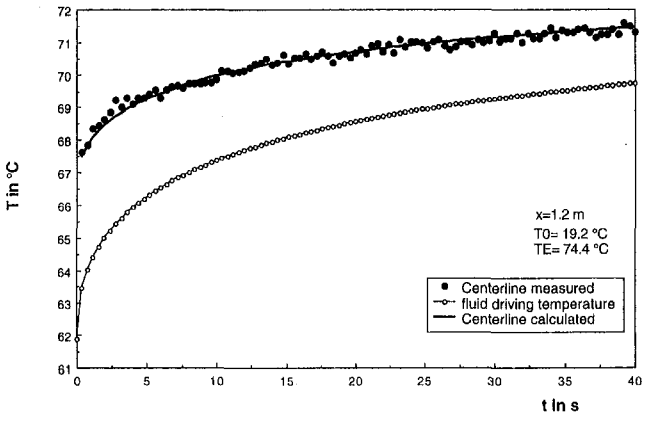

Fig. 12 Comparison of calculated and measured centerline temperature

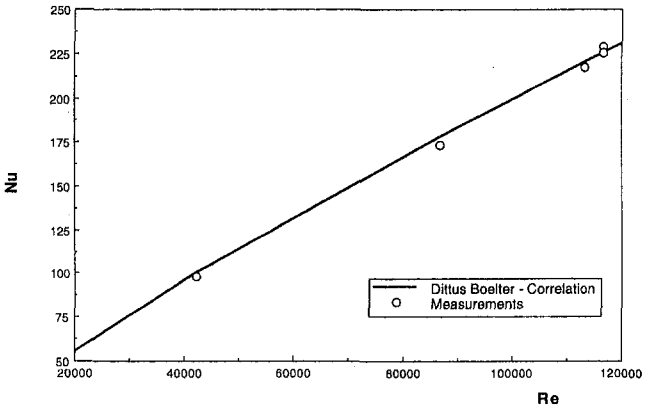

Fig. 13 Average Nusselt number

around a mean value of 0.89. This value may be compared with the theoretical value of 0.833 for a fully developed pipe flow using $\frac{1}{7}$-power laws for the velocity and temperature profiles with an isothermal surface, if $\overline{T_f}(t)$ were the bulk temperature. Since mixing is enhanced in the square duct due to the secondary flow, the determined value is quite reasonable. In Fig. 12 the measured centerline temperature is compared with the calculated value using $\gamma = 0.89$ and the average calculated fluid temperature history $\overline{T_f}(t)$.

Finally, the measured heat transfer coefficients for the different tests have been averaged over the test surface and compared to the correlation of Dittus and Boelter for various Reynolds numbers:

$$\mathrm{Nu} = 0.023\ \mathrm{Re}^{0.8}\ \mathrm{Pr}^{0.4} \tag{26}$$

in Fig. 13.

Conclusions

A simplified model describing the time-dependent local fluid temperature driving the local heat transfer in a transient heat transfer test was derived for long internal cooling channels. Using at least two surface temperature indications, the local heat transfer coefficient can be determined without an explicit energy balance. An upstream heat transfer parameter characterizes the influence of the upstream wall heat loss on the local fluid temperature, which is the adiabatic wall temperature in the general situation. As shown in the experiment, for well-mixed flow this local fluid temperature reflects the fluid bulk temperature very well. The model can be generalized to situations with varying mass flow in the streamwise direction, such as cooling channels having film cooling ejection.

Acknowledgments

The authors would like to thank H. Schaer and P. S. Wu for their help in preparing the experiments.

References

Baughn, J. W., and Yan, X., 1992, "Local Heat Transfer Measurements in Square Ducts With Transverse Ribs," *Enhanced Heat Transfer,* ASME HTD-Vol. 102, pp. 1–7.

Besserman, D. L., and Tanrikut, S., 1992, "Comparison of Heat Transfer Measurements With Computations for Turbulent Flow Around a 180 Degree Bend," ASME *Journal of Turbomachinery,* Vol. 114, pp. 865–872.

Blair, M. F., Wagner, J. H., and Steuber, G. D., 1991, "New Applications of Liquid-Crystal Thermography in Rotating Turbomachinery Heat Transfer Research," ASME Paper No. 91-GT-354.

Butler, R. J., and Baughn, J. W., 1996, "The Effect of the Thermal Boundary Condition on Transient Method Heat Transfer Measurements on a Flat Plate With a Laminar Boundary Layer," ASME JOURNAL OF HEAT TRANSFER, Vol. 118, pp. 831–837.

Chyu, M. K., Ding, H., Downs, J. P., Van Sutendael, A., and Soechting, F. O., 1997, "Determination of Local Heat Transfer Coefficient Based on Bulk Mean

Temperature Using a Transient Liquid Crystals Technique," ASME Paper No. 97-GT-489.

Clifford, R. J., Jones, T. V., and Dunne, S. T., 1983, "Techniques for Obtaining Detailed Heat Transfer Coefficient Measurements Within Gas Turbine Blade and Vane Cooling Passages," ASME Paper No. 83-GT-58.

Clifford, R. J., 1985, "Rotating Heat Transfer Investigations on a Multipass Cooling Geometry," AGARD Conference on Heat Transfer and Cooling in Gas Turbines, CP 390 Paper 2, Bergen.

Doetsch, G., 1970, *Einfuehrung in Theorie und Anwendung der Laplace-Transformation,* Birkhaeuser Verlag, Basel und Stuttgart.

Grigull, U., and Sandner, H., 1990, *Waermeleitung,* 2nd ed., Springer.

Ireland, P. T., and Jones, T. V., 1985, "The Measurement of Local Heat Transfer Coefficients in Blade Cooling Geometries," AGARD Conference on Heat Transfer and Cooling in Gas Turbines, CP 390 Paper 28, Bergen.

Metzger, D. E., and Larson, D. E., 1986, "Use of Melting Point Surface Coatings for Local Convection Heat Transfer Measurements in Rectangular Channel Flows With 90-deg Turns," ASME JOURNAL OF HEAT TRANSFER, Vol. 108, pp. 48–54.

Press, W. H., Flannery, B. P., Teukolsky, S. A., and Vetterling, W. T., 1989, *Numerical Recipes—The Art of Scientific Computing,* Cambridge University Press.

Saabas, J., Arora, S. C., and Abdel Messeh, W., 1987, "Application of the Transient Test Technique to Measure Local Heat Transfer Coefficients Associated With Augmented Airfoil Cooling Passages," ASME Paper No. 87-GT-212.

Schumann, T. E. W., 1929, "Heat Transfer: A Liquid Flowing Through a Porous Prism," *J. Franklin Inst.,* Vol. 208, pp. 405–416.

Sucec, J., 1981, "An Improved Quasi-Steady Approach for Transient Conjugated Forced Convection Problems," *Int. Journal Heat Mass Transfer,* Vol. 24, pp. 1711–1722.

Vedula, R. J., and Metzger, D. E., 1991, "A Method for the Simultaneous Determination of Local Effectiveness and Heat Transfer Distributions in Three-Temperature Convection Situations," ASME Paper No. 91-GT-345.

Wagner, J. H., Johnson, B. V., and Kopper, F. C., 1991, "Heat Transfer in Rotating Serpentine Passages With Smooth Walls," ASME *Journal of Turbomachinery,* Vol. 120, pp. 321–330.

Wang, Z., Ireland, P., Jones, T. V., and Kohler, S. T., 1994, "Measurements of Local Heat Transfer Coefficient Over the Full Surface of a Bank of Pedestals With Fillet Radii," ASME Paper No. 94-GT-307.

Wang, Z., Ireland, P. T., Jones, T. V., and Davenport, R., 1996, "A Color Image Processing System for Transient Liquid Crystal Heat Transfer Experiments," ASME *Journal of Turbomachinery,* Vol. 118, pp. 421–427.

Wang, Z., Ireland, P., Kohler, S. T., and Chew, J. W., 1998, "Heat Transfer Measurements to a Gas Turbine Cooling Passage With Inclined Ribs," ASME *Journal of Turbomachinery,* Vol. 120, pp. 63–69.

APPENDIX

Analytical Solution

The governing equations for the conjugate convection problem with uniform heat transfer coefficient are:

Fluid:

$$\frac{\partial T_f}{\partial x} = \frac{hU}{\dot{m}c_p}\left(T_W(x, t) - T_f(x, t)\right) \tag{A.1}$$

with the initial condition:

$$T_f(x, 0) = (T_E - T_0)\exp(-bx) + T_0 \tag{A.2}$$

where $b = hU/\dot{m}c_p$, and the boundary condition:

$$T_f(0, t) = T_E. \tag{A.3}$$

Solid:

$$\frac{\partial T_s}{\partial t} = \frac{\lambda_s}{\varrho_s c_{ps}}\frac{\partial^2 T_s}{\partial y^2} = a\frac{\partial^2 T_s}{\partial y^2} \quad 0 < y < \infty \tag{A.4}$$

with the initial condition:

$$T_s(x, y, 0) = T_0 \tag{A.5}$$

and the boundary condition:

$$-\lambda_s\frac{\partial T_s}{\partial y}(x, y = 0, t) = h(T_f - T_W). \tag{A.6}$$

Using the dimensionless variables

$$\Theta_f = \frac{T_f - T_0}{T_E - T_0} \quad \Theta_W = \frac{T_W - T_0}{T_E - T_0} \quad \Theta_s = \frac{T_s - T_0}{T_E - T_0} \tag{A.7}$$

we obtain for the fluid:

$$\frac{\partial \Theta_f}{\partial x} = b(\Theta_W - \Theta_f) \tag{A.8}$$

with

$$\Theta_f = \exp(-bx) \quad t = 0 \tag{A.9}$$

and

$$\Theta_f = 1 \quad x = 0 \tag{A.10}$$

and for the solid:

$$\frac{\partial \Theta_s}{\partial t} = a\frac{\partial^2 \Theta_s}{\partial y^2} \tag{A.11}$$

with

$$\Theta_s = 0 \quad t = 0 \tag{A.12}$$

and

$$-\lambda_s\frac{\partial \Theta_s}{\partial y} = h(\Theta_f - \Theta_W) \quad y = 0 \tag{A.13}$$

Using Laplace Transforms for the solid, the wall temperature in the Laplace domain is obtained as:

$$\overline{\Theta_W} = \overline{\Theta_f}\frac{\beta}{\beta + B} \tag{A.14}$$

where $\beta = h/\lambda_s$, $B = \sqrt{p/a}$, and p is the Laplace variable.

Using Laplace Transforms for the fluid and inserting Eq. (A.14) we obtain:

$$\overline{\Theta_f} = \frac{1}{p}\exp\left(\frac{-bBx}{\beta + B}\right) \tag{A.15}$$

For finding the inverse transformation of Eq. (A.15)

$$\overline{\Theta_f} = \exp(-bx)\frac{1}{p}\exp\left(\frac{b\beta x}{\beta + B}\right)$$

$$= \exp(-bx)\frac{1}{p}\exp\left(\frac{D}{\beta + B}\right) \tag{A.16}$$

the term:

$$F(p) = \exp\frac{D}{\beta + \sqrt{\frac{p}{a}}} \tag{A.17}$$

is considered. Using a power series expansion:

$$F(p) = 1 + \sum_{n=1}^{\infty}\frac{D^n}{\left(\beta + \sqrt{\frac{p}{a}}\right)^n}\frac{1}{n!} \tag{A.18}$$

and

$$\frac{1}{\left(\beta + \sqrt{\frac{p}{a}}\right)^n} = \frac{1}{\left(\frac{p}{a}\right)^{n/2}\left(1 + \beta\sqrt{\frac{a}{p}}\right)^n} \tag{A.19}$$

we can consider the binomial series:

$$\frac{1}{\left(1+\beta\sqrt{\frac{a}{p}}\right)^n}=1+\sum_{m=1}^{\infty}\binom{-n}{m}\left(\beta\sqrt{\frac{a}{p}}\right)^m \quad (A.20)$$

which is valid for $|p| > \beta^2 a$. By choosing another summation index, $k = n + m$, we obtain:

$$\frac{1}{p}F(p)=\frac{1}{p}+\sum_{n=1}^{\infty}\frac{D^n}{n!}\frac{a^{n/2}}{p^{1+(n/2)}}+\sum_{k=2}^{\infty}\left\{\sum_{n=1}^{k-1}(-1)^{k-n}\frac{D^n\beta^{k-n}}{(n-1)!n!(k-n)!}\right\}\times(k-1)!a^{k/2}\frac{1}{p^{1+(k/2)}}=G(p) \quad (A.21)$$

The inverse transformation for this expression is (Doetsch, 1970):

$$g(t)=1+\sum_{n=1}^{\infty}\frac{D^n}{n!}a^{n/2}\frac{t^{n/2}}{\Gamma\left(1+\frac{n}{2}\right)}+\sum_{k=2}^{\infty}\left\{\sum_{n=1}^{k-1}(-1)^{k-n}\frac{D^n\beta^{k-n}}{(n-1)!n!(k-n)!}\right\}\times(k-1)!a^{k/2}\frac{t^{k/2}}{\Gamma\left(1+\frac{k}{2}\right)} \quad (A.22)$$

So finally the fluid temperature is given by:

$$\frac{T_f-T_0}{T_E-T_0}=\exp(-bx)\left\{1+\sum_{n=1}^{\infty}\frac{(b\beta)^n}{n!}a^{n/2}\frac{t^{n/2}}{\Gamma\left(1+\frac{n}{2}\right)}x^n+\sum_{k=2}^{\infty}\left\{\sum_{n=1}^{k-1}(-1)^{k-n}\frac{(b\beta)^n\beta^{k-n}}{(n-1)!n!(k-n)!}x^n\right\}\times(k-1)!a^{k/2}\frac{t^{k/2}}{\Gamma\left(1+\frac{k}{2}\right)}\right\} \quad (A.23)$$

which is valid for sufficiently small $\beta^2 at$.

For large values of $\beta^2 at$ a long time solution can be obtained in the following way:

$$G(p)=\frac{1}{p}\exp\frac{D}{\beta+\sqrt{\frac{p}{a}}}=\frac{1}{p}+\frac{1}{p}\sum_{n=1}^{\infty}\frac{D^n}{\beta^n\left(1+\frac{1}{\beta}\sqrt{\frac{p}{a}}\right)^n}\frac{1}{n!} \quad (A.24)$$

Using the binomial series

$$\frac{1}{\left(1+\frac{1}{\beta}\sqrt{\frac{p}{a}}\right)^n}=1+\sum_{m=1}^{\infty}\binom{-n}{m}\left(\frac{1}{\beta}\sqrt{\frac{p}{a}}\right)^m \quad (A.25)$$

which is valid for $|p| < \beta^2 a$ and consider for large times ($p \to 0$) only the term $m = 1$, $G(p)$ can be approximated by:

$$G(p)\simeq\frac{1}{p}\exp\left(\frac{D}{\beta}\right)-\frac{1}{\beta}\frac{1}{\sqrt{pa}}\sum_{k=0}^{\infty}\left(\frac{D}{\beta}\right)^{k+1}\frac{1}{k!} \quad (A.26)$$

where $k = n - 1$.

Rewriting Eq. (A.26) gives

$$G(p)\simeq\frac{1}{p}\exp\left(\frac{D}{\beta}\right)-\frac{1}{\sqrt{p}}\frac{D}{\beta^2\sqrt{a}}\exp\left(\frac{D}{\beta}\right) \quad (A.27)$$

The inverse transformation of Eq. (A.27) is given by

$$g(t)\simeq\exp\left(\frac{D}{\beta}\right)-\frac{D}{\beta^2\sqrt{a}}\exp\left(\frac{D}{\beta}\right)\frac{1}{\sqrt{\Pi t}} \quad (A.28)$$

with $D/\beta = bx$, which leads to (using Eq. (A.16))

$$\frac{T_f-T_0}{T_E-T_0}\simeq 1-\frac{bx}{\beta\sqrt{a\Pi t}} \quad (A.29)$$

Equation (A.29) is identical to the large time approximation of Eq. (16) using

$$\exp(\gamma^2)\,\mathrm{erfc}\,(\gamma)\simeq\frac{1}{\gamma\sqrt{\Pi}} \quad (A.30)$$

for large γ and taking into account that for a constant heat transfer coefficient $\alpha = h$.

Table 1 Uncertainty analysis: contribution of individual measurands for a typical experiment

parameter (units)	value	ΔX_i	$\frac{\Delta X_i}{h}\frac{\delta h}{\delta X_i}$ x100	$\frac{\Delta X_i}{\alpha}\frac{\delta \alpha}{\delta X_i}$ x100
$\frac{Ux}{\dot{m}c_p}(\frac{m^2K}{W})$	2.e-3	2.e-4	2.5	1.5
$\sqrt{k}(\frac{W}{m^2K}\sqrt{s})$	569	29	6.5	4.3
T_E(°C)	74.4	0.2	1.1	2.9
T_0(°C)	19.2	0.1	0.1	3.8
T_{LC1}(°C)	34.8	0.1	1.6	12.5
T_{LC2}(°C)	39.7	0.1	0.1	1.5
T_{LC3}(°C)	45.2	0.1	2.0	11.9
t_1(s)	3.77	0.04	1.1	8.4
t_2(s)	7.91	0.04	0.1	0.5
t_3(s)	16.54	0.04	0.4	2.2
		uncertainty:	7.6	20.5

Temperature-Dependent Absorptances of Ceramics for Nd:YAG and CO_2 Laser Processing Applications

Z. Zhang

M. F. Modest
Fellow ASME

Department of Mechanical Engineering,
The Pennsylvania State University,
University Park, PA 16802

The absorptance of a material at the laser wavelength and as a function of temperature, ranging from room temperature to the removal point, significantly affects the efficiency of the laser machining process. A priori predictions of a laser machining process, using either simplistic or sophisticated models, require knowledge of the material's absorptance behavior. An experimental apparatus for such measurements is described. The device consists of a specimen mounted inside an integrating sphere, heated rapidly by a CO_2 or a Nd:YAG laser. Reflectances are measured with a small focused probe laser (Nd:YAG or CO_2), while specimen surface temperatures are recorded by a high-speed pyrometer. Experimental results have been obtained for wavelengths of 1.06 μm (Nd:YAG) and 10.6 μm (CO_2) for graphite, alumina, hot-pressed silicon nitride, sintered α-silicon carbide, as well as two continous-fiber ceramic matrix composites (SiC-based). Data are presented for temperatures between room temperature and the ablation/decomposition points.

Introduction

Extensive application of lasers in materials processing has led to the development of several theoretical models to predict *a priori* the interaction between lasers and materials, e.g., Dabby and Paek (1972), Abakians and Modest (1988), Chryssolouris (1991), Vorreiter et al. (1991), Ramanathan and Modest (1992), Roy and Modest (1993), Bang et al. (1993), Modest et al. (1995), Modest (1996). These range from simple one-dimensional ones to complex three-dimensional transient models. To validate and use these models, the spectral absorptance of the material at the laser wavelength and at temperatures up to its "removal temperature" (the temperature at which material removal occurs, be it by ablation, decomposition, microexplosions, etc., depending on the material) is required. Currently, sufficient and accurate experimental data of this nature are not available. To measure the temperatures during laser processing, infrared pyrometry appears most suitable. However, since the temperature obtained by the pyrometer is the radiance temperature, knowledge of the emittance of the material at the pyrometer wavelength is again required to determine the actual temperature. In this article a new experimental setup to determine high-temperature spectral absorptances rapidly at Nd:YAG and CO_2 wavelengths (1.06 μm and 10.6 μm), is presented. Results from these experiments can supply the necessary input data for these theoretical models. Since pyrometers tend to operate around 1 μm, the Nd:YAG absorptance measurements also provide the necessary emittance data for infrared pyrometry.

Various experimental techniques have been developed to measure the radiative properties of opaque materials. These may be separated into three loosely defined groups: calorimetric emission measurements, radiometric emission measurements, and reflection measurements (Modest, 1993). The calorimetric emission measurement methods and radiometric emission measurement methods require the specimen to be maintained at the temperature at which the radiative properties are to be measured. Therefore, it is unrealistic to measure the radiative properties of solids near their removal temperature using these methods. Best suited for the present task with its extreme temperatures appears to be an integrating sphere reflectometer (Jacquez and Kuppenheim, 1955).

Jacquez and Kuppenheim (1955) have provided the general theory of the integrating sphere for hemispherical spectral reflectance measurements. They describe two measurement techniques. In the first method, the so-called "substitution method," the reflected signal of the specimen and the standard reference are measured consecutively by replacing the sample by the standard, and the ratio of the respective detector readings is taken to determine the reflectance. In the second method, the so-called "comparison method," the sphere has two sample holders, and the sample and the standard reference are each placed in their own positions. The light beam is switched from sample to standard and the ratio of the respective detector readings is again determined. Efficiencies and errors for both methods were discussed by Jacquez and Kuppenheim.

Spectral hemispherical emittance measurements at high temperatures have been carried out by a number of researchers. One of the early works was done by Kneissl and Richmond (1968). Using an integrating sphere, they heated refractory metals and ceramics by induction up to 2000 K. A He–Ne laser, which operated at several visible and near-infrared wavelengths, was used together with corresponding bandpass filters to obtain high signal-to-noise ratios. A two-detector ratioing system was used to offset the power fluctuation of the He–Ne laser. Bober and co-workers (Bober and Karow, 1977; Bober, 1980; Bober et al., 1980) also measured the spectral emittance and reflectance of oxide and carbide ceramics up to 4000 K at several distinct wavelengths between visible and 10.6 μm. They developed an integrating-sphere laser reflectometer, which used one laser beam for heating together with simultaneous irradiation of the specimen's surface by a second probe laser at a different wavelength. The probe laser was modulated by either a mechanical chopper or an electro-optic ADP modulator and demodulated by a fast lock-in amplifier, which rejected the emission from the hot spot. The heating process took between 1 and 100

Contributed by the Heat Transfer Division for publication in the JOURNAL OF HEAT TRANSFER. Manuscript received by the Heat Transfer Division November 12, 1996; revision received January 23, 1998. Keywords: High Temperature, Laser, Materials, Measurement Techniques, Radiation. Associate Technical Editor: T. Tong.

ms. A simpler approach was used by Ramanathan and Modest (1993), who used a single laser beam as both heating and probe light source. To smooth out fluctuations in laser power, a thermopile detector was used for the reflectance measurements at the cost of temporal resolution.

In a reflectometer the energy falling onto the detector consists of several parts: the reflected radiation of the probe beam, the emitted radiation from the hot specimen, and, if a laser is used for heating, reflected radiation from the heating laser. The method adopted by Kneissl and Richmond (1968) cannot reject the emission from the specimen completely. Bober and co-workers used a combination of chopper and lock-in amplifier to overcome this problem, but they did not consider power fluctuations of the probe laser. In the scheme adopted by Ramanathan and Modest (1993), their thermopile detector had a response time of 0.3 s, while the heating process took only 1 s. This made it difficult for the detector to keep up with the changing signal, i.e., the detector may have lagged behind the changing signal, giving too flat a response. Another disadvantage of their scheme was that they used a single laser for both heating and probing. Therefore, the irradiated spot of the specimen was not isothermal due both to the spatial laser beam profile and to conduction losses. For a single beam, the irradiation is reflected over a range of temperatures rather than at a single temperature, the highest temperature at the beam center being reported by the pyrometer. For this reason, the use of a single laser for both heating and probing can result in significant inaccuracy.

A new experimental apparatus for the rapid measurement of solid reflectance at high temperatures has been constructed. The setup incorporates dual integrating spheres to eliminate power fluctuations of the probe light source, a combination of lock-in amplifier and chopper to reject emission from the specimen, and a separate heating laser at a different wavelength and with a substantially larger spot size to achieve an isothermal probe spot. A pyrometer with a spectral response of 0.8 $\sim$ 1.0 μm was used to measure the sample temperature. The emittance of the material at the Nd:YAG wavelength was used to infer actual temperatures from the radiance temperature measured by the instrument. The absorptance as a function of temperature at Nd:YAG and CO_2 wavelengths is presented for several materials.

Experimental Setup

The experimental setup for measuring the reflectance of a sample at elevated temperature is shown in Fig. 1, consisting of two integrating spheres, a heating laser, a probe laser, two detectors, a mechanical chopper, and two lock-in amplifiers and laser optics. The specimen was mounted at the center of the sample integrating sphere (RTC-060-IG), which was purchased from Labsphere. The inner wall of the sphere and the sample mount are coated with Infra-Gold, which has a reflectance of 95 percent over the range of 1 $\sim$ 20 μm. The sample sphere is 15 cm in diameter and has three 2.5 cm access ports on the top, and another 1.25 cm detector port is located at the side. The detector port is well baffled from the sample to ensure that the radiation is isotropically scattered before reaching the detector. The specimen was irradiated by a probe laser with an incidence angle of roughly 20 deg, and a beam diameter of approximately 100 $\sim$ 200 μm. An Apollo 575 tunable CO_2 laser was used as probe laser for 10.6 μm property measurements, while for 1.06 μm a Control 512QG Nd:YAG laser was used. In each case, the probe laser beam was modulated by a mechanical chopper (SR540, Stanford Research) running at roughly 3 kHz, near the maximum frequency of the chopper. The modulated signal was detected by an MCT detector (Graseby Infrared). This detector performs well at both 1.06 and 10.6 μm. The detector was connected to the lock-in amplifier (SR850, Stanford Research). The modulation of the probe laser, together with a laserline bandpass filter in front of the detector to block the radiation at other wavelengths, allows the measurement of the reflected

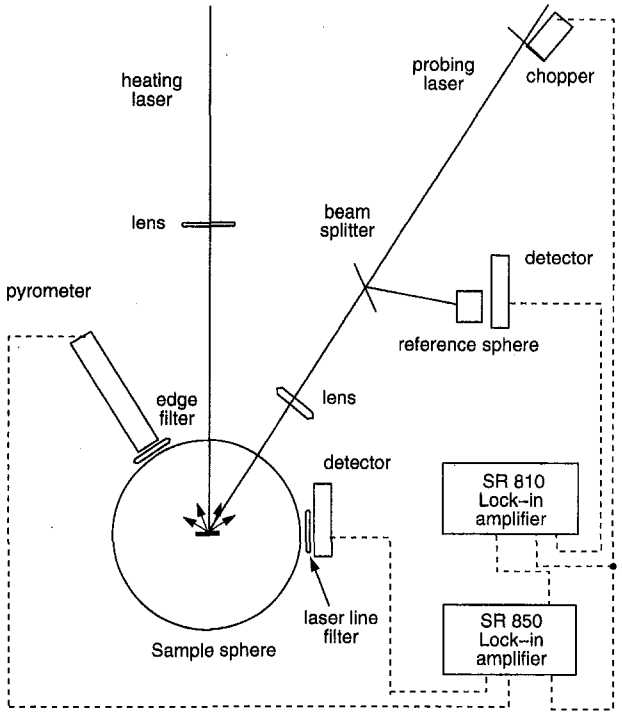

Fig. 1 Schematic of experimental setup

radiation in the presence of intense radiation emitted from the heated zone as well as reflection from the strong heating laser. The lock-in amplifier was set to run at a constant time of 1 ms, which was restricted by the chopping frequency. In order to eliminate errors due to power fluctuation of the probe laser, the probe beam was split with a part of the beam going into a reference integrating sphere (IS-020-IG, Labsphere). The signal of the reference sphere monitoring the temporal power fluctuations was recorded by another MCT detector (Graseby Infrared) and lock-in amplifier (SR810, Stanford Research).

The specimen was heated by a second laser operating at a different wavelength from the probe laser: During 1.06 μm measurements, a CO_2 laser (Coherent Everlase S51) was used for heating, while a Nd:YAG laser (Hobart HLP 3000) was used for heating during 10.6 μm property measurements. The sample sphere was purged with argon during the heating process to suppress chemical reactions. The heating laser was only partially focused to give a spot of roughly 1 mm^2. In this configuration the heating lasers were able to heat up the specimens to their removal temperature within 100–200 ms, which further minimized chemical reactions. The probe laser was focused onto the center of the heated zone. First, the two lasers were aligned by using the internal alignment laser. Then both lasers were turned on to burn spots on a test sample. The alignment was adjusted to center the probe spot to the heating spot. Accurate alignment of the probe laser to the center of the considerably larger heated zone ensured that the probed spot was essentially isothermal.

To align the pyrometer for Nd:YAG probing, the probe laser spot location was determined using an IR viewer, after which a He–Ne laser was focused onto the spot to indicate its position. For 10.6 μm measurements the probe laser, when aimed at the specimen with the chopper off, was strong enough to heat the specimen to a temperature, whose emission was strong enough to be visible in the pyrometer's eyepiece, and the pyrometer was aligned to the center of this hot spot. The pyrometer was designed and constructed specifically for this experiment by Ramanathan et al. (1996), and was aimed at the probe laser spot to measure the surface temperature of interest. The pyrometer has a viewing area of 50 μm in diameter and time constant

of 10 μs. The spectral response of the pyrometer is approximately 0.8 $\sim$ 1.1 μm. In order that the pyrometer can be used with a (heating or probe) Nd:YAG laser, a 0.95 μm short-pass filter was added in front of the pyrometer. The pyrometer was recalibrated after the filter was added.

The demodulated reflection and temperature signals were digitally recorded. The specimen was then replaced by a standard reference with known reflectance without disturbing the setup; only the probe laser was turned on this time and the radiation signals from both integrating spheres were recorded. The standard references used were a spectralon diffuse reflectance standard (SRS-99-010) and an Infra-Gold coated sample both purchased from Labsphere. The optics for the CO_2 laser path were made of zinc selenide, and the optics for the Nd:YAG laser path were made of calcium fluoride.

Jacquez and Kuppenheim (1955) showed that for an integrating sphere with uniform wall coating the radiation, which passes out of an aperture of the sphere, is proportional to the specimen's reflectance and a configuration coefficient, which is a function of the port area, the inner surface area of the sphere, and the reflectance of the wall coating. When the port area is small compared with the inner surface area of the sphere, which is an appropriate assumption for most integrating spheres, the configuration coefficient can be regarded as a constant. Furthermore, if the detectors are working in their linear range, it follows that

$$\frac{I_s}{I_r} = \frac{V_s}{V_r} = \frac{\rho_s}{\rho_r}, \tag{1}$$

where I_s and I_r are the intensities of the radiation, ρ_s and ρ_r are reflectances of the specimen and the reference, and V_s and V_r are signals produced by specimen and reference, respectively. For an opaque specimen, the spectral absorptance α and emittance ϵ are given by

$$\epsilon = \alpha = 1 - \rho_s. \tag{2}$$

Since temperature and reflectance signals are recorded simultaneously, they can be used together to provide absorptance versus temperature data. Because the pyrometer used has a radiance temperature range of 1500 K to 3500 K (after addition of the 0.95 μm bandpass filter), the experiment cannot match the absorptance data to radiance temperatures below 1500 K, although it still provides the value of absorptances at room temperature.

Results and Discussion

Between four and six different reflectance measurements were carried out at each wavelength for each material, using new specimens for each experiment. Each experiment was carried out at different power levels, to ascertain that there were no serious changes of reflectance with irradiation levels. It was observed, as noted by Ramanathan and Modest (1993) previously, that the removal temperature of each material increases somewhat with irradiation level; this is in qualitative agreement with an ablation rate according to an Arrhenius relation. Because of the limited number of runs, and because the maximum temperature reached in each experiment (but on the same material) was different, determination of standard deviations was deemed inappropriate. Instead, data for reflectance versus radiance and actual temperatures are presented in terms of average values (averaging results from different irradiation powers), together with upper and lower bounds. For the highest temperatures, whenever fewer than three data points remained, only the average reflectance is shown.

Hot-Pressed Silicon Nitride. The hot-pressed silicon nitride used in this study contains 6 wt% Y_2O_3 and 2 wt% Al_2O_3 as additives and was purchased from GTE Inc. Upon laser heating silicon nitride will decompose into liquid silicon and nitrogen. Absorptance data for Si_3N_4 at 10.6 μm and 1.06 μm are shown

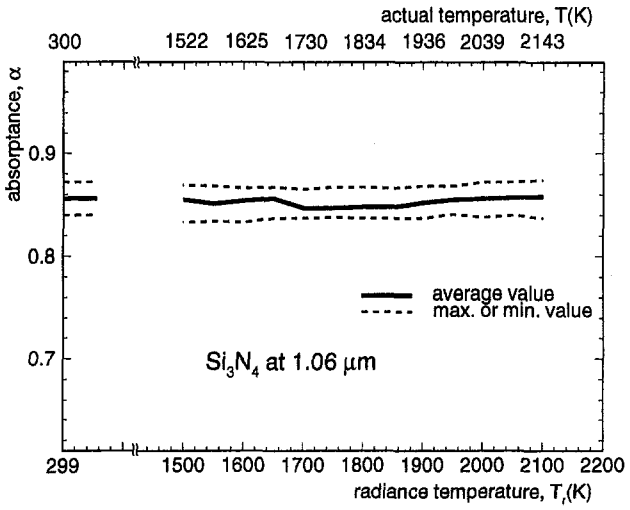

Fig. 2 Absorptance versus temperature of Si_3N_4 at 1.06 μm

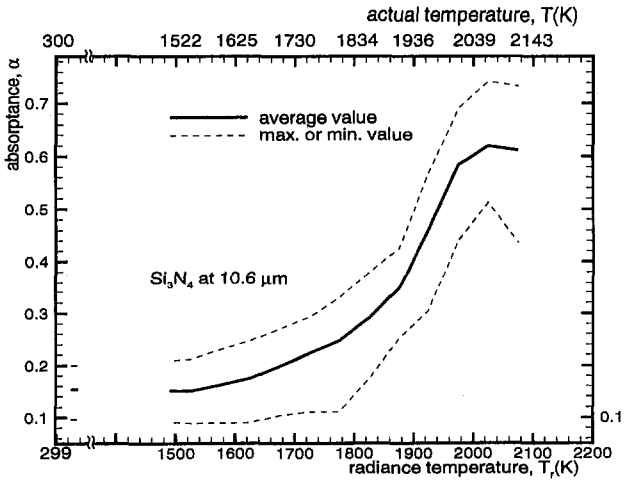

Fig. 3 Absorptance versus temperature of Si_3N_4 at 10.6 μm

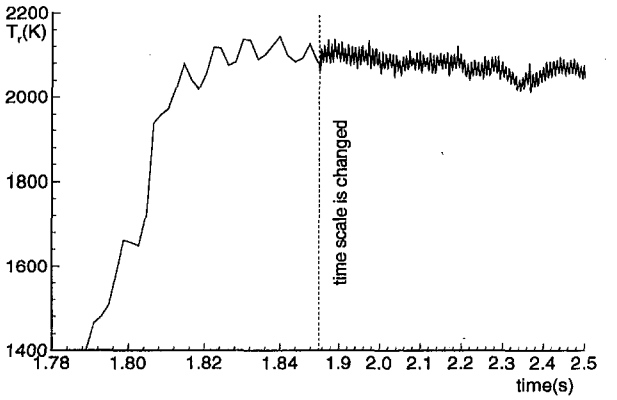

Fig. 4 Typical temperature signal of Si_3N_4 during heating process

in Figs. 2 and 3 for temperatures up to its decomposition temperature of approximately 2170 K (Pehlke and Elliot, 1959; Ramanathan and Modest, 1993). The absorptance of Si_3N_4 at 1.06 μm remains almost constant at 0.85 for temperatures all the way up to 2170 K. The heating process shows the decomposition radiance temperature when the signal from the pyrometer reaches a constant as seen in Fig. 4 for a typical run. The

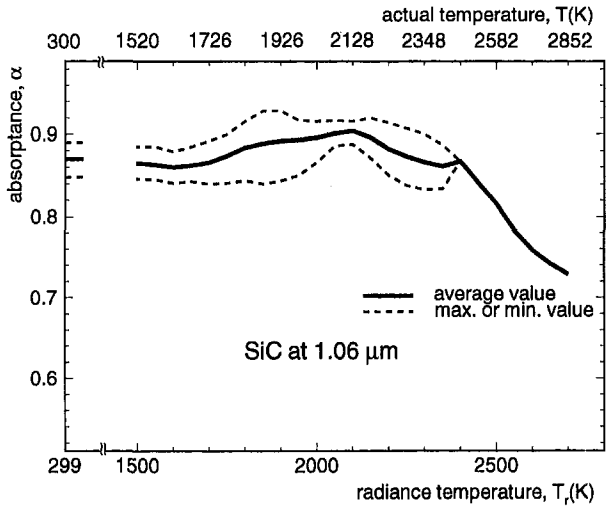

Fig. 5 Absorptance versus temperature of SiC at 1.06 μm

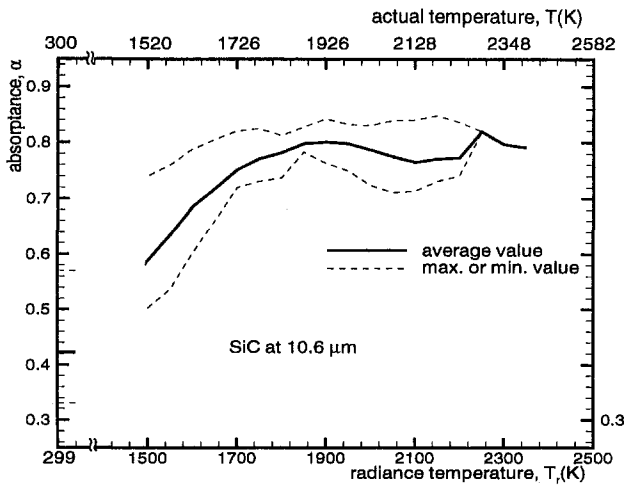

Fig. 6 Absorptance versus temperature of SiC at 10.6 μm

radiance temperature during decomposition is seen to be approximately 2100 K. Using the spectral emittance at 1.06 μm, this yields an actual decomposition temperature of 2143 K, which agrees well with the value provided by Pehlke and Elliot (1959). The periodicity in the temperature signal is due to a 120 Hz fluctuation in the power of the heating laser. Since the temporal reflected signal also shows the same periodicity, it is canceled out in the absorptance versus temperature signal.

The absorptance at 10.6 μm measured at room temperature with the present setup was found to be 0.15, which is slightly lower than that reported by Roy et al. (1993), who gave a value of 0.18. The absorptance remains low until about 1600 K and beyond that changes appreciably with temperature. Si_3N_4 is known to have a reflection band at around 10 μm (Wallace, 1983). The rapid increase of absorptance can be attributed to a band shift at elevated temperatures. The present result is considerably different from that of Ramanathan and Modest (1993), who reported that the absorptance increases only moderately as the temperature increases from 1300 K to 2200 K. As discussed earlier, due to the slow detector used in their experiment, their apparatus apparently did not respond fast enough to the rapidly changing signal.

Sintered α-Silicon Carbide. Sintered α-silicon carbide was purchased from Carborundum Inc., in the form of a 3.5-mm-thick sheet. No data are available on the additives used in the manufacture of this material. Upon laser heating SiC decomposes into several different gases. Figure 5 shows that the absorptance at 1.06 μm increases slightly with temperature up to 2200 K, after which it decreases to 0.73 at 2900 K. SiC is known to have a 12.6 μm reflection band (Spitzer et al., 1959) (fundamental lattice band), and the reflection band shifts to larger wavelengths as the temperature rises, as do other ionic crystals (Hass, 1960; Jasperse et al., 1966; Chang and Mitra, 1972). Because of the band shift one would expect to see a decrease in reflectance, and hence an increase in absorptance. Roy et al. (1993) reported that the normal absorptance of SiC at 10.6 μm increased with temperature from 0.2 at room temperature to 0.85 at 1273 K. Our data in Fig. 6 show that the absorptance at 10.6 μm increases from 0.6 at 1500 K to 0.8 at 1900 K and then decreases marginally to 0.76. This difference may be attributed to the fact that Roy et al. (1993) used furnace heating, which may have resulted in a thin SiO_2 layer on the surface at fairly low temperature, while laser heating takes only a fraction of a second, so that the oxidation can occur only close to the decomposition temperature.

Graphite. The graphite measured in this study is black graphite (McMaster-Carr), which is expected to ablate at approximately 4000 K. The absorptances at 1.06 μm and 10.6 μm are shown in Fig. 7. The absorptance at 1.06 μm is about 0.95 from 1500 K to 3400 K, which agrees well with the existing literature for the visible range (Wilson, 1964). On the other hand, the absorptance at 10.6 μm shows a slight temperature dependence, increasing from 0.73 at 1500 K to 0.84 at 3400 K.

Alumina. The alumina used in this study was AD99 and was purchased from Coors Corp. Unlike all the other ceramics in this study (which decompose mostly into gases without melting first), alumina is known to melt at around 2315 K under equilibrium conditions (Chase et al., 1985). The results presented in Fig. 9 are the absorptance at 1.06 μm, showing that alumina is highly reflective until about 1800 K, and its absorptance starts to increase sharply thereafter, reaching 0.95 at 2800 K. The results differ from those of Blair (1960), who used a "direct technique," which is known to be susceptible to large errors at short wavelengths (Battuello and Ricolfi, 1989). Due to the low emittance at 1.06 μm, the pyrometer could not detect temperatures below 1780 K (or 1500 K radiance temperature). Figure 8 does not show a distinct change in absorptance at the melting point of 2315 K. Indeed, for most of the specimen the temperature versus time signal did not show a distinct melting point. A typical temperature versus time signal is shown in Fig. 9: Because of the strong laser irradiation, the alumina apparently

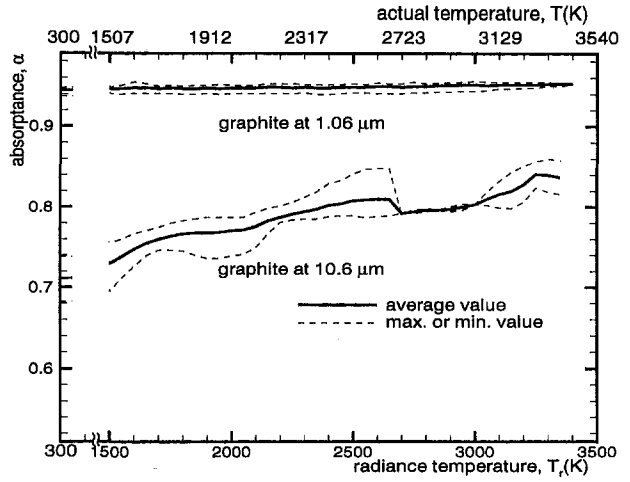

Fig. 7 Absorptance versus temperature of graphite at 1.06 and 10.6 μm

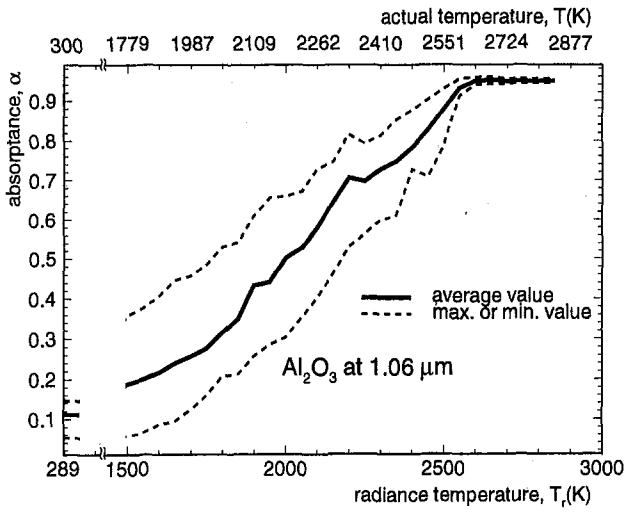

Fig. 8 Absorptance versus temperature of alumina at 1.06 μm

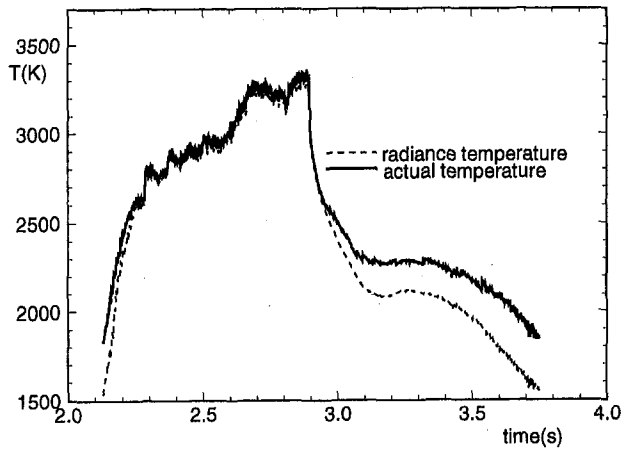

Fig. 9 Typical temperature signal of alumina during heating process

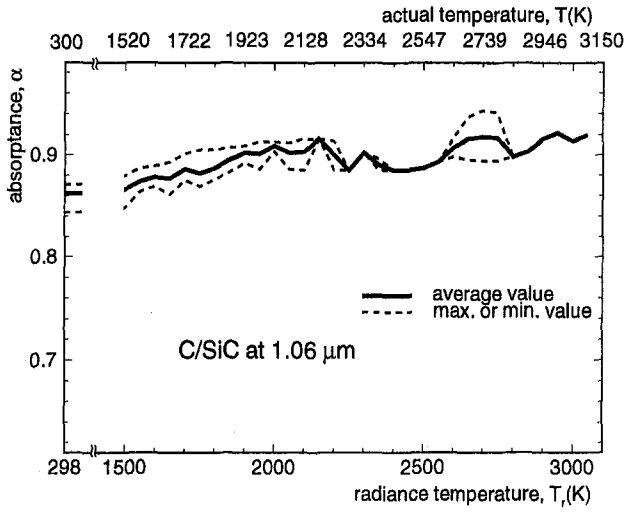

Fig. 10 Absorptance versus temperature of C/SiC at 1.06 μm

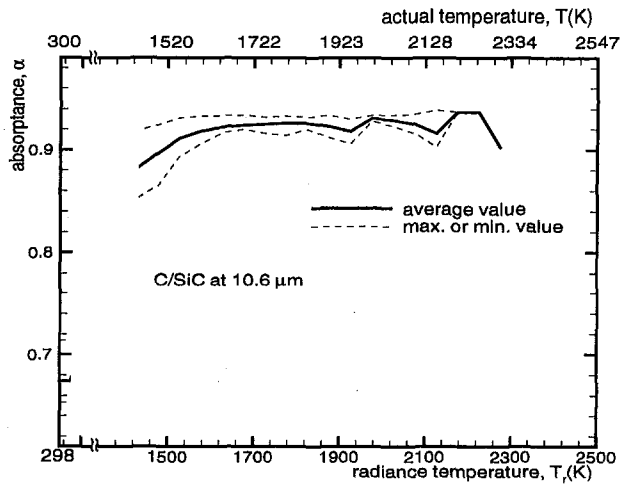

Fig. 11 Absorptance versus temperature of C/SiC at 10.6 μm

superheats to about 2600 K before starting to melt. Due to this superheating melting takes place over a range of temperatures and internal melting is possibly continuing after the laser was turned off at a surface temperature of about 3350 K. Note that during cool down there is a distinctive plateau at around 2300 K, indicating equilibrium solidification and corroborating the JANAF table's melting temperature (Chase et al., 1985). Data for the other specimens are similar, with onset of melting ranging from 2300 K to 2600 K, depending on irradiation levels. Results for 10.6 μm are not available, since the absorptance of alumina at the heating laser wavelength of 1.06 μm is only 0.18 in the temperature range between room temperature and 1800 K. This causes large amounts of heat to be dissipated to the integrating sphere, which could damage the apparatus.

Composite Materials. The composite materials considered were SiC/SiC composite (consisting of long woven β-silicon carbide fibers embedded in a β-silicon carbide matrix) and C/SiC composite (carbon fibers embedded in a β-silicon carbide matrix). They were obtained from E. I. DuPont de Nemours and Co., and contained nominally 45 vol% matrix material and 45 vol% fibers, with the rest being porosity. Upon laser heating the matrix material decomposes into gases, while some of the fibers are removed microexplosively (Ramanathan and Modest, 1995).

C/SiC. Figures 10 and 11 show the absorptance of C/SiC at 1.06 μm and 10.6 μm, respectively. The absorptance at 1.06 μm increases slightly from 0.87 at 1550 K to 0.92 at 3100 K. This is slightly higher than that of monolithic α-silicon carbide and lower than that of graphite, which was expected. The absorptance at 10.6 μm was found to be 0.7 at room temperature, which agrees with Ramanathan and Modest (1993), who reported the absorptance at 10.6 μm as 0.67 below 1250 K, and increasing almost linearly with temperature to 0.77 at 2270 K. The current study shows that the absorptance increases before the temperature reaches 1550 K, and then changes slightly from 0.9 at 1550 K to 0.93 at 2300 K. Both inherent weaknesses of Ramanathan and Modest's scheme (single beam, slow detector) would tend to have their experiment report lower-than-actual absorptance data. The absorptance of C/SiC does not have the same small peak around 2000 K as the monolithic silicon carbide. This may be attributed to the fact that the decomposition of silicon carbide is suppressed by the carbon-rich vapors (Singhal, 1976).

SiC/SiC. Figures 12 and 13 show the spectral absorptance versus temperature at 1.06 μm and 10.6 μm. At 1.06 μm the absorptance shows no appreciable change with temperature. It is higher than that of monolithic SiC, which was expected due to the material's porosity. The absorptance at 10.6 μm changes from 0.7 at 1500 K to 0.92 at 2300 K and then decreases to 0.72 at 2800 K. As expected, these value are higher than those of Ramanathan and Modest (1993), and also increase faster with temperature. The absorptance of SiC/SiC reaches a peak

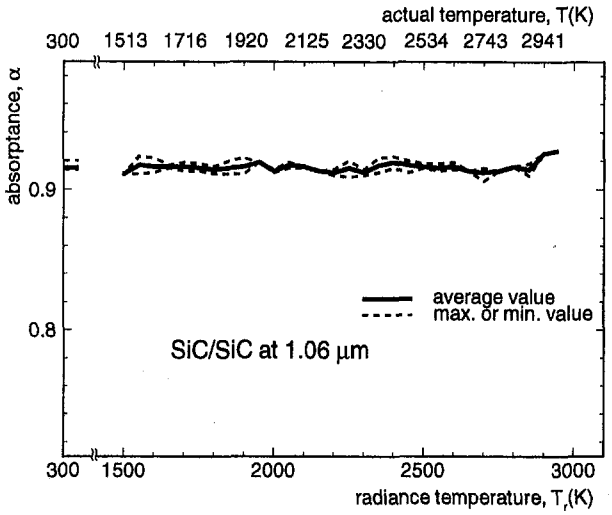

Fig. 12 Absorptance versus temperature of SiC/SiC at 1.06 μm

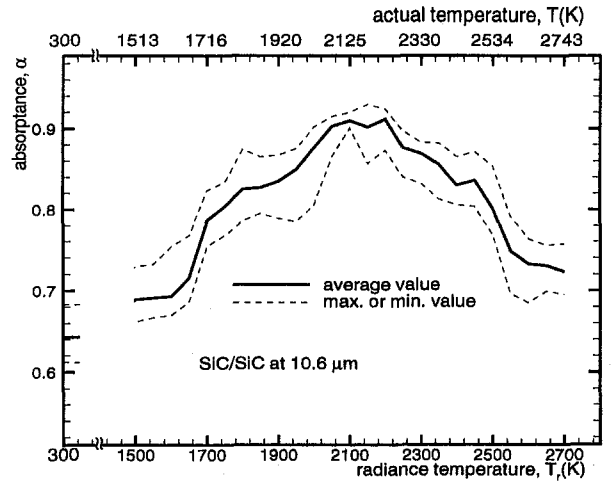

Fig. 13 Absorptance versus temperature of SiC/SiC at 10.6 μm

value at 2300 K and decreases thereafter, which is consistent with the behavior of monolithic SiC. The peak at 2300 K fades to a plateau of absorptance in Ramanathan and Modest (1993). It is also interesting to notice the peak of absorptance appearing around 2300 K in contrast to that of C/SiC, which has no peak.

Conclusions

An integrating sphere reflectometer with dual laser beams for heating and probing was constructed. The apparatus, which incorporates two integrating spheres in combination with a chopper and two lock-in amplifiers, can account for power fluctuations of the probe light source and measure the reflectance in the presence of intense ambient radiation. The hemispherical absorptances for a number of ceramics, namely silicon nitride, silicon carbide, graphite, alumina, and two composite ceramics (C/SiC and SiC/SiC), have been presented. The results can furnish reliable radiative property data for use in theoretical models of laser processing, and can improve the accuracy of infrared pyrometry.

Acknowledgments

Support for this work by National Science Foundation Grant CTS-9312325 is gratefully acknowledged.

References

Abakians, H., and Modest, M. F., 1988, "Evaporative Cutting of a Semi-Transparent Body With a Moving CW Laser," ASME JOURNAL OF HEAT TRANSFER, Vol. 110, pp. 924–930.

Bang, S. Y., Roy, S., and Modest, M. F., 1993, "CW Laser Machining of Hard Ceramics—Part II: Effects of Multiple Reflections," *International Journal of Heat and Mass Transfer,* Vol. 36, No. 14, pp. 3529–3540.

Battuello, M., and Ricolfi, T., 1989, "A Technique for Deriving Emissivity Data for Infrared Pyrometry," *High Temperatures—High Pressures,* Vol. 21, pp. 303–309.

Blair, R., 1960, "Determination of Spectral Emissivity of Ceramic Bodies at Elevated Temperature," *Journal of the American Ceramic Society,* Vol. 43, pp. 197–203.

Bober, M., and Karow, H. U., 1977, "Measurements of Spectral Emissivity of UO_2 Above the Melting Point," in: Cezairlyian, A., ed., *Proc. Seventh Symposium on Thermophysical Properties,* National Bureau of Standards, pp. 344–350.

Bober, M., Karow, H. U., and Müller, K., 1980, "Study of the Spectral Reflectivity and Emissivity of Liquid Ceramics," *High Temperatures—High Pressures,* Vol. 12, pp. 161–168.

Bober, M., 1980, "Spectral Reflectivity and Emissivity of Solid and Liquid UO_2 as a Function of Wavelength, Angle of Incidence, and Polarization," *High Temperatures—High Pressures,* Vol. 12, pp. 297–306.

Chang, I. F., and Mitra, S. S., 1972, "Temperature Dependence of Long-Wavelength Optic Phonons of NaF Single Crystals," *Physical Review B,* Vol. 5, No. 10, pp. 4094–4101.

Chase, M. W., Jr., Davies, C. A., Downey, J. R., Jr., Frurip, D. J., McDonald, R. A., and Syverud, A. N., eds., 1985, *JANAF Thermochemical Tables,* National Bureau of Standards, Washington, DC.

Chryssolouris, G., 1991, *Laser Machining: Theory and Practice,* Springer-Verlag, New York.

Dabby, F. W., and Paek, U.-C., 1972, "High-Intensity Laser-Induced Vaporization and Explosion of Solid Material," *IEEE Journal of Quantum Electronics,* Vol. QE-8, pp. 106–111.

Hass, M., 1960, "Temperature Dependence of the Infrared Reflection Spectrum of Sodium Chloride," *Physical Review,* Vol. 117, No. 6, pp. 1497–1499.

Jacquez, J. A., and Kuppenheim, H. F., 1955, "Theory of the Integrating Sphere," *Journal of the Optical Society of America,* Vol. 45, pp. 460–470.

Jasperse, J. R., Kahan, A., Plendl, J. N., and Mitra, S. S., 1966, "Temperature Dependence of Infrared Dispersion in Ionic Crystals LiF and MgO," *Physical Review,* Vol. 140, No. 2, pp. 526–542.

Kneissl, G. J., and Richmond, J. C., 1968, "A Laser Source Integrating Sphere Reflectometer," Technical Report NBS-TN-439, National Bureau of Standards.

Modest, M. F., 1993, *Radiative Heat Transfer,* McGraw-Hill, New York.

Modest, M. F., Ramanathan, S., Raiber, A., and Angstenberger, B., 1995, "Laser Machining of Ablating Materials—Overlapped Grooves and Entrance/Exit Effects," *Journal of Laser Applications,* Vol. 7, No. 4, pp. 210–218.

Modest, M. F., 1996, "Three-Dimensional, Transient Model for Laser Machining of Ablating/Decomposing Materials," *International Journal of Heat and Mass Transfer,* Vol. 39, No. 2, pp. 221–234.

Pehlke, R. D., and Elliot, J. F., 1959, "High-Temperature Thermodynamics of the Silicon, Nitrogen, Silicon-Nitride System," *Transactions of the Metallurgical Society of AIME,* Vol. 215, pp. 781–785.

Ramanathan, S., and Modest, M. F., 1992, "CW Laser Drilling of Composite Ceramics," in: *Proc. ICALEO '91, Laser Materials Processing,* Vol. 74, San Jose, CA, pp. 305–326.

Ramanathan, S., and Modest, M. F., 1993, "Measurement of Temperatures and Absorptances for Laser Processing Applications," in: *Proc. ICALEO '93, Laser Materials Processing,* Orlando, FL, pp. 30–40.

Ramanathan, S., and Modest, M. F., 1995, "High-Speed Photographic Visualization of Laser Processing Phenomena," *Journal of Laser Applications,* Vol. 7, No. 2, pp. 75–82.

Ramanathan, S., Modest, M. F., and Zhang, Z., 1996, "Design of a Fast Micro-Pyrometer for Laser Processing Applications," AIAA Paper No. 96-1885.

Roy, S., and Modest, M. F., 1993, "CW Laser Machining of Hard Ceramics—Part I: Effects of Three-Dimensional Conduction and Variable Properties and Various Laser Parameters," *International Journal of Heat and Mass Transfer,* Vol. 36, No. 14, pp. 3515–3528.

Roy, S., Bang, S. Y., Modest, M. F., and Stubican, V. S., 1993, "Measurement of Spectral, Directional Reflectivities of Solids at High Temperature Between 9 and 11 μm," *Applied Optics,* Vol. 32, No. 19, pp. 3550–3558.

Singhal, S. C., 1976, "Thermodynamic Analysis of the High-Temperature Stability of Silicon Nitride and Silicon Carbide," *Ceramurgia Int.,* Vol. 2, pp. 123–130.

Spitzer, W. G., Kleinman, D. A., and Walsh, D. J., 1959, "Infrared Properties of Hexagonal Silicon Carbide," *Physical Review,* Vol. 113, No. 1, pp. 127–132.

Vorreiter, J. O., Kaminski, D. A., and Smith, R. N., 1991, "Monte Carlo Simulation of a Laser Drilling Process," ASME Paper No. 91-WA-HT-9.

Wallace, R. J., 1983, "A Study of the Shaping of Hot Pressed Silicon Nitride With a High Power CO_2 Laser," PhD thesis, University of Southern California, Los Angeles, CA.

Wilson, R. J., 1964, "Hemispherical Spectral Emittance of Ablation Chars, Carbon, and Zirconia," NASA-SP-55, presented at Symp. on Thermal Radiation of Solids, San Francisco, CA.

Inverse Determination of Steady Heat Convection Coefficient Distributions

T. J. Martin
Graduate Research Assistant.
Student Mem. ASME

G. S. Dulikravich
Associate Professor.
Fellow ASME
FT7@PSU.EDU

Department of Aerospace Engineering,
The Pennsylvania State University,
University Park, PA 16802

An inverse Boundary Element Method (BEM) procedure has been used to determine unknown heat transfer coefficients on surfaces of arbitrarily shaped solids. The procedure is noniterative and cost effective, involving only a simple modification to any existing steady-state heat conduction BEM algorithm. Its main advantage is that this method does not require any knowledge of, or solution to, the fluid flow field. Thermal boundary conditions can be prescribed on only part of the boundary of the solid object, while the heat transfer coefficients on boundaries exposed to a moving fluid can be partially or entirely unknown. Over-specified boundary conditions or internal temperature measurements on other, more accessible boundaries are required in order to compensate for the unknown conditions. An ill-conditioned matrix results from the inverse BEM formulation, which must be properly inverted to obtain the solution to the ill-posed problem. Accuracy of numerical results has been demonstrated for several steady two-dimensional heat conduction problems including sensitivity of the algorithm to errors in the measurement data of surface temperatures and heat fluxes.

Introduction

A well-posed thermal boundary value problem requires either temperature or heat flux specified over the entire boundary of the solid region. When the surface is exposed to a moving fluid, convective heat transfer coefficients can be utilized as boundary conditions. Accurate values of the convective heat transfer coefficients are difficult to obtain experimentally because their values depend strongly on at least twelve variables or eight nondimensional groups (White, 1988). Typical semi-empirical expressions for prediction of heat convection coefficients represent curve fits through experimental data for very simple configurations covering only limited ranges of flow-field parameters. Consequently, in most practical situations, the heat convection problems are solved by using a single value of the heat convection coefficient on the entire surface exposed to a moving fluid.

This paper offers an entirely different approach to a problem of predicting the surface variation of the heat convection coefficient. The most innovative aspects of this approach are that it does not require any information about the flow-field and that it is noniterative. In other words, it is possible to treat the heat convection coefficient determination problem as an ill-posed boundary value heat conduction problem where no thermal data are available on parts of the boundary exposed to a moving fluid. This approach is capable of utilizing over-determined thermal measurements involving temperatures and heat fluxes where they are accessible. These data are then used to predict distributions of temperature, heat fluxes, and convective heat transfer coefficients on the boundaries where they are unknown.

A noniterative algorithm has been developed that reliably and efficiently solves inverse (ill-posed) boundary condition problems governed by the Laplace equation in two-dimensional and three-dimensional multiply connected domains having different thermal material properties (Martin and Dulikravich, 1996; Dulikravich and Martin, 1996). An extended version of this method was also successfully used in solving ill-posed problems in two-dimensional elasticity (Martin et al., 1994) as well as for the determination of heat sources (Martin and Dulikravich, 1996). This technique is based on the Green's function solution method, commonly referred to as the Boundary Element Method (BEM). It is an integral technique that generates a set of linear algebraic equations with unknowns confined only to the boundaries. For well-posed problems, Gaussian elimination or any other standard matrix inverter can solve the resulting solution matrix. When an ill-posed problem is encountered, the matrix becomes ill-conditioned. It has been shown that the proper solution to this matrix provides accurate results to various steady inverse heat conduction boundary value problems (Martin and Dulikravich, 1996, 1997). This method has been shown to suppress the amplification in measurement errors in the input data while both minimizing the variance in the output and preventing output bias. The algorithm is applicable to complex, multiply connected two and three-dimensional configurations.

Numerical Formulation

The governing partial differential equation for steady-state heat conduction in a two-dimensional solid with a constant coefficient of thermal conductivity is

$$k\nabla^2 T = 0. \tag{1}$$

This linear elliptic partial differential equation can be integrated subject to Dirichlet (temperature) boundary conditions, Neumann (heat flux) boundary conditions, and, when a boundary is exposed to a moving fluid, the Robin (convective heat transfer) boundary conditions given as

$$-k\left.\frac{\partial T}{\partial n}\right|_{\Gamma_{conv}} = h_{conv}(T|_{\Gamma_{conv}} - T_{amb}). \tag{2}$$

When ill-posed boundary value problems are encountered, portions of the boundary must be over-specified with both temperatures and heat fluxes, while nothing is known on boundary Γ_{conv}. Such linear boundary value problems can be solved noniteratively when using the BEM. Consequently, the BEM is more robust than the widely used iterative numerical solution tech-

Contributed by the Heat Transfer Division and presented at the National Heat Transfer Conference, Baltimore, Maryland, August 8–12, 1997. Manuscript received by the Heat Transfer Division April 7, 1997; revision received January 5, 1998. Keywords: Conduction, Conjugate Heat Transfer, Mixed Convection. Associate Technical Editor: R. D. Boyd.

niques. Analytical solutions to the partial differential equation, in the form of the Green's function, are part of the BEM solution. Therefore, high accuracy is expected because introducing the Green's functions does not introduce any error into the solution. In addition, the noniterative nature of the BEM eliminates stability, numerical dissipation, and iterative convergence problems. This is valuable because iterative procedures for the solution of inverse problems tend to amplify errors due to ill-posedness of the iteration matrix thus requiring complex regularization (smoothing) algorithms (Tikhonov and Arsenin, 1977).

The BEM is a standard numerical technique that can be found in a number of textbooks (Brebbia and Dominguez, 1989). Consequently, only pertinent concepts will be summarized in this paper. Since the objective is strictly solving a boundary value problem, the unknown temperature, T, and the unknown flux, Q, are on the boundary Γ_{conv} that is a part of the overall boundary Γ. The boundary Γ can be discretized into N_{BE} isoparametric boundary elements. Although these test cases will not be discussed in this paper (Martin and Dulikravich, 1996), internal measurement points could exist where temperature data are obtained. The T and Q can vary between the neighboring end-nodes defining each boundary element. Each boundary element can be integrated numerically using a standard Gaussian quadrature integration formula. Boundary elements containing a singularity at one end-point can be integrated analytically, resulting in a set of boundary integral equations, one for each boundary node plus one for every possible internal temperature measurement. The resulting discretized form of the BEM can be represented in matrix form (Brebbia and Dominguez, 1989) as

$$[\mathbf{H}]\{\mathbf{T}\} = [\mathbf{G}]\{\mathbf{Q}\}. \tag{3}$$

Here, $[\mathbf{H}]$ and $[\mathbf{G}]$ are full matrices containing geometrically defined coefficients.

For a well-posed boundary value problem, every point on the boundary Γ is given one Dirichlet, Neumann, or Robin boundary condition and there are no internal temperature measurements. These boundary conditions are then multiplied by their respective coefficient matrix and collected on the right-hand side to form a vector of known quantities, $\{\mathbf{F}\}$. The left-hand side remains in the standard form $[\mathbf{A}]\{\mathbf{X}\}$. This well-posed system of linear algebraic equations can be solved for the vector of unknown quantities $\{\mathbf{X}\}$ on the boundary by any standard matrix solver such as Gaussian elimination or LU factorization.

If the boundary conditions (T, Q, or h_{conv}) are unknown on parts of the boundary or if internal temperature measurements are included in the analysis, the problem becomes ill-posed. A solution of this inverse problem of determination of unknown boundary conditions may be obtained by using a procedure explained by Dulikravich and Martin (1996) and Martin and Dulikravich (1996).

In summary, after multiplying the known quantities in the vectors $\{\mathbf{T}\}$ and $\{\mathbf{Q}\}$ by their respective coefficient matrix columns, the products should be collected into the vector of known quantities, $\{\mathbf{F}\}$. The unknown boundary values of the vectors $\{\mathbf{T}\}$ and $\{\mathbf{Q}\}$ then form a single vector, $\{\mathbf{X}\}$, multiplied by a highly ill-conditioned coefficient matrix, $[\mathbf{A}]$, which is, in general, not square. The truncated Singular Value Decomposition (SVD) method (Press et al., 1986) has been often used to solve this ill-conditioned system of algebraic equations. Very small singular values of such ill-conditioned matrix $[\mathbf{A}]$ are zeroed out so that those algebraic terms that are dominated by noise and round-off error are eliminated from the matrix. In order to determine which singular values are to be truncated, it is necessary to provide a user-specified singularity threshold parameter, τ_{SVD}. One method for determining the most suitable value of τ_{SVD} has been suggested by Martin and Dulikravich (1996). Any singular value, whose ratio with the largest singular value is less than this singularity threshold, will be automatically zeroed out in the SVD algorithm.

In addition to the SVD algorithm, Tikhonov's regularization (Tikhonov and Arsenin, 1977) was also applied in a number of test cases in this study. The observation was that Tikhonov's regularization produces unacceptable levels of global bias when large regularization parameters are required for a smooth solution. Tikhonov's regularization was found to be very effective when errors were introduced into the surface heat flux measurements (Martin and Dulikravich, 1996).

Results

The equation for the boundary heat flux from the Robin boundary condition was added directly into the linear BEM system (Martin and Dulikravich, 1996; Dulikravich and Martin, 1996). The unknown temperatures were factored together with the other boundary nodal temperatures appearing on the left-hand side of the BEM matrix equation set. After the ill-conditioned coefficient matrix $[\mathbf{A}]$ has been inverted using the SVD algorithm, the unknown boundary values of T and Q were obtained from $\{\mathbf{X}\} = [\mathbf{A}]^{-1}\{\mathbf{F}\}$. Once these thermal boundary values were determined on the boundary Γ_{conv}, the convective heat transfer coefficients were determined from

$$h_{conv} = -k \left.\frac{\partial T}{\partial n}\right|_{\Gamma_{conv}} \Big/ (T|_{\Gamma_{conv}} - T_{amb}). \tag{4}$$

Here, T_{amb} is considered as known. Two test cases were used to assess the accuracy of the entire noniterative BEM inverse algorithm and its sensitivity to measurement errors in boundary temperatures and heat fluxes.

A square flat plate with side lengths of 1 m was subject to homogeneous Dirichlet boundary conditions ($T = 0$°C) on three boundaries and a Robin boundary condition (h_{conv} = 1.0 W m^{-2} °C^{-1}, T_{amb} = 1.0°C) on the bottom boundary. The thermal conductivity (k) was 1.0 W m^{-1} °C^{-1}. The analysis or well-posed formulation consisted of the Dirichlet boundary conditions on the top, left, and right boundaries of the plate, and

Nomenclature

$[\mathbf{A}]$ = coefficient matrix multiplying a vector of unknowns
Bi = Biot number = $h_{conv}\,L/k$
$\{\mathbf{F}\}$ = vector of known sources and boundary conditions
$[\mathbf{G}]$ = BEM coefficient matrix multiplying nodal fluxes
h_{conv} = convective heat transfer coefficient
$[\mathbf{H}]$ = BEM coefficient matrix multiplying nodal temperatures
k = thermal conductivity
L = characteristic length
N_{BE} = number of boundary elements
Q = normal temperature derivative or flux $\partial T/\partial n$
$\{\mathbf{Q}\}$ = vector of nodal fluxes
R = random number ($0 < R < 1$)
T = temperature
$\{\mathbf{T}\}$ = vector of nodal temperatures
$\{\mathbf{X}\}$ = vector of unknowns
Γ = boundary contour
σ^2 = statistical variance
τ_{SVD} = SVD threshold value
Ω = domain

Subscripts

amb = ambient fluid quantities
INT = internal measurement
conv = convective heat transfer
perturb = perturbed value

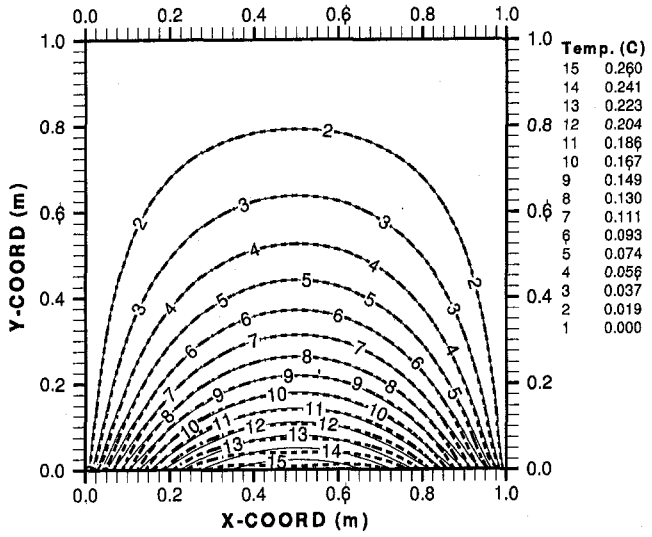

Fig. 1 Isotherms predicted within the rectangular plate by the analytical (solid lines), direct BEM (dotted lines), inverse BEM with top boundary over-specified (dashed lines), and the inverse BEM with top and side boundaries over-specified (dash-dot lines). Forty panels per side.

the Robin boundary condition on the bottom boundary. Using separation of variables, an analytical solution for this test case can be found in the following form (where a and b are the side lengths):

$$T(x, y) = \frac{2h_{\text{conv}}}{a} \sum_{n=1}^{\infty} \left[\int_0^a T_{\text{amb}} \sin\left(\frac{n\pi x}{a}\right) dx \right] \times \frac{\sinh\left(\frac{n\pi(b-y)}{a}\right) \sin\left(\frac{n\pi x}{a}\right)}{h_{\text{conv}} \sinh\left(\frac{n\pi b}{a}\right) + \frac{n\pi k}{a} \cosh\left(\frac{n\pi b}{a}\right)} \quad (5)$$

The BEM analysis predicted the heat fluxes on the top, left, and right boundaries, and temperature on the bottom boundary. When the entire computed temperature field was plotted (Fig. 1), the isotherms (thin dashed lines) obtained numerically using the BEM analysis were practically identical to the analytically obtained isotherms (full lines), having an error of less than 0.1 percent. This confirmed the very high accuracy of the analysis version of the BEM code used in this study.

The inverse problem was then formulated by specifying nothing on the bottom boundary of the rectangular plate while one or more of the remaining boundaries were over-specified with temperatures and heat fluxes taken from the analytical solution. In order to check the performance of the inverse version of the BEM code with respect to the amount of over-specified data, two variations of this numerical test case were performed.

Test Cases With Constant h_{conv}. In the first variation, only the top boundary of the square plate was over-specified with temperature and heat flux, while the side boundaries were specified with temperature only. The isotherms predicted by the inverse noniterative BEM procedure are shown as dotted lines in Fig. 1. The ambient fluid temperature was considered to be known ($T_{\text{amb}} = 1.0°\text{C}$). Therefore, the convective heat transfer coefficients can be computed directly after both the temperature and heat flux on the bottom boundary have been predicted.

The computed convective heat transfer coefficients on the bottom boundary, which in this test case should be $h_{\text{conv}} = 1.0$ W m^{-2} °C^{-1}, are plotted as square symbols in Fig. 2. The average error in h_{conv} is less than 1 percent and a peak error is 6 percent in this test case where over-specified data were provided only on a single boundary farthest from the boundary with unknown thermal boundary conditions.

Influence of the Amount of Over-specified Data. In the second variation of this test case, the opposite (top) boundary as well as both side boundaries were over-specified with both temperature and heat flux from the analytical solution. The isotherms that were predicted by the inverse noniterative BEM code are shown as dash-dot lines in Fig. 1. These isotherms cannot be seen because they lie directly on top of the isotherms predicted by the analysis version of the BEM code and by the analytical solution. The numerically predicted values of local h_{conv} from the inverse BEM procedure for this test case are plotted using triangle symbols in Fig. 2. Notice that the prediction of h_{conv} is more accurate in this test case, having a peak error of 0.4 percent. From these results it can be concluded that the inverse BEM prediction of the unknown h_{conv} is sensitive to the amount of over-specified data and the location of the over-specified boundaries.

Influence of Distance of Over-specified Boundary. To clarify that issue further, the aspect ratio ($AR = b/a$) of the rectangular plate was varied while over-specifying only the top boundary, which is the farthest away from the unspecified bottom boundary. From Fig. 3 it can be seen that for relatively thin domains ($AR < 0.25$) the peak error in the predicted h_{conv} is less than 0.3 percent. The peak error increases to approximately 10 percent, as the rectangular plate becomes a square plate (Fig. 3), while the average error remains below 1 percent.

Applicability to Different Values of Biot Number. The previous numerical results were obtained for unity Biot number ($\text{Bi} = h_{\text{conv}} L/k$). The second variation inverse problem was then repeated for a variety of Biot numbers by utilizing values of the thermal conductivity in the interval $0.01 < k < 100.0$ W m^{-1} °C^{-1}, and thus varying the Biot number over the same range since $L = 1.0$ m and $h_{\text{conv}} = 1.0$ W m^{-2} °C^{-1} were kept constant. The threshold parameter in the SVD algorithm was $\tau_{\text{SVD}} = 10^{-6}$. From Fig. 4 it can be concluded that the standard deviation and maximum error of the predicted h_{conv} were very low for $0 < \text{Bi} < 20$, after which the maximum error increased

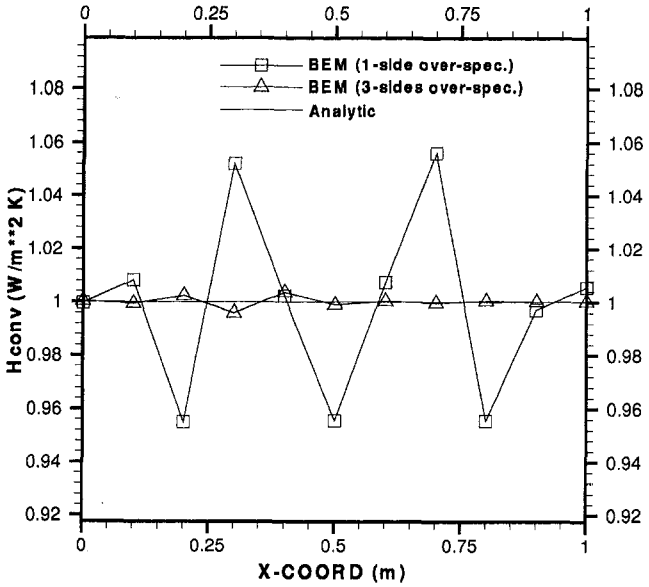

Fig. 2 Convective heat transfer coefficients, h_{conv}, numerically predicted by the inverse BEM on the bottom boundary of a square plate when: (*a*) the top boundary (squares), and (*b*) left, top, and right boundaries (triangles) were over-specified. The exact value is $h_{\text{conv}} = 1.0$ W m^{-2}°C^{-1}. Ten panels per side were used.

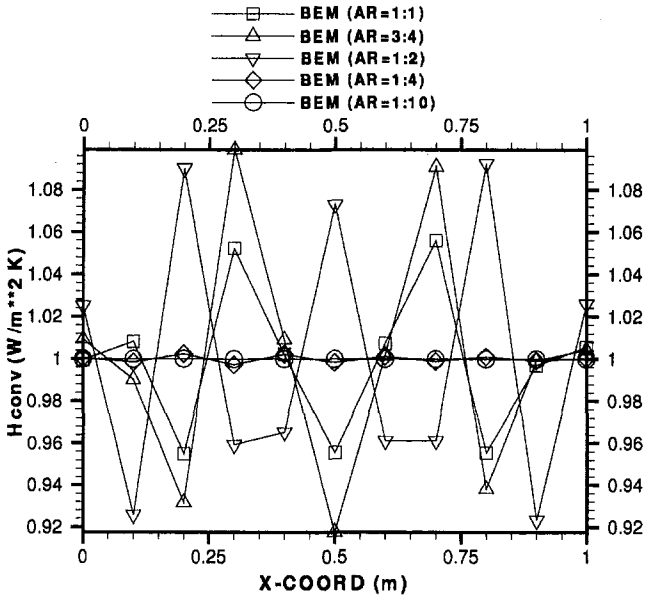

Fig. 3 Influence of the aspect ratio (height/width) of the rectangular plate and the amount of the over-specified data on the numerically predicted h_{conv} on the bottom boundary when: (*a*) the top boundary (squares), and (*b*) left, top, and right boundaries (triangles) were over-specified. The exact value is $h_{conv} = 1.0$ W m^{-2}°C^{-1}. Ten panels per side were used.

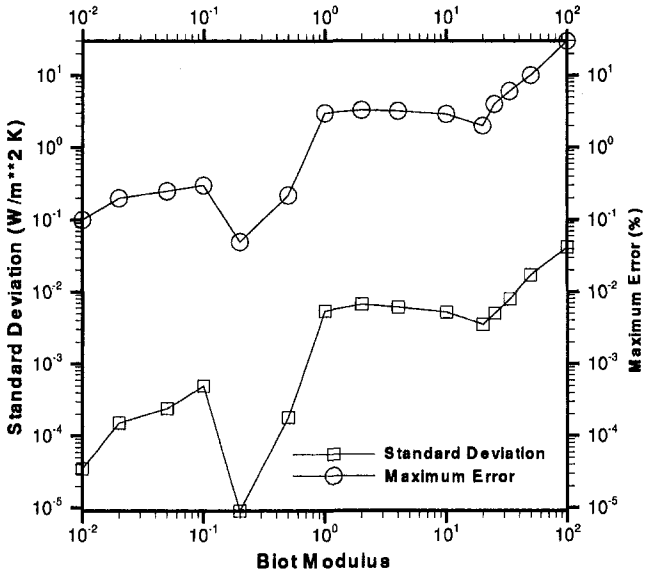

Fig. 4 Influence of Biot numbers on maximum error and standard deviation of the predicted h_{conv}

until it reached 30 percent for Bi = 100. For example, a plasma-coated gas turbine blade surface distribution of h_{conv} can be predicted quite accurately with this inverse BEM algorithm. In this example, the coating thickness (L) is 2×10^{-4} m, and k is 1.0 W m^{-1} °C^{-1}. If Bi < 20, this means that h_{conv} as high as 10^5 W m^{-2} °C^{-1} can be predicted with a maximum error of 2 percent and a standard deviation of less than 10^{-2} W m^{-2} °C^{-1}.

A Test Case With Variable h_{conv}. The inverse BEM algorithm was also evaluated for the more realistic case where the heat convection coefficient is not a constant. The same boundary conditions on the top and the vertical side boundaries were used as in the previous test cases while specifying the variable heat convection coefficient as $h_{conv} = [1.0 + \sin(2\pi x)]$ Wm^{-2}°C^{-1} on the bottom boundary. This test case does not have an analytical solution. Therefore, the BEM analysis code was run with 40 boundary elements on each of the four sides of this well-posed problem and treated the predicted isotherms as the accurate result (Fig. 5).

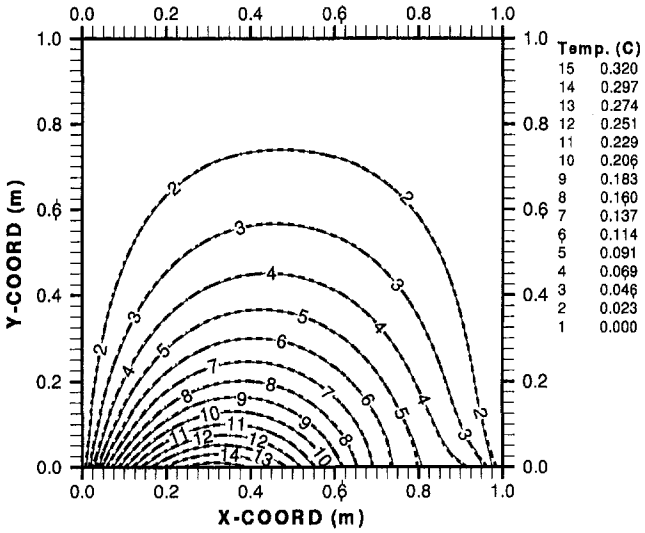

Fig. 5 Isotherms predicted by a well-posed BEM (full lines) and inverse BEM (dashed lines) for the rectangular plate with $h_{conv} = [1.0 + \sin(2\pi x)]$ W m^{-2} °C^{-1} on the bottom boundary and $T = 0.0$°C on the remaining three boundaries. Forty panels per side were used.

An inverse problem was then created by pretending that h_{conv} is unknown on the bottom boundary. These "unknown" values of h_{conv} were then predicted by over-specifying the vertical boundaries and the top boundary with the $T = 0.0$°C and with the heat fluxes that were previously predicted by the BEM solution for the forward problem with sine wave h_{conv} on the bottom boundary. The threshold parameter used in the SVD algorithm had the value $\tau_{SVD} = 10^{-4}$. The result of the inverse BEM code was a highly accurate temperature field shown as dashed lines in Fig. 5 that practically coincide with the solid lines predicted by the well-posed problem solution. An equally accurate prediction of the sine wave h_{conv} variation on the lower boundary (dashed line in Fig. 6) thus confirms the high accuracy and the applicability of this inverse BEM algorithm to prediction of variable h_{conv} values.

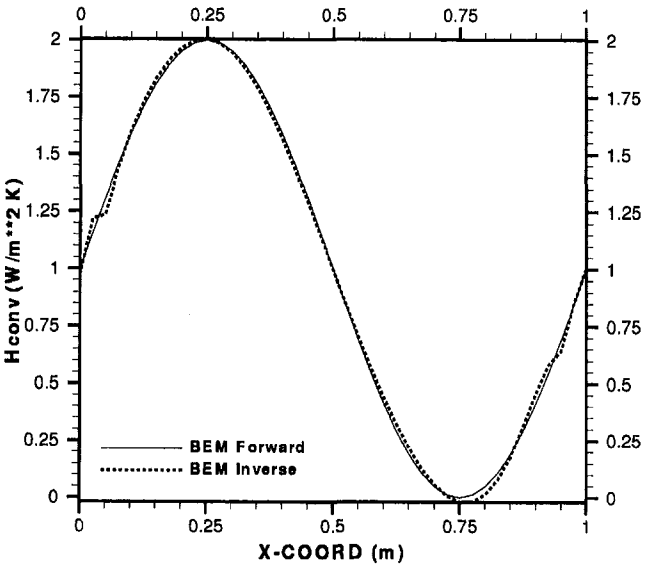

Fig. 6 Analytical (full line) and inverse BEM predicted (dotted line) variation of h_{conv} along the bottom boundary

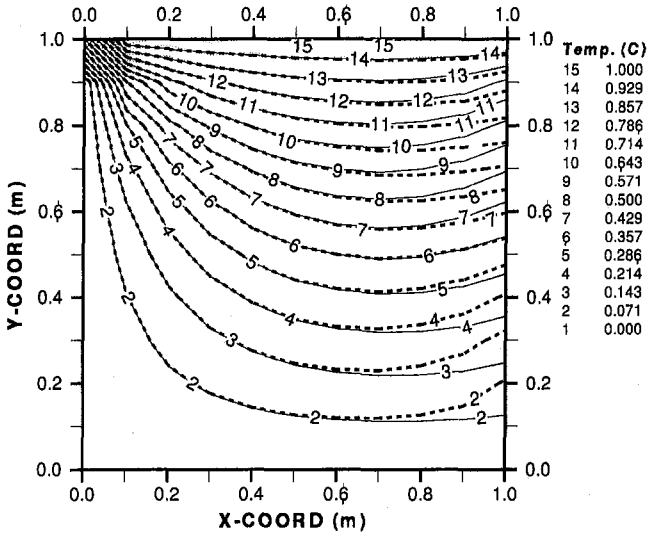

Fig. 7 Isotherms predicted analytically (solid lines) and using analysis BEM (thin dashed lines), inverse BEM with left boundary over-specified (dotted lines), and the inverse BEM with bottom, left, and top boundaries over-specified (dash-dot lines). Ten panels per side were used.

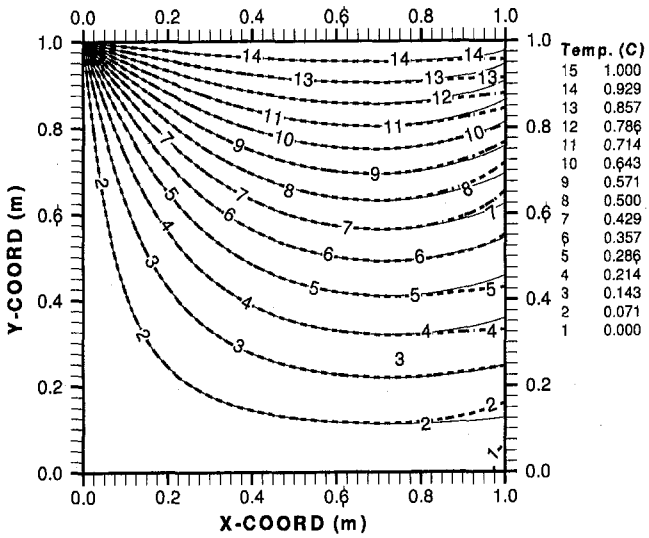

Fig. 8 Isotherms predicted analytically (solid lines) and using analysis BEM (thin dashed lines), inverse BEM with left boundary over-specified (dotted lines), and the inverse BEM with bottom, left, and top boundaries over-specified (dash-dot lines). Forty panels per side were used.

Test Cases With Asymmetric Boundary Conditions. For a second test case, the geometry was a homogeneous square plate with each side of length L discretized with 10 linear isoparametric boundary elements. The boundary conditions were altered such that the right-side boundary had the Robin boundary condition (h_{conv} = 1.0 W m^{-2}°C^{-1}, T_{amb} = 0.0°C). In the well-posed (analytical) problem, the top boundary was specified with a temperature T = 1.0°C and the left-side and bottom boundaries were specified with a temperature T = 0.0°C. The analytical solution for this problem can be found by separation of variables, and is given by

$$T(x, y) = \frac{2T_{amb}h_{conv}L}{k} \sum_{n=1}^{\infty} \frac{1 - \cos \alpha_n}{\alpha_n\left(h_{conv}\frac{L}{k} + \cos^2\alpha_n\right)} \times \frac{\sinh \frac{\alpha_n y}{L}}{\sinh \alpha_n} \sin \frac{\alpha_n x}{L}, \quad (6)$$

where

$$\tan \alpha_n = -\frac{\alpha_n k}{h_{conv}L}. \quad (7)$$

As in the previous test case, the BEM analysis was compared to the analytical solution. The analytically predicted isotherms (solid lines) and the numerical analysis or the well-posed BEM numerical prediction (dashed lines) are directly on top of each other (Fig. 7), thus confirming the high accuracy of the analysis version of the BEM code used in this study.

Again, two variations of the inverse problem were created. One variation had only the left boundary over-specified. The other variation had bottom, left, and top boundaries over-specified. In both inverse variations, nothing was specified on the right-side boundary where heat transfer coefficients were prescribed in the well-posed problem. In the case where only the opposite boundary (left side) was over-specified, the inversely predicted isotherms (dotted lines) show an appreciable error in the vicinity of the unspecified right side boundary (Fig. 7). The error in the inversely predicted isotherms was significantly reduced when a larger quantity of the over-specified data (40 panels per each side of a square) was used (Fig. 8). The value of h_{conv} on the right-side boundary was then obtained from the predicted temperatures and heat fluxes on that boundary (Fig. 9). There was a large discrepancy in the computed h_{conv} values when only the opposite boundary (left-side boundary) was over-specified, since this boundary is far away from the unspecified right-side boundary. The maximum error in predicted h_{conv} was dramatically reduced to about 2 percent when bottom, left-side, and top boundaries were over-specified (Fig. 9).

Sensitivity to Errors in the Input Temperatures. It is of utmost practical importance to access the influence of measurement errors of boundary values in any newly proposed inverse boundary value determination algorithm. Adding a random error based on the Gaussian probability density distribution to the temperature measurements numerically simulated this effect. A random number, $0 < R < 1$, was generated using a standard

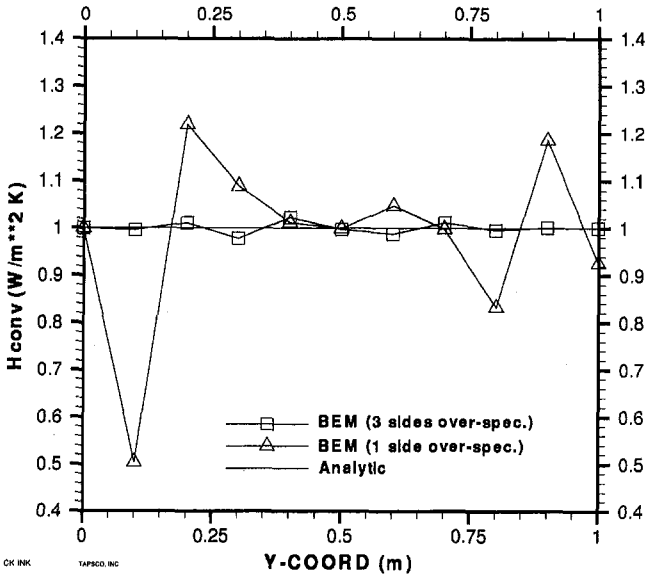

Fig. 9 Convective heat transfer coefficient predicted by the inverse BEM on the right boundary of a square plate when: (*a*) the left boundary (triangles), and (*b*) bottom, left, and top boundaries (squares) were over-specified. Ten panels per side were used.

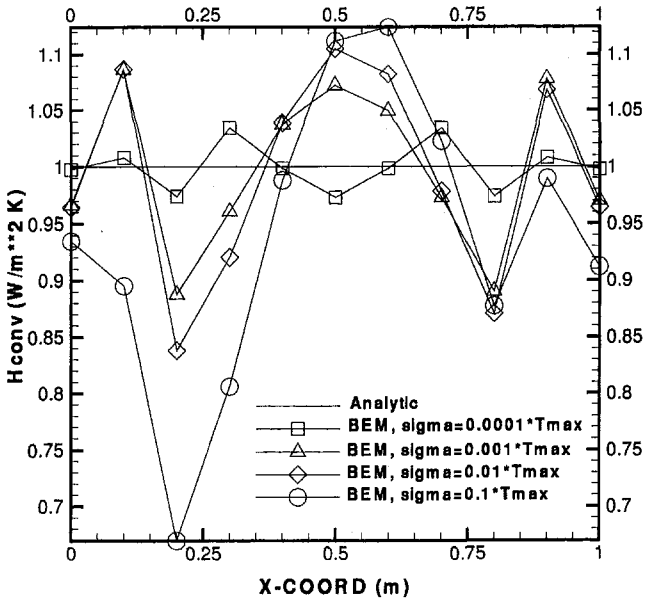

Fig. 10 Sensitivity of the predicted distributions of h_{conv} on the bottom boundary for different standard deviations of the intentionally introduced errors in over-specified temperatures on the remaining three boundaries in the first test case. SVD and ten panels per side were used.

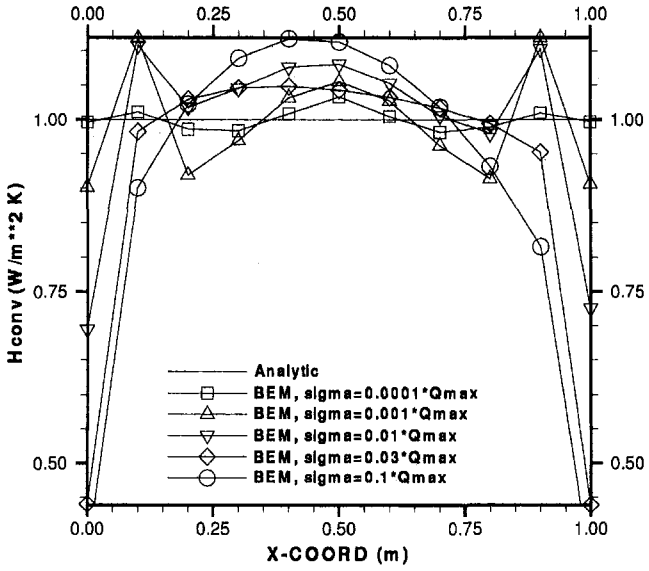

Fig. 11 Sensitivity of the predicted distributions of h_{conv} on the bottom boundary for different standard deviations of the intentionally introduced errors in over-specified fluxes on the remaining three boundaries in the first test case. Tikhonov's regularization and ten panels per side were used.

RANF utility subroutine on Cray C-90 computer. The desired variance σ^2 was specified in the input data and the error was added to the analytical temperature data points, T, according to

$$T_{perturb} = T \pm \sqrt{-2\sigma^2 \ln R}. \quad (8)$$

Here, addition and subtraction of the random error had a 50–50 chance of been chosen. The errors were assumed to be additive and the same variance was prescribed for all temperature measurements.

This simple test of sensitivity was applied to the second variant of the first test case discussed in this paper with the unknown heat convection on the bottom boundary, while the remaining three sides of the rectangle ($AR = 1$) were over-specified. The input temperatures had intentionally introduced random errors. The predicted values of h_{conv} had a maximum local error of 4 percent when average perturbation was 0.01 percent of T_{max} (Fig. 10). A maximum local error of 8.5 percent was realized when average perturbation was 0.1 percent of T_{max}. It increased to 16 percent when the average perturbation was 1 percent of T_{max}. The maximum local error in predicted h_{conv} reached 33 percent when the average perturbation of supplied (measured) boundary temperature was 10 percent of the maximum temperature in the field. At the same time, it can be seen (Fig. 10) that the average error in the predicted h_{conv} is approximately the same magnitude as the average level of the perturbations (errors) introduced in the boundary temperatures.

Sensitivity to Errors in the Input Fluxes. A similar response of this inverse BEM code was obtained when the random errors were intentionally introduced in the input heat fluxes (according to a formula similar to Eq. (8)) on the three over-specified boundaries (Fig. 11). For all practical purposes, there was no net bias in the simulated input measurement errors. For example, when an input error of $0.01 * Q_{max}$ was introduced, the net bias in the integrated boundary heat flux averaged over each boundary was 5×10^{-6} or 0.05 percent of the unperturbed average heat flux on that boundary. By comparing Figs. 11 and 10, it can be seen that the average error in the predicted values of h_{conv} is somewhat higher in the case with input errors in heat fluxes than in the case with input errors in temperatures. It is remarkable that the level of average error and the peak error in the predicted h_{conv} are of the same order of magnitude as the average errors and the peak errors in the input values of heat fluxes on the over-specified boundary.

In these test cases, Tikhonov's regularization was found to provide better results compared to SVD. Table 1 lists the optimum Tikhonov's regularization parameters, τ_{TIKH}, that were found using numerical experimentation on two different computers for two different levels of BEM discretization and then utilized in the inverse BEM code. Since Tikhonov's regularization acts as an artificial sink of energy, Martin and Dulikravich (1996) demonstrated that higher values of τ_{TIKH} lead to a rapidly increasing bias in the integrated computed heat fluxes. This could be improved significantly by increasing the amount of over-specified data. Figure 12 demonstrates improved results when each boundary was discretized with 40 panels on a higher precision computer (Table 1).

Conclusions

It has been demonstrated how a simple modification to any existing BEM analysis algorithm for the solution of Laplace's equation can transform it into an inverse non-iterative determina-

Table 1 Various levels of intentional errors in the over-specified boundary heat fluxes and the corresponding Tikhonov's regularization parameters used in the BEM inverse problems: (*a*) on a PC with 10 boundary elements per side resulting in a condition number of matrix = 7, and (*b*) on the Cray with 40 boundary elements per side resulting in a condition number of matrix = 14

σ	$0.0001Q_{max}$	$0.001Q_{max}$	$0.01Q_{max}$	$0.03Q_{max}$	$0.1Q_{max}$
τ_{TIKH} on the Cray	1×10^{-6}	1×10^{-5}	1×10^{-4}	5×10^{-4}	1×10^{-2}
τ_{TIKH} on a PC	5×10^{-7}	5×10^{-4}	5×10^{-3}	5×10^{-2}	2×10^{-1}

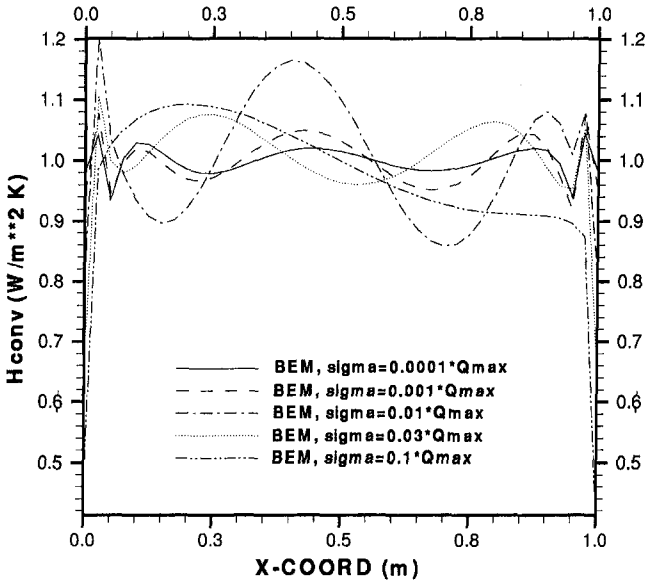

Fig. 12 Sensitivity of the predicted distributions of h_{conv} on the bottom boundary for different standard deviations of the intentionally introduced errors in over-specified fluxes on the remaining three boundaries in the first test case. Tikhonov's regularization and forty panels per side were used.

tion code for unknown distributions of steady convective heat transfer coefficients. This approach is applicable to arbitrarily shaped two and three-dimensional solids where at least part of a boundary can be over-specified with both temperatures and heat fluxes. The code is very fast and robust since it requires inversion of a single fully populated matrix. The inversion must be performed using an algorithm suitable for almost singular matrices. This method is relatively insensitive to the errors introduced in the boundary measurements of temperature while somewhat more sensitive to the errors introduced in the boundary measurements of heat fluxes. It should be noted that this method for determining unknown steady distribution of heat convection coefficients is inexpensive, since it requires only one temperature probe and one heat flux probe. These two probes can be moved from point to point on accessible boundaries, thus obtaining the over-specified thermal boundary conditions.

Acknowledgments

The authors would like to express their gratitude for the NASA–Penn State Space Propulsion Engineering Center Graduate Student Fellowship, the National Science Foundation Grant DMI-9522854 monitored by Dr. George A. Hazelrigg, the NASA Lewis Research Center Grant NAG3-1995 supervised by Dr. John K. Lytle and Dr. Kestutis Civinskas, and for ALCOA Foundation Faculty Research Fellow Award facilitated by Dr. Yimin Ruan and Dr. Owen Richmond. Special thanks are due to all the reviewers of the original manuscript for their useful suggestions.

References

Brebbia, C. A., and Dominguez, J., 1989, *Boundary Elements, An Introductory Course,* McGraw-Hill, New York.

Dulikravich, G. S., and Martin, T. J., 1996, "Inverse Shape and Boundary Condition Problems and Optimization in Heat Conduction," *Advances in Numerical Heat Transfer,* W. J. Minkowycz and E. M. Sparrow, eds., Taylor & Francis, Chap. 10, pp. 324–367.

Martin, T. J., Halderman, J., and Dulikravich, G. S., 1994, "An Inverse Method for Finding Unknown Surface Tractions and Deformations in Elastostatics," *Computers and Structures,* Vol. 56, No. 5, pp. 825–836.

Martin, T. J., and Dulikravich, G. S., 1996, "Inverse Determination of Boundary Conditions in Steady Heat Conduction With Heat Generation," ASME JOURNAL OF HEAT TRANSFER, Vol. 118, pp. 546–554.

Martin, T. J., and Dulikravich, G. S., 1997, "Non-iterative Determination of Temperature-Dependent Thermal Conductivity," *Symposium on Inverse Design Problems in Heat Transfer and Fluid Flow,* G. S. Dulikravich and K. A. Woodbury, eds., ASME HTD-Vol. 340, Vol. 2, pp. 151–158.

Press, W. H., Teukolsky, S. A., Vetterling, W. T., and Flannery, B. P., 1986, *Numerical Recipes in FORTRAN, The Art of Scientific Computing,* 2nd ed., Cambridge University Press, Cambridge.

Tikhonov, A. N., and Arsenin, V. Y., 1977, *Solutions of Ill Posed Problems,* Halsted Press, V. H. Winston & Sons, Washington, DC.

White, F. M., 1988, *Heat and Mass Transfer,* Addison-Wesley Publishing Company, Reading, MA, p. 272.

Comparison of Heat Transfer Characteristics of Radial Jet Reattachment Nozzle to In-Line Impinging Jet Nozzle

J. Seyed-Yagoobi

V. Narayanan

R. H. Page

Drying Research Center,
Department of Mechanical Engineering,
Texas A&M University,
College Station, TX 77843-3123

The heat transfer characteristics of three submerged radial jet reattachment (RJR) nozzles with exit angles of +45, 0, and −10 deg are compared to the heat transfer characteristics of a conventional submerged in-line jet (ILJ) nozzle. The nozzles are compared at their favorable spacing from the impingement surface. The comparisons are based on two criteria: (1) identical fluid flow power, and (2) identical peak pressure exerted on the impingement surface. The local and area-averaged Nusselt numbers are presented. Experiments were conducted for two different flow power conditions. Comparison under identical flow power indicates that significant enhancements in local and comparable enhancements in area-averaged Nusselt numbers can be achieved with the RJR nozzles over the conventional ILJ nozzle while being able to control the net force exerted on the impingement surface. The comparison between the ILJ and RJR nozzles on the basis of the same peak pressure exerted on the impingement surface indicates that the zero degree exit angle RJR nozzle heat transfer characteristics are superior to the ILJ nozzle.

Introduction

Impinging jets have many applications, including the heating or drying of food, paper, printer's ink, tissue, textiles, chemicals, film and the cooling of electrical equipment, turbine, and combustor components. They are also used in glass, metal, and plastics processing. The advantages of impinging jet systems include the ability to control local transport rates by varying not only flow rate and temperature, but also geometric parameters such as jet diameter, jet-to-jet spacing, and jet-to-surface distance.

In-Line Jet (ILJ) Nozzle. Systems that incorporate impinging jets are generally composed of in-line, orifice, or slot jets. The supply flow to the jet systems is provided by a reservoir at a pressure above atmospheric and the flow exits the nozzle and impinges on a surface. The conventional in-line jet (ILJ) consists of a convergent section leading to a pipe with finite length of constant cross section (see Fig. 1). The transport characteristics of the ILJ nozzle are well documented and are available in the literature (e.g., see Martin (1977), Obot et al. (1980), Goldstein et al. (1986), Polat et al. (1989), and Viskanta (1993)).

Radial Jet Reattachment (RJR) Nozzle. There have been many attempts at altering a jet's flow to increase its transport characteristics. One such innovative nozzle is the Radial Jet Reattachment (RJR) nozzle (e.g., see Page and Ostowari (1985), Page et al. (1986), and Page and Seyed-Yagoobi (1990)).

The basic concept of a submerged RJR is shown in Fig. 2. The stream of air is directed in an outward radial direction to a point where it separates from the nozzle into a free stream. The turbulent viscous mixing that occurs at the boundaries of this stream induces secondary flow by mass entrainment. When placed near a flat surface, the induced flow from the lower boundary of the radial jet stream creates a low-pressure region beneath the nozzle. The low-pressure region forces the jet stream to turn downward until the stream impinges, or reattaches, on the flat plate in a ring centered around the nozzle. The stream, now reattached to the surface of the flat plate, divides. Part of the stream turns radially outward and the remainder radially inward. This process results in a highly turbulent reattachment ring. The intense turbulence associated with this phenomenon is mainly responsible for the high heat and mass transfer between the fluid and the impingement surface.

The characteristic flow pattern of the RJR also provides another unique feature: The magnitude and direction of the net force exerted by the fluid on the reattachment surface can be controlled (Page et al., 1990). Zero and even negative net forces can be attained with different designs of the RJR nozzle. Specifically, the flow exit angle can be used to control the force on the impingement surface. The force exerted by the jet on the surface can be estimated with:

$$\text{Force} = A \cdot \rho \cdot V^2 \cdot \sin(\theta) \qquad (1)$$

where A is the exit area of the jet, ρ is the density of the fluid, V is the jet exit velocity, and θ is the jet exit angle. Negative exit angle results in the flow exiting the nozzle away from the surface and then turning down to reattach. This produces a net negative force on the surface.

Previous studies on the ILJ nozzle and the RJR nozzle have dealt with both the heat transfer and mass transfer characteristics of the nozzles (Habetz et al., 1992; Ostowari and Page, 1992). Habetz et al. (1992) reported that significant improvements in drying rates could be achieved by the RJR nozzle over the ILJ nozzle when both the nozzles were compared under the same mass flow rate condition. Ostowari and Page (1992) compared the heat transfer characteristics of the ILJ and the RJR nozzles under the same mass flow rate. They reported significant increases in the local and average heat transfer coefficients for the RJR nozzle compared to the ILJ nozzle.

The RJR technology has been successfully transferred to industry. For instance, RJR nozzles are used in the dryer sections

Contributed by the Heat Transfer Division for publication in the JOURNAL OF HEAT TRANSFER. Manuscript received by the Heat Transfer Division September 9, 1996; revision received February 9, 1998. Keywords: Augmentation and Enhancement, Jets, Materials Processing and Manufacturing Process. Associate Technical Editor: M. D. Kelleher.

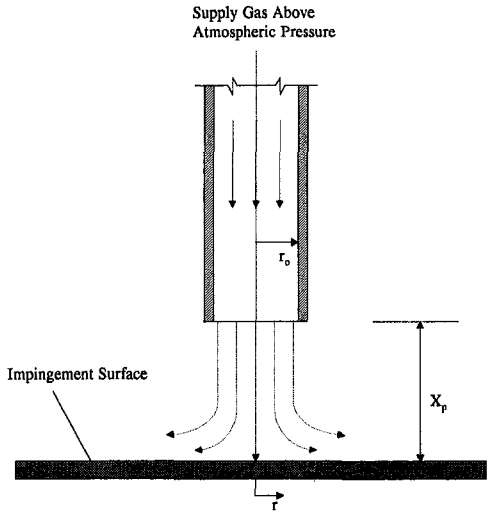

Fig. 1 Schematic of in-line jet (ILJ) nozzle

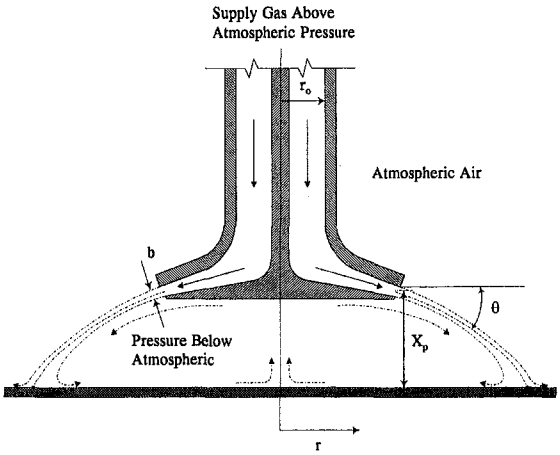

Fig. 2 Schematic of radial jet reattachment (RJR) nozzle

of paper-making machines. Significant enhancements in the drying rates have been achieved with these RJR nozzles (Thiele et al., 1995).

Objective. This paper compares the heat transfer characteristics of a single submerged RJR nozzle to the heat transfer characteristics of a single submerged ILJ nozzle. The comparisons are based on two separate criteria. The first criterion is the comparison of the nozzles under the same fluid flow power. The RJR and ILJ nozzles being two different geometries, any fair comparison between them should take into account the additional pressure drop in the RJR nozzle due to the deflection of flow caused by the bottom plate. A comparison under identical flow power condition accounts for such additional losses in the RJR, thus providing a realistic basis for comparing the two nozzles. It should be noted that this pressure drop varies for different exit angles of the bottom plate and consequently, the mass flow rate for the 45 deg exit angle RJR nozzle is larger than that of the 0 deg RJR nozzle under the same flow power condition (see Tables 1 and 2).

Previous comparisons have been made under the same exit velocity or the same mass flow rate. However, these comparisons can be misleading. In the case of the ILJ and the RJR nozzles of the same pipe diameter, a comparison of the nozzles under the identical exit velocity would favor the ILJ nozzle since the mass flow rate is larger for the ILJ nozzle under such conditions. This is true because the exit hydraulic diameter of the RJR nozzle is typically smaller than the pipe diameter of

Table 1 Operating conditions: Case 1

	ILJ	RJR θ=-10°	RJR θ = 0°	RJR θ= +45°	RJR* θ= 0°	ILJ**
Nozzle Pipe Re number	31,900	25,700	24,300	27,900	57,200	29,300
Pipe Velocity (m/s)	18.4	14.9	14.3	16.3	33.1	16.9
Mass Flow Rate (kg/s)	0.012	0.010	0.009	0.011	0.026	0.011
Flow Power (W)	2.3	2.3	2.3	2.3	32.5	2.3
Height, X_p/D	6.0	0.5	0.5	0.5	0.5	0.5

* This operating condition provided a peak pressure on the impingement surface equal to the peak pressure generated by ILJ nozzle under the operating condition given in this table.

**Corresponds to almost a wall jet.

Table 2 Operating conditions: Case 2

	ILJ	RJR θ= -10°	RJR θ= 0°	RJR θ=+45°	ILJ**
Nozzle Pipe Re Number	49,500	40,000	36,300	43,400	45,000
Pipe Velocity (m/s)	28.5	23.0	21.1	25.1	26.6
Mass Flow Rate (kg/s)	0.019	0.015	0.014	0.017	0.017
Flow Power (W)	8.4	8.4	8.4	8.4	8.4
Height, X_p/D	6.0	0.5	0.5	0.5	0.5

**Corresponds to almost a wall jet.

Nomenclature

A = exit area of the nozzle, m^2
A_{foil} = heated area of the foil, m^2
b = exit width of the RJR nozzle, m
D = inner diameter of the nozzle, m
h_{loc} = local heat transfer coefficient, W/m^2K
h_{avg} = average heat transfer coefficient defined on the basis of local heat transfer coefficient, W/m^2K
$\bar{h}$ = average heat transfer coefficient defined on the basis of area-averaged surface temperature, W/m^2K
I = current, A
ILJ = in-line jet
$\dot{m}$ = mass flow rate, kg/s
Nu_{loc} = local Nusselt number
$\overline{Nu}$ = average Nusselt number
P = fluid flow power, W
$p - p_{atm}$ = pressure drop, Pa
q''_{conv} = convected heat flux, W/m^2
q''_{gen} = generated heat flux, W/m^2
q''_{cond} = conducted heat flux, W/m^2
q''_{rad} = radiated heat flux, W/m^2
r = distance in the radial direction, m
r_o = inner radius of the nozzle, m
r_f = final radial integration distance for area averaging, m
Re = pipe Reynolds number = $u \cdot D/\nu$
RJR = radial jet reattachment
T_h = local heated foil temperature, °C
T_{ad} = local adiabatic foil temperature, °C
ΔT = local surface temperature differential, °C
$\overline{\Delta T}$ = area-averaged surface temperature differential, °C
u = pipe velocity, m/s
V = exit velocity of the RJR nozzle, m/s
X_p = height of nozzle exit from the impingement surface, m
θ = exit angle of the free jet, deg
ν = kinematic viscosity, m^2/s
ρ = density, kg/m^3
ϕ = voltage, V

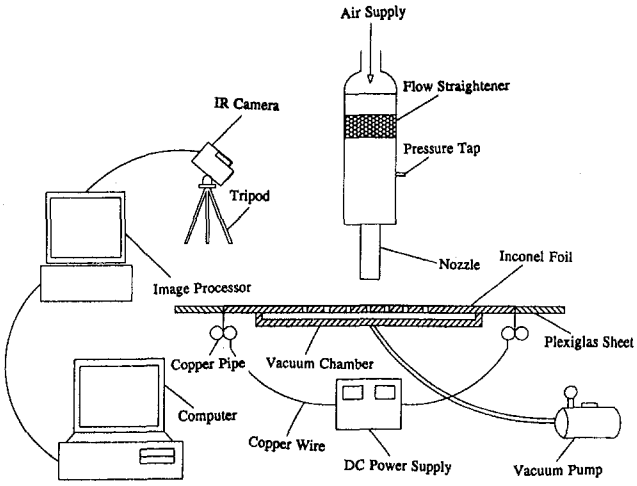

Fig. 3 Schematic of heat transfer jet impingement facility

the ILJ nozzle. In contrast, a comparison under equivalent mass flow rate would bias the results toward the RJR nozzle since the exit velocity for the RJR nozzle is typically larger than the exit velocity of the ILJ nozzle, contributing to higher heat transfer rates. In the case where the exit hydraulic diameters of the two nozzles are identical, a comparison under the same Reynolds number (and consequently, same mass flow rate and exit velocity) would still be meaningless owing to dynamically dissimilar flows. A comparison of the two nozzles under identical fluid flow power, on the other hand, properly accounts for the different nozzle geometries, by compensating for the pressure losses due to deflection of flow from the normal direction for the RJR nozzles. Hence, for an operational comparison, the power requirement to operate the nozzles should be considered. This paper highlights the importance and application of fluid flow power as a comparison criterion by choosing a particular case of identical pipe diameters of the ILJ and RJR nozzles. Such a case is typical when one is interested in retrofitting existing ILJ nozzles into RJR nozzles.

The second comparison criterion is based on the same peak pressures exerted by the nozzles on the surface. This type of a comparison is important when the peak pressure exerted on the surface by the nozzle is restricted in certain industrial applications.

Experimental Setup

Nozzle Geometry. The ILJ and RJR nozzles used for this study consisted of a 2.7 cm inner diameter pipe nozzles with a length of 15.2 cm. Three RJR nozzles with exit angles of +45, 0, and −10 deg were considered. The RJR nozzle exit width, b, was 0.5 cm and the bottom disk diameter was 3.8 cm (see Fig. 2).

Test Facility. The experimental setup used for this study is shown in the Fig. 3. The test apparatus consisted of a rigid frame to which a plenum and nozzle assembly was attached above a flat impingement foil. The plenum was provided with a flow straightener at its entry in order to eliminate any flow disturbances initiated upstream of the plenum. A pressure tap was provided downstream of the flow straightener in the plenum. An elliptically convergent piece provided the transition from the plenum to the nozzles. The nozzles could be screwed into this transition piece interchangeably. Dry air was supplied from two dedicated compressors and a heatless dryer that provided a dew point of −40°C. The supply air was maintained at a constant temperature by upstream heaters. The flow rate to the nozzles was measured by a choked flow converging nozzle located upstream of the flow. An inclined tube manometer was used to measure the pressure drop between the plenum and the ambient air.

The facility utilized a thin electrically heated stationary foil upon which the air jet impinged. The flat foil consisted of a sheet of Inconel alloy 600, 0.42 m wide by 0.72 m long, with a thickness of 0.0254 mm. This material was chosen because of its high electrical resistance and uniform physical properties. Furthermore, the small foil thickness ensured a negligible temperature difference between its top and bottom surfaces. The Inconel foil was stretched over a Plexiglas sheet and clamped between two copper tubes, which also served as the electrical bus source. A vacuum was applied to the bottom of the Inconel sheet via 609 holes (21 × 29) drilled within the Plexiglas. This design assured a flat surface during the experiment and low conductivity below the Inconel foil. The upper surface of the Inconel sheet was painted dull black to provide a high constant emissivity, approaching 0.98. The Inconel foil was heated by applying direct current across the copper bus bars. Due to the homogeneous nature of the Inconel material, the energy release per unit area of the foil was constant throughout the foil and could be accurately determined by knowing the heated area, and the input current and voltage. The electrical contact resistance between the copper rods and the Inconel foil was negligible, and hence no correction was made for the electrically generated heat flux calculations.

The foil surface temperatures were measured with an infrared camera and recording system (Mikron Model 6T62). This thermal imaging system has a temperature resolution of up to 0.025°C. A pressure tap, located on the impingement surface, was used for surface pressure measurements. The differential pressure ($p - p_{atm}$) was measured using a pressure transducer (Validyne model DP103-16). The plenum and nozzle assembly could be moved horizontally to provide for localized pressure measurements along a radial line on the surface.

Testing Procedure. All experiments were conducted while ensuring that the supply air temperature at nozzle exit was kept close to the ambient room temperature (within ±0.1°C), so that any thermal entrainment between the exiting jet and the surrounding would be minimized. The pressure drop across the plenum was noted for each experiment, and the mass flow rate was controlled accordingly to provide for a constant flow power for both the ILJ and RJR nozzles. The foil heat flux was maintained at around 272 W/m^2, which provided a temperature differential of less than 5°C with respect to ambient air for all parts of the foil. This temperature differential ensured low radiation losses from the foil to the surroundings, and also minimized conduction losses below the foil. The free convection at such temperature difference was found to be negligible in comparison with the forced convection effect due to the impinging jet. For each steady-state flow condition, a typical measurement included a recorded thermal image of an adiabatic foil (no electrical heating), followed by another recorded thermal image of the heated foil. The analysis then involved a digital subtraction of the two stored thermal images, followed by converting these temperature differentials to corresponding heat transfer coefficients. The infrared images were found to be fairly symmetric in the radial direction, from the nozzle centerline. Pressure measurements along the impingement surface were conducted for the ILJ and the RJR nozzles to measure the local pressures exerted by the jets on the surface.

Calculation Procedure. The local heat transfer coefficient corresponding to the local temperature differential at each location along a radial line, starting from the nozzle centerline, was calculated as follows:

$$h_{loc} = \frac{q''_{conv}}{T_h - T_{ad}} \tag{2}$$

where the local adiabatic foil temperature, T_{ad}, and local foil

heated temperature, T_h, are known at each surface point. At these locations, the convected heat flux needed for the local heat transfer coefficient calculation was determined from

$$q''_{conv} = q''_{gen} - q''_{cond} - q''_{rad} \quad (3)$$

The electrically generated resistance heating was calculated from measured values of the heated foil area, and the voltage and current as follows:

$$q''_{gen} = \frac{\phi \cdot I}{A_{foil}} \quad (4)$$

At each of the radial locations, the conduction losses were determined from known apparatus conductance values and measured temperatures. The radiation losses at these locations were calculated from room and foil temperatures. Radiation and conduction losses accounted for less than 3 percent of the total heat flux in all the experimental cases.

The local Nusselt number was calculated based on the thermal conductivity of the jet at nozzle exit condition and the inner pipe diameter for the in-line jet nozzle and the RJR nozzle as follows

$$Nu_{loc} = \frac{h_{loc} \cdot D}{k} \quad (5)$$

Practically, the area-averaged heat transfer coefficient is more important than the local heat transfer values in the design of impinging nozzle applications. This is because the area of concern in process industries is typically larger than the nozzle cross-sectional area. The average heat transfer coefficient can be defined in two ways. For an axisymmetric jet, the local heat transfer coefficients can be integrated over possible areas of concern (πr_f^2) as follows:

$$h_{avg} = \frac{2}{r_f^2} \int_0^{r_f} h_{loc}(r) r dr \quad (6)$$

which follows from the mathematical definition of integration. Equation (6) has been used in our previous publications (for example, see Ostowari and Page (1992) and Page et al. (1993)). A more correct definition of average heat transfer coefficient for a constant heat flux surface in terms of an average surface temperature (for example, see Viskanta (1993)) is as follows:

$$\bar{h} = \frac{q''_{conv}}{\overline{\Delta T}} \quad (7)$$

where the area average temperature differential is defined as

$$\overline{\Delta T} = \overline{(T_h - T_{ad})} = \frac{2}{r_f^2} \int_0^{r_f} (T_h(r) - T_{ad}(r)) r dr \quad (8)$$

In the present paper, the local heat transfer data were averaged based on the average surface temperature using Eq. (7). The average Nusselt number was calculated based on the average heat transfer coefficient as follows:

$$\overline{Nu} = \frac{\bar{h} \cdot D}{k} \quad (9)$$

The fluid flow power was calculated from

$$P = \frac{\dot{m}}{\rho} \cdot \Delta P \quad (10)$$

where $\dot{m}$, ρ, and ΔP are the mass flow rate, fluid density, and pressure drop across the nozzle. The pressure differential, ΔP, across the nozzles was measured between the pressure tap located in the plenum and the ambient air. Since the flow velocity was small in the plenum, no velocity correction term was added to the pressure drop in Eq. (10). The mass flow rate for the ILJ nozzle was larger than for the RJR nozzle operating under the same flow power (see Tables 1 and 2). This was because the pressure drop across the RJR nozzle was higher than the pressure drop across the ILJ nozzle, thus resulting in a lower mass flow rate in order to maintain the same flow power for both the nozzles. The Reynolds numbers in the Tables 1 and 2 are based on the inner pipe diameter and pipe velocity for the ILJ and the RJR nozzles.

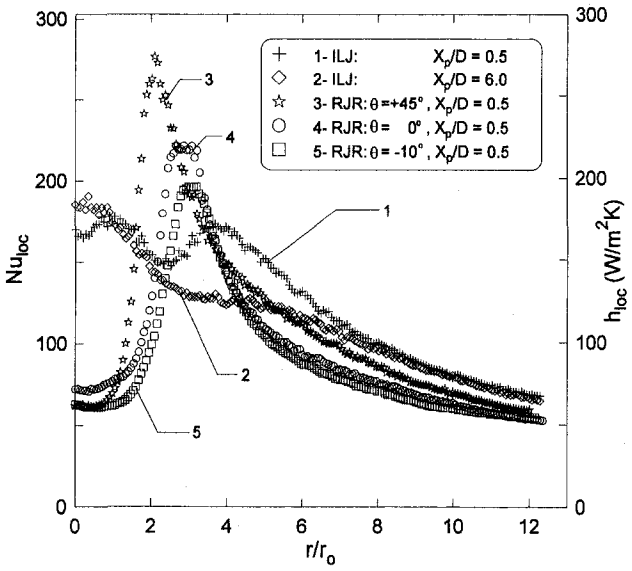

Fig. 4 Local Nusselt number for ILJ and RJR nozzles: P = 2.3 W

Experimental Results

Initial experiments for the ILJ nozzle were conducted at various nozzle heights. The optimum height criterion used for the ILJ nozzle was based upon determining the height that produced the maximum value of Nu_{loc} at the nozzle centerline. The optimum height for the ILJ nozzle corresponded to six nozzle diameters, which is in agreement with the reported data in the literature (Downs and James, 1987). This nozzle-to-surface spacing is also in agreement with the average heat transfer correlation (based on a circular area with a radius of ten times the nozzle diameter) reported by Klammer and Schupe (Viskanta, 1993). In addition, another experiment was conducted for the ILJ nozzle at a close nozzle to surface spacing of 0.5 D. Initial detailed experiments were also conducted for the zero degree RJR nozzle at various heights. It was observed that the RJR nozzle performed better (both local and average heat transfers over the entire surface) as the nozzle to surface spacing was reduced. The test case of X_p/D = 0.5 produced the best overall results for the RJR nozzle over the heights tested. Experiments below X_p/D of 0.5 were not possible to conduct because of adverse viewing requirement for the infrared imaging system. This height of 0.5 D for the RJR nozzles agrees well with previously published data by Ostowari and Page (1992).

Comparison Based on Identical Fluid Flow Power. Two different flow powers were investigated. The first flow power of 2.3 W corresponded to the ILJ Reynolds number of 31,900. The results presented here are based on the operating conditions given in Table 1. Figure 4 shows the local Nusselt number and the local heat transfer coefficient as a function of nondimensional radius, r/r_o, where r_o is the nozzle pipe inner radius. The radius, r, originates from the center point directly below the nozzle. The results indicate that the local Nusselt number was higher at the nozzle center point (r/r_o = 0) for the ILJ nozzle, but less than the RJR nozzles near the corresponding reattach-

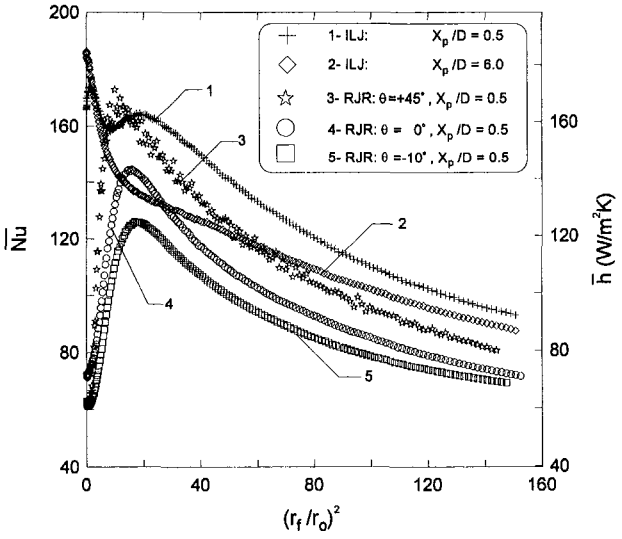

Fig. 5 Average Nusselt number for ILJ and RJR nozzles: P = 2.3 W

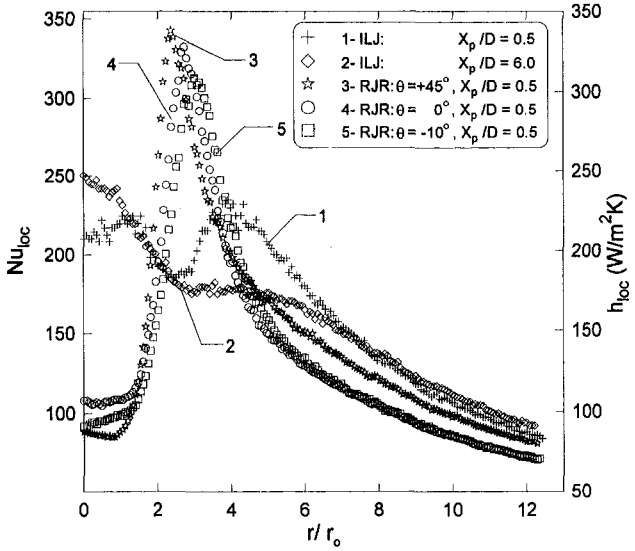

Fig. 6 Average Nusselt number for ILJ and RJR nozzles: P = 8.4 W

ment rings. According to Fig. 4, the location of peak local Nusselt number, which occurred within the reattachment ring for RJR nozzles with +45, 0, and −10 deg exit angles, were at r/r_o of 2.0, 2.9, and 3.1, respectively. The reattachment ring used in this context is a boundary or region of a physical space where the recirculating flow beneath the RJR nozzle was separated from the flow that was following the impingement wall curvature (flat plate), similar to a wall jet. For the RJR nozzle, the local Nusselt number was low in the recirculation region but increased rapidly near the reattachment region, with a maximum peak in the reattachment region, followed by an exponential decay past the reattachment region. The peak local Nusselt numbers were significantly higher for the +45 and 0 deg RJR nozzles than for the ILJ nozzle while that of a −10 deg RJR nozzle was comparable to that of the ILJ nozzle. For example, the RJR nozzle with a +45 deg exit angle produced a peak local Nusselt number of 277 while the ILJ nozzle operating at X_p/D = 6.0 produced a peak local Nusselt number of 188. A direct comparison of the Nusselt numbers between the ILJ and the RJR nozzles was possible since the Nusselt numbers were based on the same inner pipe (for the ILJ nozzle) or approach inner pipe (for the RJR nozzle) diameter for both the nozzles. The Nusselt numbers were not significantly different from the heat transfer coefficient values because the magnitudes of the inner pipe diameter and the thermal conductivity of ambient air were almost the same. Also shown in this figure is a plot of the ILJ nozzle operating at close nozzle to surface spacing of 0.5 D, for the same flow power, which will be discussed later.

Figure 5 presents the area-averaged Nusselt number and heat transfer coefficient as a function of dimensionless area ratio, $(r_f/r_o)^2$. This dimensionless ratio represents the area, πr_f^2, over which the data were averaged divided by the nozzle inner pipe area, πr_o^2. The presentation of data by this averaging technique provides for a better comparison of the effectiveness of one nozzle over the other for the same flow power. For the RJR nozzle with +45 deg exit angle, the maximum enhancement of 19.7 percent in average Nusselt number over the ILJ nozzle at a X_p/D = 6.0, is obtained at an $(r_f/r_o)^2$ of 9.9. The maximum enhancement in the average Nusselt number for the 0 deg exit angle RJR nozzle was 4.8 percent while the −10 deg RJR nozzle showed a reduction of 7.4 percent in its peak average Nusselt number. Enhancement was defined as the ratio of the difference in $\overline{Nu}$ between the RJR nozzle and the ILJ nozzle, over the $\overline{Nu}$ of the ILJ nozzle, at a particular nondimensional area from the centerline. Thus, the maximum enhancements for the RJR nozzles corresponded to the location of their peak $\overline{Nu}$ values. The ILJ nozzle at X_p/D = 6.0 showed higher area-averaged heat transfer than all the RJR nozzles for areas larger than $(r_f/r_o)^2$ = 63. Although the average Nusselt number was low or at best comparable for the 0 and −10 deg RJR nozzles to the ILJ nozzle, the true advantage of the 0 and −10 deg RJR nozzles was that it exerted a zero or a net negative force on the reattachment surface.

Additional similar sets of experiments were conducted to compare the heat transfer characteristics of the RJR nozzle to the ILJ nozzle at a higher flow power of 8.4 W, which corresponded to a highly turbulent ILJ nozzle Reynolds number of 49,500. The operating conditions for these sets of experiments are given in Table 2. Figures 6 and 7 illustrate the local and average Nusselt number values, respectively. An interesting observation was that the maximum enhancements in $\overline{Nu}$ for the RJR nozzle cases of 0 and −10 deg were significantly higher (8.1 percent and 4.8 percent, respectively) for the higher flow power case (Fig. 7), compared to their corresponding maximum enhancements in the lower flow power case, as seen in Fig. 5 (4.1 percent and −7.4 percent, respectively). The RJR nozzle with the 45 deg exit angle, on the other hand, showed a decrease in enhancement for the higher flow power case (5.5 percent)

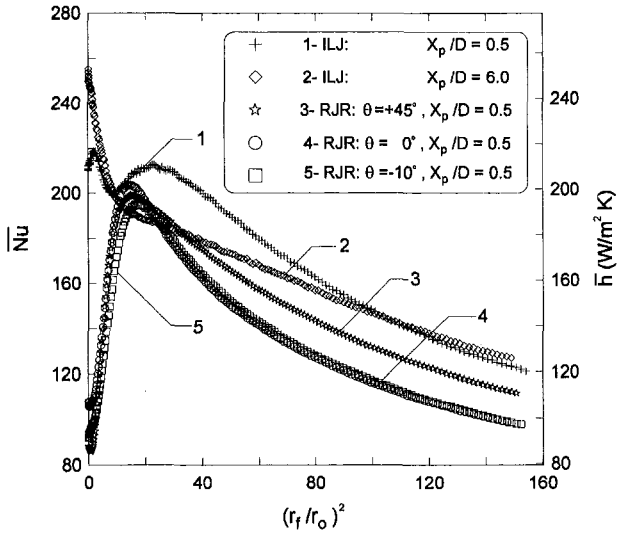

Fig. 7 Local Nusselt number for ILJ and RJR nozzles: P = 8.4 W

compared to the lower flow power case (19.7 percent). Again, the ILJ nozzle at $X_p/D = 6.0$ showed higher Nu than all the RJR nozzles at areas larger than $(r_f/r_o)^2 = 39$.

Finally, included in Figs. 4–7 are the heat transfer results for the ILJ nozzle operated at X_p/D of 0.5. Such close spacing to the impingement surface represents almost a wall-jet-type of flow for the ILJ nozzle. As seen in Figs. 6 and 7, the local and average values of Nusselt number for the ILJ nozzle operated at X_p/D of 6 were higher within the stagnation region than the corresponding values of ILJ nozzle operated at X_p/D of 0.5. However, the ILJ nozzle at X_p/D of 0.5 produced higher average Nusselt number values than the ILJ nozzle at X_p/D of 6, beyond $(r_f/r_o)^2$ of approximately 9.5. At X_p/D of 0.5, the ILJ nozzle Nu_{loc} data showed two local maxima occurring at r/r_o of 1.5 and 3.9. The same trend was observed for the ILJ nozzle at the low flow power as well (Fig. 4). These observations were similar to those reported by Lytle and Webb (1991). There has been speculation and disagreement among investigators as to the physical explanation for the second peak in the local Nusselt number value (see Viskanta, 1993). This second peak could be due to ring-shaped wall eddies induced consecutively by the large-scale toroidal vortices hitting the plate (Popiel and Trass, 1991). It is also suggested that the second maximum is a result of a transition from laminar to turbulent flow in the boundary layer (Lytle and Webb, 1991). The ILJ at this nozzle-to-surface spacing shows significantly higher average heat transfer coefficient than the RJR nozzles.

Comparison Based on Identical Peak Pressure. The results for comparison under identical peak pressures exerted on the impingement surface are shown in Fig. 8. Figure 8(*a*) shows the pressure distribution on the surface as a function of the nondimensional radial distance from the nozzle centerline, r/r_o. The data have not been presented in the form of a nondimensional pressure coefficient because the exit velocities for the ILJ and RJR nozzles are different. As seen from the graph, the ILJ nozzle at $X_p/D = 0.5$ and $X_p/D = 6.0$ exerts high local surface pressures at the impingement point, followed by a decrease away from the nozzle centerline. For the ILJ nozzle at $X_p/D = 0.5$, the peak pressure was slightly higher and was more spread in the region close to the nozzle compared to the $X_p/D = 6.0$ case. The 0 deg RJR nozzle surface pressure profile, at the same peak pressure as the ILJ nozzle of $X_p/D = 0.5$ case, had the flow power increased to 32.5 W (see Table 1 for corresponding operating conditions). Also shown in the figure is the pressure exerted on the surface by the 0 deg RJR nozzle operating at the same flow power as the ILJ nozzle cases. The net force exerted by the ILJ nozzle at a height of 0.5 D from the impingement surface was 0.4184 N while that of the RJR 0 deg nozzle for the same flow power of 2.3 W was only 0.071 N (5.9 times lower than the ILJ case).

The flow under the RJR nozzle is at subatmospheric pressure. Thus, we have both positive and negative surface pressures exerted on the surface with the RJR nozzle. At high flow rates, this may tend to warp a delicate surface. This condition can be avoided by installing RJR nozzles on both sides of the surface in order to balance the local negative and positive pressures to prevent warping.

The local and average Nusselt number for the RJR nozzle with 0 deg exit angle with a matching peak pressure to ILJ nozzle at $X_p/D = 0.5$ are shown in Figs. 8(*b*) and 8(*c*), respectively. The RJR nozzle local peak Nusselt number was higher by a factor of 2.2 over the ILJ nozzle case of $X_p/D = 0.5$. The 0 deg RJR nozzle showed a maximum average Nusselt number enhancement of 70.0 percent at $(r_f/r_o)^2$ of 18.6. Similar enhancements could also be demonstrated if the RJR nozzle was compared to the ILJ nozzle case of $X_p/D = 6.0$. It should be mentioned that the enhancement in heat transfer is at the expense of a significant increase in flow power (14 times that of the ILJ nozzle) for the 0 deg RJR nozzle.

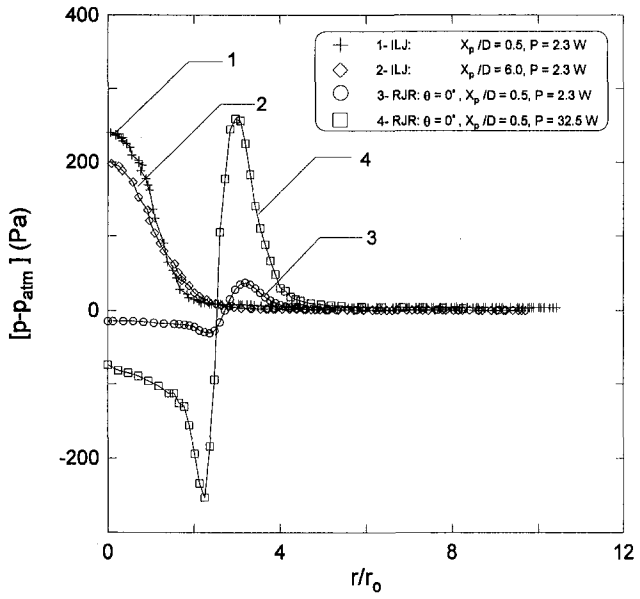

Fig. 8(*a*) Surface pressure measurements for the ILJ and RJR nozzles

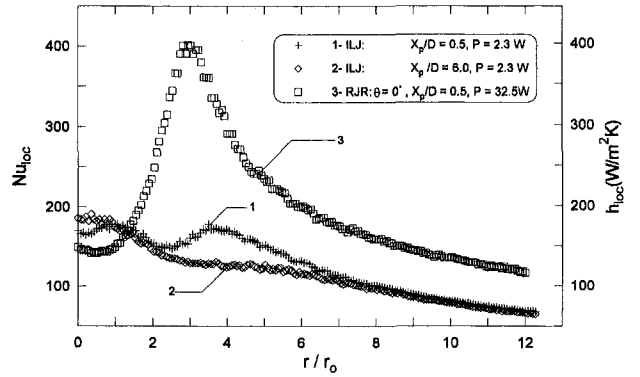

Fig. 8(*b*) Local Nusselt number for ILJ and RJR nozzles

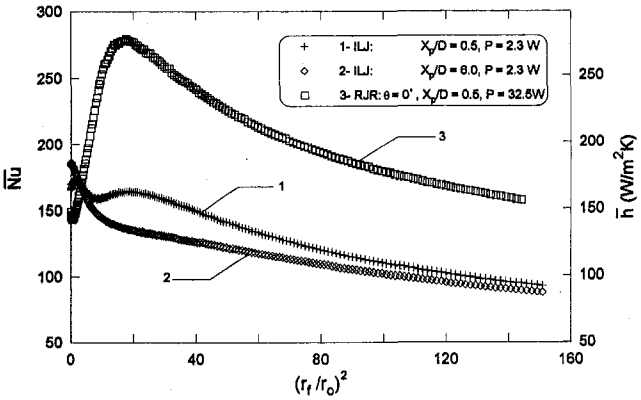

Fig. 8(*c*) Average Nusselt number for ILJ and RJR nozzles

Fig. 8 Comparison under identical peak pressures for ILJ and RJR nozzles

Error Analysis

An error analysis was performed based on the method proposed by Kline and McClintock (1953). In particular, for the optimum ILJ nozzle case of $X_p/D = 6.0$ and for the 0 deg RJR nozzle case of $X_p/D = 0.5$ (both for the higher Reynolds number set of experiments), the maximum and minimum values of uncertainty for the local Nusselt number were found to be 10 percent and 7.4 percent, respectively, for the ILJ nozzle. The maximum and minimum values of uncertainty for the local

Nusselt number of the 0 deg RJR nozzle were found to be 15.5 and 8.0 percent, respectively.

To confirm repeatability of the results, several cases of selected experiments were studied. The minimum and maximum standard deviation of Nu_{loc} values for the ILJ nozzle at $X_p/D = 6.0$ (at higher flow power) were 0.0 and 14.0, respectively, over three cases. The minimum and maximum standard deviations for $\overline{Nu}$ for this ILJ case were 0.8 and 11.1. The minimum and maximum standard deviation for the Nu_{loc} and $\overline{Nu}$ values of the 0 deg RJR nozzle case at higher flow power were 0.2, 22.4 and 0.3, 5.1, respectively, over four repeated cases. The minimum and maximum standard deviation of Nu_{loc} and $\overline{Nu}$ for the +45 deg RJR nozzle, at the high flow power case were 0.3, 16.3, and 1.6, 7.4 respectively, over four repeated cases. In all of the above-mentioned values of Nu_{loc} and $\overline{Nu}$, the maximum percentage error was not greater than 8.6 percent. The high values of standard deviation for the ILJ corresponded to the stagnation point, whereas the maximum value of standard deviation for the RJR nozzle corresponded to the reattachment or recirculation region.

Conclusions

The heat transfer characteristics of RJR nozzles with exit angles of +45, 0, and −10 deg were compared to the heat transfer characteristics of an ILJ nozzle. The comparisons were made at each nozzle's favorable spacing from the impingement surface and based on two criteria: (1) identical flow power, and (2) identical peak pressure. Comparison under identical fluid flow power was shown to be important from a practical point of view when comparing dissimilar flows, such as those of ILJ and RJR nozzles.

The results for the comparison under identical flow power indicated that considerable enhancements in local Nusselt numbers were achieved with the +45 deg RJR nozzle, while the 0 and −10 deg nozzles provided comparable or lower heat transfer. The ILJ nozzle showed higher area-averaged Nusselt number over large areas of integration compared to the RJR nozzles. The surface pressure exerted by the 0 deg RJR nozzle was very low compared to the ILJ nozzle at the same flow power. Comparison of the nozzles under identical peak pressures indicated that high enhancement was achieved with the RJR nozzle.

The RJR nozzle provided a mechanism to control the magnitude and the direction of the exerted force on the impingement surface. This is particularly important in heating, cooling, or drying of fragile surfaces. Also, since the RJR nozzle operates at close nozzle to surface spacing, it is suitable for the design of compact equipment.

Acknowledgments

This work was financially supported by the Texas A&M University Drying Research Center and the Department of Mechanical Engineering.

References

Downs, S. J., and James, E. H., 1987, "Jet Impingement Heat Transfer—A Literature Survey," ASME Paper No. 87-H-35.

Goldstein, R. J., Behbahani, A. I., and Heppelmann, K. K., 1986, "Stream-wise Distribution of the Recovery Factor and the Local Heat Transfer Coefficient to an Impinging Circular Air Jet," *International Journal Heat Mass Transfer,* Vol. 29, pp. 1227–1235.

Habetz, D. K., Page, R. H., and Seyed-Yagoobi, J., 1992, "A Drying Comparison of Radial Jet Reattachment and Standard In-Line Jet Impingement," *Drying '92,* Majumdar, A. S., ed., pp. 953–962.

Kline, S. J., and McClintock, F. A., 1953, "Describing Uncertainties in Single Sample Experiments," *Mechanical Engineering,* Vol. 75, Jan., pp. 3–8.

Lytle, D., and Webb, B. W., 1991, "Secondary Heat Transfer Maxima for Air Jet Impingement at Low Nozzle-to-Plate Spacings," *Experimental Heat Transfer, Fluid Mechanics, and Thermodynamics,* J. F. Keffer, R. K. Shah, and E. N. Ganic, eds., Elsevier, New York, pp. 776–783.

Martin, H., 1977, "Heat and Mass Transfer Between Impinging Gas Jets and Solid Surfaces," *Advances in Heat Transfer,* Vol. 13, pp. 1–60.

Obot, N. T., Mujumdar, A. S., and Douglas, W. J. M., 1980, "Design Correlations for Heat and Mass Transfer Under Various Turbulent Impinging Jet Configurations," *Drying '80,* Vol. 1, pp. 338–402.

Ostowari, C., and Page, R. H., 1992, "Convective Heat Transfer From a Radial Jet Reattachment," *AIChE Symposium Series,* Vol. 88, No. 288, pp. 189–197.

Page, R. H., and Ostowari, C., 1985, "Radial Jet Reattachment Flow," *Bulletin American Physical Society,* Vol. 30, p. 1698.

Page, R. H., Ostowari, C., and Carbone, J. S., 1986, "Radial Jet Flow," *Proc. 4th International Symposium on Flow Visualization,* Paris, France, pp. 512–521.

Page, R. H., Carbone, J., and Ostowari, C., 1990, "Radial Jet Reattachment Force," *Experiments in Fluids,* Vol. 8, No. 5, pp. 297–298.

Page, R. H., and Seyed-Yagoobi, J., 1990, "A New Concept for Air or Vapor Impingement Drying," *TAPPI Journal,* Vol. 73, pp. 229–234.

Page, R. H., Ostowari, C., Seyed-Yagoobi, J., and Gruber, T. C., Jr., 1993, "Measurement of Impinging Jet Heat Transfer Utilizing Infrared Techniques," *Experimental Heat Transfer, Fluid Mechanics, and Thermodynamics,* Elsevier Science Publishers, New York, Vol. I, pp. 726–731.

Polat, S., Huang, B., Mujumdar, A. S., and Douglas, W. J. M., 1989, "Numerical Flow and Heat Transfer Under Impinging Jets: A Review," *Ann. Rev. Num. Fluid Mech. Heat Transfer,* Vol. 2, pp. 157–197.

Popiel, C. O., and Trass, O., 1991, "Visualization of Free and Impinging Round Jets," *Exp. Thermal Fluid Sci.,* Vol. 4, pp. 253–261.

Thiele, E. W., Seyed-Yagoobi, J., Page, R. H., and Castillo-Garcia, H., 1995, "Enhancement Drying Rate, Moisture Profiling, and Sheet Stability on an Existing Paper Machine With RJR Blow Boxes," *Proc. TAPPI Papermakers Conference,* Chicago, IL, pp. 223–228.

Viskanta, R., 1993, "Heat Transfer to Impinging Isothermal Gas and Flame Jets," *Experimental Thermal and Fluid Science,* Vol. 6, pp. 111–134.

Heat Transfer Enhancement in Electronic Modules Using Various Secondary Air Injection Hole Arrangements

B. A. Jubran[1]
Department of Mechanical Engineering,
International Islamic University, Malaysia,
53100 Kuala Lumpur, Malaysia

M. S. Al-Haroun
Department of Mechanical Engineering,
University of Jordan,
Amman, Jordan

This paper reports an experimental investigation to study the effects of using various designs of secondary air injection hole arrangements on the heat transfer coefficient and the pressure drop characteristics of an array of rectangular modules at different values of free-stream Reynolds numbers in the range 8×10^3 to 2×10^4. The arrangement used is either one staggered row of simple holes or one row of compound injection holes. The pitch distances between the injection holes, as well as the injection angles, were varied in both the streamwise and spanwise directions. Generally, the presence of secondary air through the injection hole arrangement can give up to 54 percent heat transfer enhancement just downstream of the injection holes. The amount of heat transfer enhancement and pressure drop across the electronic modules is very much dependent on the design of the injection holes. The simple angle injection hole arrangement tends to give a better heat transfer enhancement and less pressure drop than the compound angle holes.

1 Introduction

Heat transfer enhancement in electronic components continues to attract a lot of research activity toward achieving better cooling techniques to meet the design and development of rather complex circuits and dense electronic boards, characterized by high rate of heat dissipation per unit of component area. The topography of the electronic board plays a significant role on the heat transfer rate and the pressure drop characteristics of these boards.

Numerous experimental investigations on heat transfer enhancements in electronic modules, using various fin designs, have been reported in the literature such as those of Sparrow et al. (1983), Torikoshi et al. (1988), and Jubran et al. (1996). Ratts et al. (1988) presented an experimental study of internal flow modulation induced by vortex shedding from cylinders in crossflow and its effect on cooling an array of chips. They concluded that a heat transfer coefficient increase of up to 82 percent could be obtained when cylinders are placed periodically above the back edge of each row of chips. Myrum et al. (1993) investigated the heat transfer and the pressure characteristics of airflow in a ribbed duct with vortex generator placed immediately upstream or just downstream of selected rib elements. Provided the diameter of the generator is large, the average Nusselt number was increased by as much as 21 percent.

Lau et al. (1989) studied the effects of lateral flow ejection on the overall heat transfer coefficient and pressure drops for turbulent flow through pin fin channels and found that the Nusselt number has increased with increasing the Reynolds number and is reduced by as much as 25 percent as the ejection ratio is increased from 0 to 1.0. Lehmann and Huang (1991) investigated the potential of using secondary flow mixing to enhance convective air cooling of board-mounted electronic components through the use of vortex generators. Hollworth and Durbin (1992) investigated the potential of using low-velocity potential impinging air jets for cooling simulated electronic modules and obtained heat transfer enhancement of up to 50 percent. Jubran and Al-Salaymeh (1996) reported preliminary results on the use of secondary airflow for heat transfer enhancement and obtained up to 51 percent increase in the heat transfer rate.

The aim of the present investigation is to study the heat transfer enhancement and the pressure drop characteristics for a uniform array of blocks using secondary air flow injection holes. The parameters under consideration will include the shape of injection holes, namely simple injection holes and compound injection holes, the distance between the injection of the holes, the injection angles of the holes, and the blowing rate ratio.

2 Experimental Rig and Experimentation

The basic experimental setup used in this investigation is basically a modified version of that used by Hollworth and Durbin (1992). The setup consists mainly of a suction-type wind tunnel with maximum flow rate of 0.24 m^3/s. The main body of the test section is a channel-like box 2 m in length, 0.33 m in width, and 0.04 m in height. The test section and the wind tunnel have been constructed from 3 mm sheet metal. The front sidewall of the test section accommodates at its middle section a double glazing window to ease observation of the array configurations during tests. At the air intake side of the wind tunnel a bellmouth is attached, and a flow straightener is placed at the front and at the trailing edge of the wind tunnel test section with a gradual contraction, which is connected to a circular cross-sectional pipe of the fan, Fig. 1.

The module array consists of uniform individual rectangular elements manufactured from the light metal aluminum alloy Duralumin. The modules in the array are arranged in 8 rows each containing 5 elements. The basic dimensions of the modules are 25 mm side length, 15 mm width, and 10 mm height. It should be pointed out that the long side of the module is always parallel to the airflow. The spacings between the modules are 25 mm and 15 mm, in the streamwise and spanwise directions, respectively. Figure 2(*a*) shows a typical basic array configuration in the test section.

[1] On leave from University of Jordan.

Contributed by the Heat Transfer Division for publication in the JOURNAL OF HEAT TRANSFER. Manuscript received by the Heat Transfer Division August 6, 1997; revision received January 5, 1998. Keywords: Electronics, Heat Transfer, Packaging. Associate Technical Editor: Y. Jaluria.

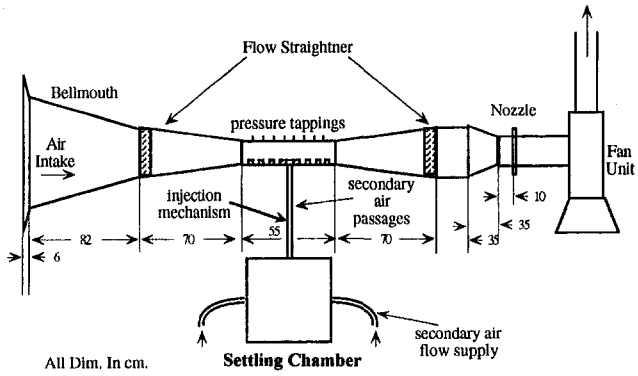

Fig. 1 Schematic diagram of the experimental setup

The secondary air flow injection is carried out by drawing air from a fan and then feeding it to a settling chamber, which accommodates the injection mechanism. The injection mechanism consists of one row of brass tubes of 6.2 mm outside diameter and 6 mm inside diameter. The injection mechanisms used have different pitch-to-diameter ratios between the holes, namely P/D = 1.7, 2.5, and 5. The injection tubes are interconnected by a flat plate to form an injection box, which again is flush with the modules, Fig. 2(b). Three injection angles were also used; 45, 60, and 90 deg. The angles were taken with reference to the streamwise direction for the simple injection holes and with reference to the spanwise direction for the compound angle holes. The injection mechanism is located between the third and fourth rows of modules. Table 1 summarizes the geometric design of the injection models with reference to their injection angles and the P/D ratios. The ratio of injection air to free-stream is quantified using the blowing rate ratio, which is defined as $M = \rho_i U_i / \rho_\infty U_\infty$. Different blowing rates for the secondary air injection were used in the range 0.25 to 2.96. These experiments were conducted at free-stream Reynolds numbers of 8×10^3 to 2×10^4.

Each of the eight heat transfer active modules of the middle column of the array is hollowed to the same size of the heater such as to accommodate a 22 Ω resistance heater; each rated at 2 W. This means that each row of the array will have an active module in the middle of the row. The leads of the heaters are insulated, and are connected to a variable DC power supply.

Table 1 Summary of injection model specifications

Injection Model	P/D	β°	Ω°
A	5.0	60	
B	2.5	60	
C	1.7	60	
D	5.0	45	
E	1.7	45	
F	5.0	90	
G	2.5	90	
H	1.7	90	
A′	5.0		60
B′	2.5		60
C′	1.7		60
D′	5.0		45
E′	2.5		45

The module's power is held constant during the experiment, such that the per module heat flux is kept constant. The modules on the array test surface are fixed to a piece of 2.5 mm balsa wood, which is fixed to a 5-mm wood sheet, Fig. 2(a). Each module in the array is threaded to accommodate a 3 mm screw, so that the modules are well attached to the base sheet.

The steady-state temperature of the rectangular modules was obtained by embedding two copper constantan thermocouples to the surface of each module of interest. All thermocouples were connected via the 3530 Orion-A data logger. The pressure drop across the modules arrays was determined by a total of 24 static pressure tappings mounted on the roof of the test section just over the module array, and these were connected to an inclined manometer sensitive to the measurements of small deflections as low as 0.05 mm of ethanol. This arrangement of pressure tapping enables pressure drop to be obtained along the module array as well as at locations before and after the array. At each row there exist three tappings, and the average of these was taken as the static pressure at that location. The air flow rate was determined using a standard nozzle 7.02 cm in diameter with a coefficient of discharge of 0.96 installed at the inlet

Nomenclature

A_c = flow cross-sectional area of the gap above the module, m^2
A_{surf} = modules exposed area, m^2
b = module height, m
C = distance between rows of modules, m
C_p = pressure coefficient in presence of secondary airflow injection
C_{po} = pressure coefficient of basic uniform array without secondary airflow injection
D = diameter of injection cylinders or holes
E = input voltage to the elements heater, V
h = heat transfer coefficient, $W/m^2 \cdot K$
H = height of test section channel, m
I = input current to the element heater, amp
k_{air} = thermal conductivity of air, $W/m \cdot K$
L = module side length, m
M = blowing rate ratio
N = denotes downstream row number, or the total number of modules downstream of the module of interest
Nu = Nusselt number for the array configurations with secondary air injection
Nu_o = Nusselt number for uniform array configurations without secondary air injection
P = distance between injection holes
q = heat flux rate, W
St_o = Stanton number for array configurations without secondary air injection
T_{act} = surface temperature of the active module, K
T_{ref} = reference temperature of fluid, K
$\dot{w}$ = air flow rate through channel, m^3/s
β = injection hole angle with respect to test surface as projected into streamwise/normal plane
ν = kinematic viscosity for air, m^2/s
ρ = air density, kg/m^3
Ω = injection hole angle with respect to test surface as projected into spanwise/normal plane

Subscripts

a = air
act = active
conv = convection
I = injection
ref = reference
∞ = free stream

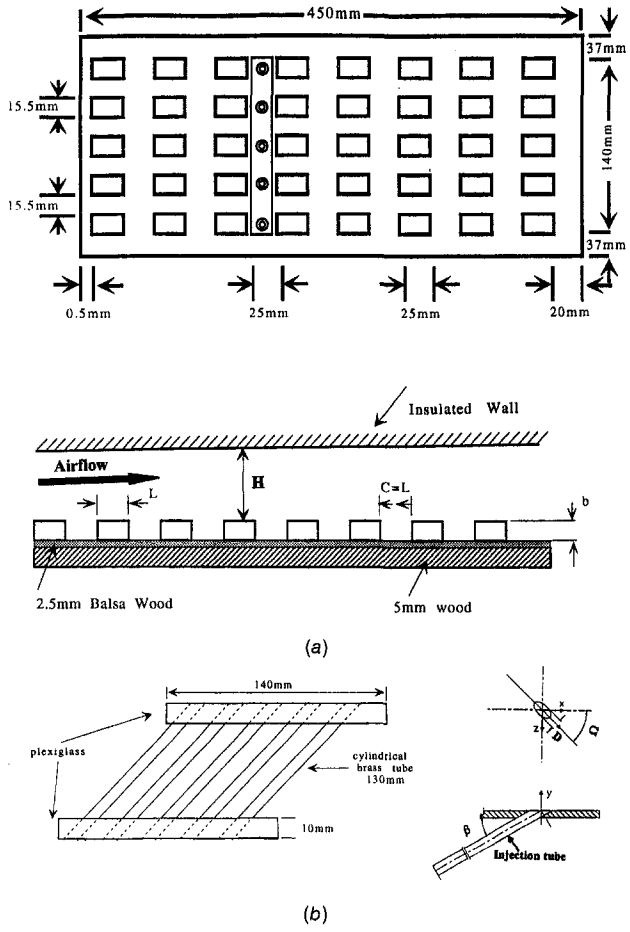

Fig. 2 Details of test sections: (*a*) view of basic array configuration, (*b*) injection mechanism

section of the fan. Various flow rates were obtained by varying the speed of the fan.

Once the desired injection air mechanism installed in the test section, the fan was switched on with the right amount of airflow. The temperature of the secondary injected air is the same as that of the main flow in the test section. The heaters were also switched on and the experimental setup was allowed to reach steady state, which was obtained after about one hour. At this instant of time, readings of temperature, input power, pressure drop, and inlet temperature were recorded. The same procedure was repeated for different injection air mechanisms and free-stream velocities.

3 Data Reduction

The connective heat transfer rate q was determined from the electrical power input to the module using

$$q = EI - \Delta q \tag{1}$$

where the term Δq is a small correction for conduction and radiation heat losses from the module. In order to minimize the radiation losses, the modules have been polished. Fixing the modules to the balsa wood plate has minimized the conduction heat losses. Hollworth and Durbin (1992) reported that the conduction losses through such surfaces never exceed 4 percent of the heat input to the module. Furthermore, Wirtz and Dykshoorn (1984) used the same test surface and it was shown, by a thermal imaging technique, that very little heat was conducted into the balsa wood surface adjacent to the heat dissipating modules. A correction factor was computed and applied during the calculation of the heat transfer coefficients in order to account for these heat losses. Assuming an emissivity of 0.04 for the module's surface, the correction factor combining both of these losses was found not to exceed 10 percent of the electrical power input.

The heat transfer coefficient was calculated from

$$h = \frac{q}{A_{\text{surf}}(T_{\text{act}} - T_{\text{ref}})} \tag{2}$$

where q is the heat input to the active module, A_{surf} is the five-surface area of the active module exposed to the air flow, T_{act} is the active module surface temperature, and T_{ref} is the steady-state temperature of the passive modules at the first row of the array.

Reynolds number (Re) and Nusselt number (Nu) are calculated from:

$$\text{Re} = \frac{\dot{w}L}{A_c \nu} \tag{3}$$

$$\text{Nu} = \frac{hL}{k_{\text{air}}} \tag{4}$$

where $\dot{w}$, L, A_c, ν, and k_{air} are the air volumetric flow rate, the module side length that is parallel to the direction of the airflow, the cross-sectional area of the empty space over the modules, the kinematic viscosity of air, and the thermal conductivity of the air, respectively.

Presentations of the pressure drop results were classified into two groups. The first group is that for basic uniform module array configuration where a fully developed regime is established. In this region, the per-row pressure drop Δp_{row} is expressed in terms of the per-row pressure coefficient as

$$C_{po} = \frac{\Delta p_{\text{row}}}{(1/2)\rho V^2} \tag{5}$$

where V is calculated as $\dot{w}/A_c$ and ρ is the air density. The second group of pressure drop results is for when the various air injection mechanisms are present in the array of modules. This is expressed in dimensionless form as C_p/C_{po}, where C_p represents the per-row pressure drop coefficient in the presence of the injection holes.

4 Results and Discussions

Throughout the measurements made to establish the data presented in this paper, care was taken to note possible sources of error, and an error analysis based on the method of Kline and McClintock (1953) was carried out. The error analysis indicated a ±5 percent uncertainty in the heat transfer, ±2 percent for pressure coefficients, and ±2 percent in the velocity. Tests were repeated a few times to ensure the repeatability of the results.

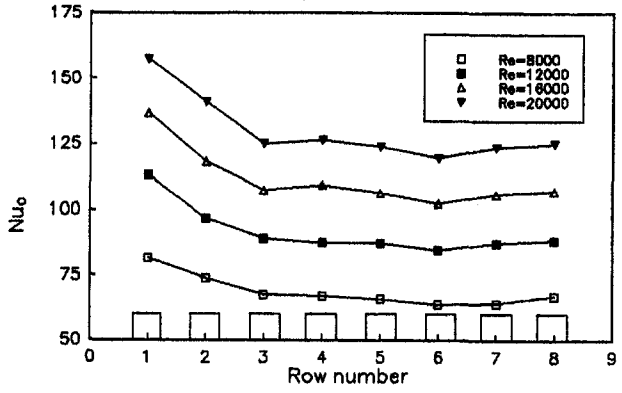

Fig. 3 Row-by-row Nusselt number distributions for the basic array configuration without secondary air injection

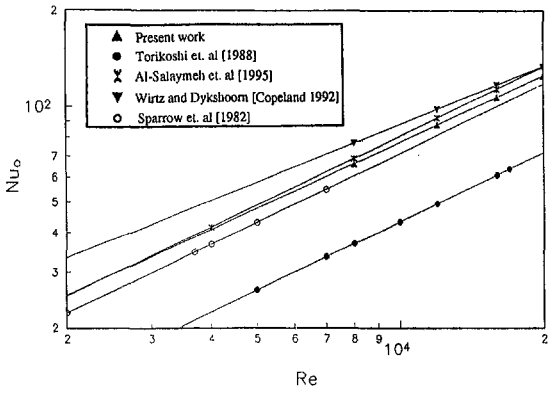

Fig. 4 Comparison of fully developed Nusselt number of the present work with previous works

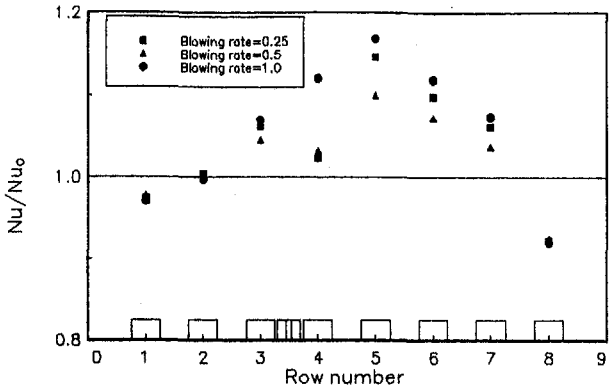

Fig. 5 Row-by-row Nusselt number distributions of model A, P/D = 5 and β = 60 deg

4.1 Heat Transfer Results and Discussion. The row-by-row distribution of the per-block Nusselt number for the basic uniform module array configuration is shown in Fig. 3, for different values of Reynolds numbers ranging from 8×10^3 to 2×10^4. These results show that for all Re values, the maximum Nu is attained at the first row of modules, which is attributed to the impingement of the flow on the first row of modules. Downstream of the first row, Nu decreases with the distance up to the third row of modules after which Nu is independent of the row location. These rows are consequently considered as the fully developed region in the array. The results for the basic uniform module array configuration at different Re values together with those of Sparrow et al. (1982), Torikoshi et al. (1988), Wirtz and Dykshoorn (1984), and Jubran and Al-Salaymeh (1996) are shown in Fig. 4. These results were correlated using the following form:

$$\mathrm{Nu}_o = a\mathrm{Re}^m \tag{6}$$

$$\mathrm{St}_o = b\mathrm{Re}^{m-1} \tag{7}$$

where Nu_o and St_o are the average values of the Nusselt number and the Stanton number in the fully developed region of the array, respectively. It is interesting to note that the values of the exponent, m, for all investigations that are shown in Fig. 4 are in the range 0.65 to 0.86. On the other hand, the values of the constants a and b are very much dependent on the dimensions of the modules and the other array configurations parameters. Although the Prandtl number was not variable in the present study, it is included in the coefficients of Eqs. (6) and (7). For the present investigation with L/H = 0.625 and the range of Re used, the following correlations were obtained:

$$\mathrm{Nu}_o = 0.10\ \mathrm{Re}^{0.72} \tag{8}$$

$$\mathrm{St}_o = 0.14\ \mathrm{Re}^{-0.28} \tag{9}$$

These correlations are in good agreement with those reported in the literature. Sparrow et al. (1982), Torikoshi et al. (1988), Jubran and Al-Salaymeh (1996), and Jubran et al. (1996) who found the exponential, m, to be 0.72. It seems that the present work, with the exception of Jubran et al. (1996), is the only one that has made use of rectangular modules, while the other investigations mentioned used square ones. It can be concluded from this that when rectangular modules are used in an array configuration, they tend to enhance the heat transfer rate over that when square modules are used.

The effects of inserting different designs of secondary air injection mechanisms between the third and fourth rows at a fixed mainstream Reynolds number, Re = 1.6×10^4, and blowing rate ratios in the range 0.25 to 2.96, on the heat transfer characteristic of the uniform array configuration are shown in

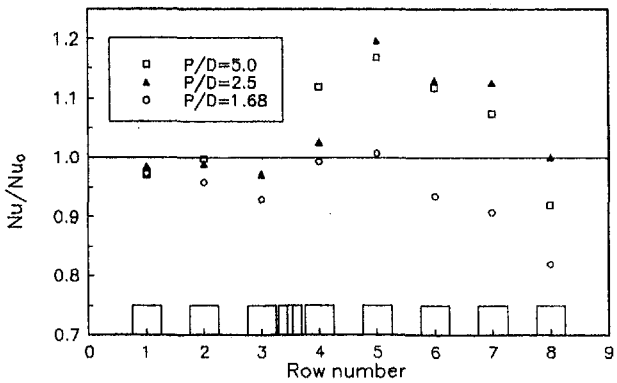

Fig. 6 Effect of P/D on Nusselt number ratio for 60 deg simple angle injection holes at M = 1.0

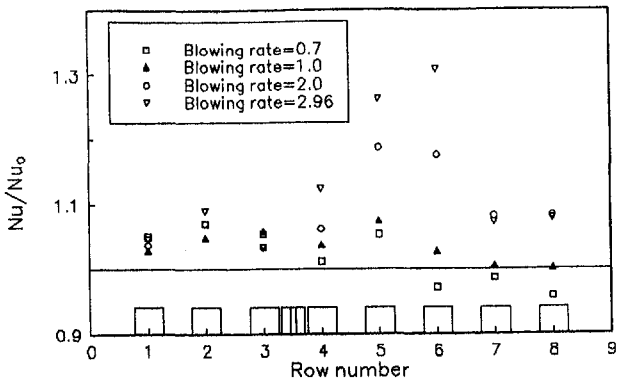

Fig. 7 Row-by-row Nusselt number distributions of model A', P/D = 5 and Ω = 60 deg

Figs. 5–10. The results are plotted in terms of the ratio of Nu of the array with secondary air injection, to that Nu_o of the basic array configuration with a uniform module array without air injection.

The per-row distributions of $\mathrm{Nu/Nu}_o$ of injection model A at blowing rate ratios 0.25, 0.5, and 1.0 is shown in Fig. 5. This figure reveals that for all blowing rate ratios, the ratio $\mathrm{Nu/Nu}_o$ increases with increasing streamwise distance up to the fifth row, where the maximum enhancement is attained, and then decreases steeply to 8 percent lower than the fully developed value without air injection at the last module. In particular the maximum values of heat transfer enhancement at the fifth row are approximately 15, 10, and 17 percent for blowing rate ratios M = 0.25, 0.5, and 1.0, respectively. The effect of increasing

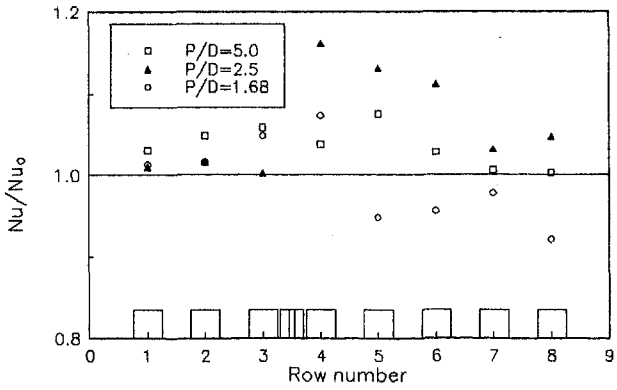

Fig. 8 Effect of P/D on Nusselt number ratio for 60 deg compound angle injection holes at M = 1.0

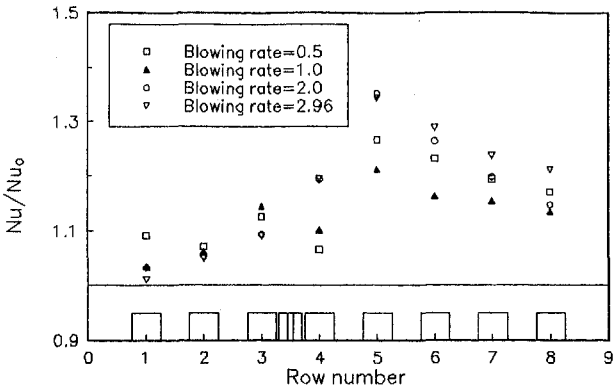

Fig. 9 Row-by-row Nusselt number distributions of model D, P/D = 5 and β = 45 deg

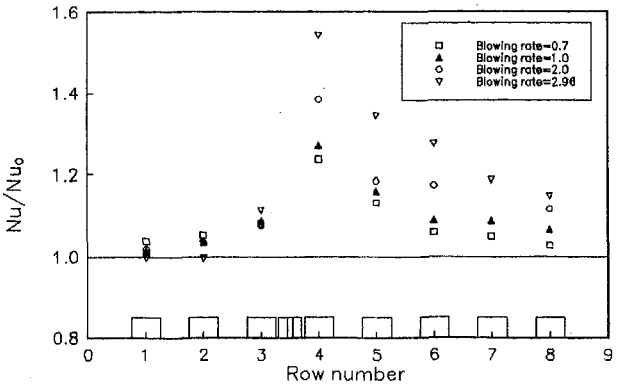

Fig. 10 Row-by-row Nusselt number distributions of model D′, P/D = 5.0 and Ω = 45 deg

pitch to diameter ratio between the holes, P/D = 1.68, 2.5, and 5 for 60 deg simple angle air injection model and blowing rate ratio M = 1.0, on the heat transfer enhancement, is shown in Fig. 6. It is clear that the optimum P/D is 2.5. This optimum P/D is found to be the same for all blowing rate ratios investigated.

The effect of using compound angle air injection holes where the secondary air is injected at 60 deg angle to the lateral direction of the mainstream flow (model A′) and M = 0.7, 1.0, 2.0, and 2.96 is shown in Fig. 7. The figure indicates that upstream of the injection holes the enhancement does not exceed 10 percent for all blowing rate ratios and it can be noted that the enhancement is almost blowing rate independent. However, downstream of the injection holes, a significant increase in the heat transfer enhancement is noted, with the maximum values occurring at the fifth row for all blowing rates, except for the highest blowing rate ratio M = 2.96, where the maximum enhancement in heat transfer is shifted to the sixth row with a value of 30 percent. The effect of increasing pitch-to-diameter ratio between the holes, P/D = 1.68, 2.5, and 5 for 60 deg compound angle air injection model and blowing rate ratio M = 1.0, on the heat transfer enhancement is shown in Fig. 8. It is clear that the optimum P/D is 2.5, the same as that for simple angle injection holes. A comparison between Figs. 6 and 8 indicates that the simple angle injection holes are slightly better than the compound angle injection holes.

The results of the Nu/Nu$_o$ for simple angle injection holes of 45 deg inclination to the streamwise directions and P/D = 5.0 (Model D) are shown in Fig. 9 for M = 0.5, 1.0, 2.0, and 2.96. It can be seen from this figure that a maximum heat transfer enhancement of 35 percent is obtained for both M = 2.0 and 2.96. The results of Nu/Nu$_o$ for compound angle injection holes of 45 deg with respect to the lateral direction (model D′) are shown in Fig. 10. The figure shows that as the distance downstream is increased, the Nu/Nu$_o$ is increased up to the maximum value at the fourth row, after which it decreases steeply, but is still higher than 1. The presence of the secondary air injection from this model tends to enhance the heat transfer by 24, 27, 38, and 54 percent for M = 0.7, 1.0, 2.0, and 2.96, respectively. Figure 11 compares the results of Nu/Nu$_o$ for simple angle injection holes at 45 deg and compound injection holes at 45 deg in the spanwise direction at M = 1 and P/D = 5.0. In general, the simple angle injection holes model tends to give better heat transfer enhancement than the compound angle injection holes model. Furthermore, rows 4 and 6 are favored by receiving better cooling, which might suggest that the present cooling technique could be used for modules with increased cooling needs.

Although no flow visualization was carried out in the present investigation, one may use similar arguments to that used in film cooling of gas turbine blades, which uses similar injection models to the one used in the present investigation, to explain the heat transfer enhancement in the presence of secondary air flow. In particular at blowing rates $M > 0.5$, jets from the injection holes tend to lift off from the surface of the injection models to form vortices, which tend to increase the mixing between the mainstream flow and the secondary flow injection and hence increase the heat transfer rate. The results reported here show clearly that as the blowing rate is increased, the heat transfer enhancement is increased.

4.1 Pressure Drop Results and Discussion. The effect of the presence of various injection hole models located between the third and fourth rows at different blowing rates has been investigated. The results of C_p/C_{po} are shown in Figs. 12 and

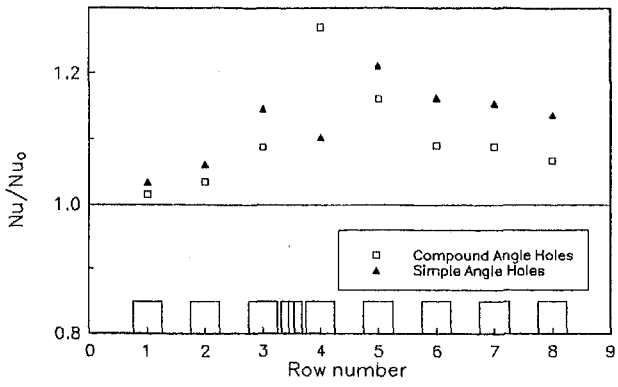

Fig. 11 Effect of the injection angle type on Nusselt number ratio for 45 deg, M = 1 and P/D = 5.0

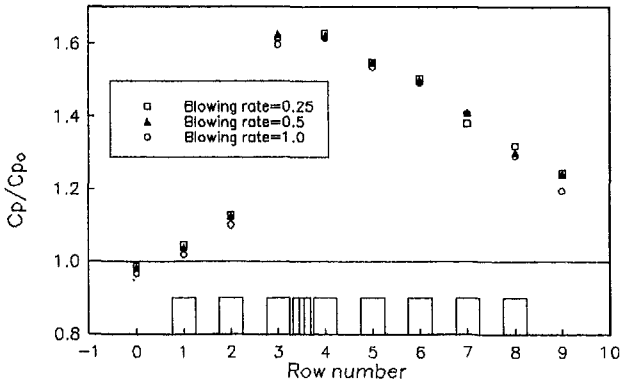

Fig. 12 Row-by-row pressure drop coefficient ratio of model A, P/D = 5 and β = 60 deg

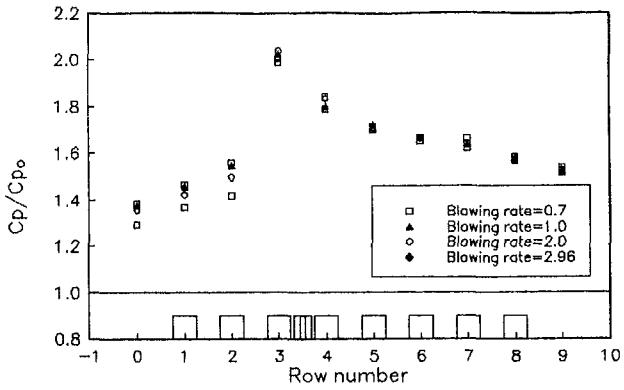

Fig. 13 Row-by-row pressure drop coefficient ratio of model A′, P/D = 5 and Ω = 60 deg

13, where C_p is the local pressure coefficient in the presence of the secondary airflow injection holes models, and C_{po} is the local pressure coefficient of the basic uniform array without secondary airflow injection. The parameters investigated include the blowing rate ratio, the injection angle, and the pitch-to-diameter ratio, P/D.

Figure 12 shows the effect of secondary airflow injection from simple angle injection holes at 60 deg in the streamwise direction and P/D = 5.0 (model A), on the pressure drop ratio C_p/C_{po}, for blowing rates M = 0.25, 0.5, and 1. The figure indicates clearly that the presence of the secondary air injection tends to increase the pressure drop, especially at the location of the injection model by as much as 60 percent. However, the results also show that the C_p/C_{po} is a weak function of the blowing rate M. The results of the pressure drop ratio for the compound angle injection model at 60 deg in the spanwise direction (model A′) is shown in Fig. 13. The figure reveals that the pressure drop coefficient increases steeply as the streamwise distance is increased up to the third, where an abrupt increase of 100 percent pressure drop is observed. Downstream of the third row of modules, the pressure drop coefficient is decreased progressively to nearly 53 percent at the outlet position. Again, the results indicate that the pressure drop is a weak function of the blowing rate for compound angle holes injection.

The comparison between Figs. 12 and 13 shows that the use of compound angle injection tends almost to double the pressure drop over that obtained for simple angle injection holes. This may be attributed to the lateral injection of the jets for the compound angle, which tends to give a bigger obstruction to the mainstream flow and hence cause a higher pressure drop than that obtained for the simple injection holes where the jet is injected parallel to the main flow. The effect of changing the P/D and the angles of the injection holes for both simple and compound angle hole injection tends to have negligible effects on the pressure drop ratio.

5 Conclusions

An experimental investigation was conducted to explore the effects of using secondary air through various injection hole arrangements on the heat transfer coefficient and pressure drop characteristics of array configurations composed of rectangular individual modules. The experimental results suggest the following conclusions:

1 The heat transfer enhancement characteristics of array configurations composed of rectangular individual modules in the presence of secondary air injection holes are very much dependent on the P/D ratio between the holes. In general, the optimum P/D in the present investigation is found to be 2.5.

2 Reducing the injection angles of the secondary air tends to enhance the heat transfer from the electronic modules for both the compound angle and simple angle injection holes. In general the simple injection holes tend to give better heat transfer enhancement than the compound injection holes, except at the location of the injection holes, where the compound angle holes give better heat transfer enhancement of 54 percent.

3 The optimum blowing rate ratio that gives the highest heat transfer enhancement is dependent on the injection angle of the holes and P/D. For high P/D, the secondary air flow should be injected at high blowing rate ratio, while for low P/D, blowing rate ratio should be small.

4 The pressure drop coefficient ratio across the electronic modules is essentially a weak function of the blowing rates for both compound and simple angle holes. For the same experimental conditions, the simple injection holes tend to have lower pressure drop coefficient ratio than that of the compound injection holes.

References

Hollworth, B. R., and Durbin, M., 1992, "Impingement Cooling of Electronics," ASME JOURNAL OF HEAT TRANSFER, Vol. 114, pp. 607–613.

Jubran, B. A., and Al-Salaymeh, A. S., 1996, "Heat Transfer Enhancement in Electronic Modules Using Riblets and "Film cooling-like" Techniques," *Int. J. Heat Fluid Flow,* Vol. 17, pp. 148–154.

Jubran, B. A., Swiety, S. A., and Hamdan, M. A., *1996,* "Convective Heat Transfer and Pressure Drop Characteristics of Various Array to Simulate the Cooling of Electronic Modules," *Int. J. Heat Mass Transfer,* Vol. 39, pp. 3519–3529.

Kline, S. J., and McClintock, F. A., 1953, "Describing Uncertainties in Single Sample Experiments," *Mechanical Engineering,* Vol. 75, Jan., pp. 3–8.

Lau, S. C., Han, J. C., and Kim, Y. S., 1989, "Turbulent Heat Transfer and Friction in Pin Fin Channels With Lateral Flow Ejection," ASME JOURNAL OF HEAT TRANSFER, Vol. 111, pp. 51–58.

Lehmann, G. L., and Huang, Y., 1991, "Enhanced Direct Air Cooling of Electronic Components Using Secondary Flow Mixing," *Heat Transfer in Electronic Equipment,* A. Ortega, D. Agonafer, and B. W. Webb, eds., ASME HTD-Vol. 171.

Myrum, T. A., Qiu, X., and Acharya, S., 1993, "Heat Transfer Enhancement in a Ribbed Duct Using Vortex Generators," *Int. J. Heat Mass Transfer,* Vol. 36, pp. 3497–3508.

Ratts, E., Amon, C. H., Mikic, B. B., and Patera, A. T., 1988, "Cooling Enhancement of Forced Convection Air Cooled Chip Array Through Flow Modulation Induced Vortex Shedding Cylinders in Cross-flow," *Cooling Technology for Electronic Equipment,* Wing Aung, ed., Hemisphere, pp. 183–194.

Sparrow, E. M., Niethammer, J. E., and Chaboki, A., 1982, "Heat Transfer and Pressure Drop Characteristics of Array of Rectangular Modules Encountered in Electronic Equipment," *Int. J. Heat Mass Transfer,* Vol. 25, No. 7, pp. 961–973.

Sparrow, E. M., Vemuri, S. B., and Kadle, D. S., 1983, "Enhanced and Local Heat Transfer, Pressure Drop and Flow Visualization for Arrays of Block-like Electronic Components," *Int. J. Heat Mass Transfer,* Vol. 26, No. 5, pp. 689–699.

Torikoshi, K., Kawazoe, M., and Kurihara, T., 1988, "Convective Heat Transfer Characteristics of Arrays of Rectangular Blocks Affixed to One Wall of a Channel," *Natural and Mixed Convection in Electronic Equipment Cooling,* ASME HTD-Vol. 100, R. A. Wirtz, ed.

Wirtz, R. A., and Dykshoorn, P., 1984, "Heat Transfer From Array of Flatpacks in a Channel Flow," *Proc. Fourth Annual International Electronics Packaging Society,* Baltimore, pp. 318–326.

Heat Transfer Characteristics of a Slot Jet Reattachment Nozzle

V. Narayanan

J. Seyed-Yagoobi

R. H. Page

Drying Research Center,
Department of Mechanical Engineering,
Texas A&M University,
College Station, TX 77843-3123

A two-dimensional reattachment nozzle called the Slot Jet Reattachment (SJR) nozzle was designed and built with a zero degree exit angle. The heat transfer characteristics of this submerged nozzle were investigated by varying the Reynolds number, nozzle exit opening, and nozzle to surface spacing. The pressure distribution on the impingement surface for different Reynolds numbers and exit openings were measured. Correlations for location of the maximum local Nusselt number and local Nusselt number distribution along the minor axis of the SJR nozzle were determined. A nondimensional scheme for generalized representation of heat transfer data for two-dimensional separated/reattaching flows was developed. The local and average heat transfer characteristics along the minor axis of the SJR nozzle were compared to a conventional slot jet nozzle under identical flow power condition. The comparison showed that the peak local heat transfer coefficient for the SJR nozzle was 9 percent higher than that for a standard slot jet nozzle, while its average heat transfer coefficient was lower or at best comparable to the slot jet nozzle based on the same averaged area. The net force exerted per unit width by the SJR nozzle flow was 13 times lower than the slot jet nozzle flow under this criterion. Additional experiments were conducted to compare the SJR and slot jet nozzles under matching local peak pressures exerted by the jet flow on the impingement surface. The results indicated 52 percent increase in the peak local heat transfer coefficient, and a maximum enhancement of 35 percent in average heat transfer coefficient for the SJR nozzle over the slot jet nozzle based on the same averaged area under this criterion.

Introduction

Impinging jets are used extensively in various applications, such as heating, cooling or drying of paper, pulp, printer's ink, food, tissue, textiles, chemicals, film, and in the cooling of electronic equipment, turbine and combustor components. The attraction of these jet systems lies in their ability to control local transport rates by varying different parameters such as the jet diameter, jet-to-surface spacing, jet-to-jet spacing, and also the jet flow rate and temperature. Systems that incorporate impinging jets generally consist of in-line, orifice, or slot jets. For a slot jet nozzle, a reservoir upstream of the nozzle provides the necessary flow pressure, and the flow exits the nozzle and impinges directly on the surface. The transport characteristics of the in-line jet and slot jet nozzles are well documented by Martin (1977) and Viskanta (1993).

Two-dimensional jet impingement research dates back to over four decades. Korger and Krizek (1966) clearly illustrated the effect of nozzle-to-surface spacing on the local mass transfer coefficient on the impingement surface using the technique of sublimation from naphthalene plates. The parameters studied included slot widths, nozzle-to-surface spacings, and nozzle efflux Reynolds number ranging from 6040 to 37,800. They observed a secondary maximum in local mass transfer coefficient along the impingement surface for close nozzle-to-surface spacing, but observed that the stagnation point mass transfer coefficient for this spacing was lower than that for larger spacings. They concluded that the maximum stagnation point mass transfer coefficient was obtained at a nozzle-to-surface spacing of 8.5 slot widths, below which it was lower until about 2.5 slot width height, and then went on to increase at lower values.

Gardon and Akfirat (1966) reported both local and average heat transfer coefficients for single and multiple two-dimensional air jets impinging on an isothermal flat plate using a heat-flow transducer for three different aspect ratios. They identified four regimes of heat transfer corresponding to low and high Reynolds numbers, and for small and large nozzle to plate spacings. They observed the same trend as observed by Korger and Krizek (1966), and developed correlations for the stagnation point Nusselt number in terms of the Reynolds number and nozzle-to-surface spacing for the four regimes. Sparrow and Wong (1975) measured the mass transfer coefficients as a result of jet impingement due to initially laminar slot jets using the naphthalene sublimation technique. They observed that the stagnation point mass transfer coefficient generally decreased with increasing nozzle-to-surface spacing, but showed evidence of nonmonotonicity at the highest (laminar) Reynolds number investigated. They showed that increasing Reynolds number, as expected, showed higher transfer coefficients, and suggested that the shape of the exit velocity profile had a significant effect on the transfer characteristics.

Martin (1977) summarized the then currently available research on slot jet impingement nozzles and developed correlations for integral mean heat transfer coefficients for single slot jet nozzles, as well as arrays, based on the local mass transfer measurements of Schlünder et al. (1970). Gau and Lee (1992) studied the effect of rectangular jets impinging on rib-roughened walls for four different slot widths over a Reynolds number range of 2500 to 11,000, and nozzle-to-surface spacings of 2 to 16 slot widths. The rib heights and pitch-to-height ratios were also varied. They observed a significantly different flow structure from that of the flat plate case and proposed correlations for the stagnation point Nusselt number as a function of slot width, rib height, Reynolds number, and nozzle-to-surface spacing. Kataoka et al. (1994) investigated the effect of longitudinal vortices on heat transfer on the impingement surface and concluded that the heat transfer in the inner impingement region was enhanced due to the surface renewal effects of intermittently colliding vortices on the surface. Also, they concluded that the surface renewal motion in the outer impingement region

Contributed by the Heat Transfer Division and based on a paper presented at the International Mechanical Engineering Congress & Exposition, Atlanta, Georgia, November 17–22, 1996. Keywords: Jets, Impingement, Enhancement. Associate Technical Editor: B. W. Webb.

is controlled by the intermittent collision of large-scale turbulent eddies with the surface.

Relatively few studies have been reported on a different geometry of the jet. Lee et al. (1994) studied the local heat transfer characteristics of an impinging elliptic jet with an aspect ratio of 2.14 for various Reynolds numbers and nozzle to surface spacings. They reported that the optimum nozzle-to-surface spacing for the elliptic jet was closer than that for the in-line impinging jet. The investigators observed changes in the shape of the isothermal contour on the impingement surface with nozzle-to-surface spacing. The Nusselt number in the impingement region was found to be larger than for the axisymmetric jet, and this increase was attributed to the large entrainment rate and large-scale coherent structures associated with elliptic jet flow.

The Radial Jet Reattachment (RJR) nozzle (Page et al., 1986, 1989) was developed in an attempt to enhance heat and mass transfer characteristics while effectively controlling the impingement surface force exerted by the jet flow. In the RJR nozzle, the jet is directed outward from the nozzle exit and it then reattaches on an adjacent surface in its vicinity. The turbulent mixing that occurs at the boundaries of the free stream induces secondary flow by mass entrainment and causes the flow to reattach to the surface in the form of a circular "reattachment ring" at close nozzle-to-surface spacing. The jet at this ring splits such that part of it recirculates under the nozzle while the rest flows outward. Thus, turbulent reattachment enhances the transport characteristics over a wide area. The main feature of the RJR nozzle, as mentioned earlier, is that a net zero or even negative force can be exerted on the reattachment surface by simply varying the exit angle, θ, of the nozzle. Multiple RJR configurations have been studied (for example, Gruber et al., 1995, Mohr et al., 1997, Peper, 1996), and the RJR nozzle technology is currently being used in industry. One such example is the application of RJR blowboxes in the dryer section of paper machines (Thiele et al., 1995). Recently, Seyed-Yagoobi et al. (1998) compared the ILJ and RJR nozzles under identical fluid flow power and peak surface pressures exerted by the two nozzles.

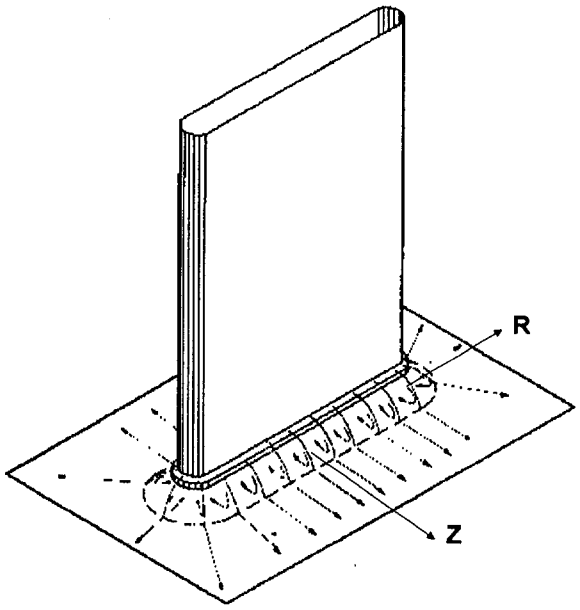

Fig. 1 Schematic of SJR nozzle

Objectives

The present paper introduces a two-dimensional submerged jet reattachment nozzle called the Slot Jet Reattachment (SJR) nozzle, with a zero degree exit angle, shown schematically in Figs. 1 and 2. This nozzle is a modification of the existing submerged slot jet nozzle based on the RJR nozzle concept. The heat transfer characteristics of this innovative nozzle are investigated by varying the nozzle-to-surface spacing, the exit Reynolds number, and the exit opening. The local pressures on the impingement surface are also measured for various Reynolds numbers and exit openings along the direction of the minor axis. Correlations for location of the maximum local Nusselt

Nomenclature

A_{foil} = surface area of heated foil, m^2
b = SJR nozzle exit opening, m
C_p = pressure coefficient = $(p - p_{atm}/0.5\rho V^2)$
D_h = cross-sectional hydraulic diameter of slot jet nozzle, m
$D_{h,exit}$ = exit hydraulic diameter for SJR nozzle, = $2b$
h = heat transfer coefficient, W/m^2K
I = current, A
k = thermal conductivity of air, W/m K
$\dot{m}$ = flow rate, kg/s
Nu = local Nusselt number
P = fluid flow power, W
Δp = pressure drop between plenum and ambient, representing pressure drop across nozzle, Pa
p = local pressure exerted on impingement surface by jet flow from nozzle, Pa
p_{atm} = atmospheric pressure, Pa
q'' = local heat flux, W/m^2
R = radial direction on impingement surface corresponding to ends of nozzle, m
Re = Reynolds number; for SJR nozzle: Re = $(V \cdot D_{h,exit}/\nu)$; for slot jet nozzle: Re = $(V \cdot D_h/\nu)$
RJR = Radial Jet Reattachment
SJR = Slot Jet Reattachment
T = local surface temperature of heated inconel foil with air flow impingement, K
V = exit velocity of nozzle, m/s
X_p = distance from centerline of nozzle exit to impingement surface, m
Z = direction along minor axis of nozzle on reattachment surface, m
Δ = difference
θ = exit angle of SJR nozzle, deg
λ = characteristic length for SJR flow = $(\sqrt{X_p^2 + (Z_r - (Z_w/2))^2})$, m
ν = kinematic viscosity, m^2/s
ρ = fluid density, kg/m^3
Φ = voltage (V)

Subscripts

ad = adiabatic
cond = conductive contribution (to the local heat flux)
conv = convective contribution (to the local heat flux)
gen = electrically generated (heat flux)
h = heated
L = limit of integration along Z direction for area averaging
max = maximum
r = reattachment
rad = radiative contribution (to the local heat flux)
w = width of bottom plate of SJR nozzle along minor axis, Z_w = 0.018 m
ws = slot jet nozzle inside width, Z_{ws} = 0.010 m
wso = slot jet nozzle outside width, Z_{wso} = 0.014 m

Superscripts

* = nondimensional length
" = flux quantity
− = average quantity

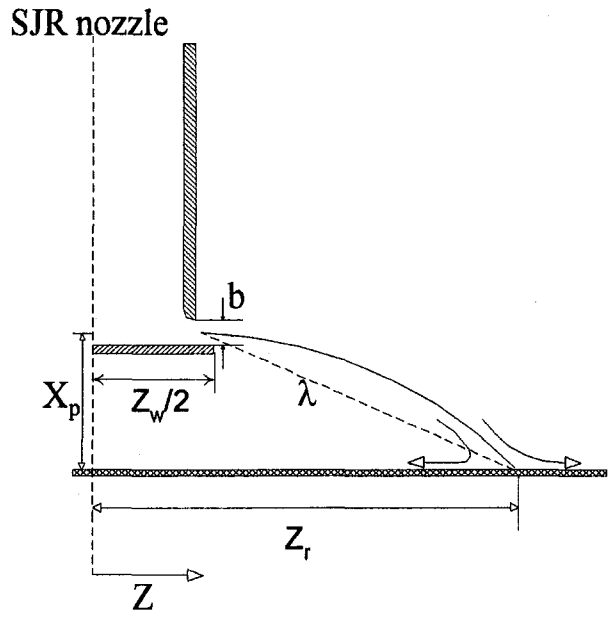

Fig. 2 Schematic showing the geometric parameters of a 0 deg SJR nozzle (minor axis direction)

number, and the local Nusselt number distribution along the minor axis of the SJR nozzle are presented. A nondimensionalization scheme to generalize the representation of heat transfer data for two-dimensional reattachment flows is presented.

The local and average heat transfer characteristics along the minor axis of the submerged SJR nozzle are compared with the conventional submerged slot jet nozzle, at each nozzle's optimum nozzle to surface spacing. The comparisons of the nozzles are based on two separate criteria of identical fluid flow power and matched peak pressure on the reattachment surface along the minor axis direction.

Experimental Set-Up and Procedure

Nozzle Geometry. The SJR nozzle was built with a rectangular cross section and circular ends to ensure proper reattachment (see Fig. 1). The slot jet nozzle internal width, Z_{ws} (along minor axis), was 10.2 mm, and a major axis length was 77.5 mm, giving it an aspect ratio of 7.6. The aspect ratio and the major axis length were calculated without considering the circular ends of the nozzle cross section. The slot hydraulic diameter, D_h, was 22.0 mm. The external width of the slot jet nozzle, Z_{wso} (see Fig. 2), was 14.0 mm. The approach length of 230 mm was long enough to ensure fully developed turbulent condition prior to the exit. The exit was contoured to direct the flow parallel to the reattachment surface, resulting in a flow exit angle of zero degree. The bottom plate of the SJR was made larger than the slot external width in the minor and major axis directions by 4.0 mm, in order to direct the flow properly at a zero degree exit angle. The exit opening, b, of the nozzle could be varied. The exit hydraulic diameter of the SJR nozzle was twice the exit opening, b. The slot jet was essentially the same nozzle as the SJR, but without the bottom plate.

Test Facility. The experimental setup used for this study is described in detail elsewhere (e.g., see Seyed-Yagoobi et al., 1998). Briefly, the facility utilized a thin electrically heated stationary foil upon which the air jet impinged. The foil surface temperatures were measured nonintrusively, with an infrared camera and recording system (Mikron Model 6T62), which had a temperature resolution as high as 0.025°C. The ambient air temperature and nozzle exit temperatures were recorded using calibrated T-type thermocouples. A pressure tap located on a Plexiglas impingement surface was used for surface pressure measurements. The differential pressure, $p - p_{atm}$, was measured using a pressure transducer (Validyne model DP103-16), directly interfaced to a computer.

Experimental Procedure. All experiments were conducted while ensuring that the supply air temperature at nozzle exit was kept close to the ambient room temperature (within ±0.1°C), minimizing any thermal entrainment between the nozzle flow and the surrounding. The pressure drop across the nozzle was noted for each experiment. The foil heat flux for the SJR nozzle low-Reynolds-number cases of Re = 4800 and Re = 9500 was maintained at around 650 W/m^2, while that for the other cases was around 1000 W/m^2. This was done to obtain a good resolution of the local temperatures for the low-Reynolds-number cases as well as to ensure that the maximum foil temperature differentials were less than 10°C with respect to ambient air for all parts of the foil in every experiment. This temperature differential ensured low radiation losses from the foil to the surroundings, and also minimized conduction losses below the foil. Also, the free convection at such a temperature difference was found to be negligible in comparison with the forced convection effect due to the impinging jet. For each steady-state flow condition, a typical measurement included a recorded thermal image of an adiabatic foil (no electrical heating), followed by another recorded thermal image of the heated foil. The analysis involved a digital subtraction of the two stored computer thermal images, followed by conversion of these temperature differentials to corresponding heat transfer coefficients. The mass flow rate for the slot jet and SJR nozzles was adjusted according to the pressure drop for the constant flow power experiments. Pressure measurements along the centerline of the major axis in the direction of the minor axis, Z, of the impingement surface were recorded for the slot jet nozzle and the SJR nozzle to determine the local pressures exerted by the jets on the surface.

Calculation Procedure

The temperature differential was related to a corresponding local heat transfer coefficient as given by Eq. (1)

$$h_{loc} = \frac{q''_{conv}}{(T_h - T_{ad})}. \quad (1)$$

The convective heat flux for Eq. (1) was calculated from

$$q''_{conv} = q''_{gen} - q''_{cond} - q''_{rad}. \quad (2)$$

The conduction losses were determined from known apparatus conductance values and temperatures. The radiation losses were calculated from the room and foil temperatures under blackbody surrounding radiation condition. These two losses were always included in the analysis and were less than 5 percent of q''_{gen}. The electrically generated heat flux was calculated from the voltage and current readings:

$$q''_{gen} = \frac{(\Phi \cdot I)}{A_{foil}} \quad (3)$$

where A_{foil} is the surface area of the electrically heated surface. The local Nusselt number was determined as follows:

$$Nu = \frac{h_{loc} \cdot \lambda}{k} \quad (4)$$

where λ is the characteristic length of the flow, defined in the following section. The average heat transfer coefficient in the Z direction was given by

$$\bar{h} = \frac{q''_{conv}}{\overline{\Delta T}} \quad (5)$$

where the area-averaged temperature differential is defined as

$$\overline{\Delta T} = \overline{(T_h - T_{ad})} = \frac{1}{Z_L}\int_0^{Z_L} (T_h(r) - T_{ad}(r))dZ. \quad (6)$$

The fluid flow power was calculated as follows:

$$P = \left\{\frac{\dot{m} \cdot \Delta p}{\rho}\right\} \quad (7)$$

No corrections were added to the measured pressure drop since the air velocity in the plenum was small, and the flow was considered incompressible.

Error Analysis

An error analysis was performed for all experiments based on the method by Kline and McClintock (1953). In particular, for the optimum slot jet nozzle case of $X_p/Z_{ws} = 9.9$, Re = 48,600, and for the SJR nozzle case of $X_p/Z_{ws} = 1.0$, with optimum exit opening of $b/Z_w = 0.29$, and the highest Reynolds number of Re = 28,600, the average values of uncertainty in the local heat transfer coefficient were 2.0 percent and 3.1 percent, respectively. To confirm repeatability of results, these experimental cases were repeated several times. The minimum and maximum percent standard deviations of the local heat transfer coefficient values for the slot jet nozzle were respectively 1.8 and 4.4, with an average value of 2.4. The minimum and maximum percent standard deviations of the local heat transfer coefficient for the SJR nozzle case were 0.4 and 6.7, with an average value of 3.9, respectively. The high values of standard deviation for the slot jet corresponded to the stagnation region while those for the SJR were around the reattachment region.

Experiments were conducted for the slot jet nozzle to compare our local heat transfer data to reported values in the literature (Gau and Lee, 1992, Schlünder et al., 1970), under similar operating conditions. Our data were in good agreement (less than 9 percent different in the stagnation region) with those of Gau and Lee (1992) while they were around 35 percent higher than the data reported by Schlünder et al. (1970).

Experimental Results

The temperature image of the heated plate showed two distinct regions implying that the flow characteristic of the slot jet and SJR nozzles was two dimensional in nature. The two directions, Z and R, corresponded to the nozzle minor axis direction and the radial direction at the ends of the nozzle, respectively (see Fig. 1). In the Z direction, the temperature distribution consisted of isothermal sections of fairly uniform rectangular strips of constant temperatures. The R direction consisted of radial isothermal sections at the ends of the nozzle. Since the Z direction was the main direction of interest, all the data in this paper will pertain to this direction only. The heated image was relatively symmetric about the two axes. Hence, the results for Nusselt number are presented only in the positive Z direction.

Experiments were conducted over a range of operating parameters to study the individual effect of exit Reynolds number, Re, exit opening, b, and nozzle-to-surface spacing, X_p, on the heat transfer characteristics of the SJR nozzle. Initially, X_p was varied to determine an optimum (based on heat transfer) operating height for the SJR nozzle at a fixed b. In general, the SJR nozzle was operated at close nozzle-to-surface spacings to ensure that the flow reattached on the surface. The centerline velocity of the jet decreased rapidly due to jet mixing and resulted in a decrease in heat transfer with an increase in X_p. A X_p of 11 mm provided the highest local heat transfer values in the range experimented. X_p of less than 11 mm was not investigated since the bottom plate touched the surface at such close spacings. A majority of the experiments were conducted at this "optimum" nozzle-to-surface spacing, by varying b and Re. Based on the analysis of data from these experiments, a scheme for generalized, nondimensional representation of the heat transfer and pressure data was determined and will now be presented.

Scheme for Generalization of Two-Dimensional Reattachment Jet Data. It is a standard practice to represent heat transfer data in the form of a Nusselt number, the characteristic length for which is selected such that it is critical to the heat transfer phenomenon. For a regular jet, the length of jet prior to impingement is the critical characteristic length, and it is proportional to the nozzle hydraulic diameter. Hence, the Nusselt number is generally based on the hydraulic diameter of the nozzle for impinging jet flows. In the case of a reattachment nozzle (such as an SJR nozzle), the jet length prior to reattachment is not directly proportional to any single geometric parameter associated with the nozzle. The path of the jet prior to reattachment is determined by a combination of entrainment on both sides of the jet, conservation of mass in the recirculation region, and momentum balance along the jet path, which are in turn dependent on nozzle parameters. The nozzle parameters are X_p, b, Z_w, and θ (see Fig. 2). Among these, the exit opening (note that exit hydraulic diameter of SJR nozzle is equal to $2b$) decides the flow condition at the exit, and hence, the flow exit Reynolds number should be based on this parameter. The width of the bottom plate does not play a role in the similarity of flow field, since the similar flow region begins at the edge of the plate, and not from the nozzle centerline. In this study, θ was a constant (0 deg). Since the jet path is a combined effect of various parameters, we cannot directly choose any one of the nozzle dimensions as the characteristic length for Nusselt number.

The characteristic length, then, should be based on the jet length from separation to reattachment. This region is most critical to convective heat transfer. Accordingly, we use a straight line between separation and reattachment points in the SJR nozzle flow field as a reasonable approximation of that critical length (see Fig. 2). In reality, this line is curved, but the determination of the rectified length is a second-order correction that is not significant for the current representation. Therefore, the heat transfer coefficient is nondimensionalized with this length, λ, for the Nusselt number representation where

$$\lambda = \left(X_p^2 + \left(Z_r - \frac{Z_w}{2}\right)^2\right)^{0.5} \quad (8)$$

Note that Z_r is based on the location of maximum local heat transfer coefficient.

The distance from the nozzle centerline, Z, along the minor axis can be nondimensionalized with respect to the same characteristic length, λ. However, the distance $Z_w/2$ should be subtracted from Z since the geometrically similar flow field begins at the point of separation and not from the centerline of the nozzle. Representation of Nusselt number and Z^* [$Z^* = (Z - Z_w/2)/\lambda$] in terms of λ enables us to combine the effects of changes of X_p and b into a single parameter, X_p/b. This parameter represents the geometric similarity criterion of SJR nozzles, i.e., if two nozzles have the same X_p/b, the Nusselt numbers will be the same if the exit Reynolds numbers are identical.

Varying X_p while keeping b fixed results in a shift in the reattachment location. However, changing b with X_p fixed does not have any significant effect on the location of reattachment point, for the range of experiments conducted. This will be clarified in the following section. As mentioned before, two dynamically similar SJR nozzle flows should result in identical Nusselt number distributions. This implies that if, say, we have the same ratio of X_p/b by changing X_p or b, the location of reattachment (in terms of the proper nondimensional distance, Z^*) should not differ. This can be true only if Z is nondimensionalized with a length that is sensitive to changes in reattachment point location. It is for this reason that Z is nondimension-

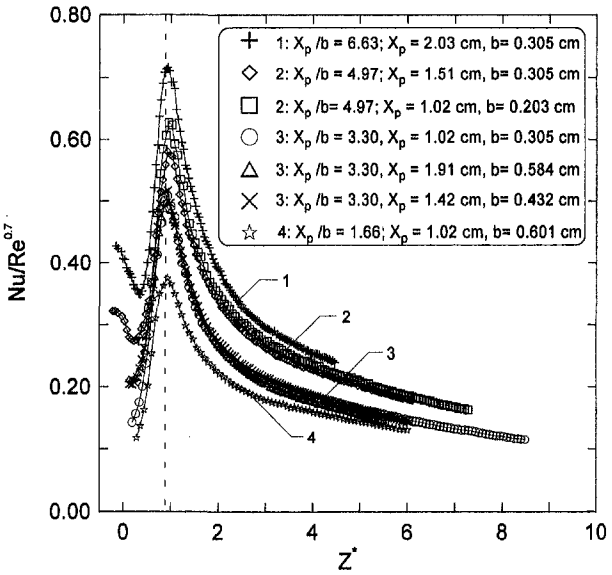

Fig. 3 Nu/Re$^{0.7}$ variation with X_p/b at Re = 14,500

alized with the characteristic length, λ, used in the definition of Nusselt number.

The local gage pressure on the reattachment surface was made nondimensional by introducing pressure coefficient, C_p, based on the exit conditions of the SJR nozzle.

Effect of Variation of X_p/b. Figure 3 represents a graph of Nu/Re$^{0.7}$ as a function of Z^* for various X_p/b values at a fixed Reynolds number of 14,500. The reason for normalization by Re$^{0.7}$ will be clear in the next section. It should again be mentioned that the centerline of the nozzle is at $Z^* = -Z_w/2\lambda$. In most cases, data points directly beneath the nozzle could not be obtained due to adverse viewing requirements of the IR camera. The general trend for all cases was an increase in Nu/Re$^{0.7}$, culminating in a peak around the stagnation region, followed by monotonically decaying region of heat transfer, typical of a turbulent boundary layer growth. The overall trend in heat transfer distribution was that of separated and reattaching flows, like that in a backward-facing step.

In the case where X_p was kept fixed and b varied, the ratio X_p/b decreased with increasing values of b. This resulted in a lower Nusselt number for a fixed Reynolds number. Physically, this implied that when two SJR nozzles operate at the same nozzle-to-surface spacing and Reynolds number, the nozzle with a smaller exit opening would have a larger exit momentum than the nozzle with a larger exit opening. Since the length of the free jet (hence, λ) was the same for both cases, the nozzle with a smaller exit opening had a higher heat transfer coefficient, and consequently higher Nusselt number.

In a case where b was fixed and X_p varied, the ratio X_p/b decreased with decreasing nozzle to surface spacing. Figure 3 indicates that the Nusselt number for a lower X_p/b ratio is lower than that for a large ratio. However, a decrease in Nusselt number did not correspond to a decrease in heat transfer coefficient. Physically, the heat transfer coefficient actually increased with lower nozzle-to-surface spacing. However, the characteristic length, λ, decreased for a lower nozzle-to-surface spacing, which resulted in a net decrease in Nusselt number. Also, in Fig. 3, when X_p and b were varied over three different values to yield the same value of $X_p/b = 3.30$, the data for all three cases essentially collapsed, indicating that for a dynamically similar SJR nozzle flow (i.e., where X_p/b and Re are fixed), the Nusselt number distributions were identical.

In the case where X_p was varied with b fixed, the reattachment location changes, moving toward the nozzle for closer nozzle to surface spacings (X_p). However, since Z^* is nondimensionalized with λ (which reduces with decrease in nozzle to surface spacing), the net location of reattachment in terms of Z^* remained unchanged (see Fig. 3). Thus, varying X_p while keeping b fixed, or vice versa, had no different effect on the location of the reattachment point when represented as Z^*. This allowed us to represent the combined effects of variations of X_p and b as a single parameter, X_p/b.

Figure 4 shows C_p as a function of Z^* for varying X_p/b values and fixed Reynolds number of 14,300. A mirror image of the data points in the negative Z^* direction is plotted along with the positive values to indicate the symmetry of data. The data in Fig. 4 were recorded at the "optimum" nozzle-to-surface spacing of 11 mm. Thus, for a fixed X_p, an increase in X_p/b corresponded to a decrease in b, and vice versa. C_p values for higher X_p/b were lower than for the lower X_p/b cases. The increase in C_p value for the lower X_p/b (larger exit opening) cases was caused by the low value of exit velocity. Thus, the dynamic exit pressure, $0.5V^2\rho$, with which the static pressure on the surface was made nondimensional, was itself changing at a faster rate than the static pressure on the reattachment surface, and resulted in the observed trend. Also, lower value of C_p would result with increased X_p at a fixed b due to a decrease in the local surface pressure differential, $p - p_{atm}$, for the same exit velocity.

Effect of Variation of Exit Reynolds Number. The effect of variations of X_p/b and Re can be combined into a single graph, shown in Fig. 5, to represent the cumulative effect of the two parameters on heat transfer characteristics of the 0 deg SJR nozzle. As observed in Fig. 3, Nu/Re$^{0.7}$ increased with an increase in X_p/b. In a situation when X_p/b was fixed and Re varied, it is apparent that Nusselt number increases with increasing Reynolds number, due to an increase in the exit velocity. However, it can be seen from Fig. 5 that the data points of Nu/Re$^{0.7}$ for all Reynolds numbers for a fixed X_p/b collapsed into a single graph, indicating the power law dependence of Nusselt number on Reynolds number. The collapse of data around the reattachment region is not perfect, and may partly be due to the high experimental uncertainties in this region. In general, however, we can conclude that Nu/Re$^{0.7}$ was essentially independent of Re for a fixed X_p/b. Goldstein et al. (1986) found a similar dependence for Nusselt number in a circular impinging jet. They found that Nu/Re$^{0.76}$ was essentially independent of

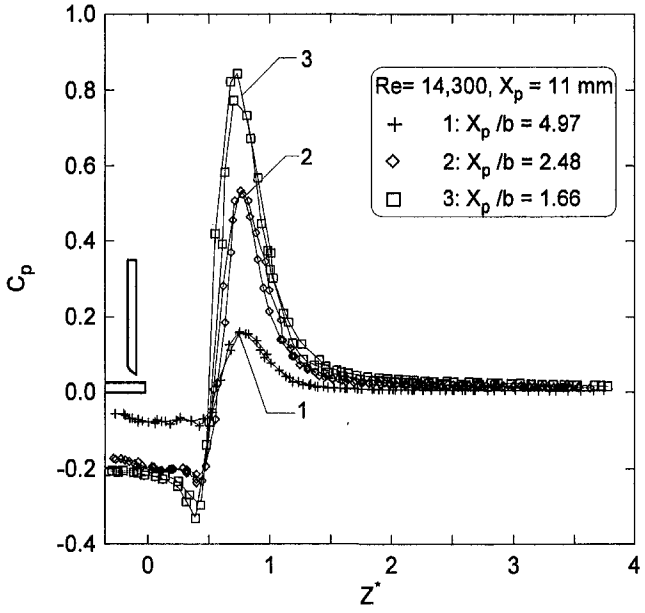

Fig. 4 C_p variation with X_p/b at Re = 14,300

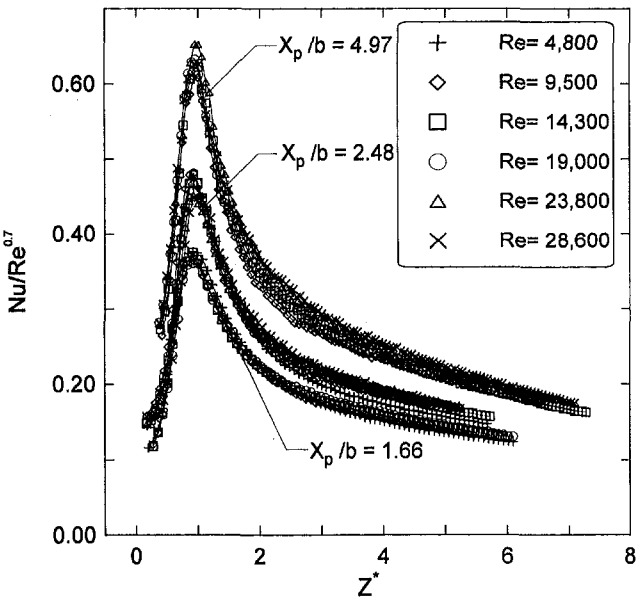

Fig. 5 Generalized representation of the heat transfer characteristics of SJR nozzle

Re for all nozzle-to-surface spacing tested except close to the stagnation region, where the data did not collapse completely. Note that the exponent on the Reynolds number differs slightly for the SJR nozzle from that proposed by Goldstein et al. (1986) for in-line jet nozzles.

It can be seen from Fig. 5 that the location of maximum local Nusselt number was independent of Re for the range experimented. The variation of Re was directly proportional to the exit velocity for a fixed X_p/b. In order to draw precise conclusions about the effect of exit velocity on the reattachment region, the interactions between the various components of the SJR nozzle flow would have to be considered. Interactions occur due to the jet entraining air on both sides, the momentum conservation along the curved jet path, the momentum balance at reattachment, and the conservation of mass within the recirculation region. For the turbulent flow present in the SJR nozzle reattachment region, the flow field pattern is dependent on the nozzle-to-surface spacing and the nozzle exit opening, but weakly dependent on the exit velocity. However, the exit velocity strongly affects the heat transfer on the reattachment surface.

A graph representing the cumulative effect of C_p variation with X_p/b and Re is shown in Fig. 6. As seen from this graph, C_p increases with a decrease in X_p/b for a fixed Re, and remains essentially unaltered at a fixed X_p/b for varying Re. Figure 6 shows that for a fixed $X_p/b = 3.31$, the data for three different Reynolds numbers collapse onto a single graph, further strengthening the heat transfer observations in Fig. 5. The gage pressure exerted on the surface increased (both the positive and negative pressure differences) with Reynolds number for a fixed X_p/b. However, the exit velocity (used in the denominator of C_p) also increased with increasing Reynolds number, thus countering the effect of increased pressure. As expected, negative gage pressures were observed within the recirculation zone.

Correlations for 0° SJR Nozzle. Based on experiments conducted over six different Reynolds numbers, and five exit openings, at a nozzle-to-surface spacing of 11 mm, correlations were developed to represent the location and value of the maximum local Nusselt number. As seen from Figs. 3 and 5, the location of maximum local Nusselt number was relatively independent of X_p/b and Re, and was a constant value. Hence, we can represent the location of maximum local Nusselt number as

$$Z_r^* = \left[\frac{Z_r - \frac{Z_w}{2}}{\sqrt{\left(X_p^2 + \left(Z_r - \frac{Z_w}{2}\right)^2\right)}}\right] = 0.933 \qquad (9)$$

Equation (9) predicted the experimental values of Z_r^* to within 5 percent. Z_w was kept a constant in all experiments. It should be mentioned again that Z_r is the location of the maximum local Nusselt number. This correlation is extremely useful in order to utilize the information provided in the figures since the characteristic length, λ, is dependent on Z_r. Once Z_r is made known by this correlation, λ and heat transfer coefficients can be back calculated from the graphs.

Equation (9) helps us to determine the location of the peak local Nusselt number. In practical applications, the variation of Nu with Z^* is of prime importance since the spatial nonuniformities associated with impingement heat transfer can be estimated. Since the trend of Nu with Z^* (for example, see Fig. 3) is not a monotonically decreasing trend, it is split into two regions (the first, from the nozzle centerline to the point of maximum local heat transfer, Z_r^*, and the second from Z_r^* onward). The two correlations combined can effectively describe the entire heat transfer distribution of the SJR nozzle. Accordingly, the following Nu correlations were developed:

$$\mathrm{Nu} = \mathrm{Re}^{0.7} \cdot \left(\frac{X_p}{b}\right)^{0.402} \cdot \exp[a + bZ^* + cZ^{*2} + d\exp(-Z^*)];$$

$$0 \le Z^* \le Z_r^* \qquad (10)$$

where $a = -66.2090$, $b = 60.1880$, $c = -18.8270$, and $d = 64.3570$; and

$$\mathrm{Nu} = \mathrm{Re}^{0.7} \cdot \left(\frac{X_p}{b}\right)^{0.387} \cdot \exp[a + bZ^{*2} + c \cdot \exp(-Z^*)];$$

$$Z_r^* < Z^* \le 8 \qquad (11)$$

where $a = -1.9290$, $b = -0.0091$, and $c = 2.2350$.

The ranges of validity of Eqs. (9), (10), and (11) are

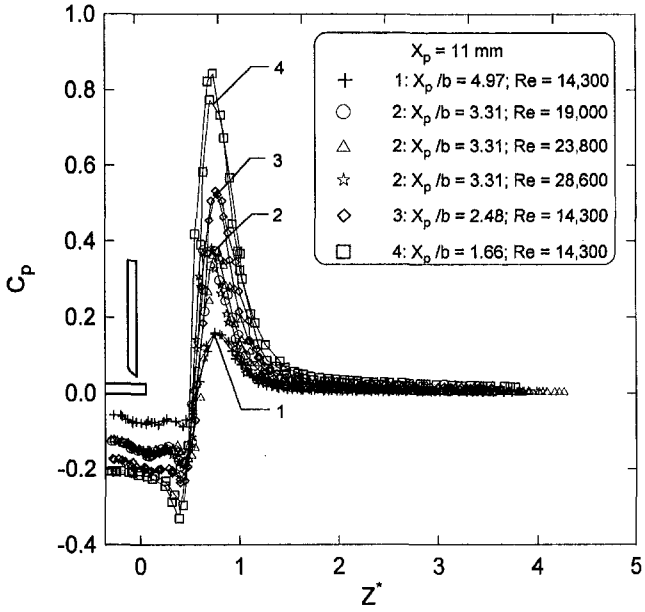

Fig. 6 Generalized representation of C_p for the SJR nozzle

$$1.66 \leq X_p/b \leq 4.97$$

$$4{,}800 \leq \mathrm{Re} \leq 28{,}600$$

$$\mathrm{Pr} = 0.71, \quad \text{and} \quad \theta = 0°$$

The coefficient of determination values for Eqs. (10) and (11) are 0.974 and 0.988, respectively. Equation (10) predicts 94 percent of the correlated data to within 15 percent while Eq. (11) predicts 99 percent of the data to within 10 percent of the experimental values. Equation (10) can be used to determine the magnitude of peak local Nusselt number by substituting the value of Z_r^* from Eq. (8). To illustrate the accuracy of the prediction, local heat transfer values calculated from Eqs. (9), (10), and (11) are plotted with an experimental case that was not used to develop the correlation. Their agreement, as shown later in Fig. 9, is quite good in all regions, and the maximum deviation between calculated and experimental values is 13 percent at $Z^* = 8.0$.

Comparison of Heat Transfer Characteristics of SJR and Slot Jet Nozzles. When comparing slot jet nozzle and SJR nozzle with the same pipe hydraulic diameter, although the transport characteristics for the SJR nozzle were superior to the slot jet nozzle under the same mass flow rate condition (since the exit hydraulic diameter of the SJR was smaller than the pipe hydraulic diameter), a fair comparison would have to include the additional pressure drop in the SJR nozzle due to the deflection of the flow by the bottom plate. Comparison under the same exit velocity was also not proper since we could have a different mass flow rate but still have the same exit velocity for both the SJR and slot jet nozzles. A comparison under identical exit momentum for the two nozzles would have been a better comparison, since the product of mass flow rate and exit velocity would have to be kept constant. However, such a comparison would not account for the additional pressure losses associated with the SJR nozzle. Hence, the two nozzles are compared under identical fluid flow power at each nozzles' "optimum" height from the impingement surface. This section of the paper highlights the importance and application of fluid flow power as a comparison criterion by choosing a particular case of identical pipe hydraulic diameters of the slot jet and SJR nozzles. Such a case is typical when one is interested in modifying existing slot jet nozzles into SJR nozzles.

The representation scheme used for a performance comparison of the two nozzles is discussed below. The height of the slot jet nozzle from the impingement surface was made nondimensional with respect to the slot width, Z_{ws}. The Reynolds number for the slot jet nozzle was based on the slot velocity and the slot hydraulic diameter. As before, the Reynolds number for SJR nozzle was based on the exit hydraulic diameter and exit velocity. In the following graphs, $Z = 0$ m corresponds to the nozzle centerline. Also, the nozzle-to-surface spacing of the SJR nozzle was made dimensionless with respect to the slot width, Z_{ws}, for ease of comparison with the slot jet nozzle. The heat transfer data are reported in terms of local and average heat transfer coefficients since the definition of characteristic length in the Nusselt number is different for the two nozzles.

The first set of experiments was conducted to determine the slot jet's optimum spacing from the impinging surface under a flow power of 45 W (Narayanan et al., 1996). The results indicated that the optimum height for the slot jet nozzle was at $X_p/Z_{ws} = 9.9$, based on the peak local Nusselt number in the Z direction. This optimum height is in excellent agreement with the optimum height results reported by Gardon and Akfirat (1966). As mentioned before, the "optimum" height of the SJR nozzle corresponded to its closest X_p value of 11 mm ($X_p/Z_{ws} = 1.0$).

Figure 7 illustrates the local and average heat transfer coefficient distributions in the Z direction at a flow power of 45 W, for the slot jet nozzle at $X_p/Z_{ws} = 9.9$ and for the SJR nozzle

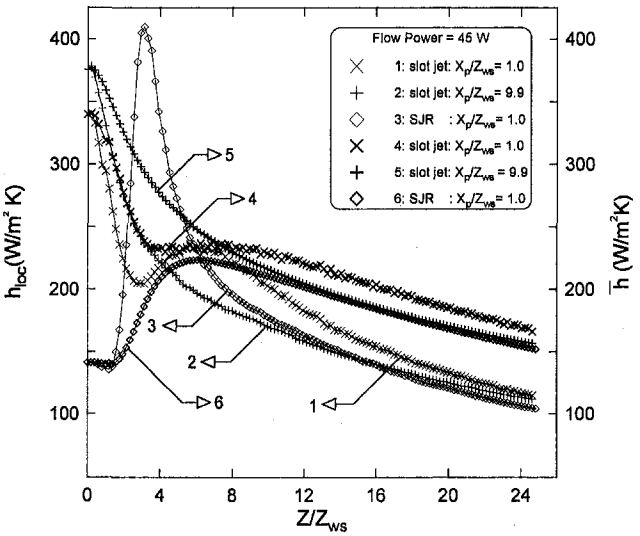

Fig. 7 Comparison of local and average heat transfer distributions of slot jet and SJR nozzles under P = 45 W

at $X_p/Z_{ws} = 1.0$. In addition, the data for the slot jet nozzle at $X_p/Z_{ws} = 1.0$ are also shown. The Reynolds number for the slot jet nozzle corresponded to 48,600 for $X_p/Z_{ws} = 9.9$, while it was 47,000 for the slot jet at $X_p/Z_{ws} = 1.0$. The exit Reynolds number for the SJR nozzle for the corresponding flow power was 15,000. The peak local heat transfer coefficient for the slot jet case of $X_p/Z_{ws} = 9.9$ occurred in the stagnation region and was equal to 376 W/m^{2}K, while that for the SJR nozzle occurred in the reattachment band and was equal to 410 W/m^{2}K, corresponding to an enhancement in the peak local heat transfer coefficient of around 9 percent. The slot jet nozzle at $X_p/Z_{ws} = 1.0$ showed a second peak at around $Z/Z_{ws} = 5.47$. This trend was observed in the in-line jet as well (Lytle and Webb, 1994, Popiel and Trass, 1991, Viskanta, 1993, and Seyed-Yagoobi et al., 1998). The second maximum in the case of the slot jet nozzle was found to be less pronounced than the in-line jet case.

Figure 7 also shows the average heat transfer coefficient as a function of Z/Z_{ws}. For the SJR nozzle, data directly below the nozzle could not be recorded. Based on local heat transfer data in the R direction, it was observed that the local heat transfer increased slightly in this region toward the centerline. Hence, constant values (corresponding to the lowest $\bar{h}$) of average heat transfer was chosen for these points. It was observed that although the SJR nozzle peak local heat transfer coefficient was higher than the slot jet case of $X_p/Z_{ws} = 9.9$, its average heat transfer coefficient was actually lower, or at best equal to the slot jet nozzle over the same averaged areas. The heat transfer characteristics of the SJR nozzle could be improved greatly with positive exit angles, as reported by Narayanan et al. (1997). Also, the force exerted on the surface by the SJR nozzle was quite negligible compared to the strong force of the slot jet for similar average heat transfer coefficient. The net force per unit depth exerted on the impingement surface (from $Z/Z_{ws} = -11.3$ to 11.3) by the SJR nozzle was 1.7 N/m compared to a force per unit depth of 22.1 N/m exerted by slot jet nozzle under the same flow power condition.

Figure 8 shows the local gage pressure distribution on the impingement surface for both nozzles under the same fluid flow power at each nozzles' "optimum" height from the impingement surface. The surface gage pressure is not presented in the dimensionless form in this case because the exit velocities for the slot jet and the SJR nozzles are different, not allowing for a direct comparison of surface gage pressure in terms of C_p. As seen in Fig. 8, the SJR nozzle exerts significantly lower

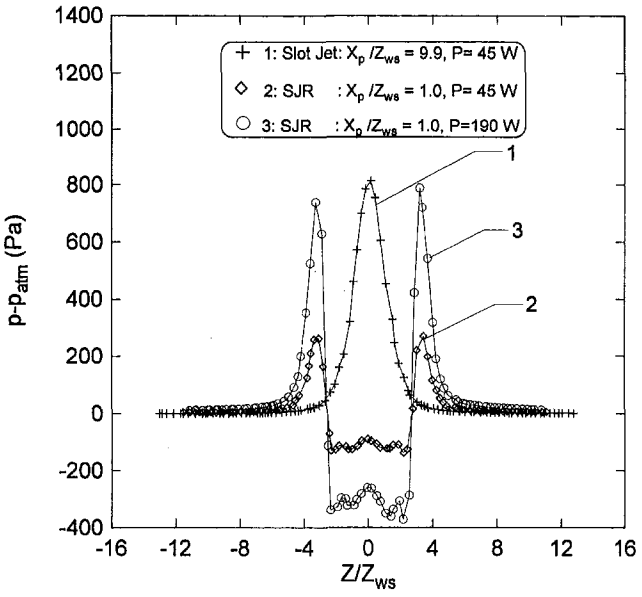

Fig. 8 Comparison of surface pressure distribution of slot jet and SJR nozzles

pressure on the surface compared to the slot jet nozzle under identical flow power of 45 W. The peak local gage pressure exerted by the slot jet nozzle on the surface was found to be 3.1 times larger than the peak pressure exerted by the SJR nozzle, although the SJR nozzle operated at much closer nozzle-to-surface spacing.

Additional heat transfer experiments were conducted while matching the local peak pressure exerted by the SJR nozzle to the local peak pressure exerted by the slot jet nozzle. Such a comparison is important since the peak pressure exerted by the nozzle on the substrate is critical in certain applications. The SJR nozzle flow power in this case had to be increased to 190 W, which was around 4.2 times the flow power of the slot jet nozzle. Figure 9 illustrates the local and average heat transfer coefficient for this case compared to the slot jet nozzle. The 0 deg exit angle SJR nozzle provided better heat transfer compared to the slot jet nozzle when the peak pressure exerted on the impingement surface was the basis of comparison. The SJR

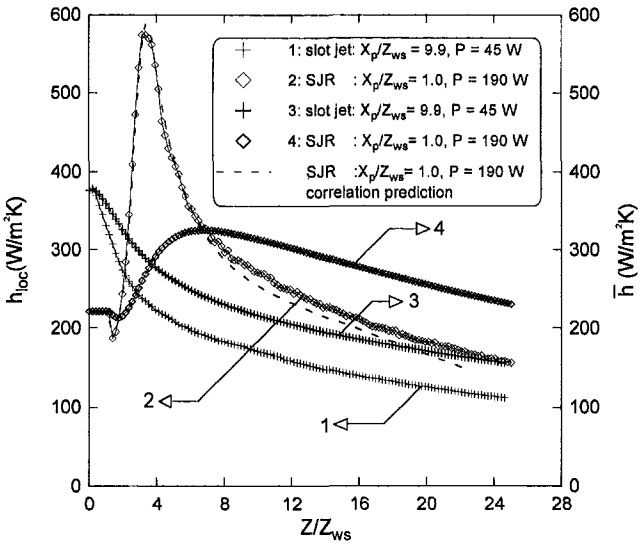

Fig. 9 Comparison of local and average heat transfer distribution of slot jet and SJR nozzles under constant surface peak pressure

nozzle peak local heat transfer coefficient was approximately 52 percent higher than that for the slot jet nozzle. The peak value of the average heat transfer coefficient for the SJR nozzle showed an enhancement of 35 percent over the slot jet nozzle at a Z/Z_{ws} = 6.84. Under this comparison, the net force per unit depth exerted by the SJR nozzle was 4.0 N/m as compared to a force per unit depth of 22.1 N/m exerted by the slot jet nozzle.

Conclusions

A new impingement nozzle called Slot Jet Reattachment (SJR) nozzle was designed and built with a zero degree exit angle. The heat transfer characteristics of this nozzle were investigated by varying the nozzle-to-surface spacing, Reynolds number, and the nozzle exit opening. Correlations for the location of the peak local Nusselt number and for the variation of Nu along the minor axis centerline were presented. These correlations can be very useful in the design of single SJR nozzles. A nondimensional scheme for generalized representation of heat transfer data for two-dimensional separated/reattaching flows was developed. Specifically, a length scale that truly represented the heat transfer phenomenon of two-dimensional reattachment jets was identified.

The SJR nozzle's performance was compared to a slot jet nozzle under identical flow power condition. The local heat transfer coefficient comparison results indicated a 9 percent enhancement in the peak local Nusselt number for the SJR nozzle under identical flow power condition, while the average heat transfer was at best only comparable to the slot jet nozzle. A comparison under identical peak surface pressures for the SJR and the slot jet nozzles indicated an enhancement of 52 percent in the peak local Nusselt number could be obtained by the use of the SJR nozzle. The peak value of the average heat transfer coefficient, under this condition, for the SJR nozzle showed an enhancement of 35 percent against the slot jet nozzle over the same averaged area.

The true benefit of the SJR nozzle lies in the fact that the force on the reattachment surface can be controlled. Specifically, this could make a significant impact in the cooling, drying, or heating of fragile materials. Since the force can be effectively controlled with the SJR nozzle, it is possible to operate this nozzle at high flow rates, resulting in significant enhancements in heat transfer values. The SJR nozzle operates closer to the impingement surface than a slot jet nozzle, thus permitting compact new equipment and retrofitting of existing slot jet nozzle equipment.

Acknowledgments

This study was financially supported by the Texas A&M University Drying Research Center and the Texas A&M University Energy Resources Program.

References

Gardon, R., and Akfirat, J. C., 1966, "Heat Transfer Characteristics of Impinging Two-Dimensional Air Jets," ASME JOURNAL OF HEAT TRANSFER, Vol. 88, pp. 101–108.

Gau, C., and Lee, C. C., 1992, "Impingement Cooling Flow Structure and Heat Transfer Along Rib-Roughened Walls," *Int. J. Heat Mass Transfer,* Vol. 35, No. 11, pp. 3009–3018.

Goldstein, R. J., Behbahani, A. I., and Heppelmann, K. K., 1986, "Streamwise Distribution of the Recovery Factor and the Local Heat Transfer Coefficient to an Impinging Circular Air Jet," *Int. J. Heat Mass Transfer,* Vol. 29, No. 8, pp. 1227–1235.

Gruber, T. C., Page, R. H., Seyed-Yagoobi, J., and Albrecht, S. L., 1995, "Drying With Two Radial Jets: Development of RJR Drying Arrays," *Technical Association of Pulp and Paper Industries Journal,* Vol. 78, No. 7, pp. 124–128.

Kataoka, K., Kawasaki, H., Tsujimoto, M., and Ohmura, N., 1994, "Effect of Longitudinal Vortices on Heat Transfer Surfaces Which a Two-Dimensional Jet Strikes Against," *Heat Transfer 1994, Proc. 10th International Heat Transfer Conference,* Brighton, UK, Vol. 3, 4 EC-8, pp. 31–36.

Kline, S. J., and McClintock, F. A., 1953, "Describing Uncertainties in Single Sample Experiments," *Mechanical Engineering,* Vol. 75, Jan., pp. 3–8.

Korger, M., and Krizek, F., 1966, "Mass Transfer Coefficient in Impingement Flow From Slotted Nozzles," *Int. J. Heat Mass Transfer,* Vol. 9, pp. 337–344.

Lee, Sang-Joon, Lee, Jung-Ho, and Lee, Dae-Hee, 1994, "Local Heat Transfer Measurements From an Elliptic Jet Impinging on a Flat Plate Using Liquid Crystal," *Int. J. Heat Mass Transfer,* Vol. 37, No. 6, pp. 967–976.

Lytle, D., and Webb, B. W., 1994, "Air Jet Impingement Heat Transfer at Low Nozzle-Plate Spacing," *Int. J. Heat Mass Transfer,* Vol. 37, No. 12, pp. 1687–1697.

Martin, H., 1977, "Heat and Mass Transfer Between Impinging Gas Jets and Solid Surfaces," *Advances in Heat Transfer,* Vol. 13, pp. 1–60.

Mohr, J. W., Seyed-Yagoobi, J., and Page, R. H., 1997, "Heat Transfer From a Pair of Radial Jet Reattachment Flames," ASME JOURNAL OF HEAT TRANSFER, Vol. 119, No. 3, pp. 633–635.

Narayanan, V., Seyed-Yagoobi, J., and Page, R. H., 1996, "Comparison of Heat Transfer Characteristics of a Slot Jet Reattachment Nozzle and a Conventional Slot Jet Nozzle," *Proc. ASME Heat Transfer Division,* Vol. 2, ASME HTD-Vol. 333, pp. 151–157.

Narayanan, V., Seyed-Yagoobi, J., Page, R. H., and Alam, S. A., 1997, "Effect of Exit Angle on the Heat Transfer Characteristics of a Slot Jet Reattachment Nozle and Its Comparison to a Slot Jet Nozzle," *Proc. 1997 ASME National Heat Transfer Conference,* ASME HTD-Vol. 347, Vol. 9, pp. 119–127.

Page, R. H., Ostowari, C., and Carbone, J. S., 1986, "Radial Jet Flow," *Proc. 4th International Symposium on Flow Visualization,* Paris, France, pp. 512–521.

Page, R. H., Hadden, L. L., and Ostowari, C., 1989, "A Theory for Radial Jet Reattachment Flow," *AIAA Journal,* Vol. 27, No. 11, pp. 1500–1505.

Peper, F., 1997, "Strömungsstruktur, Wärmeübergang, Strahlkraftund Druckverlust Radialer Prallstrahlfelder," Ph.D. Dissertation, Ruhr University, Bochum, Germany.

Popiel, C. O., and Trass, O., 1991, "Visualization of a Free and Impinging Round Jet," *Experimental Thermal and Fluid Science,* Vol. 4, pp. 253–264.

Schlünder, E. U., Krötzsch, P., Hennecke, Fr.-W., 1970, "Gesetzmäßigkeiten der Wärme- und Stoffübertragung bei der Prallströmung aus Rund- und Schlitzdüsen," *Chemie-Ing.-Techn.,* Vol. 42, pp. 333–338.

Seyed-Yagoobi, J., Narayanan, V., and Page, R. H., 1998, "Comparison of Heat Transfer Characteristics of Radial Jet Reattachment Nozzle to In-Line Impinging Jet Nozzle," ASME JOURNAL OF HEAT TRANSFER, Vol. 120, this issue, pp. 335–341.

Sparrow, E. M., and Wong, T. C., 1975, "Impingement Transfer Coefficients Due to Initially Laminar Slot Jets," *Int. J. Heat Mass Transfer,* Vol. 18, pp. 597–605.

Thiele, E. W., Seyed-Yagoobi, J., Page, R. H., and Castillo-Garcia, H., 1995, "Enhancement Drying Rate, Moisture Profiling, and Sheet Stability on an Existing Paper Machine With RJR Blow Boxes," *Proc. TAPPI Papermakers Conference,* Chicago, IL, pp. 223–228.

Viskanta, R., 1993, "Heat Transfer to Impinging Isothermal Gas and Flame Jets," *Experimental Thermal and Fluid Science,* Vol. 6, pp. 111–134.

ERRATA

To the paper, "Buoyancy-Induced Convection in a Narrow Open-Ended Annulus," by K. Vafai, published in the ASME JOURNAL OF HEAT TRANSFER, Vol. 119, August 1997, pp. 483–494:

The correct form of Eq. (28) is:

$$\overline{\mathrm{Nu}} = 0.2(\mathrm{Ra})^{0.14}(1 - 1.41x)(1 + 27.74g); \quad \mathrm{Ra} < 1 \times 10^5$$

$$\overline{\mathrm{Nu}} = 0.2(\mathrm{Ra})^{0.1/4}(1 - 1.05x)(1 + 28.01g); \quad \mathrm{Ra} \geq 1 \times 10^5$$

It should also be noted that the Rayleigh number used in both Eq. (28) and Section 4.3 is based on the radius of the inner cylinder.

Constructal Optimization of Internal Flow Geometry in Convection

R. A. Nelson, Jr.
MS K575,
Nuclear Systems and Design
Analysis Group,
Technology and Safety
Assessment Division,
Los Alamos National Laboratory,
Los Alamos, NM 87545
Mem. ASME

A. Bejan
Department of Mechanical Engineering
and Materials Science,
Box 90300,
Duke University,
Durham, NC 27708-0300
Fellow ASME

In this paper "constructal theory" is used to predict the formation of geometric shape and structure in finite-size fluid systems subjected to heating from below. Two classes of system are considered as tests: (i) single-phase fluid layers, and (ii) porous layers saturated with single-phase fluids. It is shown that the minimization of thermal resistance across the layer can be used to account for the appearance of organized macroscopic motion (streams) on the background of disorganized motion (diffusion). By optimizing the shape of the flow, it is possible to predict analytically the main structural and heat transfer characteristics of the system, e.g., the onset of convection, the relation between Nusselt number and Rayleigh number, the geometric shape of the rolls, and the decreasing exponent of Ra_H as Ra_H increases. The convective flow structure emerges as the result of a process of geometric optimization of heat flow path, in which diffusion is assigned to length scales smaller than the smallest macroscopic flow element (elemental system). The implications of this test of constructal theory are discussed in the context of the wider search for a physics law of geometric form generation in natural flow systems.

1 Objective

It was shown in a recent paper that by geometrically minimizing the thermal resistance between one point and a finite-size volume (an infinity of points), it is possible to predict a most common natural shape that previously was considered nondeterministic: the tree (Bejan, 1997a). Tree network patterns abound in nature, in both animate and inanimate systems (e.g., botanical trees, river basins, lungs, vascularized tissues, lightning, neural dendrites, dendritic crystals). The key to solving this famous problem was the optimization of the shape of each finite-size element of the flow volume, such that the flow resistance of the element is minimal. The optimal structure of the flow—the tree network—was then *constructed* by putting together the shape-optimized building blocks. This geometric optimization method was named "constructal theory."

The deterministic power of constructal theory is an invitation to new theoretical work on natural flow structures that have evaded determinism in the past. This paper is about one such flow: convection in a fluid layer heated from below. We shall examine this problem in two settings (two fields, really): pure single-phase fluid (Bénard convection), and porous layer saturated with single-phase fluid.

The constructal approach employed in this paper is based on the view that a naturally occurring flow—its geometric structure—is the end result of a process of internal geometric optimization, i.e., self-organization. According to the theory, the objective of this process is to construct an assembly of paths of minimal resistance for the current that must flow through the system. Natural convection in heating from below is the testing ground chosen for the theory. We show that macroscopic shape and structure can be predicted based on the geometric minimization of thermal resistance. In other words, we show that the constructal approach is deterministic with respect to the very existence of organized fluid motion (streams).

The reason for using Bénard convection as a test case for constructal theory is that this type of organized heat transfer is very well known. An added reason is to renew interest in a piece of classical work that, from today's point of view, looks even more important. The maximization of heat transfer rate (or Nusselt number) in Bénard convection was a hypothesis introduced by Malkus (1954) and used in several studies of convection in pure fluids and fluid-saturated porous media. It was related by Glansdorff and Prigogine (1971) to a principle of entropy generation minimization subject to imposed boundary conditions. In the present study we develop the connection between conductance maximization and the optimization of geometric shape of a single, finite-size flow element. In this way we recognize the importance of Malkus' hypothesis and entropy generation minimization principle as part of a more direct and transparent theory of geometrical shape and pattern formation in nature. Constructal theory brings many of the advances made by others in the past under the same deterministic umbrella. We comment on this aspect further in section 4.

The present extension of constructal theory is very timely because a large segment of the physics and biology communities works on identifying the single physics principle that controls geometric form in natural systems, both animate and inanimate. This challenge was summarized by Kadanoff (1986) in his critique of the proliferation of computer simulations (fractal algorithms) of naturally occurring structures. Kadanoff wrote that "further progress depends upon establishing a more substantial theoretical base in which geometrical form is *deduced* from the mechanisms that produce it." The constructal (geometric optimization) principle invoked in this paper answers this challenge, and shows that geometric form can indeed be deduced.

2 Single-Phase Natural Convection

The geometric optimization of the flow pattern can be demonstrated in single-phase convection. We limit this discussion to two-dimensional geometries without a free surface, first, heated from below, and, later, heated from the side (Section 2.2). Our objective is not to refine the mathematical models used by previous researchers; rather it is to demonstrate self-organization as a geometric optimization process, and for this we rely on the simplest and most transparent approach.

Contributed by the Heat Transfer Division for publication in the JOURNAL OF HEAT TRANSFER. Manuscript received by the Heat Transfer Division June 13, 1997; revision received February 17, 1998. Keywords: Natural Convection, Porous Media, Thermodynamics and Second Law. Associate Technical Editor: Y. Jaluria.

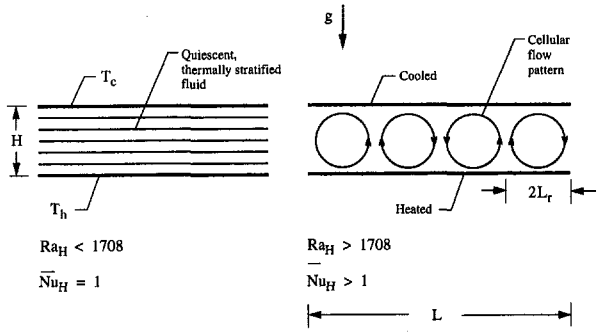

Fig. 1 Horizontal fluid layer held between parallel plates and heated from below

2.1 Establishment of Organized Motion (Streams) in Heating From Below. Why should a disorganized motion and heat transfer mechanism (chaotic, molecular thermal diffusion) change abruptly such that the disorganized entities ride together, in a macroscopic motion visible as streams? Why should shapelessness (diffusion) coexist with shape and structure (streams)?

Consider the single-phase fluid layer shown in Fig. 1, which is characterized by the thickness H and the bottom excess temperature $\Delta T = T_h - T_c$. In line with the access-optimization principle of constructal theory, we search for the fastest (most direct) route for heat transfer across the fluid layer. To start with, the classical solution for time-dependent thermal diffusion near a wall with a sudden jump in temperature (ΔT) is

$$\frac{T - T_c}{\Delta T} = \text{erfc}\left[\frac{y}{2(\alpha t)^{1/2}}\right] \tag{1}$$

where T_c is the far-field temperature in the fluid. The effect of the temperature jump is felt to the distance

$$\frac{y}{2(\alpha t)^{1/2}} \sim 1 \tag{2}$$

which represents the knee in the temperature profile indicated by Eq. (1). The time needed by this heating effect to travel by thermal diffusion the distance H is

$$t_0 \sim \frac{H^2}{4\alpha} \tag{3}$$

The time t_0 corresponds to the heating of the entire layer ($y \sim H$). The factor 4 in the denominator arises from the geometry (shape) of the time-dependent temperature profile in Eq. (1).

Pure conduction continues to be the preferred heat transfer mechanism, and the fluid layer remains macroscopically motionless as long as H is small enough that t_0 is the shortest time to transport heat across the layer. The alternative to conduction is convection, or the channeling of energy transport on the back of fluid streams, which act as conveyor belts (rolls, Fig. 1, right side). The question is whether the convection time (t_1) around the convection cell is shorter than t_0. The convection time is $t_1 \sim 4H/v$, where v is the vertical velocity of the fluid (the peripheral velocity of the roll).

To evaluate the v and t_1 scales, we rely on scale analysis. First, we note that the effective diameter of each roll is of order H, but smaller; for example, $H/2$. When the roll turns, an excess temperature of order $\Delta T/2$ is created between the moving stream and the average temperature of the fluid layer. This excess temperature induces buoyancy (modified gravitational acceleration) of order $g\beta\Delta T/2$. The total buoyancy force that drives the roll is of order $(g\beta\Delta T/2)\rho(H/2)^2$. When the Prandtl number is of order 1 or greater, the driving force is balanced by the viscous shearing force $\tau H/2$, where the shear stress scale is $\tau \sim \mu v/(H/4)$. The force balance buoyancy $\sim$ friction yields the velocity scale $v \sim g\beta\Delta T H^2/(16\nu)$ and the corresponding convection time scale

$$t_1 \sim \frac{64\nu}{g\beta\Delta T H} \tag{4}$$

To see the emergence of an opportunity to optimize the geometric features of the flow pattern, imagine that H increases. As the system grows, the thermal diffusion time t_0 increases in accelerated fashion, Eq. (3), whereas the convection time t_1 (a *property* of the H system, even if quiescent) decreases monotonically [Eq. (4)]. Setting $t_1 \lesssim t_0$ and using Eqs. (3) and (4), we find that the first streams occur when $Ra_H = 256 \sim O(10^2)$, where $Ra_H = g\beta\Delta T H^3/(\alpha\nu)$ is the Rayleigh number.

The exact solution for this critical condition is $Ra_H = 1708$; in other words, $Ra_H = O(10^3)$. The factor of 6.7 error in the result of scale analysis is understandable (and unimportant) because it can be attributed to the imprecise geometric ratios (factors of order one) introduced along the argument made in Eq. (4). A more exact estimate can be achieved in an analysis that better reflects the scales of the flow, as we demonstrate in section 2.3.3: see feature (b).What is important is that the predicted critical Ra_H is a *constant* considerably greater than 1. This constant is a conglomerate of all the geometric ratios of the roll-between-plates configuration. Had we neglected the geometric reality of how the rolls fit, or the geometric fact that 4 belongs in the denominator of Eq. (3), we would have obtained only $Ra_H \sim 1$, i.e., the correct dimensionless group but not the

Nomenclature

c_P = specific heat at constant pressure, J/kg K
f = function; dimensionless factor, Eq. (14)
g = gravitational acceleration, m/s^2
h = heat transfer coefficient, W/m^{2}K
H = height, m
k = thermal conductivity, W/m K
K = permeability, m^2
L = length, m; horizontal dimension, m
L_r = horizontal dimension, m
$\dot{m}'$ = mass flow rate, kg/s m
Nu = Nusselt number
q' = heat transfer rate per unit length, W/m
q'' = heat flux, W/m^2
Ra_H =Rayleigh number
Ra_p = porous medium Rayleigh number
t = time, s
T = temperature, K
T_∞ = temperature outside the boundary layer, K
u, v = velocity components, m/s
x, y = Cartesian coordinates, m
α = thermal diffusivity, m^2/s
β = volume expansivity, K^{-1}
δ = thickness, m
ΔT = temperature difference, K
θ = temperature difference, K
μ = viscosity, kg/m^3
ν = kinematic viscosity, m^2/s
ρ = density, kg/m^3
τ = shear stress, N/m^2

Subscripts

b = bulk
c = cold
f = fluid in porous medium
h = hot
H = height
in = inlet
L = horizontal dimension
m = porous medium
max = maximum
opt = optimum
out = outlet
t = transverse
$(\bar{\ })$ = average
0 = diffusion regime
1 = stream regime

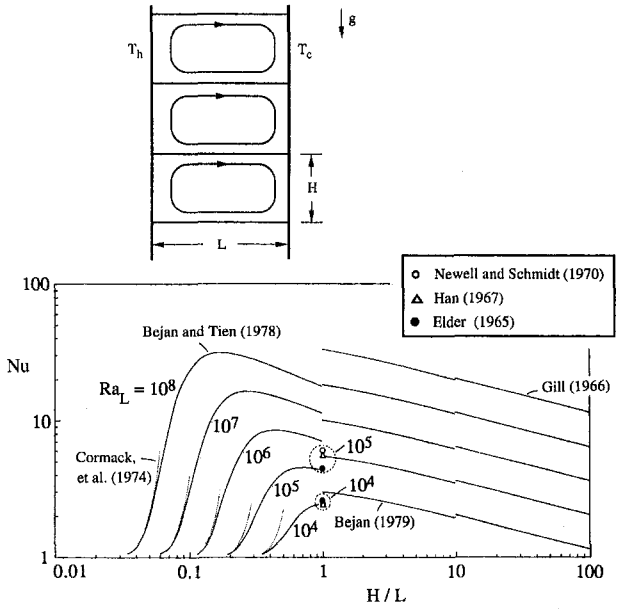

Fig. 2 The optimization of roll shape and the maximization of overall thermal conductance in a cellular vertical fluid layer heated from the side (Bejan, 1980)

fact that the critical Ra_H is a *geometric* (structural) constant. All the transition (critical) numbers of fluid mechanics are constants that reflect the geometry (shape) of the elemental system—the first roll, or the first eddy.

When convection occurs, there are two heat transfer mechanisms, not one. Each roll characterized by $t_0 \sim t_1$ is an "elemental system" in the sense of constructal theory (Bejan, 1997a, b). The equipartition of time $t_0 \sim t_1$ is the analog of the equipartition of temperature drop across an optimized element of the heat-generating volume of constructal theory. Conduction, or thermal diffusion, is present and does its job at every point inside the elemental volume $H \times 2L_r$ shown in Fig. 1. Superimposed on this volumetric heat flow is an optimal pattern of convection "streets" that channel the imposed heat current *faster* across H.

The usual terminology for "faster" in the field of heat transfer is to say that the onset of convection is followed by an increase in the overall Nusselt number $\overline{Nu}_H = \bar{q}''H/k\Delta T$. In the present discussion of heating from below, we have been fixing the heat current. If we fix the uniform heat flux q'' in Bénard convection, we see once again that the optimization of the heat flow pattern at the elemental level leads to a smaller overall ΔT, and thus a larger $\overline{Nu}_H$ (Fig. 1). We comment on this aspect further in section 4.

The geometric minimization of the temperature difference across H continues to manifest itself as H (or Ra_H) increases, as convection becomes more intense. In this case, geometric optimization means the selection of the number of rolls that fill a layer of horizontal dimension L (Fig. 1), or the selection of the roll aspect ratio $H \times L_r$. This principle is known as the Malkus hypothesis, and was proposed heuristically in the usual context of maximizing $\bar{q}''$ when ΔT is imposed (Malkus, 1954).

2.2 Cellular Fluid Space Heated From the Side. An illustration of the minimization of thermal resistance through the optimization of the shape of each roll is provided by the man-made configuration shown in Fig. 2 (Bejan, 1980). The fluid layer is heated from the side ($\Delta T = T_h - T_c$), and its thickness—the horizontal dimension—is fixed. The ensuing flow is segmented into rolls by inserting horizontal partitions, which are impermeable and adiabatic. The partitions are equidistant, but their vertical spacing H may vary.

Figure 2 shows what happens to the overall thermal conductance [$Nu = q'/(k\Delta T/L)$] of the L layer when the shape of each roll (H/L) varies. These changes occur at constant L, which means a constant Rayleigh number based on L, $Ra_L = g\beta\Delta TL^3/(\alpha\nu)$. The thermal conductance reaches a maximum when each roll has a certain, intermediate shape (not too tall, not too shallow). The evidence that supports the maxima exhibited in Fig. 2 is strong and comes from seven independent studies, which are indicated on the figure. The optimal roll shape becomes more slender as the convection becomes more intense (i.e., as Ra_L increases).

The analogy between the geometric optimization of segmented vertical layers (Fig. 2) and the geometric maximization of thermal conductance in layers heated from below (Fig. 1) was not noted until now. An analogous geometric principle governs the maximization of thermal conductance across a cellular vertical layer filled with a fluid-saturated porous medium (Bejan, 1980).

2.3 Optimization of Flow Structure in Heating From Below. The flow geometry resulting from the optimization process in the man-made system of Fig. 2 shows the way to a pure and very simple theory of convection in a fluid layer heated from below (Fig. 1). The key is to regard the natural flow pattern as the result of an "engineering process" in which many flow patterns are evaluated until the flow with minimal thermal resistance is identified. We can describe this process analytically by intersecting the two asymptotes of the geometric configuration: many cells versus few cells. This method has been used with consistently good results in the geometric optimization of cooling arrangements for electronics, as shown in a recent review (Bejan, 1996).

2.3.1 The Many Cells Limit. All the physical parameters of the system of Fig. 1 are fixed except for L_r, or the number of cells. For simplicity, we assume that the flow is two dimensional; however, a three-dimensional flow can be optimized by using the same method. Because we are free to vary L_r, we can imagine the "many cells" limit shown in Fig. 3. Each cell is a very slender counterflow, which has the important property that it can sustain a longitudinal (i.e., vertical) temperature gradient of the same order as the imposed gradient $\Delta T/H$. This property of slender counterflows is well known: The longitudinal gradient occurs because one branch of the counterflow loses heat to (or gains heat from) the other branch.

We are interested in more than just the orders of magnitude of the flow variables: As we showed in Section 2, we want to compare quantitatively the results of geometric optimization with the observed features of natural flows. This is why in addition to using scale analysis we assume a reasonable shape for the laminar temperature profile. If the temperature profile is parabolic across each branch (Fig. 3), and if the maximum

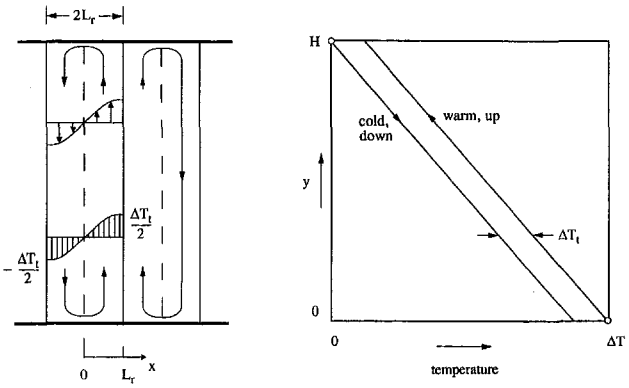

Fig. 3 The geometry of flow of Fig. 1 in the "many cells" limit

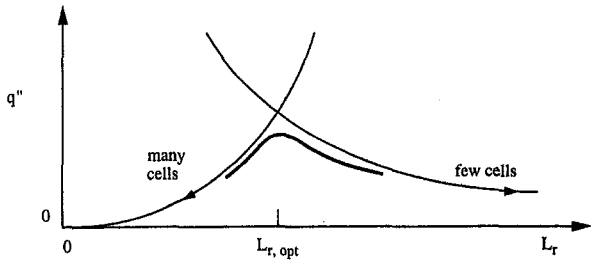

Fig. 4 The intersection of the many cells and the few cells asymptotes, and the optimal cell thickness

temperature difference across one branch is $\Delta T_t/2$, then the average temperature difference between the two branches is $\frac{2}{3}\Delta T_t$.

The mass flow rate of one branch, $\dot{m}'$, can be estimated by writing the momentum equation for fully developed flow in the upflowing branch (e.g., Bejan, 1995, pp. 186–187):

$$\frac{d^2v}{dx^2} = -\frac{g\beta}{\nu}(\bar{T}_{up} - \bar{T}_{down}) \tag{5}$$

In this equation $\bar{T}_{up}$ and $\bar{T}_{down}$ are the average temperatures of the upflowing and downflowing branches. Noting that $(\bar{T}_{up} - \bar{T}_{down}) \cong \frac{2}{3}\Delta T_t$ and integrating Eq. (5) subject to the conditions of no-slip at $x = 0$ and zero-shear at $x = L_r$, we obtain $v(x)$ and the mass flow rate as

$$\dot{m}' = \frac{2\rho g\beta L_r^3 \Delta T_t}{9\nu} \tag{6}$$

The enthalpy lost by the upflowing branch is $\dot{m}' c_P(T_{in} - T_{out})$, where T_{in} and T_{out} are the "start" and "finish" bulk temperatures of the branch. The right side of Fig. 3 shows that $T_{in} - T_{out} = \Delta T - \Delta T_t$. This enthalpy loss is being conducted horizontally to the downflowing branch. The horizontal temperature gradient across the interface between the two branches ($x = 0$; dashed line in Fig. 3) is $2(\frac{1}{2}\Delta T_t/L_r)$, where the leading factor of 2 is the mark of the assumed parabolic temperature profile. Finally, the first law of thermodynamics written for the upflowing branch as a flow system of size $H \times L_r$ is

$$\dot{m}c_P(\Delta T - \Delta T_t) = kH\frac{\Delta T_t}{L_r} \tag{7}$$

Combining Eqs. (6) and (7), we find the relation between the transversal temperature difference ΔT_t and the difference imposed vertically (ΔT):

$$\frac{\Delta T_t}{\Delta T} = 1 - \frac{9}{2\mathrm{Ra}_H}\left(\frac{H}{L_r}\right)^4 \tag{8}$$

Another property of the counterflow is that it convects energy longitudinally (upward) at the rate $\dot{m}' c_P(\bar{T}_{up,b} - \bar{T}_{down,b})$. The present analysis is sufficiently approximate so that we may replace the bulk temperature difference with the mean temperature difference $\frac{2}{3}\Delta T_t$. The counterflow carries this energy current upward through a space of thickness $2L_r$. Consequently, the average heat flux removed by the counterflow from the bottom wall is

$$q'' = \frac{\dot{m}' c_P(2/3)\Delta T_t}{2L_r} \tag{9}$$

or, after using Eqs. (6)–(8),

$$q'' = \frac{2kg\beta L_r^2}{27\alpha\nu}(\Delta T)^2\left[1 - \frac{9}{2\mathrm{Ra}_H}\left(\frac{H}{L_r}\right)^4\right]^2 \tag{10}$$

This result has been sketched qualitatively in Fig. 4: The heat flux decreases approximately as L_r^2 as $L_r \to 0$, i.e., as the cells become more numerous.

2.3.2 The Few Cells Limit. Consider now the opposite limit where the flow is spread out, by design, using a small number of upflows and downflows. This limit is illustrated in Fig. 5. Each vertical flow is a plume formed over a long portion of horizontal wall of length $L = 4\ L_r$. The thermal resistance is due to the horizontal boundary layers that line each section of length $2L_r$. Although it is possible to obtain a purely theoretical estimate for the heat transfer rate across such a boundary layer, by using boundary layer theory, in this section we rely on the most accurate estimate, which is derived from an experimental correlation.

We begin with the observation that the plume rises or sinks in a quiescent and thermally stratified fluid of average temperature difference $\Delta T/2$. This means that the effective temperature difference between the horizontal base of each plume and the fluid reservoir that surrounds it is $\theta = \Delta T/2$. The average heat flux removed by the plume is known from direct measurements (e.g., Lloyd and Moran, 1974):

$$\frac{q''L}{\theta k} = 0.54\ \mathrm{Ra}_{L,\theta}^{1/4} \tag{11}$$

where $\mathrm{Ra}_{L,\theta}$ is the Rayleigh number based on L and θ, and $\mathrm{Ra}_{L,\theta} < 10^7$. Note that according to Eq. (11), the heat flux is independent of the vertical dimension of the system, H. Expressed in terms of L_r and ΔT, the correlation (11) reads as

$$q'' = 0.161\frac{k\Delta T}{H}\left(\frac{H}{L_r}\right)^{1/2}\mathrm{Ra}_H^{1/4} \tag{12}$$

In conclusion, when the horizontal surfaces are covered sparsely with isolated plumes, the wall-averaged heat flux decreases monotonically as the spacing L_r increases. This asymptotic trend has been added to Fig. 4 to show that a flow geometry with maximal heat flux exists.

2.3.3 The Intersection of the Asymptotes. The optimal flow structure (L_r) can be located by intersecting the asymptotes (10) and (12). Eliminating q'' between Eqs. (10) and (12), we obtain

$$\mathrm{Ra}_H^{1/3}\left(\frac{L_{r,opt}}{H}\right)\left[1 - \frac{9}{2\mathrm{Ra}_H}\left(\frac{H}{L_{r,opt}}\right)^4\right]^{8/9} = 1.41 \tag{13}$$

It is convenient to define the dimensionless factor f as

$$f = \frac{L_{r,opt}}{H\mathrm{Ra}_H^{-1/3}} \tag{14}$$

such that Eq. (13) provides implicitly the function $f(\mathrm{Ra}_H)$:

$$f^4 - 1.474f^{23/8} = \frac{9}{2}\mathrm{Ra}_H^{1/3} \tag{15}$$

Equations (14) and (15) pinpoint the optimal value of the

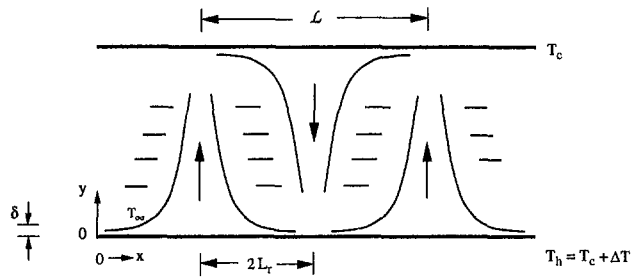

Fig. 5 The geometry of the flow of Fig. 1 in the "few cells" limit

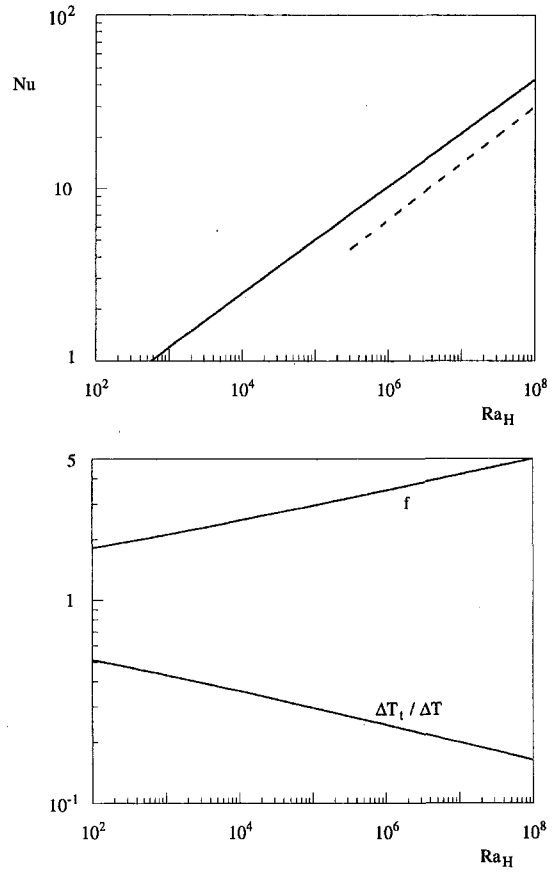

Fig. 6 The heat transfer characteristics of the cellular flow of Fig. 1, after its L_r dimension has been optimized

flow slenderness ratio $L_{r,\text{opt}}/H$ as a function of Ra_H. The maximum heat flux that corresponds to this geometry is obtained by substituting $L_r = L_{r,\text{opt}}$ into Eq. (10) or Eq. (12):

$$\text{Nu}_{\max} \leq 0.161 f^{-1/4} \text{Ra}_\text{H}^{1/3} \tag{16}$$

The inequality sign is a reminder that the actual peak of the $q''_{\max}(L_r)$ curve is situated under the intersection of the two asymptotes (Fig. 4). Electronics cooling applications of the intersection-of-asymptotes method have shown that the inequality sign accounts for a factor of approximately $\frac{1}{2}$ between the height of the point of intersection and the peak of the actual curve. Finally, at the optimum, Eq. (8) reads

$$\frac{\Delta T_t}{\Delta T} = 1.47 f^{-9/8} \tag{17}$$

Figure 6 shows the main features of the optimal geometry derived based on this simple analysis. The plotted $\text{Nu}_{\max}$ curve is based on Eq. (16) with the equal sign, which means that the actual $\text{Nu}_{\max}$ should be lower, by a factor of order 1/2. Several features of this solution are worth noting:

(*a*) The $\text{Nu}_{\max}(\text{Ra}_\text{H})$ curve comes close to the experimental data, e.g., the $P_r \sim 1$ range of the correlation due to Globe and Dropkin (1959). If the expected factor of order 1/2 is applied, then the $\text{Nu}_{\max}$ curve falls right on top of Globe and Dropkin's correlation, which is shown with dashed line in Fig. 6 (top). At the same point, $L_{r,\text{opt}}/H \cong 0.35$, which agrees with the linear stability solution $L_{r,\text{opt}}/H \sim 0.5$.

(*b*) The $\text{Nu}_{\max}(\text{Ra}_\text{H})$ curve cuts the $\text{Nu}_{\max} = 1$ line at an $\text{Ra}_\text{H} \cong 526$, which is a value of $O(10^3)$. In other words, the predicted transition between pure diffusion and stream flow is in agreement with the time minimization (or access maximization) argument of Section 2.1. This improved estimate of the critical Ra_H for the onset of convection validates the comments made in the second paragraph under Eq. (4).

(*c*) The $\text{Nu}_{\max}(\text{Ra}_\text{H})$ curve is described approximately by $\text{Nu}_{\max} \sim \text{Ra}_\text{H}^n$, where the exponent n decreases from 0.333 to 0.313 as Ra_H increases. Over most of the Ra_H range of Fig. 6, the n value is close to 0.313 as the f factor approaches $1.033\ \text{Ra}_\text{H}^{1/12}$. This $\text{Nu}_{\max}(\text{Ra}_\text{H})$ behavior also agrees with observations. The minor and gradual decrease of the Ra_H exponent is well known, and is one of the points of controversy in the field of Bénard convection (e.g., Yang and Lloyd, 1982). In this section we predicted this trend analytically.

(*d*) The transversal temperature difference between the vertical branches of the roll (ΔT_t) decreases as Ra_H increases, i.e., as convection intensifies. Although this trend may seem counterintuitive, it is explained by the fact that the rolls become more slender as Ra_H increases. In this limit the vertical streams find themselves in a more intimate thermal contact.

(*e*) The optimized slenderness ratio is given by $L_{r,\text{opt}} = H f \text{Ra}_\text{H}^{-1/3}$, and approaches $L_{r,\text{opt}} \cong 1.033 H \text{Ra}_\text{H}^{-1/4}$ as Ra_H increases, i.e., when $f \cong 1.033\ \text{Ra}_\text{H}^{1/12}$.

3 Fluid-Saturated Porous Layer Heated From Below

There is an analogy between the geometric optimization of flow structure in a space filled with fluid and the optimization of structure in a space filled with a porous medium saturated with fluid. In this section we illustrate the determinism that results from geometrically minimizing the thermal resistance across a fluid-saturated porous layer. For brevity, we rely once more on Figs. 1 and 3–5, and list only the analytical highlights that differ from those of section 2.3. One difference is that in this section the two asymptotes of the flow geometry are described in exact analytical terms.

Assume that the system of Fig. 1 is a porous layer saturated with fluid, and that, if present, the flow is two dimensional and in the Darcy regime. The height H is fixed, and the horizontal dimensions of the layer are infinite in both directions. The fluid has nearly constant properties such that its density–temperature relation is described well by the Boussinesq linearization. The volume-averaged equations that govern the conservation of mass, momentum, and energy are (e.g., Nield and Bejan, 1992)

$$\frac{\partial u}{\partial x} + \frac{\partial v}{\partial y} = 0 \tag{18}$$

$$\frac{\partial u}{\partial y} - \frac{\partial v}{\partial x} = -\frac{Kg\beta}{\nu}\frac{\partial T}{\partial x} \tag{19}$$

$$u\frac{\partial T}{\partial x} + v\frac{\partial T}{\partial y} = \alpha_m\left(\frac{\partial^2 T}{\partial x^2} + \frac{\partial^2 T}{\partial y^2}\right) \tag{20}$$

where T, u, and v are the volume-averaged temperature and velocity components, and K, g, β, and ν are the permeability constant, gravitational acceleration, coefficient of volumetric thermal expansion, and kinematic viscosity. The thermal diffusivity $\alpha_m = k_m/(\rho c_P)_f$ is based on the thermal conductivity of the porous matrix saturated with fluid (k_m) and the heat capacity of the fluid alone, $(\rho c_P)_f$. The horizontal length scale of the flow pattern ($2L_r$), or the geometric aspect ratio of one roll, is unknown.

In the limit $L_r \to 0$ each roll is a very slender vertical counterflow, Fig. 3. Because of symmetry, the outer planes of this structure ($x = \pm L_r$) are adiabatic: They represent the center planes of the streams that travel over the distance H. The scale analysis of the $H \times (2L_r)$ region indicates that in the $L_r/H \to 0$ limit the horizontal velocity u vanishes. This scale analysis is not shown because it is well known as the defining statement of fully developed flow (e.g., Bejan, 1995, p. 97). Equations (18)–(20) reduce to

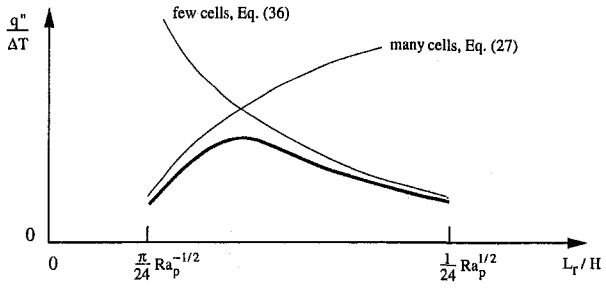

Fig. 7 The geometric maximization of the thermal conductance of a fluid-saturated porous layer heated from below

$$\frac{\partial v}{\partial x} = \frac{Kg\beta}{\nu}\frac{\partial T}{\partial x} \tag{21}$$

$$v\frac{\partial T}{\partial y} = \alpha_m \frac{\partial^2 T}{\partial x^2} \tag{22}$$

which can be solved exactly for v and T. The boundary conditions are $\partial T/\partial x = 0$ at $x = \pm L_r$, and the requirement that the extreme (corner) temperatures of the counterflow region are dictated by the top and bottom walls, $T(-L_r, H) = T_c$ and $T(L_r, 0) = T_h$. The solution is

$$v(x) = \frac{\alpha_m}{2H}\left[\mathrm{Ra}_p - \left(\frac{\pi H}{2L_r}\right)^2\right]\sin\left(\frac{\pi x}{2L_r}\right) \tag{23}$$

$$T(x, Y) = \frac{\nu}{Kg\beta}v(x) + \frac{\nu}{Kg\beta}\left(2\frac{y}{H} - 1\right) \times \frac{\alpha_m}{2H}\left[\mathrm{Ra}_p - \left(\frac{\pi H}{2L_r}\right)^2\right] + (T_h - T_c)\left(1 - \frac{y}{H}\right) \tag{24}$$

where the porous-medium Rayleigh number $\mathrm{Ra}_p = Kg\beta H(T_h - T_c)/(\alpha_m\nu)$ is a specified constant. The right side of Fig. 3 shows the temperature distribution along the vertical boundaries of the flow region ($x = \pm L_r$): The vertical temperature gradient $\partial T/\partial y$ is independent of altitude. The transversal (horizontal) temperature difference (ΔT_t) is also a constant,

$$\Delta T_t = T(x = L_r) - T(x = -L_r) = \frac{\nu}{Kg\beta}\frac{\alpha_m}{H}\left[\mathrm{Ra}_p - \left(\frac{\pi H}{2L_r}\right)^2\right] \tag{25}$$

The counterflow convects heat upward at the rate q', which can be calculated using Eqs. (23) and (24):

$$q' = \int_{-L}^{L}(\rho c_P)_f v T dx \tag{26}$$

The average heat flux convected in the vertical direction is $q'' = q'/2L_r$, hence the thermal conductance expression

$$\frac{q''}{\Delta T} = \frac{k_m}{8H\mathrm{Ra}_p}\left[\mathrm{Ra}_p - \left(\frac{\pi H}{2L_r}\right)^2\right]^2 \tag{27}$$

This result is valid provided the vertical temperature gradient does not exceed the externally imposed gradient, $(-\partial T/\partial y) < \Delta T/H$. This condition translates into

$$\frac{L_r}{H} > \frac{\pi}{2}\mathrm{Ra}_p^{-1/2} \tag{28}$$

which in combination with the assumed limit $L_r/H \to 0$ means that the domain of validity of Eq. (27) is wide when Ra_p is large. In this domain the thermal conductance $q''/\Delta T$ decreases monotonically as L_r decreases, cf. Fig. 7.

As L_r increases, the number of rolls decreases and the vertical counterflow is replaced by a horizontal counterflow in which the thermal resistance between T_h and T_c is dominated by two horizontal boundary layers, Fig. 5. Let δ be the scale of the thickness of the horizontal boundary layer. The thermal conductance $q''/\Delta T$ can be deduced from the heat transfer solution for natural convection boundary layer flow over a hot isothermal horizontal surface facing upward, or a cold surface facing downward. The similarity solution for the horizontal surface with power-law temperature variation (Cheng and Chang, 1976) can be used to develop an analytical result, as we show at the end of this section.

A simpler analytical solution can be developed in a few steps using the integral method. Consider the slender flow region $\delta \times (2L_r)$, where $\delta \ll 2L_r$, and integrate Eqs. (18)–(20) from $y = 0$ to $y \to \infty$, i.e., into the region just above the boundary layer. The surface temperature is T_h, and the temperature outside the boundary layer is T_∞ (constant). The origin $x = 0$ is set at the tip of the wall section of length $2L_r$. The integrals of Eqs. (18) and (20) yield

$$\frac{d}{dx}\int_0^\infty u(T - T_\infty)dy = -\alpha_m\left(\frac{\partial T}{\partial y}\right)_{y=0} \tag{29}$$

The integral of Eq. (19), in which we neglect $\partial v/\partial x$ (cf. boundary layer theory), leads to

$$u_0(x) = \frac{Kg\beta}{\nu}\frac{d}{dx}\int_0^\infty T dy \tag{30}$$

where u_0 is the velocity along the surface, $u_0 = u(x, 0)$. Reasonable shapes for the u and T profiles are the exponentials

$$\frac{u(x, y)}{u_0(x)} = \exp\left[-\frac{y}{\delta(x)}\right] = \frac{T(x, y) - T_\infty}{T_h - T_\infty} \tag{31}$$

which transform Eqs. (29) and (30) into

$$\frac{d}{dx}(u_0\delta) = \frac{2\alpha_m}{\delta} \tag{32}$$

$$u_0 = \frac{Kg\beta}{\nu}(T_h - T_\infty)\frac{d\delta}{dx} \tag{33}$$

These equations can be solved for $u_0(x)$ and $\delta(x)$. Necessary in heat transfer calculations is the thickness

$$\delta(x) = \left[\frac{9\alpha_m\nu}{Kg\beta(T_h - T_\infty)}\right]^{1/3}x^{2/3} \tag{34}$$

The corresponding solution for $u_0(x)$ is of the type $u_0 \sim x^{-1/3}$, which means that the horizontal velocities are large at the start of the boundary layer, and decrease as x increases. This is consistent with the geometry of the $H \times 2L_r$ roll sketched in Fig. 5, where the flow generated by one horizontal boundary layer turns the corner and flows vertically as a relatively narrow plume (narrow relative to $2L_r$), to start with high velocity (u_0) a new boundary layer along the opposite horizontal wall.

The thermal resistance of the geometry of Fig. 5 is determined by estimating the local heat flux $k_m(T_h - T_\infty)/\delta(x)$ and averaging it over the total length $2L_r$:

$$q'' = \left(\frac{3}{4}\right)^{1/3}\frac{k_m\Delta T}{H}\left(\frac{T_h - T_\infty}{\Delta T}\right)^{4/3}\mathrm{Ra}_H^{1/3}\left(\frac{H}{L_r}\right)^{2/3} \tag{35}$$

The symmetry of the sandwich of boundary layers requires $T_h - T_\infty = \frac{1}{2}\Delta T$, such that

$$\frac{q''}{\Delta T} = \frac{3^{1/3}k_m}{4H}\,\mathrm{Ra}_p^{1/3}\left(\frac{H}{L_r}\right)^{2/3} \tag{36}$$

To check the goodness of this result we used the similarity solution for a hot horizontal surface that faces upward in a porous medium and has an excess temperature that increases as x^λ (Cheng and Chang, 1976). The only difference is that the role that was played by $(T_h - T_\infty)$ in the preceding analysis is now played by the excess temperature averaged over the surface length $2L_r$. If we use $\lambda = 1/2$, which corresponds to uniform heat flux, then it can be shown that the Cheng and Chang (1976) solution leads to the same formula as Eq. (36) except that the factor $3^{1/3} = 1.442$ is replaced by $0.816(3/2)^{4/3} = 1.401$. The difference between the results of the two methods is only 3 percent.

Equation (36) is valid when the specified Ra_p is such that the horizontal boundary layers do not touch. We write this geometric condition as $\delta(x = 2L_r) < \frac{1}{2}H$ and, using Eq. (34), we obtain

$$\frac{L_r}{H} < \frac{1}{24}\,\mathrm{Ra}_p^{1/2} \tag{37}$$

Since in this analysis L_r/H was assumed to be very large, we conclude that the L_r/H domain in which Eq. (36) is valid becomes wider as the specified Ra_H increases. The important feature of Eq. (36) is that in the "few rolls" limit the thermal conductance decreases as the horizontal dimension L_r increases. This second asymptotic trend has been added to Fig. 7.

Figure 7 presents a bird's-eye view of the effect of flow shape on thermal conductance. Even though we did not completely draw $q''/\Delta T$ as a function of L_r, the two asymptotes tell us that the thermal conductance is maximum at an optimal L_r value that is close to their intersection. There is a family of such curves, one curve for each Ra_p. The $q''/\Delta T$ peak of the curve rises, and the L_r domain of validity around the peak becomes wider as Ra_p increases. Looking in the direction of small Ra_p values we see that the domain vanishes (and the cellular flow disappears) when the following requirement is violated:

$$\frac{1}{24}H\,\mathrm{Ra}_p^{1/2} - \frac{\pi}{2}H\,\mathrm{Ra}_p^{-1/2} > 0 \tag{38}$$

This inequality means that the flow exists when $\mathrm{Ra}_p > 12\pi = 37.7$. This conclusion agrees very well with the stability criterion for the onset of two-dimensional convection, $\mathrm{Ra}_p > 4\pi^2 = 39.5$.

The optimal shape of the flow, $2L_{r,\mathrm{opt}}/H$, is obtained by intersecting the asymptotes (27) and (36):

$$\pi^2\left(\frac{H}{2L_{r,\mathrm{opt}}}\,\mathrm{Ra}_p^{-1/2}\right)^2 + 2^{5/6}3^{1/6}\left(\frac{H}{2L_{r,\mathrm{opt}}}\,\mathrm{Ra}_p^{-1}\right)^{1/3} = 1 \tag{39}$$

Over most of the Ra_p domain (38), Eq. (39) is approximated well by its high-Ra_p asymptote:

$$\frac{2L_{r,\mathrm{opt}}}{H} \cong \pi\mathrm{Ra}_p^{-1/2} \tag{40}$$

The maximum thermal conductance is obtained by substituting the $L_{r,\mathrm{opt}}$ value of Eq. (39) in either Eq. (36) or Eq. (27). This estimate is an upper bound, as explained under Eq. (16). In the high-Ra_p limit (40) this upper-bound assumes the analytical form

$$\left(\frac{q''}{\Delta T}\right)_{\max}\frac{H}{k_m} \lesssim \frac{3^{1/3}}{2^{4/3}\pi^{2/3}}\,\mathrm{Ra}_p^{2/3} \tag{41}$$

Toward lower Ra_p values the slope of the $(q''/\Delta T)_{\max}$ curve increases such that the exponent of Ra_p approaches 1. This behavior is an excellent agreement with the large volume of experimental data collected for Bénard convection in saturated porous media (e.g., Cheng, 1978). The "less than 1" exponent of Ra_p in the empirical $\mathrm{Nu}(\mathrm{Ra}_p)$ curve, and the fact that this exponent decreases as Ra_p increases has attracted considerable attention from theoreticians during the last two decades (e.g., Cheng, 1978; Nield and Bejan, 1992). Equation (41) is the first instance in which this behavior is predicted theoretically, i.e., in purely deterministic fashion.

4 Geometric Form in Natural Flow Systems

In this paper we showed that if we start from the basic idea of constructal theory—the optimization of access to flow by optimizing the internal geometry of finite-size systems—it is possible to anticipate the structural features of fluid systems heated from below. We demonstrated these deterministic steps for two classes of fluid system: fluid layers, and porous layers saturated with fluid.

The occurrence of the first sign of organized motion (stream, roll, cell) has been connected theoretically to the shape changes (multiplication of rolls) that are observed at higher heat fluxes. The same theoretical viewpoint explains why organized motion (rolls) must always coexist with disorganized motion (diffusion), such that the latter is assigned to cover length scales smaller than the smallest roll.

The geometric optimization of access for internal currents—the minimization of resistance in the present paper—is a more general statement than the optimization principles invoked in the past. If resistance minimization means that we fix the heat current and minimize the overall temperature difference, then it also means that we minimize the total entropy generation rate, and that we recover Prigogine's principle. On the other hand, if we regard the temperature difference as fixed and maximize the heat current, we achieve entropy generation *maximization*, not minimization. The point is that, contrary to Prigogine's approach, thermodynamics is not needed in order to achieve access optimization through geometric (shape) optimization. Thermodynamics is not needed because access optimization is a separate, self-standing law that accounts for the generation of macroscopic form in natural flow systems.

Prigogine is only one in a growing series of theoreticians who suspect that a new and very powerful law rules the formation of geometric form in nature. Kadanoff is another. Our geometric optimization approach is related even more closely to the much older argument used by biologists to explain the nearly round cross sections of blood vessels and bronchial passages. The billions of such cross sections, just like the billions of tree networks and billions of river cross sections (whose depth is universally proportional to the width; Bejan, 1997b), support the geometric optimization of flow access principle. Presently, there is no law in our physics books to account for these observations. This is why we need to hear and test new theories. We need to continue to extend our physics over currently unexplained phenomena.

In this paper we analyzed a system with fixed size and imposed throughflow, and proceeded to minimize global resistance through the creation and optimization of internal geometric form. If, on the other hand, the system is isolated and in an initial state of internal nonuniformity (nonequilibrium), then the constructal optimization of flow access is equivalent to the minimization of the time of approach to uniformity (equilibrium, zero internal flow). If the volume is unbounded, the constructs of internal streams compound themselves and continue to spread in space indefinitely. Their complexity continues to increase in time.

The major feature of this work is that it was carried out purely theoretically, i.e., without any trace of empiricism. This is also true about the first paper on constructal theory (Bejan, 1997a), where every geometric feature was a result of resistance

minimization. Even dichotomy (bifurcation, or pairing) was deduced, as a result of geometric optimization. This also leads to a somewhat different perspective on "stability," which now emerges as *the need* of a system to organize itself in order to optimize its geometry. At the same time, "chaos" is the inability of a flow system to find a stationary optimal configuration i.e., the continual, dynamic search for a configuration that does not exist.

The conclusion that follows logically from this paper and other tests of constructal theory is this: Nature exhibits geometric form everywhere (trees, round and river cross sections, eddies), in both animate and inanimate flow systems. If a single theory accounts for the occurrence of geometric form in flow systems, then that theory unites the physical and biological fields recognized by scientists.

Acknowledgments

Professor Bejan's research was supported by the National Science Foundation.

References

Bejan, A., 1979, "Note on Gill's Solution for Free Convection in a Vertical Enclosure," ASME *J. Fluid Mech.*, Vol. 90, pp. 561–568.

Bejan, A., 1980, "A Synthesis of Analytical Results for Natural Convection Heat Transfer Across Rectangular Enclosures," *Int. J. Heat Mass Transfer*, Vol. 23, pp. 723–726.

Bejan, A., 1995, *Convection Heat Transfer*, 2nd ed., Wiley, New York, Chaps. 4 and 5.

Bejan, A., 1996, "Geometric Optimization of Cooling Techniques," in: *Air Cooling Technology for Electronic Equipment*, Kim, S. J., and Lee, S. W., eds., CRC Press, Boca Raton, FL, Chap. 1.

Bejan, A., 1997a, "Constructal-Theory Network of Conducting Paths for Cooling a Heat Generating Volume," *Int. J. Heat Mass Transfer*, Vol. 40, pp. 799–816.

Bejan, A., 1997b, *Advanced Engineering Thermodynamics*, 2nd ed., Wiley, New York.

Bejan, A., and Tien, C.-L., 1978, "Laminar Natural Convection Heat Transfer in a Horizontal Cavity With Different End Temperatures," ASME JOURNAL OF HEAT TRANSFER, Vol. 100, pp. 641–647.

Cheng, P., 1978, "Heat Transfer in Geothermal Systems," *Adv. Heat Transfer*, Vol. 14, pp. 1–105.

Cheng, P., and Chang, I. D., 1976, "On Buoyancy Induced Flows in a Saturated Porous Medium Adjacent to Impermeable Horizontal Surfaces," *Int. J. Heat Mass Transfer*, Vol. 19, pp. 1267–1272.

Cormack, D. E., Leal, L. G., and Imberger, J., 1974, "Natural Convection in a Shallow Cavity With Differentially Heated End Walls," *J. Fluid Mech.*, Vol. 65, pp. 209–229.

Elder, J. W., 1965, "Laminar Free Convection in a Vertical Slot," *J. Fluid Mech.*, Vol. 23, pp. 77–98.

Gill, A. E., 1966, "The Boundary Layer Regime for Convection in a Rectangular Cavity," *J. Fluid Mech.*, Vol. 26, pp. 515–536.

Glansdorff, P., and Prigogine, I., 1971, *Thermodynamic Theory of Structure, Stability and Fluctuations*, Wiley, London.

Globe, S., and Dropkin, D., 1959, "Natural Convection Heat Transfer in Liquids Confined by Two Horizontal Plates and Heated From Below," ASME JOURNAL OF HEAT TRANSFER, Vol. 81, pp. 24–28.

Han, J. T., 1967, M. A. Sc. Thesis, Dept. of Mech. Eng., University of Toronto.

Kadanoff, L. P., 1986, "Fractals: Where's the Physics?" *Physics Today*, Feb., pp. 6–7.

Lloyd, J. R., and Moran, W. R., 1974, "Natural Convection Adjacent to Horizontal Surfaces of Various Platforms," ASME Paper No. 74-WA/HT-66.

Malkus, W. V. R., 1954, "The Heat Transport and Spectrum of Thermal Turbulence," *Proc. Royal Society*, Series A, Vol. 225, pp. 196–212.

Newell, M. E., and Schmidt, F. W., 1970, "Heat Transfer by Natural Convection Within Rectangular Enclosures," ASME JOURNAL OF HEAT TRANSFER, Vol. 92, pp. 159–167.

Nield, D. A., and Bejan, A., 1992, *Convection in Porous Media*, Springer Verlag, New York, p. 224.

Yang, K. T., and Lloyd, J. R.,1982, *Proc. of a Workshop on Natural Convection*, July 18–21, Breckenridge, CO.

Steady-State Subcooled Nucleate Boiling on a Downward-Facing Hemispherical Surface

K. H. Haddad

F. B. Cheung
Fellow ASME

Department of Mechanical Engineering,
The Pennsylvania State University,
University Park, PA 16802

Steady-state nucleate boiling heat transfer experiments in saturated and subcooled water were conducted. The heating surface was a 0.305 m hemispherical aluminum vessel heated from the inside with water boiling on the outside. It was found that subcooling had very little effect on the nucleate boiling curve in the high heat flux regime where latent heat transport dominated. On the other hand, a relatively large effect of subcooling was observed in the low-heat-flux regime where sensible heat transport was important. Photographic records of the boiling phenomenon and the bubble dynamics indicated that in the high-heat-flux regime, boiling in the bottom center region of the vessel was cyclic in nature with a liquid heating phase, a bubble nucleation and growth phase, a bubble coalescence phase, and a large vapor mass ejection phase. At the same heat flux level, the size of the vapor masses was found to decrease from the bottom center toward the upper edge of the vessel, which was consistent with the increase observed in the critical heat flux in the flow direction along the curved heating surface.

Introduction

Steady-state nucleate pool boiling heat transfer on curved heating surfaces has received considerable attention owing to its relevance in the thermal management of cryogenic fluids, cooling of high-power-density electronic devices, handling of hazardous liquid chemicals containers during a fire, and external passive heat removal from a core melt in the lower head of an advanced light water reactor. In the latter case, the decay heat generated in the core melt is removed by boiling of water on the outer surface of the reactor lower head. Owing to the downward-facing orientation of the heating surface, the vapor dynamics and the two-phase liquid/vapor motions resulting from the boiling process can be radically different from those observed during pool boiling on upward-facing surfaces.

Experimental studies dealing with boiling on the outside of curved and downward-facing surfaces have been performed by many researchers, including Thibault and Hoffman (1978), Hwalek (1982), Subramanian and Witte (1987), Dix and Orozco (1990), Chu et al. (1994), Cheung et al. (1994), and Haddad et al. (1995). Most of them employed the transient quenching method to determine the boiling curve. Spherical test sections were used by most of these authors except Thibault and Hoffman (1978), who used a cylindrical surface. Hwalek (1982), Dix and Orozco (1990), Cheung et al. (1994), and Haddad et al. (1995) all reported that the critical heat flux increased from the bottom center toward the equator of the spherical test section. The data of Thibault and Hoffman (1978) indicated that subcooling had essentially no effect on the nucleate boiling curves at several locations on the outer surface of the cylinder. This was also supported by the findings of Dix and Orozco (1990) using a hollow sphere. Observations by Chu et al. (1994) of the boiling phenomenon on the external bottom center region of a downward-facing torispherical surface revealed information about the bubble dynamics. The CHF condition was characterized by a cyclic explosive vaporization. When the process entered the nucleate boiling regime, the explosions became far less reaching and less violent, but the phenomenon was still cyclic in nature.

Besides the transient quenching method, the steady-state heating method has also been employed to study nucleate boiling on downward facing curved surfaces. Most of the studies performed using this method [i.e., Haselden and Peters (1949), Lance and Myers (1958), Flynn et al. (1961), and Theofaneous et al. (1994)] used a cylindrical heating surface. Lance and Myers (1958) used cylinders with diameters of 50.8 and 31.75 mm. They observed that the bubbles formed at the bottom of the tubes were larger than those formed on the sides. Theofaneous et al. (1994) performed a full-scale simulation of the flooding of a reactor lower head using a large two-dimensional cylindrical strip. They found that the critical heat flux increased from the bottom center toward the upper edge of the test section. Chu et al. (1995) performed steady-state heating experiments using a torispherical downward-facing surface with a crown radius of curvature of 3.35 m and a knuckle radius of 0.66 m for a large-scale simulation of a reactor lower head. Rhea and Nevins (1968) was the only study that used a spherical heating surface, with a diameter of 63.5 mm, to perform steady-state heating experiments. Unfortunately, they did not investigate the effect of subcooling on the nucleate boiling heat transfer, nor did they report the bubble dynamics on the heating surface.

In the present study, an aluminum hemispherical vessel with a diameter of 0.305 m was used to conduct steady-state heating experiments in saturated and subcooled water. Nucleate boiling curves were deduced from temperature measurements at different subcooling levels. The vapor dynamics around the bottom center was observed and investigated using a high-speed video system and a high-speed camera.

Experimental Method

Experimental Apparatus. The experimental setup employed in this study consisted of three major parts, i.e., a water tank with a reflux condenser unit, a heated hemispherical vessel,

Contributed by the Heat Transfer Division and presented at the National Heat Transfer Conference, Houston, Texas, August 3–5, 1996. Manuscript received by the Heat Transfer Division August 16, 1996; revision received January 14, 1998. Keywords: Boiling, Multiphase Flows, Phase-Change Phenomena. Associate Technical Editor: M. D. Kelleher.

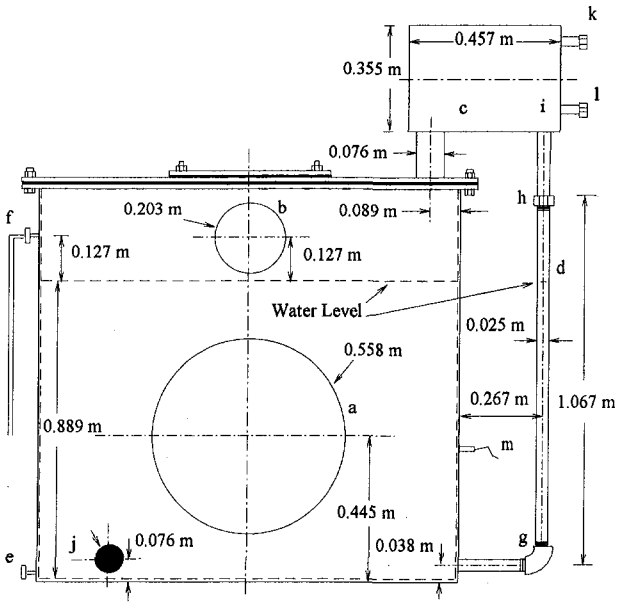

a Viewing Window
b Viewing Window
c Condenser
d Condensate Return
e Drain
f Water Inlet and Pressure Relief Valve
g Elbow
h Pipe Connection
i Condenser Access
j Immersion Heater
k Cold Water Inlet
l Hot Water Outlet
m 2.54 mm Tube for Thermocouples

Fig. 1 Front view of the water tank with the condenser

and a data acquisition/photographic system. The tank and condenser assembly and the hemisphere are shown in Figs. 1 and 2. The condenser was used during the experiment to help maintain a constant water level inside the tank. Thermal insulation was placed on the outside surface of the tank that was not occupied by the three viewing windows. This helped minimize the heat loss from the tank and allowed for better control of the water temperature during the experiment. Three thermocouples were inserted through the tank wall to allow for the monitoring of the ambient water temperature at different locations along the water column.

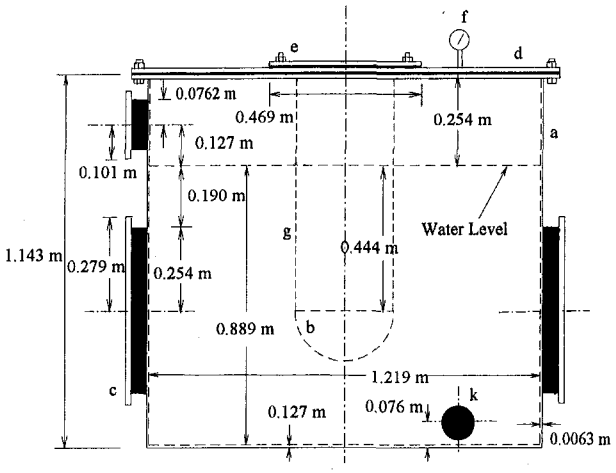

a Cylindrical Tank
b Hemisphere
c Viewing Window
d Tank Cover
e Tank Access Hole
f Pressure Gage
g Cylindrical Pipe
k Immersion Heaters

Fig. 2 Side view of the water tank and the test vessel

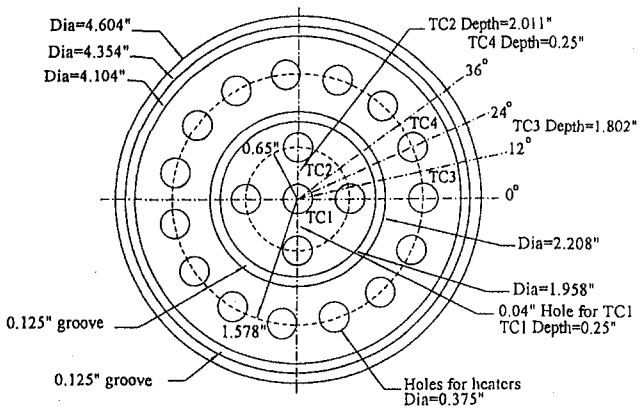

Fig. 3 Heaters placement in the inner and outer segments

The hemispherical vessel employed in the experiment was made of aluminum and had a diameter of 12 in. (0.305 m). The vessel was divided into five segments that could be heated independently at prescribed power levels. Subminiature thermocouple probes with stainless steel sheathing were inserted through the interior surface of the vessel inside the walls of the segments. The hemisphere was attached to an aluminum pipe that was 12 in. (0.305 m) in diameter and 24 in. (0.610 m) in length. The other end of the pipe was fastened to the tank cover through a flange. This allowed for the hemisphere to be suspended vertically in the middle of the tank, which was necessary for videotaping and photographing the two-phase boundary layer through the large viewing windows.

Figure 3 shows the heater's placement in the bottom center segment (i.e., the inner segment) and the segment adjacent to it (i.e., the outer segment). Along the circumference that separated the inner and outer segments, there was a 3.18 mm air gap (i.e., groove) to minimize conduction heat transfer between the two segments. The holes for the cartridge heaters (31.8 mm long and 9.5 mm thick) were drilled and then re-aimed to provide a 0.025 mm fit. This was very important to assure good contact between the heaters and the aluminum test vessel. Before inserting them into the holes, the heaters were treated with a special coating Watlube to protect against high-temperature oxidation and to enhance the heat transfer between the heaters and the test segments. Each heater had a power rating of 480 W when subjected to a voltage of 120 V. Two thermocouples were embedded in each segment specifically for monitoring the performance of the heaters. Five heaters were used in the inner segment and fifteen were used in the outer segment. This would allow heat flux levels of up to 1.2 MW/m^2 to be achieved.

It was very important to prevent the temperature of the vessel from exceeding the melting point of aluminum, which would happen if the heat flux were increased beyond the critical heat flux. In order to achieve this, a power control system, which consisted of the data acquisition system, constant DC power sources, and solid state relays, was used. Temperatures at various locations inside the heated segments were continually monitored and compared against a set point value using the data acquisition system. When one of the monitored temperatures exceeded the set point, all the digital I/O channels became open and the solid-state relays were not powered anymore. As a result the power supplies to all the segments were discontinued and the vessel was protected from melting associated with the occurrence of the local dryout on the heating surface.

A Minolta X-370 camera with a 70–210 mm zoom was used for direct photographing of the two-phase boundary layer. The speed of the camera could be adjusted to a value as high as 1000 frames/s. Videotaping of the two-phase boundary layer was achieved using a Kodak Ektapro high-speed video system consisting of a motion analyzer, an imager, a cassette condi-

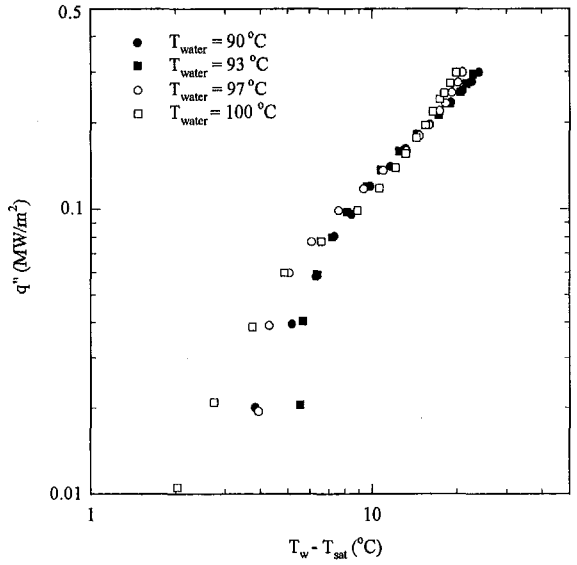

Fig. 4 Steady-state nucleate boiling data measured at the bottom center of the vessel (θ = 0 deg)

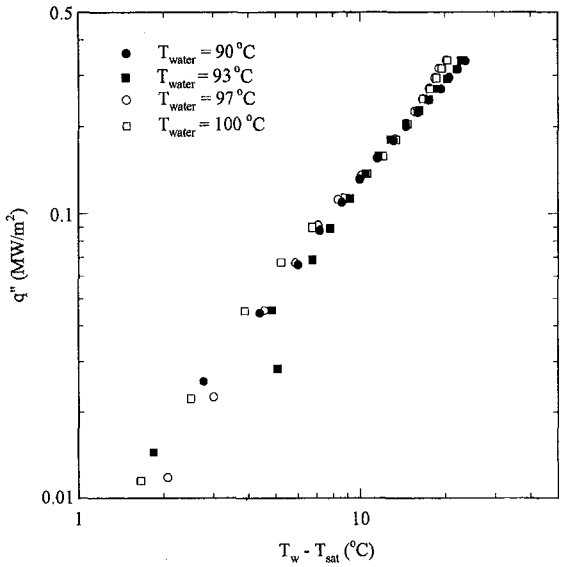

Fig. 5 Steady-state nucleate boiling data measured at an off-center location of the vessel (θ = 18 deg)

tioner, and a TV set. Different settings in the speeds of the camera and the video system were used to accommodate different heat flux levels.

Experimental Procedure. To prepare for a run, the tank was first filled with water to the desired water level. Then a pump was used to circulate the water through a high-grade filter. After the water had been conditioned, the outside surface of the hemisphere was polished with fine emery paper (#220) and cleaned with acetone. The hemisphere and the pipe assembly were then fastened to the tank cover. The immersion heaters were then turned on to heat the water pool to the desired temperature. The power level for a specific segment of the hemisphere was set to the desired value by adjusting the voltage of the power controllers connected to the heaters of that part of the hemisphere. The voltage across and the current through each of the power controllers were then measured using a multimeter. The temperatures at various locations inside the wall of the segment were monitored on the computer screen through the data acquisition system. When these temperatures stabilized around certain mean values, it was decided that steady-state conditions were attained and it was time to record the temperatures indicated by the data acquisition software.

Results and Discussion

Steady-State Heat Transfer Measurements. Steady-state heating experiments were conducted for water temperatures varying from 90° to 100°C. During these experiments, the heat flux levels and the corresponding wall superheats were recorded to construct nucleate boiling curves. Data were collected for the bottom center (i.e., inner) segment and the outer segment adjacent to it. The local boiling heat flux was determined by performing an inverse heat conduction analysis (Liu, 1995) of the temperatures recorded through the thermocouples embedded inside the walls of the inner and outer segments. The boiling heat flux was found to agree satisfactorily with the local power input. The uncertainty in the embedded thermocouple locations was about ±0.001 m, the maximum error in the temperature reading was ±0.1°C, and the uncertainty in the calculated heat flux was ±7 percent.

Figures 4 and 5 show the nucleate boiling curves for the inner segment (θ = 0 deg) and for the outer segment (θ = 18 deg). Each figure includes four curves for water temperatures of 90°, 93°, 97°, and 100°C. It can be seen from the figures that subcooling has a strong effect on the nucleate boiling heat transfer in the low-to-moderate heat flux levels. This is in contrast to the conventional case of pool boiling for which subcooling has very little effect on the nucleate boiling heat transfer. Observations of the two-phase boundary layer indicated that the bubble size decreased considerably as the subcooling level was increased. As a result the local bubble agitation was reduced along with the two-phase boundary layer flow, which reduced the convective heat transfer associated with the local bubble agitation and the convective boundary layer motion. It was because of this that the local heat flux actually decreased as the degree of subcooling was increased. At high heat flux levels, latent heat transfer dominated the convective heat transfer, and subcooling had very little effect on the nucleate boiling heat flux in this region.

Comparison of Steady-State and Transient Quenching Results. The present steady-state boiling data are compared to the transient quenching data of Haddad et al. (1995) in Figs. 6 and 7. At the bottom center location, the critical heat flux was found to be 0.4 MW/m^2 for saturated boiling and 0.59

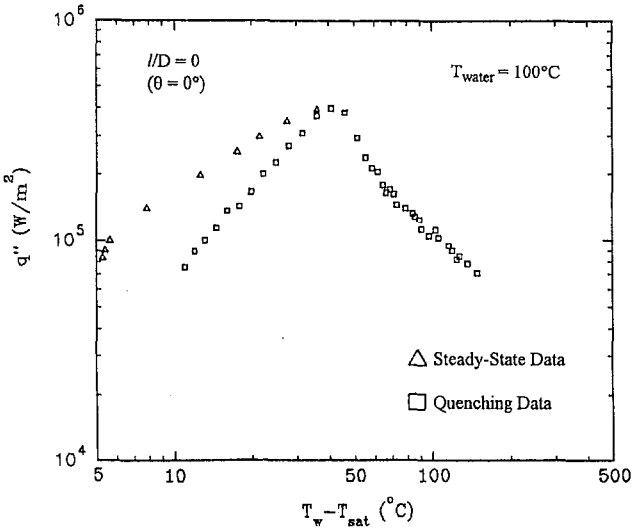

Fig. 6 Comparison of the steady-state and transient quenching data for water at 100°C

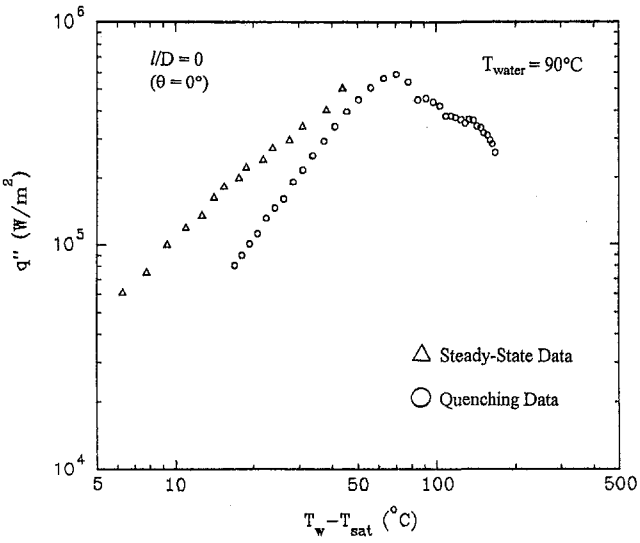

Fig. 7 Comparison of the steady-state and transient quenching data for water at 90°C

MW/m^2 for subcooled boiling with 10°C of subcooling. For both saturated and subcooled boiling, the steady-state data were always higher than the corresponding transient quenching data in the nucleate boiling regime. However, the two sets of data tended to merge together as the critical heat flux limit was reached. The same trend was observed in the outer segment (not shown in the text due to space limitation) where the critical heat flux was found to be higher than the value at the bottom center.

The present results are consistent with the findings of Bergles and Thompson (1970) and Verez and Florschuetz (1971) who compared in depth the steady-state method and the transient quenching method in predicting the nucleate boiling curve. Both found that the transient quenching method always underpredicted the results obtained through the steady-state method. The differences between the two sets of data depicted in Figs. 6 and 7 are due to relatively small quench period beyond the critical heat flux in the nucleate boiling regime toward the end of the quenching process observed by Haddad et al. (1995).

Effect of Subcooling on the Behavior of the Two-Phase Boundary Layer. Steady-state pool boiling experiments were conducted at two subcooling levels and three heat flux levels of 0.01, 0.09, and 0.30 MW/m^2 corresponding to a low, intermediate, and high power level, respectively. When the heat flux was low and the water was subcooled at 90°C, the outer surface of the vessel was covered with a large number of very small isolated water bubbles. When the water was saturated at the same heat flux level, the bubble size increased drastically while the bubble frequency decreased. The boiling process started by the heating of the liquid in contact with the surface of the vessel. When the required local level of superheat was attained, the nucleation site became active and a very tiny bubble could be observed on the heating surface. Then, the vapor mass grew larger and larger as more liquid was evaporating at the surface. Finally, the bubble detached from the surface when it reached a certain critical size (on the order of 5 to 10 mm) and the whole process was repeated again.

At the intermediate heat flux level, it was also possible to distinguish the four stages of the bubble formation process through direct observation of the two-phase boundary layer. The bubble frequency for the saturated and the subcooled boiling was higher in this case than in the case of the low heat flux level. In the subcooled boiling case, the surface was still covered by a large number of isolated bubbles that did not interfere with each other. On the other hand, some local bubble coalescence started to occur in the saturated boiling case.

The high heat flux case shown in Fig. 8 was characterized by a very different vapor dynamic than in the cases of low and intermediate heat flux levels. In the case of saturated boiling, it was not possible to distinguish the various stages of the bubble formation process through direct observation of the boiling phenomenon. This was due to the very fast bubble activity at this heat flux level. It appeared as if the bottom center region of the hemisphere was covered by one large vapor mass. In this case, it was not possible to discover, by direct visual observation, the bubble coalescence that led to the formation of the large vapor mass. It was only possible to observe the bubble coalescence process when the boiling phenomenon was observed in slow motion using the video system.

These observations revealed that the boiling process in the bottom center region was cyclic in nature with four distinct phases. First there was the phase of direct contact between the liquid and the solid during which water from the liquid pool was heated next to the heating surface. When the liquid superheat reached a critical value, bubble nucleation and growth started at various locations on the heating surface. At a certain point, the bubbles started to coalesce and formed a large vapor mass that covered the entire heating surface. This large bubble was ejected from underneath the hemisphere when it reached the critical size (on the order of 40 to 60 mm). Away from the bottom center, the ejected large vapor mass formed a ring, as shown very clearly in Fig. 8(*b*). As it traveled toward the upper edge of the vessel, the ring was broken into vapor slugs due to the diverging area of the vessel.

These four phases of the boiling process and the cyclic nature of the evaporation around the bottom center of the vessel were also reported by Chu et al. (1994) for a small heating surface with a large radius of curvature. Chu et al. (1995) also reported the same boiling characteristics for a large torispherical downward-facing surface that was used for a full-scale simulation of a reactor lower head. In the present study, the video system was used to observe the characteristics of the interface between the spherical heating surface and the large vapor mass in the bottom center. It was revealed that individual nucleation sites were feeding the envelope of the large vapor mass. This is also consistent with the observations of Chu et al. (1995), Gaertner (1965), and Katto and Haramura (1983). Therefore, it seems that the size of the heating surface does not influence the nature of the vapor dynamics for pool boiling on a downward-facing curved surface.

The photographic records of Fig. 9 were taken with the heaters of the inner segment of the hemisphere turned off and the heaters of the outer segment were still delivering a heat flux of 0.3 MW/m^2. The subcooled boiling case, Fig. 9(*a*), was characterized by isolated bubbles with the absence of any coalescence. This confirmed the fact that bubble coalescence in the subcooled boiling case of Fig. 8(*a*) was a local phenomenon limited to the region very close to the bottom center of the vessel. On the other hand, the bubbles formed on the outer segment in the saturated boiling case exhibited a high level of coalescence, as shown in Fig. 9(*b*). Therefore, the bubble coalescence of Fig. 8(*b*), when the two segments were heated, was not limited to a certain region of the hemisphere but rather a characteristics of boiling everywhere on the heating surface.

Variation of the Vapor Size Along the Vessel Outer Surface. A growing vapor mass stays attached to the surface as long as the surface tension force remains larger than the forces that tend to pull the vapor mass away from the heating surface. These latter forces include buoyancy, drag, lift, and/or inertia forces associated with the motion of the bulk fluid. In the case of pool boiling on the outer surface of a downward-facing hemispherical vessel, only the component of the buoyancy force tangential to the vessel outer surface will aid in the release of

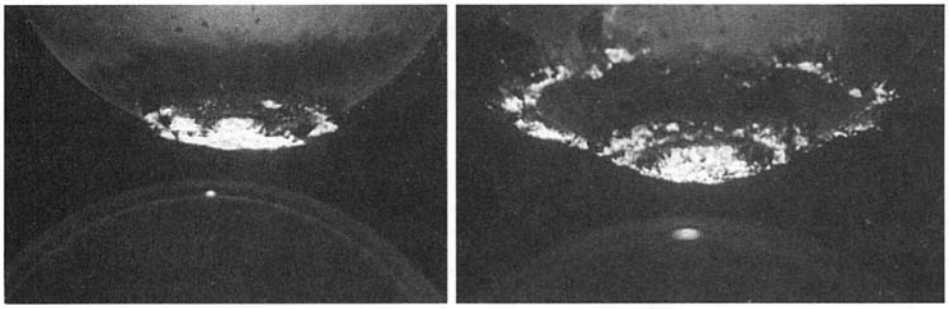

(*a*) Water temperature = 90°C (*b*) Water temperature = 100°C

Fig. 8 Nucleate boiling in the bottom center region of the vessel at a high heat flux level

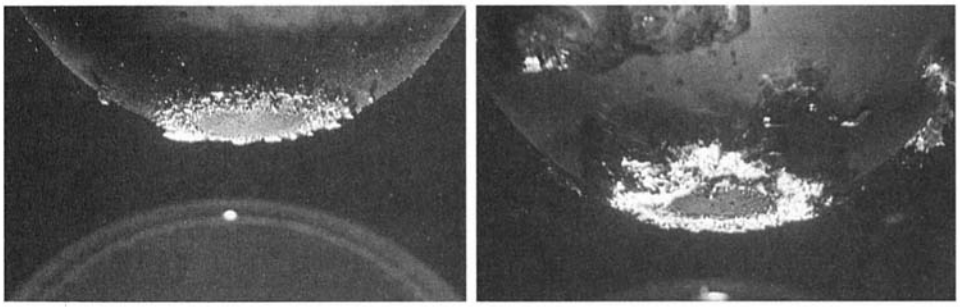

(*a*) Water temperature = 90°C (*b*) Water temperature = 100°C

Fig. 9 Nucleate boiling in the bottom center region of the vessel with heating of the outer segment only

the vapor mass. This component is the highest near the upper edge of the vessel and the lowest near the bottom center of the hemisphere. At exactly the bottom center of the vessel, buoyancy does not have any component along the tangent to the vessel surface and it will act solely to keep the vapor mass attached to the hemisphere. In addition, the two-phase boundary layer flow rate is very small near the bottom center and it increases toward the upper edge of the vessel. As a result, the drag and the inertia forces associated with the two-phase flow increase toward the upper edge of the hemisphere. Thus, both the buoyancy force and the forces associated with the two-phase flow increase toward the upper edge of the hemisphere. This explains the fact that the vapor masses in the bottom center region were large, flattened, and elongated, whereas those near the upper edge were relatively small and spherical.

The decrease in the vapor size, away from the bottom center of a downward facing curved surface, provides an explanation for the increase in the critical heat flux from the bottom center toward the upper edge of a curved downward facing surface. This increase in the CHF was observed by Cheung et al. (1994), Theofaneous et al. (1994), and Haddad et al. (1995). When the size of the bubbles is large, coalescence will occur at a lower heat flux. Therefore, vapor blanketing of the heating surface will occur at lower heat flux levels. It is very well known that the occurrence of the CHF is linked to vapor blanketing of the heating surface. As a result, the decrease in the vapor size from the bottom center toward the upper edge of the vessel is responsible for the associated increase in CHF reported in the literature. It should be noted that the vapor masses are considerably smaller at higher levels of subcooling, leading to appreciably higher CHF limits.

Conclusions

1 Subcooling has very little effect on the nucleate boiling curve on the outer surface of the hemispherical test vessel in the high-heat-flux regime where latent heat transfer dominates. On the other hand, in the low-heat-flux regime where sensible heat transfer is important, subcooling has a strong effect on nucleate boiling.

2 In the high-heat-flux regime, boiling around the bottom center region of the vessel becomes cyclic in nature. The boiling cycle consists of liquid heating, bubble nucleation and growth, bubble coalescence, and ejection of large vapor masses from underneath the heating surface.

3 With the outer surface being heated uniformly, the size of the vapor masses always decreases from the bottom center toward the upper edge of the vessel. This is due to the increase in the tangential component of the buoyancy force and the influence of the two-phase boundary layer flow in the downstream locations. This explains the increase in the CHF from the bottom toward the upper edge of the vessel that has been reported in the literature.

4 The observations of the boiling phenomenon reported in this study for a small test vessel agree very well with the observations reported by Chu et al. (1995) for a full-scale simulation of a reactor lower head. The vessel size does not seem to affect the nature of the bubble dynamics for pool boiling on a downward-facing curved heating surface.

Acknowledgments

This work was sponsored by the U.S. Nuclear Regulatory Commission under contract No. NRC-04-93-061.

References

Bergles, A. E., and Thompson, W. G., 1970, "The Relationship of Quench Data to Steady State Pool Boiling Data," *Int. J. Heat Mass Transfer,* Vol. 13, pp. 58–68.

Cheung, F. B., Haddad, K., Chamra, L., Otero, F., and Brundage, A, 1994, "Boundary Layer Boiling on the External Bottom Surface of a Hemispherical Vessel," ANS Winter Meeting, *10th Proc. of Nuclear Thermal Hydraulics,* pp. 155–162.

Chu, T. Y., Brainbridge, B. L., Bentz, J. H., and Simpson, R. B., 1994, "Observations of Quenching Downward Facing Surfaces," Sandia Report No. SAND93-0688.

Chu, T. Y., Bentz, J. H., and Simpson, R. B., 1995, "Observation of the Boiling Process From a Large Downward-Facing Torispherical Surface," *Proc. 30th National Heat Transfer Conference.*

Dix, D., and Orozco, J., 1990, "An Experimental Study in Nucleate Boiling Heat Transfer From a Sphere," ASME JOURNAL OF HEAT TRANSFER, Vol. 112, pp. 258–263.

Flynn, T. M., Draper, J. W., and Roos, J. J., 1961, "The Nucleate and Film Boiling Curve of Liquid Nitrogen at One Atmosphere," *Adv. Cryogenic Eng.,* Vol. 7, pp. 537–545.

Gaertner, R. F., 1965, "Photographic Study of Nucleate Pool Boiling on a Horizontal Surface," ASME JOURNAL OF HEAT TRANSFER, Vol. 87, pp. 17–29.

Haddad, H. K., Cheung, F. B., and Liu, Y. C., 1995, "Spatial Variation of the Critical Heat Flux on a Downward Facing Hemispherical Surface," *Proc. 30th National Heat Transfer Conference,* Vol. 14, pp. 23–32.

Haselden, G. G., and Peters, J. I., 1949, "Heat Transfer to Boiling Liquid Oxygen and Liquid Nitrogen," *Trans. of the Institution of Chemical Engineers,* Vol. 27, pp. 201–208.

Hwalek, J. J., 1982, "The Quenching Method of Determining Boiling Curves on Spheres," Ph.D Thesis, Department of Chemical Engineering, University of Illinois, Urbana, IL.

Katto, Y., and Haramura, Y., 1983, "Critical Heat Flux on a Uniformly Heated Horizontal Cylinder in an Upward Cross Flow of Saturated Liquid," *Int. J. Heat Mass Transfer,* Vol. 26, No. 8, pp. 1199–1205.

Lance, R. P., and Myers, J. E., 1958, "Local Boiling Coefficient on a Horizontal Tube," *AIChE J.,* Vol. 4, No. 1, pp. 75–80.

Liu, Y. C., 1995, "Inverse Heat Conduction in a Segmented Hemispherical Vessel With Downward Facing Boiling Boundary Conditions," M.S. Thesis, The Pennsylvania State University, University Park, PA.

Rhea, L. G., and Nevins, R. G., 1968, "Nucleate Boiling Heat Transfer From an Oscillating Sphere in Liquid Nitrogen," *Adv. Cryogenic Eng.,* Vol. 14, pp. 178–184.

Subramanian, S., and Witte, L. C., 1987, "Quenching of a Hollow Sphere," ASME JOURNAL OF HEAT TRANSFER, Vol. 109, pp. 262–264.

Theofaneous, T. G., Syri, S., Salmassi, T., Kymäläinen, O., and Tuomisto, H., 1994, "Critical Heat Flux Through Curved, Downward Facing, Thick Walls," *Nuclear Engineering and Design,* Vol. 151, pp. 247–258.

Thibault, J., and Hoffman, T. W., 1978, "Local Boiling Heat Flux Density Around a Horizontal Cylinder Under Saturated and Subcooled Conditions," *Proc. Sixth Int. Heat Transfer Conf.,* Toronto, Vol. 1, pp. 199–204.

Verez, D. R., and Florschuetz, L. W., 1971, "A Comparison of Transient and Steady-State Pool-Boiling Data Obtained Using the Same Heating Surface," ASME JOURNAL OF HEAT TRANSFER, Vol. 93, pp. 229–232.

Competing Effects of Dielectrophoresis and Buoyancy on Nucleate Boiling and an Analogy With Variable Gravity Boiling Results

T. J. Snyder
Color Printing and Imaging Division,
Tektronix, Inc.,
Wilsonville, OR

J. N. Chung
School of Mechanical
and Materials Engineering,
Washington State University,
P. O. Box 642920
Pullman, WA 99164-2920

J. B. Schneider
School of Electrical Engineering
and Computer Science,
Washington State University,
Pullman, WA

An experiment was performed that produced a controlled electrical body force (dielectrophoretic force or DEP force) over the length of a horizontal platinum wire heater during boiling. The DEP force was generated such that it either aided or opposed terrestrial gravity or acted nearly alone in microgravity. The net effect can be thought of as simply either "reducing" or "increasing" buoyancy. To account for this change in force an "effective gravity ratio" $g'_{(b,e)}$ was defined that represents the ratio of the total DEP and buoyancy body forces to the constant terrestrial-gravity buoyancy force. Based on our own experimentation and on the published literature, it was argued that the nucleate boiling will be enhanced if the effective gravity acts to hold the vapor bubbles near the heater surface, while at the same time permitting access of the liquid to the surface in order to prevent dryout. However, a large electroconvection effect can dominate and reverse the trend. The nonboiling portion of the heat transfer coefficient was shown to be significant with an applied electric field, especially at high subcoolings. It was found that for $1 < g'_{(b,e)} < 3$ a quarter power dependence appears to be a reasonable engineering approximation for the increase in critical heat flux with effective gravity.

Background

Numerous investigators have shown that the presence of an electric field appreciably modifies the boiling heat transfer process. The electrohydrodynamic (EHD) effects on convective heat transfer, nucleate, transition, and film boiling along with condensation heat transfer were reviewed by Jones (1978). This review showed that most of the earliest work supports the conclusion that the electric field has practically no effect on the heat transfer coefficient in nucleate boiling; however, it increases the critical heat flux (CHF) significantly. In a more recent review, Di Marco and Grassi (1993) reported that the electric field enhances the heat exchange in the nucleate boiling region for both smooth and finned surfaces. Geppert et al. (1995) presents a short overview of recent, selected EHD-enhanced boiling studies on different horizontal tube and flat plate configurations. They conclude that the results are not consistent due to many reasons that include the following: the use of different working fluids, the control of impurities, the evaporator size differences, inaccuracies in thermocouple mounting, the difference between single-tube and bundled-tube tests, and the method of evaporator heating (electrical or water flow). Therefore, when comparing all the references, it became clear that the results are not unified because the conclusions are based on data for very drastically different experiments. The conclusions are not based on generalizations specific to the effect of the electric field on the generally accepted boiling heat transfer mechanisms, i.e., the boiling bubble dynamics and the nonboiling convection effects. Therefore, many of the preceding conclusions are not generalizations but merely results specific to the experiment to which they were performed. In this paper, we attempt to form more general conclusions about EHD-enhanced boiling that are independent or that can be formulated as a function of the system parameters, i.e., different boiling regimes, electrode/heater couplings, fluid properties, and orientation with respect to gravity.

Theory

The EHD force that is produced by an electric field acting on a unit volume element of fluid has no unique formulation. One generally accepted expression is (Stratton, 1941)

$$\mathbf{F}^e = \rho_f \mathbf{E} - 0.5|\mathbf{E}|^2\nabla\epsilon - \nabla\left(0.5\rho\left(\frac{\partial\epsilon}{\partial\rho}\right)|\mathbf{E}|^2\right), \quad (1)$$

where $\mathbf{F}^e$ is the force per unit volume, ρ_f is the free charge density, $\mathbf{E}$ is the electric field, ϵ is the dielectric permittivity of the fluid, and ρ is the density. The first term is the force per unit volume on a medium containing free electric charge of density ρ_f and is small in an insulating dielectric fluid. The direction of this force depends on the polarities of the free charge and the direction of the electric field. The second term describes the force exerted on a fluid due to spatial gradients in the permittivity, and it can dominate for very strong and highly diverging electric fields, such as those used in this paper. The third term in Eq. (1) describes effects associated with the deformation of the fluid (electrostriction) and is important when considering application of a nonuniform electric field to a compressible fluid. Since the compressibility of a liquid is small, the electrostriction effect has no practical influence on hydrodynamics for an incompressible flow (Jones, 1978; Di Marco and Grassi, 1993). In general, this equation shows that the electric field can produce forces on both the liquid and vapor in a two-phase boiling system. Also, because of these forces, the

Contributed by the Heat Transfer Division for publication in the JOURNAL OF HEAT TRANSFER and presented at IMECE 96. Manuscript received by the Heat Transfer Division January 21, 1997; revision received October 8, 1997; Keywords: Boiling; Microgravity Heat Transfer; Phase-Change Phenomena. Associate Technical Editor: R. A. Nelson, Jr.

application of an electric field has two strong mechanisms which can change the heat transfer in the nucleate boiling regime. The first is the effect of the electrical body force on the generated vapor bubbles (the interfacial EHD effect), and the second is the effect of the electrical forces on the liquid (the electroconvection effect).

The DEP force is a polarization force. Under the influence of an electric field, a neutral body (dispersed-phase component) will become polarized due to the difference in permittivity. If the field over the surface of the neutral body is unequal, then the polarized neutral body will experience a net force due to the imbalance in Coulomb forces. This is the basis for the DEP force shown in the second term in Eq. (1). Since ϵ is not differentiable at a liquid-vapor interface, it is appropriate to directly formulate the dielectrophoretic force acting on a spherical vapor bubble or liquid droplet in a two-phase mixture. The resulting DEP force for a vapor bubble, given by Pohl (1978) and Jones and Bliss (1976), is

$$\mathbf{F}_{\text{dep}} = 2\pi R^3 \epsilon_o \epsilon_l \left(\frac{\epsilon_v - \epsilon_l}{\epsilon_v + 2\epsilon_l} \right) \nabla(|\mathbf{E}|^2), \tag{2}$$

where R is the radius of the bubble and ϵ_l and ϵ_v are the relative permittivity of the liquid and vapor, respectively. The direction of this force is such that the medium with relatively smaller permittivity will be driven away from regions of high electric field towards regions of low electric field. Equation (2) assumes that the dielectric is isotropically, linearly, and homogeneously polarizable. The neutral body (liquid droplet or vapor bubble) is assumed to be spherical, and both the dispersed phase and continuous phase are assumed to be "perfect" dielectrics with finite dielectric constants and zero conductivity. Finally, the neutral body is assumed to be a "small sphere" so that the amount of polarization can be obtained by approximating the local field as uniform; however, the field is nonuniform enough to produce appreciably different forces on the positive and negative portions of the induced polarization charges. While it is questionable how well these assumptions were maintained in the boiling experiments due to the amount and size of bubbles, the results found are consistent with the theory.

To account for the relative magnitude of the DEP force to the buoyancy force, a dimensionless parameter named G_{be} has been used in the past (Di Marco and Grassi, 1993) and is defined as

$$G_{be} = \frac{|F_{\text{DEP}}|}{|F_b|} = \frac{3}{2} \frac{(\epsilon_l - \epsilon_n)\epsilon_o \epsilon_l \nabla |\mathbf{E}|^2}{(\epsilon_v + 2\epsilon_l)(\rho_l - \rho_v) g}. \tag{3}$$

However, for the case when gravity decreases to near zero (microgravity), this equation is singular. Also, this equation does not represent the total DEP and buoyancy forces at the heater surface and only provides a ratio of forces, which does not adequately determine the resulting bubble dynamics. A new dimensionless parameter was formulated and used in this study called the "DEP and buoyancy effective gravity ratio" or simply the "effective gravity ratio" and is defined as

$$g'_{(b,e)} = (b + e); \quad b = \frac{\mathbf{F}_b \cdot \hat{n}}{|\mathbf{F}_b^*|} \quad \text{and} \quad e = \frac{\mathbf{F}_e \cdot \hat{n}}{|\mathbf{F}_b^*|}, \tag{4}$$

where $\mathbf{F}_b$ is the actual buoyancy force as defined with the gravity level encountered in the test conditions, $\mathbf{F}_e$ is given by Eq. (2) for the DEP force, and $\mathbf{F}_b^*$ is the constant buoyancy force based on terrestrial-gravity conditions; $\hat{n}$ is a unit vector in the direction of terrestrial buoyancy. Substituting Eq. (2) for the DEP force and using the definition of the buoyancy force, the effective gravity ratio can be written as

$$g'_{(b,e)} = \frac{\left(g(\rho_l - \rho_v)\hat{n} + \frac{3}{2} \frac{\epsilon_o \epsilon_l (\epsilon_l - \epsilon_v)}{(\epsilon_v + 2\epsilon_l)} \nabla |\mathbf{E}|^2 \right) \cdot \hat{n}}{|g^*(\rho_l - \rho_v)\hat{n}|} = \frac{g_{\text{eff}}}{g^*}; \tag{5a}$$

$$b = \frac{g(\rho_l - \rho_v)}{|g^*(\rho_l - \rho_v)\hat{n}|} \quad \text{and}$$

$$e = \frac{\left(\frac{3}{2} \frac{\epsilon_o \epsilon_l (\epsilon_l - \epsilon_v)}{(\epsilon_v + 2\epsilon_l)} \nabla |\mathbf{E}|^2 \right) \cdot \hat{n}}{|g^*(\rho_l - \rho_v)\hat{n}|}. \tag{5b}$$

This dimensionless number represents a ratio of the sum of both DEP and buoyancy body forces (on the vapor phase) to the constant terrestrial-gravity buoyancy force in the direction of $\hat{n}$, and g_{eff} represents the effective gravity. Note that $g'_{(b,e)}$ could be negative if the effective gravity is opposed to terrestrial gravity. Also, by defining the parameters b and e in this way, one can immediately understand the relative contributions of the individual forces. For example, $g'_{(b=0,e=0)} = 0$ corresponds to no electric field and zero-gravity conditions, while $g'_{(b=1,e=-1)} = 0$ corresponds to terrestrial gravity with an imposed dielectrophoretic force of equal magnitude but opposite direction. When considering the interfacial EHD effect alone, this definition provides an effective way to compare variable-gravity boiling results with electric field boiling results because both change the total body force. The normalization with earth gravity provides a baseline for comparison, as nearly all boiling results are based on this level.

The basis for this experiment was to produce boiling curves using an electric-field distribution, which allowed a controllable and nearly constant DEP force to exist over the entire length of the heater wire. Also, the DEP force was produced normal to the buoyancy force so that the effective gravity could be

Nomenclature

A = heater surface area
a = acceleration
$b = \mathbf{F}_b/\mathbf{F}_b^*$
$e = \mathbf{F}_e/\mathbf{F}_b^*$
$\mathbf{E}$ = electric field
$\mathbf{F}_b$ = variable gravity buoyancy force
$\mathbf{F}_b^*$ = terrestrial-gravity buoyancy force
$\mathbf{F}_e$ = dielectrophoretic force
$\mathbf{F}_{\text{DEP}}$ = dielectrophoretic force
$\mathbf{F}^e$ = electrohydrodynamic force per unit volume
g = variable gravity
g^* = terrestrial gravity
$g'_{(b,e)}$ = effective gravity ratio, refer to Eq. (5)
g_{eff} = effective gravity (buoyancy + dielectrophoretic forces)
G_{be} = ratio of F_{DEP} to F_b
h = heat transfer coefficient
h_{fg} = latent heat of vaporization
I_H = current through heater
$\hat{n}$ = unit vector in the direction of terrestrial buoyancy
Q = heat flux
Q_c = critical heat flux
R = bubble radius
R_s = shunt resistance
T = temperature
V_A = voltage measured at current tap
V_H = voltage across heater
V_{HV} = high voltage
ϵ = relative permittivity
ρ_f = free charge density
ρ = density
σ_s = surface tension

Subscripts

l = liquid
o = free space
sat = saturated
sub = subcooling

calculated from simply the scalar sum of the two forces. Also, the experiment was designed to control the DEP force with the electrode geometry instead of the applied voltage so that different effective gravities could be produced with the same electrode voltage. Boiling curves were generated with different DEP forces, either aiding or opposing gravity and in a microgravity environment. Therefore, the net effect was designed to either "reduce" or "increase" buoyancy.

In order to form an analogy with variable gravity boiling, it must first be decided what to expect, in terms of heat transfer, when the gravitational field is changed. Recent experimental results have shown that lowering gravity increases heat transfer, and increasing gravity decreases the heat transfer (Merte, 1990). For a number of fluids and test parameters Merte (1990) showed that an increased buoyancy force reduces the extent of superheated liquid in the vicinity of the heat transfer surface, reducing the number of nucleation sites, and also reducing the microlayer area and/or increases its thickness. The relative contribution of nonboiling convection increases with gravity and can reverse this trend at the lower levels of heat flux. Conversely, for body forces below 1 g, buoyancy keeps the heated fluid adjacent to the heating surface, increases the nucleation site area, and keeps the growing vapor bubbles closer to the heating surface, increasing the microlayer area and/or decreasing its thickness (Merte, 1990). There have been numerous other articles that attribute microlayer evaporation to increased heat transfer when the bubbles remain near the heater surface. Bankoff (1959) showed that the latent heat transport (condensation at the cap of the bubble and evaporation from the surrounding microlayer) are the key transport mechanisms for subcooled boiling. Kirk et al. (1992) varied the orientation of the heater for low velocity flow boiling tests and found that enhancement of heat transfer may be attributed not to increased agitation effects, but rather to the evaporation of the thin superheated liquid film. A similar result was given by Nishikawa and Fujita (1990), which attributed the same orientation effect in pool boiling. Computations demonstrated that the effect on heat transfer from variable orientations can be due to the influence of the latent heat transport, which was shown to account for nearly 80 percent of the heat transfer in some cases. Cornwell and Schuller (1982) recorded increased heat transfer rates at the upper tubes of bundles in a horizontal reboiler, and attributed the increase to the sliding of bubbles and the formation of a microlayer under the bubbles. For boiling around the periphery of a tube, Cornwell and Einarsson (1983) found the highest boiling heat transfer rates underneath the tube where the bubbles were pushed back against the heater surface by buoyancy. Many other investigators have reported increased heat transfer rates for inverted surfaces under earth's gravity for low heat fluxes (Jung et al., 1987; Chen, 1978; Tong et al., 1988). These effects have been said to decrease the thickness of the microlayer and increase nucleation site density.

Experimental Apparatus, Test Matrix, and Uncertainties

Experimental Apparatus. A 1.91 cm platinum wire 0.025 cm in diameter with a resistance of approximately 0.05 Ω was used as the heater. The heat flux was calculated from the power given to the heater and the heater area. The temperature in the heater was measured using the standard resistometry technique. For the purpose of this study, an electrode geometry was sought that could provide a uniform DEP force along the entire platinum heater wire, could provide good visualization, and, in order to vary $g'_{(b,e)}$, could produce DEP forces equal to two times the terrestrial buoyancy force. Two finite-sized square plates (2.54 cm × 2.54 cm) separated by an angle of 13 deg were used. The plates were mounted to a Lexan base and were supported by a Plexiglas structure. A 600 Å gold film was plated on the surface of the plates and was utilized as conducting surfaces. Also, two separate electrode spacings were used so that a 23 kV potential corresponded to both a 1 g and a 2 g DEP force, thus eliminating the voltage as a variable. In order to control whether the DEP force aided or opposed buoyancy, the direction of the buoyancy force was changed relative to the electrodes. Laplace's equation was solved using the moment method for the finite electrodes in order to find the DEP force. The platinum heater wire was positioned along the equipotenential line at zero potential located at the midplane of the two electrodes. This eliminated nearly all of the coupling effects between the wire

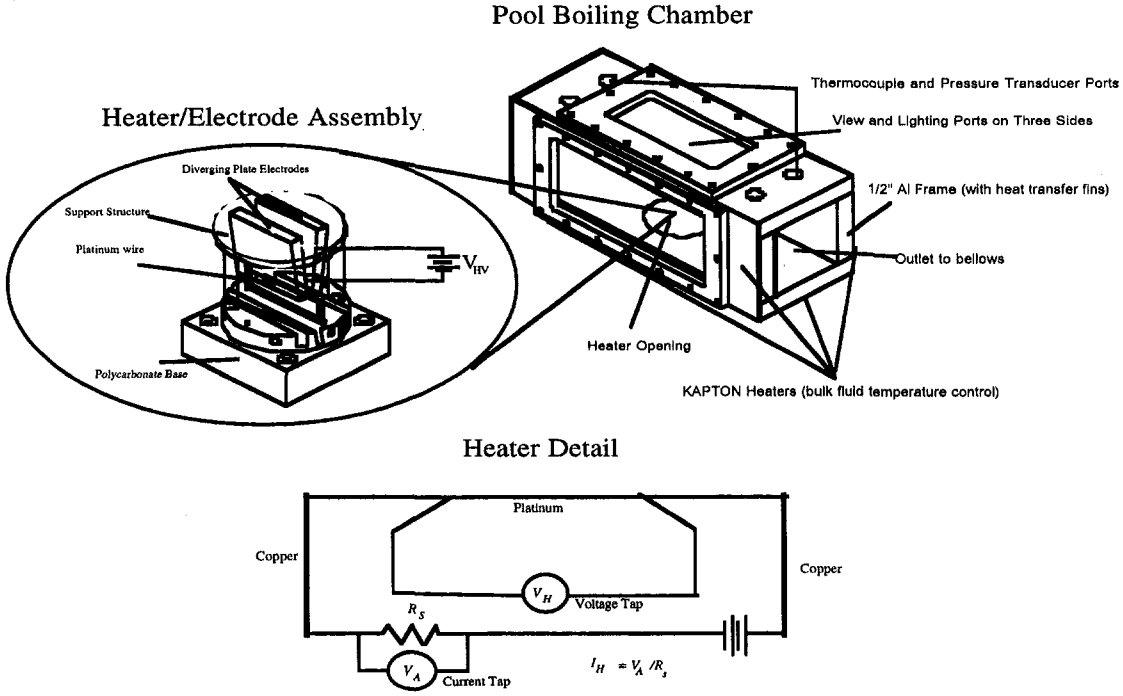

Fig. 1 Experimental apparatus

and the electric field. Refer to Fig. 1 for an overall schematic of the apparatus and to Snyder (1995) for further details.

Composite video (30 Hz) was used for visualization, and FC-72 was used as the working fluid. The permittivity of FC-72 is 1.76 and 1.01 for the liquid and vapor phases, respectively. The other thermophysical properties were taken from a temperature-dependent thermophysical properties chart (3M Product Manual). Degassing was performed prior to each experiment by boiling through a reflux condenser according to the 3M product manual recommendations. In order to bring the buoyancy force to nearly zero and measure the effects from a variable DEP force only, a drop tower was used. The drop tower utilized a drag shield and provided 2.1 s of microgravity. The microgravity level achieved in the drop tower testing was measured to be approximately 10^{-4} g. Complete details can be found in Snyder et al. (1995).

Test Matrix. For this study, saturated conditions and one subcooling (15°C) were employed. The uncertainty in subcooling was ±2°C. For simplicity, these will be referred to as saturated, or $\Delta T_{sub} \cong 0$°C, and subcooled, or $\Delta T_{sub} \cong 15$°C, respectively. The following two tables contain a listing of the effective gravity test matrix used in this study.

Performed under terrestrial-gravity conditions

$g'(b = 1, e = -2) = -1$	$1g$ buoyancy, $2g$ DEP opposing buoyancy.
$g'(b = 1, e = -1) = 0$	$1g$ buoyancy, $1g$ DEP opposing buoyancy.
$g'(b = 1, e = 0) = 1$	$1g$ buoyancy, $0g$ DEP—terrestrial-gravity boiling.
$g'(b = 1, e = 1) = 2$	$1g$ buoyancy, $1g$ DEP aiding buoyancy.
$g'(b = 1, e = 2) = 3$	$1g$ buoyancy, $2g$ DEP aiding buoyancy.

Performed under microgravity conditions

$g'(b = 0, e = 0) = 0$	$0g$ buoyancy, $0g$ DEP—Microgravity boiling.
$g'(b = 0, e = -1) = -1$	$0g$ buoyancy, $1g$ DEP opposing buoyancy*.
$g'(b = 0, e = -0.5) = -0.5$	$0g$ buoyancy, $0.5g$ DEP opposing buoyancy*.
$g'(b = 0, e = -0.1) = -0.1$	$0g$ buoyancy, $0.1g$ DEP opposing buoyancy*.

* Opposing buoyancy means that the DEP force was against the terrestrial gravity force prior to the drop.

Uncertainties. The following are the uncertainties for the most significant quantities used in this paper:

Quantity	Uncertainty*
Heat Flux, Q	±5200 W/m^2
Surface Temperature, T_s	±2.148°C
High Voltage, V_{HV}	±0.25 kV
DEP Force, F_{DEP} or F_e	±0.25g

* The uncertainties were estimated based on equations given in Kline and McClintock (1953). Further details are provided in Snyder (1995).

Heat Transfer and Visualization Results

In terrestrial gravity, boiling curve measurements were performed for each effective gravity test (i.e., three at standard gravity, and three more with the electric field active). This was done to insure repeatability due to the fact that the changes in heat transfer were small, and, therefore, could be susceptible to the aging of the wire and other uncertainties. A single wire was used for all the tests. Less data was taken for the tests performed in microgravity. The entire test matrix consisted of approximately 800 individual data points. Figures 2 and 3 are the boiling curves for the saturated and subcooled conditions for $g'_{(b,e)} = -1$ to 3.

Convection Regime. Increases in heat transfer efficiency are seen by a shift in the boiling curve to the left, i.e., an increase in heat flux for a constant surface temperature. First, note that for $g'_{(b=1,e=-1)} = 0$ and $g'_{(b=1,e=1)} = 2$ and for $g'_{(b=1,e=-2)} = -1$ and $g'_{(b=1,e=2)} = 3$ the contribution from the electroconvection prior to the onset of nucleate boiling (ONB) is very similar. This is due to the electrode geometry and potential being the same for effective gravity ratios of 0 and 2, and −1 and 3. The only difference was the orientation of the electrode with respect to gravity, which did not significantly affect the convective heat transfer. Based on Figs. 2 and 3, it is apparent that the heat transfer in the convection regime increased with the addition of the electric field, however, it did not scale with $g'_{(b,e)}$. The DEP force for this study was calculated based on the interfacial force on a vapor bubble, and, therefore, it was not expected to scale as such. These increases in heat transfer are attributed to the disruption of the laminar layer and the production of turbulence. This turbulence acted to reduce the thermal laminar boundary layer thickness, and provided a thinner superheated region. For the purpose of this study, the heat transfer trends in the convection regime are mainly used in order to elucidate the effect on the heat transfer from the DEP force on the bubbles.

Nucleate Boiling Regime. The effects from the electric field were small in the boiling regime, but were repeatable. For $g'_{(b=1,e=-1)} = 0$ there was a significant reduction in the heat transfer efficiency and the critical heat flux for the saturated case. The combination of the balance in forces and the saturated conditions did not allow access of the liquid to the heater surface in order to prevent dryout. Similar conditions for the subcooled case showed an increase in heat transfer in the nucleate boiling regime, but a reduction in the CHF. The combination of the balance in forces and the subcooled conditions resulted in the bubbles remaining near the heater surface, but still allowed access of the liquid to the heater to prevent dryout until nearing the CHF. At this point, the balance in forces again resulted in a decrease in the CHF. Since there is boiling all around the periphery of the wire, the direction of the net body force should not influence the heat transfer. For saturated boiling, this was found to be the case, i.e., the difference in heat transfer between $g'_{(b=1,e=0)} = 1$ and $g'_{(b=1,e=2)} = -1$ was small. However, under the same effective gravity for the subcooled conditions, there was a noticeable increase in heat transfer efficiency. This was presumably due to the dominance of, and the increase in, electroconvection. The effect of the electroconvection on the boiling heat transfer can also be seen between the saturated and subcooled tests. The heat transfer efficiency was increased for the subcooled tests relative to the saturated tests.

In general, we conclude, and will continue to argue in this paper, that the boiling heat transfer coefficient can be considered as a summation of an effect from the bubble dynamics, which is a strong function of the effective gravity, plus an effect from the electroconvection. Therefore, the bulk of the differences in heat transfer in Figs. 2 and 3 can be explained by considering a combined effect from both the effective gravity and the electroconvection. Therefore, we propose that the overall heat transfer coefficient with an applied electric field consists of a nonboiling heat transfer coefficient due to electroconvection and a boiling heat transfer coefficient due to the bubble dynamics:

$$h_{total} = h_{electroconvection} + h_{bubble\ dynamics}. \quad (6)$$

Figure 4 shows the bubble dynamics for the different effective gravities at a single heat flux. For the saturated conditions when the effective gravity was zero, the bubbles grew to much larger sizes and remained near the heater wire for much longer times due to the net force at the heater wire being zero. For the case of $g'_{(b=1,e=-2)} = -1$, the bubble dynamics were similar to, but still different from, the case of $g'_{(b=1,e=0)} = 1$. The bubbles at the wire surface did move down against gravity, but only for

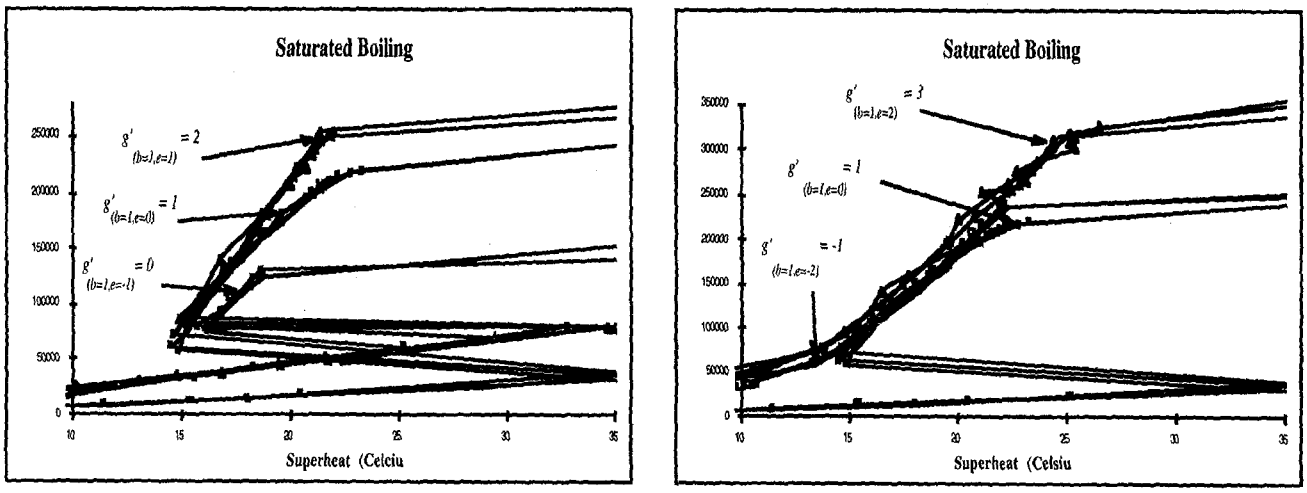

Fig. 2 Boiling curve ($\Delta T_{sub} \cong 0$) – $g'_{(b,e)} = -1$ to 3

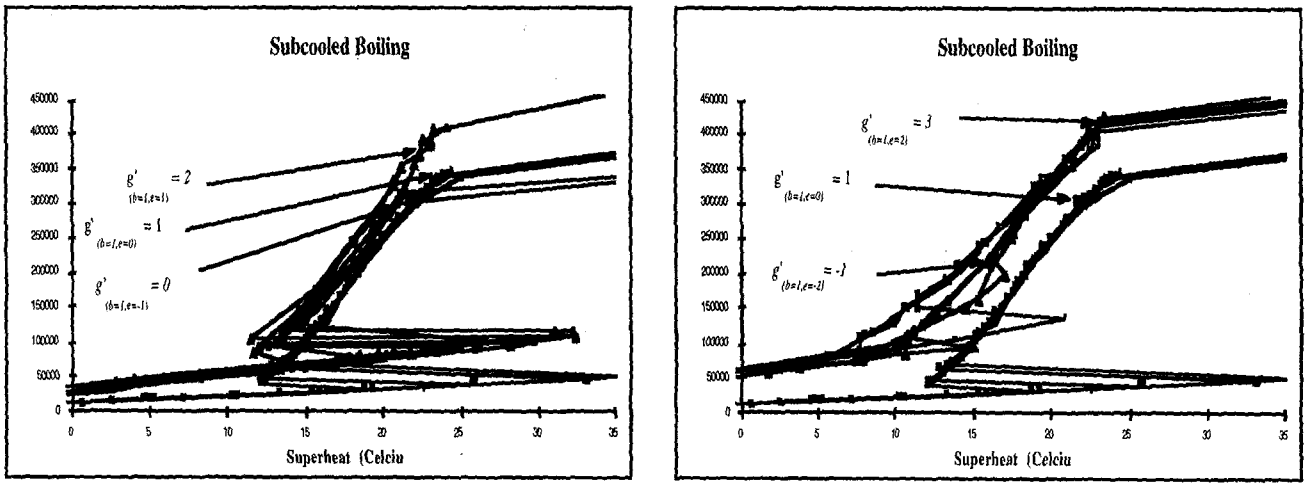

Fig. 3 Boiling curve ($\Delta T_{sub} \cong 15$) – $g'_{(b,e)} = -1$ to 3

a short distance; they then moved out, away from the electrode, and back up. This behavior was a result of the DEP force decreasing rather quickly away from the electrodes, while the gravity force remained constant. While not apparent from the pictures presented here, it was unquestionably determined that as the effective gravity increases, the bubble detachment diameter decreases. Please refer to Chap. 9 in Snyder (1995) for details.

Nucleate boiling results were also obtained in microgravity with the magnitude of the effective gravity due to the DEP force only. Figure 5 shows the bubble dynamics in microgravity with an effective gravity ratio of 0 to −1 ($b = 0$ and $e = 0$, −0.1, −0.5, and −1). Here, because of the difficulty in experimentation, the electric potential was varied to vary the DEP force. Note from the pictures that even for these short duration experiments the application of an effective gravity reverted film boiling ($b = 0$, $e = 0$) back to nucleate boiling ($b = 0$, $e = -1$) in a manner similar to the addition of a gravitational field. Three important results were found from the tests in microgravity. First, the bubble detachment diameters are very similar between $g'_{(b=1,e=0)} = 1$ and $g'_{(b=1,e=1)} = 1$. This can be seen by comparing the boiling picture in Fig. 4 at $g'_{(b=1,e=0)} = 1$ to the picture in Fig. 5 at $g'_{(b=1,e=1)} = 1$. These two pictures are shown in Fig. 6 with the microgravity picture inverted for easier comparison (there is no up or down in microgravity, and the orientation in Fig. 6 corresponded to the initial conditions of the test with respect to gravity). Second, the heat transfer for $g'_{(b=1,e=0)} = 1$ and $g'_{(b=1,e=1)} = 1$ are similar. This is shown in the boiling curve in Fig. 7; however, this would require much longer microgravity times to verify. Third, the CHF for $g'_{(b=1,e=-1)} = 0$ ($\sim$12.5 W/cm^2) was consistent with $g'_{(b=1,e=0)} = 0$ ($\sim$12.1 W/cm^2), at least for short-term microgravity. Much longer microgravity durations and more testing would be required for further verification. From these results it can be concluded that the effective gravity, either from buoyancy or dielectrophoresis, has a similar influence on the bubble dynamics. Therefore, it is reasonable to assume that sustained boiling in microgravity is possible with the application of an electric field. Also, because of the recorded bubble dynamic, the nucleate boiling heat transfer, and the CHF similarities with gravity-driven boiling, one could possibly use a known terrestrial gravity or variable-gravity heat transfer correlation for boiling in microgravity with an applied electric field by simply knowing the effective gravity over the heater surface.

Previously published results have shown increases in the CHF by a factor of up to four in an applied electric field with a heated wire (Jones, 1978). The reason that this was not found in this study is that the heater wire was decoupled with the high voltage electric field by placing it between the electrodes where the potential from the electric field nearly matched that of the wire. This was done to control the DEP force magnitude and direction in order to repeatably vary the effective gravity. To

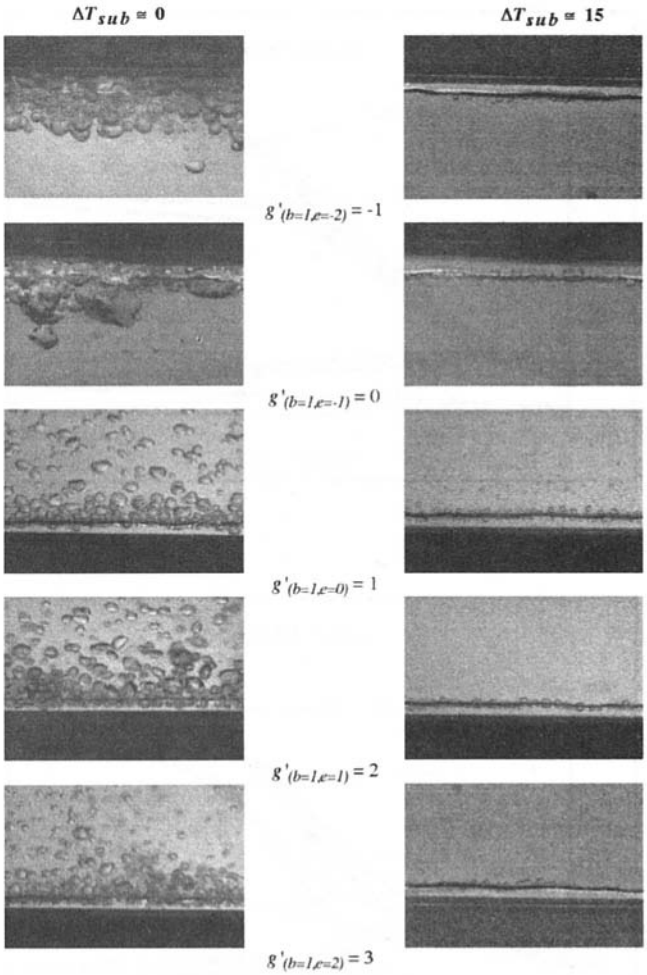

Fig. 4 Pool boiling, 12.1 × 10^4 W/m^2, $g'_{(b,e)}$ = −1 to 3

simulate some of the previous work with this experiment, boiling curves were performed with one of the electrodes disconnected. This resulted in much larger electric field gradients because of the coupling with the small radius of curvature wire. Figures 8(*a*) and 8(*b*) show the boiling curves for this electric field distribution with either the positive electrode active or the negative electrode active for the saturated and subcooled

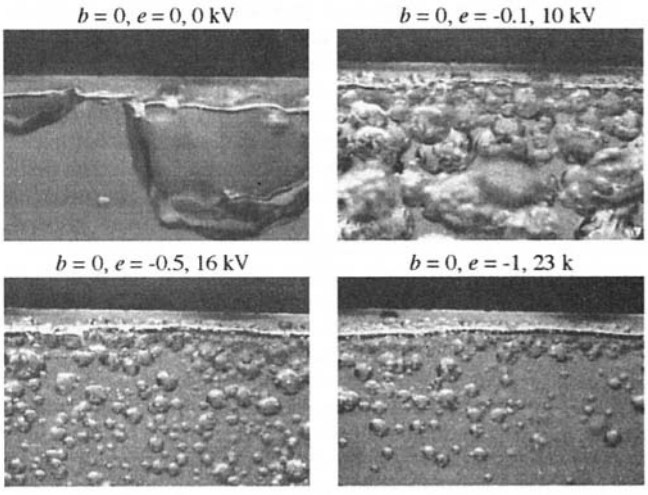

Fig. 5 Microgravity boiling (b = 0) with various DEP forces (e = −1, −0.5, −0.1, 0), Q'' = 12.1 × 10^4 W/m^2

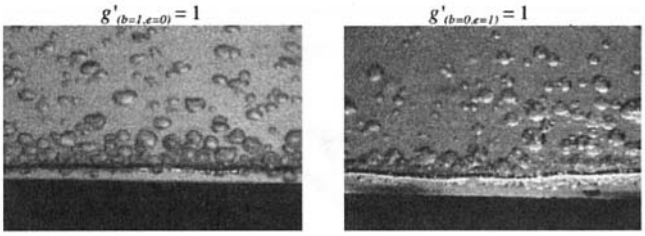

Fig. 6 Comparison of the bubble dynamics between terrestrial gravity with no DEP force and microgravity with an applied 1g DEP force, Q'' = 12.1 × 10^4 W/m^2

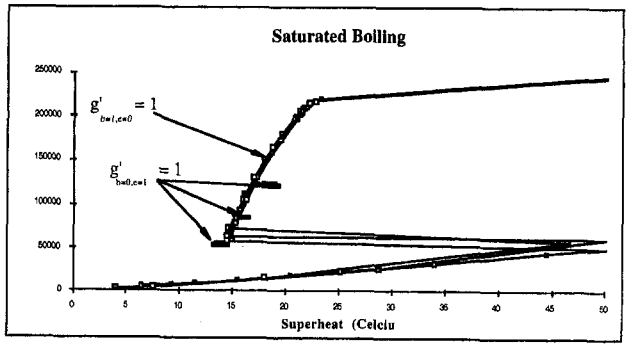

Fig. 7 Boiling curve ($\Delta T_{sub} \cong 0$) − $g'_{(b=1,e=0)}$ = 1 compared to $g'_{(b=0,e=)}$ = 1

conditions, respectively. These results show the normally large increase in CHF with applied voltage. Because of the very small radius of curvature of the wire, the DEP force on the vapor bubbles at the heater surface is extremely large and oriented

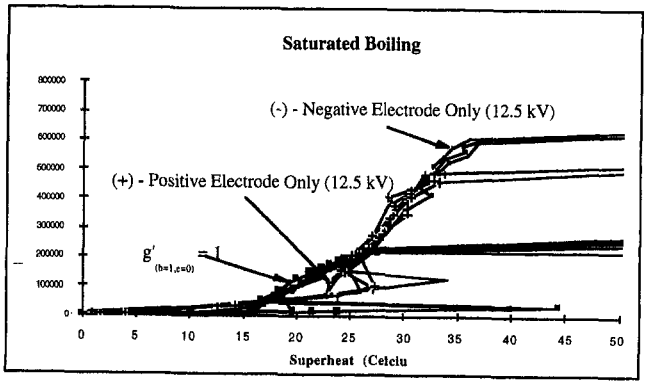

Fig. 8(*a*) Platinum wire boiling curve with electric field setup between the wire and either the positive or negative electrode ($\Delta T_{sub} \cong 0$)

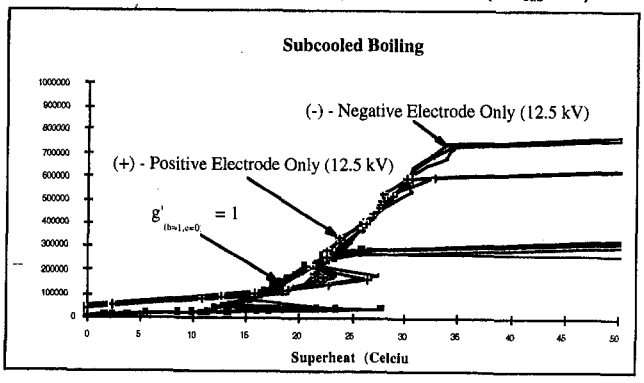

Fig. 8(*b*) Platinum wire boiling curve with electric field setup between the wire and either the positive or negative electrode ($\Delta T_{sub} \cong 15$)

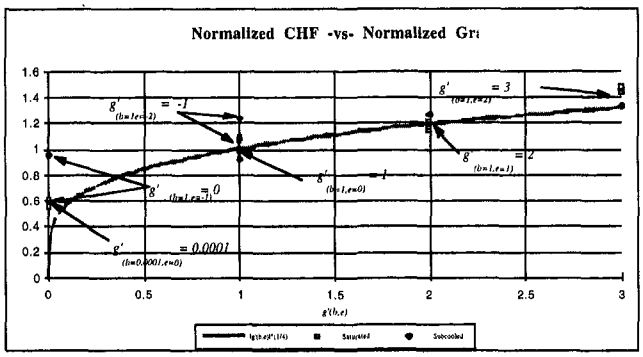

Fig. 9 Normalized CHF versus effective gravity ratio

radially out from the heater wire. The large DEP forces caused the bubbles to detach vigorously and emanated in a radial direction from a limited number of nucleation sites on the heater wire. The DEP force appeared to pump the vapor with a "jet-like" action. The bubble detachment diameters were very small. At the higher heat fluxes, the extremely large number of very small sized bubbles formed a "blanket" or "froth" of bubbles around the heater wire. Most importantly, note that the very strong DEP forces on the bubbles (which resulted in a very high effective gravity ratio) caused the heat transfer to decrease in the nucleate boiling regime. Also, the heat transfer for the subcooled tests was increased relative to the saturated tests. These are both consistent with the analogy being presented in this paper with variable gravity theory, i.e., that as the gravity or "effective gravity" increases, the heat transfer decreases; however, a large electroconvection effect can dominate and reverse the trend.

It is interesting to note that the transition to film boiling was much smoother when the wire served as an electrode. Instead of an abrupt and very large increase in superheat, say 200 to 300°C, the CHF was accompanied by approximately a 25 to 50°C increase in superheat. The large DEP forces produced by the applied electric field acted equally on the entrained liquid droplets in the vapor boundary layer and kept portions of the heater surface wetted. This phenomena changed the CHF process drastically and was recorded as an average increase in surface temperature instead of an instant dryout.

Critical Heat Flux. Many correlations have indicated that the critical heat flux depends on $g^{1/4}$ (Noyes, 1963; Zuber, 1959). The relation derived for pool boiling from a horizontal surface takes the following form (Zuber, 1959):

$$\frac{Q_c}{A} = \frac{\pi}{24} h_{fg} \rho_v \left[\frac{\sigma_s g^* g(\rho_l - \rho_v)}{\rho_v^2} \right]^{1/4} \left(\frac{\rho_l + \rho_v}{\rho_l} \right)^{1/2}. \quad (7)$$

This can be normalized with terrestrial-gravity conditions (Siegel, 1967) and written as

$$\frac{Q_c(g)}{Q_c(g^*)} = \left(\frac{g}{g^*} \right)^{1/4}, \quad (8)$$

where Q_c is the critical heat flux at terrestrial gravity (g^*) and variable gravity conditions (g), respectively. This assumes that the fluid properties are not significantly influenced by gravity reductions. An analogy can be formed by simply replacing the gravity field (g/g^*) in Eq. (8) with $g'_{(b,e)}$, the DEP and buoyancy effective gravity ratio, this yields

$$\frac{Q_c(g_{\text{eff}})}{Q_c(g^*)} = (|g'_{(b,e)}|)^{1/4}. \quad (9)$$

This assumes that the fluid properties are not significantly influenced by gravity reductions or the imposed electric field. Experimental CHF data from this investigation is given in Fig. 9 along with the theoretical dependence of Eq. (9). These results, which were previously used to correlate CHF data for variable gravity, can be used surprisingly well to correlate boiling results with an effective gravity produced from both buoyancy and DEP forces. However, note that $g'^{1/4}_{(b,e)}$ correlates the saturated boiling results much better than the subcooled results. This is because subcooled boiling has a much stronger dependence on the electroconvective effects. It has been shown that the DEP forces, when the wire serves as an electrode, are easily thousands of times the buoyancy force (Snyder et al., 1996). However, under these conditions, the CHF only increases 3 or 4 times the terrestrial gravity CHF. Therefore, there appears to be a mechanism or condition where the $g^{1/4}$ dependence breaks down and approaches a constant value.

As outlined by Siegel (1967), concerning the microgravity data point on Fig. 9, the test duration is short and a period of time is required for the vapor pattern to be formed at the critical flux in order to obtain a transition from nucleate to film boiling. Therefore, it would be expected that the measured critical heat flux might often be greater than the critical flux that would be measured in a long-duration microgravity test. Siegel (1967) states that, "it still cannot be ascertained whether the critical flux is zero at zero gravity and tests of longer duration with carefully measured values of low gravity fields are still needed." However, we might add that the impossible-to-obtain case of $g \to 0$ exactly corresponds to CHF $\to 0$, if there is no limit imposed on the time duration and there is no heat sink (insulated walls). While this case is somewhat unrealistic, it is the only data point that is actually know for certain in Fig. 9. The remaining points (i.e., different fluids, heat transfer surfaces, subcoolings, gravity levels, time durations, etc.) are that which need longer duration and higher quality tests in order to quantify. Also, small changes in the system variables (heat flux, gravity level, or even the size of thermal heat sink of the experimental boiling chamber) will cause the measured CHF in microgravity to change if the time duration is long enough. A system-dependent analysis is possible; however, a general correlation, based on this discussion, appears nearly impossible when g approaches zero. The issues of "transients," i.e., "time" and "the amount of heat sink available to sustain the subcooling," are complex issues that must be faced in order to obtain further general results for boiling in microgravity.

Discussion

It has been well established that boiling heat transfer is very different for flat surfaces than for small radius of curvature wires, thus making it difficult to formulate an analogy with variable gravity boiling with the heater wire results from this study alone. However, a review of the literature shows that others have formulated and/or recorded trends in heat transfer for EHD boiling studies similar to those encountered with variable gravity boiling. Kronig and Ahsmann (1949) and Turnbull (1969) developed Nusselt-type correlations for convective heat transfer taking the electric field force into account. Chandra and Smylie (1972) also used the idea of an electrohydrodynamic thermal convection analogy. The heat transfer data were correlated using the Nusselt number plotted versus an electric Rayleigh number. Choi (1962) proposed the use of a modified Zuber-Kutateladse hydrodynamic approach to predict the effect of the electric field on the CHF. He also derived an effective gravitational acceleration utilizing the DEP force for concentric cylinders. Smylie (1966) and Gross (1967) recognized the possible use of EHD forces as a controllable laboratory analogy for the nonuniform, spherically symmetric gravitational forces. Markels and Durfee (1964, 1965) studied EHD enhanced pool boiling with AC and DC electric fields in semi-insulating liquids using a steam heated tube. They noted a strong dependence of the heat transfer to the magnitude and direction of the electric body forces. In a set of experiments by Baboi et al. (1968), it

was concluded that dielectrophoretic forces tend to pull nucleating bubbles off the heated wire surface more rapidly, thus increasing the CHF.

More recently, Cooper (1990) completed a study on boiling under 1 g with two concentric cylinders. The outer cylinder was of constant diameter, and the inner cylinder was the shape of a finned tube (refer to the paper for a description). In this study, a column of vapor was seen trapped on the upper part of the tube in each interfin space. The lower liquid-vapor interface of each column oscillated at a frequency that increased with increasing field strength. These results appear to be caused from the EHD forces (very likely DEP forces) holding the vapor onto the heater surface, which maintained a thin superheated microlayer over the heater and increased the heat transfer similar to that recorded for microgravity boiling. Ogata and Yabe (1993a, b) showed that an electric field can cause bubbles to be pushed back against the heating surface while, simultaneously, the radial component of force moves the bubbles over the heater surface. This force distribution was concluded to be one of the causes of heat transfer augmentation. They also concluded that the microlayer was enlarged by the deformed bubble shape, thus giving rise to augmented heat transfer. Geppert et al. (1995) showed similar results, i.e., that the already departed bubbles are pushed back to the heat transfer surface, which further enhanced the heat transfer during nucleate boiling.

Finally, based on the previous results and discussion, we conclude that the effect of the DEP force on the bubbles is analogous to reducing or increasing the gravity locally or inducing gravity-driven vapor flow across the heater surface similar to forced-convection. In terms of the relationship between the bubble dynamics and the heat transfer, it appears that nucleate boiling heat transfer will be enhanced if the effective gravity acts to hold the vapor bubbles near the heater surface, while at the same time permitting access of the liquid to the surface in order to prevent dryout. However, a large electroconvection effect can dominate and possibly reverse this trend. Therefore, we propose that the overall heat transfer coefficient with an applied electric field consists of a nonboiling heat transfer coefficient due to electroconvection and a boiling heat transfer coefficient due to the bubble dynamics as given in Eq. (6). Furthermore, it appears that the heat transfer coefficient due to the bubble dynamics can be correlated with the effective gravity ratio ($g'_{(b,e)}$) using theory for variable gravity and/or gravity-driven forced convection. The conclusions are based on the fact that one of the main effects from the electric field is simply to add an electrical body force on the generated vapor bubbles that can increase or decrease the gravity and/or induce vapor flow across the heater surface. Also, the second main effect of the electric field is to change the convective heat transfer (electroconvection) which, in terms of heat transfer, can compete with the generalizations formed due to the bubble dynamics alone. Finally, this competing effect between the heat transfer due to the effective gravity (that due to the bubble dynamics) and the heat transfer due to the electroconvection is analogous to results previously published for variable gravity boiling between a variable gravity field and natural convection (Merte, 1990), i.e., as the effective gravity increases the heat transfer will decrease, however, a large electroconvective component can dominate and reverse the trend.

Because the DEP force does not generally act in one direction with respect to gravity as simulated in this experiment, it may be advantageous to separate the heat transfer coefficient due to the bubble dynamics further into a coefficient due to an effective gravity normal $[((\mathbf{F}_b + \mathbf{F}_e)/|\mathbf{F}_b^*|) \cdot \hat{n}_\perp]$ and an effective gravity parallel $[((\mathbf{F}_b + \mathbf{F}_e)/|\mathbf{F}_b^*|) \cdot \hat{n}_\parallel]$ to the heating surface, as well as to the nonboiling heat transfer coefficient. Of course, the most difficult aspect in implementing a correlation for DEP-driven boiling using gravity-driven theory is, admittedly, the spatial dependence in the DEP force for any practical heater/electrode geometry. Nevertheless, the separation of the heat transfer coefficient in this way may allow more general correlations to be formed, which unite EHD boiling results with variable gravity boiling results.

Conclusion

An experiment was performed which produced a controlled dielectrophoretic (DEP) force over the length of a horizontal platinum wire heater. Boiling curves were produced for variable DEP forces and buoyancy forces by varying the electric field geometry, by varying the orientation of the electric field with respect to gravity, and by performing experiments in a drop tower with very small buoyancy forces. An effective gravity ratio $g'_{(b,e)}$ was defined that represents the ratio of the total DEP and buoyancy body forces on the vapor bubbles to the constant terrestrial-gravity buoyancy force. It was also concluded that the overall boiling heat transfer coefficient in the presence of an electric field can be modeled as the summation of a heat transfer coefficient due to bubble dynamics and a heat transfer coefficient due to electroconvection. The effect of the DEP force on the bubbles was shown to be analogous to reducing or increasing the gravity locally or inducing gravity-driven vapor flow across the heater surface. In terms of the relationship between the bubble dynamics and the heat transfer, it was concluded that the effect of a variable DEP force is similar to the effect of a variable buoyancy force. The heat transfer will be enhanced if the effective gravity acts to hold the vapor bubbles near the heater surface, while at the same time permitting access of the liquid to the surface in order to prevent dryout. However, a large electroconvective effect can dominate and possibly reverse this trend. It was found that for $1 < g'_{(b,e)} < 3$, a quarter power dependence is a reasonable engineering approximation for the increase in critical heat flux with effective gravity.

Acknowledgments

The research was supported by NASA Grant NAG3-1387. Dr. Fran Chairmonte was the project monitor and provided constant support. The first author was a NASA Graduate Student Research Program fellow for $3\frac{1}{2}$ years. The third author received support from the Office of Naval Research Code 321OA.

References

Baboi, N. F., Bologa, M. K., and Klyukanov, A. A., 1968, "Some Features of Ebullition in an Electric Field," *Appl. Electr. Phenom.*, (USSR), Vol. 20, pp. 57–70.

Bankoff, S. G., 1959, "On the Mechanism of Subcooled Nucleate Boiling," Jet Prop. Lab., Memo 30-38.

Bochirol, L., Bonjour E., and Weil, L., 1960, "Echanges Thermiques-Etude de l'Action de Champs Electriques sur les Transferts de Chaleur dans les Liquids Bouillants," *C. R. Hebd. Seance Acad. Sci (Paris)*, Vol. 250, pp. 76–78.

Chandra, B., and Smylie, D. E., 1972, "A Laboratory Model of Thermal Convection Under a Central Force Field," *Geophys. Fluid Dyn.*, Vol. 3, pp. 211–224.

Chen, L. T., 1978, "Heat Transfer to Pool Boiling Freon From Inclined Heating Plate," *Letters in Heat Mass Transfer*, Vol. 5, pp. 111–120.

Cheng, K. J., 1984, "Electric Field Effects on Nucleation During Phase Transitions of a Dielectric Fluid," *Physics Letters*, Vol. 106A, pp. 403–404.

Choi, H. Y., 1962, "Electrohydrodynamic Boiling Heat Transfer," Ph.D. thesis, Dept. Mech. Eng., Massachusetts Institute of Technology, Cambridge, MA.

Cooper, P., 1990, "EHD Enhancement of Nucleate Boiling," ASME JOURNAL OF HEAT TRANSFER, Vol. 112.

Cornwell, K., and Einarsson, J. G., 1983, "Periperal Variation of Heat Transfer Under Pool Boiling on Tubes," *International Journal of Heat and Fluid Flow*, Vol. 5, pp. 141–144.

Cornwell, K., and Schuller, M. J., 1982, "A Study of Boiling Outside a Tube Bundle Using High Speed Photography," *International Journal of Heat and Mass Transfer*, Vol. 25, pp. 683–690.

Di Marco, P., and Grassi, W., 1993, "Saturated Pool Boiling Enhancement by Means of an Electric Field," *Enhanced Heat Transfer*, Vol. 1, No. 1, pp. 99–114.

Geppert, C. A., Geppert, L. M., and Seyed-Yagoobi, J., 1995, "Electrohydrodynamically Enhanced Heat Transfer in Pool Boiling," *1995 National Heat Transfer Conference*, Vol. 6. ASME HTD-Vol 308.

Gross, M. J., 1967, Laboratory Analogies for Convection Problems, "Mantles of the Earth and Terrestrial Planets," Wiley, New York, pp. 499–503.

Jones, T. B., 1978, "Electrodynamically Enhanced Heat Transfer in Liquids—A Review," in: *Advances in Heat Transfer,* Vol. 14, pp. 107–148, T. F. Irvine and J. P. Hartnett, eds., Academic Press, New York.

Jones, T. B., and Bliss, G. W., 1976, "Bubble Dielectrophoresis," *Journal of Applied Physics,* Vol. 48, No. 4, pp. 1412–1417.

Jung, D. S., Venart, J. S., and Sousa, A. M., 1987, "Effects of Enhanced Surfaces and Surface Orientation on Nucleate and Film Boiling Heat Transfer in R11," *Int. J. Heat Mass Transfer,* Vol. 30, No. 12, pp. 2627–2639.

Kirk, K. M., Merte, H., Jr., and Keller, R. B., 1992, "Low Velocity Nucleate Flow Boiling at Various Orientations," *Fluid Mechanics Phenomena in Microgravity,* AMD-Vol. 154, FED-Vol. 142.

Kline, S. J., and McClintock, F. A., 1953, "Describing Uncertainties in Single-Sample Experiments," *Mechanical Engineering,* ASME, NY, pp. 3–12.

Kronig, R., and Ahsmann, G., 1949, "The Influence of an Electric Field on the Convective Heat Transfer in Liquids," *Appl. Sci. Res. Sect.,* A2, pp. 31–32.

Markels, M., and Durfee, R. L., 1964, "The Effect of Applied Voltage on Boiling Heat Transfer," *AIChE Journal,* Vol. 10, pp. 106–110.

Markels, M., and Durfee, R. L., 1965, "Studies of Boiling Heat Transfer With Electrical Fields: Part I.—Effect of Applied A.C. Voltage on Boiling Heat Transfer to Water in Forced Circulation; Part II.—Mechanistic Interpretations of Voltage Effects on Boiling Heat Transfer," *AIChE Journal,* Vol. 11, pp. 716–723.

Marston, P. L., and Apfel, R. E., 1977, "Effect of an Electric Field on the Limits of Liquid Stability," *Physics Letters,* Vol. 60A, No. 3, pp. 225–226.

Merte, H., Jr., 1990, "Nucleate Pool Boiling in Variable Gravity," *Low-Gravity Fluid Dynamics and Transport Phenomena,* Progress in Astronautics and Aeronautics, Vol. 130.

Nishikawa, K., and Fujita, Y., 1990, "Nucleate Boiling Heat Transfer and Its Augmentation," *Advances in Heat Transfer,* Vol. 20, pp. 1–82.

Noyes, R. C., 1963, "An Experimental Study of Sodium Pool Boiling Heat Transfer," ASME JOURNAL OF HEAT TRANSFER, Vol. 85, p. 125.

Ogata, J., and Yabe, A., 1993a, "Basic Study on the Enhancement of Nucleate Boiling Heat Transfer by Applying Electric Fields," *Int. J. of Heat and Mass Transfer,* Vol. 36, No. 3, pp. 775–782.

Ogata, J., and Yabe, A., 1993b, "Augmentation of Boiling Heat Transfer by Utilizing the EHD Effect—EHD Behaviour of Boiling Bubbles and Heat Transfer Characteristics," *Int. J. of Heat and Mass Transfer,* Vol. 36, No. 3, pp. 783–791.

Pohl, H. A., 1978, "Dielectrophoresis, The Behavior of Neutral Matter in Nonuniform Electric Fields," Cambridge University Press, New York.

Siegel, R., 1967, "Effects of Reduced Gravity on Heat Transfer," *Advances in Heat Transfer,* Vol. 4, pp. 143–228.

Smylie, D. E., 1966, "Thermal Convection in Dielectric Liquids and Modelling in Geophysical Fluid Dynamics," *Earth Planet Sci. Letters,* pp. 339–340.

Snyder, T. J., 1995, "Studies on the Dielectrophoretic Force and its Effects on Boiling Bubble Dynamics and Heat Transfer in Terrestrial and Microgravity Environments," Ph.D. thesis, Wash. State Univ., Pullman, WA.

Snyder, T. J., Sitter, J. S., Wang, T.-C., and Chung, J. N., 1995, "2.1 Second Drop Tower With Airbag Deceleration System—Design, Instrumentation, and Initial Results," *Microgravity Quarterly,* Vol. 5.2.

Snyder, T. J., Schneider, J. B., and Chung, J. N., 1996, "A Second Look at Electrokinetic Phenomena in Boiling," *J. of Applied Physics,* Vol. 79, pp. 6755–6760.

Stratton, J. A., 1941, *Electromagnetic Theory,* Chap. 2, McGraw-Hill, New York.

Tong, W., Simon, J. W., and Bar-Cohen, A., 1988, "A Bubble Sweeping Heat Transfer Mechanism for Low Flux Boiling on Downward Facing Inclined Surfaces," *Collected Papers in Heat Transfer,* ASME HTD-Vol. 104, Vol. 2, pp. 173–178.

Turnbull, R. J., 1969, "Free Convection From a Heated Vertical Plate in a Direct-Current Electric Field," *Phys. Fluids,* Vol. 12, pp. 2255–2263.

Zuber, N., 1959, "Hydrodynamic Aspects of Boiling Heat Transfer," Ph.D. thesis, Univ. of California, Los Angeles, CA.

Boiling Heat Transfer With Binary Mixtures: Part I—A Theoretical Model for Pool Boiling

S. G. Kandlikar
Mechanical Engineering Department,
Rochester Institute of Technology,
Rochester, New York 14623-5604

Experimental evidence available in the literature indicates that the pool boiling heat transfer with binary mixtures is lower than the respective mole- or mass-fraction-averaged value. Although a few investigators have presented analytical work to model this phenomenon, empirical methods and correlations are used extensively. In the present work, a theoretical analysis is presented to estimate the mixture effects on heat transfer. The ideal heat transfer coefficient used currently in the literature to represent the pool boiling heat transfer in the absence of mass diffusion effects is based on empirical considerations, and has no theoretical basis. In the present work, a new pseudo-single component heat transfer coefficient is introduced to account for the mixture property effects more accurately. The liquid composition and the interface temperature at the interface of a growing bubble are predicted analytically and their effect on the heat transfer is estimated. The present model is compared with the theoretical model of Calus and Leonidopoulos (1974), and two empirical models, Calus and Rice (1972) and Fujita et al. (1996). The present model is able to predict the heat transfer coefficients and their trends in azeotrope forming mixtures (benzene/methanol, R-23/R-13 and R-22/R-12) as well as mixtures with widely varying boiling points (water/ethylene glycol and methanol/water).

1 Introduction

Boiling of binary and multicomponent mixtures constitutes an important process in chemical, process, air-separation, refrigeration, and many other industrial applications. Reboilers feeding the vapors to distillation columns and flooded evaporators generally employ pool boiling, while the in-tube evaporation process involves flow boiling. Although the multicomponent boiling is of greater interest from a process standpoint, a fundamental understanding of the mechanism can be obtained first with binary mixtures.

The present work is directed toward reviewing the existing theories on pool boiling heat transfer with binary mixtures, and developing a theoretical model to predict the effect of mass diffusion on heat transfer. The results from the model will be compared with the available experimental data for water/ethylene glycol, methanol/water, benzene/methanol, R-22/R-12, and R-23/R-12 systems. The model will be extended to flow boiling heat transfer with binary mixtures in Part II of this paper.

2 Review of Previous Work

2.1 Pool Boiling Models and Correlations for Binary Mixtures. Table 1 provides a summary of some of the important models and correlations available in the literature. Success of a purely theoretical treatment of this subject has been limited and these investigators have generally resorted to empirical methods.

Stephan and Körner (1969) recognized the importance of the term $|y_1 - x_1|$ in the reduction of heat transfer with binary mixtures. An empirical constant specific to the mixture was introduced along with a pressure correction. Several later investigators modified this equation, and provided values of the empirical constant for specific binary systems. Jungnickel et al. (1979) modified this correlation by including a heat flux multiplier, $\dot{q}^{(0.48+0.1x_1)}$. Using their own experimental data, Jungnickel et al. determined the values of the empirical constant K_{ST} for R-23/R-12 and R-22/R-12 systems.

Calus and Rice (1972) were among the first investigators to develop an empirical model based on the bubble growth theories presented by Scriven (1959) and Van Stralen (1967). The term representing the reduction in bubble growth in binary systems was used to represent the reduction in heat transfer rate directly in the pool boiling correlation. Starting with the term $[1 + |y_1 - x_1|(\kappa/D_{12})^{0.5}(c_p/\Delta h_{LG})(dT/dx_1)]^{-1}$, Calus and Rice empirically observed that it could be reduced to a simpler form, $[1 + |y_1 - x_1|(\kappa/D_{12})^{0.5}]^{-1}$, while retaining the same functional dependence for isopropanol/water, acetone/water, and water/glycerol mixtures. Further, an exponent of 0.7 was added to this term as it provided a better match with the experimental data. Since their method yields the pool boiling coefficients directly, it cannot utilize the more accurate pure component correlations or data available in the literature. Their model was unable to predict the severe suppression seen in their own experimental data.

Calus and Leonidopoulos (1974) provided a model based on theoretical considerations. They retained the entire term $[1 + |y_1 - x_1|(\kappa/D_{12})^{0.5}(c_p/\Delta h_{LG})(dT/dx)]^{-1}$ in Calus and Rice's model, and dropped the empirically derived exponent of 0.7. Although this model could not represent the effect of composition on heat transfer well, it provided a lower mean error than the Stephan and Körner (1969) and Calus and Rice (1972) correlations.

Schlünder (1982) introduced the difference between the saturation temperatures of the pure components at the same pressure as a parameter in his correlating scheme. Also, a correction

Contributed by the Heat Transfer Division and presented at the National Heat Transfer Conference, Baltimore, Maryland, August 8–12, 1997. Manuscript received by the Heat Transfer Division November 19, 1996; revision received January 30, 1998. Keywords: Boiling, Evaporation, Phase-Change Phenomena. Associate Technical Editor: M. S. Sohal.

factor incorporating the mass transfer coefficient was introduced to modify Stephan and Körner's (1969) correlation. The value of the mass transfer coefficient was calculated from the experimental data and was found to be in agreement with the values observed in the case of falling film evaporation. In the absence of any reliable method to predict this coefficient, it was treated as an empirical constant specific to a system. Their correlation scheme, shown in Table 1, formed the basis for a number of modifications proposed later in literature.

Thome (1983) recognized the need to account for the rise in the saturation temperature at the liquid–vapor interface of a bubble. He introduced the boiling range (difference between the dew point and the bubble point temperatures at a given composition) as a parameter in reducing the available temperature difference with $\alpha_{PB,B} = \alpha_{PB,B,id}/[1 + \Delta T_{bp}/\Delta T_{id}]$. Later, Thome and Shakir (1987) introduced the mass transfer correction factor proposed by Schlünder (1982) as shown in Table 1.

Wenzel et al. (1995) followed a similar approach to Schlünder (1982), but set out to obtain the actual value of the interface concentration by applying the mass transfer equation at the bubble boundary. This approach required a knowledge of the mass transfer coefficient at the interface. It was empirically set at 10^{-4} m/s. The interface concentration was then used in determining the interface temperature.

Fujita and Tsutsui (1994) modified Thome and Shakir's (1987) correlation by replacing the mass transfer term with a heat flux-dependent term as shown in Table 1. The empirical constant in their correlation was evaluated from the experimental data. Fujita et al. (1996) modified the Fujita and Tsutsui correlation by replacing the heat flux term with a term including the ideal wall superheat, ΔT_{id}. They compared their correlation with several data sets from literature as well as with their own experimental results. The mean deviation between the predicted and experimental values ranged between 3.6 to 14 percent.

2.2 Ideal Pool Boiling Heat Transfer Coefficient for Mixtures. There are two approaches followed in the literature for developing a pool boiling correlation for binary mixtures. In the first one, an ideal mixture heat transfer coefficient is defined on the basis of a mole fraction-weighted average of the wall superheat for the pure fluids, which results in the reciprocal mole average of the pure component heat transfer coefficients at the same temperature or pressure as the mixture:

$$\alpha_{PB,B,id} = \left[\frac{\tilde{x}_1}{\alpha_{PB,1}} \bigg|_{p \text{ or } T} + \frac{\tilde{x}_2}{\alpha_{PB,2}} \bigg|_{p \text{ or } T} \right]^{-1} \quad (1)$$

The associated ideal temperature difference is obtained from a linear variation with mole fraction:

$$\Delta T_{id} = \tilde{x}_1 \Delta T_1 + \tilde{x}_2 \Delta T_2 \quad (2)$$

Calus and Rice (1972) and Calus and Leonidopoulos (1974) used mass fractions instead of mole fractions in these equations. The effects of mass transfer resistance, and the rise in the interface temperature, are then introduced to modify the equations in a semi-empirical way.

The second approach for calculating the ideal heat transfer coefficient utilizes the pool boiling correlation using mixture properties, as followed by Thome and Shakir (1987). They employed the Stephan–Abdelsalam (1980) pool boiling correlation using mixture properties. However, since correlations often introduce considerable errors in predicting pool boiling heat transfer coefficients for pure fluids, it becomes very difficult to separate the effects due to the pure fluid correlation error and the error associated with modeling the mixture effects. This approach is therefore generally not followed, and Eqs. (1) and (2) are used as the starting point.

3 Estimating the Pseudo-Single Component Pool Boiling Heat Transfer Coefficient, $\alpha_{PB,B,psc}$

The ideal heat transfer coefficient used in the literature is intended to represent the heat transfer coefficient of the mixture in the absence of any mass diffusion effects. It is determined by various investigators using one of the averaging techniques

Nomenclature

c_p = specific heat, J/kg K
D_{12} = diffusion coefficient of component 1 in mixture of 1 and 2
D^0_{12}, D^0_{21} = diffusion coefficient of component 1 (2) present in infinitely low concentration of liquid mixture
d_B = departure bubble diameter, m
F_D = diffusion factor = α/α_{id}
g = acceleration due to gravity in Eq. (4)
g = $(x_1 - x_{1,s})/(y_{1,s} - x_{1,s})$, defined by Eq. (23)
Δh_{LG} = latent heat of vaporization, J/kg
Ja_0 = modified Jakob number, defined by Eq. (21)
K, K_{st}, K_p = constants employed in different correlations
M = molecular weight
$\dot{m}$ = mass flux, kg/m^2
p = pressure, Pa
$\dot{q}$ = heat flux, W/m^2
R = bubble radius, m
T = temperature, K
t = time from bubble inception, s
ΔT_{bp} = boiling point range, difference between the dew point and bubble point temperatures
ΔT_{id} = wall superheat for ideal mixture as defined by earlier investigators
ΔT_s = $(T_s - T_{sat})$, K
ΔT_1, ΔT_2 = wall superheats for components 1 and 2 in pool boiling
$v_{m,1}$, $v_{m,2}$ = molar specific volumes of components 1 and 2 in liquid phase, m^3/kg-mol
V_1 = volatility parameter, defined by Eq. (33)
x_1, x_2 = mass fraction of components 1 and 2 in liquid phase
$\tilde{x}_1$, $\tilde{x}_2$ = mole fraction of components 1 and 2 in liquid phase
y_1, y_2 = mass fraction of components 1 and 2 in vapor phase
$\tilde{y}_1$, $\tilde{y}_2$ = mole fraction of components 1 and 2 in vapor phase
z = distance from bubble interface in liquid phase, m
α = heat transfer coefficient, W/m^2 K
β_0 = contact angle, rad
δ_m = thickness of mass diffusion boundary layer, m
η = viscosity, kg/m s
κ = thermal diffusivity, m^2/s
λ = thermal conductivity, W/m K
ρ = density, kg/m^3
σ = surface tension, N/m
ϕ = association parameter

Subscripts

1, 2 = components of a binary system; 1 = more volatile component
avg = average
B = binary
BL = boundary layer
D = mass diffusion
G = vapor
id = ideal
L = liquid
m = mixture
PB = pool boiling
psc = pseudo-single component
s = liquid-vapor interface of a bubble
sat = saturation

Table 1 Summary of some important methods for predicting pool boiling heat transfer coefficients in binary mixtures

Author and Year	Correlation Scheme	Comments
Stephan and Körner (1969)	$\alpha = \dfrac{\alpha_{id}}{1 + A\lvert y_1 - x_1\rvert(0.88 + 0.12p)}$ α_{id} - reciprocal mole-fraction average	The composition difference in the two phases was recognized as an important factor in the heat transfer reduction. Empirical constant A is specific to a mixture (range (0.43-0.56), p is in bar.
Calus and Rice (1972). Binary mixtures of isopropanol with water and acetone.	$\left[\dfrac{Nu}{K_p^{0.67}}\right]\left[\dfrac{T_{sat}}{T_{sat,water}}\right]^4 = E\left[\dfrac{P_e}{1+\lvert y-x\rvert(K/D_{12})^{0.5}}\right]^{0.7}$ $K_p = p/[g\sigma(\rho_L-\rho_G)]^{0.5}$, E – empirical constant $P_e = \dfrac{q}{\Delta h_v}\dfrac{\rho_L}{\rho_G}\dfrac{c_L}{\lambda_L}\left(\dfrac{\sigma}{g(\rho_L-\rho_G)}\right)^{0.5}$	The diffusion resistance term derived by Van Stralen (1966) in bubble growth equation is applied to modify the pool boiling correlation. ($c_L/\Delta h_v$)(dT/dx) term is neglected and an empirical constant is introduced.
Calus and Leonidopoulos (1974). n-propanol/water.	$\Delta T = (\Delta T_1 x_1 + \Delta T_2 x_2)\cdot$ $\left[1+(y-x)\left(\dfrac{K}{D_{12}}\right)^{0.5}\left(\dfrac{c_L}{\Delta h_v}\right)\left(\dfrac{dT}{dx}\right)\right]$ (Effectively, α_{id} is reciprocal mass fraction averaged value)	This scheme introduces the averaging equation from pure-fluid temperature differences. Original form of diffusion resistance term by Van Stralen (1966) is retained without introducing empirical constants.
Schlünder (1982)	$\alpha = \alpha_{id}\dfrac{1}{1+\dfrac{\Delta T_s}{\Delta T_{id}}\lvert y_1 - x_1\rvert\left[1-\exp\left(-\dfrac{B_o q}{\beta_L \rho_L h_{LG}}\right)\right]}$; $B_o = 1, \beta_L = 2\times 10^{-4} m/s$ α_{id} - reciprocal mole-fraction average	Introduced the boiling range of the respective pure components at the same pressure, and a term representing the mass transfer effects. B_o represents the evaporation component, assumed to be 1, and β_L set as a constant
Thome and Shakir (1987). ethanol/water, acetone/water, ethanol/benzene, nitrogen/argon, nitrogen/oxygen, and nitrogen/methane	$\alpha = \alpha_{id}\dfrac{1}{1+\dfrac{\Delta T_{bp}}{\Delta T_{id}}\left[1-\exp\left(-\dfrac{B_o q}{\beta_L \rho_L h_{LG}}\right)\right]}$; $B_o = 1, \beta_L = 3\times 10^{-4} m/s$ α_{id} - reciprocal mole-fraction average	The boiling range and the mass diffusion effects from Schlünder's model were combined. New value of β_L was determined empirically from experimental data sets.
Wenzel et al. (1995). Binary mixtures of acetone, isopropanol, and water	$\alpha = \dfrac{\alpha_{id}}{1+(\alpha_{id}/q)(T_s - T_{sat})}$; $\dfrac{y_{1,s}-x_1}{y_{1,s}-x_{1,s}} = \exp\left(-\dfrac{q}{B_o\beta_L\rho_L\Delta h_v}\right)$; $B_o = 1$, and $\beta_L \approx 10^{-4} m/s$ α_{id} - reciprocal mole-fraction average	Bubble interface temperature replaces saturation temperature in calculating α. Empirically determined values of the constant, B_o, and mass transfer coefficient, β_L, employed.
Fujita et al. (1996). methanol/water, ethanol/water, methanol/ethanol, ethanol/n-butanol, methanol/benzene, benzene/n-heptane, and water/ethylene glycol.	$\alpha = \dfrac{\alpha_{id}}{1+K_s(\Delta T_{bp}/\Delta T_{id})}$; $K_s = [1-\exp(-2.8\,\Delta T_{id}/\Delta T_{sat,1-2})]$; $\Delta T_{id} = \bar{x}_1\Delta T_1 + \bar{x}_2\Delta T_2$, $\Delta T_{sat,1-2} = \lvert T_{sat,1} - T_{sat,2}\rvert_p$ α_{id} - reciprocal mole-fraction average	It is an extension of earlier models by Stephan and Korner (1969), and Jungnickel et al. (1980). The mass diffusion effect expressed as an empirical function of boiling temperature range and difference in saturation temperatures of pure components at the same pressure.

between the respective pure component values. Since the pool boiling heat transfer is a highly nonlinear phenomenon with respect to temperature difference or fluid properties, there is little justification in using any of these methods for determining an "ideal" value for the mixture. There is also no clear indication, or justification, as to the state at which the respective pure component values should be determined. All investigators listed in Table 1 have determined them at the same pressure as the mixture. Many investigators, however, including Gorenflo et al. (1988), have calculated the pure component values at the same reduced pressure as in the binary system.

The concept of using the pure component correlation directly with mixture properties for estimating α_{id} was proposed by Thome and Shakir (1987). In the present work, the pure component values available from experiments are utilized, and the pure component correlation by Stephan and Abdelsalam (1980) is employed to apply the mixture property corrections.

Stephan and Abdelsalem (1980) correlation for pool boiling of pure fluids

$$\alpha_{PB} = \frac{\lambda_L}{d_B}\,0.23\left(\frac{\dot{q}d_B}{\lambda_L T_{\rm sat}}\right)^{0.674}\left(\frac{\rho_G}{\rho_L}\right)^{0.297}\left(\frac{\Delta h_{LG} d_B^2}{\kappa_L^2}\right)^{0.371} \times \left(\frac{\kappa_L^2\rho_L}{\sigma d_B}\right)^{0.674}\left(\frac{\rho_L-\rho_G}{\rho_L}\right)^{-1.73} \quad (3)$$

where d_B is the departure bubble diameter given by

$$d_B = 0.851\beta_0\sqrt{\frac{2\sigma}{g(\rho_L-\rho_G)}} \quad (4)$$

In this correlation, the property effect on α_{PB} can be expressed as follows by approximating $(\rho_L - \rho_G) \approx \rho_L$, and introducing a constant C_1 to replace other parameters:

$$\alpha_{PB} = (C_1)T_{\rm sat}^{-0.674}\Delta h_{LG}^{0.371}\rho_G^{0.297}\sigma^{-0.317} \times \lambda_L^{0.284}\beta_0^{0.066}\rho_L^{0.062}c_{p,L}^{0.042} \quad (5)$$

For conditions close to the critical point, the term $(\rho_L - \rho_G)$ could be retained and the equation modified appropriately. The last three properties, β_0, ρ_L, and $c_{p,L}$ in Eq. (5), have relatively small values of exponents, and their effect could be neglected in comparison to other properties. For example, a twofold change in the contact angle will result in only a 4.7 percent change in α. Introducing another constant C_2 in Eq. (5), the property effect can be expressed as:

$$\alpha_{PB} = (C_2)T_{\rm sat}^{-0.674}\Delta h_{LG}^{0.371}\rho_G^{0.297}\sigma^{-0.317}\lambda_L^{0.284} \quad (6)$$

For predicting the ideal mixture heat transfer coefficient based on Eq. (6), the individual property variations with composition are needed. First, the following averaging equations are employed:

$$T_{{\rm sat},m,{\rm avg}} = x_1 T_{{\rm sat},1} + x_2 T_{{\rm sat},2} \quad (7)$$

$$\rho_{G,m,{\rm avg}} = x_1\rho_{G,1} + x_2\rho_{G,2} \quad (8)$$

$$\Delta h_{LG,m,{\rm avg}} = x_1\Delta h_{LG,1} + x_2\Delta h_{LG,2} \quad (9)$$

$$\sigma_{m,{\rm avg}} = x_1\sigma_1 + x_2\sigma_2 \quad (10)$$

and

$$\lambda_{L,m,{\rm avg}} = x_1\lambda_{L,1} + x_2\lambda_{L,2} \quad (11)$$

The average mixture heat transfer coefficient, $\alpha_{PB,B,{\rm avg}}$ is defined as the heat transfer coefficient obtained with a pseudo-single component fluid having the mixture properties given by Eqs. (7)–(11). It can be found from Eqs. (6)–(11) by assuming Const.2 in Eq. (6) to be independent of mixture composition. Alternatively, the following averaging scheme is found to predict $\alpha_{PB,B,{\rm avg}}$ directly from α_1 and α_2 for pure fluids within less than 5 percent of the predictions from Eq. (6) even when the individual properties were varied by a factor of 2–3. For this purpose, all mixtures investigated in this study were included in the analysis.

$$\alpha_{PB,B,{\rm avg}} = 0.5\left[(x_1\alpha_1 + x_2\alpha_2) + \left(\frac{x_1}{\alpha_1} + \frac{x_2}{\alpha_2}\right)^{-1}\right] \quad (12)$$

This equation is used to find the average pool boiling heat transfer coefficient of the mixture with properties given by Eqs. (7)–(11) in the absence of mass diffusion effects. The actual mixture properties are, however, different from those described by Eqs. (7)–(11), and can be obtained from the property information for the particular binary system. The pseudo-single phase coefficient $\alpha_{PB,B,{\rm psc}}$ for the mixture is based on the actual mixture properties, and the following equation is employed to incorporate this effect:

$$\alpha_{PB,B,{\rm psc}} = \alpha_{PB,B,{\rm avg}}\left(\frac{T_{{\rm sat},m}}{T_{{\rm sat,avg}}}\right)^{-0.674}\left(\frac{\Delta h_{LG,m}}{\Delta h_{LG,{\rm avg}}}\right)^{0.371}\left(\frac{\rho_{G,m}}{\rho_{G,{\rm avg}}}\right)^{0.297} \times \left(\frac{\sigma_m}{\sigma_{\rm avg}}\right)^{-0.317}\left(\frac{\lambda_{L,m}}{\lambda_{L,{\rm avg}}}\right)^{0.284} \quad (13)$$

The subscript "m" in this equation refers to the actual mixture properties, while "avg" refers to the average properties calcu-

lated from Eqs. (7)–(11). For mixtures close to the critical state, the approximation $(\rho_L - \rho_G) \approx \rho_L$ is no longer valid, and Eq. (13) could be modified with the inclusion of ρ_L and an appropriate reciprocal mass fraction weighted average for determining $\rho_{L\text{avg}}$. In many cases, only one or two properties, such as surface tension, vapor density or saturation temperature, may exhibit severely nonlinear behavior. This is especially true in the low concentration region. In such cases, the property correction factors for only these properties may be employed in Eq. (13).

The pseudo-single phase coefficient $\alpha_{PB,B,\text{psc}}$ defined by Eqs. (13) and (12) offers several advantages over the commonly used $\alpha_{PB,B,id}$. Actual mixture properties are employed in calculating $\alpha_{PB,B,\text{psc}}$ rather than using a general reciprocal mole or mass fraction-averaged equation to represent the property effects for all mixtures with different nonideal mixture characteristics. Mixtures with a high degree of nonideality are therefore represented more accurately with the present method. The second advantage is that the pure fluid coefficients α_1 and α_2 can be calculated from any appropriate correlation, such as Stefan and Abdelsalam (1982), Gorenflo (1984), Rohsenow (1952), or any proprietary correlation technique. Note that the Stefan–Abdelsalam correlation is used only to capture the effect of properties in the present analysis, and does not require its usage in estimating the pure component values. Alternatively, experimental values of α_1 and α_2, if available, could be directly employed in Eq. (13). A third advantage is that it is possible to use α_1 and α_2 obtained at the same total pressure, or at the same reduced pressure, or at the same system temperature as the mixture while calculating $\alpha_{PB,B,\text{psc}}$ from the present method. Experimental data in laboratories is generally obtained by keeping the total pressure constant.

4 Pool Boiling Heat Transfer Coefficient for Binary Mixtures

The nucleate boiling heat transfer in a binary system is affected by the changes in the nucleation and bubble growth characteristics. As a first step, the present analysis focuses on the effect of the changes in the bubble growth characteristics on pool boiling heat transfer. As a bubble grows, the more volatile component evaporates preferentially at the interface, thereby depleting the nearby liquid, and setting a diffusion process from the bulk toward the interface. The equilibrium interface phase concentrations are first calculated as a bubble grows asymptotically under the diffusion-controlled growth. A one-dimensional transient heat and mass transfer analysis is then conducted to estimate the effect of mass diffusion on the heat transfer process.

Liquid Concentration at the Interface. Consider a bubble growing on a heated wall in a binary system as shown in Fig. 1. The mass concentration of the more volatile component 1 varies from $x_{1,s}$ at the interface to x_1 in the bulk liquid across a concentration boundary layer of uniform thickness δ_m around the bubble. According to Van Stralen (1979), the interface concentration reaches an asymptotic value during the bubble growth period. Consider an instant when the bubble radius is R and the concentration gradient in the liquid extends from R to $R + \delta_m$. The evaporated vapor leaves the interface at the equilibrium vapor phase concentration of $y_{1,s}$.

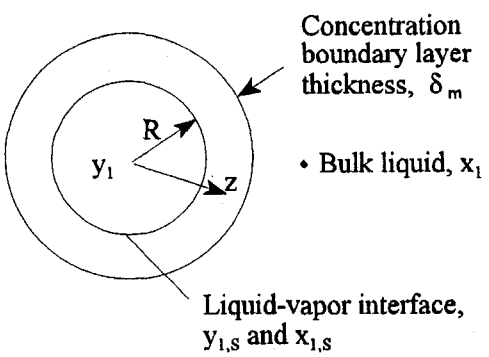

Fig. 1 Schematic representation of concentration around a bubble growing in a binary mixture

The increase in the pressure inside a bubble due to interface curvature is negligible in the latter stages of the bubble growth, during which the majority of the evaporation occurs. The system pressure is therefore used in determining the equilibrium concentrations at the interface. The concentration gradient in the vapor inside the bubble is neglected. The average concentration in the boundary layer is represented by $x_{1,BL,\text{avg}}$. The higher concentration of component 1 in the vapor comes from its depletion in the boundary layer. A mass balance of component 1 in the boundary layer thickness δ_m and inside the bubble yields:

$$x_{1,BL,\text{avg}} = x_1 - \frac{1}{3}\frac{R}{\delta_m}\frac{\rho_G}{\rho_L}(y_{1,s} - x_1) \tag{14}$$

Following the analysis by Mikic and Rohsenow (1969) for transient heat transfer under one-dimensional assumption with a planar interface, the liquid concentration at a distance z from the interface at any instant t from the bubble inception is obtained from a similar one-dimensional transient mass transfer analysis on a semi-infinite surface and is given by:

$$\frac{x_{1,z} - x_{1,s}}{x_1 - x_{1,s}} = \text{erf}\left(\frac{z}{2\sqrt{D_{12}t}}\right) \tag{15}$$

The thickness of the concentration boundary layer is given by:

$$\delta_m = (\pi D_{12} t)^{1/2} \tag{16}$$

Combining Eqs. (15) and (16),

$$\frac{x_{1,z} - x_{1,s}}{x_1 - x_{1,s}} = \text{erf}\left(\frac{\sqrt{\pi}}{2}\frac{z}{\delta_m}\right) \tag{17}$$

Integrating Eq. (17), the average concentration in the boundary layer can be obtained in terms of the bulk and the interface liquid compositions as follows:

$$\frac{x_{1,BL,\text{avg}} - x_1}{x_{1,s} - x_1} = 0.313 \tag{18}$$

Combining Eqs. (14) and (18), the interface concentration $x_{1,s}$ is obtained:

$$x_{1,s} = x_1 - 1.06\frac{R}{\delta_m}\frac{\rho_G}{\rho_L}(y_{1,s} - x_1) \tag{19}$$

R is obtained by applying the bubble growth equations developed by Van Stralen (1975) for the one-dimensional planar approximation.

$$R = \frac{2}{\pi^{1/2}}\text{Ja}_0(\kappa t)^{1/2} \tag{20}$$

where Ja_0 is the modified Jakob number to account for the mass diffusion effects and the rise in the interface temperature. It is given by

$$\text{Ja}_0 = \frac{(T_W - T_{L,\text{sat}})}{\left(\frac{\rho_G}{\rho_L}\right)\left[\frac{\Delta h_{LG}}{c_{p,L}} + \left(\frac{\kappa}{D_{12}}\right)^{1/2}\frac{\Delta T_S}{g}\right]} \tag{21}$$

and ΔT_s and g are given by

$$\Delta T_s = T_{\text{sat},s} - T_{\text{sat}} \tag{22}$$

and

$$g = \frac{x_1 - x_{1,s}}{y_{1,s} - x_{1,s}} \tag{23}$$

Dividing Eq. (20) by Eq. (16), the ratio R/δ_m is obtained as

$$\frac{R}{\delta_m} = \frac{2}{\pi} \mathrm{Ja}_0 \left(\frac{\kappa}{D_{12}}\right)^{1/2} \tag{24}$$

and the interface concentration is obtained by combining Eqs. (19) and (24) as:

$$x_{1,s} = x_1 - \frac{2.13}{\pi} \mathrm{Ja}_0 \left(\frac{\kappa}{D_{12}}\right)^{1/2} \frac{\rho_G}{\rho_L} (y_{1,s} - x_1) \tag{25}$$

It can be seen from Eq. (25) that the interface concentration is independent of time t, and it represents the asymptotic value reached at the interface.

Effect of Mass Diffusion Resistance in Liquid at Interface on Pool Boiling Heat Transfer. The more volatile component diffuses from the bulk, which has a higher concentration toward the bubble interface. The following analysis is presented for the case where the mass diffusion is the controlling mechanism for heat transfer, and limits the availability of the more volatile component at the interface.

The pool boiling heat transfer coefficient for a binary mixture, $\alpha_{B,PB}$, is expressed in terms of the pseudo-single component heat transfer coefficient as:

$$\alpha_{PB,B} = \alpha_{PB,B,\mathrm{psc}} F_D \tag{26}$$

where F_D is the diffusion-induced suppression factor to account for the reduction in the heat transfer coefficient due to the mass diffusion effects. The heat transfer coefficient is assumed to be proportional to the evaporation rate at the bubble interface. F_D is then obtained by comparing the mass transfer rates with and without the diffusion resistance. In the absence of mass diffusion effects, the interface temperature corresponds to the saturation temperature of the bulk liquid, and following the analysis by Van Stralen (1979), the heat flux due to transient conduction at the interface under one-dimensional approximation is given by:

$$\dot{q}_S = \frac{\lambda_L (T_W - T_{\mathrm{sat}})}{(\pi \kappa t)^{1/2}} \tag{27}$$

The resulting evaporation mass flux is given by:

$$\dot{m}_s = \frac{\dot{q}_s}{\Delta h_{LG}} = \frac{1}{\Delta h_{LG}} \frac{\lambda_L (T_W - T_{\mathrm{sat}})}{(\pi \kappa t)^{1/2}} \tag{28}$$

A similar analysis could be conducted for the mass diffusion in the boundary layer. For relatively low values of the total mass flux, the transient mass diffusion equation similar to Eq. (27) can be applied for the diffusion of component 1 toward the interface. The resulting mass flux is given by:

$$\dot{m}_{1,s} = \frac{\rho_L D_{12} (x_1 - x_{1,s})}{(\pi D_{12} t)^{1/2}} \tag{29}$$

The total evaporation rate in the binary system is obtained by dividing Eq. (29) with $(y_{1,s} - x_1)$:

$$\dot{m}_{s,D} = \frac{\dot{m}''_{1,s}}{(y_{1,s} - x_1)} = \frac{\rho_L D_{12}}{(\pi D_{12} t)^{1/2}} \frac{x_1 - x_{1,s}}{y_{1,s} - x_1} \tag{30}$$

The reduction in the heat transfer coefficient, represented by the factor F_D, is obtained by comparing the two evaporation rates given by Eqs. (28) and (30):

$$F_D = \left(\frac{D_{12}}{\kappa}\right)^{1/2} \frac{x_1 - x_{1,s}}{y_{1,s} - x_1} \frac{\Delta h_{LG}}{c_p (T_W - T_{\mathrm{sat}})} \tag{31}$$

Equation (31) can be further simplified by substituting for $(x_1 - x_{1,s})/(y_{1,s} - x_1)$ from Eq. (25) as follows:

$$F_D = \frac{2.13}{\pi} \left(\frac{1}{1 + \left(\frac{c_{p,L}}{\Delta h_{LG}}\right)\left(\frac{\kappa}{D_{12}}\right)^{1/2} \frac{\Delta T_s}{g}}\right) \tag{32}$$

Equation (32) represents the suppression factor in the diffusion-controlled region. At small values of the parameter $(\Delta T_s/g)$, such as near the azeotropic compositions, or in the vicinity of pure fluids, Eq. (30) will not be applicable as the total mass flux is much higher than the diffusion flux. Also, the diffusion factor F_D should reduce to 1 to represent the pure fluid case. In the present work, this transition is seen to occur at $(\Delta T_s/g) \approx 0.3$.

Further simplification is obtained by using the slope of the bubble point curve, and using y_1 in-stead of $y_{1,s}$ and introducing a new parameter V_1, called the volatility parameter:

$$V_1 = \frac{c_{p,L}}{\Delta h_{LG}} \left(\frac{\kappa}{D_{12}}\right)^{1/2} \left| \frac{dT}{dx_1} (y_1 - x_1) \right| \tag{33}$$

At $V_1 = 0.005$, the bracketed term in Eq. (32) is close to 1, and a linear interpolation is used in the region $0 < V_1 < 0.005$, with $F_D = 1$ at $V_1 = 0$, and $F_D = 0.678$ at $V_1 = 0.005$. The final expression for F_D is given below.

Final Expression for F_D

For $V_1 > 0.005$

$$F_D = 0.678 \left(\frac{1}{1 + \left(\frac{c_{p,L}}{\Delta h_{LG}}\right)\left(\frac{\kappa}{D_{12}}\right)^{1/2} \frac{\Delta T_s}{g}}\right) \tag{34}$$

For $0 < V_1 \leq 0.005$,

$$F_D = 1 - 64.0 V_1 \tag{35}$$

Although the expression derived here for F_D looks similar to that of Calus and Leonidopoulos (1974) except for the leading constant, there is another major difference. The expression for g incorporates the vapor phase composition, $y_{1,s}$ at the interface condition, and not y_1, corresponding to the bulk condition. This requires the calculation of interface compositions using Eq. (25). An iterative scheme is therefore needed to solve this set of equations. Note that the graphic method of determining $\Delta T_s/g$ employed by earlier investigators is no longer applicable; however it can be used to calculate V_1. Using y_1 in stead of $y_{1,s}$ introduces an error that is significant for mixtures with large V_1, such as water/ethylene glycol.

5 Usage of the Equations

The binary pool boiling heat transfer coefficient is given by Eq. (26) in conjunction with Eqs. (33)–(35). ΔT_s and g are obtained from Eqs. (22) and (23), and the interface concentration is obtained from Eq. (25) with Ja_0 from Eq. (21). An iterative procedure is needed to find $x_{1,s}$ and α. The following procedure is recommended.

1 Calculate T_{sat} corresponding to the bulk liquid concentration and system pressure.
2 Assume $x_{1,s}$. Determine $T_{\mathrm{sat},s}$ and $y_{1,s}$ from the thermodynamic property data for the mixture.
3 Assume α and calculate $T_w = T_{\mathrm{sat}} + q/\alpha$.

4 Calculate Ja_0, ΔT_s and g from Eqs. (21)–(23).
5 Calculate $x_{1,s}$ from Eq. (25).
6 Calculate V_1 from Eq. (33).
7 Calculate α from Eq. (26).
8 Iterate steps 2 through 7 until $x_{1,s}$ and α are converged.

The diffusion coefficient D_{12} is obtained from Eqs. (36) and (37) given in the next section.

6 Comparison With Experimental Data

The model developed in this work is compared with the experimental data available in the literature. For this purpose, the data reported by Fujita et al. (1996) on ethylene glycol/water, methanol/water, and methanol/benzene systems, and by Jungnickel et al. (1979) on R-22/R-12 and R-23/R-13 are utilized. The mixtures represent diverse combinations; the ethylene glycol/water system has a large difference in volatility and boiling points of the two components, and methanol/benzene, R-23/R-13, and R-22/R-12 have azeotropic combinations in certain ranges of pressure and temperature. The properties of the mixtures were obtained from NIST (1995) and HYSIM (1996) programs. The diffusion coefficients were calculated following the procedure outlined by Kandlikar (1975), with the thermodynamic factor set equal to 1 in the Vignes correlation (1971):

$$D_{12} = (D_{12}^0)^{x_2}(D_{21})^{x_1} \tag{36}$$

This correlation was found to be very suitable for nonideal mixtures. D_{12}^0 and D_{21}^0 in this equation are self-diffusion coefficients given by the Wilke–Change (1955) correlation

$$D_{12}^0 = 1.1782 \times 10^{-16} \frac{(\phi M_2)^{1/2} T}{\eta_{L,2} v_{m,1}} \tag{37}$$

M is the molecular weight, and ϕ is the association factor for the solvent (2.26 for water, 1.9 for methanol, 1.5 for ethanol, 1.9 for ethylene glycol, and 1.0 for unassociated solvents including benzene, ether, heptane, and refrigerants; Taylor and Krishna, 1993; Wilke and Chang, 1955), and $v_{m,1}$ is the molar specific volume of component 1.

Figure 2 shows a comparison of the ideal heat transfer coefficient, $\alpha_{PB,B,id}$, used by previous investigators, and the proposed pseudo-single component heat transfer coefficient, $\alpha_{PB,B,psc}$ for ethylene glycol mixture at 100 kPa. It can be seen that the two are quite different over the concentration range. The main reason for this difference is the abrupt change in the vapor density with the slight addition of water to pure ethylene glycol. The resulting bubbles in the mixture have a high concentration of water vapor. Pool boiling heat transfer is expected to be affected by this behavior. $\alpha_{PB,B,id}$ does not reflect this property effect, and therefore shows an almost monotonous variation with the composition. For azeotropic compositions, $\alpha_{PB,B,psc}$ represents the heat transfer coefficient for the mixture without the diffusion effects, and is expected to be more accurate than $\alpha_{PB,B,id}$.

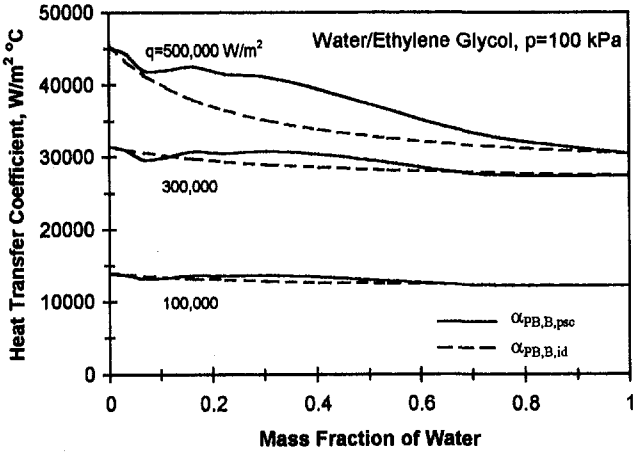

Fig. 2 Variation of pseudo-single component and ideal heat transfer coefficients with composition, water/ethylene glycol, p = 100 kPa

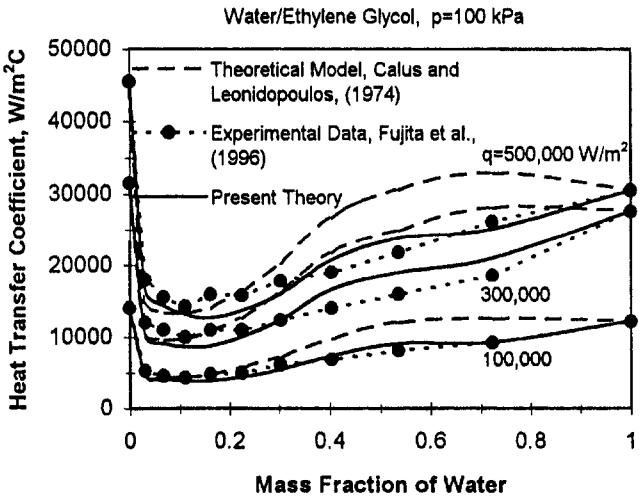

Fig. 3 Comparison of present model and Calus–Leonidopoulos (1974) model with experimental data of Fujita et al. (1996), water/ethylene/glycol, p = 100 kPa

Figure 3 shows a comparison of the experimental data of Fujita et al.'s (1996) for ethylene glycol/water mixtures with the theoretical model of Calus and Leonidopoulos (1974) and the present model at 100 kPa and three values of heat flux. The Calus–Leonidopoulos model predicts reasonably well for low concentrations of water, but overpredicts in the rest of the range. The present model shows an excellent agreement over the entire range for all the three heat fluxes with an average error of less than 12 percent.

Figure 4 shows a comparison of the same data of Fig. 3 with the two empirical correlations, those of Calus and Rice (1972) and Fujita et al. (1996). It can be seen that both correlations perform well at lower water concentrations, while that of Fujita et al. is slightly better in the higher concentration range. It may be noted that the data set under discussion was used by Fujita et al. (1996) in their correlation development.

Figure 5 shows a comparison of the present data with the data of Fujita et al. on methanol/benzene at 100 kPa, similar

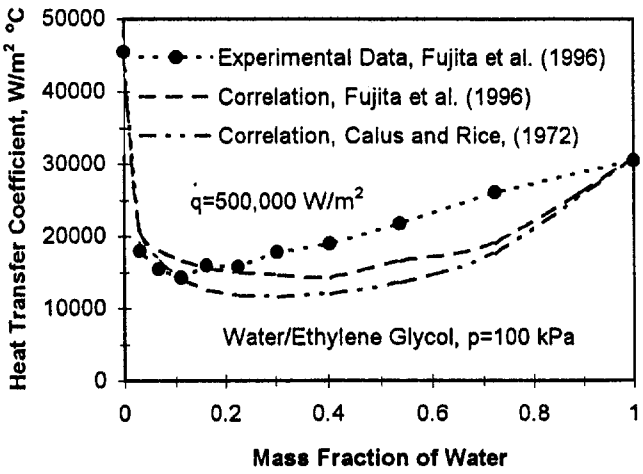

Fig. 4 Comparison of Fujita et al. (1996) and Calus and Rice (1972) correlations with data of Fujita et al., water/ethylene glycol, p = 100 kPa

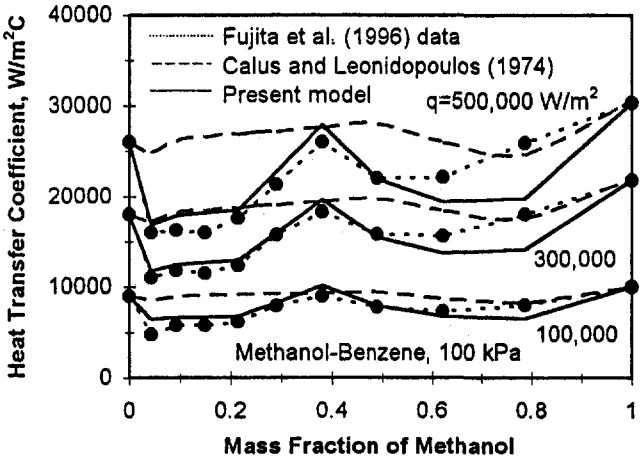

Fig. 5 Comparison of present model and Calus and Leonidopoulos (1974) model with experimental data of Fujita et al. (1996), methanol/benzene, p = 100 kPa

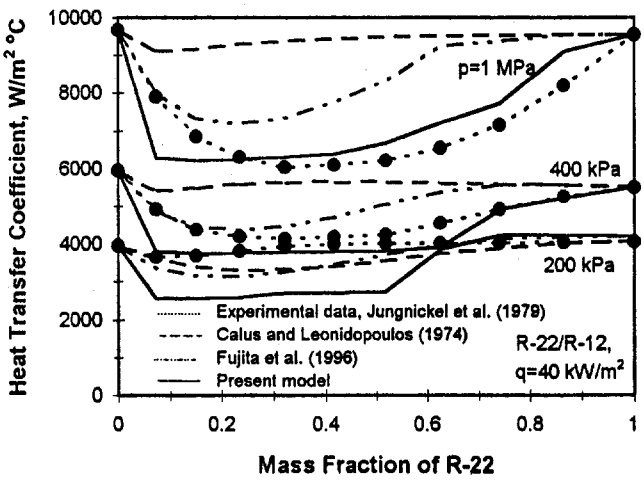

Fig. 7 Comparison of present model and Calus and Leonidopoulos (1974) model with experimental data of Jungnickel et al. (1979), R-22/R-12, q = 40 kW/m²

to the comparison in Fig. 3. The present model shows the same behavior as the data, and accurately predicts the behavior near the azeotropic composition. It underpredicts the heat transfer coefficient at higher heat fluxes and at higher concentrations of methanol. However, the mean error is less than 12 percent for each heat flux data set. The Calus and Leonidopoulos (1974) model is not able to predict the suppression in the range between the pure component and the azeotropic compositions. The main reason is that the ethylene glycol has a large dT/dx_1 slope, and the concentration difference between the two phases at interface is quite high. For methanol/benzene, the slope dT/dx_1 is not as steep, and the concentration difference between the two phases is also smaller.

Figure 6 shows the comparison with the data of Fujita et al. for methanol/water at 100 kPa and three values of heat fluxes. The agreement between the present theoretical model and the experimental data is excellent in the entire range resulting in an absolute deviation between 5.6 and 9.3 percent. The model slightly overpredicts the suppression at higher heat fluxes, still within less than 10 percent mean error. The Calus and Leonidopoulos model shows a behavior similar to the methanol/benzene mixture.

Figure 7 shows the comparison with the data of Jungnickel et al. (1979) for R-22/R-12 refrigerant mixtures for three different pressures. The agreement between the proposed method and data is very good at higher pressures. At low pressure, however, the proposed method predicts a lower value of heat transfer coefficient. The Calus–Leonidopoulos (1974) model consistently overpredicts over the entire range. To investigate the pressure effect further, the correlation of Fujita et al. (1996) is also shown in Fig. 7. Their correlation does well for the low-pressure data, but overpredicts considerably at higher pressures. It was not possible to make any conclusive comments on these trends.

Figure 8 shows the comparison with the R-23/R-13 data of Jungnickel et al. (1979). For this set, the present model is able to predict the heat transfer coefficient quite well for high as well as low-pressure data sets, with an average error of less than 15 percent. The Calus and Leonidopoulos (1974) model is unable to predict the mixture effects in the entire range.

7 Conclusions

The following conclusions are drawn from the present work:

1 The ideal heat transfer coefficient, $\alpha_{PB,B,id}$, used by earlier investigators does not truly represent the pool boiling heat trans-

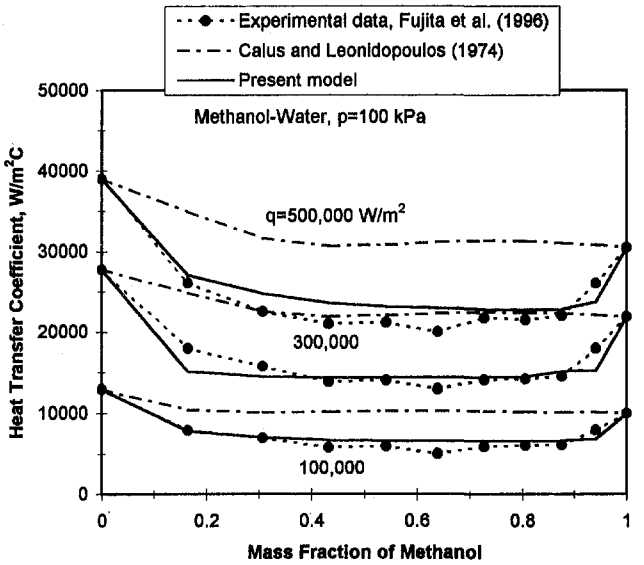

Fig. 6 Comparison of present model and Calus and Leonidopoulos (1974) Model with experimental data of Fujita et al. (1996) methanol/water, p = 100 kPa

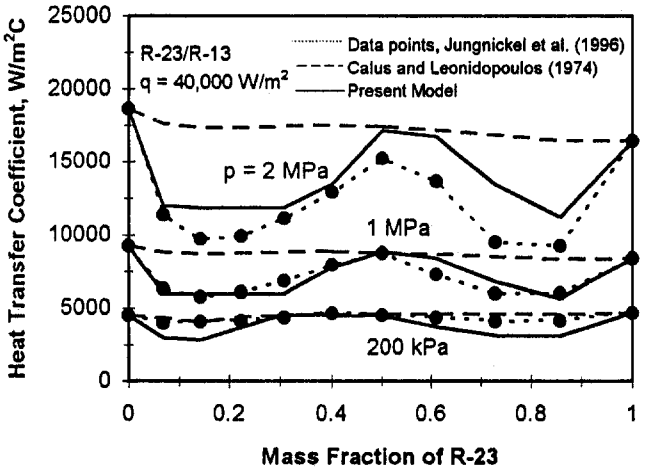

Fig. 8 Comparison of present model and Calus and Leonidopoulos (1974) model with experimental data of Jungnickel et al. (1979), R-23/R-13, q = 40 kW/m²

fer of binary mixtures before incorporating mass diffusion effects. A new pseudo-single component pool boiling heat transfer coefficient, $\alpha_{PB,B,psc}$, is proposed to account for the property effects in binary mixtures.

2 A theoretical model is developed to calculate the equilibrium concentrations at the interface of a bubble as it approaches the asymptotic growth condition. This is a major improvement over Schlünder's (1982) model, which assumes a constant value of the mass transfer coefficient in the liquid at the interface.

3 The heat transfer coefficient for the binary mixtures is derived, based solely on theoretical considerations, by applying the transient one-dimensional model for heat and mass transfer at the liquid–vapor interface of a bubble under diffusion-controlled growth conditions. In the region where both heat and mass transfer effects are important, a volatility parameter V_1, represented by $V_1 = (\kappa/D_{12})^{0.5}(c_p/\Delta h_{LG})(|(y_1 - x_1)dT/dx_1|)$, is utilized to represent the mixture effects.

4 The present model is compared with the other theoretical model available in the literature by Calus and Leonidopoulos (1974) for five data sets covering a wide range of volatility difference and boiling temperature range, including azeotropic combinations. The Calus–Leonidopoulos model is unable to predict the heat transfer coefficients and their trends accurately, generally overpredicting in the entire range. The present model is able to predict the heat transfer coefficient quite well, comparable to one of the latest empirical methods proposed in literature by Fujita et al. (1996), developed using the same data sets as used in the present comparison.

5 The final expression for the present model is given by Eq. (26) in conjunction with Eqs. (26), (13), (12), (7)–(11), (34), (35), (25), and (21)–(23). The procedure for calculation is outlined in section 4 under usage of the equations.

6 It is recommended in future to incorporate the effects resulting from the changes in the nucleation characteristics with binary mixtures by conducting experimental as well as analytical work in this area.

Acknowledgments

The author is thankful to Dr. Vijay Srinivasan of Praxair, Inc., Tonawanda, NY, for his help in mixture property evaluation using HYSIM property routines.

References

Calus, W. F., and Rice, P., 1972, "Pool Boiling—Binary Liquid Mixtures," *Chem. Engng. Sci.,* Vol. 27, pp. 1687–1697.

Calus, W. F., and Leonidopoulos, D. J., 1974, "Pool Boiling—Binary Liquid Mixtures," *Int. J. Heat Mass Transfer,* Vol. 17, pp. 249–256.

Fujita, Y., and Tsutsui, M., 1994, "Heat Transfer in Nucleate Pool Boiling of Binary Mixtures," *Int. J. Heat Mass Transfer,* Vol. 37, pp. 291–302.

Fujita, Y., Bai, Q., and Tsutsui, M., 1996, "Heat Transfer of Binary Mixtures in Nucleate Pool Boiling," *2nd Eur. Therml. Sci. and 14th UIT Nat. Heat Trans. Conf.,* Celata, G. P., Di Marco, and Mariani, A., eds., pp. 1639–1646.

Gorenflo, D., 1984, *Behältersieden,* Kap. Ha., VDI-Wärmeatlas, 4. Aufl., VDI-Verlag, Düsseldorf.

Gorenflo, D., Blein, P., Herres, G., Rott, W., Schömann, H., and Solol, P., 1988, "Heat Transfer at Pool Boiling of Mixtures With R-22 and R-114," *Rev. Int. Froid,* Vol. 11, 257–263.

HYSIM, Version 6, 1996, Hyprotech Ltd., Calgary, Alberta, Canada.

Jungnickel, H., Wassilew, P., and Kraus, W. E., 1979, "Investigation on the Heat Transfer of Boiling Binary Refrigerant Mixtures," *Proc. XVth Int. Cong. Refrig.,* Vol. II, pp. 525–536.

Kandlikar, S. G., Bijlani, C. A., and Sukhatme, S. P., "Predicting the Properties of R-22 and R-12 Mixtures—Transport Properties," *ASHRAE Transactions,* Vol. 81, Part 1, 1975.

Mikic, B. B., and Rohsenow, W. M., 1969, "Bubble Growth Rates in Non-uniform Temperature Field," *Progress in Heat and Mass Transfer,* Vol. II, pp. 283–293.

NIST, 1995, *REFPROP,* National Institute for Science and Technology, Washington, DC.

Rohsenow, W. M., 1952, "A Method of Correlating Heat Transfer Data for Surface Boiling Liquids," *Trans. ASME,* Vol. 74, p. 969.

Schlünder, E. U., 1982, "Heat Transfer in Nucleate Pool Boiling of Mixtures," *Proc. 7th Int. Heat Transfer Conf.,* Vol. 4, pp. 2073–2079.

Scriven, L. E., 1959, "On the Dynamics of Phase Growth," *Chem. Engng. Sci.,* Vol. 10, pp. 1–13.

Stephan, K., and Körner, M., 1969, "Berechnung des Wärmeübergangs Verdamp Fender Binärer Flüssigkeitsgemische," *Chemie Ing. Techn.,* Vol. 41, pp. 409–417.

Stephan, K., and Abdelsalam, M., 1980, "Heat Transfer Correlations for Natural Convection Boiling," *Int. J. Heat Mass Transfer,* Vol. 23, pp. 73–87.

Taylor, R., and Krishna, P., 1993, *Multicomponent Mass Transfer,* Wiley, New York.

Thome, J. R., 1983, "Prediction of Binary Mixture Boiling Heat Transfer Coefficients Using Only Phase Equilibrium Data," *Int. J. Heat Mass Transfer,* Vol. 26, pp. 965–974.

Thome, J. R., and Shakir, S., 1987, "A New Correlation for Nucleate Pool Boiling of Binary Mixtures," *AIChE Symp. Ser.,* Vol. 83, pp. 46–51.

Van Stralen, S., 1967, "The Mechanism of Nucleate Boiling in Pure Liquids and Binary Mixtures," *Int. J. Heat Mass Transfer,* pp. 990–1046, 1469–1498.

Van Stralen, S., 1979, "Growth Rate of Vapor and Gas Bubbles," Chap. 7, *Boiling Phenomena,* Van Stralen, S., and Cole, R., eds., Hemisphere Publishing Corp., USA.

Vignes, A., 1966, "Diffusion in Binary Solutions," *Ind. Eng. Chem. Fundam.,* Vol. 5, pp. 189–199.

Wenzel, U., Balzer, F., Jamialahmadi, M., and Müller-Steinhagen, H., 1995, "Pool Boiling Heat Transfer Coefficients for Binary Mixtures of Acetone, Isopropanol, and Water," *Heat Tr. Engng.,* Vol. 16, pp. 36–43.

Wilke, C. R., and Chang, P., 1955, "Correlation of Diffusion Coefficients in Dilute Solutions," *AIChE J.,* Vol. 1, pp. 264–270.

Boiling Heat Transfer With Binary Mixtures: Part II—Flow Boiling in Plain Tubes

S. G. Kandlikar
Mechanical Engineering Department,
Rochester Institute of Technology,
Rochester, New York 14623-5604

Flow boiling heat transfer with pure fluids comprises convective and nucleate boiling components. In flow boiling of binary mixtures, in addition to the suppression effects present in pool boiling, the presence of flow further modifies the nucleate boiling characteristics. In the present work, the flow boiling correlation by Kandlikar (1990, 1991b) for pure fluids is used as the starting point, and the mixture effects derived in Part I (Kandlikar, 1998) of this paper are incorporated. Three regions are defined on the basis of a volatility parameter, $V_l = (c_p/\Delta h_{LG})(\kappa/D_{12})^{1/2}|(y_l - x_l)dT/dx_l|$. They are: region I—near azeotropic, region II—moderate diffusion-induced suppression, and region III—severe diffusion-induced suppression. The resulting correlation is able to correlate over 2500 data points within 8.3 to 13.3 percent mean deviation for each data set. Furthermore, the $\alpha-x$ trend is represented well for R-12/R-22, R-22/R-114, R-22/R-152a, R-500, and R-132a/R-123 systems. Electrically heated stainless steel test sections as well as fluid-heated copper test sections are both covered under this correlation.

1 Introduction

Heat transfer in flow boiling of binary mixtures is receiving increasing attention in the refrigeration industry as refrigerant mixtures are being evaluated to replace the conventional pure refrigerants. The advantages of using refrigerant mixtures over pure refrigerants include the improvement of coefficient of performance, better match with the product thermal load, and safer, environmentally friendly refrigerants. The pure refrigerant systems in reality contain binary mixtures with the presence of dissolved oil. While ternary refrigerants (four components with oil) are currently being tested as potential replacements, a fundamental understanding of binary systems is essential before attempting multicomponent heat transfer modeling. Among other applications, chemical, petrochemical and process industry applications of binary mixtures are noteworthy.

2 Review of Literature

There are relatively few studies available in the open literature on modeling the flow boiling heat transfer compared to those on pool boiling of binary mixtures. Table 1 provides a summary of some of the available correlations. One of the early developments was proposed by Calus et al. (1973) who extended the pool boiling suppression factor derived by Calus and Rice (1972). Calus et al. modified an existing flow boiling correlation, which included only the convective term, and introduced an additional correction factor to account for the rise in the saturation temperature at the liquid–vapor interface of a bubble. As their correlation did not include a nucleate boiling term, it underpredicted the results considerably at higher heat flux.

Bennett and Chen (1980) presented a correlation scheme based on the Chen (1966) correlation. The convective component was modified to incorporate the bubble interface temperature. The suppression factor suggested by Calus and Leonidopoulos (1974) for pool boiling was introduced in the nucleate boiling term with some modifications. The mass transfer coefficient in the liquid near a bubble interface was calculated from a correlation with the same form as the Dittus–Boelter correlation for heat transfer, but employing the Sherwood and Schmidt numbers and the same values of constants, although these constants were obtained independently from their own data sets. Jung (1988) found that the Chen correlation overpredicted the heat transfer coefficient for pure refrigerants, and the Bennett and Chen correlation was unable to correlate the heat transfer data for refrigerant mixtures.

Jung (1988) conducted an extensive study on the flow boiling of refrigerant mixtures of R-12/R-152*a*, including azeotrope R-500, and R-22/R-114. He developed a correlation shown in Table 1, using an ideal heat transfer coefficient for mixtures in flow boiling, similar to that employed for pool boiling by earlier investigators. This approach implicitly incorporates the convective component of flow boiling in the averaging scheme. Jung's correlation utilizes the phase equilibrium data, and critical pressure and temperature, along with 25 constants, which were determined empirically from their own experimental data sets.

Kandlikar (1991a) extended his earlier pure component flow boiling correlation (Kandlikar, 1990) to binary mixtures as shown in Table 1. It was postulated that only the nucleate boiling component would be affected in binary systems due to diffusion effects, which were modeled after a semi-empirical approach proposed by Calus and Rice (1972) for pool boiling. The results were satisfactory when compared to Jung's (1988) data. However, with the availability of new data sets, it was seen that the Kandlikar (1991a) correlation for binary mixtures yielded larger errors, usually underpredicting the mixture effects. One of the main reasons was the inability of the underlying Calus and Rice's suppression model to predict the severe suppression seen for mixtures with large volatility differences as shown in Part I.

3 Objectives of the Present Work

From this discussion it can seen that there is a need for developing a flow boiling correlation applicable to binary systems and azeotropes, particularly with the current interest in refrigerant mixtures. The present work is aimed toward incorporating the pool boiling model developed in Part I of this paper in a flow boiling model for binary mixtures. The new model is

Contributed by the Heat Transfer Division and presented at the National Heat Transfer Conference, Baltimore, Maryland, August 8–12, 1997. Manuscript received by the Heat Transfer Division November 19, 1996; revision received January 30, 1998. Keywords: Boiling, Evaporation, Phase-Change Phenomena. Associate Technical Editor: M. S. Sohal.

Table 1 Summary of available methods for predicting binary flow boiling heat transfer

Authors (Year)	Correlation	Comments
Calus et al. (1973)	$(\alpha_{TP}/\alpha_L) = 0.065(1/X_{tt})T_{sat}/\Delta T_{sat})(\sigma_{water}/\sigma_L^*)^{0.9}F^{0.6}$; $F = 1-(y_1-x_1)(c_{p,L}/h_{LV})(\kappa/D_{12})^{0.5}(dT/dx_1)$	Considers only convective contribution, large errors are seen when nucleate boiling is present.
Bennett and Chen (1980)	$\alpha_{TP}/\alpha_{LO} = \{[(dP/dz)_{2\phi}/(dP/dz)_L](\mathrm{Pr}_L+1)/2\}^{0.444}[\Delta T_m/\Delta T_s]+$ $0.00122(\lambda_L^{0.79}c_{p,L}^{0.45}\rho_L^{0.49}g_c^{0.25})/(\sigma^{0.5}\mu_L^{0.29}h_{LV}^{0.24}\rho_V^{0.24})(\Delta T_{sat})^{0.24}(\Delta P_{sat})^{0.75}S_B\mathrm{Re}_{2\phi}^{0.99}$; $S_B = [1-(c_{p,L}/h_{LV})(y_1-x_1)(dT/dx_1)(\kappa/D_{12})]^{0.5}S$; $[\Delta T_m/\Delta T_s] = 1-(1-y_1)(\dot{q}/\Delta T_s)(dT/dx_1)\big\vert_p;\alpha_m = 0.023(\mathrm{Re}_{2\phi})^{0.8}(\mathrm{Sc})^{0.4}\rho_L D_{12}/d$; $\mathrm{Re}_{2\phi} = \mathrm{Re}_L\{[(dP/dz)_{2\phi}/(dP/dz)_L](\mathrm{Pr}_L+1)/2\}^{0.555}$; S – Chen(1966) *Suppression factor, function of* $\mathrm{Re}_{2\phi}$	Mass transfer analogy employed to predict the suppression in nucleate boiling. Convective component modified through a temperature difference correction term.
Jung (1988)	$\alpha_{TP} = (N/C_{UN})\alpha_{UN} + C_{me}F_p\alpha_L$ $N = 4048X_{tt}Bo^{1.13}$ *for* $X_{tt} < 1$; $N = 2-0.1\ X_{tt}^{-0.28}Bo^{-0.33}$ *for* $1 \le X_{tt} \le 5$; $\alpha_{SA} = 207(\lambda_L/b_d)(q\,b_d/(\lambda_L T_{sat}))^{0.674}(\rho_V-\rho_L)^{0.581}\mathrm{Pr}_L^{0.533}$; $b_d = 0.0146\beta\{2\sigma/[g((\rho_V-\rho_L)]\}^{0.5}$ *with* $\beta = 35°$; $F_p = 2.37(0.29+1/X_{tt})^{0.85}$; $C_{UN} = [1+(b_2+b_3)(1+b_4)(1+b_5)$; $b_2 = (1-\tilde{x}_1)\ln[(1.01-\tilde{x}_1)/(1.01-\tilde{y}_1)]+\tilde{x}_1\ln(\tilde{x}_1/\tilde{y}_1)+\lvert\tilde{x}_1-\tilde{y}_1\rvert^{1.5}$; $b_3 = 0$ *for* $\tilde{x}_1 \ge 0.01$; $b_3 = (\tilde{x}_1/\tilde{y}_1)^{0.1}-1$ *for* $\tilde{x}_1 < 0.01$; $b_4 = 1.52(p/p_{cmnc})^{3.9}$; $b_5 = 0.92\lvert\tilde{x}_1-\tilde{y}_1\rvert^{0.001}(p/p_{cmnc})^{0.66}$; $x_1/y_1 = 1$ *for* $x_1 = y_1 = 0$; $\alpha_{UN} = \alpha_l/C_{UN}$; $\alpha_l = [\tilde{x}_1/\alpha_1+x_2/\alpha_2]^{-1}$; $C_{me} = 1-0.35\lvert\tilde{x}_1-\tilde{y}_1\rvert^{1.56}$	The ideal mixture α concept for pool boiling is extended for flow boiling. It causes the averaging of the convection contribution as well from the pure component flow boiling α values. A large number of empirically determined constants are introduced.
Kandlikar (1991)	$\alpha_{TP,B} = \alpha_{Conv} + \dfrac{\alpha_{Nucl}}{\left[1+\lvert y_1-x_1\rvert(\kappa/D_{12})^{1/2}\right]^{0.7}}$ α_{Conv} and α_{Nucl} obtained from Kandlikar (1990) correlation for flow boiling	The nucleate boiling term was modified to account for the mixture effects.

tested with the experimental data available from five different sources covering a broad range of variables. The parametric trends in the flow boiling heat transfer with binary mixtures are also investigated.

4 Development of a Flow Boiling Model for Mixtures

4.1 Pure Component Correlation (Kandlikar, 1990). In developing the present model, the Kandlikar (1990) correlation is used as the starting point. This correlation was able to represent the dependence of α on quality x, mass flux G, and heat flux q. The flow boiling correlation for pure fluids is as follows:

$$\alpha_{TP} = \text{larger of} \begin{cases} \alpha_{TP,\mathrm{NBD}} \\ \alpha_{TP,\mathrm{CBD}} \end{cases} \quad (1)$$

The subscripts NBD and CBD in Eq. (1) refer to the nucleate boiling dominant and the convective boiling dominant regions, for which the respective α_{TP} are given by:

$$\alpha_{TP,\mathrm{NBD}} = 0.6683Co^{-0.2}(1-x)^{0.8}\alpha_{LO} + 1058.0Bo^{0.7}(1-x)^{0.8}F_{Fl}\alpha_{LO} \quad (2)$$

and

$$\alpha_{TP,\mathrm{CBD}} = 1.136Co^{-0.9}(1-x)^{0.8}\alpha_{LO} + 667.2Bo^{0.7}(1-x)^{0.8}F_{Fl}\alpha_{LO} \quad (3)$$

Additionally, for horizontal tubes with Froude number, $\mathrm{Fr}_{\mathrm{LO}}$, less than 0.04, a multiplier $(25\mathrm{Fr}_{\mathrm{LO}})^{0.324}$ is applied to the first terms in Eqs. (2) and (3). For $\mathrm{Fr}_{\mathrm{LO}} > 0.04$, and for vertical tubes no correction is needed. This correction is usually not needed for the range of mass fluxes employed in the refrigerant evaporators.

F_{Fl} in Eqs. (2) and (3) is a fluid-surface parameter related to the nucleation characteristics. Table 2 lists its value for several refrigerants. The single-phase heat transfer coefficient, α_{LO}, is obtained from the Petukhov and Popov (1963), and Gnielinski (1976) correlations, as suggested later by Kandlikar (1991b).

Petukhov and Popov (1963) for $0.5 \le \mathrm{Pr}_{\mathrm{L}} \le 2000$ *and* $10^4 \le \mathrm{Re}_{\mathrm{LO}} \le 5 \times 10^6$:

$$\mathrm{Nu}_{\mathrm{LO}} = \alpha_{LO}D/\lambda_L = \mathrm{Re}_{\mathrm{LO}}\,\mathrm{Pr}_{\mathrm{L}}(f/2)/[1.07 + 12.7(\mathrm{Pr}_{\mathrm{L}}^{2/3}-1)(f/2)^{0.5}] \quad (4a)$$

Gnielinski (1976) for $0.5 \le \mathrm{Pr}_{\mathrm{L}} \le 2000$ *and* $2300 \le \mathrm{Re}_{\mathrm{LO}} < 10^4$:

$$\mathrm{Nu}_{\mathrm{LO}} = \alpha_{LO}D/\lambda_L = (\mathrm{Re}_{\mathrm{LO}}-1000)\,\mathrm{Pr}_{\mathrm{L}}(f/2)/[1.0 + 12.7(\mathrm{Pr}_{\mathrm{L}}^{2/3}-1)(f/2)^{0.5}] \quad (4b)$$

Nomenclature

Bo = boiling number = $q/(G\Delta h_{LG})$
c_p = specific heat, J/kg K
Co = convection number = $(\rho_G/\rho_L)^{0.5}((1-x)/x)^{0.8}$
D = diameter of tube, m
D_{12} = diffusion coefficient of component 1 in mixture of 1 and 2
D_{12}^0, D_{12}^0 = diffusion coefficient of component 1 present in infinitely low concentration of liquid mixture
f = friction factor
F_D = diffusion factor = α/α_{id}
F_{Fl} = fluid-surface parameter, values listed in Table 2
$\mathrm{Fr}_{\mathrm{LO}}$ = Froude number with all flow as liquid = $G^2/(\rho^2 gD)$
G = mass flux, kg/m^{2}s
g = = $(x_1 - x_{1,s})/(y_{1,s} - x_{1,s})$
Δh_{LG} = latent heat of vaporization, J/kg
Ja_0 = modified Jakob number, defined by Eq. (12)
M = molecular weight
q = heat flux, W/m^2
Pr = Prandtl number = $c_p\eta/\kappa$
Re = Reynolds number = GD/η
T = temperature, K
ΔT_s = $(T_s - T_{\mathrm{sat}})$, K
$v_{m,1}$, $v_{m,2}$ = molar specific volume of components 1 and 2, m^3/kg-mol
V_1 = volatility parameter, defined by Eq. (6)
x = quality
x_1, x_2 = mass fraction of components 1 and 2 in liquid phase
y_1, y_2 = mass fraction of components 1 and 2 in vapor phase
$\tilde{x}_1$, $\tilde{x}_2$ = mole fraction of components 1 and 2 in liquid phase
α = heat transfer coefficient, W/m^2 K
η = viscosity, kg/m s
κ = thermal diffusivity, m^2/s
λ = thermal conductivity, W/m K
ρ = density, kg/m^3
σ = surface tension, N/m
ϕ = association parameter of the solvent

Subscripts

1, 2 = components of a binary system; 1 = more volatile component
B = binary
CBD = convective boiling dominant
D = mass diffusion
G = vapor
id = ideal
L = liquid
LG = latent quantity
LO = entire flow as liquid
m = mixture
NBD = nucleate boiling dominant
PB = pool boiling
psc = pseudo-single component
s = liquid-vapor interface of a bubble
sat = saturation
TP = two-phase

Table 2 Fluid-surface parameter F_{Fl} for refrigerants in copper or brass tubes

Fluid	F_{Fl}
Water	1.00
R-11	1.30
R-12	1.50
R-13B1	1.31
R-22	2.20
R-113	1.30
R-114	1.24
R-124	1.9
R-134a	1.63
R-152a	1.10

For all fluids in stainless steel tubes, F_{Fl}=1.0

The friction factor in Eqs. (4*a*) and (4*b*) is given by

$$f = [1.58 \ln (\mathrm{Re}_{LO}) - 3.28]^{-2} \quad (5)$$

The first terms in Eqs. (2) and (3) for the NBD and CBD regions, respectively, represent the convective components, while the second terms, which include the heat flux, represent the nucleate boiling component. The demarcation between the NBD and CBD regions is made automatically by comparing α_{TP} predicted by Eqs. (2) and (3), respectively, and taking the larger of the two as indicated by Eq. (1).

4.2 Pool Boiling Model for Mixtures From Part I. The mixture effect in the nucleate boiling is derived on the basis of the diffusion-induced suppression factor F_D presented in Part I of this paper. A volatility parameter V_1 is used to distinguish between the regions where the diffusion effects are significant and where they are small as in azeotropic systems.

$$V_1 = \frac{c_{p,L}}{\Delta h_{LG}} \left(\frac{\kappa}{D_{12}}\right)^{0.5} \frac{dT}{dx_1} (y_1 - x_1) \quad (6)$$

The diffusion-induced suppression factor F_D in pool boiling is given by the following equation. For $V_1 > 0.005$,

$$F_D = 0.678 \left(\frac{1}{1 + \left(\frac{c_{p,L}}{\Delta h_{LG}}\right)\left(\frac{\kappa}{D_{12}}\right)^{1/2} \frac{\Delta T_s}{g}}\right) \quad (7)$$

and for $0 < V_1 \leq 0.005$,

$$F_D = 1 - 64.0 V_1 \quad (8)$$

The bubble interface concentration is given by:

$$x_{1,s} = x_1 - (2.13/\pi)\mathrm{Ja}_0(\kappa/D_{12})^{1/2}(\rho_G/\rho_L)(y_{1,s} - x_1) \quad (9)$$

where

$$g = (x_1 - x_{1,s})/(y_{1,s} - x_{1,s}) \quad (10)$$

$$\Delta T_s = T_{\mathrm{sat},s} - T_{\mathrm{sat}} \quad (11)$$

and the Jakob number for the binary system is given by

$$\mathrm{Ja}_0 = \frac{(T_W - T_{L,\mathrm{sat}})}{(\rho_G/\rho_L)[(\Delta h_{LG}/c_{p,L}) + (\kappa/D_{12})^{1/2}(\Delta T_s/g)]} \quad (12)$$

The diffusion coefficient D_{12} was calculated as follows:

$$D_{12} = (D_{12}^0)^{x_2}(D_{21}^0)^{x_1} \quad (13)$$

D_{12}^0 and D_{21}^0 in this equation are self-diffusion coefficients given by

$$D_{12}^0 = 1.1782 \times 10^{-16} \frac{(\phi M_2)^{1/2} T}{\eta_{L,2} V_{m,1}} \quad (14)$$

ϕ is the association factor for the solvent (2.26 for water, 1.9 for methanol, 1.5 for ethanol, 1.9 for ethylene glycol, and 1.0 for unassociated solvents, including benzene, methane, and refrigerants).

4.3 Flow Boiling Model for Binary Mixtures. The diffusion-induced suppression factor F_D given by Eq. (7) is derived for pool boiling. Before this factor can be applied to the nucleate boiling component in flow boiling, a valuable insight is obtained from a plot of wall superheat versus heat transfer coefficient obtained by Kandlikar and Raykoff (1997), shown in Fig. 1. The experiments were conducted with subcooled flow of water/ethylene glycol solutions over a flat 9.5 mm circular heater placed flush on the lower wall of a 3 mm × 40 mm horizontal flow channel. Figure 1 shows the variation of heat transfer coefficient with wall superheat for pure water, and for 20–80 percent mass concentration of water/ethylene glycol solution. The heat transfer coefficient with pure water is almost constant at lower values of wall superheat. Nucleation begins at ONB (onset of nucleate boiling), and α increases slowly with wall superheat. This region is similar to the CBD region. Beyond a certain value of wall superheat, α begins to rise rapidly due to increased nucleation activity, and this region corresponds to the NBD region. The results for the aqueous ethylene glycol solution, also shown in Fig. 1, indicate the same trend of slowly increasing α in the CBD region, but the sharp increase in α corresponding to the NBD region is not seen even for a superheat of 33°C. This shows that the nucleate boiling dominant region is not present, or pushed significantly toward the higher wall superheats for binary mixtures. Therefore, it can be surmised that the convective mechanism is the dominant mechanism in flow boiling of binary mixtures.

From this discussion, it can be concluded that the CBD region extends into considerably higher values of wall superheats for flow boiling of binary mixtures. For conditions near azeotropic compositions, the pure component correlation should, however, hold good. For the conditions where the mixture effects are significant, the diffusion-induced suppression factor could be

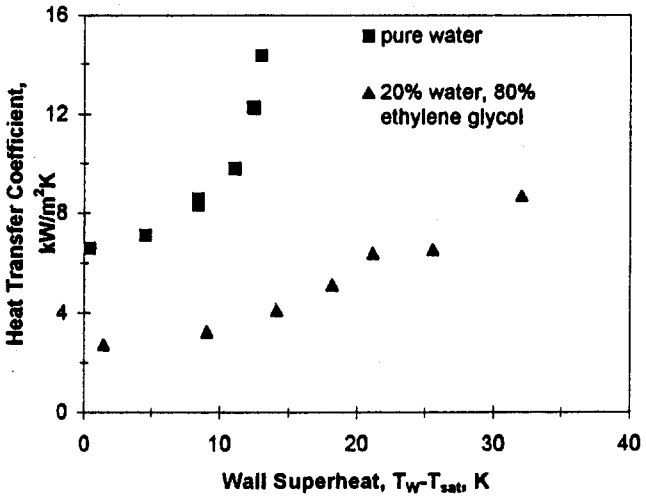

Fig. 1 Heat transfer characteristics of water/ethylene glycol solution under subcooled flow boiling, flow velocity = 0.4 m/s in 3 mm × 40 mm rectangular channel (Kandlikar and Raykoff, 1997)

applied to the nucleate boiling component in the CBD region correlation. The volatility parameter, V_1, given by Eq. (6), derived for pool boiling of binary mixtures, is again utilized here to define three regions with different levels of diffusion-induced suppression. The criteria identifying these regions are obtained by analyzing over 2500 data points for five different binary systems reported by five investigators. Table 3 gives the details of the experimental conditions and ranges of parameters for these data sources. The data contains the entire range of concentrations, including the azeotropes of R-12/R-22 and R-12/R-152a.

The following correlation is presented to predict the flow boiling of binary mixtures. The properties of the mixtures at saturation are employed in the following equations.

Flow Boiling Correlation for Binary Mixtures

Region I: Near-azeotropic region; $V_1 < 0.03$,

$$\alpha_{TP,B} = \text{larger of} \begin{cases} \alpha_{TP,B,\text{NBD}} \\ \alpha_{TP,B,\text{CBD}} \end{cases} \quad (15)$$

In this region, the general correlation for pure fluids is applicable. $\alpha_{TP,\text{NBD}}$ and $\alpha_{TP,\text{CBD}}$ are obtained from Eqs. (2) and (3), respectively, using the mixture properties. The fluid-surface parameter is obtained as the mass fraction-averaged value given by the following equation:

$$F_{Fl} = x_1 F_{Fl,1} + x_2 F_{Fl,2} \quad (16)$$

Table 2 lists F_{Fl} for different refrigerants flowing in copper or brass tubes. F_{Fl} for all liquids in stainless steel tubes is 1.0.

The near-azeotrope region covers azeotropes and low-volatility difference mixtures. Although the nucleate boiling may be slightly affected for these mixtures, its effect on the flow boiling heat transfer coefficient is insignificant.

Region II. Moderate diffusion-induced suppression region, $0.03 < V_1 < 0.2$, and $Bo > 1E-4$,

$$\alpha_{TP,B} = \alpha_{\text{CBD},B} = 1.136Co^{-0.9}(1-x)^{0.8}\alpha_{LO} + 667.2Bo^{0.7}(1-x)^{0.8}F_{Fl}\alpha_{LO} \quad (17)$$

F_{Fl} for mixtures is obtained from Eq. (16). In the moderate diffusion-induced suppression region, the nucleation effects are suppressed due to the mass diffusion resistance, and the convective heat transfer becomes dominant. In the CBD region, the bubble growth is primarily limited to the early stages in the growth cycle. The correlation for the CBD region without any suppression factor is therefore able to predict this region well.

Table 3 Details of the experimental data available for flow boiling of binary mixtures

Source (Year)	Binary System	Press. (bar)	Tube/ Orient.	Mass Fraction	Quality	Heat Flux kW/m²	Mass Flux, kg/m²s
Jung et al (1988)	R-12/R-152a R-22/R-114 R-500	3.1-4.8	9 mm, SS, Hor.	0-1	0-0.9	10-45	250-720
Hihara et al. (1989)	R-12/R-22 R-22/R-114	0.23-0.83	8 mm, SS, Hor.	0-1	0-1	5.8-28.5	100-350
Takamatsu et al. (1993)	R-22/R-114	4 - 8.1	7.9 mm, Copper, Hor.	0-1, Only 0.5 1used	0-0.9	1.8-72.8	214-393
Celata et al. (1993)	R-12/R-114	10 - 30	7.57 mm, SS, Hor.	0 - 1	0 - 1	10 - 45	300 - 1800
Murata and Hashizume (1993)	R-34a/R-123	2.2 and 2.4	10.3 mm, Copper, Hor.	90/30 mole-fraction	0.1-1	10 - 30	100 - 300

Region III. Severe diffusion-induced suppression region, (a) for $0.03 < V_1 < 0.2$ and $Bo \leq 1E-4$, and (b) $V_1 \geq 0.2$,

$$\alpha_{TP,B} = 1.136Co^{-0.9}(1-x)^{0.8}\alpha_{LO} + 667.2Bo^{0.7}(1-x)^{0.8}F_{Fl}\alpha_{LO}F_D \quad (18)$$

This region covers the two ranges as indicated in (a) and (b) above. F_D is obtained from

$$F_D = 0.678[1 + (c_{p,L}/\Delta h_{LG}) \times (\kappa/D_{12})^{1/2}|(y_1 - x_1)(dT/dx_1)|]^{-1} \quad (19)$$

where dT/dx_1 is the slope of the bubble point temperature versus x_1 curve. Equation (19) is simplified from Eq. (7) to eliminate the iteration for the equilibrium concentrations at the interface. Instead, bulk liquid and vapor concentrations are used along with the slope of the bubble point curve. The error in F_D due to this simplification is small, usually less than 5 percent for the refrigerant mixtures, and F_D is applied only to the nucleate boiling term. The fluid-surface parameter F_{Fl} in these equations is obtained from Eq. (16).

The severe diffusion-induced suppressed region is dominated by the convective effects. The nucleate boiling contribution in this region is further reduced due to the large difference in composition between the two phases, and the resulting mass diffusion resistance at the liquid–vapor interface of a growing bubble.

4 Results and Discussion

Table 3 shows the details of the experimental data sets used to compare the results from the correlation. The data covers a broad range of the volatility parameter, V_1. Table 4 shows the mean deviation from each data set listed in Table 3. The ranges of Bo, Co, and V_1 for each data set are also listed in Table 4. The correlation is applicable for qualities from near zero to about 0.8. The dryout and near-dryout regions are not covered by the correlation. The properties of the mixtures are evaluated using REFPROP by NIST (1995).

It can be seen from Table 4 that the mean absolute error for each data set is between 8.3 and 13.3 percent. Additional discussion on the comparison for specific ranges of V_1 covering different suppression regions is presented in the following paragraphs.

Region I—Near-Azeotropic Region. In this region, the compositions of the two phases are nearly equal. The data by Jung et al. (1988) on azeotrope R-500 are representative of this region. R-500, which is an azeotrope of R-12 and R-152a, shows a small volatility difference, with V_1 in the range of 0.0006–0.002. Figure 2 shows a comparison between the predicted and the experimental variation of α with quality x. It can be seen that the nucleate boiling dominant region at lower x and the convective boiling dominant region at higher x are well represented by the correlation. The mean absolute error for this data set is 11.4 percent.

Some of the experimental data of Hihara et al. (1989) also fall in this region for the R-22/R-12 system. Figure 3 shows a comparison between the predicted and the experimental values. It can be seen that the trend in α versus x is well represented by the correlation showing the transition between NBD and CBD regions. No diffusion-induced suppression is observed in the entire region and the pure fluid correlation correctly represents α and its trends with x.

Region II—Moderate Diffusion-Induced Suppression Region. This region covers the range $0.03 < V_1 < 0.2$ with $Bo > 1E-4$. In this region, the nucleate boiling dominant region is not present, and the heat transfer is mainly in the CBD region. However, the diffusion-induced suppression is quite moderate, and does not affect the nucleate boiling term in the CBD region. The data of Celata et al. (1993) for R-12/R-114 falls in this

Table 4 Parameter ranges of data sources and comparison with correlation

Data source	Binary System	Bo x 10e-5	Co	V	Mean Abs. Deviation, %
Jung et al. (1988)	R-12/R-152a R-12/R-152a R-22/R-114 R-500	6.1-6.3 8.8 - 71 7.1- 77 7.5 - 77	0.52-1.8 0.01 - 1.45 0.04 - 1.39 0.01 - 1.83	0.025-0.044 0.013 - 0.022 0.1 - 0.72 0.0006 - 0.002	8.3 % 10.4 % 13.0 % 11.4 %
Hihara et al. (1989)	R-12/R-22 R-22/R-114	47 - 61 37 - 60	0.01 - 1.91 0.023- 1.64	0.015 - 0.064 0.07 - 0.67	13.3 % 9.0 %
Takamatsu et al. (1993)	R-22/R-114	19 - 76	0.018 - 3.2	0.28 - 0.54	9.2 %
Celata et al. (1993)	R-12/R-114	9.4 - 88	0.52 - 1.83	0.06 - 0.15	8.9 %
Murata and Hashizume (1993)	R-134a/R-123	20 - 185	0.004 - 0.05	0.28 - 0.34	12.1 %

region. Some of the data points from Hihara et al. (1989) for R-12/R-22 and R-22/R-114 also fall in this region.

Figure 4 shows the data from Celata et al. (1993) for R-22/R-114 obtained in an electrically heated stainless steel test section. F_{Fl} for this case is 1.0 in the entire range of concentrations. As seen from Fig. 4, the correlation is able to predict the data well. The mean absolute error with this data set is 8.9 percent. Similar observations are made with Jung's (1988) data sets for R-22/R-114 and R-22/R-152*a* mixtures employing an electrically heated stainless-steel test section. Figure 5 shows the comparison with Jung's R-12/R-152*a* data falling in the moderate diffusion-induced suppression region, with a good agreement between the observed and predicted trends.

Region III—Severe Diffusion-Induced Suppression. In this region, the nucleate boiling mechanism is strongly affected by the mass diffusion effects, and the nucleate boiling component in the CBD region is suppressed considerably. A large number of data investigated in the present work falls in this region.

Figure 6 shows Murata and Hashizume's (1989) data for R-134*a*/R-123 system. This data set is obtained using a copper tube with an electrical heater element wrapped around it. The fluid-surface parameter F_{Fl} given by equation (16) is applied for this case. Again the correlation does a good job in predicting the heat transfer coefficient in this region as well, with a mean error of 12.1 percent for the entire data set.

Figure 7 shows the data of Takamatsu et al. (1993) obtained using a copper test section exchanging heat with hot water. This

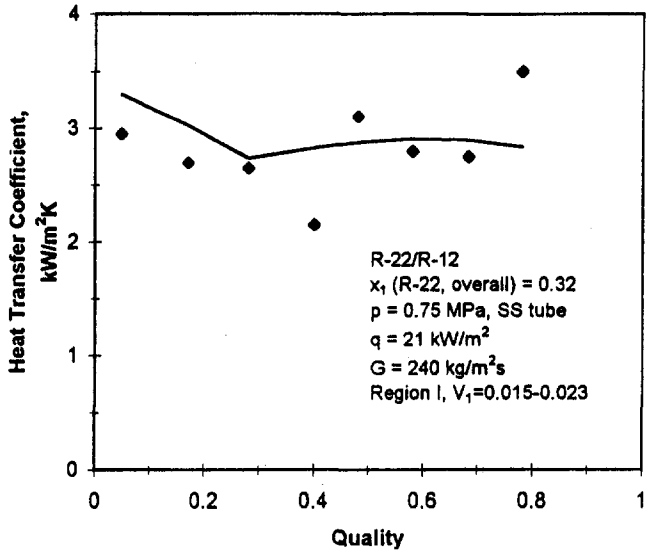

Fig. 3 Comparison of model predictions with the experimental data of Hihara et al. (1989) for *R*-22/*R*-12 in region I, near azeotropic region

corresponds to a fluid-heated test section. The fluid-dependent parameter F_{Fl} is applicable to copper and brass tubes. The correlation is able to represent this data set also quite well and the trends in α versus x are also accurately represented. The mean absolute error is seen from Table 4 to be 9.2 percent for the entire data set.

Figure 8 shows the data set Hiahara et al. (1989) for R-22/R-114 under the severe diffusion-induced suppression region. These data were obtained in an electrically heated stainless-steel test section for which $F_{Fl} = 1.0$ applies. The agreement between the correlation and the data is very good, with the mean absolute error seen from Table 4 as 9.0 percent.

Additional Comments. The experimental error in a binary system is higher than that with pure components due to additional uncertainties associated with equilibrium phase compositions. The saturation temperature along the length of the evaporator tube varies due to changing liquid and vapor compositions as well as changing pressure. Additional factors are introduced

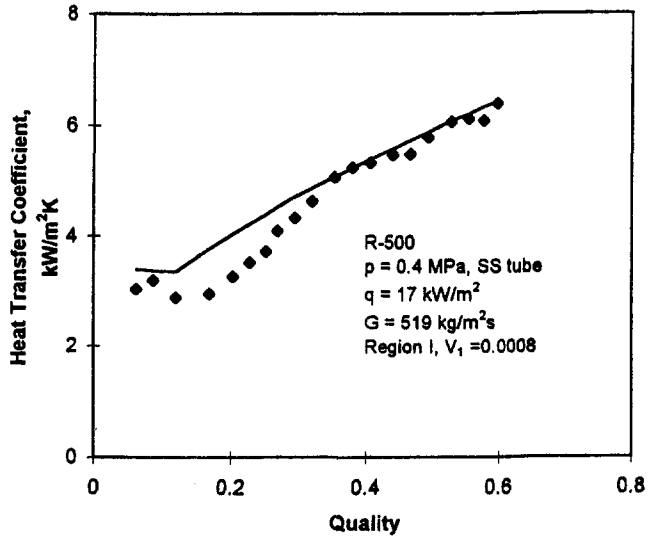

Fig. 2 Comparison of model predictions with the experimental data of Jung (1989) for *R*-500 azeotrope in region I, near azeotropic region

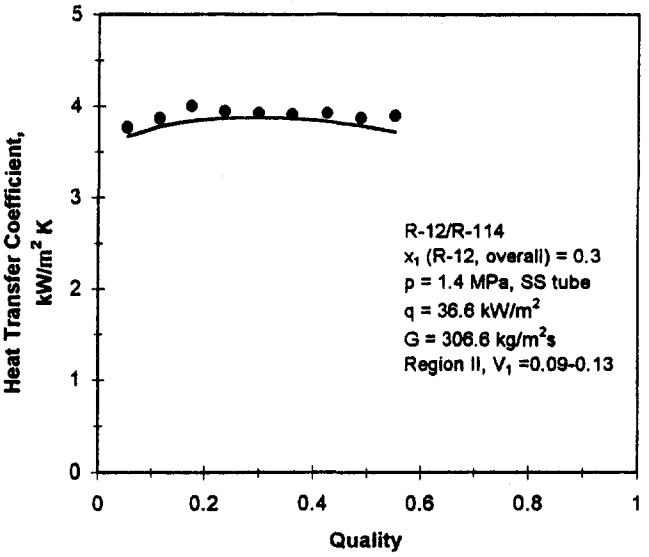

Fig. 4 Comparison of model predictions with the experimental data of Celata et al. (1993) for *R*-12/*R*-114 in region II, moderate diffusion-induced suppression region

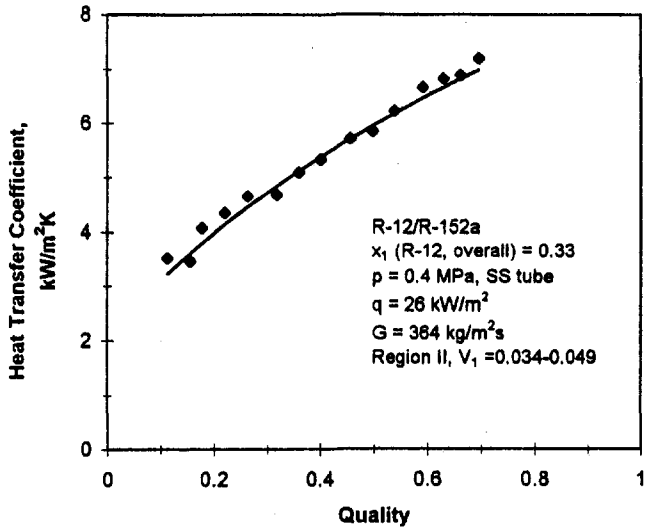

Fig. 5 Comparison of model predictions with the experimental data of Jung (1989) for *R*-12/*R*-152*a* in region II, moderate diffusion-induced suppression region

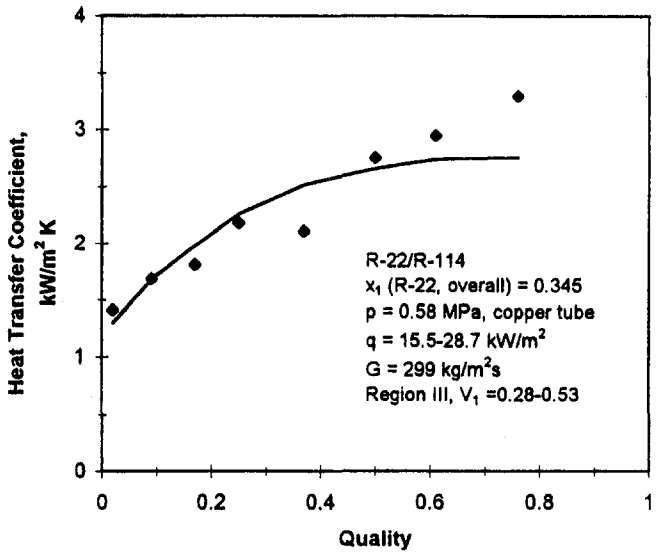

Fig. 7 Comparison of model predictions with the experimental data of Takamatsu et al. (1993) for *R*-22/*R*-114 in region III, severe diffusion-induced suppression region; data obtained from a water-refrigerant heat exchanger

by the fluid heated or electrically heated test sections, and stainless steel or copper tubes. The present correlation is still able to predict well for all these cases.

Another comment may be made regarding a somewhat larger error associated with the first one or two thermocouple locations in many experimental data sets. The heat transfer coefficients measured at these locations are much lower than those at the subsequent locations. The main reason for this is believed to be the delay in initiating nucleation with binary mixtures as the flow enters the heated test section. The nucleation characteristics are also believed to be affected for mixtures and additional work in this area is warranted to quantify these effects.

5 Conclusions

1 A flow boiling correlation is developed for binary systems. It incorporates the diffusion-induced suppression factor developed in Part I of this paper. The basic correlation by Kandlikar (1990) for pure liquids is extended to cover the binary systems under three regions depending on the volatility parameter: region I—near-azeotropic region, region II—moderate diffusion-induced suppression region, and region III—severe diffusion-induced suppression region.

2 The correlation is compared with the experimental data for five binary systems of refrigerant mixtures reported in the literature. The overall absolute mean deviation for over 2500 data points is around 10 percent.

3 The trend in the heat transfer coefficient α versus quality x is well represented by the correlation in all three regions.

4 The correlation performs equally well for fluid-heated as well as electrically heated test sections. Also, the tube material effect, stainless steel or copper/brass, is well accounted by the fluid dependent parameter, which reduces to 1.0 for stainless-steel test sections.

Acknowledgments

The author gratefully acknowledges the support provided by Taavo Raykoff in the programming for data analysis.

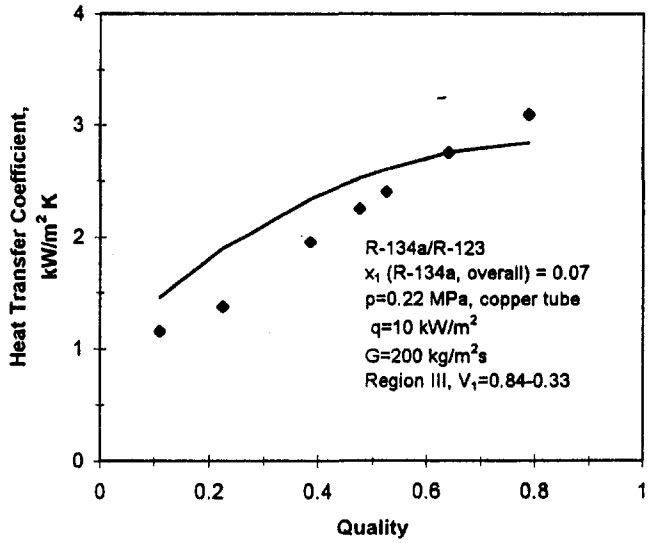

Fig. 6 Comparison of model predictions with the experimental data of Murata and Hashizume (1989) for *R*-134*a*/*R*-123 in region III, severe diffusion-induced suppression region

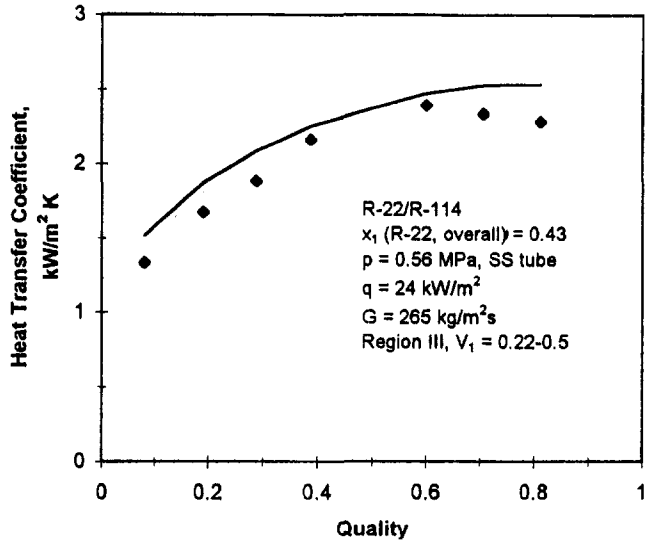

Fig. 8 Comparison of model predictions with the experimental data of Hihara et al. (1989) for *R*-22/*R*-114 in region III, severe diffusion-induced suppression region

References

Bennett, D. L., and Chen, J. C., 1980, "Forced Convective Boiling in Vertical Tubes for Saturated Pure Components and Binary Mixtures," *AIChE J.,* Vol. 26, No. 3, pp. 454–461.

Calus, W. F., and Rice, P., 1972, "Pool Boiling—Binary Liquid Mixtures," *Chemical Engineering Science,* Vol. 27, pp. 1687–1697.

Calus, W. F., di Montegnacco, A., and Kenning, D. B. R., 1973, "Heat Transfer in a Natural Circulation Single Tube Reboiler, Part II: Binary Liquid Mixtures," *The Chem. Eng. J.,* Vol. 6, pp. 251–264.

Calus, W. F., and Leonidopoulos, D. J., 1974, "Pool Boiling—Binary Liquid Mixtures," *Int. J. Heat Mass Transfer,* Vol. 17, pp. 249–256.

Celata, G. P., Cumo, M., and Setaro, T., 1993, "Forced Convective Boiling in Binary Mixtures," *Int. J. Heat Mass Transfer,* Vol. 36, No. 13, pp. 3299–3309.

Chen, J. C., 1966, "A Correlation for Boiling Heat Transfer to Saturated Fluids in Convective Flow," *Industrial and Engineering Chemistry, Process Design and Development,* Vol. 5, No. 3, pp. 322–329.

Gnielinski, V., 1976, "New Equations for Heat and Mass Transfer in Turbulent Pipe and Channel Flow," *International Chemical Engineer,* Vol. 16, pp. 359–368.

Hihara, E., Tanida, K., and Saito, T., 1989, "Forced Convective Boiling Experiments of Binary Mixtures," *JSME Int. J.,* Ser. II, Vol. 32, No. 1, pp. 98–106.

Jung, D. S., McLinden, M., Radermacher, R., and Didion, D., 1988, "Horizontal Flow Boiling Experiments With a Mixture of R-22/R-114," *Int. J. Heat Mass Transfer,* Vol. 32, No. 1, pp. 131–145.

Jung, D. S., 1988, "Horizontal Flow Boiling Heat Transfer Using Refrigerant Mixtures," Ph.D. Dissertation, University of Maryland.

Kandlikar, S. G., 1990, "A General Correlation for Saturated Two-Phase Flow Boiling Heat Transfer Inside Horizontal and Vertical Tubes," ASME JOURNAL OF HEAT TRANSFER, Vol. 112, pp. 219–228.

Kandlikar, S. G., 1991a, "Correlating Heat Transfer Data in Binary Systems," *Phase Change Heat Transfer,* Hensel, E., Dhir, V. K., Greif, R., and Fillo, J., eds., ASME HTD-Vol. 159, pp. 163–170.

Kandlikar, S. G., 1991b, "A Model for Predicting the Two-Phase Flow Boiling Heat Transfer Coefficient in Augmented Tube and Compact Heat Exchanger Geometries," ASME JOURNAL OF HEAT TRANSFER, Vol. 113, Nov., pp. 966–972.

Kandlikar, S. G., and Raykoff, T., 1997, "Investigating Bubble Characteristics and Convective Effects on Flow Boiling of Binary Mixtures," presented at the Engineering Foundation Conference on Pool and Convective Flow Boiling, Irsee, Germany, June.

Kandlikar, S. G., 1998, "Boiling Heat Transfer With Binary Mixtures: Part I— A Theoretical Model for Pool Boiling," ASME JOURNAL OF HEAT TRANSFER, Vol. 120, this issue, pp. 380–387.

Murata, K., and Hashizume, K., 1989, "Forced Convection Boiling of Nonazeotropic Refrigerant Mixtures Inside Tubes," ASME JOURNAL OF HEAT TRANSFER, Vol. 115, pp. 680–689.

NIST, 1995, REFPROP, National Institute for Science and Technology, Washington, DC.

Petukhov, B. S., and Popov, V. N., 1963, "Theoretical Calculation of Heat Exchange and Frictional Resistance in Turbulent Flow in Tubes of an Incompressible Fluid With Variable Physical Properties," *Teplofiz. Vysok. Temperatur (High Temperature Heat Physics),* Vol. 1, No. 1.

Takamatsu, H., Momoki, S., and Fujii, T., 1993, "A Correlation for Forced Convection Boiling Heat Transfer of Nonazeotropic Refrigerant Mixture of HCFC22/CFC114 in a Horizontal Smooth Tube," *Int. J. Heat Mass Transfer,* Vol. 36, No. 14, pp. 3555–3563.

Heat Transfer Characteristics in Partial Boiling, Fully Developed Boiling, and Significant Void Flow Regions of Subcooled Flow Boiling

S. G. Kandlikar
Mechanical Engineering Department,
Rochester Institute of Technology,
Rochester, NY 14623
sgkeme@rit.edu

Subcooled flow boiling covers the region beginning from the location where the wall temperature exceeds the local liquid saturation temperature to the location where the thermodynamic quality reaches zero, corresponding to the saturated liquid state. Three locations in the subcooled flow have been identified by earlier investigators as the onset of nucleate boiling, the point of net vapor generation, and the location where $x = 0$ is attained from enthalpy balance equations. The heat transfer regions are identified as the single-phase heat transfer prior to ONB, partial boiling (PB), and fully developed boiling (FDB). A new region is identified here as the significant void flow (SVF) region. Available models for predicting the heat transfer coefficient in different regions are evaluated and new models are developed based on our current understanding. The results are compared with some of the experimental data available in the literature.

1 Overview and Regions of Subcooled Flow Boiling

Consider a subcooled liquid flowing in a heated channel. As long as the channel wall is below the local saturation temperature of the liquid, heat transfer is by single-phase mode. As the wall temperature exceeds the saturation temperature, boiling can be initiated depending on the wall, heater surface, and flow conditions.

The boiling process in the subcooled flow improves the heat transfer rate considerably over the single-phase value. Subcooled flow boiling has therefore received considerable attention where high-heat-flux cooling is required, such as in emergency core cooling of nuclear reactors, first-wall cooling of fusion reactors, neutron generators for cancer therapy and material testing, high-power electronic applications, cooling of rocket nozzles, and pressurized water reactors (Bergles, 1984; Boyd, 1988).

Figure 1 shows a schematic illustrating important locations and regions of subcooled flow boiling. For the sake of simplicity, the discussion is presented for a circular tube. The discussion is valid for other geometries, and the analysis can be easily extended for other simple geometries using the concept of hydraulic diameter. Liquid enters the tube at **A** under subcooled conditions and the tube wall is below the local saturation temperature. The bulk liquid temperature and the wall temperature vary along the length of the tube. Under a constant heat flux surface boundary condition for a circular tube of diameter D, the bulk fluid temperature variation in the flow direction in the nonboiling region can be obtained from an energy balance over the tube length L. In the single-phase, fully developed, nonboiling region, the heat transfer coefficient α_l is almost constant (neglecting property variation with temperature), and the wall temperature rises linearly and parallel to the bulk liquid temperature. At location **B**, the wall temperature reaches the saturation temperature of the liquid. However, nucleation does not occur immediately, as a certain amount of wall superheat is needed to nucleate cavities existing on the wall.

The first bubbles appear on the wall at location **C**, which is identified as the *onset of nucleate boiling,* or ONB. The wall temperature begins to level off, as more nucleation sites are activated beyond ONB. Farther downstream, as more sites are activated, the contribution to heat transfer from the nucleate boiling continues to rise while the single-phase convective contribution diminishes. This region is called the *partial boiling* region. At **E** the convective contribution becomes insignificant and the *fully developed boiling,* or FDB, is established. Subsequently, the mean wall temperature remains almost constant in the FDB region until some point where the convective effects become important again due to the two-phase flow in the newly defined *significant void flow* region.

The bubbles generated at the wall immediately following ONB cannot grow due to the condensation occurring at the bubble surface exposed to the subcooled liquid flow. A thin layer of bubbles is formed on the wall. As the bulk liquid temperature increases in the flow direction, the layer becomes populated with more bubbles, whose size also increases with decreasing subcooling. At some location **G**, the bubbles eventually detach from the wall and flow toward the liquid core. Some bubbles condense along the way. Point **G** is identified as the point of *net vapor generation,* or NVG, (also called OSV, *Onset of Significant Void*), prior to which the vapor volumetric flow fraction is insignificant. Heat transfer subsequent to NVG can be considered to be in the two-phase region.

The vapor present in the subcooled flow following NVG is at the saturation temperature. This gives rise to a thermodynamic nonequilibrium condition with the liquid temperature falling below the equilibrium subcooled liquid temperature dictated by the local enthalpy. As heat addition continues downstream, the saturation condition under thermodynamic equilibrium is reached at **H**. A nonequilibrium condition exists and the true liquid temperature is indicated by a dashed line. Flow beyond **H** is covered under saturated flow boiling.

The state of the subcooled liquid can be defined in terms of an equilibrium "quality" based on the liquid enthalpy relative to the saturation state:

$$x = (h_l - h_{l,\text{sat}})/h_{lg} = -c_p \Delta T_{\text{sub}}/h_{lg} \quad (1)$$

Contributed by the Heat Transfer Division for publication in the JOURNAL OF HEAT TRANSFER. Manuscript received by the Heat Transfer Division July 18, 1997; revision received February 2, 1998. Keywords: Boiling, Evaporation, Phase-Change Phenomena. Associate Technical Editor: P. S. Ayyaswamy.

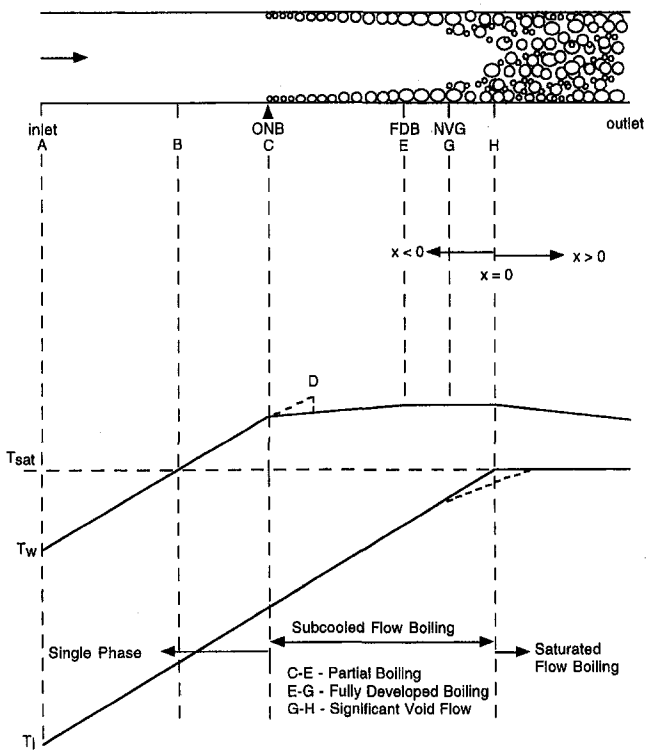

Fig. 1 Schematic representation of subcooled flow boiling

Equation (1) results in a negative quality in the subcooled region. In the single-phase region of the subcooled flow before any boiling is initiated, the heat transfer rate is expressed in terms of the single-phase liquid heat transfer coefficient and the wall-to-liquid temperature difference:

$$\dot{q} = \alpha_l(T_w - T_l) = \alpha_l(\Delta T_{sat} + \Delta T_{sub}) \qquad (2)$$

Further discussion on the heat transfer rates in different regions is presented in the following sections. Kandlikar (1997) presented a comprehensive summary of heat transfer in different regions. In the present paper, further refinements are incorporated in the nondimensionalizing of ONB criterion, and in the heat transfer models for the *fully developed subcooled flow boiling* and the *significant void flow* regions. Additional data from McAdams et al. (1949) are included in the comparison.

2 Onset of Nucleate Boiling (ONB)

As long as the wall temperature is below the local saturation temperature, nucleate boiling cannot be initiated under steady flow conditions. The bubbles are nucleated on cavities present on the heater surface and require a certain amount of wall superheat depending on the cavity size and the flow conditions. Presence of trapped gases or vapor in the cavities initiates the nucleus formation. Generally, at the beginning of the boiling process at start-up, the cavities are flooded and require a higher degree of wall superheat. Once boiling is initiated, the required superheat to sustain the bubble activity is lower due to the presence of vapor inside the cavities. This behavior is known as the hysteresis effect and is marked for highly wetting liquids such as refrigerants.

In the absence of the hysteresis effect, the nucleation criterion suggested by Hsu and Graham (1961) has shown to predict the nucleation data reasonably well by many later investigators (e.g., Kandlikar and Cartwright, 1995). Bergles and Rohsenow (1964) described the nucleation criterion graphically in terms of the tangency condition and presented an empirical correlation for the ONB condition. Hsu (1962) and Sato and Matsumura (1964) presented equations for $\Delta T_{sat,ONB}$ and $\dot{q}_{ONB}$:

$$\Delta T_{sat,ONB} = \frac{4\sigma T_{sat} v_{lg} \alpha_l}{\lambda_l h_{lg}} \left[1 + \sqrt{1 + \frac{\lambda_l h_{lg} \Delta T_{sub}}{2\sigma T_{sat} v_{lg} \alpha_l}} \right] \qquad (3)$$

and

$$\dot{q}_{ONB} = [\lambda_l h_{lg}/(8\sigma v_{lG} T_{sat})][\Delta T_{sat,ONB}]^2 \qquad (4)$$

The range of active cavity radii were also presented by Hsu, and Sato and Matsumura. This equation was recently nondimen-

Nomenclature

a, b = constants in Eq. (15)
Bo = boiling number = $\dot{q}/(\dot{m}h_{lg})$
c_p = specific heat, J/kg K
C = const
D = diameter of flow channel, m
D_h = hydraulic diameter of flow channel, m
F_{fl} = fluid-surface parameter in Kandlikar (1990) correlation
f = friction factor
h = enthalpy, J/kg
h_{lv} = latent heat of vaporization, J/kg
m = constant in Eq. (17), given by Eq. (20)
$\dot{m}$ = mass flux, kg/m^{2}s
n = constant in Eq. (20), given by Eq. (22)
Nu = Nusselt number
Pr = Prandtl number
p = constant in Eq. (20), given by Eq. (21)
$\dot{q}$ = heat flux, W/m^{2}K
r_c = cavity radius
r_c^* = nondimensional cavity radius, given by Eq. (5)
Re = Reynolds number
T = temperature, K
v = specific volume, m^3/kg
x = equilibrium quality
x_a = apparent quality, given by Eq. (25)
α = heat transfer coefficient, W/m^{2}K
α^* = α based on wall superheat, W/m^{2}K
δ_t = thickness of the thermal boundary layer thickness = λ/α_1, m
ΔT_{sat} = wall superheat = $T_w - T_{sat}$, K
ΔT_{sat}^* = nondimensional wall superheat, given by Eq. (6)
ΔT_{sub} = liquid subcooling = $T_{sat} - T_l$, K
ΔT_{sub}^* = nondimensional liquid subcooling, given by Eq. (7)
λ = thermal conductivity, W/m K
μ = viscosity, N s/m^2
σ = surface tension, N/m

Subscripts

A–E = corresponding to A–E in Fig. 7.
b = bulk
cp = constant property
FDB = fully developed boiling
g = vapor
l = liquid
lo = all flow as liquid
lg = latent
NBD = nucleate boiling dominant
ONB = onset of nucleate boiling
PB = partial boiling
sat = saturated state
sub = subcooled state
SVF = significant void flow
w = wall

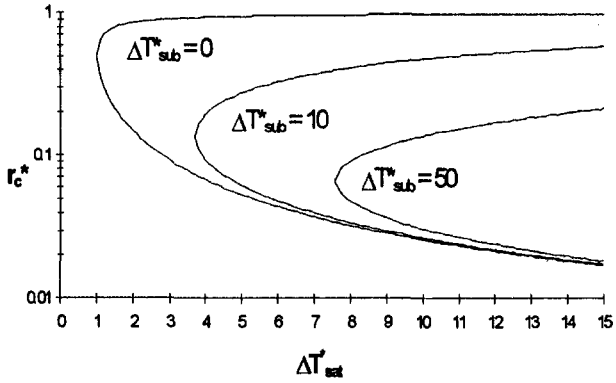

Fig. 2 Nondimensional form of nucleation criterion presented by Kandlikar and Spiesman (1997)

sionalized by Kandlikar and Spiesman (1997) by introducing the following parameters:

$$r_c^* = r_c/\delta_t \tag{5}$$

$$\Delta T^*_{sat} = \Delta T_{sat} h_{lv} \delta_t / (8\sigma T_{sat} v_{lv}) \tag{6}$$

$$\Delta T^*_{sub} = \Delta T_{sub} h_{lv} \delta_t / (8\sigma T_{sat} v_{lv}) \tag{7}$$

The nondimensional form of the active cavity range is then given by the following equation:

$$r^*_{max}, r^*_{min} = \frac{1}{2}\left[\frac{\Delta T^*_{sat}}{\Delta T^*_{sat} + \Delta T^*_{sub}} \pm \sqrt{\left(\frac{\Delta T^*_{sat}}{\Delta T^*_{sat} + \Delta T^*_{sub}}\right)^2 - \frac{1}{(\Delta T^*_{sat} + \Delta T^*_{sub})}}\right] \tag{8}$$

The properties in Eqs. (3) – (8) are evaluated at the saturation temperature and α_l is determined from an appropriate correlation incorporating the wall temperature correction factor. Figure 2 shows the nondimensional plot for the nucleation criterion given by Eq. (8) for three values of ΔT^*_{sub}. Note that $\Delta T^*_{sub} = 0$ corresponds to the saturation condition. Additional factors such as the dissolved gases and surface characteristics further affect the nucleation characteristics.

3 Fully Developed Boiling Region

After ONB, nucleation activity increases along the flow as the liquid subcooling decreases. Heat transfer is by a combination of single-phase convective, and nucleate boiling modes. At some point, heat transfer is essentially by the nucleate boiling mode with little contribution from the single-phase convective mode. This region is called *fully developed boiling* and has been studied extensively for water by earlier investigators in nuclear reactor applications. Table 1 provides a summary of some of the important work reported in literature. Jens and Lottes' (1951) correlation was one of the first ones reported with water data. Thom et al. (1965) later found that this correlation underpredicted their data and proposed a correlation recommended by Collier (1981) and Rohsenow (1985) for water. The Thom et al. correlation agrees well with the low-heat-flux data of Brown (1967) as reported by Rohsenow (1985).

Shah (1977) compiled the available experimental data on twelve fluids from fifteen different sources. The FDB and the *partial boiling* regions are not clearly identified in his correlation; instead he employs the level of subcooling relative to the wall superheat as a criterion and recommends separate correlations for the two regions. The demarcation between the two regions is made by a hand-drawn line through the data sets on a plot of $\Delta T_{sub}/\Delta T_{sat}$ versus Bo.

In the present work, the Kandlikar (1990) correlation for saturated flow boiling heat transfer is re-examined. One of the features of this correlation as reported by Kandlikar (1991) is its ability to predict the trends in α versus x in the low-quality region, explaining the reasons for increasing or decreasing α for different cases. The correlation employed the additive model of the nucleate boiling component and the two-phase convective heat transfer in the saturated boiling region. In the subcooled *fully developed boiling* region, the convective contribution is insignificant and the term representing the nucleate boiling component is expected to represent the total heat transfer coefficient. The heat transfer coefficient α^* in the *fully developed boiling* region is thus given by the following equation derived from the nucleate boiling dominant region of the Kandlikar correlation:

$$\alpha^* = 1058.0 Bo^{0.7} F_{fl} \alpha_{lo} \tag{9}$$

Note that α^* is based on the wall superheat with $q = \alpha^* \Delta T_{sat}$, $Bo = q/(\dot{m} h_{lg})$. Note that $\dot{m}$ is the total mass flux, kg/m^{2}s. F_{fl} is the fluid-surface parameter, and α_{lo} is the single-phase heat transfer coefficient for all liquid flow (same as α_l in the subcooled region) obtained from Gnielinski (1976) and Petukhov–Popov (1963) correlations along with the property correction factor recommended by Petukhov (1970):

$$\mathrm{Nu}_{lo} = \mathrm{Nu}_{lo,cp} (\mu_b/\mu_w)^{0.11} \tag{10}$$

where $\mathrm{Nu}_{lo,cp}$ is the Nusselt number with constant properties obtained from the following equations, and the subscripts b and w refer to the properties at bulk and wall temperatures, respectively.

Petukhov and Popov (1963) found, for $0.5 \le \mathrm{Pr} \le 2000$ and $10^4 \le \mathrm{Re}_{lo} \le 5 \times 10^6$:

$$\mathrm{Nu}_{lo} = \frac{\mathrm{Re}_{lo}\mathrm{Pr}_l (f/2)}{[1.07 + 12.7(\mathrm{Pr}^{2/3} - 1)(f/2)^{0.5}]} \tag{11}$$

Gnielinski (1976) found, for $0.5 \le \mathrm{Pr} \le 2000$ and $2300 \le \mathrm{Re}_{lo} < 10^4$:

$$\mathrm{Nu}_{lo} = \frac{(\mathrm{Re}_{lo} - 1000)(f/2)\mathrm{Pr}_l}{[1 + 12.7(\mathrm{Pr}^{2/3} - 1)(f/2)^{0.5}]} \tag{12}$$

where f is the friction factor given by the following equation:

$$f = [1.58 \ln (\mathrm{Re}_{lo}) - 3.28]^{-2} \tag{13}$$

The heat transfer coefficient in the FDB region of the subcooled flow is expressed in terms of the temperature difference between the wall and the fluid, or $q = \alpha^* \Delta T_{sat} = \alpha_{FDB} (\Delta T_{sub}$

Table 1 Some important correlations for fully developed heat transfer in subcooled flow boiling

Investigator Year	Fluid	Correlation	Comments
McAdams et al. (1949)	water	$q = C\,(\Delta T_{sat})^{3.86}$	Perhaps the first reported correlation for *FDB*. The constant C depends on the dissolved air content.
Jens and Lottes (1951)	water	$\Delta T_{sat} = 25\, q^{0.25} \exp(p/62)$; p - bar, q - MW/m^2, T - K	Earlier correlation, modified by later investigators.
Thom et al. (1965)	water	$\Delta T_{sat} = 22.65\, q^{0.5} \exp(p/87)$; p - bar, q - MW/m^2, T - K	$q \propto \Delta T_{sat}^2$ from the correlation, data indicates an exponent of 3, tested for low heat flux water data.
Mikic and Rohsenow (1969)	water	$q = 1.89 \times 10^{-4} \cdot g^{1/2} h_{lg}^{1/2} \rho_l^{1/2} c_{p,l}^{3/2} \rho_g^{1/2} (\Delta T_{sat})^3 / [\sigma^{3/2} (\rho_l - \rho_g)^{3/2} T_{sat}^{1/2}]$	Developed for pool boiling, includes surface effects, recommended by Rohsenow (1985) for *FDB*.
Shah (1977)	R-11, R-12, R-113, water, other fluids.	$q = [230\,(\dot{m} h_{lv})^{-0.5} \alpha_{lo} \Delta T_{sat}]^2$ α_{lo} from Dittus-Boelter correlation	$q \propto \Delta T_{sat}^2$, not supported by data; no clear distinction between *partial* and *fully developed boiling*; hand-drawn line through data to include the effect of subcooling.
Present work	water, refrigerants	$q = [1058\,(\dot{m} h_{lv})^{-0.7} F_{fl} \alpha_{lo} \Delta T_{sat}]^{10.3}$ α_{lo} from Gnielinski, and Petukhov and Popov correlations; F_{fl} - fluid-surface parameter, given by Kandlikar (1991).	Represents correct dependence of q on ΔT_{sat}; compares well with Bergles and Rohsenow's (1964), McAdams et al. (1949) and Del Valle and Kenning (1985) water data, and other refrigerant data.

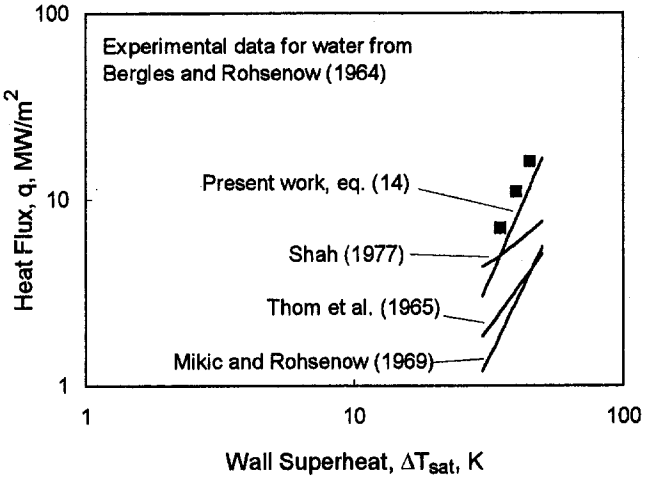

Fig. 3 Comparison of *fully developed boiling* correlations with experimental data from Bergles and Rohsenow (1964); subcooled water, 4.5 m/s flow velocity, 109-72°C subcooling, 2.2 bar pressure.

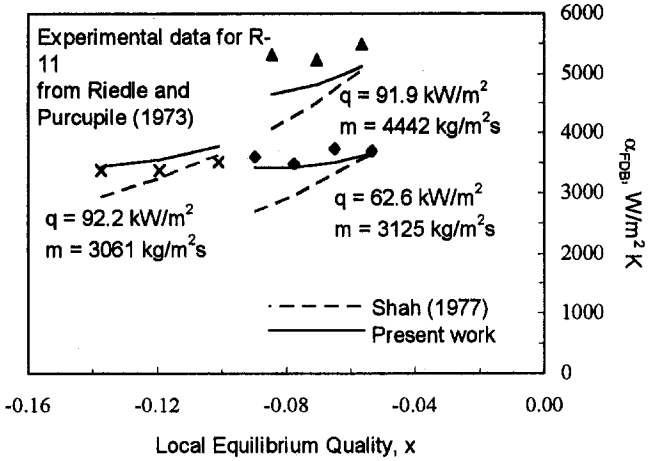

Fig. 4 Comparison of present work, Eq. (9), and Shah (1977) correlations with Riedle and Purcupile (1973) experimental data in the *fully developed boiling* (FDB) region

$+ \Delta T_{sat}$). Combining the definition of α^* and Bo with Eq. (9) results in the following expression for $\dot{q}$ in the FDB region:

$$\dot{q} = [1058(\dot{m}h_{lg})^{-0.7} F_{fl} \alpha_{lo} \Delta T_{sat}]^{1/0.3} \qquad (14)$$

The present correlation given by Eq. (14) and the other correlations listed in Table 1 are compared with the experimental data of Bergles and Rohsenow (1984) for water flowing in an annulus over a heated stainless steel tube. The results are shown in Fig. 3. The Thom et al. (1965) correlation considerably underpredicts the results. This was also noted by Rohsenow (1985) who reported that the Thom et al. correlation is able to predict Brown's (1967) data, which are in the low heat flux range. The pool boiling curve represented by the Mikic and Rohsenow (1969) correlation is below the FDB curve, but has the same slope as the experimental FDB data. The Shah (1977) correlation underpredicts the results, and exhibits a lower slope. The dependence of $\dot{q}$ on ΔT_{sat} is expressed through an exponent of 3.86 by McAdams et al. (1949), whereas it is 2.0 in the correlations of Shah and Thom et al., and 3.33 in the present work. The present work agrees closely with the data and displays the same trend as seen from Fig. 3.

To compare the present correlation with the Shah (1977) correlation further, the refrigerant data by Riedle and Purcupile (1973) employed in Shah's correlation development are used. The FDB region is identified by the method described in the next section. Figure 4 shows the results of the comparison in the FDB region for R-11 under two different conditions. The agreement with both the Shah correlation and the present work is excellent; the absolute mean error with the Shah correlation is 14.5 percent, while it is 13.0 percent with the present work. The data points close to $x = 0$ sometimes show larger deviation as they may fall under the *significant void flow* region. Use of the saturated flow boiling correlation (Kandlikar, 1990) with the nonequilibrium quality calculated from Saha and Zuber (1974) improves the results, and is discussed in greater detail in section 6.

To verify the FDB model given by Eq. (14) further, it is compared with the data reported by McAdams et al. (1949). They conducted experiments with subcooled flow of water at 2.07, 4.14, and 6.2 bar pressures in annuli with an inner diameter of 6.35 mm, and jacket diameters of 4.32 mm, 10.92, and 18.54 mm ID tubes. The corresponding hydraulic diameters were 4.32, 12.19, and 13.21 mm. Water velocity was varied from 0.3 m/s to 11 m/s.

Figures 5 and 6 show the comparison of the McAdams et al. (1949) data for two conditions with the present model in the PB and FDB regions. The steep vertical line represents the present model given by Eq. (14) in the FDB region. As can be seen, the agreement is excellent.

4 Location of FDB

Figure 7 shows a plot of $\dot{q}$ versus T_w at constant subcooling. **A-B** lies in the single-phase region, with ONB starting at **C**, and the *fully developed boiling* beginning at **E**. The location **E** where the FDB begins has been investigated by many investigators, and the model by Bowring (1962) is widely recommended. In the present work, the same model is employed. The intersection of the extension of the single-phase line **A-B-F** given by Eqs. (2) and (10)–(13), and the fully developed boiling curve E-F-G given by Eq. (14) identifies **F**, and $\dot{q}_F$ is obtained by solving the two-equation sets:

$$1058 F_{fl}(\dot{m}h_{lg})^{-0.7}\dot{q}_F - \dot{q}_F^{0.3} - 1058\alpha_{lo}F_{fl}(\dot{m}h_{lg})^{-0.7}\Delta T_{sub} = 0 \qquad (15)$$

An iterative scheme is needed to solve Eq. (15) for $\dot{q}_F$ at given

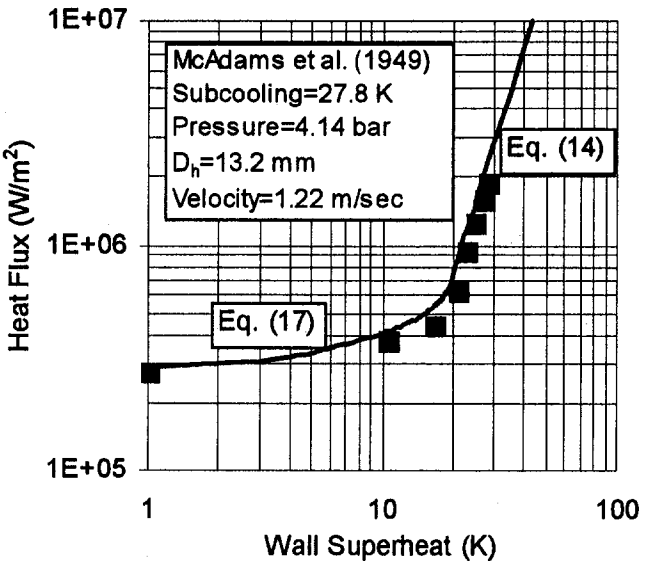

Fig. 5 Comparison of the present model, Eqs. (17) and (14), with McAdams et al. (1949) data in the *partial boiling* and the FDB regions, water velocity 1.22 m/s

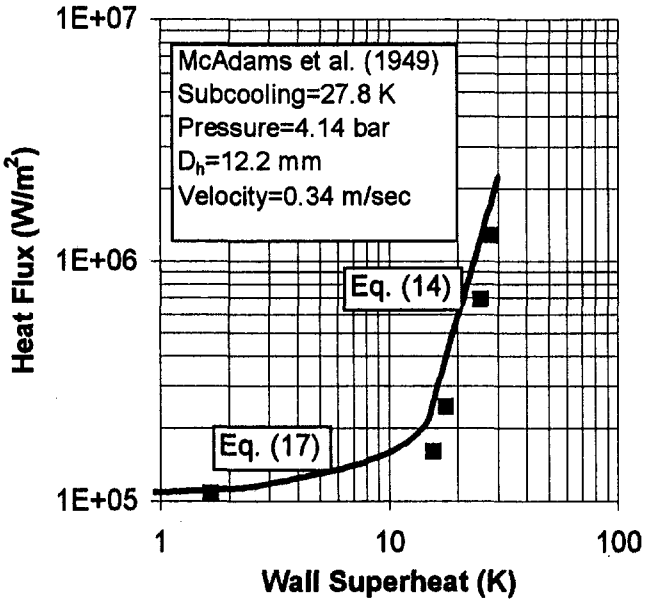

Fig. 6 Comparison of the present model, Eqs. (17) and (14), with McAdams et al. (1949) data in the *partial boiling* and the FDB regions, water velocity 0.34 m/s

values of $\dot{m}$ and ΔT_{sub}. After locating **F**, $\dot{q}_E$ is obtained from the Bowring (1962) model given by the following equation:

$$\dot{q}_E = 1.4\ \dot{q}_F \tag{16}$$

The wall superheat at **E** can be calculated from the FDB equation, Eq. (14).

5 Partial Boiling Region

The *partial boiling* region is identified as the region between **C**, where ONB begins, and **E**, where FDB begins, as shown in Fig. 7. The heat transfer in this region is calculated by slightly modifying the procedure outlined by Kandlikar (1991) as follows.

The heat flux $\dot{q}_E$ at **E** is obtained from Eq. (14), and $\dot{q}_C$ at **C** is obtained from Eqs. (3) and (4) at ONB. In the *partial boiling* region **C-E**, the following equation is employed:

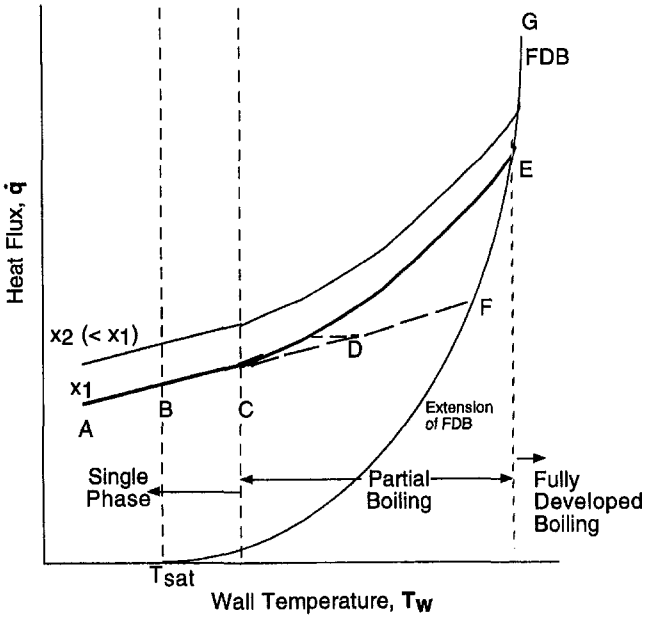

Fig. 7 Heat transfer in *partial boiling* region

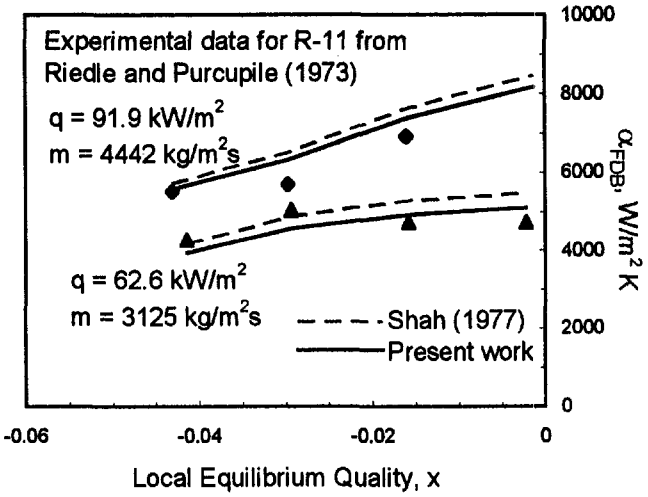

Fig. 8 Comparison of present work, Eqs. (15)–(22), and Shah (1977) correlation with Riedle and Purcupile (1973) data for R-11 in the *partial boiling* region

$$\dot{q} = a + b(T_w - T_{sat})^m \tag{17}$$

The constants a and b are obtained from the known heat fluxes at **C** and **E**:

$$b = \frac{\dot{q}_E - \dot{q}_C}{(\Delta T_{sat,E})^m - (\Delta T_{sat,C})^m} \tag{18}$$

and

$$a = \dot{q}_C - b(\Delta T_{sat,C})^m \tag{19}$$

The exponent m is treated as a constant in Eqs. (17)–(19), and is determined as follows:

$$m = n + p\dot{q} \tag{20}$$

where the constants n and p are obtained by matching the slopes of $m = 1$ at **C** to $m = 1/0.3$ at **D**:

$$p = (1/0.3 - 1)/(\dot{q}_E - \dot{q}_C) \tag{21}$$

and

$$n = 1 - p\dot{q}_C \tag{22}$$

This procedure assures smooth transitions from the single-phase region to the *partial boiling* region, and then to the FDB region. The gradual change in the slope also reflects the fact that an increasing number of nucleation cavities are activated as wall superheat increases.

The model outlined above for heat transfer in the *partial boiling* region is compared with the experimental data of Riedle and Purcupile (1973) for R-11 for three conditions. In the experiments, the liquid temperature increases as it is heated along the length of the tube. The results are therefore plotted on α versus x coordinates, where $\alpha = \dot{q}/(\Delta T_{sub} + \Delta T_{sat})$. Figure 8 shows a comparison of the present model and Shah's (1977) correlation with Riedle and Purcupile's data. This data set was used in the correlation development by Shah. As can be seen from Fig. 8, the present model results in a slightly better agreement than the Shah correlation. For the entire data set, the absolute mean error with the Shah correlation is 11 percent, while it is 7.9 percent with the present method. It may be noted that the present model utilizes the earlier correlations for the FDB and ONB conditions, and that no additional empirical

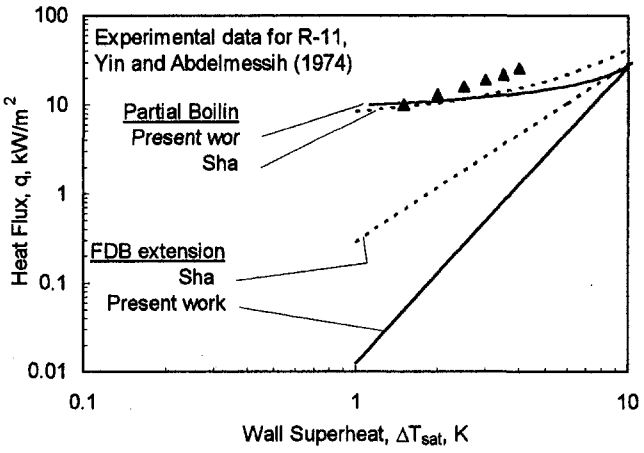

Fig. 9 Comparison of present work, Eqs. (15)–(22), and Shah (1977) correlation with Yin and Abdelmessih (1974) data for R-11 in the *partial boiling* region; 1.4 bar and 611 kg/m²s

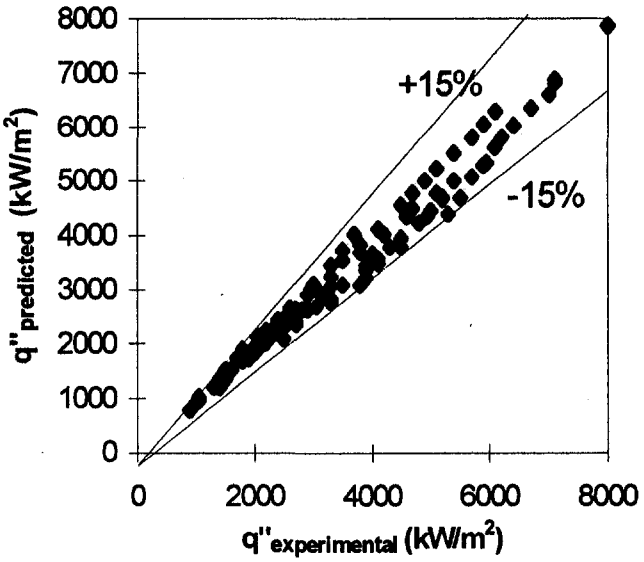

Fig. 11 Comparison of the present work using the nonequilibrium quality in the Kandlikar (1990) correlation with subcooled water data by Del Valle and Kenning (1985) for 0.2 mm heater thickness

constants are introduced. Figures 9 and 10 show similar comparisons with Yin and Abdelmessih's (1974) data for R-11, and Hino and Ueda's (1985) data for R-113, respectively. The local subcooling for the each data point was not available, and it is suspected that some of the data points, especially in Fig. 9, may be under the *fully developed boiling* region. Further improvement is expected from the present model after correcting each data point for the local subcooling.

Comparison of McAdams et al. (1949) data in the PB region can also be seen from Figs. 5 and 6. The agreement is seen to be excellent. It can be seen that the Bowring's model for the transition to FDB is also well represented.

6 Significant Void Flow Region

The point of net vapor generation identifies the location in the subcooled flow where the net void fraction begins to be significant. It is postulated by Kandlikar (1997) that the two-phase flow effects would become important and the saturated flow boiling correlations should be applicable. Although the thermodynamic quality is negative in this region, the nonequilibrium quality based on the void fraction would be positive. An apparent quality, x_a, is therefore introduced to account for the nonequilibrium effects.

Saha and Zuber (1974) correlations are employed to locate the thermodynamic quality x_{NVG} at location **G** shown in Fig. 1.

$\mathrm{Re}_{lo}\mathrm{Pr}_l < 70{,}000$:

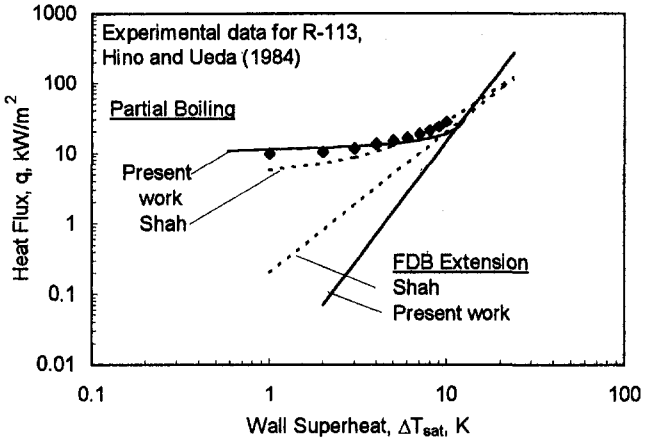

Fig. 10 Comparison of present work, Eqs. (15)–(22), and Shah (1977) correlation with Hino and Ueda (1984) data for R-113 in the *partial boiling* region; 1.47 bar and 515 kg/m²s

$$x_{\mathrm{NVG}} = -0.0022\,\frac{\dot{q}D}{\rho_l h_{lg} \kappa_l} = -0.0022 Bo\ \mathrm{Re}_{lo}\mathrm{Pr}_l \qquad (23)$$

$\mathrm{Re}_{lo}\mathrm{Pr}_l > 70{,}000$:

$$x_{\mathrm{NVG}} = -154 Bo \qquad (24)$$

The apparent quality in the *significant void flow* region beyond x_{NVG} is obtained from a correlation also recommended by Saha and Zuber (1974):

$$x_a = \frac{x - x_{\mathrm{NVG}} \exp(x/x_{\mathrm{NVG}} - 1)}{1 - x_{\mathrm{NVG}} \exp(x/x_{\mathrm{NVG}} - 1)} \qquad (25)$$

where x is the actual thermodynamic quality (negative value in the subcooled region).

The apparent quality x_a is then used in the Kandlikar (1990) correlation for saturated flow boiling. Kandlikar (1997) have proposed the model given above and compared the available experimental data for water and refrigerants from literature. Figure 11 shows the results of comparison with the subcooled flow boiling data obtained by Del Valle and Kenning (1985) for a heater thickness of 0.2 mm and three different velocities. The experimental data are obtained for the flow of water in a rectangular channel. Del Valle and Kenning compared their data with the available models for the fully developed boiling and found large errors (predicted heat fluxes were lower by a factor of over two). The data reported by Del Valle and Kenning correspond to the thermocouple location toward the exit of the test section located 130 mm from the inlet. In the present analysis, their data are corrected to obtain the local temperature and the equilibrium quality by applying the heat balance equation over the heated length between the inlet section and the thermocouple location. It can be seen from Fig. 11 that the agreement is excellent for all three velocities.

7 Additional Remarks

The experimental data reported in literature on subcooled boiling should be used with caution. In applying the equations and models in this region, it is essential to determine the local subcooling at the section where wall temperature is measured. In many data sets, including Del Valle and Kenning (1985), the subcooling at the inlet to the test section is reported. As the liquid flows through the test section, it gets heated and the local

subcooling decreases in the flow direction. This effect is quite significant in long test sections under high-heat-flux conditions.

8 Conclusions

Subcooled flow boiling is divided into three regions, *partial boiling, fully developed boiling,* and a newly defined *significant void flow* region. A comprehensive methodology with appropriate correlations is presented to predict the heat transfer in each region. Highlights of the proposed methodology are given below.

(a) The onset of boiling is determined from the bubble nucleation criterion proposed by Hsu and Graham (1961). The nondimensional form of equations presented by Kandlikar and Spiesman (1997) provide a clear way to study the parametric effects.

(b) Bowring's (1962) method is employed to identify the beginning of the *fully developed boiling* region.

(c) The nucleate boiling component in the Kandlikar correlation (1990) for saturated flow boiling in the nucleate boiling dominant region is employed to describe the heat transfer in the *fully developed boiling* region.

(d) The method proposed by Kandlikar (1991) is slightly modified/corrected for heat transfer in the *partial boiling* region.

(e) The Saha and Zuber (1974) correlation is used to determine the location of the NVG point and the nonequilibrium quality at a given section in the *significant void flow* region.

(f) The correlation for the nucleate boiling dominant (NBD) region in the Kandlikar (1990) correlation is used to calculate the heat transfer coefficient in the *significant void flow* region using the nonequilibrium quality.

(g) It is recommended that the nonequilibrium quality be employed, instead of the thermodynamic equilibrium quality, in the low-quality saturated flow boiling region as well for estimating the heat transfer coefficient using the Kandlikar (1990) correlation.

The methodology described in (b) – (f) has been compared with some of the available experimental data on water and refrigerants with very good agreement, generally within less than 10–15 percent.

References

Bergles, A. E., 1984, "Heat Transfer Mechanisms in Nuclear Reactor Thermal-Hydraulics," *Latin American Journal of Heat and Mass Transfer,* Vol. 8, pp. 107–129.

Bergles, A. E., and Rohsenow, W. M., 1984, "The Determination of Forced-Convection Surface-Boiling Heat Transfer," ASME JOURNAL OF HEAT TRANSFER, Vol. 86, pp. 365–372.

Boyd, R. D., 1988, "Subcooled Water Flow Boiling Experiments Under Uniform High Heat Flux Conditions," *Fusion Technology,* Vol. 13, pp. 131–142.

Bowring, W. R., 1962, "Physical Model of Bubble Detachment and Void Volume in Subcooled Boiling," OECD Halden Reactor Project Report No. HPR-10.

Brown, W., 1967, "Study of Flow Surface Boiling," *Sc.D. Thesis,* Massachusetts Institute of Technology, Cambridge, MA.

Collier, J. G., 1981, "Subcooled Boiling Heat Transfer," Chap. 5, *Convective Boiling and Condensation,* McGraw-Hill, New York.

Del Valle, V. H., and Kenning, D. B. R., 1985, "Subcooled Boiling at High Heat Flux," *Int. J. Heat Mass Trans.,* Vol. 28, No. 10, pp. 1907–1920.

Gnielinski, V., 1976, "New Equations for Heat and Mass Transfer in Turbulent Pipe and Channel Flow," *International Chemical Engineer,* Vol. 16, pp. 359–368.

Hino, R., and Ueda, T., 1985, "Studies on Heat Transfer and Flow Characteristic in Subcooled Flow Boiling—Part I. Boiling Characteristics," *Int. J. Heat Mass Transfer,* Vol. 11, No. 3, pp. 269–281.

Hsu, Y. Y., and Graham, R. W., 1961, "An Analytical and Experimental Study of the Thermal Boundary Layer and Ebullition Cycle in Nucleate Boiling," NASA TN-D-594.

Hsu, Y. Y., 1962, "On the Size Range of Active Nucleation Cavities on a Heating Surface," ASME JOURNAL OF HEAT TRANSFER, Vol. 84, pp. 207–216.

Jens, W. H., and Lottes, P. A., 1951, "An Analysis of Heat Transfer, Burnout, Pressure Drop, and Density Data for High Pressure Water," Argonne Natl. Lab Report No. ANL-4627-1951.

Kandlikar, S. G., 1990, "A General Correlation for Saturated Two-Phase Flow Boiling Heat Transfer Inside Horizontal and Vertical Tubes," ASME JOURNAL OF HEAT TRANSFER, Vol. 112, pp. 219–228.

Kandlikar, S. G., 1991, "Development of a Flow Boiling Map for Subcooled and Saturated Flow Boiling of Different Fluids Inside Circular Tubes," ASME JOURNAL OF HEAT TRANSFER, Vol. 113, pp. 190–200.

Kandlikar, S. G., and Cartwright, M. D., 1995, "A Photographic Study of Nucleating Bubble Characteristics in Flow Boiling," *Convective Flow Boiling, Proc. Convective Flow Boiling,* An International Conference held at the Banff Center for Conferences, Banff, Alberta, Canada, Apr. 30–May 5, Taylor and Francis, pp. 73–78.

Kandlikar, S. G., 1997, "Further Developments in Predicting Subcooled Flow Boiling Heat Transfer," presented at the Engineering Foundation Conference on Convective Flow and Pool Boiling, May, Irsee, Germany.

Kandlikar, S. G., and Spiesman, P., 1997, "Effect of Surface Characteristics on Subcooled Flow Boiling Heat Transfer," presented at the Engineering Foundation Conference on Convective Flow and Pool Boiling, May, Irsee, Germany.

McAdams, W. H., Minden, C. S., Carl, R., Picornell, D. M., and Dew, J. E., 1949, "Heat Transfer at High Rates to Water With Surface Boiling," *Ind. Eng. Chem.,* Vol. 41, No. 9, pp. 1945–63.

Mikic, B. B., and Rohsenow, W. M., 1969, "New Correlation of Pool Boiling Data Including the Effect of Heating Surface Characteristics," ASME JOURNAL OF HEAT TRANSFER, Vol. 91, pp. 241–250.

Petukhov, B. S., and Popov, V. N., 1963, "Theoretical Calculation of Heat Exchange in Turbulent Flow in Tubes of an Incompressible Fluid With Variable Physical Properties," *High Temp.,* Vol. 1, No. 1, 69–83.

Petukhov, B. S., 1970, "Heat Transfer and Friction in Turbulent Pipe Flow With Variable Physical Properties," in: *Advances in Heat Transfer,* T. F. Irvine et al., eds., Vol. 6, pp. 503–564.

Riedle, K., and Purcupile, J. C., 1973, "Experimental and Analytical Investigation—Boiling Heat Transfer in Evaporator Tubes—Horizontal Flow," *ASHRAE Trans.,* Part I, pp. 142–155.

Rohsenow, W. M., 1985, "Boiling," Chap. 12, *Handbook of Heat Transfer,* Rohsenow, W. M., Hartnett, J. P., and Ganic, E. N., eds., McGraw-Hill, New York.

Saha, P., and Zuber, N., 1974, "Point of Net Vapor Generation and Vapor Void Fraction in Subcooled Boiling," *Proc. 5th International Heat Transfer Conference,* Tokyo, Paper B4.7, pp. 175–179.

Sato, T., and Matsumura, H., 1964, "On the Conditions of Incipient Subcooled Boiling With Forced Convection," *Bulletin of JSME,* Vol. 7, No. 26, pp. 392–398.

Shah, M. M., 1977, "A General Correlation for Heat Transfer During Subcooled Boiling in Pipes and Annuli," *ASHRAE Trans.,* Vol. 83, Part 1, pp. 205–215.

Thom, J. R. S., Walker, W. M., Fallon, T. A., and Reising, G. F. S., 1965, "Boiling in Subcooled Water During Flow up Heated Tubes or Annuli," presented at the Symposium on Boiling Heat Transfer in Steam Generating Units and Heat Exchengers, Manchester, Sept. 15–16, Institute of Mech. Eng., London.

Yin, S. T., and Abdelmessih, A. H., 1974, "Prediction of Incipient Flow Boiling From a Uniformly Heated Surface," *AIChE Symposium Series,* Vol. 73, No. 164, pp. 236–243.

Film Boiling Incipience at the Departure From Natural Convection on Flat, Smooth Surfaces

J. Y. Chang[1]

S. M. You
email: you@uta.edu

A. Haji-Sheikh

Department of Mechanical and Aerospace Engineering, The University of Texas at Arlington, Arlington, TX 76019-0023

The present research is an experimental study of pool boiling nucleation behavior using flat, smooth surfaces immersed in saturated highly wetting liquids, FC-72 and FC-87. A flush-mounted, copper surface of 10 mm × 10 mm is used as a heat transfer surface, simulating a microelectronic chip surface. At the nucleation incipient points of higher wall superheats with steady increase of heat flux, vapor film blankets the smooth surface and remains on the surface. To predict this film boiling incipience phenomenon from the smooth surface, an incipience map is developed over the boiling curve. When the incipient heat flux is higher than the minimum heat flux (MHF) and the incipient wall superheat value is higher than the transition boiling curve value at the incipient heat flux, the transition from single-phase natural convection to film boiling is observed at the incipient point. To prevent film boiling incipience, a microporous coating is applied over the smooth surface, which decreases incipient wall superheat and increases minimum heat flux. The film boiling incipience should be avoided to take advantage of highly efficient nucleate boiling heat transfer for the cooling of high-heat-flux applications.

Introduction

For many years, the electronics industry has improved performance of electronic components. During the same period, there has been a strong drive to reduce the size and cost of these electronic assemblies. These trends have resulted in problems because power densities have increased rapidly as volume has decreased. The ever-increasing thermal load is expected to be the most challenging problem for high-flux thermal management systems (Mackowski, 1991). A liquid cooling scheme utilizing boiling heat transfer has been considered to be a practical method for handling the large amount of heat generated from high-density devices (Bar-Cohen, 1983). In particular, direct immersion cooling with dielectric fluids (e.g., refrigerants and fluorinerts) has emerged as an effective cooling technology. Recently, some researchers have constructed different module packages employing immersion cooling, and tested their feasibility (Jimenez and Mudawar, 1994; Mudawar et al., 1994; Nelson et al., 1994).

Although immersion cooling research has been conducted, most of the previous experimental reports with immersion cooled packages concerned only cooling performance during steady-state operations. As the power density of the electronic system continues to increase, unstable transient operating conditions can be expected to be a serious consideration in future cooling systems. Unfavorable incipient characteristics of transient heat load have been reported in the field of high-heat-flux applications, such as nuclear power plants and high-temperature superconductors. The transient heat load induced during an accident from such plants is known to be higher than the stationary critical heat flux (CHF) of the working coolant. Usually, the high transient heat load was accompanied by a direct incipient transition from nonboiling forced or natural convection to film boiling, which resulted in a deterioration of the cooling performance. The transition was due to the spontaneous formation of massive vapor over the heated surface. Because of the extremely high heat dissipation rate, the development of heterogeneous nucleation from the surface cavity structures was delayed. Instead, the superheating process of the liquid by the diffusive heat transfer mode produced a large amount of accumulated thermal energy in the thin superheated liquid layer over the heated surface. At a certain superheat limit, the explosive vapor growth was prompted by the high vaporization rate associated with such a high superheated liquid layer. Skripov et al. (1965) and Skripov and Pavlov (1970) tested several organic liquids with a 20 μm platinum wire heater and demonstrated that the superheat limit agrees well with the theoretical homogeneous nucleation superheat.

In contrast to Skripov's results, several researchers observed the incipient transition to the film boiling regime even at a superheat lower than the homogeneous nucleation limit and at a heat flux smaller than the stationary CHF during their transient boiling heat transfer tests. Sinha et al. (1979) investigated transient boiling characteristics of liquid nitrogen at a stepwise heat input into a horizontal wire. They observed that the boiling transition to film boiling occurred even at a heat load of about 40 percent of stationary CHF. Okuyama and Iida (1990) investigated transient bubble patterns from a platinum wire heater within liquid nitrogen by applying various heights of stepwise heat input. They found that a higher incipient superheat of the boiling transition was obtained with a higher magnitude of the heat load. Their experimental data showed that lower superheat of the incipient transition was about 50 percent of homogeneous nucleation limit at a heat load of about 70 percent of stationary CHF. Sakurai et al. (1990, 1992) extensively studied system pressure effects on the direct incipient transition phenomenon using various increasing rates of exponential heat input into a wire heater. During their research, they assumed that the direct incipient transition was due to the initiation of heterogeneous spontaneous nucleation (HSN) in the originally flooded cavities

[1] Current address: Post-Doc Scholar, Dept. of Mechanical Engineering, The Pennsylvania State University, University Park, PA 16802.

Contributed by the Heat Transfer Division and presented at the ASME International Mechanical Engineering Congress & Exposition, Atlanta, Georgia, November 17–22, 1996. Manuscript received by the Heat Transfer Division July 30, 1996; revision received January 30, 1997. Keywords: Augmentation and Enhancement, Boiling, Phase-Change Phenomena. Associate Technical Editor: J. R. Howell.

on the heater surface. The HSN phenomenon occurs when a new phase appears at an interface or a boundary rather than in the bulk fluid similar to the homogeneous spontaneous nucleation (Stralen and Cole, 1979). From their experiments with liquid nitrogen, they found the lower limit of HSN superheat agrees well with the minimum film-boiling superheat (or MTD, minimum temperature difference). Even without transient heat-flux conditions, some researchers observed the incipient transition phenomena with steady-state increases of heat flux (Kutateladze et al., 1973; Straub, 1994). However, they did not conduct any additional research about these phenomena.

As reviewed previously, many researchers have reported the unfavorable incipient characteristics of direct film boiling transition phenomena. However, all the previous experiments were done with fine metallic heaters (wire or thin foil heaters) utilizing benign characteristics of thermal response and thermometry. In the present research, a flush-mounted, smooth copper surface of 10 mm × 10 mm was used as a heat transfer area, simulating a micro-electronic chip surface. Experiments were performed to investigate the pool boiling nucleation behaviors of copper heaters immersed in saturated highly wetting liquids, FC-72 and FC-87. Both liquids are widely accepted in the electronic industry as leading candidates for the application of direct immersion cooling. These liquids are known to have no potential to deplete the stratospheric ozone layer. Two different heater surfaces were tested: a plain surface, and a plain surface coated with a micro-porous-enhancement coating. With steady-state increases or decreases of heat flux, nucleate boiling, film boiling, and direct incipient transition behaviors were investigated with the plain surface heater. Also, the effects of surface microgeometries on the pool boiling nucleation behaviors were investigated.

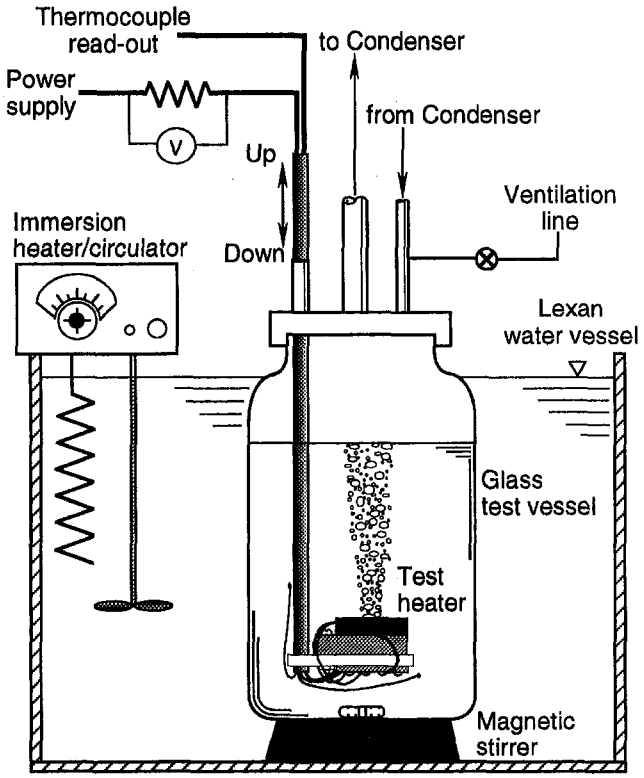

Fig. 1 Schematic of test apparatus

Experimental Apparatus and Procedure

Test Facility. The pool boiling test facility used for this research is shown in Fig. 1. The test liquid was contained within a glass vessel, 260 mm high and 160 mm in diameter, which was submerged in a Lexan water container. The water container served as an isothermal bath. Water temperature was controlled by a 1000 W immersion heater/circulator. A magnetic stirring bar was located inside the test vessel and was used to accelerate the degassing process before each test. A water-cooled condenser, which is not shown in the figure, was used during degassing and testing to minimize loss of the test liquid. Atmospheric pressure was maintained by venting the test vessel to ambient. Two copper-constantan thermocouples were placed within the test vessel to measure bulk liquid temperature. The test heater assembly was mounted horizontally to a vertical traversing mechanism, which enabled movement of the heater to a desired height within the glass vessel.

A power supply was connected in series with a shunt resistor and the test heater. The shunt resistor rated at 100 mV and 10 A was used to determine the current in the electric circuit. Direct current was supplied to the heating element by a DC power supply. A measured voltage drop across the test heater was used to estimate heat flux applied by the power supply.

Figure 2 shows the test heater assembly used during this study. Serpentine windings of a thin nichrome wire (0.144 mm diameter) were attached to a Teflon substrate (11 mm thick) using Omegabond 200 high-temperature epoxy ($k \approx 1.4$ W/mK). A 1.5-mm-thick block of copper (10 mm × 10 mm) was bonded on top of the heating element, also using Omegabond 200 epoxy. Two layers of epoxy assured electrical insulation between the copper and the nichrome. To minimize the epoxy thickness, it was cured in an oven maintained at 423 K with a weight resting on top of the copper block. Electrical leads were soldered to each end of the nichrome wire. The resulting heating element resistance was about 12 Ω. This heating element was set in a Lexan frame and surrounded by a two-part, 3M epoxy (1832L-B/A, $k \approx 0.067$ W/mK) to generate a flush-mounted heating surface. The copper block had two holes (1 mm diameter and 5 mm depth) drilled into its center from one edge. Two copper-constantan thermocouples (30 wire gage, 0.255 mm diameter) were inserted and soldered in the holes to provide surface temperature measurements.

Test Procedure. The immersion heater/circulator was used to heat the water bath to the saturation temperature of the test liquid. Once the test liquid reached its saturation temperature, it was left at this state for two hours to remove dissolved gases. A magnetic stirrer was used during this process to accelerate dissolved gas removal. After degassing, the magnetic stirrer was turned off and data acquisition begun.

Heat flux was controlled by the voltage input of a DC power supply. For the nucleate boiling experiments under increasing heat-flux condition, after each voltage increase (heat-flux increment), a 15-second delay was imposed before initiating data acquisition. After the delay, the computer collected and aver-

Nomenclature

A = heater surface area, cm^2
CHF = critical heat flux, W/cm^2
MHF = minimum heat flux, W/cm^2
MTD = minimum temperature difference, K
$q''(t)$ = transient heat flux, W/cm^2
q''_0 = applied heat flux, W/cm^2
$(dU/dt)_{copper}$ = rate of change of stored thermal energy in copper block, W
$(dU/dt)_{IM}$ = rate of change of stored thermal energy in insulation material, W

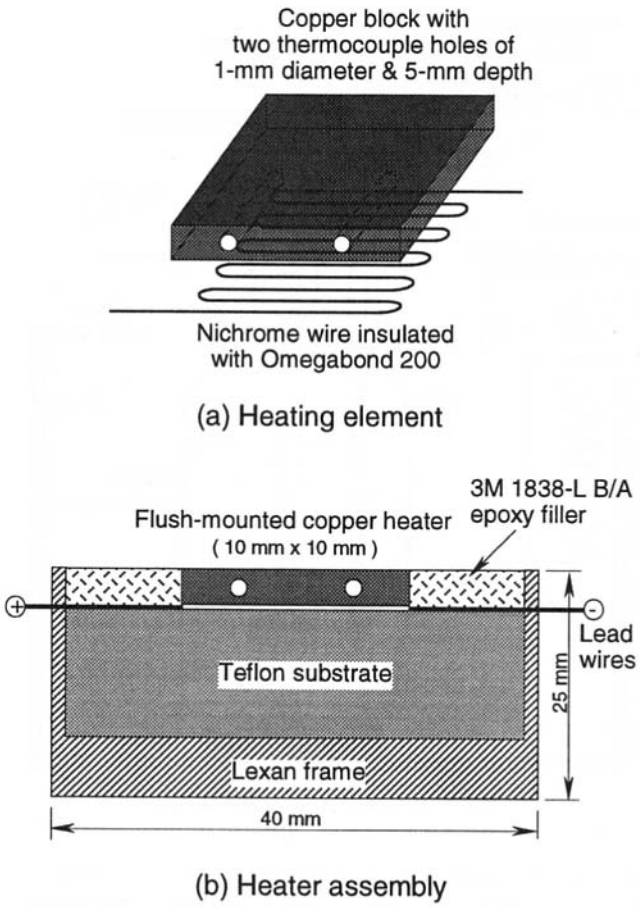

Fig. 2 Test heater geometry

aged 125 surface-temperature data points from each thermocouple, which took about 15 seconds. This was immediately followed by the acquisition and averaging of an additional 125 data points per thermocouple. A comparison was then made between these two average temperatures for each thermocouple. This procedure was repeated until the temperature differences for the thermocouples were less than 0.2 K. The test section at this point was assumed to be at steady state. Usually it took about 45 seconds to reach the steady-state condition after each heat-flux increment. After reaching steady state, bulk fluid temperature was measured and heat flux was calculated.

For heat-flux values greater than ≈80 percent of CHF, instantaneous surface temperature was monitored for 45 seconds after each heat-flux increment to prevent heater burnout. Each instantaneous surface temperature measurement was compared with the average surface temperature from the previous heat flux. If a temperature difference larger than 30 K from any thermocouple was detected, the data acquisition algorithm assumed CHF and immediately shut down the power supply. The CHF value was computed as the steady-state heat-flux value just prior to power supply shutdown plus half of the increment. If CHF was not detected during the 45-second delay, collecting and averaging of 125 surface temperature data points from each thermocouple was initiated and repeated until the steady-state condition was achieved. At least two consecutive runs were conducted for each surface tested. The time interval between these runs was determined by monitoring the test heater surface temperature. The surface was allowed to reach thermal equilibrium within ±0.1 K of the saturated bulk fluid temperature. In all cases, this time interval between runs was greater than one hour.

For the film boiling experiments, voltage input was gradually increased to produce a desired heat flux from the heater, which was initially located within the liquid. The heater was then taken out of the liquid and left in vapor/air space until it was heated to a desired temperature. At that instant, the heater was reimmersed quickly into the liquid. This procedure involved partial quenching as the liquid contacted the heater surface. However, the heat flux was continuously provided to the heater so that a stable film boiling point could be achieved as long as the heat-flux and surface superheat conditions were satisfied, which will be discussed later. After reaching the stable film boiling point, heat flux was incrementally reduced to the MHF point by a step of 0.2 W/cm^2 for measuring the film boiling curve of the heater surface. At each applied heat flux, the steady-state point was determined using the same algorithm employed in the nucleate boiling curve measurement.

Since the thermocouples were embedded within the copper block, temperatures measured with them were averaged and corrected by a one-dimensional heat conduction model to obtain the representative heater surface temperature at each applied heat flux. This correction was less than 0.5 K for all cases.

Substrate conduction losses were estimated based upon a numerical analysis conducted by O'Connor and You (1995), whose heater had a design similar to the present one. Heat losses were estimated to be between 15 and 5 percent for heat fluxes between 0.5 and 15 W/cm^2, respectively. The overall uncertainty estimates in heat flux were 15.5 and 5 percent for the above referred heat-flux conditions. The uncertainty estimates of the present heater can be estimated to be smaller than those of O'Connor and You (1995) for the larger surface area (1.0 versus 0.825 cm^2) with comparable thicknesses.

Results and Discussion

Experiments were conducted using saturated FC-72 and FC-87 at 1 atm. Some selected properties of FC-87 and FC-72 are listed in Table 1 for comparison. The tested surfaces included a smooth or "plain" reference surface and a plain surface coated with a micro-porous-enhancement coating.

Pool Boiling Tests of Plain Surface. Pool boiling tests with a plain surface in saturated FC-72 and FC-87 were first conducted. Before these tests were performed, the copper surface was highly polished. Polishing was conducted with a finger for over four hours using Brasso polishing solution. The polished surface was mirrorlike with no evidence of visible scratches or cavities. After polishing, a small amount of 3M epoxy (1832L-B/A) was carefully applied around the perimeter of the heater surface to prevent undesired edge nucleation sites.

Representative results of the plain surface pool boiling tests are shown in Fig. 3. The FC-72 and FC-87 boiling curves are fairly consistent with each other. The natural convection and nucleate boiling curves are nearly identical for both liquids. These similarities are thought to be due to the similar physical

Table 1 Selected properties of saturated FC-72 and FC-87 at 12 atm

Property	FC-72	FC-87	Ratio
Chemical formula	C_6F_{14}	C_5F_{12}	
Molecular weight [kg/kmol]	340	290	
Boiling point [K]	329.7	302.3	
Critical pressure [atm]	18.4	20.1	0.915
Density-liquid [kg/m^3]	1598.9	1571.6	1.02
Density-vapor [kg/m^3]	13.37	12.38	1.08
Specific heat-liquid [J/kg·K]	1121	1103	1.02
Heat of vaporization [J/kg]	9.428E+4	9.897E+4	0.953
Thermal conductivity-liquid [W/m·K]	5.45E-2	5.50E-2	0.991
Viscosity-liquid [kg/m·sec]	4.47E-4	6.69E-4	0.668
Surface tension [N/m]	8.10E-3	8.90E-3	0.910

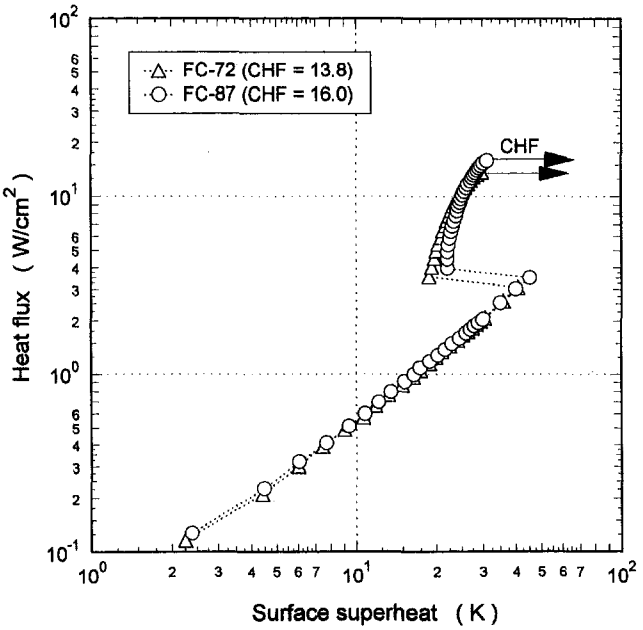

Fig. 3 Plain surface boiling data in saturated liquids

properties of the two liquids, as compared in Table 1. Incipient superheat values ranged from 25 to 45 K. The CHF values for FC-72 and FC-87 were observed to be 13.8 and 16.0 W/cm^2, respectively. These CHF values are within 10 percent of the predictions by Zuber (1959): 15.1 W/cm^2 for saturated FC-72 and 15.6 W/cm^2 for saturated FC-87.

Photographs of an incipient process from natural convection to nucleate boiling are shown in Fig. 4. The photographs were taken during the test with FC-72 at the heat flux of 3.6 W/cm^2 and at the incipient superheat of 38.9 K. Within the very short time of about 0.1 s, the initial vapor bubble grew and departed from the heater surface. The departed initial bubble size was over 20 times larger than that of the steady-state bubble size in Fig. 4(f). This large-size initial bubble was due to the combined contributions from the rapid dissipation of thermal energy stored within the heater block and the spontaneous vaporization from superheated liquid layer developed over the heated surface before the initial nucleation.

Pool boiling tests of the plain surface in FC-72 and FC-87 were repeated many times, with almost all tests producing consistent results as described previously. However, during the tests, an interesting phenomenon occurred. While performing a pool boiling test of a highly polished plain surface in FC-87, film boiling incipience at the departure from natural convection was observed. The results of this test are shown in Fig. 5. After the transition, the heater remained within the stable film boiling regime as heat flux was increased steadily in 0.5 W/cm^2 increments. Under exactly identical test conditions, the only difference between this test and the other pool boiling tests that produced nucleate boiling incipience was the incipient point. As long as the natural convection regime continued to a superheat higher than about 52 K at the heat flux of about 4.4 W/cm^2, initiation of incipient vaporization always transferred to the film boiling regime. From the test results, the incipient point (superheat and heat flux) seems to be critical to determine the direct transition behavior with FC-87. For the tests with FC-72, a nearly identical incipient point with that of FC-87 was obtained, however, the film boiling incipience could not be observed.

Photographs of the transition process from natural convection to film boiling for FC-87 are shown in Fig. 6. Compared to the initial spherical vapor bubble observed in Fig. 4, the current initial vapor bubble shows a different shape. At the initial stage

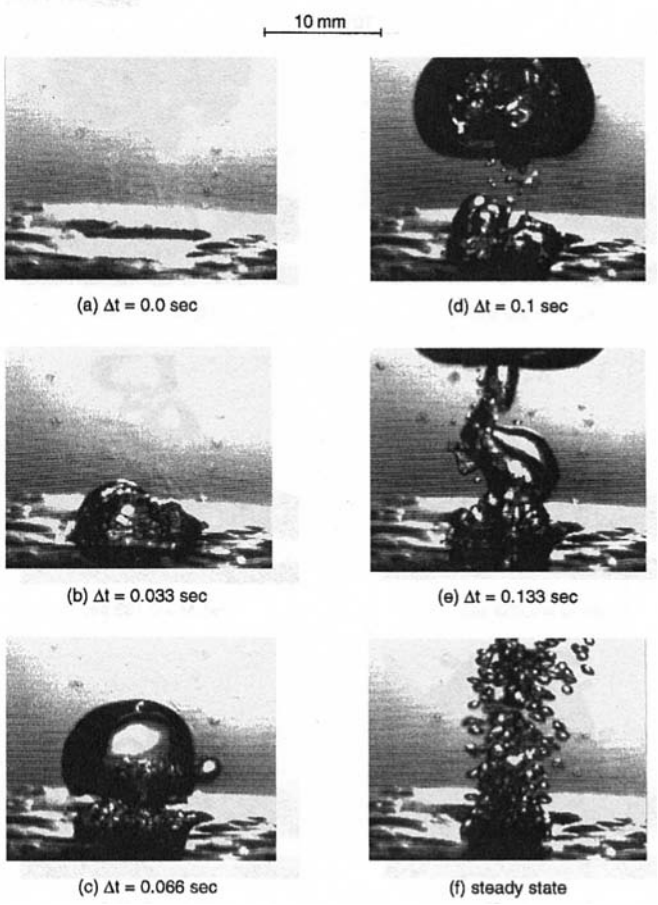

Fig. 4 Photographs of nucleate boiling incipience

(Fig. 6(b)), it looks like a cluster of many tiny vapor bubbles, and in Fig. 6(c), a lumped vapor mass forms, around which some bubbles exist. As soon as the initial vapor lump departed from the surface, a film boiling pattern was observed on the

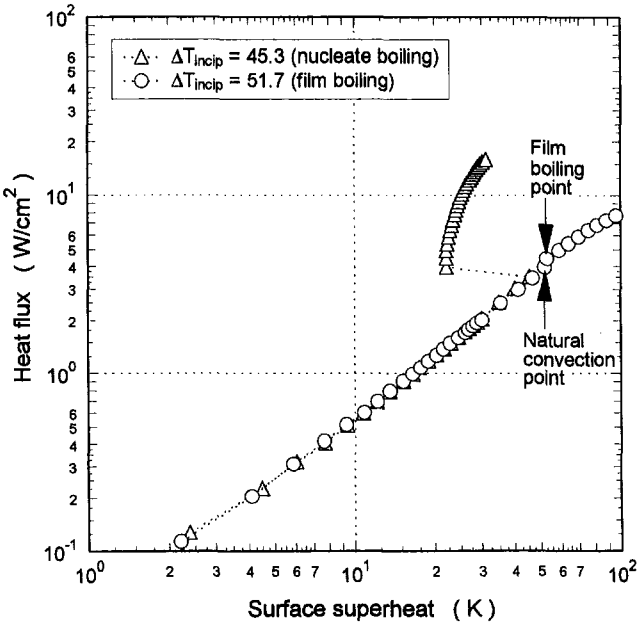

Fig. 5 Plain surface boiling incipiences in saturated FC-87: nucleate boiling incipience versus film boiling incipience

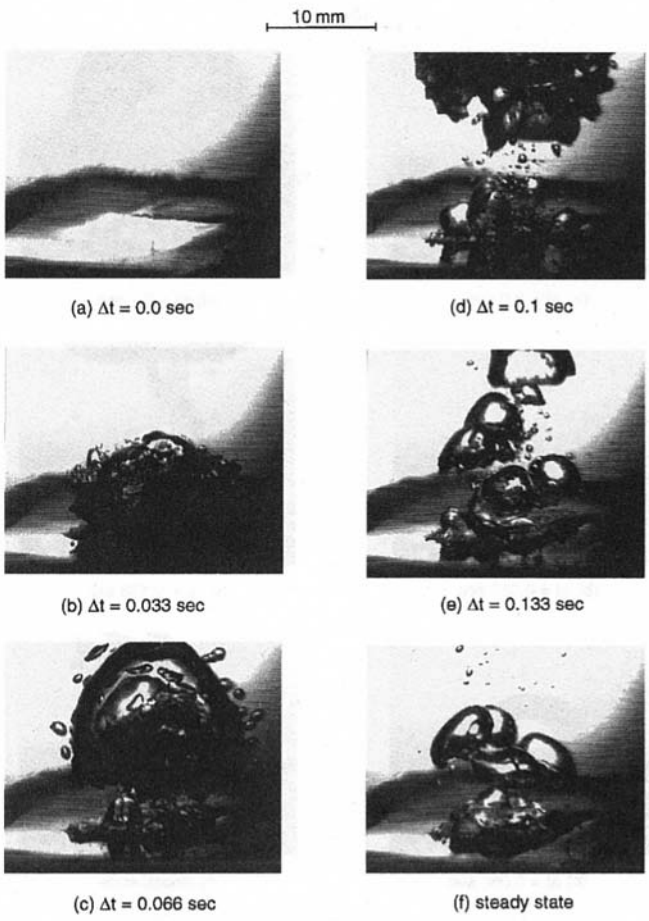

Fig. 6 Photographs of film boiling incipience

heater surface (Figs. 6(*d*, *e*)). During the steady-state observation, a four-bubble pattern (Fig. 6(*f*)) and a single bubble pattern were alternately formed from the heater surface, and this pattern combination was fairly consistent. Based upon Lienhard and Dhir (1973), the Taylor instability wave length was estimated to be approximately 8 mm for saturated FC-87. Considering the cell sizes formed by the four-bubble and one-bubble patterns, the observed vapor bubbles from the node points of alternately formed Taylor waves confirmed the transition process to film boiling upon departure from single-phase natural convection.

There was some doubt regarding how the film boiling curve in Fig. 5 could be compared with the film boiling curve produced with steady-state decreases of heat flux. Film boiling curves were generated using the decreasing heat-flux manner (DHF) introduced in the test procedure. The measured film boiling curves for FC-72 and FC-87 are shown in Fig. 7. Nearly identical film curves were observed for both liquids. The MHFs and MTDs were measured to be 5.8 W/cm^2 and 60.0 K for FC-72 and 5.4 W/cm^2 and 55.6 K for FC-87. For comparison, the FC-87 film boiling curve generated using the increasing heat-flux manner (IHF) is also plotted in Fig. 7. The FC-87 film boiling curves of IHF and DHF are parallel, with superheat differences of ≈8 K over the corresponding heat fluxes. Interestingly, the figure shows that the extended point from the last natural convection point in the curve of IHF, which is thought to be the true film boiling incipient point, coincides with the MTD in the curve of DHF. Referring to Sakurai et al. (1990, 1992), the incipient film boiling transition observed during the FC-87 tests was thought to be due to the initiation of heterogeneous spontaneous nucleation (HSN). Sakurai et al. showed that the lower limit of HSN superheat agrees well with the MTD. During their tests, the lower limit of HSN was obtained by increasing transient exponential heat input with a time constant of 500 ms. Using this theory, an explanation can be given for why the incipient film boiling transition could not be observed for the tests with FC-72, even with the same incipient superheat: The MTD of FC-72 was higher than the highest incipient superheat obtained during the tests.

Pool Boiling Transitions of Plain Surface by Quenching Method. Although Sakurai et al. (1990, 1992) showed that the MTD is the lower limit of film boiling transition, other researchers observed film boiling transition at a superheat lower than the MTD (Kutateladze et al., 1973; Okuyama and Iida, 1990). Also, interestingly, the heat fluxes of all the previously observed transition points were found to be located above the MHF. From these survey results, the development of an incipience map from which a film boiling incipience regime could be predicted might be possible. For this map, MTD as well as MHF was thought to be useful information. More incipient data were required to examine different incipience behaviors. For the film boiling incipience points generated by Sakurai et al. (1990, 1992) and Okuyama and Iida (1990), they varied increasing rate (for ramp or exponential inputs) or height (for step input) of applied heat load at a system pressure to examine transient response from a thin wire heater. For the present copper heater with much higher heat capacity, the quenching method was used to investigate transient paths after initiation of nucleation from the heater surface. By heating the surface to a desired superheat with a desired heat flux before immersing into a liquid, various incipient points could be simulated. For this test, saturated FC-87 was used as a test liquid. The 16 simulated incipient points generated during a series of quenching tests are shown in Fig. 8. The transient response of the heater temperature was recorded at a time interval of 0.121 s between two consecutive data points. The data acquisition was initiated before immersion of the heater so that the incipient points shown in Fig. 8 were determined by checking the recorded heater temperature histories. As the liquid contacted the heater surface and subsequent vaporization occurred, sudden slope changes of the heater temperature over time were always observed.

Figure 8 shows the grouping of the incipient points based upon their characteristics of boiling transition upon quenching.

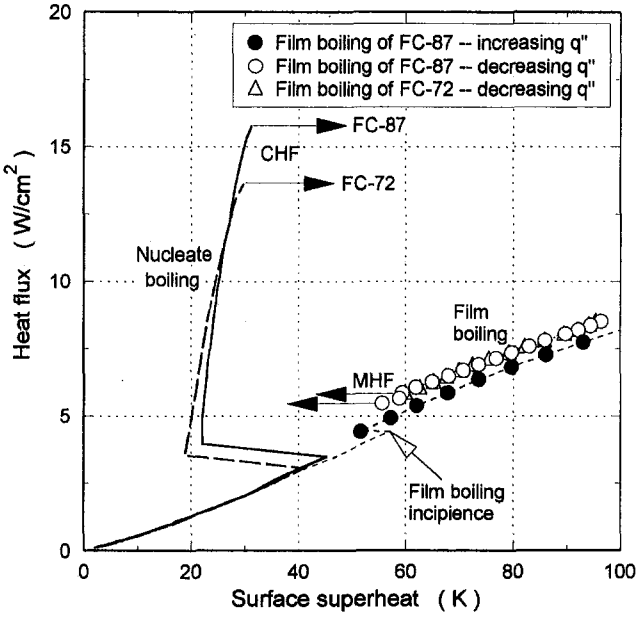

Fig. 7 Film boiling data of plain surface

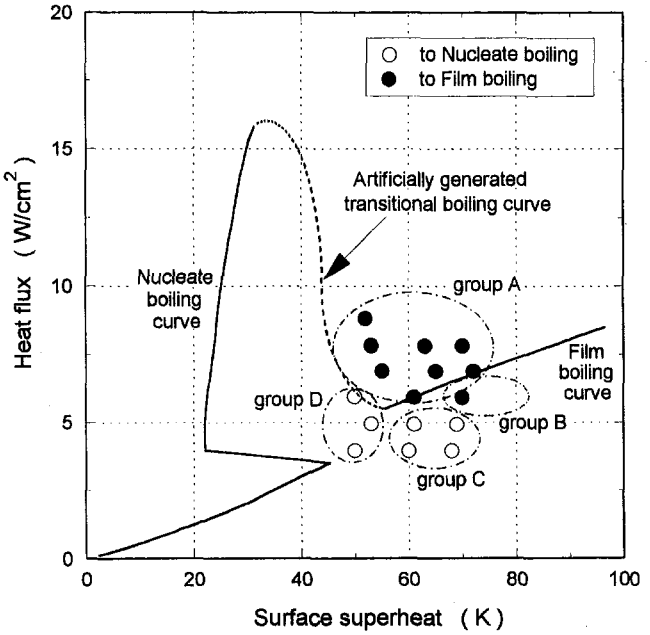

Fig. 8 Pool boiling transitions by quenching method in saturated FC-87

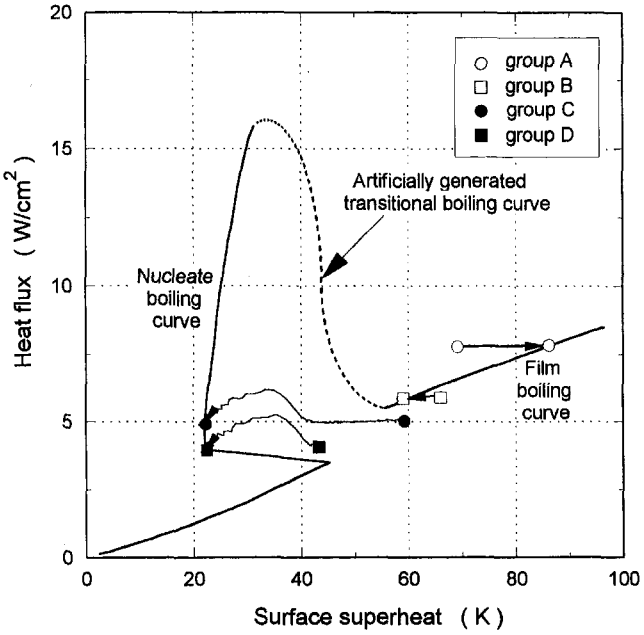

Fig. 10 Transient paths after immersions in saturated FC-87

The eight data points in group A experienced a gradual increase in their surface temperatures and returned to the film boiling curve. The single point in group B experienced a decrease in the surface temperature and also returned to the film boiling curve. The data in groups C and D experienced a rapid decrease in their surface temperatures and returned to the nucleate boiling curve. The only difference between groups C and D is that the data in group C initially experienced temporal formation of a vapor film over the heater surface, and within a short time, the vapor film vanished.

Figure 9 details the transient superheat data of one incipient point sample from each group found in Fig. 8. The surface superheat of the sample from group A gradually increased until reaching steady state at the film boiling curve after approximately two minutes. The transition to steady state was much longer than those of other group samples. The superheat of the sample from group B smoothly decreased and reached steady state after approximately twenty seconds. The superheat of the group C sample decreased to approximately 42 K and then quickly dropped to approximately 25 K. The sample then quickly reached steady state. While the superheat decreased from the initial point to 42 K, vapor film was observed to cover the heater surface. The superheat of the group D sample exhibited a rapid decrease immediately after quenching, reaching steady state in under twenty seconds. The rapid drop in surface superheat for groups C and D was attributed to the formation of nucleate boiling at the heater surface.

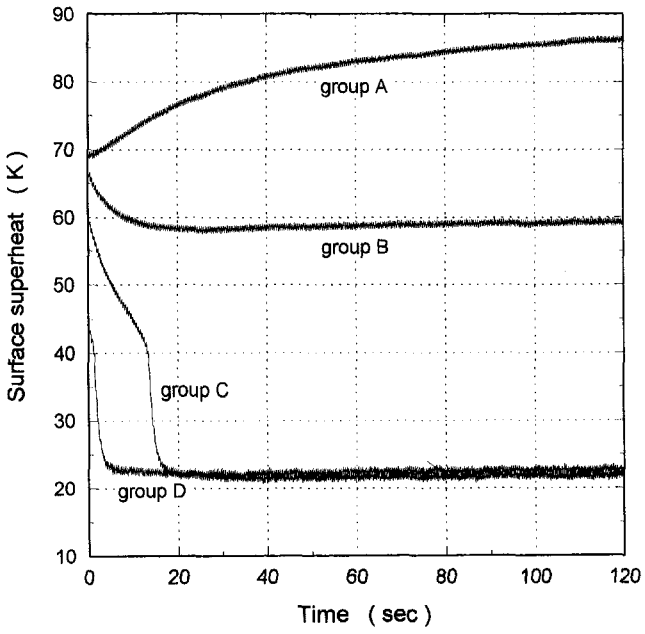

Fig. 9 Transient superheat data in saturated FC-87

Using the transient heater temperature data in Fig. 9, transient surface heat fluxes were estimated. The transient surface heat flux was calculated considering the applied heat flux and the rate of change of the stored thermal energy in the copper block and the surrounding insulation material:

$$q''(t) = q''_0 - \frac{1}{A}\left[\left(\frac{dU}{dt}\right)_{\text{copper}} + \left(\frac{dU}{dt}\right)_{IM}\right]$$

To reduce the high-frequency, low-magnitude oscillation in the recorded temperatures seen in Fig. 9, numerical filtering of the raw temperature data was performed before calculating the surface heat fluxes. The transient heat flux was estimated by solving a one-dimensional heat-conduction equation. Figure 10 shows the transient path of the same sample point from each group shown in Fig. 9. As previously mentioned, group A and B samples moved to the film boiling curve. The paths of both the A and B samples are fairly horizontal, reflecting nearly constant transient heat fluxes during the transition to the steady-state superheats. Group C and D samples moved to the nucleate boiling curve. Both of these samples show a small peak in their heat fluxes due to the rapid temperature drops, as seen in Fig. 9. The thermal energy stored in the copper block and the insulation material was released during the rapid temperature drops.

Based upon the present and previous studies, an incipience map was developed in Fig. 11. In the boiling incipience map, region A covers where the heat flux is higher than the MHF and the superheat is higher than the transitional boiling curve and lower than the film boiling curve. Region B covers where the heat flux is higher than the MHF and the superheat is higher than the film boiling curve. Region C covers where the heat

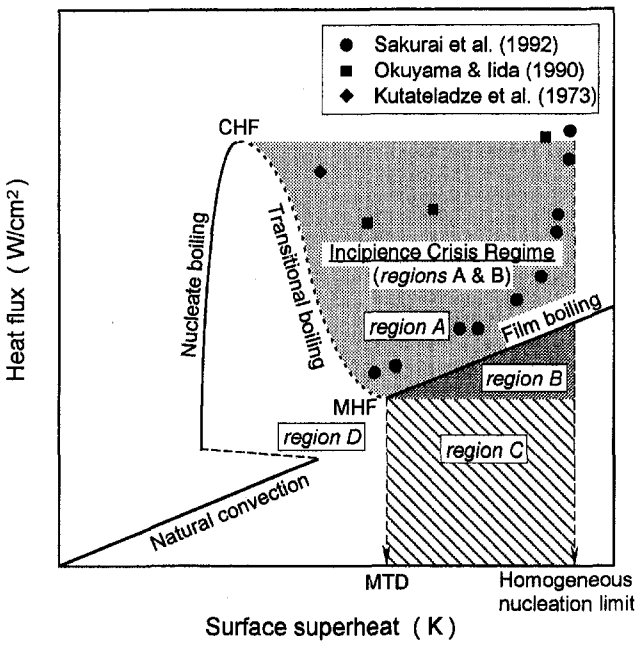

Fig. 11 Boiling incipience map

flux is lower than the MHF and the superheat is higher than the MTD. Region D covers where the superheat is lower than the transitional boiling curve and the MTD. For regions A, B, and C, the incipient superheats have the upper limit of homogeneous nucleation. The boiling incipience characteristic for each region is already discussed in Figs. 8, 9, and 10. The combined area of regions A and B is termed the Incipience Crisis Regime (ICR). When the incipient heat flux is higher than the MHF and the wall superheat value is higher than the transition boiling curve, the transition from single-phase natural convection to film boiling is observed at the incipient point. Available incipient transition data points from previous researchers are plotted together based upon their relative positions to the boiling curves. All the data points are located within the ICR.

Referring to the film boiling incipience phenomenon presented in Figs. 5 and 6, examination of the incipient point and subsequent film boiling points strongly suggest that the incipience occurred within region B of the FC-87 boiling incipience map. The slight difference between the film boiling curves generated using the increasing and decreasing heat-flux manners indicates that further study is required to reveal the hysteresis behavior.

Pool Boiling of Microporous Enhanced Surface. From the present study, it was found that FC-72 and FC-87 have quite low MTD's: 60.0 K for saturated FC-72 and 55.6 K for saturated FC-87. Since these liquids are the leading candidates for high-heat-flux, immersion electronic cooling, the possible incipience crisis problem should be resolved for design requirements. The incipient superheat can be expected to reach the Incipience Crisis Regime from the immersion-cooled electronic system when the component surface is smooth and when a transient power jump is induced to the component. In the present study, a microporous enhancement coating technique is suggested, which can be directly implemented on the microelectronic chip surface. The microscale enhancement coating has been proven to augment boiling heat transfer with highly wetting dielectric fluids (O'Connor and You, 1995; O'Connor et al., 1995; Chang and You, 1996, 1997a, b). In the present study, the ABM coating developed by Chang and You (1996) was applied to the heater surface, simulating a microelectronic chip surface. Detailed descriptions of the ABM coating are provided by Chang and You. The coated surface was used to generate the boiling curves of natural convection, nucleate boiling, and film boiling for FC-72 and FC-87, respectively.

Figure 12 shows the effect of applying a microporous coating to the test surface. The incipient superheat of the coated surface was always lower than 10 K, significantly lower than that of the plain surface. For the nucleate boiling regime, the coated surface consistently augmented heat transfer coefficients by more than 300 percent for FC-72 and FC-87 compared to those of the plain surface. The ABM coating provided repeatable CHF values with approximately 100 and 50 percent enhancements over the plain surface for FC-72 and FC-87, respectively. For the film boiling regime, the coated surface augmented the MHF and MTD by approximately 70 and 36 percent, respectively, for FC-72, and 90 and 60 percent, respectively, for FC-87. The microporous coating significantly reduced the possibility of an incipience crisis problem by decreasing the incipient point (heat flux and superheat) and increasing MHF and MTD for FC-72 and FC-87. The microporous coating magnified the difference between the incipient point and Incipient Crisis Regime. A further benefit was the higher cooling performance over an extended operation range, achieved by highly enhanced nucleate boiling and CHF of the coated surface. The present test result showed that the microporous coating, which can be easily implemented with the high-heat-flux application, can prevent the possible incipience crisis and enhance the nucleation performance effectively.

Conclusions

Experiments were performed to investigate the pool boiling nucleation behavior of a flush-mounted copper heater. Two heater surfaces (plain and microporous-enhanced) were tested in a pool of saturated FC-72 and FC-87 at atmospheric pressure.

1 With steady-state increases or decreases of heat flux, a film boiling incipience was observed from a highly polished plain surface. As the surface heat flux and superheat reached higher than a certain point, the nucleation incipience transferred to the film boiling regime. The photographic study showed that the explosively growing initial vapor bubble shape of the film boiling incipience was different from that of the nucleate boiling incipience.

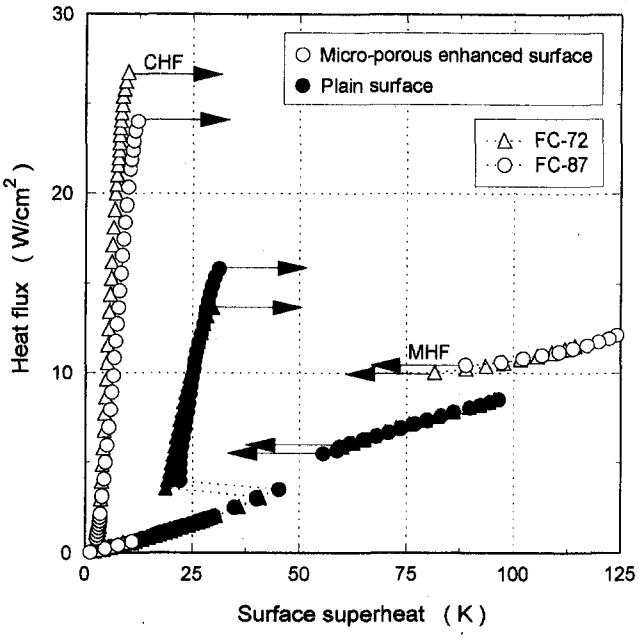

Fig. 12 Pool boiling data of microporous enhanced surface

2 Using a quenching method, a stable film boiling point was obtained. Using these points as initial positions, and with steady-state decreases of heat flux, film boiling curves were generated for FC-72 and FC-87. The measured film boiling curve of FC-87 was parallel to the film boiling curve generated with the increasing heat-flux manner, maintaining a temperature difference of ≈ 8 K. The measured MTD of FC-87 agreed well with the film boiling incipience superheat. Based upon the theory of Sakurai et al. (1990, 1992), the film boiling incipience was concluded to be the initiation of heterogeneous spontaneous nucleation.

3 By quenching the heater at desired heat flux and superheat, incipience behaviors from various points were simulated. Using these incipience data, the boiling incipience map was developed to predict the film boiling incipience regime (Incipience Crisis Regime) from the boiling curves.

4 Microporous-enhanced coating magnified the difference between the incipient point and the MHF–MTD point, and also enhanced the nucleation performance significantly. From the present test results, the microporous coating technique is highly recommended for immersion cooling of high-heat-flux applications to avoid the incipience crisis and to take advantage of highly efficient nucleate boiling heat transfer.

Acknowledgments

This study was supported by the Texas Higher Education Coordinating Board: Advanced Research/Technology Program grant number 003656-014. The authors extend their thanks to the 3M Industrial Chemical Products Division for the donation of FC-72 and FC-87 test liquids. Thanks are also due to Mr. Alan Herda for assistance in preparing the manuscript.

References

Bar-Cohen, A., 1983, "Thermal Design of Immersion Cooling Modules for Electronic Components," *Heat Transfer Engineering,* Vol. 4, Nos. 3–4, pp. 35–50.

Chang, J. Y., and You, S. M., 1996, "Heater Orientation Effects on Pool Boiling of Micro-Porous-Enhanced Surfaces in Saturated FC-72," ASME JOURNAL OF HEAT TRANSFER, Vol. 118, pp. 937–943.

Chang, J. Y., and You, S. M., 1997a, "Boiling Heat Transfer Phenomena From Micro-porous and Porous Surfaces in Saturated FC-72," *Int. J. Heat Mass Transfer,* Vol. 40, No. 18, pp. 4437–4447.

Chang, J. Y., and You, S. M., 1997b, "Enhanced Boiling Heat Transfer From Micro-Porous Surfaces; Effects of Coating Composition and Method," *International Journal of Heat and Mass Transfer,* Vol. 40, No. 18, pp. 4449–4460.

Jimenez, P. E., and Mudawar, I., 1994, "A Multi-Kilowatt Immersion-Cooled Standard Electronic Clamshell Module for Future Aircraft Avionics," ASME *Journal of Electronic Packaging,* Vol. 116, pp. 220–229.

Kutateladze, S. S., Moskvicheva, V. N., Bobrovich, G. I., Mamontova, N. N., and Avksentyuk, B. P., 1973, "Some Peculiarities on Heat Transfer Crisis in Alkali Metals Boiling Under Free Convection," *Int. J. Heat Mass Transfer,* Vol. 16, pp. 705–713.

Lienhard, J. H., and Dhir, V. K., 1973, "Hydrodynamic Prediction of Peak Pool-Boiling Heat Fluxes From Finite Bodies," ASME JOURNAL OF HEAT TRANSFER, Vol. 95, pp. 152–158.

Mackowski, M. J., 1991, "Requirements for High Flux Cooling of Future Avionics Systems," SAE Paper No. 912104.

Mudawar, I., Jimenez, P. E., and Morgan, R. E., 1994, "Immersion-Cooled Standard Electronic Clamshell Module: A Building Block for Future High-Flux Avionic Systems," ASME *Journal of Electronic Packaging,* Vol. 116, pp. 116–125.

Nelson, R. D., Sommerfeldt, S., and Bar-Cohen, A., 1994, "Thermal Performance of an Integral Immersion Cooled Multichip Module Package," *IEEE Trans. CPMT—Part A,* Vol. 17, No. 3, pp. 405–412.

O'Connor, J. P., and You, S. M., 1995, "A Painting Technique to Enhance Pool Boiling Heat Transfer in Saturated FC-72," ASME JOURNAL OF HEAT TRANSFER, Vol. 117, pp. 387–393.

O'Connor, J. P., You, S. M., and Price, D. C., 1995, "Thermal Management of High Power Microelectronics via Immersion Cooling," *IEEE Trans. CPMT,* Part A, Vol. 18, No. 3, pp. 656–663.

Okuyama, K., and Iida, Y., 1990, "Transient Boiling Heat Transfer Characteristics of Nitrogen (Bubble Behavior and Heat Transfer Rate at Stepwise Heat Generation)," *Int. J. Heat Mass Transfer,* Vol. 33, No. 10, pp. 2065–2071.

Sakurai, A., Shiotsu, M., and Hata, M., 1990, "Effects of System Pressure on Minimum Film Boiling Temperature for Various Liquids," *Exp. Thermal and Fluid Science,* Vol. 3, No. 5, pp. 450–457.

Sakurai, A., Shiotsu, M., and Hata, M., 1992, "Boiling Heat Transfer Characteristics for Heat Inputs With Various Increasing Rates in Liquid Nitrogen," *Cryogenics,* Vol. 32, No. 5, pp. 421–429.

Sinha, D. N., Brodie, L. C., Semura, J. S., and Young, F. M., 1979, "Premature Transition to Stable Film Boiling Initiated by Power Transients in Liquid Nitrogen," *Cryogenics,* Vol. 19, pp. 225–229.

Skripov, V. P., Pavlov, P. A., and Sinitsyn, E. N., 1965, "Heating of Liquids to Boiling by a Pulsating Heat Supply," *High Temperature,* Vol. 3, pp. 670–674.

Skripov, V. P., and Pavlov, P. A., 1970, "Explosive Boiling of Liquids and Fluctuation Nucleus Formation," *High Temperature,* Vol. 8, pp. 782–787.

Straub, J., 1994, "The Role of Surface Tension for Two-Phase Heat and Mass Transfer in the Absence of Gravity," *Exp. Thermal and Fluid Science,* Vol. 9, pp. 253–273.

Stralen, S. V., and Cole, R., 1979, *Boiling Phenomena,* Vol. 1, Hemisphere Publ. Co., pp. 83–86.

Zuber, N., 1959, "Hydrodynamic Aspects of Boiling Heat Transfer," AEC Report No. AECU-4439, Physics and Mathematics.

K. W. Moser
Mem. ASME

R. L. Webb
Professor.
Fellow ASME

Department of Mechanical Engineering,
The Pennsylvania State University,
University Park, PA 16802

B. Na
LG Electronics, Inc.,
Changwon, Korea

A New Equivalent Reynolds Number Model for Condensation in Smooth Tubes

In 1959, Akers et al. developed an in-tube condensation model, which defines the all-liquid flow rate that provides the same heat transfer coefficient as an annular condensing flow. This liquid flow rate was expressed by an "equivalent" Reynolds number and used in a single-phase, turbulent flow equation to predict the condensation coefficient. However, the assumptions on which the equivalent Reynolds number is based are shown in the present work to be faulty. This results in the underprediction of many researchers' data. A new equivalent Reynolds number model, based on the heat-momentum analogy, is developed in this study. This model is then shown to predict the experimental Nusselt number of 1197 data points from 18 sources with an average deviation of 13.64 percent. The data are for tube internal diameters between 3.14 and 20 mm.

Introduction

When a vapor is reduced below its saturation temperature, condensation occurs. As the vapor condenses inside a tube, its latent heat is transferred through the tube wall to a cooling fluid. If the vapor velocity inside the tube is sufficiently high, the condensate flows as an annular film on the tube wall. Typically much of the condensation process occurs in the annular flow regime. Many of the existing in-tube condensation correlations are based on annular flow. Generally, these correlations can be classified into three categories: shear-based correlations, boundary layer-based correlations, and two-phase multiplier-based correlations.

Carpenter and Colburn (1951) pioneered the development of shear-based correlations. These correlations assume that the dominant thermal resistance occurs in the laminar sublayer of the liquid film and that the vapor core causes the film to become turbulent at much lower Reynolds numbers than for single-phase flow. Other shear-based correlations include those of Altman et al. (1960) and Soliman et al. (1968). Boundary layer-based correlations are similar to shear-based correlations, except that the thermal resistance throughout the entire liquid film thickness is considered, not just in the laminar sublayer. Traviss et al. (1973), Azer et al. (1972), and Cavallini and Zecchin (1974) all developed boundary layer-based correlations.

Two-phase multiplier-based correlations assume that two-phase flows are similar to single-phase flows. Consequently, predicting two-phase heat transfer is as simple as multiplying a single-phase heat transfer relationship by an unknown factor. This concept uses the same rationale as the Lockhart and Martinelli (1949) two-phase multiplier, developed for the prediction of frictional pressure drop. Several examples of two-phase multiplier-based condensing correlations are those of Cavallini and Zecchin (1971), Boyko and Kruzhilin (1967), and Shah (1979).

An interesting two-phase multiplier-based correlation was developed by Akers et al. (1959) and became known as the "equivalent Reynolds number" model. This model defines the all-liquid flow rate that provides the same heat transfer coefficient as an annular condensing flow. This liquid flow rate was expressed by an "equivalent" Reynolds number (Re_{eq}) and used in a single-phase, turbulent flow equation to predict the condensation coefficient. Akers et al. proposed that the resulting Nusselt number should be equal to the Nusselt number of the condensing flow. However, the assumptions on which the equivalent Reynolds number is defined are shown in the present work to be faulty and the result will be underprediction of the condensation coefficient. A new equivalent Reynolds number model, based on the heat-momentum analogy, is developed in this study.

Akers Equivalent Reynolds Number Definition

To define Re_{eq}, Akers et al. (1959) sought to replace the vapor core with a liquid flow that produces the same liquid–vapor interfacial shear stress. Therefore, the equivalent liquid mass velocity is equal to the sum of the mass velocities of: (1) the liquid condensate film (G_l) and (2) a liquid flow (G_l'), which produces the same interfacial shear stress as the vapor core:

$$G_{eq} = G_l + G_l' \tag{1}$$

Equating the interfacial shear stress caused by the vapor core to that caused by an equivalent liquid core, they obtained:

$$\tau_i = \frac{f_v G_v^2}{2\rho_v} = \frac{f_l G_l'^2}{2\rho_l} \tag{2}$$

From Eq. (2), the liquid flow that replaces the vapor core can be represented by:

$$G_l' = G_v \sqrt{\frac{\rho_l}{\rho_v}} \sqrt{\frac{f_v}{f_l}} \tag{3}$$

Akers et al. then assumed that for fully developed turbulent flow of the vapor core and liquid film, the interface was so rough that f_v becomes constant, independent of Reynolds number. They also inappropriately assumed that f_l would be independent of Reynolds number. Consequently, $f_v/f_l = 1$, allowing Eq. (1) to be simplified to:

$$G_{eq} = G_l + G_v \sqrt{\frac{\rho_l}{\rho_v}} \tag{4}$$

Akers et al. (1959) subsequently converted G_{eq} into Re_{eq} and introduced it into the single-phase Sieder–Tate (1936) equation to predict the two-phase Nusselt number. While this approach

Contributed by the Heat Transfer Division for publication in the JOURNAL OF HEAT TRANSFER. Manuscript received by the Heat Transfer Division May 29, 1997; revision received January 8, 1998. Keywords: Condensation. Associate Technical Editor: R. A. Nelson, Jr.

predicted their own data well, many researchers, including Bae et al. (1968), Azer et al. (1972), and Shah (1979) have found that this model significantly underpredicts their data.

The failure of the Akers model to predict accepted data is believed to be because of two factors. First, the driving temperature differences for a single-phase flow and two-phase flow are different. In a single-phase flow, the difference between the bulk fluid and wall temperatures ($T_b - T_w$) controls the heat transfer. In an annular, two-phase flow, the temperature difference across the liquid film ($T_\delta - T_w$) controls the heat transfer. The second shortcoming is that the assumption $f_v/f_l = 1.0$ is not appropriate. While it is possible that a rough liquid–vapor interface may cause f_v to be independent of Reynolds, it is very unlikely that f_l would be independent of Re. For a smooth tube, it is more likely that f_l will be governed by the friction relationship for a smooth pipe. Consequently, the friction factor ratio f_v/f_l would not be equal to one.

New Equivalent Reynolds Number Definition

The equivalent Reynolds number is based on the heat–momentum analogy, which states that a relationship exists between heat transfer and the wall shear stress. In a single-phase flow, an increase in wall shear stress results in an increase in the heat transfer. Similarly, in a two-phase flow, it is expected that as the wall shear stress increases, the heat transfer will also increase. Therefore, if a condensing two-phase flow were replaced by an all-liquid flow with the same wall shear stress, the analogy suggests that the single-phase heat transfer coefficient would be equal to the condensation coefficient, providing the driving temperature differences that define the single-phase and condensing heat transfer coefficients are the same.

Consider a control volume on a two-phase flow in a smooth-walled tube. For such a control volume, the following three assumptions are made: First, the static pressure drop of the liquid is the same as the static pressure drop of the vapor. Second, the volume occupied by the liquid phase plus the volume occupied by the vapor phase at any instant is equal to the total tube volume. Third, there is no liquid entrainment in the vapor core. Using these assumptions, the static pressure gradient for the two-phase flow may be expressed as the sum of the pressure gradients due to friction, gravity, and momentum change. From the definition of the frictional pressure gradient, the wall shear stress caused by the two-phase flow is given by:

$$\tau_w = -\left(\frac{dP}{dz}\right)_f\left(\frac{A}{p}\right) = -\left(\frac{dP}{dz}\right)_f\left(\frac{D}{4}\right) \tag{5}$$

Next, consider an equivalent all liquid flow that imparts the same wall shear stress as the two-phase flow. The wall shear stress for such a flow is given by:

$$\tau_w = \frac{f_{l,eq}}{2\rho_l}\left(\frac{\mathrm{Re}_{eq}\mu_l}{D}\right)^2 \tag{6}$$

where Re_{eq} and $f_{l,eq}$ are the Reynolds number and friction factor of the equivalent all-liquid flow, respectively. Combining Eqs. (5) and (6):

$$\mathrm{Re}_{eq} = \sqrt{-\left(\frac{dP}{dz}\right)_f\left(\frac{\rho_l D^3}{2\mu_l^2 f_{l,eq}}\right)} \tag{7}$$

The two-phase frictional pressure gradient, $(dP/dz)_f$, can be predicted using a variety of methods. The most popular method is to multiply the single-phase frictional pressure drop by a two-phase multiplier (ϕ_{lo}), as shown in Eq. (8):

$$\left(\frac{dP}{dz}\right)_f = \phi_{lo}^2\left(\frac{dP}{dz}\right)_{lo} \tag{8}$$

Nomenclature

A = surface area, m^2
A_c = cross-sectional area, m^2
c_p = constant pressure specific heat, J/kg-K
dP/dz = pressure gradient, Pa/m
D = tube inner diameter, m
F = correction factor defined by Eq. (36)
f = Fanning friction factor
Fr = Froude number = $G^2/(gD\rho_{ip}^2)$
G = mass velocity, kg/m^2-s
G_{eq} = equivalent mass velocity [Eq. (1)], kg/m^2-s
G_l' = liquid mass velocity, which replaces the vapor core, kg/m^2-s
h = heat transfer coefficient, W/m^2-K
k = thermal conductivity, W/m-K
N = number of increments the tube is split into
Nu = local Nusselt number
Nu_{avg} = average Nusselt number
P = pressure, Pa
p = perimeter, m
Pr = Prandtl number
q'' = heat flux, W/m^2
R = tube inner radius, m
r = radial coordinate measured from the tube centerline, m
R^+ = dimensionless pipe radius = $Ru*/\nu_l$
Re_{eq} = equivalent Reynolds number [Eq. (7) for present model]
Re_l = liquid phase Reynolds number = $G(1-x)D/\mu_l$
Re_{lo} = Reynolds number for entire flow as a liquid = GD/μ_l
T_b = bulk fluid temperature, °C
T_w = wall temperature, °C
T_δ = temperature at the edge of the liquid film, °C
T^+ = dimensionless temperature = $(T_\delta - T_w)/(q_w''/\rho_l c_{p,l} u*)$
u = velocity, m/s
u^+ = dimensionless velocity profile = $u/u*$
$u*$ = friction velocity = $(\tau_w/\rho_l)^{1/2}$, m/s
We = Weber number = $G^2D/(\rho_{ip}\sigma)$
x = vapor quality
y = coordinate normal to the pipe wall = $R - r$, m
y^+ = dimensionless distance = $yu*/\nu_l$
z = coordinate along the pipe length, m
α = thermal diffusivity, m^2/s
δ = film thickness, m
δ^+ = dimensionless film thickness = $\delta u*/\nu_l$
ϵ = eddy diffusivity, m^2/s
μ = dynamic viscosity, $N\text{-}s/m^2$
ν = kinematic viscosity, m^2/s
ρ = density, kg/m^3
σ = surface tension, N/m
τ = shear stress, Pa
ϕ_{lo}^2 = two-phase multiplier

Subscripts

1-ph = single-phase
2-ph = two-phase
avg = average
eq = equivalent
exp = experimental
f = frictional
h = thermal
i = liquid–vapor interface
l = liquid phase
lo = corresponding to the entire flow as a liquid
pred = predicted
tp = two-phase
v = vapor phase
vo = corresponding to the entire flow as a vapor
w = wall

$(dP/dz)_{lo}$ is the frictional pressure gradient that would result if only liquid flowed through the tube at Reynolds number Re_{lo} $(=GD/\mu_l)$:

$$\left(\frac{dP}{dz}\right)_{lo} = -\frac{2f_{lo}G^2}{\rho_l D} \tag{9}$$

Assuming that $f_{l,eq}$ and f_{lo} can be predicted by the Blasius friction factor for turbulent flow at Re_{eq} and Re_{lo}, respectively, Eq. (7) can be simplified to:

$$\mathrm{Re}_{eq} = \phi_{lo}^{8/7}\,\mathrm{Re}_{lo} \tag{10}$$

Many researchers, including Lockhart and Martinelli (1949), Baroczy (1966), and Chisholm (1973), have developed equations for the two-phase multiplier. However, based on a comparison with an extremely large database, Hewitt (1992) recommends the Friedel (1979) correlation for fluids with liquid to vapor viscosity ratios (μ_l/μ_v) less than 1000. This viscosity ratio range includes many fluids of practical interest, including refrigerants and water.

The Friedel (1979) correlation is an empirical relationship developed from a database of over 25,000 points and is valid for both vertical upward and horizontal flows in round tubes. The two-phase multiplier is given by:

$$\phi_{lo}^2 = A_1 + \frac{3.24A_2}{\mathrm{Fr}^{0.045}\,\mathrm{We}^{0.035}} \tag{11}$$

where

$$A_1 = (1-x)^2 + x^2\left(\frac{\rho_l}{\rho_v}\right)\left(\frac{f_{vo}}{f_{lo}}\right) \tag{12}$$

$$A_2 = x^{0.78}(1-x)^{0.24}\left(\frac{\rho_l}{\rho_v}\right)^{0.91}\left(\frac{\mu_v}{\mu_l}\right)^{0.19}\left(1-\frac{\mu_v}{\mu_l}\right)^{0.70} \tag{13}$$

and

$$\rho_{tp} = \left(\frac{x}{\rho_v} + \frac{1-x}{\rho_l}\right)^{-1} \tag{14}$$

Once the equivalent Reynolds number has been calculated, a single-phase heat transfer correlation is needed to predict the condensation coefficient. Because of its predictive ability over a wide range of Reynolds and Prandtl numbers, the Petukhov (1970) equation was chosen.

Correction Factor

The prediction of the condensation coefficient using the equivalent Reynolds number and a single-phase heat transfer equation requires a correction factor, because the driving temperature difference for a single-phase and an annular two-phase flow are different. In a single-phase flow, the heat flux is defined as:

$$q'' = h_{1-ph}(T_b - T_w) \tag{15}$$

where T_b is the bulk fluid temperature and T_w is the wall temperature. However, for an annular, two-phase flow, the heat flux is given by:

$$q'' = h_{2-ph}(T_\delta - T_w) \tag{16}$$

where T_δ is the temperature at the outer edge of the liquid film, which is equal to the saturation temperature, and T_w is the wall temperature.

Consequently, at the same heat flux, Eqs. (15) and (16) can be combined to define the two-phase heat transfer coefficient as the product of the single-phase heat transfer coefficient and the ratio of single-phase to two-phase driving temperature differences:

$$h_{2-ph} = Fh_{1-ph} \tag{17}$$

where

$$F = \frac{T_b - T_w}{T_\delta - T_w} \tag{18}$$

The two-phase temperature difference $(T_\delta - T_w)$ can be determined using a boundary layer analysis similar to that of Traviss et al. (1973). The single-phase temperature difference $(T_b - T_w)$ was determined with the Petukhov (1970) equation. The complete derivation is given in the appendix, and the final, simplified form of the correction factor is given by:

$$F = 1.31(R^+)^{C_1}\,\mathrm{Re}_l^{C_2}\,\mathrm{Pr}_l^{-0.185} \tag{19}$$

where C_1 and C_2 are defined by Eqs. (37) and (38) in the appendix.

Figure 1 was prepared to gain physical insight of the Eq. (19) correction factor. Figure 1 illustrates how the correction factor varies with Re_{eq} at $\mathrm{Pr}_l = 3$ for four different values of liquid Reynolds number (Re_l). This figure shows that for small values of Re_l, the single-phase temperature difference $(T_b - T_w)$ is 10 to 30 percent greater than the two-phase temperature difference $(T_\delta - T_w)$. Small liquid Reynolds numbers are generally associated with thin condensate films, where little temperature change exists across the thickness. In contrast, as the liquid film thickness increases, the two-phase temperature difference increases. Consequently, the two temperature differences approach each other as Re_l approaches 30,000.

The variation of the correction factor with Re_{eq} at Re_l = 10,000 and four different liquid Prandtl numbers is shown in Fig. 2. The figure shows that $(T_b - T_w)$ is greater than $(T_\delta - T_w)$ for small Prandtl numbers. Since the Prandtl number relates the relative thicknesses of the hydrodynamic and thermal boundary layers, small Prandtl numbers are associated with larger thermal boundary layers. Consequently, the temperature difference across the condensate film would be small, making $(T_b - T_w) > (T_\delta - T_w)$. As the liquid Prandtl number increases, the thermal boundary layer thickness decreases, creating larger temperature differences across the condensate film. Thus $(T_\delta - T_w)$ may become larger than $(T_b - T_w)$, making $F < 1$.

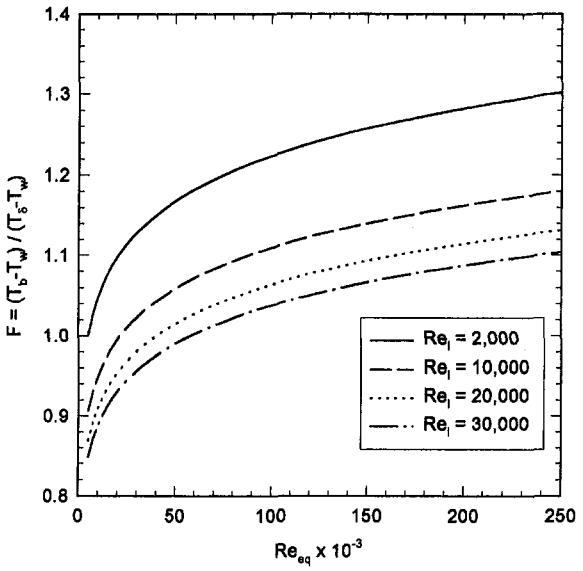

Fig. 1 Variation of the correction factor for four liquid Reynolds numbers at $\mathrm{Pr}_l = 3$

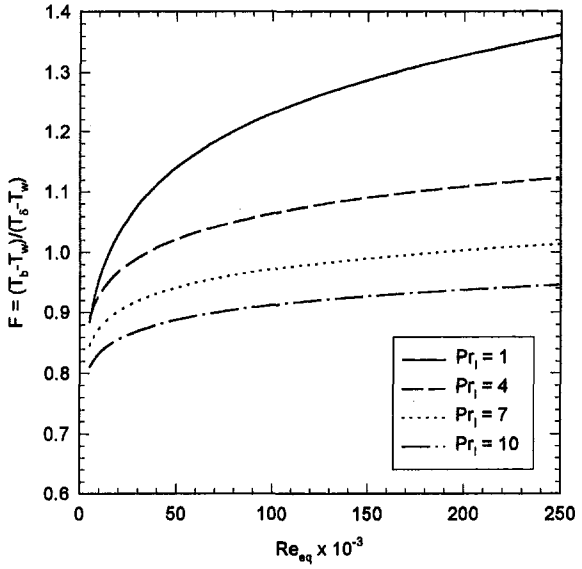

Fig. 2 Variation of the correction factor for four liquid Prandtl numbers at Re_l = 10,000

Local Nusselt Number Expression

Using Eq. (19) along with the Petukhov (1970) equation, the local heat transfer coefficient for an annular condensing flow, Eq. (17), can be written in the form of a Nusselt number as:

$$\mathrm{Nu} = \frac{h_{2-ph}D}{k_l} = \frac{0.0994^{C_1}\,\mathrm{Re}_l^{C_2}\,\mathrm{Re}_{eq}^{1+0.875C_1}\,\mathrm{Pr}_l^{0.815}}{(1.58\ln \mathrm{Re}_{eq} - 3.28)(2.58\ln \mathrm{Re}_{eq} + 13.7\,\mathrm{Pr}_l^{2/3} - 19.1)} \quad (20)$$

where C_1 and C_2 are given by Eqs. (37) and (38), respectively, in the appendix.

Prediction of Local Heat Transfer Data

Table 1 summarizes the local heat transfer data predicted with the new equivalent Reynolds number model. This table shows that the data include tube inner diameters between 4.57 and 12.7 mm, which were tested with five different refrigerants (R-12, R-22, R-113, R-134a, and R-410a). Overall, there are 558 local data points.

Table 1 Local heat transfer data analyzed for the verification of the present model

Source	Fluid	Tube I.D. (mm)	T_{sat} (°C)	Mass Flux (kg/m²-s)	Vapor Quality (%)
Wijaya and Spatz (1995)	R-22	4.57	35	495	22 - 92
	R-22	7.06	35 - 45	495	15 - 90
	R-22	7.75	35 - 52	480 - 495	22 - 83
	R-410a	7.75	46 - 52	481	26 - 79
Dobson et al. (1994a)	R-134a	4.57	35	300 - 650	29 - 91
	R-12	4.57	35	300 - 500	33 - 83
Bae et al. (1969)	R-22	12.52	27 - 39	340 - 658	17 - 96
Altman et al. (1960)	R-22	8.71	35 - 56	298 - 859	13 - 92
Chitti and Anand (1995)	R-22	8.00	36 - 46	148 - 439	23 - 76
Traviss et al. (1971)	R-12	8.00	21 - 56	161 - 1,532	10 - 95
	R-22	8.00	24 - 47	188 - 1,002	14 - 96
Azer et al. (1971)	R-12	12.7	37 - 50	210 - 446	34 - 100
Goodykoontz and Brown (1967)	R-113	7.4	33 - 79	841 - 1,482	17 - 91

Each data point was predicted using the local Nusselt number expression evaluated at the equivalent Reynolds number defined in Eq. (10). In addition, each point was also predicted with the Shah (1979) and Traviss et al. (1973) equations. The overall ability of the three equations to predict the experimental data was determined by the mean absolute deviation, defined as:

$$\text{Mean Abs. Dev.} = \left(\frac{100}{N}\right)\sum_{i=1}^{N}\frac{|\mathrm{Nu}_{pred,i} - \mathrm{Nu}_{exp,i}|}{\mathrm{Nu}_{exp,i}} \quad (21)$$

where N is the total number of data points. The mean absolute deviation gives the average difference between the predicted and experimental values for each data set, without considering whether the difference was positive or negative.

The results of the predictions of the present model are shown in Fig. 3, which shows that more data points were underpredicted than overpredicted. Overall, 72 percent of the 558 local data points were predicted within ±20 percent. The mean absolute deviations of the predictions of the present model, the Shah (1979) equation, and the Traviss et al. (1973) equation for each local data set are shown in the upper half of Table 2. The table indicates that the present model and the Shah (1979) equation provide similar predictions for the experimental data. The Traviss et al. (1973) equation gives a higher prediction of the Nusselt number than the other two equations, resulting in a larger mean absolute deviation for every data set but their own.

Prediction of Average Heat Transfer Data

Table 3 summarizes the average heat transfer data predicted with the new equivalent Reynolds number model. This table shows that the data includes tube inner diameters between 3.14 and 20 mm tested with six different refrigerants (R-11, R-12, R-22, R-125, R-134a, and R-410a). Overall, the database includes 639 average data points.

The average Nusselt number can be defined as the average of the local values with respect to the length of the condenser tube:

$$\mathrm{Nu}_{avg} = \frac{1}{L}\int_0^L \mathrm{Nu}\,dz \quad (22)$$

However, due to the complexity of the local Nusselt number expression, Eq. (22) cannot be integrated to provide a closed-form solution. Therefore, for each data point, the tube was

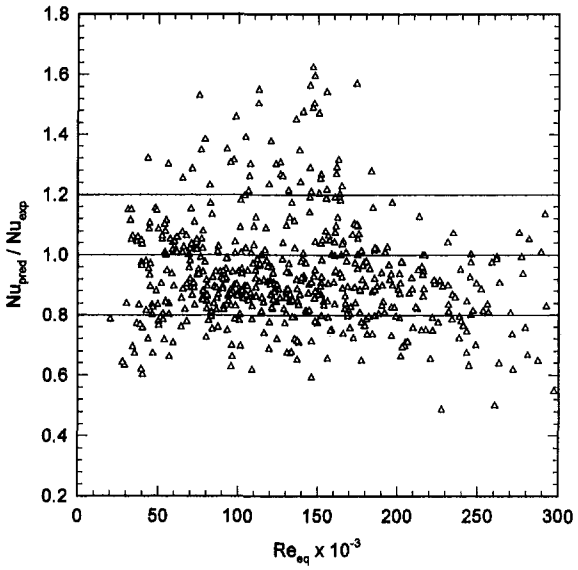

Fig. 3 Predictions of the local heat transfer data using the present model

Table 2 Summary of the comparison of experimental data with the predictions of the present model, the Shah (1979) equation, and the Traviss et al. (1973) equation

Type of Data	Source	# of Data Points	Mean Absolute Deviation (%)		
			Present Model	Shah Equation	Traviss Equation
LOCAL	Wijaya and Spatz (1995)	65	9.68	6.31	19.70
	Dobson et al. (1994a)	36	7.36	9.27	29.72
	Bae et al. (1969)	48	8.15	7.80	13.55
	Altman et al. (1960)	16	8.25	7.65	14.67
	Chitti and Anand (1995)	12	16.87	16.96	16.95
	Traviss et al. (1971)	157	20.27	19.34	15.42
	Azer et al. (1971)	40	22.50	25.82	39.80
	Goodykoontz and Brown (1967)	184	15.25	14.55	20.17
AVERAGE	Dobson et al. (1994b)	423	13.67	13.36	18.60
	Eckels and Pate (1991)	20	13.90	15.18	18.91
	Eckels et al. (1994)	4	9.30	10.33	15.80
	Schlager et al. (1990)	10	8.95	12.83	21.27
	Schlager et al. (1989)	5	2.58	10.48	20.06
	Doerr et al. (1994)	29	12.56	17.14	22.67
	Chitti and Anand (1996)	62	9.13	17.60	29.97
	Wijaya and Spatz (1995)	32	11.63	17.87	23.62
	Bogart (1996)	24	7.55	18.27	32.14
	Cavallini (1971)	30	4.49	3.83	4.23
OVERALL		1,197	13.64	14.27	20.01

separated into many increments, each having a small vapor quality change ($\Delta x < 0.15$). After the local Nusselt number was calculated in each increment using Eq. (22), the results were averaged to give the average Nusselt number.

Figure 4 shows how the local Nusselt number predictions vary with vapor quality for three data points taken at different mass velocities by Bogart (1996). For each data point, the refrigerant vapor quality was approximately 0.85 at the tube inlet and 0.12 at the exit. The figure shows that the predictions of Eq. (22) are linear with vapor quality, which suggests that the average of many incremental Nusselt number calculations gives the same result as a single calculation at the average vapor quality (x_{avg}). To verify this hypothesis, the average Nusselt numbers for all 639 average data points were calculated using both the incremental method and a single calculation of Eq. (22) at x_{avg}. Both methods resulted in predictions within ±2 percent of each other. Consequently, the simplest way to predict the average Nusselt number is to make a single calculation of Eq. (22) at x_{avg}.

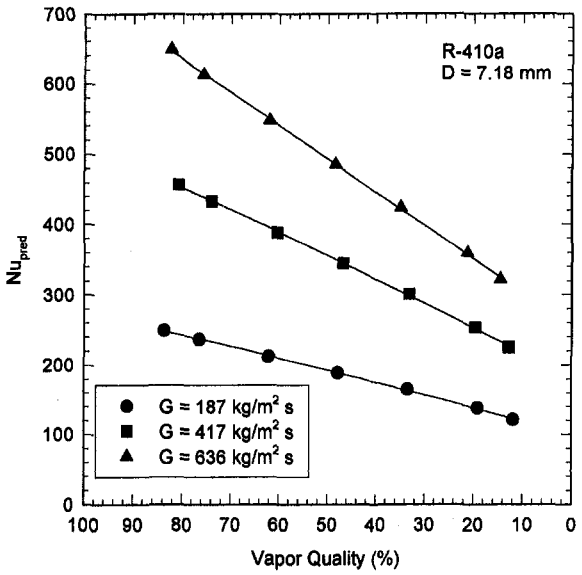

Fig. 4 Variation of the predicted Nusselt number with vapor quality for the average heat transfer data of Bogart (1996)

The results of the predictions of the present model for the average heat transfer data are shown in Fig. 5. This figure shows that 79 percent of the 639 data points are predicted within ±20 percent, with more data points underpredicted than overpredicted. The mean absolute deviations of the present model, the Shah (1979) mean heat transfer equation, and the Traviss et al. (1973) equation are shown for each average heat transfer data set in the lower half of Table 2. Note that the incremental calculation procedure was used to obtain the predictions for the Traviss et al. (1973) equation. The table indicates that the present model generally provides the best prediction of the data.

Table 3 Average heat transfer data analyzed for the verification of the present model

Source	Fluid	Tube I.D. (mm)	T_{sat} (°C)	Mass Flux (kg/m²-s)	Vapor Quality (%)
Dobson et al. (1994b)	R-22	3.14	34 - 46	148 - 828	10 - 97
	R-22	7.04	34 - 46	147 - 676	2 - 100
	R-134a	3.14	34 - 46	148 - 678	1 - 100
	R-134a	7.04	33 - 46	151 - 665	2 - 100
	R-410a	7.04	35 - 45	152 - 667	3 - 99
Eckels and Pate (1991)	R-134a	8.00	30 - 40	136 - 407	10 - 85
	R-12	8.00	30 - 50	126 - 417	10 - 85
Eckels et al. (1994)	R-134a	8.00	40	121 - 368	15 - 85
Schlager et al. (1990)	R-22	10.9	39 - 42	100 - 397	15 - 85
Schlager et al. (1989)	R-22	8.00	39 - 42	205 - 500	10 - 90
Doerr et al. (1994)	R-22	8.00	30 - 40	125 - 376	9 - 83
	R-125	8.00	30 - 40	198 - 375	9 - 89
Chitti and Anand (1996)	R-22	8.00	35 - 36	206 - 373	5 - 90
	R-410a	8.00	24 - 39	161 - 491	5 - 96
Wijaya and Spatz (1995)	R-22	7.75	46 - 52	160 - 560	25 - 87
	R-410a	7.75	46 - 52	165 - 560	25 - 87
Bogart (1996)	R-22	8.81	38 - 41	222 - 822	11 - 85
	R-410a	7.18	39 - 43	187 - 862	11 - 85
Cavallini (1971)	R-11	20.0	22 - 36	87 - 360	31 - 100

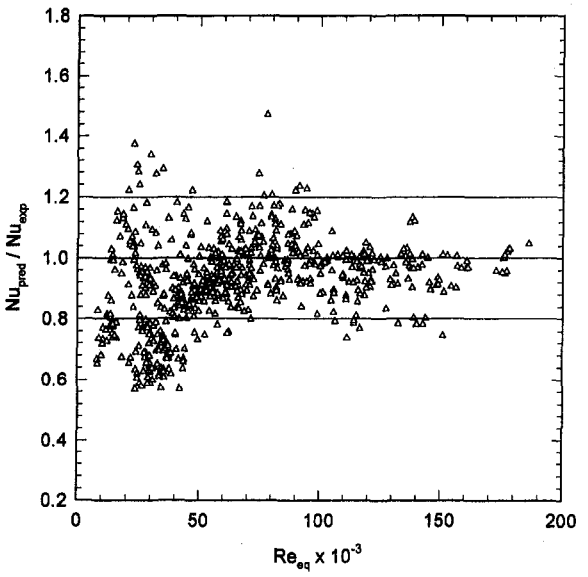

Fig. 5 Predictions of the average heat transfer data using the present model

The Shah (1979) mean heat transfer equation did not predict the average heat transfer data as well as the local heat transfer data, and the Traviss et al. (1973) equation often overpredicted the experimental data by more than 20 percent.

Summary of the Nusselt Number Predictions

A summary of the Nusselt number predictions for all 1197 data points in the database is given at the bottom of Table 2. The present model has an overall mean absolute deviation of 13.64 percent, the best of the three equations. The Shah (1979) equation gave a mean absolute deviation of 14.27 percent, consistent with the 15.4 percent mean deviation reported in his paper. The Traviss et al. (1973) equation gave the largest mean absolute deviation, 20.01 percent. Overall, the present model predicts the local heat transfer data as well as Shah (1979) and better than Traviss et al. (1973). For the average heat transfer data, the present model gives better predictions than the other two equations.

Discussion

For both the local and average heat transfer data, the present model was found to underpredict the experimental Nusselt number more often than it overpredicted it. These underpredictions occurred primarily for three reasons: underpredictions of the two-phase pressure drop, liquid entrainment in the vapor core, and stratification of the annular flow.

The two-phase pressure drop is an important part of the equivalent Reynolds number model, as seen in Eq. (7). If underpredicted, the resulting equivalent Reynolds number will be too low, producing an underprediction of the experimental Nusselt number. In the data sets that included both heat transfer and pressure drop, the Friedel (1979) correlation provided reasonably accurate predictions of the frictional pressure drop (within ±20 percent), even for diameters as small as 3.14 mm. However, in cases where the Friedel (1979) correlation did not predict the pressure drop well, it gave underpredictions more often than overpredictions. As seen in Fig. 6, many of the pressure drop measurements of Traviss et al. (1971) were underpredicted by more than 20 percent. Consequently, many of the Nusselt number predictions were also underpredicted by more than 20 percent. Ultimately, the predictive ability of the equivalent Reynolds number model is constrained by the accuracy of the two-phase frictional pressure drop prediction.

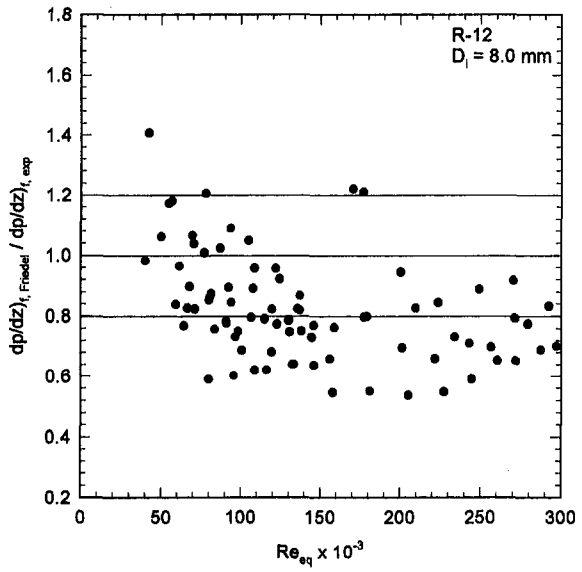

Fig. 6 Predictive ability of the Friedel (1979) correlation for the experimental pressure drop data of Traviss et al. (1971)

The second cause of the underpredictions was liquid entrainment in the vapor core of the annular flow. As the difference in the liquid and vapor phase velocities increases, some of the condensate is entrained into the vapor core flow, thus thinning the liquid film on the wall. A thinner liquid film provides less thermal resistance, leading to increased heat transfer. Since the equivalent Reynolds number model assumes no entrainment, the experimental Nusselt number will be underpredicted when it occurs.

The final cause of the underprediction of some of the experimental data at low mass velocities and vapor qualities was nonannular flow. An examination of the Taitel and Dukler (1976) flow map suggests that many of the local data points having mass velocities under 200 kg/m^2-s and vapor qualities less than 40 percent were on the borderline between the annular and stratified flow regimes. In addition, many of the average heat transfer data points in the database had exit vapor qualities below 20 percent, where the flow may become stratified. Because the present model assumes that the flow is annular, it will not provide accurate predictions for other flow regimes.

The present model shows a significant improvement over Shah (1979) for several of the average heat transfer data sets, including those of Bogart (1996), Chitti and Anand (1996), and Schlager et al. (1989). This may be due mainly to two simplifications Shah (1979) made in the formulation of his equation for average heat transfer in a tube. First, he assumed a linear vapor quality variation in the tube. Second, he neglected several "small" terms in the integration of the local heat transfer coefficient along the tube length so that the final solution would not be too cumbersome to use. Such assumptions are not valid for all mass fluxes and vapor qualities.

Shah (1979) recommends that his correlation be used for tube inner diameters between 7 and 40 mm, because his database did not include tubes with diameters less than 7.4 mm. However, the present work shows that the Shah equation is valid for diameters as low as 3.14 mm. We note that the Shah (1979) equation is basically an empirical correlation. However, the present equivalent Reynolds number formulation is an analytically based application of the two-phase heat and momentum analogy.

Conclusions

The equivalent Reynolds number model for shear-controlled condensation inside smooth tubes is attractive because of its rational basis and inherent simplicity. The present formulation corrects deficiencies in the original Akers et al. (1959) model and shows that the present formulation predicts the condensation coefficient as well as the previous correlations. The model requires predictive equations for the single-phase heat transfer coefficient, and the two-phase frictional pressure gradient.

The present model includes an analytically based correction factor, which accounts for the different driving temperature differences between the two-phase and the equivalent all-liquid flows. Using this model, the Nusselt number was predicted for 1197 data points obtained from 18 sources. For the local heat transfer data, the new equivalent Reynolds number model predicted the data as accurately as the Shah (1979) equation and more accurately than the Traviss et al. (1973) equation. For the average heat transfer data, the new equivalent Reynolds number model predicted the data more accurately than the other two equations. Overall, the mean absolute deviation for the predictions of all 1197 data points was 13.64 percent for the new equivalent Reynolds number model, 14.27 percent for the Shah (1979) equation, and 20.01 percent for the Traviss et al. (1973) equation.

A final important element of the present work is that it extends range of validity of the present model and the other correlations to tube internal diameters as small as 3.14 mm.

References

Akers, W. W., Deans, H. A., and Crosser, O. K., 1959, "Condensing Heat Transfer Within Horizontal Tubes," *Chemical Engineering Progress Symposium Series,* Vol. 55, No. 29, pp. 171–176.

Altman, M., Staub, F. W., and Norris, R. H., 1960, "Local Heat Transfer and Pressure Drop for Refrigerant-Condensing in Horizontal Tubes," *Chemical Engineering Progress Symposium Series,* Vol. 56, No. 30, pp. 151–159.

Azer, N. Z., Abis, L. V., and Swearingen, T. B., 1971, "Local Heat Transfer Coefficients During Forced Convection Condensation Inside Horizontal Tubes," *ASHRAE Transactions,* Vol. 77, No. 1, pp. 182–201.

Azer, N. Z., Abis, L. V., and Soliman, H. M., 1972, "Local Heat Transfer Coefficients During Annular Flow Condensation," *ASHRAE Transactions,* Vol. 78, No. 1, pp. 135–143.

Bae, S., Maulbetsch, J. S., and Rohsenow, W. M., 1968, "Refrigerant Forced Convection Condensation Inside Horizontal Tubes," Report No. 79760-59, Department of Mechanical Engineering, Heat Transfer Lab., MIT, Cambridge, MA.

Bae, S., Maulbetsch, J. S., and Rohsenow, W. M., 1969, "Refrigerant Forced Convection Condensation Inside Horizontal Tubes," Report No. 79760-64, Department of Mechanical Engineering, Heat Transfer Lab., MIT, Cambridge, MA.

Bogart, J. E., 1996, personal communication, Wolverine Tube Inc., Decatur, AL.

Baroczy, C. J., 1966, "A Systematic Correlation for Two-Phase Pressure Drop," *Chemical Engineering Progress Symposium,* Vol. 62, No. 44, pp. 232–249.

Boyko, L. D., and Kruzhilin, G. N., 1967, "Heat Transfer and Hydraulic Resistance During Condensation of Steam in a Horizontal Tube and a Bundle of Tubes," *International Journal of Heat and Mass Transfer,* Vol. 10, pp. 361–373.

Carpenter, E. F., and Colburn, A. P., 1951, "The Effect of Vapor Velocity of Condensation Inside Tubes," *General Discussion on Heat Transfer,* published by the Institute of Mechanical Engineers and ASME, pp. 20–26.

Cavallini, A., and Zecchin, R., 1971, "High Velocity Condensation of Organic Refrigerants Inside Tubes," *Proc. Eighth International Congress of Refrigeration,* Vol. 2, pp. 193–200.

Cavallini, A., and Zecchin, R., 1974, "A Dimensionless Correlation for Heat Transfer in Forced Convection Condensation," *Proc. Fifth International Heat Transfer Conference,* Vol. 3, pp. 309–313.

Chisholm, D., 1973, "Pressure Gradients Due to Friction During the Flow of Evaporating Two-Phase Mixtures in Smooth Tubes and Channels," *Journal of Heat and Mass Transfer,* Vol. 16, pp. 347–358.

Chitti, M. S., and Anand, N. K., 1995, "An Analytical Model for Local Heat Transfer Coefficients for Forced Convective Condensation Inside Smooth Horizontal Tubes," *International Journal of Heat and Mass Transfer,* Vol. 38, No. 4, pp. 615–627.

Chitti, M. S., and Anand, N. K., 1996, "Condensation Heat Transfer Inside Smooth Horizontal Tubes for R- and R-32/125 Mixture," *HVAC&R Research,* Vol. 2, No. 1, pp. 79–100.

Dobson, M. K., et al., 1994a, "Experimental Evaluation of Internal Condensation of Refrigerants R-12 and R-134a," *ASHRAE Transactions,* Vol. 100, No. 1, pp. 744–754.

Dobson, M. K., et al., 1994b, "Heat Transfer and Flow Regimes During Condensation in Horizontal Tubes," ACRC Technical Report 57, University of Illinois.

Doerr, T. M., Eckels, S. J., and Pate, M. B., 1994, "In-Tube Condensation Heat Transfer of Refrigerant Mixtures," *ASHRAE Transactions,* Vol. 100, No. 2, pp. 547–555.

Eckels, S. J., and Pate, M. B., 1991, "Evaporation and Condensation of HFC-134a and CFC-12 in a Smooth Tube and a Microfin Tube," *Alternative Refrigerants: ASHRAE Technical Data Bulletin,* Vol. 7, No. 3, pp. 10–20.

Eckels, S. J., Doerr, T. B., and Pate, M. B., 1994, "In-Tube Heat Transfer and Pressure Drop of R-134a and Ester Lubricant Mixtures in a Smooth Tube and a Micro-fin Tube: Part II—Condensation," *ASHRAE Transactions,* Vol. 100, No. 2, pp. 283–294.

Friedel, L., 1979, "Improved Friction Pressure Drop Correlations for Horizontal and Vertical Two Phase Pipe Flow," Paper E2, European Two Phase Flow Group Meeting, Ispra, Italy.

Goodykoontz, J. H., and Brown, W. F., 1967, "Local Heat Transfer and Pressure Distributions for Freon-113 Condensing in Downward Flow in a Vertical Tube," NASA TN D-3952.

Hewitt, G. F., 1992, "Gas-Liquid Flow," *Handbook of Heat Exchanger Design,* Begell House Inc., New York, pp. 2.3.2-9–2.3.2-12.

Lockhart, R. W., and Martinelli, R. C., 1949, "Proposed Correlation of Data for Isothermal Two-Phase, Two-Component Flow in Pipes," *Chemical Engineering Progress,* Vol. 45, No. 1, pp. 39–48.

Moser, K. W., 1997, "A New Definition of the Equivalent Reynolds Number for Vapor Shear-Controlled Condensation Inside Smooth Tubes." M.S. Thesis, The Pennsylvania State University.

Petukhov, B. S., 1970, "Heat Transfer and Friction in Turbulent Pipe Flow With Variable Physical Properties," *Advances in Heat Transfer,* Vol. 6, Academic Press, New York.

Schlager, L. M., Pate, M. B., and Bergles, A. E., 1989, "Heat Transfer and Pressure Drop During Evaporation and Condensation of *R* in Horizontal Microfin Tubes," *International Journal of Refrigeration,* Vol. 12, pp. 6–13.

Schlager, L. M., Pate, M. B., and Bergles, A. E., 1990, "Evaporation and Condensation Heat Transfer and Pressure Drop in Horizontal, 12.7 mm Microfin Tubes With Refrigerant," ASME JOURNAL OF HEAT TRANSFER, Vol. 112, pp. 1041–1047.

Sieder, E. N., and Tate, C. E., 1936, "Heat Transfer and Pressure Drop of Liquids in Tubes," *Ind. Eng. Chem.,* Vol. 28, pp. 1429.

Shah, M. M., 1979, "A General Correlation for Heat Transfer During Film Condensation Inside Pipes," *International Journal of Heat and Mass Transfer,* Vol, pp. 547–556.

Soliman, M., Schuster, J. R., and Berenson, P. J., 1968, "A General Heat Transfer Correlation for Annular Flow Condensation," ASME JOURNAL OF HEAT TRANSFER, Vol. 90, pp. 267–276.

Taitel, Y., and Dukler, A. E., 1976, "A Model for Predicting Flow Regime Transitions in Horizontal and Near Horizontal Gas-Liquid Flow," *American Institute of Chemical Engineering Journal,* No. 1, pp. 47–55.

Traviss, D. P., Baron, A. G., and Rohsenow, W. M., 1971, "Forced Convection Condensation Inside Tubes," Report No. 72591-74, Department of Mechanical Engineering, Heat Transfer Lab., MIT, Cambridge, MA.

Traviss, D. P., Rohsenow, W. M., and Baron, A. B., 1973, "Forced-Convection Condensation Inside Tubes: A Heat Transfer Equation for Condenser Design," *ASHRAE Transactions,* Vol. 79, No. 2, pp. 31–39.

Wijaya, H., and Spatz, M. W., 1995, "Two-Phase Flow Heat Transfer and Pressure Drop Characteristics of R- and R-32/125," *ASHRAE Transactions,* Vol. 101, No. 1, pp. 1020–1027.

APPENDIX

Derivation of the Correction Factor (F)

The correction factor was derived using a boundary layer analysis of the liquid condensate film. To simplify the analysis, the following five assumptions were made:

1 The von Karman universal velocity profile describes the motion of the liquid film:

$$u^+ = y^+ \quad 0 < y^+ < 5$$

$$u^+ = -3.05 + \ln y^+ \quad 5 < y^+ < 30$$

$$u^+ = 5.5 + 2.5 \ln y^+ \quad y^+ > 30 \tag{23}$$

2 The film thickness is small compared to the tube radius ($\delta \ll R$).

3 A uniform film thickness exists around the tube circumference.

4 No liquid entrainment in the vapor core.

5 Eddy viscosity is equal to the eddy conductivity ($\epsilon_m = \epsilon_h$).

To begin the analysis, consider the turbulent z-momentum equation in cylindrical coordinates. Integration of this equation with respect to the radial coordinate, r, reveals a linear shear stress distribution in the film. A variable transformation is used such that $y = R - r$ describes the distance outward from the tube wall, and the shear stress distribution is given by:

$$\tau = \left(1 - \frac{y}{R}\right)\tau_w \tag{24}$$

In the region close to the wall, both the molecular and turbulent contributions to shear stress can be important. Therefore, the shear stress is

$$\tau = \rho_l(\nu_l + \epsilon_m)\frac{du}{dy} \tag{25}$$

The combination of Eqs. (24) and (25) yields an expression for ϵ_m/ν_l. In dimensionless variables,

$$\frac{\epsilon_m}{\nu_l} = -1 + \frac{(1 - y^+/R^+)}{du^+/dy^+} \tag{26}$$

Utilizing the von Karman universal velocity profile, Eq. (26) becomes:

$$\frac{\epsilon_m}{\nu_l} \approx 0 \quad 0 < y^+ < 5$$

$$\frac{\epsilon_m}{\nu_l} \approx \frac{y^+}{5} - 1 \quad 5 < y^+ < 30$$

$$\frac{\epsilon_m}{\nu_l} = -1 + \frac{y^+}{2.5}\left(1 - \frac{y^+}{R^+}\right) \quad y^+ > 30 \tag{27}$$

The energy equation in the liquid film relates the radial heat flux to the temperature gradient:

$$q'' = \rho_l c_{p,l}(\alpha_l + \epsilon_h)\frac{dT}{dy} \tag{28}$$

Assuming that, as with the shear stress, the heat flux varies linearly in the liquid film,

$$\frac{q''}{q''_w} = \frac{\tau}{\tau_w} \tag{29}$$

and that $\epsilon_m = \epsilon_h$, the temperature difference $(T_\delta - T_w)$ can be obtained in a dimensionless form:

$$T^+ = \int_0^{\delta^+} \frac{1 - \dfrac{y^+}{R^+}}{\dfrac{\epsilon_m}{\nu_l} + \dfrac{1}{\mathrm{Pr_l}}}\, dy^+ \tag{30}$$

Substituting ϵ_m/ν_l from Eq. (25) into Eq. (30), T^+ becomes:

$$T^+ = \delta^+ \mathrm{Pr_l} \quad 0 < \delta^+ < 5$$

$$T^+ = 5\,\mathrm{Pr_l} + \int_5^{\delta^+} \frac{\mathrm{Pr_l}}{1 + \mathrm{Pr_l}\left(\dfrac{y^+}{5} - 1\right)}\, dy^+ \quad 5 < \delta^+ < 30$$

$$T^+ = (T^+)_{\delta^+=30} + \int_{30}^{\delta^+} \frac{1 - \dfrac{y^+}{R^+}}{\dfrac{1}{\mathrm{Pr_l}} - 1 + \dfrac{y^+}{2.5}\left(1 - \dfrac{y^+}{R^+}\right)}\, dy^+$$

$$\delta^+ > 30 \tag{31}$$

The equations for T^+ can be solved analytically to obtain the temperature profile across the liquid film. The only remaining unknowns in Eq. (31) are the dimensionless pipe radius (R^+) and the dimensionless film thickness (δ^+). However, both can be written in terms of known values. Combining the definition of R^+ with the friction velocity (u^*) and Eq. (6), the dimensionless pipe radius is given by:

$$R^+ = \mathrm{Re_{eq}}\sqrt{\frac{f}{8}} \tag{32}$$

Using the Blasius friction factor, this equation becomes:

$$R^+ = 0.0994\ \mathrm{Re_{eq}^{7/8}} \tag{33}$$

Using the continuity equation, Traviss et al. (1973) showed that the dimensionless film thickness can be approximated within ±4 percent with the following expressions:

$$\delta^+ = 0.7071\ \mathrm{Re_l^{0.5}} \quad 0 < \mathrm{Re_l} < 50$$

$$\delta^+ = 0.4818\ \mathrm{Re_l^{0.585}} \quad 50 < \mathrm{Re_l} < 1125$$

$$\delta^+ = 0.0095\ \mathrm{Re_l^{0.812}} \quad \mathrm{Re_l} > 1125 \tag{34}$$

Using the preceding derivation for the two-phase temperature difference $(T_\delta - T_w)$ and the derivation of Petukhov (1970) for the single-phase temperature difference $(T_b - T_w)$, the correction factor, F, becomes:

$$F = \frac{1.07\sqrt{2/f} + 12.7(\mathrm{Pr_l^{2/3}} - 1)}{T^+} \tag{35}$$

Due to the complexity of the relationships for T^+, the correction factor can be tedious to solve. Consequently, a more convenient form of this equation is desired. Assuming that $\delta^+ > 30 (\mathrm{Re_l} > 1125)$, the correction factor was calculated for a wide range of R^+ and Pr. Using a curve-fitting program, F can be defined to an accuracy of ±1 percent with the following expression:

$$F = 1.31(R^+)^{C_1}\,\mathrm{Re_l^{C_2}}\,\mathrm{Pr_l^{-0.185}} \tag{36}$$

where C_1 and C_2 are defined as:

$$C_1 = 0.126\ \mathrm{Pr_l^{-0.448}} \tag{37}$$

$$C_2 = -0.113\ \mathrm{Pr_l^{-0.563}} \tag{38}$$

Convective Condensation of Superheated Vapor

R. L. Webb
Professor,
Department of Mechanical Engineering,
Penn State University,
University Park, PA 16802
r5w@psu.edu

This paper provides a rationally based method to calculate the condensation coefficient of superheated vapor for condensation inside tubes. The method is theoretically based, and is applicable to any pure vapor. The method may be easily extended to condensation inside enhanced tubes, or to shell-side condensation. This work is an extension of a theory previously presented by Lee et al. (1991).

Introduction

There are many applications in which the vapor entering a condenser is superheated. Important among these are refrigerant condensers, where the vapor leaving the compressor is significantly superheated. If the tube wall is at a greater temperature than the saturation value, the vapor will be cooled without condensation. However, the vapor will condense if the tube wall is below the vapor saturation temperature.

Very little has been published on methodology to calculate the heat transfer coefficient for convective condensation of superheated vapor. The author's review of applicable books on two-phase heat transfer or heat-exchanger design gives no discussion of a general calculation methodology. Survey papers (e.g., Marto, 1988), or handbook chapters (e.g., Butterworth, 1983, or Marto, 1991) do not discuss convective condensation of superheated vapor. One may find a brief reference to use of the Nusselt condensation equation with superheated vapor (e.g., Hewitt et al., 1994). This is not the same issue as addressed here, because it does not address the rate at which the vapor loses its superheat, and how that affects the local condensation coefficient.

Altman et al. (1960) measured the average condensation coefficient of R-22 flowing inside a 1.2-m-long horizontal tube with entering superheat. They proposed the following empirical correlation for their average condensing coefficient with superheated vapor:

$$\frac{h_{sup}}{h_{sat}} = 0.29(T_{sat} - T_w)^{0.52} \quad (1)$$

where the units on $(T_{sat} - T_w)$ are degrees Fahrenheit. Equation (1), applicable only to R-22, shows that the average condensing coefficient is independent of the entering superheat (up to their maximum tested superheat of 21 K). Further work has been reported for condensation of superheated refrigerants. Miropolsky et al. (1974) and Fujii et al. (1978) experimentally studied condensation of superheated vapor and offered empirical correlations.

Although not treated in the literature, discussion with heat exchanger designers suggests that the condensing superheated vapor will quickly lose its superheat, followed by condensation of saturated vapor. The work to be presented herein shows that this supposition is incorrect. There are two issues of concern: (1) What is the heat transfer coefficient in the superheated region, and (2) How fast will the vapor lose its superheat? Lee et al. (1991) appear to be the first investigators to propose a semi-rationally based prediction method for the local condensation coefficient of superheated vapor. They performed a detailed experimental and theoretical study of convective superheated condensation for Refrigerant-22 flowing in a horizontal tube. They proposed an empirical model that they argue is similar in concept to the Chien (1966) model for convective vaporization inside tubes. The model assumes that the condensation coefficient for superheated vapor can be written as the sum of a forced convection (sensible heat) term and a saturated condensation term. They show that the model provides good agreement with their data. This model will be discussed later.

The purpose of this paper is to provide a theoretically based model for superheated condensation. The model has the same structure as the Colburn and Hougen (1934) equation for condensation in the presence of noncondensible gas. The Colburn and Hougen equation includes the sum of a vapor sensible cooling term, and a latent heat term. The same basic terms apply to the present problem. Hence, the present model is rationally based. We will show that the model of Lee et al. (1991) can be transformed to the proposed model. Hence, the proposed model and the Lee et al. model will give the same results. The key advantage of the proposed model is that it is rationally based, and can be extended to both condensation inside enhanced tubes, and shell-side condensation.

Mechanism of Superheated Condensation

Consider convective condensation of superheated vapor inside a tube with $T_w < T_{sat}$. There will be two components to the heat flux arriving at the liquid–vapor interface surface, which is at temperature T_{sat}. These components are the sensible component (resulting from cooling of the superheated vapor from T_b to T_{sat}) and the latent component, resulting from the condensing process:

$$q_{sup} = q_{sens} + q_{lat} \quad (2)$$

The sensible component is given by $q_{sens} = h_{fc}(T_b - T_{sat})$, where h_{fc} is the heat transfer coefficient for forced convection to a gas. The latent component is given by $q_{lat} = h_{sat}(T_{sat} - T_w)$, where h_{sat} is the condensation coefficient for saturated vapor. We wish to define a composite heat transfer coefficient (h_{sup}), which accounts for the combined effect of the sensible and latent components. The h_{sup} is defined in terms of the conventional driving temperature difference for condensation, $(T_{sat} - T_w)$. Thus, the total heat flux (q_{sup}) is defined as $h_{sup}(T_{sat} - T_w)$. Substituting these definitions into Eq. (2) gives

$$h_{sup}(T_{sat} - T_w) = h_{fc}(T_b - T_{sat}) + h_{sat}(T_{sat} - T_w) \quad (3)$$

For condensation inside a plain tube, the h_{fc} and h_{sat} terms are calculated using the following equations:

- h_{sat}: Equation for convective condensation of saturated vapor inside tubes, e.g., the Shah (1979) correlation.
- h_{fc}: Equation for single-phase convection to a gas flowing in a tube, e.g., the Petukhov equation as given by Incropera and DeWitt (1996), or the Dittus–Boelter equation.

Contributed by the Heat Transfer Division for publication in the JOURNAL OF HEAT TRANSFER. Manuscript received by the Heat Transfer Division May 30, 1997; revision received November 21, 1997. Keywords: Condensation, Forced Convection. Associate Technical Editor: M. Kaviany.

We note that Eq. (2) is identical to the Colburn and Hougen (1934) model for condensation in the presence of noncondensible gases. However, the formulation of the q_{lat} term is specialized to the present problem of condensation of a saturated, pure vapor. Dividing each term in Eq. (3) by $(T_{sat} - T_w)$ yields

$$h_{sup} = h_{fc}\left(\frac{T_b - T_{sat}}{T_{sat} - T_w}\right) + h_{sat} \quad (4)$$

where

$$F = \frac{T_b - T_{sat}}{T_{sat} - T_w} = \frac{\Delta T_{sh}}{T_{sat} - T_w} \quad (5)$$

Thus, the model may be written as

$$h_{sup} = Fh_{fc} + h_{sat} \quad (6)$$

As shown by Eq. (5), this F-factor is physically interpreted as the degrees of superheat ($\Delta T_{sh} = T_b - T_{sat}$) divided by the condensing temperature difference for saturated vapor ($T_{sat} - T_w$). The F-factor asymptotically approaches zero as the superheat is depleted. Hence, the superheat term Fh_{fc} in Eq. (6) equals zero after the superheat is depleted.

Correction for Mass Transfer

Equation (3) calculates the sensible cooling rate of the superheated vapor by the expression $q_{sens} = h_{fc}(T_b - T_{sat})$. This equation applies for no accompanying mass transfer. The movement of the condensing vapor to the condensing surface will also result in bulk convection of superheated vapor, which will aid in cooling of the superheated vapor. The bulk convection rate of superheated vapor to the liquid–vapor interface is given by $q_{bc} = (m_v/A)c_{pv}(T_b - T_{sat})$, where m_v/A is the mass flux of condensation. The $\dot{m}_v/A = q_{lat}/i_{fg}$ where i_{fg} is the latent heat of the condensing vapor. Thus, the bulk convection contribution is given by $q_{bc} = (q_{lat}/i_{fg})c_{pv}(T_b - T_{sat})$. To account for both convection components of the superheated vapor, we may write

$$h^*_{fc}(T_b - T_{sat}) = h_{fc}(T_b - T_{sat}) + (q_{lat}/i_{fg})c_{pv}(T_b - T_{sat}) \quad (7)$$

Or, one may replace h_{fc} by h^*_{fc}, where

$$h^*_{fc} = h_{fc} + c_{pv}q_{lat}/i_{fg} \quad (8)$$

Substituting Eq. (8) into Eq. (3) gives

$$h_{sup}(T_{sat} - T_w) = h^*_{fc}(T_b - T_{sat}) + h_{sat}(T_{sat} - T_w) \quad (9)$$

Whether it is important to include the contribution of bulk convection depends on the magnitude of $c_{pv}q_{lat}/i_{fg}$ as compared to h_{fc}. Typically, inclusion of the $c_{pv}q_{lat}/i_{fg}$ term will have little effect on the calculated total heat flux, because the latent term is large, relative to the sensible heat term.

We provide an example to calculate the magnitude of h^*_{fc}/h_{fc} for R-22 condensing at 49°C in a 15.0 mm inside diameter smooth tube at 0.050 kg/s mass flow rate for $q_{lat} = 34.5$ kW/m^2. The h_{fc} is calculated using the Dittus–Boelter equation (the previously noted Petukhov equation is equally applicable). The calculated value for h^*_{fc}/h_{fc} is 1.40, which is sufficiently large that one should consider the correction. If one were condensing steam at the same q_{lat}, the correction factor would be significantly smaller, because of the high latent heat of steam.

The recognition that mass flux can affect sensible heat transfer was first discussed by Ackermann (1937). Ackermann (1937) formulated a slightly different form of the correction. The present formulation is believed to be more accurate and simpler than the Ackermann derivation. Hewitt et al. (1994) provide further discussion of this subject, and give Ackermann's 1937 derivation.

Lee Model

Lee et al. (1991) used the same formulation as for Eq. (3), except they defined the composite condensing coefficient for the superheated vapor in terms of the local driving temperature difference vapor temperature $(T_b - T_w)$ for which $q_{sup} = h_{sup,L}(T_b - T_w)$. Using the Lee definition for q_{sup} in Eq. (3) gives

$$q_{sup} = h_{sup,L}(T_b - T_w) = h_{fc}(T_b - T_{sat}) + h_{sat}(T_{sat} - T_w) \quad (10)$$

Dividing each term in Eq. (10) by $(T_b - T_w)$ and defining $S_1 = (T_b - T_{sat})/(T_b - T_w)$ and $S_2 = (T_{sat} - T_w)/(T_b - T_w)$ allows Eq. (4) to be written as

$$h_{sup,L} = S_1h_{fc} + S_2h_{sat} \quad (11)$$

The term S_1 is a measure of the degrees of superheat and can be written as $S_1 = \Delta T_{sh}/(T_b - T_w)$. When the superheat is depleted, $S_1 = 0$, and $S_2 = 1.0$. The F-factor defined by Eq. (5) is related to S_1 and S_2 by the relation $F = S_1/S_2$. The present author's formulation (Eq. (6)) is simpler than that of Lee, and it will give the same result. We note that Lee did not propose inclusion of the mass flux contribution to h_{fc} as given by Eq. (9).

Lee et al. used Eq. (11) to test their ability to predict their local condensation coefficient data for R-22 condensation in a 7.95 mm inside diameter, horizontal tube 5.3 m long. Cooling water flowed in the annulus of the double-pipe condenser. The coolant annulus was instrumented at nine points along the length

Nomenclature

c_{pv} = specific heat of superheated vapor
d_i = tube internal diameter
F = F-factor defined by Eq. (5)
h = heat transfer coefficient: h_{fc} (sensible heat transfer to superheated vapor), h^*_{fc} (defined by Eq. (8)), h_{sat} (from condensing saturated vapor), h_{sup} (condensation coefficient for superheated vapor), $h_{sup,L}$ (condensing coefficient of superheated vapor defined by the Lee et al. correlation, Eq. (11)), h_{Nu} (condensing coefficient on a vertical gravity drained plate as given by the Nusselt Eq. (12))
i_{fg} = latent heat
K_g = mass transfer coefficient used in Eq. (14)
m_v/A = mass flux of vapor toward condensing surface
p_v = partial pressure of diffusing vapor: p_{vb} (in bulk mixture), p_{vi} (at liquid vapor interface)
p_{am} = log-mean pressure of noncondensible gas in mixture
q = heat flux: q_{bc} [$=(m_v/A)c_{pv}(T_b - T_{sat})$], q_{sens} (sensible heat flux from superheated vapor), q_{lat} (from condensing saturated vapor), q_{sup} (from condensing superheated vapor)
S_1 = term used in Eq. (11) defined as $\Delta T_{sh}/(T_b - T_w)$
S_2 = term used in Eq. (11) defined as $(T_{sat} - T_w)/(T_b - T_w)$
T = temperature: T_b (mixed temperature of superheated vapor), T_c (coolant temperature), T_i (temperature of liquid–vapor interface), T_{sat} (saturation temperature), T_w (wall temperature)
ΔT_{sh} = degrees of superheat = $T_b - T_{sat}$
X = vapor quality
Z = axial length along test section

to allow measurement of the local heat flux. Data were taken for 150–350 kg/s-m^2 mass velocity, 7.64–13.55 bar saturation pressure, inlet superheats between 1.9 and 65°C, and a range of heat fluxes. Figure 1 is taken from Lee et al. (1991) and shows that their predicted heat flux for superheated vapor using Eqs. (10) and (11) plotted versus their experimental data. Figure 1 shows that their model predicts the experimental data within ±20 percent.

Figure 2 shows one of their experimental runs, which is for 21.3 K entering superheat and an exit vapor quality near zero. The solid lines on the lower part of the figure show the experimental F-Factor (Eq. (5)) and the predicted condensing coefficient. The plotted vapor quality (x) shows a near linear decrease along the test section length. The F-factor, which indicates the superheat, decreases from 4.0 at $Z/d_i = 50$ to $F \cong 0$ at $Z/d_i = 275$. The asymptotic value of the condensing coefficient (horizontal line for $Z/d_i = 350$) is that predicted by the Shah (1979) equation. The figure shows that the superheat does not dissipate quickly. Figure 2 shows that the superheat is finally dissipated at $Z/d_i = 275$, at which $x \cong 0.45$. The solid line through the q'' points is the predicted local heat flux.

Discussion

Application to Other Geometries. The fundamental form of Eq. (6) is applicable to any geometry. Thus, it may be applied to condensation inside enhanced tubes (e.g., the micro-fin tube) or condensation on the outside of a bundle of tubes. To use Eq. (6) for such other geometries, one must have the appropriate equations for h_{fc} and h_{sat} for the geometry of interest.

Relation to Other Work. In the Introduction, brief reference was made to use of the Nusselt condensation equation with superheated vapor, as noted on page 578 of Hewitt et al. (1994). The average condensation coefficient of saturated vapor on a vertical plate with a gravity drained laminar film is given by

$$h_{Nu} = 0.943\left(\frac{k^3 g(\rho_l - \rho_v) i_{fg}}{L\nu_l(T_w - T_{sat})}\right)^{1/4} \tag{12}$$

If the vapor is superheated, one may replace the latent heat (λ) by a fictitious superheat given by

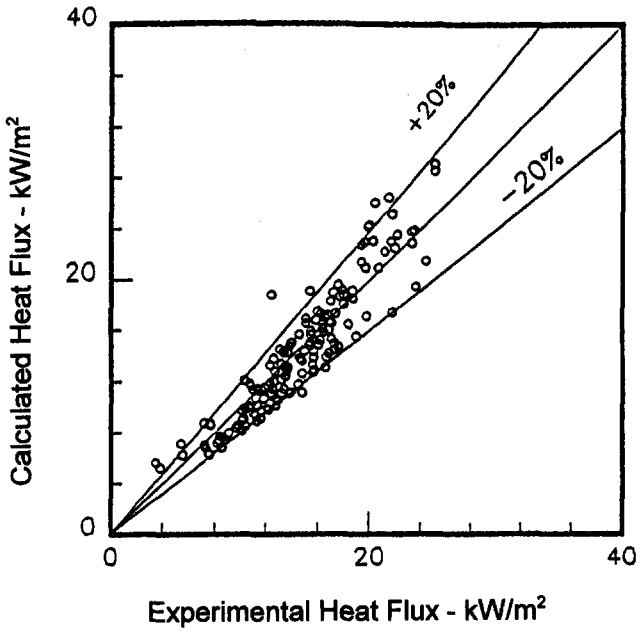

Fig. 1 Comparison of predicted heat flux using Eq. (11) and the superheated R-22 condensation data of Lee et al. (1991)

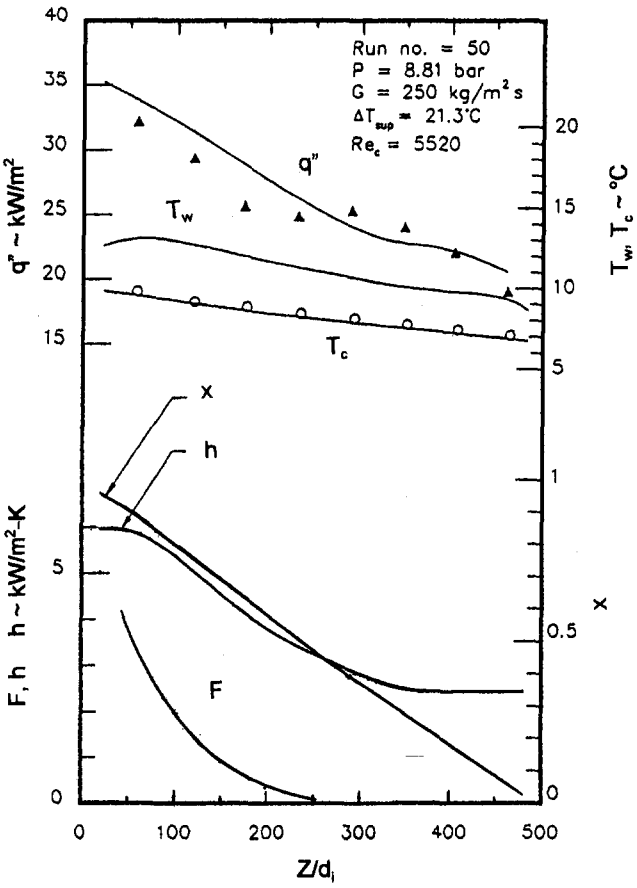

Fig. 2 Illustration of the model for R-22 data of Lee et al. (1991)

$$i'_{fg} = i_{fg} + c_{pv}(T_b - T_{sat}) \tag{13}$$

The i'_{fg} accounts for the effect of superheated vapor on the latent heat flux. This method assumes that the vapor is uniformly superheated over the entire length of the condensing surface. It is not the same issue as addressed here, because it does not address the rate at which the vapor loses its superheat along the condensing length, and how that affects the local condensation coefficient. Nor is the Nusselt equation applicable to condensation inside tubes.

In the introduction, we also noted that the model has the same structure as the Colburn and Hougen (1934) equation for condensation in the presence of noncondensible gas. This equation is given in Chap. 10 of Collier and Thome (1994) as

$$q = h^*_{fc}(T_b - T_i) + \frac{K_g i_{fg} \rho_v}{p_{am}}(p_{vb} - p_{vi}) \tag{14}$$

Equation (14) has the same form as Eqs. (9) and (2). The two terms on the right-hand side of Eq. (14) are the vapor sensible cooling term, and the latent heat term. The latent term is written in terms of the diffusion rate of the condensing vapor through the mixture containing the noncondensible gas. The driving temperature difference for the sensible term is $(T_b - T_i)$. The vapor is saturated at the liquid–vapor interface temperature (T_i). Hence, this term is the same as in Eq. (9). Equation (14) is well accepted for calculation of the effect of noncondensible gases.

Conclusions

This work formulates an alternate equation for calculation of the condensation coefficient of superheated vapor. Although the equation is simpler than that of Lee, it gives the same result.

The basic formulation of the model is applicable to condensation inside or outside tubes of any geometry, including enhanced surfaces.

References

Ackermann, G., 1937, "Heat Transfer and Molecular Mass Transfer in the Same Field at High Temperatures and Large Partial Pressure Differences," *Forsch. Ing. Wes. VDI, Forschungesheft,* Vol. 8, p. 232.

Altman, M., Staub, F. W., and Norris, R. H., 1960, "Local Heat Transfer and Pressure Drop for Refrigerant-22 Condensing in Horizontal Tubes," *Chem. Eng. Progress Symp. Ser.,* Vol. 56, No. 30, pp. 151–159.

Butterworth, D., 1983, "Film Condensation of Pure Vapor," Sec. 2.6.2 in Vol. 2 of *Heat Exchanger Design Handbook,* E. U. Schlunder, ed.-in-chief, Hemisphere Pub. Co., New York.

Chien, J. C., 1966, "Correlation for Boiling Heat Transfer to Saturated Fluids in Convective Flow," *Ind. Eng. Chem. Pressure Design Development,* Vol 5, No. 3, pp. 322–329.

Collier, J. G., and Thome, J. R., 1994, *Convective Boiling and Condensation,* 3rd ed., Clarendon Press, Oxford, p. 439.

Colburn, A. P., and Hougen, O. A., 1934, "Design of Cooler Condensers for Mixtures of Vapors With Non-condensing Gases," *Ind. Eng. Chemistry,* Vol. 26, p. 1178.

Fujii, T., Honda, H., Nozu, S., and Nakarai, S., 1978, "Condensation of Superheated Vapor Inside a Horizontal Tube," *Heat Transfer—Japanese Research,* Vol. 4, No. 3, pp. 1–48.

Hewitt, G. F., Shires, G. L., and Bott, T. R., 1994, *Process Heat Transfer,* CRC Press, pp. 578 and 604.

Incropera, F. P., and DeWitt, D. P., 1996, *Fundamentals of Heat and Mass Transfer,* 4th ed., Wiley, New York, p. 445.

Lee, C. C., Teng, Y. J., and Lu, D. C., 1991, "An Investigation of Condensation Heat Transfer of Superheated R-22 Vapor in a Horizontal Tube," *Proc. World Conf. on Experimental Heat Transfer, Fluid Mechanics, and Thermodynamics,* pp. 1051–1057.

Marto, P. J., 1988, "An Evaluation of Film Condensation on Horizontal Integral-Fin Tubes," ASME JOURNAL OF HEAT TRANSFER, Vol. 110, pp. 1287–1305.

Marto, P. J., 1991, *Boilers, Evaporators & Condensers,* S. Kakac, ed., Hemisphere, Washington, DC, Chap. 10.

Miropolsky, Z. L., Shneersva, R. I., and Teernakova, L. M., 1974, "Heat Transfer at Superheated Steam Condensation Inside Tubes," *Proc. 5th Int. Heat Transfer Conference,* Vol. 3, pp. 246–249.

Shah, M. M., 1979, "A General Correlation for Heat Transfer During Film Condensation Inside Pipes," *Int. J. Heat Mass Transfer,* Vol. 22, pp. 547–556.

Freezing and Melting With Multiple Phase Fronts Along the Outside of a Tube

B. Vick

D. J. Nelson

X. Yu

Mechanical Engineering Department,
Virginia Polytechnic Institute
and State University,
Blacksburg, VA 24061-0238

This paper addresses the modeling and analysis of thermal storage systems involving phase change with multiple phase fronts. The problem involves a fluid flowing inside a long tube surrounded by a phase-change material (PCM). The fluid temperature at the tube inlet cycles above and below the freezing temperature of the PCM, causing alternating liquid and solid layers to form and propagate from the tube outside surface. The objective of this paper is to predict the dynamic performance, temperature distribution, and phase front distribution along the tube. The problem is modeled as axisymmetric and two dimensional. Axial conduction is neglected and the problem is discretized into axial segments. Each of these axial sections is modeled as a transient, one-dimensional problem involving phase change with the possibility of multiple phase boundaries. The boundary element method (BEM) is used to obtain the transient solution in each axial section. Each axial segment communicates with downstream segments through the fluid flowing inside the tube. In order to ensure numerically stable results, a fully implicit discretization is used in both the axial and time variables. Results are presented for the time and axial evolution of the phase fronts and temperatures in response to a fluid inlet temperature that periodically alternates between values above and below the freezing temperature. This BEM is tested against the thermal network method (TNM) and the negligible sensible heat approximation (NSH) by comparing the outlet temperature and the latent state of charge. Results are found to be consistent and accurate.

Introduction

The problem under investigation is shown in Fig. 1 and involves a fluid flowing through a long tube surrounded by a phase-change material (PCM). The inlet temperature of the fluid cycles across the freezing temperature of the PCM, T_{fr}, and causes the temperature of the tube outer surface to change across T_{fr}. This causes alternating layers of liquid or solid to form and propagate from the tube wall. This situation is encountered in thermal energy storage systems. While no literature has been found that reports multiple layers, the authors and others have observed this phenomenon in operating thermal storage systems. The issue of off-design partial charge and discharge operation that causes these multiple phase fronts was the subject of a recent ASHRAE research project (Vick et al., 1996).

The present work is applicable to modeling of ice-on-pipe thermal storage systems where both the charge and discharge of the PCM (usually water) occur only from the flow inside the pipes. These systems typically consist of a large tank with a network of long tubes of relatively small diameter submerged in static water. A region of the PCM can be associated with each tube such that an outer symmetry (insulated) boundary approximation can be used. Due to the small temperature difference between the tube outside surface and the PCM (less than 5°C) and the short vertical extent of the tubes, natural convection is largely absent in these systems. Experimental observations by the authors indicate that nearly cylindrical layers of ice form, also indicating a lack of convective motion within the PCM.

Single-front phase-change problems have attracted many investigators and there are numerous publications addressing these problems. Among the proposed numerical techniques, the finite difference and finite element methods have been widely used. In recent years, the boundary element method (BEM) has been applied to phase-change and moving boundary problems. The BEM requires discretization only over the boundaries, and thus has a major advantage over the finite difference and finite element methods, which require a discretization over the complete domain, especially for the phase-change problems where nonlinearity is concentrated on the moving boundaries.

Phase-change problems in cylindrical systems with one or more moving fronts arise mainly in thermal storage applications. There is very little research on multiple phase front problems available, especially for problems in cylindrical systems. Numerous authors have addressed problems involving a single phase front (Banerjee and Shaw, 1982; Kim and Kaviany, 1990; Pasquetti and Caruso, 1990; Vick and Nelson, 1993) but only a few have addressed multiple-front phase-change problems (Choi and Hsieh, 1992; Nelson and Vick, 1994; Vick and Nelson, 1994; Yu et al., 1995), especially in cylindrical systems. Wrobel and Brebbia (1981) addressed the basic formulation using the BEM for axisymmetric transient heat conduction problems, but phase change was not investigated. Sadegh et al. (1987) addressed a buried tube problem in a semi-infinite domain where quasi-steady heat conduction was assumed. Recently, Vick et al. (1996) developed a thermal model and approximate solution for ice thermal storage systems in which multiple phase fronts were included. The distributed effects of sensible heat were approximated as lumped capacities at the boundaries and the quasi-steady assumption was used.

This paper is the extension of the work of Yu et al. (1995), where multiple phase fronts in one-dimensional cylindrical systems were studied. The current work extends the analysis to include both the radial and the axial development of multiple phase fronts along the outside of a tube containing a flowing fluid. With the assumption that axial conduction is negligible, the problem may be discretized into axial segments. Each of

Contributed by the Heat Transfer Division for publication in the JOURNAL OF HEAT TRANSFER. Manuscript received by the Heat Transfer Division August 11, 1995; revision received January 13, 1998. Keywords: Moving Boundaries, Phase-Change Phenomena, Thermal Energy Storage. Associate Technical Editor: S. Ramadhyani.

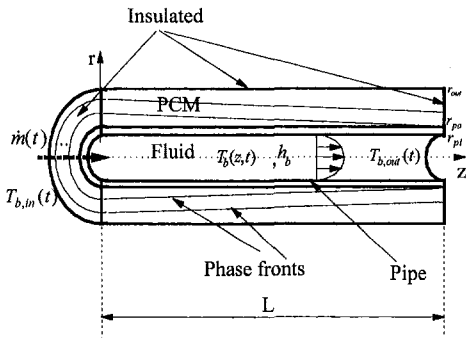

Fig. 1 A typical tube showing details of boundary/inlet conditions

these axial segments is treated as a transient, radially one-dimensional problem involving phase change with the possibility of multiple phase boundaries, as addressed by Yu et al. (1995). The boundary element method is used to obtain the transient solution in each axial section. Since the BEM needs numerical discretization only over the boundaries, it is particularly well suited to problems with multiple moving phase fronts.

This paper is motivated by the need for a theoretical model and computational algorithm to solve the freezing and melting problem of a PCM surrounding a long tube. This problem occurs in ice thermal energy storage systems. The objective of this paper is to develop an accurate method to predict the dynamic performance, temperature distribution, and phase front distribution along the tube.

Problem Formulation

As shown in Fig. 1, the problem under investigation involves the radial and axial evolution of multiple phase fronts along the outside of a tube. A pure substance with a freezing and melting temperature of T_{fr} is contained between two concentric cylindrical walls of length L. The thin outside wall is insulated and has a radius of r_{out}. The tube wall has inside and outside radii of r_{pi} and r_{po}. There is a fluid of bulk temperature $T_b(z, t)$ and mass flow rate of $\dot{m}(t)$ flowing inside the tube. The fluid enters the tube at the temperature of $T_{b,in}$ and leaves the pipe at $T_{b,out}$. If the fluid inlet temperature cycles across T_{fr}, the temperature at the outside tube wall will change back and forth across T_{fr}, causing alternating layers of solid and liquid to form and propagate from the tube outside surface.

Equations in the Fluid. Assuming that axial conduction is negligible and fully developed conditions exist, the energy equation of the fluid can be expressed as,

$$k_b \frac{1}{r}\frac{\partial}{\partial r}\left(r\frac{\partial T_f}{\partial r}\right) = (\rho c_p)_b\left(u_z\frac{\partial T_f}{\partial z} + \frac{\partial T_f}{\partial t}\right) \tag{1}$$

The initial and inlet conditions are,

$$T_f = T_{\text{init}}, \quad t = 0$$
$$T_f = T_{b,\text{in}}(t), \quad z = 0 \tag{2}$$

Here, T_f represents the local temperature of fluid and is a function of r, z and t.

Integrating over the cross section of the tube and using the axisymmetric condition at $r = 0$ reduces Eq. (1) to

$$\pi r_{pi}^2(\rho c_p)_b\frac{\partial T_m}{\partial t} + (\dot{m}c_p)_b\frac{\partial T_b}{\partial z} = k_b\left(\frac{\partial T_f}{\partial r}\right)_{r=r_{pi}} \tag{3}$$

where $\dot{m}$ is the mass flow rate, T_b is the bulk temperature, and T_m is the mean temperature of the fluid.

Note that T_b and T_m are defined as

$$T_b = \frac{\int_0^{r_{pi}}(\rho c_p)_b u_z T_f dA_c}{\int_0^{r_{pi}}(\rho c_p)_b u_z dA_c} = \frac{\int_0^{r_{pi}} u_z T_f dA_c}{UA_c} \tag{4}$$

$$T_m = \frac{\int_0^{r_{pi}}(\rho c_p)_b T_f dA_c}{\int_0^{r_{pi}}(\rho c_p)_b dA_c} = \frac{\int_0^{r_{pi}} T_f dA_c}{A_c} \tag{5}$$

As defined in Eqs. (4) and (5), T_b is the bulk fluid temperature at a given cross section, A_c, and is defined in terms of the thermal energy transported with the bulk motion of the fluid as it moves past the cross section. The temperature T_m is the average temperature defined in terms of the lumped capacity or heat storage of the fluid. These two temperatures differ since the velocity is involved in T_b but is not involved in T_m. Thermal

Nomenclature

A = ratio of the thermal diffusivities = α/α_l
Bi = Biot number = $h_b r_{\text{out}}/k_l$
c_p = specific heat
G = Green's function
h_b = heat transfer coefficient
h_{if} = latent heat of fusion
k = thermal conductivity
K = thermal conductivity ratio = k/k_l
L = length of tube
Lz = dimensionless length of tube = L/r_{out}
$\dot{m}$ = mass flow rate
Pe = Peclet number of fluid = Ur_{pi}/α_b
r = radial position
R = dimensionless radial position = r/r_{out}
r_{out} = radial position of outside wall surface
s = phase front position
S = dimensionless phase front position = s/r_{out}
Ste = Stefan number = $(\rho c_p)_l(T_h - T_{fr})/(\rho_l h_{if})$
t = time
T = temperature
T_{fr} = phase change temperature of PCM
u_z = local fluid velocity
U = mean fluid velocity
z = axial position
Z = dimensionless axial position, z/r_{out}
α = thermal diffusivity
θ = dimensionless temperature = $(T - T_{fr})/(T_h - T_{fr})$
ρ = density
τ = dimensionless time = $\alpha_l t/r_{\text{out}}^2$
τ_c, τ_h = dimensionless cooling and heating time

Subscripts

b = fluid, average or bulk variable
c = cold
f = fluid, local variable
h = hot
i = typical axial segment
in = inlet conditions, $z = 0$
init = initial condition
j = general radial region
j_{in} = radial region adjacent to $r = r_{po}$
j_{out} = radial region adjacent to $r = r_{\text{out}}$
l = liquid
out = outside wall surface, $r = r_{\text{out}}$
p = tube
pi = tube inside surface, $r = r_{pi}$
po = tube outside surface, $r = r_{po}$
s = solid

Superscripts

n = general time level
nn = current time level

storage applications for the problem under investigation seldom involve sensible temperature differences of more than 10°C above or below T_{fr}. Thus the maximum possible difference between T_b and T_m is 7 percent with actual values much closer.

While the energy equation is defined in Eq. (3), the convective boundary condition between the fluid and the pipe wall can be expressed as

$$-k_f \frac{\partial T_f}{\partial r} = h_b(T_b - T_{pi}) = -k_p \frac{\partial T_p}{\partial r}, \; r = r_{pi} \qquad (6)$$

where T_{pi} represents the tube inside surface temperature and the forced convection heat transfer coefficient h_b is calculated using empirical correlations for laminar or turbulent flow.

Substituting Eq. (6) and replacing T_m with T_b reduces Eq. (3) to

$$\pi r_{pi}^2 (\rho c_p)_b \frac{\partial T_b}{\partial t} + (\dot{m} c_p)_b \frac{\partial T_b}{\partial z} = 2\pi r_{pi} h_b [T_{pi}(z, t) - T_b(z, t)] \qquad (7)$$

Equations in the PCM. Since alternating layers of PCM are separated by surfaces all at T_{fr} (zero Rayleigh number), convection in the liquid layers is negligible. Also, thermal storage systems typically have long thin geometry (length to tube spacing of 1000 to 3000), resulting in temperature gradients in the radial direction orders of magnitude higher than those in the axial direction. Conduction effects in the axial direction can thus be neglected. The energy equation in each layer of PCM is

$$\frac{1}{r}\frac{\partial}{\partial r}\left(r \frac{\partial T_j}{\partial r}\right) = \frac{1}{\alpha_j}\frac{\partial T_j}{\partial t}, \quad \text{in layer } j \qquad (8)$$

with the initial condition of

$$T_j = T_{\text{init}}, \quad t = 0 \qquad (9)$$

where j indicates the radial layers as shown in Fig. 2.

The appropriate boundary conditions for this problem are described as follows:

1 Insulated outside wall:

$$\frac{\partial T_1}{\partial r} = 0, \quad j = 1, \quad r = r_{\text{out}} \qquad (10)$$

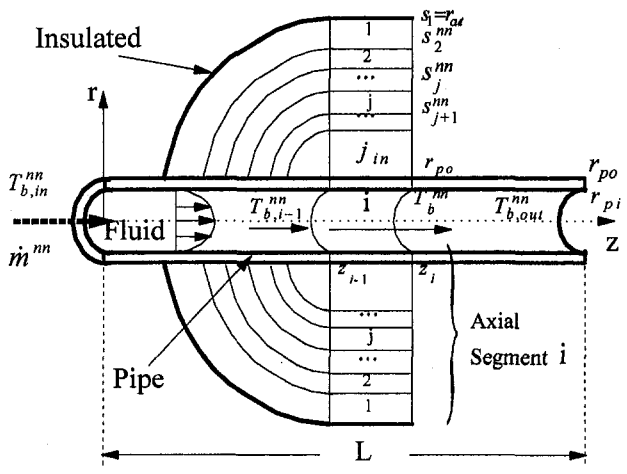

Fig. 2 A typical tube showing details of axial segment *i*

2 Moving phase front:

$$\left.\begin{aligned} -k_l \frac{\partial T_l}{\partial r} &= -k_s \frac{\partial T_s}{\partial r} + \rho h_{if} \frac{ds_j}{dt} \\ T_j &= T_{j-1} = T_{fr} \end{aligned}\right\} \text{at } r = s_j(z, t), \quad j = 2 \ldots, j_{\text{in}} \qquad (11)$$

where $s_j(z, t)$ is the location of phase boundary j.

3 Composite boundaries:
When one phase front overtakes another, a layer is consumed and a boundary separating two layers of the same phase is employed for numerical purposes. The boundary conditions at this kind of boundary are given by

$$\left.\begin{aligned} -\frac{\partial T_j}{\partial r} &= -\frac{\partial T_{j-1}}{\partial r} \\ T_j &= T_{j-1} \end{aligned}\right\} r = s_j(t) \qquad (12)$$

4 Pipe outside surface:

$$\left.\begin{aligned} -k_p \frac{\partial T_p}{\partial r} &= -k_{j_{\text{in}}} \frac{\partial T_{j_{\text{in}}}}{\partial r} \\ T_{j_{\text{in}}} &= T_{po} \end{aligned}\right\} \text{at } r = r_{po} \qquad (13)$$

where T_{po} represents the pipe temperature at $r = r_{po}$ and j_{in} represents the layer adjacent the tube. The convective boundary condition at the tube inside surface that connects the fluid and the tube is given by Eq. (6).

Solution

By neglecting axial conduction, the tube of total length L may be divided into I_{out} axial segments of length $\Delta z = L/I_{\text{out}}$, as shown in Fig. 2, where all quantities are assumed uniform in the axial direction over each segment. Radially one-dimensional heat transfer is then valid for the alternating liquid/solid layers and the tube wall in each axial segment. The problem can then be solved as a sequence of radially one-dimensional problems in each axial segment. An axial segment communicates with downstream segments through the fluid flowing inside the tube.

After discretization in the axial direction, all the governing equations, Eqs. (6)–(13), still keep the same form except all quantities should have a subscript i representing the ith axial segment. For convenience, the subscript i is not included in the following expressions and all the quantities are assumed to be of the ith axial segment unless mentioned specifically or subscripted.

Time and Axial Discretization of Fluid Energy Equation. Referring to Figs. 2 and 3, the fluid energy equation, Eq. (7), can be discretized in time and in the axial direction. The fully implicit scheme is employed in both the time and the axial variables to ensure unconditionally stable results. The discretized form of the fluid energy equation, Eq. (7), can be expressed as

$$\pi r_{pi}^2 (\rho c_p)_b \frac{(T_b^{nn} - T_b^{nn-1})}{\Delta t} + (\dot{m} c_p)_b \frac{(T_b^{nn} - T_{b,i-1}^{nn})}{\Delta z} = 2\pi r_{pi} h_b (T_{pi}^{nn} - T_b^{nn}) \qquad (14)$$

where the superscript nn indicates the current time step, as shown in Fig. 3.

General BEM Solution in Axial Segment *i*. The PCM initially starts as a single phase of liquid or solid at temperature T_{init}. In a typical axial segment i, when $T_b(z, t)$ cycles across the freezing temperature of the PCM, alternating layers of liquid and solid could form and propagate from the tube wall. Referring to Fig. 2, a general layer is represented as layer j and any

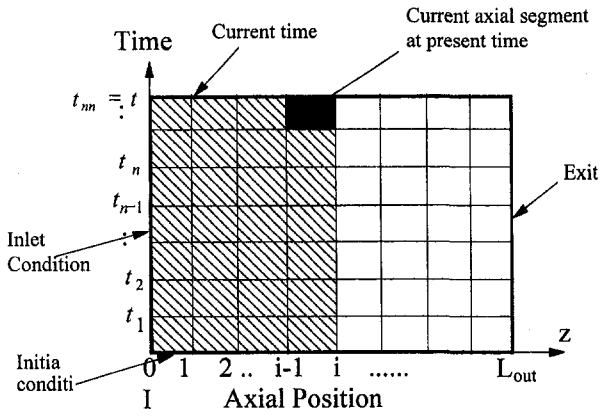

Fig. 3 Discretization in axial direction and time

newly formed layer is numbered sequentially from the tube wall. Note that a configuration change can occur due to the complete freezing of a liquid layer or complete melting of a solid layer. Whenever a configuration change occurs, all the layers are renumbered sequentially from outside to inside. Thus, the outermost layer is always layer $j = 1$ but is not necessarily the one that existed initially, since the moving front could reach the outer surface. Also, adjacent layers are not necessarily formed sequentially, since a layer could be consumed when one front overtakes the other.

The BEM is used to develop the solution for an axial segment as described in the work by Yu et al. (1995). For more details, the reader is referred to this work. The boundary element method is applied by developing a general solution that applies in a layer of liquid, layer of solid, or the tube wall. The general solution is constructed using the full space Green's function (or the fundamental solution), corresponding to the energy equation, Eq. (8). This Green's function is given by

$$G_j(r, t|r_0, t_0) = \frac{1}{4\pi\alpha_j(t - t_0)} \times \exp\left(-\frac{r^2 + r_0^2}{4\alpha_j(t - t_0)}\right) I_0\left(\frac{rr_0}{2\alpha_j(t - t_0)}\right) \quad (15)$$

The solution for a particular layer can be expanded in terms of integrals of the Green's function. The resulting integrals can be discretized in time to obtain

$$\frac{\lambda}{2\pi\alpha_j} T_j^{nn}(r) = F_j(z, t) + \sum_{n=n_j+1}^{nn} \left[r_o\left(\frac{\partial T_j}{\partial r_o}\right)^n (GI)^n - T_j^n r_o (HI)^n + T_{fr} V_j^n (GI)^n \right]_{r_o = s_j(t_o)} - \sum_{n=n_j+1}^{nn} \left[r_o\left(\frac{\partial T_j}{\partial r_o}\right)^n (GI)^n - T_j^n r_o (HI)^n + T_{fr} V_j^n (GI)^n \right]_{r_o = s_{j+1}(t_o)} \quad (16)$$

where λ is $\frac{1}{2}$ on the boundaries and 1 inside a layer. F_j represents the influence of the initial condition and is zero except for the original layer of PCM that existed at $t = 0$ and the tube wall. Also, V_j^n is the velocity of a moving front. The time integrals of the Green's function, $(GI)^n$ and $(HI)^n$, are defined as

$$(GI)^n = \int_{t^{n-1}}^{t^n} G_j(r, t|r_0, t_0) dt_0$$

$$(HI)^n = \int_{t^{n-1}}^{t^n} \frac{\partial G_j(r, t|r_0, t_0)}{\partial r_0} dt_0 \quad (17)$$

and can be interpreted as the influence coefficients.

For each PCM layer j and the tube wall at current time step nn, two simultaneous equations can be obtained by evaluating Eq. (16) at both boundaries of this layer, $r = s_{j+1}^{nn}$ and $r = s_j^{nn}$. These equations can be written in matrix form as

$$\mathbf{A_j U_j} = \mathbf{B_j} \quad (18)$$

where $\mathbf{A_j}$ is a 2×2 matrix that depends on geometry, thermal properties, and the time step. $\mathbf{U_j}$ and $\mathbf{B_j}$ are 2×1 matrices where $\mathbf{U_j}$ represents the unknown boundary information, and $\mathbf{B_j}$ accounts for the history of this layer. At a stationary boundary, such as the tube surface or the outer wall surface, the unknowns in $\mathbf{U_j}$ are temperature or heat flux, depending on the boundary conditions. At a moving front, the unknowns are the heat flux (since the temperature is locked to the freezing temperature T_{fr} of the PCM) and the phase front location. For a fixed boundary separating two layers of the same phase, both temperature and heat flux are unknown.

Multiplying Eq. (11) by $2\pi s_j$ and integrating over time from t_{nn-1} to t_{nn} produces the discretized form of the energy balance at a moving boundary in the form

$$[(s_j^{nn})^2 - (s_j^{nn-1})^2]\rho h_{if} = 2s_j^{nn}\Delta t\left[k_s\left(\frac{\partial T_s}{\partial r}\right)^{nn} - k_l\left(\frac{\partial T_l}{\partial r}\right)^{nn}\right], \quad \text{at} \quad r = s_j^{nn} \quad (19)$$

Computational Algorithm. Beginning with a single layer of pure liquid or solid in the PCM, all temperatures are initialized to T_{init} at time $t = 0$. A marching procedure is then implemented in both the time and axial variables with the notation indicated in Fig. 3. First time is incremented and the solution in each axial segment is calculated, beginning with the tube inlet and marching downstream to the exit. Due to the hyperbolic nature of the fluid equation, Eq. (7), the order of the time and axial marching procedure could be reversed; however, it is more suitable for system simulation in thermal storage systems to increment time first.

At a given time and axial position, a set of simultaneous equations is assembled for the unknown boundary data at the various radial locations. Equation (14) is used in the fluid while Eq. (16) is used at the two boundaries of the pipe wall and at the two boundaries of each solid and liquid layer in the PCM. Boundary conditions, such as Eq. (19) at moving phase fronts, supply the remaining conditions necessary to assemble a simultaneous set of equations for the unknown temperatures, heat fluxes, and phase front positions at the radial boundaries in each axial segment.

The unknown temperatures and heat fluxes enter the BEM formulation in Eq. (16) in a linear fashion; however, the positions of the phase boundaries enter in a highly nonlinear fashion. As a result, the following iteration procedure is used to solve the radial problem at the current time and axial position:

- All moving phase front positions, s_j^{nn}, are guessed using the velocity at the previous time step.
- Simultaneous equations generated from Eqs. (14) and (16) are solved for the unknown boundary temperatures and heat fluxes.
- Equation (19) is used to improve the values of s_j^{nn}.
- Iteration is continued until Eq. (19) at all phase fronts is satisfied to within a specified accuracy.

After a converged solution is obtained at the current time and axial location, the solution is examined for possible configuration changes due to any one of the following occurrences:

1 The outer pipe wall surface crosses the freeze temperature, initiating the formulation of a new layer.
2 A phase front consumes an adjacent layer and merges with another phase boundary, producing a stationary composite boundary separating two layers of the same phase.

If any one of these events occurs, the configuration is updated and the solution is recalculated. Note that more than one configuration change can occur.

Results

The results of this investigation are presented in terms of dimensionless parameters defined in the nomenclature, where the thermal diffusivity and thermal conductivity of the liquid, the outside wall radius, and the freeze temperature are chosen as reference quantities. A sample case is chosen where the dimensionless fluid inlet temperature $\theta_{b,\text{in}}$ switches back and forth between values below (-1) and above (1) the freezing point of the PCM. The dimensionless cooling and heating times are τ_c and τ_h, respectively. Water is used as the PCM and the dimensionless parameters are listed in Table 1. Numerical results are shown for $I_{\text{out}} = 21$ axial segments of equal length of $\Delta Z = Lz/I_{\text{out}}$. Also, equal heating and cooling times are used (τ_c and τ_h) with 20 time steps in each heating and cooling period, $\Delta\tau = \tau_c/20$. Numerical experimentation showed that these choices produced results that were independent of time step and axial segment size.

Figures 4–6 display the time evolution of temperatures and phase fronts at three different axial locations. In each figure, the bottom portion shows the radial position of each front varying with time. When one front overtakes another, a layer between them is consumed and the front separating these two adjacent layers is fictitious (shown as a dotted line) because these two layers are of the same phase. When a moving front reaches the upper limit ($S_j^{nn} = 1.0$), the layer adjacent to the outer wall surface is consumed. All the phase fronts are represented with solid lines except for the fictitious boundaries. The layers are labeled in each region with Liq or Sol, representing liquid or solid, respectively. The top portion shows the variation of the fluid inlet temperature, the fluid bulk temperature at the particular axial location, and the tube outer surface temperature. A new layer forms when θ_{po} crosses the freezing temperature of the PCM ($\theta_{fr} = 0.0$).

Figure 4 shows the variation of temperatures and the phase fronts at the exit of the first axial segment $i = 1$. The hot and cold periods are $\tau_c = \tau_h = 1$. The PCM starts as an all-liquid layer at an initial condition of $\theta_{\text{init}} = 0.0$. At time $\tau = 0$, the inlet temperature is set to $\theta_{b,\text{in}} = -1$. The first freeze phase front starts at the first time step. Because of the higher conductivity of the ice and no stored sensible energy at the initial condition, this freeze front reaches the outer boundary and consumes the whole liquid layer before the inlet temperature $\theta_{b,\text{in}}$ switches. The PCM becomes one layer of solid and is subcooled quickly until the melting period begins. At time $\tau = 1$, the inlet temperature switches to $\theta_{b,\text{in}} = +1$. Because of the subcooling of the PCM and the high Stefan number, the energy stored in the subcooled solid slows down the formation and propagation of the liquid layer. This first melt front starts late in the second time step of this melting period, $\tau = 1.1$, and does not reach the outer wall at the end of this period because of the sensible energy stored in the first solid layer and the lower conductivity of liquid. Thus, there is less energy stored in this liquid layer.

Table 1 Geometry, property ratios, and parameters for the sample case

Geometry	$R_{pi} = 0.2$; $R_{po} = 0.25$; $R_{out} = 1$; $Lz = 3000$
Thermal Diffusivity Ratios	$A_l = 1$; $A_s = 8.60$; $A_p = 1.70$; $A_b = 0.21$
Thermal Conductivity Ratios	$K_l = 1$; $K_s = 3.88$; $K_p = 0.88$; $K_b = 0.20$
Stefan Number	$Ste = 1.0$
Peclet Number	$Pe = 10^4$
Biot Number	$Bi = 1.0$
Initial Temperature	$\theta_{\text{init}} = 0.0+$ (all liquid)

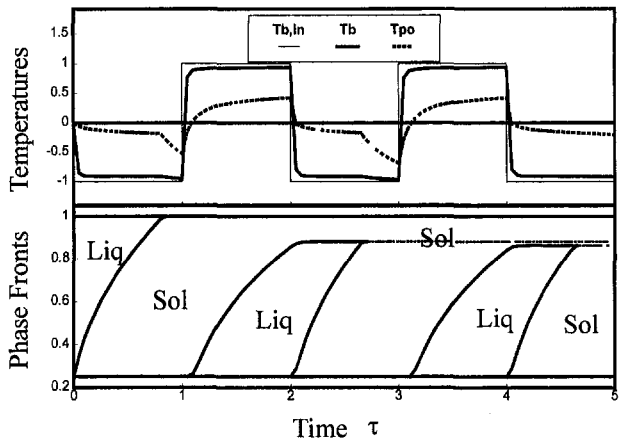

Fig. 4 Time evolution of temperatures and phase fronts at the exit of the first axial segment ($i = 1$, $z = 142.86$). Parameters are listed in Table 1.

In the next freezing period, the freezing front overtakes the first melting front and consumes the liquid between the two solid layers. Thus, the PCM becomes two layers of solid separated by a fictitious boundary, shown as a dotted, stationary line. The PCM is subcooled more than in the first freezing period until the fluid temperature switches back to $\theta_{b,\text{in}} = +1$ at time $\tau = 3$. The second melt front starts at the third time step of this melting period, $\tau = 3.15$, and thus propagates more slowly than the first melting front. Because of more stored sensible energy in the solid layers and lower conductivity and diffusivity of the liquid, this melt front propagates slightly less than previous melting front. The next cooling period starts at $\tau = 4$ and the third freeze front starts at the first time step of the freezing period and overtakes the previous melt front.

Figure 5 shows the variation of temperatures and the phase fronts at the exit of the middle axial segment, $i = 11$. The behaviors of the freezing and melting fronts are similar to those in Fig. 4. Because of the energy transferred in the upstream axial segments, the driving potentials in both freezing and melting periods decrease quickly in this case. Thus, the first freezing front is far away from the outer wall. Because the fluid driving potential is smaller, and thus less sensible energy is stored, the PCM never gets to a fully charged or discharged condition (never becomes all liquid or all solid). The influence of sensible energy is not apparent in this segment. Even though the driving potential in the freezing period decreases faster than that in the melting period, the freezing fronts still propagate faster than

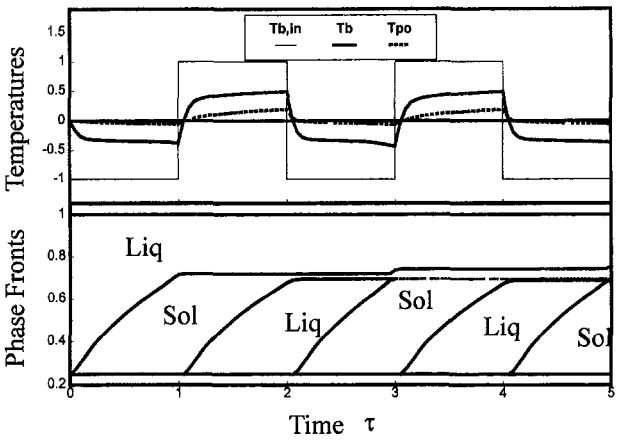

Fig. 5 Time evolution of temperatures and phase fronts at the exit of the middle axial segment of the tube ($i = 11$, $z = 1571.42$). Parameters are listed in Table 1.

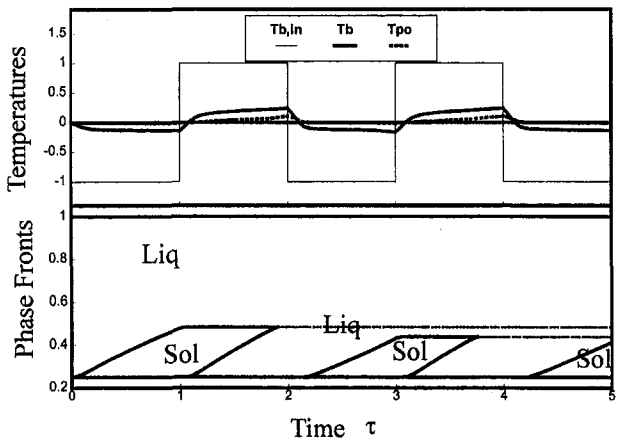

Fig. 6 Time evolution of temperatures and phase fronts at the outlet of the tube (i = 21, z = 3000). Parameters are listed in Table 1.

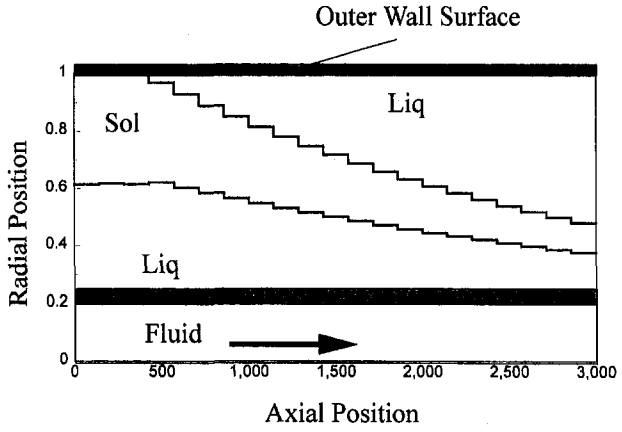

Fig. 8 Moving front distribution at the middle of the first melting period (τ = 1.5, nn = 30). Parameters are listed in Table 1.

the melting fronts. It is hard to notice that all the temperatures have a slight time delay in responding to the inlet temperature since the tube is long and it needs time to propagate the inlet condition downstream to this segment. This phenomenon could be exaggerated for cases with low Peclet numbers (low mass flow rate).

Figure 6 shows the temperature and phase front curves at the outlet of the tube, i = 21. In this axial segment, the fluid temperature has a longer time delay than that in segment i = 11. Since the absolute value of the fluid temperature is much closer to the freeze temperature of the PCM than that in previous segment i = 11, the phase fronts propagate much more slowly than in segment i = 11. Even though the fluid has lower conductivity and the first solid layer has some stored sensible energy, the melting fronts overtake the first freeze fronts in the melting cycles. This is because the fluid driving potential in the freezing period decreases faster than that in the melting period. Thus, the driving potential difference of the fluid in the melting and freezing periods is large enough to cause the melt front to overtake the freeze front in this segment. The PCM is then heated to store some sensible energy. Because of this, the second freeze front starts late at the fourth time step in this freezing period, τ = 2.2. Because the driving potential is relatively small in this segment, the stored sensible energy in the liquid plays an important role in slowing down the formation of the freeze fronts.

Figures 7–9 are snapshots of the freeze and melt front distributions around the tube taken in the middle of each heating/cooling period. These figures are not to scale in geometry and the radial direction scale is strongly exaggerated for illustration. The physical ratio of axial scale to radial scale should be 3000:1.

Figure 7 shows the freeze front distribution along the tube at time τ = 0.5, in the middle of the first freezing period. The stepwise pattern is a representation of the fully implicit axial discretization. There are a total of two axial segments. Figure 8 shows the front distributions at τ = 1.5, in the middle of the first melting period. Note that the melt front at the entrance of the tube is slowed down once the freeze front reaches the outer wall surface. The solid layer at the entrance was subcooled and the stored sensible energy slows down the formation of the melt front.

Figure 9 shows the distributions at τ = 2.5, in the middle of the second cooling period. Note that the melting front is overtaking the freezing front at this moment. Due to the energy transferred in upstream axial segments, the driving potential of the fluid in the melting period is larger than that in the freezing period at the latter portion of the tube. This causes the melt front to overtake the freeze front. The fictitious boundary separating two layers of the phase is shown as a dotted line.

To validate the BEM algorithm, several cases with different Stefan numbers are tested against the thermal network method (TNM) developed by Vick et al. (1996) and against the negligible sensible heat (NSH) approximation, where only latent heat effects are considered. The TNM has been extensively validated with experimental data for low Stefan numbers and a single phase front (Nelson et al., 1996). No experimental data are available for multiple phase fronts for direct comparison with the present BEM. Since the strength of this BEM algorithm is

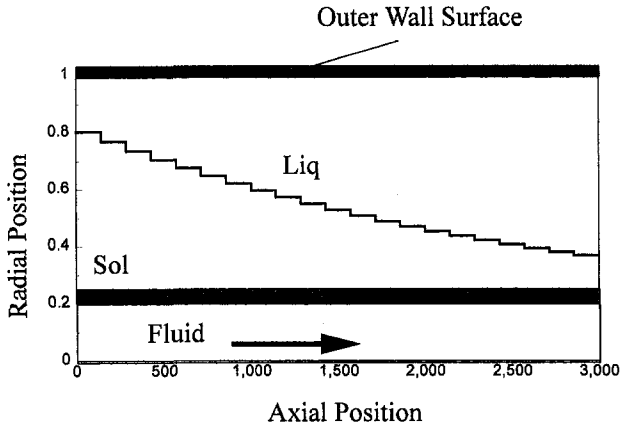

Fig. 7 Moving front distribution at the middle of the first freezing period (τ = 0.5, nn = 10). Parameters are listed in Table 1.

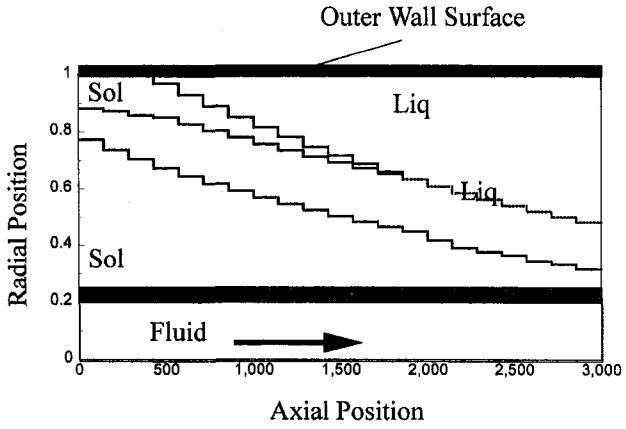

Fig. 9 Moving front distribution in the middle of the second freeing period (τ = 2.5, nn = 50). Parameters are listed in Table 1.

the ability to track multiple phase fronts without the restriction of small Stefan number, partial charge/discharge cases for high and low Ste are compared.

The exit temperature and latent state of charge (mass percent of ice) from the three different methods are compared in Figs. 10 and 11. In these figures, the upper portion shows the latent state of charge (L-SOC), which represents the accumulated energy transferred while the lower portion of the figures shows the outlet temperature, $\theta_{b,\text{out}}$, which reflects the heat transfer rate at current time.

Figure 10 shows the results of a case with Ste = 1.0. Since the NSH does not consider the sensible heat at all, the L-SOC is far off from those of the BEM and TNM. The outlet temperature of fluid, $\theta_{b,\text{out}}$, is also off from those of the other two methods. The results from the BEM and the TNM have very good agreement. Because of the neglect of the sensible energy, the L-SOC from NSH method gets to a fully charged condition at each freezing period while those from the other methods do not. Note that at each freezing period, there is a sudden drop of the fluid outlet temperature in the NSH method. After the PCM around the tube becomes one single phase, only the sensible energy physically exists in the PCM. Thus, $\theta_{b,\text{out}}$ drops in the NSH abruptly and the discrepancy shows up. In the melting period, due to the low conductivity in the liquid PCM, $\theta_{b,\text{out}}$ is very close to the inlet temperature, $\theta_{b,\text{in}}$. There is no sudden rise of $\theta_{b,\text{out}}$ when the PCM around part of the tube becomes single-phase liquid.

Figure 11 shows the same case as shown in Fig. 10, except that the Stefan number is one tenth of that in Fig. 10, Ste = 0.1, and the time for each period is increased by 10. As expected for a low Stefan number, the discrepancy of L-SOC and $\theta_{b,\text{out}}$ is much smaller comparing with case in Fig. 10. All the other behaviors are similar to those in Fig. 10. Note that $\theta_{b,\text{out}}$ in all three methods has a dip in the freezing period because of the small Stefan number. The offset of the L-SOC due to θ_{init} in the NSH method gets smaller after the first freezing period.

The agreement between the results from the BEM model and the TNM model is excellent for low Stefan number cases and good for high Stefan numbers cases. The NSH method works very well for small Stefan numbers even when the system is superheated or subcooled during the process. For high Stefan number cases, the NSH method also works well until all the PCM or the PCM at some axial segments becomes one single layer.

Conclusions

A general method for analysis of multiple phase front problems encountered in thermal energy storage systems is developed in the present work. A multiple front problem arises when the system experiences partial charge and discharge, as shown in Figs. 4–9, while a fully charged/discharged system has at most one single moving front. For the case described in Figs. 4–9, if the heating and cooling periods are increased, this case could become a single front or fully charged/discharged problem. On the other hand, a fully charged/discharged system can become a partial charged/discharged system by reducing the length of the freezing and the melting periods. In applications, ice thermal energy storage systems experience many partial charge and discharge cycles due to off-design operation.

The freezing and melting processes are modeled as a series of radially one-dimensional problems in axial segments along the flow direction. A boundary element method is applied in each axial segment, including the full effect of sensible and latent energy, as well as different thermal properties in the solid and liquid phases. The boundary element method is well suited to multiple phase front problems, since it requires discretization only on the boundaries and phase fronts, while the finite element and finite difference methods require complete spatial discretization.

Stable and accurate results are generated using a fully implicit scheme in both the axial direction and in time. The results are tested against the thermal network method (TNM) and the negligible sensible heat approximation (NSH). The agreement between the exit temperature and the volume percentage of the ice (Latent State-of-Charge) obtained with the BEM and TNM models are excellent. The NSH model works well for low-Stefan-number cases, for cases without subcooling and superheating and for cases with high Peclet numbers.

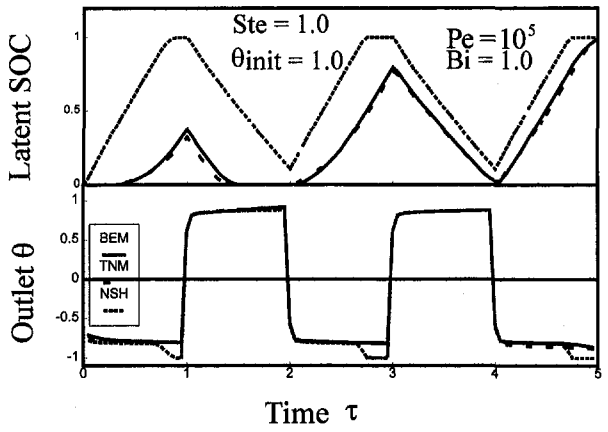

Fig. 10 Comparison of BEM with TNM and NSH. High Stefan number and high initial temperature.

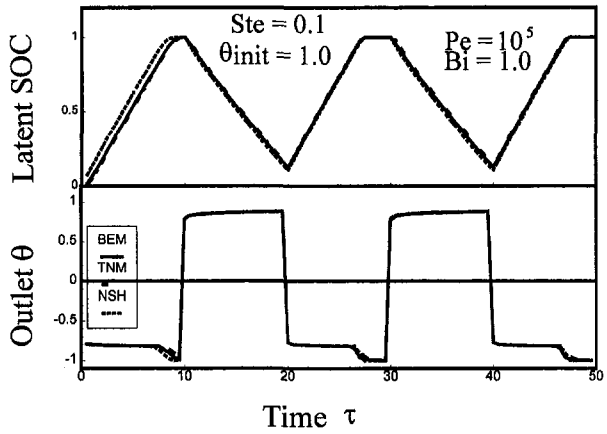

Fig. 11 Comparison of BEM with TNM and NSH. Low Stefan number, high initial temperature.

References

Abramowitz, M., and Stegun, I. A., 1972, *Handbook of Mathematical Functions,* Dover, New York.

Banerjee, P. K., and Shaw, R. P., 1982, "Boundary Element Formulation for Melting and Solidification Problems," in: *Developments in Boundary Element Methods—2,* Banerjee and Shaw, eds., Applied Science Publishers, NJ.

Beck, J. V., and Cole, K. D., 1992, *Heat Conduction Using Green's Functions,* Hemisphere Publishing Corporation, Bristol, PA.

Choi, C. Y., and Hsieh, C. K., 1992, "Solution of Stefan Problems Imposed With Cyclic Temperature and Flux Boundary Conditions," *Int. J. Heat Mass Transfer,* Vol. 35, No. 5, pp. 1181–1195.

Kim, C. J., and Kaviany, M., 1990, "A Numerical Method for Phase-Change Problems," *Int. J. Heat Mass Transfer,* Vol. 33, No. 12, pp. 2721–2734.

Nelson, D. J., and Vick, B., 1994, "Freezing and Melting With Multiple Phase Fronts Using the Boundary Element Method, Part I: Analysis," *Proc. 10th International Heat Transfer Conference,* Brighton, England, Aug. 14–18.

Nelson, D. J., Vick, B., and Yu, X., 1996, "Validation of the Algorithm for Ice-on-Pipe Brine Thermal Storage Systems," *ASHRAE Transactions,* Vol. 102, Part 1, pp. 55–62.

O'Neill, K., 1983, "Boundary Integral Equation Solution of Moving Boundary Phase Change Problems," *Int. J. Numerical Methods Engineering,* Vol. 19, pp. 1825–1850.

Pasquetti, R., and Caruso, A., 1990, "Boundary Element Approach for Transient and Nonlinear Thermal Diffusion," *Numerical Heat Transfer,* part B, Vol. 17, pp. 83–99.

Sadegh, A. M., Jiji, L. M., and Weinbaum, S., 1987, "Boundary Integral Equation Technique With Application to Freezing Around a Buried Pipe," *Int. J. Heat Transfer,* Vol. 30, No. 2, pp. 223–232.

Vick, B., and Nelson, D. J., 1993, "The Boundary Element Method Applied to Freezing and Melting Problems," *Numerical Heat Transfer, Part B: Fundamentals,* Vol. 24, pp. 263–277.

Vick, B., and Nelson, D. J., 1994, "Freezing and Melting With Multiple Phase Fronts Using the Boundary Element Method, Part II: Results," *Proc. 10th International Heat Transfer Conference,* Brighton, England, Aug. 14–18.

Vick, B., Nelson, D. J., and Yu, X., 1996, "Model of an Ice-on-Pipe Brine Thermal Storage Component," *ASHRAE Transactions,* Vol. 102, Part 1, pp. 45–54.

Wrobel, L. C., and Brebbia, C. A., 1981, "Boundary Elements in Thermal Problems," in: *Numerical Methods in Heat Transfer,* Wiley, New York, pp. 91–113.

Wrobel, L. C., and Brebbia, C. A., 1981, "A Formulation of the Boundary Element Method for Axisymmetric Transient Heat Conduction," *Int. J. Heat Mass Transfer,* Vol. 24, No. 5, pp. 843–850.

Yu, X., Nelson, D. J., and Vick, B., 1995, "Phase Change With Multiple Fronts in Cylindrical Systems Using the Boundary Element Method," *Engineering Analysis With Boundary Elements,* Vol. 16, No. 2, pp. 161–170.

L. L. Zheng
Research Scientist,
Department of Materials Science
and Engineering.
lzheng@thermsa.eng.sunysb.edu

H. Zhang
Assistant Professor,
Department of Mechanical Engineering.
Assoc. Mem. ASME

D. J. Larson, Jr.
Professor,
Department of Materials Science
and Engineering.

V. Prasad
Professor,
Consortium for Crystal Growth Research.
Fellow ASME

State University of New York
at Stony Brook,
Stony Brook, NY 11794

A Model for Solidification Under the Influence of Thermoelectric and Magnetohydrodynamic Effects: Application to Peltier Demarcation During Directional Solidification With Different Gravitational Conditions

A physics-based model is developed to study the gravitational (convection), thermoelectric (Peltier, Seebeck, Joule, and Thomson) and magnetohydrodynamic (Lorentz force) effects on solidification phenomena. A scaling analysis is carried out to examine the importance and contributions of various governing parameters. Directional solidification with Peltier Interface Demarcation under varying gravitational conditions is simulated for the Bridgman–Stockbarger configuration. The predicted interface location and movement during current pulsing are studied and the microstructures corresponding to different current polarities are analyzed based on Jackson–Hunt theory.

1 Introduction

Owing to its importance in many industrial applications, the fundamental aspects of directional solidification have received much attention in recent years. Many of these studies are devoted to studying the effects of heat and mass transfer on growth rate and interface morphology. Peltier Interface Demarcation (PID) has been successfully applied to the study of directional solidification of single-phase (Lichtensteiger et al., 1971) and multiphase (Pirich and Larson, 1982; Holmes and Gatos, 1978) systems. The microscopic growth rate and interface morphology during solidification of a nontransparent system have been recorded by these authors. Experiments using PID have been conducted in orbit and on earth to study the effects of buoyancy-induced convection on single and multiphase directional solidification (Lichtensteiger et al., 1971; Pirich and Larson, 1982; Wang et al., 1984; Favier et al., 1994; Quenisset and Naslain, 1981). In these experiments, the PID technique has also been used to acquire information on the evolution of the solid/liquid interface.

Peltier Interface Demarcation is achieved by passing a current pulse through the directionally solidifying sample to create a rapid thermal perturbation at the solid/liquid interface due to the Peltier effect. This results in a morphological (chemical, microstructural, and/or strain) perturbation corresponding to the solid/liquid interface shape at the instant of the current pulse. Due to the presence of the electric current, additional thermoelectric responses are also observed including Joule, Thomson, and Seebeck effects (Shercliff, 1979). Different from the Peltier effect, the Joule and Thomson effects are the volumetric heat production or absorption and occur not only in the vicinity of the solid/liquid interface but throughout the bulk liquid and solid. In addition to the thermoelectric effects, magnetohydrodynamic (MHD) effects are also produced in the presence of electron motion in the magnetic field induced by the electric field. In a gravitational environment, the MHD effect can interact with buoyancy convection so as to complicate the heat and mass transport during directional solidification and interface demarcation.

To understand the nature of thermal transients induced by PID and their significance in directional solidification, Silberstein and Larson (1987) experimentally studied the thermoelectric and morphological effects of PID on directional solidification of a Bi/MnBi eutectic. In particular, the spatial variation of thermoelectric effects during Peltier pulsing in Bi and Bi/MnBi eutectic were studied. Their experimental data indicated that the thermal perturbation due to thermoelectric effects can be resolved into Thomson/Peltier and Joule heating contributions. Based on experimental observations, a semi-empirical expression was suggested to estimate the thermal perturbation caused by the individual thermoelectric effects. Schaefer and Glicksman (1968) studied Bi interface movement resulting from Peltier heating and cooling, and Li et al. (1996) applied the PID technique to study the dynamic process of solid/liquid interface instability during directional solidification in Bi-1 wt% Sb alloys, and quantitatively analyzed the correlation between the morphological effects of PID and pulsing conditions.

Due to limited experimental data, the understanding of thermoelectric effects on interface demarcation in directional solidification is not complete. To obtain more detailed information on thermal perturbations due to thermoelectric effects, Brush et al. (1990) performed a numerical study of directional solidification in the presence of thermoelectric effects with the electromigration of solute. Their model was, however, based on a one-dimensional configuration and the solid/liquid interface was assumed to be planar. Recently, Zheng and Larson (1997a) have developed a computer model to investigate PID during directional solidification of Bi in a microgravity (diffusion-

Contributed by the Heat Transfer Division and presented at the National Heat Transfer Conference, Baltimore, Maryland, August 8–12, 1997. Manuscript received by the Heat Transfer Division May 22, 1997; revision received February 8, 1998. Keywords: Magnetohydrodynamics, Materials Processing and Manufacturing Processes, Microgravity Heat Transfer, Thermoelectric. Associate Technical Editor: P. S. Ayyaswamy.

controlled) environment. Dynamic growth in an axisymmetric system has been investigated and the individual influence of the Joule, Peltier, and Thomson effects has been quantitatively identified. Although several theoretical studies have been conducted to examine PID on directional solidification, most of them have focused on either the effects of thermoelectric forces alone, or gravitationally dependent convection. The influence of combined convective, thermoelectric, and magnetohydrodynamic effects on interface demarcation is not well understood.

To understand the mechanisms of interface demarcation during directional solidification, we have extended our previous numerical study (Zheng and Larson, 1997a) from diffusion-controlled to varying gravitational (convection) conditions. The work will be presented in this paper as follows:

- A physics-based mathematical model is proposed to describe the directional solidification including thermoelectric and magnetohydrodynamic effects.
- Based on the proposed model, a scaling analysis of magnetohydrodynamic effects is carried out, and its impact on the flow and temperature field evolution is qualitatively examined.
- The mathematical model for an axisymmetric system representing the Bridgman–Stockbarger system is incorporated into the existing MASTRAPP algorithm (Zhang and Moallemi, 1995; Zhang et al., 1996).
- Finally, numerical simulations of Peltier interface demarcation under varying gravitational conditions, and the thermoelectric and magnetohydrodynamic effects on interface demarcation and directional solidification are examined in detail.

2 Mathematical Formulation

For the system involving external electric current pulsing, under a varying gravitational environment, the directional solidification can be described by a set of conservation equations for mass, momentum, and energy as follows:

$$\frac{\partial \rho}{\partial t} + \nabla\cdot(\rho\vec{u}) = 0, \tag{1}$$

$$\frac{\partial}{\partial t}(\rho\vec{u}) + \nabla\cdot(\rho\vec{u}\vec{u}) = -\nabla p + \mu\nabla^2\vec{u} + \sum_i \vec{F}_i, \tag{2}$$

$$\frac{\partial}{\partial t}(\rho C_p T) + \nabla\cdot(\rho C_p T\vec{u}) = \dot{Q}, \tag{3}$$

where $\vec{F}_i$ is the body force, and $\dot{Q}$ is the rate of local energy storage. The body forces in Eq. (2) can be written as:

$$\sum \vec{F}_i = \rho\vec{g} + \vec{j}\times\vec{B} \tag{4}$$

where $\rho\vec{g}$ is the gravitational force, $\vec{j}\times\vec{B}$ is the Lorentz force, and $\vec{g}$, $\vec{j}$, and $\vec{B}$ are the gravitational acceleration, current density, and magnetic induction field, respectively.

Considering that a conduction current, of intensity $\vec{j}$, can be caused by a temperature gradient ∇T as well as by an electric field $\vec{E}$ or an electromotive force $\vec{u}\times\vec{B}$ (due to motion at velocity $\vec{u}$ in a magnetic induction field $\vec{B}$), Ohm's law can be generalized as (Panofsky and Phillips, 1956):

$$\vec{j}/\sigma = \vec{E} + \vec{u}\times\vec{B} - S\nabla T \tag{5}$$

in which S is the absolute thermoelectric power of the conducting medium in question, and σ is the electrical conductivity measured under isothermal conditions. Electric current flow causes additional heat flow, and as a consequence, the heat flow intensity $\vec{q}$ is given by a modified version of Fourier's law as (Panofsky and Phillips, 1956):

$$\vec{q} = -k\nabla T + ST\vec{j} \tag{6}$$

in which k is the thermal conductivity, measured under conditions where $\vec{j}$ is absent.

In a current- and heat-conducting medium at equilibrium with a given temperature distribution at a given instant, there is an electrical energy input to the medium at a rate $\dot{W} = \vec{E}\cdot\vec{j}$ per unit volume and time. Hence the rate at which energy is stored locally in the medium is given by

$$\dot{Q} = -\nabla\cdot\vec{q} + \dot{W} = \nabla\cdot(k\nabla T) - \nabla\cdot(ST\vec{j}) + j^2/\sigma + \vec{j}S\cdot\nabla T \tag{7}$$

Nomenclature

b = inner radius of ampoule, m
B = magnetic induction field, T (tesla)
C_p = specific heat, J kg^{-1} K^{-1}
E = electric field, V m^{-1}
F = force, N m^{-3}
g = acceleration due to gravity, m^2 s^{-1}
Gr = Grashof number = $\beta(T_h - T_{mp})gb^3/\nu_l^2$
Ha = Hartman number = $j_0 b$
$\vec{i}$ = unit vector
j = current density, A m^{-2}
k = thermal conductivity, W/mK
N_J = Joule number = $2\rho C_{pl}(T_h - T_{mp})\mu_e/B_0^2$
N_P = Peltier number = $\Pi_{sl} j_0 b/k(T_h - T_{mp})$
N_T = Thomson number = $\tau(T_h - T_{mp})/bj_0$
p = pressure, Pa
Pr = Prandtl number = $\mu C_{pl}/k$
q = heat flux, W/m
$\dot{Q}$ = energy storage, W
$\mathrm{Re_m}$ = magnetic Reynolds number = $\mu_e\sigma_s b u_0$
S = absolute thermo-electric power (Seebeck coefficient), V K^{-1}
St = Stefan number = $C_{pl}(T_h - T_{mp})\Delta H^{-1}$
t = time, s
T = temperature, K
T_{mp} = melting temperature, K
$\vec{u}$ = vector velocity, m s^{-1}
u_n = interface moving velocity, normal to the interface, ms^{-1}
u_p = pulling velocity, m s^{-1}
V = centerline interface moving velocity, μms^{-1}
V_R = average interface moving velocity, μms^{-1}
$\dot{W}$ = work done by electric field, Js^{-1}
x_{int} = interface location, m
x, y = distance, m
α = thermal diffusivity, m^2 s^{-1}
β = volume expansion coefficient, K^{-1}
ΔH = latent heat of fusion, J kg^{-1}
θ = dimensionless temperature
λ = lamellar/rod spacing, μm
μ = dynamic viscosity, kg m^{-1} s^{-1}
μ_e = magnetic permeability, A m^2
ν = kinematic viscosity, m^2 s^{-1}
Π_{sl} = Peltier coefficient, V
ρ = density, kg m^{-3}
σ = electric conductivity, Ω^{-1} m^{-1}
τ = Thomson coefficient, V K^{-1}

Subscripts

a = adiabatic zone
c = cold zone
h = hot zone
l = liquid (melt)
s = solid (crystal)
0 = reference to the external electric field

Superscripts

$\hat{}$ = dimensionless
$\vec{}$ = vector

where Eqs. (5) and (6) have been invoked. If we apply the normal, "low-frequency" approximation (Shercliff, 1979),

$$\nabla \cdot \vec{j} = 0, \tag{8}$$

Eq. (7) reduces to

$$\dot{Q} = \nabla \cdot (k \nabla T) + j^2/\sigma - \vec{j} T \cdot \nabla S. \tag{9}$$

The extra local heating due to the electric current exceeds the Joule heating j^2/σ by the final term $\vec{j} S \cdot \nabla T$. Note that this effect occurs even when the electric current is due to electromotive forces other than the thermoelectric ones, or when S varies, because of variable composition, provided the current density $\vec{j}$ has a component parallel to ∇T. The effect is produced because the variation of S in Eq. (6) means that a given current flux transports a varying entropy flux. When the medium is of uniform composition and S is a function of T only, the last term in Eq. (9) can be written as

$$-T \frac{dS}{dT} \vec{j} \cdot \nabla T, \tag{10}$$

which describes the Thomson effect. The quantity $\tau = T(dS/dT)$ is called the Thomson coefficient.

Considering an electric field where the movement of the in-situ electrode is negligible, the current density $\vec{j}$ and the magnetic field $\vec{B}$ can be evaluated via Maxwell's equations (Panofsky and Phillips, 1956),

$$\nabla \times \vec{E} = -\frac{\partial \vec{B}}{\partial t}$$

$$\nabla \times \vec{B} = \mu_e \vec{j}$$

and

$$\nabla \cdot \vec{B} = 0 \tag{11}$$

where μ_e is the magnetic permeability. By substituting Eq. (5) into Maxwell's equations, an equation for magnetic field is obtained as

$$\frac{\partial \vec{B}}{\partial t} = \frac{1}{\mu_e \sigma} \nabla^2 \vec{B} + \nabla \times (\vec{u} \times \vec{B}) - \nabla \times (S \nabla T), \tag{12}$$

where the last two terms on the right-hand side of Eq. (12) can be rewritten as

$$\vec{u} \nabla \cdot \vec{B} + \vec{B} \nabla \cdot \vec{u} - \nabla S \times \nabla T - S \nabla \times \nabla T. \tag{13}$$

For an electrically homogeneous material in an incompressible flow, we have

$$\nabla \cdot \vec{u} = 0, \text{ and } S = S(T) \tag{14}$$

Substituting Eqs. (11) and (14) into Eq. (13), the last two terms in Eq. (12) reduce to zero, and the magnetic field Eq. (12) is simplified as

$$\frac{\partial \vec{B}}{\partial t} = \frac{1}{\mu_e \sigma} \nabla^2 \vec{B}. \tag{15}$$

With respect to directional solidification involving a phase change process, an additional equation

$$-k_s \left.\frac{\partial T}{\partial x_n}\right|_s + k_l \left.\frac{\partial T}{\partial x_n}\right|_l - \Pi_{sl} j_n = \rho \nabla H u_n \tag{16}$$

is required to determine the movement of the solid/liquid interface, where Π_{sl} is the Peltier coefficient (a material property), and the subscript n indicates the direction normal to the solid/liquid interface. In the discussion that follows, the solid/liquid interface is assumed to be isothermal, applicable to a single component system.

3 Dimensionless Parameters and Order of Magnitude Analysis

A scaling analysis is performed here to estimate the order of magnitude of the buoyancy and thermoelectric effects. We nondimensionalize the conservation equations using the following dimensionless parameters:

$$\hat{x} = \frac{x}{b}, \quad \hat{u} = \frac{ub}{\nu_l}, \quad \hat{t} = \frac{t\nu_l}{b^2}, \quad \hat{\rho} = \frac{\rho}{\rho_l},$$

$$\theta = \frac{T - T_{mp}}{\Delta T}, \quad \hat{C}_p = \frac{C_p}{C_{p,l}} \quad \hat{k} = \frac{k}{k_l},$$

$$\hat{j} = \frac{j}{j_0}, \quad \hat{\sigma} = \frac{\sigma}{\sigma_s}, \quad \hat{B} = B/(j_0 b/\sigma_s \nu_0)$$

where b is the reference length scale, ν/b is the velocity scale, $\Delta T = T_h - T_{mp}$ is the difference between the highest temperature of the system T_h and the melting temperature T_{mp}, the subscripts 0, s, and l represent reference, solid, and liquid. The dimensionless conservation equations for mass, momentum, energy, and magnetic field (Eqs. (1)–(3) and (15)) are then obtained as

$$\frac{\partial \hat{\rho}}{\partial \hat{t}} + \nabla \cdot (\hat{\rho} \vec{\hat{u}}) = 0, \tag{17}$$

$$\frac{\partial}{\partial \hat{t}} (\hat{\rho} \vec{\hat{u}}) + \nabla \cdot (\hat{\rho} \vec{\hat{u}} \vec{\hat{u}}) = -\nabla \hat{p} + \hat{\mu} \nabla^2 \vec{\hat{u}} - \mathrm{Gr} \hat{\rho} \theta \vec{i}_g + Ha^2 \vec{\hat{j}} \times \vec{\hat{B}}, \tag{18}$$

$$\frac{\partial}{\partial \hat{t}} (\hat{\rho} \hat{C}_p \theta) + \nabla \cdot (\hat{\rho} \hat{u} \hat{C}_p \theta) = \frac{1}{\mathrm{Pr}} \nabla (\hat{k} \nabla \theta) + 2 \frac{\mathrm{Re}_m}{N_J} \hat{j}^2/\hat{\sigma} - \frac{N_T}{\mathrm{Pr}} \vec{\hat{j}} \cdot \nabla \theta, \tag{19}$$

$$\frac{\partial}{\partial \hat{t}} (\vec{\hat{B}}) = \frac{1}{\mathrm{Re}_m} \nabla^2 \vec{\hat{B}} \tag{20}$$

and the equation for the solid/liquid interface movement (Eq. (16)) is given by:

$$\frac{\mathrm{St}_l}{\mathrm{Pr}} \left(-\hat{k}_s \left.\frac{\partial \theta}{\partial \hat{x}_n}\right|_s + \left.\frac{\partial \theta}{\partial \hat{x}_n}\right|_l \right) - \frac{\mathrm{St}_l}{\mathrm{Pr}} N_P \hat{j}_n = \hat{u}_n. \tag{21}$$

In Eq. (18), $\hat{p} = (p - \rho_l g x)/(\rho \nu_l^2/b^2)$ is the dimensionless pressure. The governing parameters

$$\mathrm{Gr} = \beta \Delta T g b^3/\nu_l^2 \tag{22}$$

and

$$\mathrm{Ha} = j_0 b^2/\sigma_s \nu_l (\sigma_s/\rho \nu_l)^{1/2} \tag{23}$$

are the Grashof and Hartman numbers, representing the dimensionless buoyancy and magnetic forces, respectively.

$$\mathrm{Pr} = \nu_l/\alpha_l \tag{24}$$

and

$$N_J = 2\rho C_{pl} \Delta T/(B_0^2/\mu_e) \tag{25}$$

in Eq. (19) are the Prandtl and Joule numbers that measure the ratios of kinetic to viscous heat and Joule to magnetic heat in the system, respectively, and $B_0 = j_0 b/(\sigma_s \nu_l)$ is the reference magnetic induction.

$$N_T = \tau j_0/(k/b) \tag{26}$$

and

$$N_P = \Pi_{sl} j_0/(k\Delta T/b) \tag{27}$$

are the ratios of the Thomson and Peltier effects to the heat flux, and we name them after Thomson and Peltier.

$$\mathrm{St} = C_{pl}\Delta T/\Delta H \tag{28}$$

is the Stefan number for the melt, which measures the ratio of heat capacity to latent heat.

$$\mathrm{Re_m} = \mu_e \sigma_s \nu_l \tag{29}$$

is the magnetic Reynolds number, which can also be expressed in an alternative form as $\mathrm{Re_m} = \mu_e \sigma_s b u_0$ with the reference velocity $u_0 = \nu_l/b$.

3.1 Magnetic Induction Field. It is interesting to find that the governing equation for the magnetic field, Eq. (20), preserves the features of the Navier–Stokes equation where inertia terms are absent. The magnetic Reynolds number in this equation quantifies the transport of the magnetic effects. For most liquid metals and semiconductors, the magnetic Reynolds number is much smaller than unity, e.g., for bismuth $\mathrm{Re_m}$ is approximately 10^{-7}. Due to the small value of $\mathrm{Re_m}$, the distribution of magnetic induction is predominantly determined by a diffusion process rather than a transient process. Therefore, Eq. (20) can be simplified as a Laplace equation:

$$\nabla^2 \vec{B} = 0. \tag{30}$$

The magnetic induction in the present system (Fig. 1) is primarily induced by the externally imposed current field. According to Savart's law (Panofsky and Phillips, 1956), the magnetic field, as a function of current density for a cylindrical system can be expressed as:

$$\vec{B} = \frac{\mu_e}{4\pi} \int \frac{\vec{j} \times \vec{r}}{r^3} d\mathscr{V}' \tag{31}$$

where $\vec{r}$ is the distance from the point of integration or source point (where $\vec{j}$ is located) toward the field point where $\vec{B}$ is determined, and $\mathscr{V}'$ is the integral volume. Assuming a constant current density, $\vec{j} = j_0 \vec{i}_x$, we find:

$$\vec{B} = \tfrac{1}{2} \mu_e j_0 y \, \vec{i}_x \times \vec{i}_y$$

and

$$\vec{j} \times \vec{B} = \tfrac{1}{2} \mu_e j_0 |j_0| \, y \vec{i}_x \times (\vec{i}_x \times \vec{i}_y) \tag{32}$$

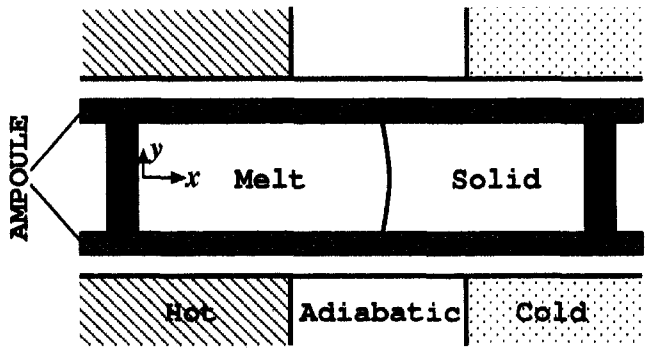

Fig. 1 Schematic diagram of directional solidification in a Bridgman–Stockbarger system

where $\vec{i}_x$ and $\vec{i}_y$ are the unit vectors of Cartesian coordinates x and radius y, respectively. The cross product of $\vec{j}$ and $\vec{B}$, associated with $\vec{j} = j_0 \vec{i}_x$, is then derived as

$$\vec{j} \times \vec{B} = -\tfrac{1}{2} \mathrm{Re_m} \frac{j_0}{|j_0|} y \vec{i}_y. \tag{33}$$

The $\vec{j} \times \vec{B}$ expression in Eq. (33) indicates that the Lorentz force due to the imposed axial electric current is proportional to the magnetic Reynolds number and dimensionless radius pointing to the axis.

3.2 Gravitational and Magnetic Effects. In Eq. (18), the fluid motion can be induced by either the gravitational force or Lorentz force even when initial fluid motion and the pressure gradient are absent. Given the gravitational force $\rho \vec{g} = \rho g \vec{i}_x$ (or $\vec{i}_g = \vec{i}_x$), the buoyancy force, $-\mathrm{Gr}\hat{\rho}\theta \vec{i}_g$, is aligned with the x direction and varies from $-\mathrm{Gr}\hat{\rho}$ (hot side) to zero (interface) due to the temperature change. The Lorentz force, $\mathrm{Ha}^2 \vec{j} \times \vec{B}$, is aligned with the radial direction, pointing to the center of the ampoule, and varies from zero at the center of the ampoule to $\frac{1}{2}\mathrm{Ha}^2\,\mathrm{Re_m}$ near the wall. Assigning the reference length $b = 3$ mm and a temperature difference $\Delta T = 175$°C, Gr for Bismuth under unit gravity is 10^5. Under these conditions, the Hartmann number Ha, at $j_0 = 80$ A/cm^2, is 1.156×10^6, and the magnetic Reynolds number $\mathrm{Re_m}$ is 1.8×10^{-7}. Considering these dimensionless numbers, we find that $\mathrm{Ha}^2\,\mathrm{Re_m} \sim 2.4 \times 10^5$ and $\mathrm{Gr} \sim 10^5$, indicating that the maximum magnetic force induced by the electric current is of the same order of magnitude as that of the maximum gravitational force. However, these two forces cannot cancel each other due to the fact that the gravitational force is in the longitudinal direction and the magnetic force is in the radial direction.

3.3 Thermoelectric Effects. Thermoelectric effects include Seebeck, Thomson, Peltier, and Joule effects. By definition, the Seebeck effect is the electric potential generated by a temperature difference in a uniform material, or materials difference at constant temperature. The Joule, Thomson, and Peltier effects are cooling or heating generated by the electric field. It must be emphasized that for a given local temperature distribution, the "extra" local heating/cooling due to j is contributed by Joule heating as well as the Thomson effect. The Thomson effect exists even when $\vec{j}$ is due to electromotive forces other than the thermoelectric forces, provided $\vec{j}$ has a component parallel to ∇S. The Peltier effect arises because of the ability of the current to transport or generate heat abruptly at the interface. The magnitude of the Peltier effect can be determined by the difference of the Thomson effect across the solid/liquid interface (Zheng and Larson, 1997a). Thus, the thermoelectric effects on energy redistribution are represented by the Joule and Thomson effects, as seen in Eq. (19). The dimensionless parameters for Joule heating and the Thomson effect have been identified as $2\,\mathrm{Re_m}/N_J$ and N_T/Pr, respectively. For the chosen material Bi, given $\Delta T = 175$°C and $j_0 = 80$ A/cm^2, $\mathrm{Re_m} = 1.8 \times 10^{-7}$, $\mathrm{Pr} = 0.01613$, and $N_J = 5 \times 10^{-7}$ are obtained. N_T, proportional to the Thomson coefficient, is $1.7 \times 10^2\,\tau$. The Thomson coefficient for liquid bismuth, plotted in Fig. 2, is almost zero, while that for solid bismuth is of the order of 10^{-4} (Zheng and Larson, 1997a). Based on the aforementioned dimensionless parameters, $2\,\mathrm{Re_m}/N_J \approx 0.72$ and $N_T/\mathrm{Pr} \simeq 1.06$ are obtained. This confirms that in liquid bismuth, Joule heating is a dominant thermoelectric effect, while in solid bismuth, the Thomson effect can be of the same order of magnitude as Joule heating. The maximum Thomson effect is achieved when the current direction is anti-parallel to the temperature gradient. Quantitative information with respect to Joule heating and the Thomson effect for bismuth can be found from Zheng and Larson (1997a).

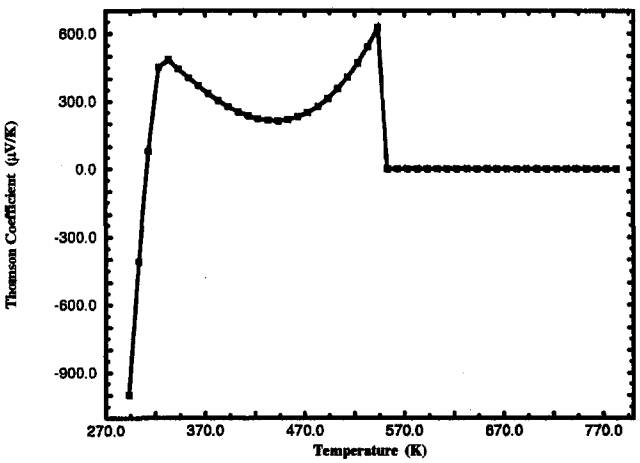

Fig. 2 Thomson coefficient for bismuth as a function of temperature

4 Numerical Method and Accuracy

The governing equations for mass, momentum, and energy together with the formulations for body force, heat flux, current density, and interface movement have been solved using the adaptive curvilinear finite volume scheme (MASTRAPP) developed by Zhang and Moallemi (1995) and Zhang et al. (1996). The principal components of this scheme include multizone adaptive grid generation (MAGG) and curvilinear finite volume discretization (CFV).

The MAGG scheme is based on a constrained variational method in which a linear combination of integrals, measuring different grid characteristics, is optimized using Euler–Lagrange equations. A mesh for the current calculations is created with the optimization of important grid characteristics; namely the smoothness, orthogonality, weighted cell area, and inertia of the grids for the entire domain with the exception of the zonal interfaces. At the zonal interfaces, the Euler–Lagrange equations together with the constrained formulation (the interface shapes) provide necessary conditions to determine the grid distribution and Lagrange multipliers. The finite difference approximation of the Euler–Lagrange equations are solved by a SOR method to obtain coordinates of the grid points.

The CFV scheme employs a flux discretization in the physical domain. Due to its simplicity in the multidomain system, a nonstaggered grid arrangement is chosen. Pressure oscillation induced by the chosen grid arrangement is prevented by using the momentum interpolation scheme. The solution procedure follows the SIMPLER algorithm (Patankar, 1980), which solves a pressure equation to obtain the pressure field and then uses a pressure-correction equation to correct the predicted velocities.

The solution algorithm has been validated against experimental and numerical results by simulating natural convection in an eccentric annulus, liquid metal solidification in a rectangular cavity, and many other problems (Zhang et al., 1996). The new features of the numerical procedure used in this paper have been validated by comparing the predicted temperature at the centerline of the sample with measurements (Zheng and Larson, 1997b) during directional solidification in a Bridgman–Stockbarger furnace. The maximum discrepancy between the prediction and the experiment is about 5 percent.

Due to the axisymmetric feature of unidirectional solidification in a Bridgman–Stockbarger system (see next section), the computational domain is limited to half of the region of interest. The symmetry axis is aligned with the x coordinate, and the radius is in the y direction. A 80 × 30 five-zone nonorthogonal mesh is generated using the multizone adaptive grid generation. Grid lines are arranged to be aligned with the moving interface, and the grids are migrated so as to distribute the numerical grids evenly in solid and liquid zones in terms of their lengths (see Zhang et al., 1997, for details). A comparison of predicted interface position, and maximum and minimum values of the stream function was made for the simulations using 80 × 30 and 160 × 60 nonuniform grids and 230 × 30 uniform grids. Differences among the results using different grids are within 3 percent for varying values of gravitational acceleration.

5 System Configuration and Boundary/Initial Conditions

5.1 Bridgman Stockbarger Crystal Growth System. For clarity of the formulation and boundary conditions, we briefly describe the experimental PID procedure in a Bridgman–Stockbarger system. Figure 1 shows a schematic diagram of directional solidification in a Bridgman–Stockbarger system. In terms of temperature distribution, the furnace is constituted of three parts: The upper part of the furnace is the hot zone where the temperature is maintained at an almost constant value T_h by a resistance heater; the lower part of the furnace is the cold zone where the cooling temperature T_c is sustained by a water-cooled chill block; and the middle part of the furnace is the adiabatic zone where heat exchange with the surroundings is negligible. The sample crystal (Bi), sealed in a fused silica ampoule, is initially positioned inside the furnace within the region where the temperature is above the Bi melting point T_{mp}. The directional solidification is initiated by translating the furnace vertically after the system achieves thermal, and hydrodynamic (if the gravitational force is present) equilibrium. The ampoule is a fused silica tube with an inner radius of b = 3 mm and a wall thickness of 1 mm. The investigated sample length is at least 30 times the ampoule's inner radius.

5.2 Boundary Conditions. In our calculations, the numerical region covers the sample (both solid and liquid) and the ampoule. With respect to the coordinate system in Fig. 1, the boundary conditions for temperature and velocity are specified as follows:

at the central axis, $\hat{y} = 0$:

$$\frac{\partial \theta}{\partial \hat{y}} = 0, \quad \frac{\partial \hat{u}}{\partial \hat{y}} = 0, \quad \text{and} \quad \hat{v} = 0.$$

at the ampoule outer wall, $\hat{y} = 1.33$:

$$\theta = 1 \text{ if } \hat{x} < \hat{L}_h,$$

$$\frac{\partial \theta}{\partial \hat{y}} = 0 \quad \text{if} \quad \hat{L}_h < \hat{x} < (\hat{L}_h + \hat{L}_a),$$

$$\theta = -1.44 \text{ if } \hat{x} > (\hat{L}_h + \hat{L}_a)$$

at the ampoule inner wall, $\hat{y} = 1$: $\hat{u} = \hat{v} = 0$.
at the bottom $\hat{x} = 30$:

$$\theta = -1.44.$$

at the top, $\hat{x} = 0$:

$$\frac{\partial \theta}{\partial \hat{x}} = 0, \quad \frac{\partial \hat{u}}{\partial \hat{x}} = 0, \quad \text{and} \quad \hat{v} = 0.$$

at the interface $\hat{x}_{\text{int}}$:

$$\theta = 0.$$

where $\hat{L}_h$ = 18 and $\hat{L}_a$ = 5 are initial dimensionless lengths of the hot and adiabatic regions, respectively, and $\hat{L}$ = 30 is the total dimensionless length of the sample (computational domain). The interface position $\hat{x}_{\text{int}}$ varies with time and is determined by Eq. (21).

5.3 Initial Conditions. The initial distributions of temperature and velocity are obtained by solving the governing Eqs. (17)–(19), (21), and the boundary conditions discussed above with the following constraints: (1) steady state $\partial/\partial\hat{t} = 0$, (2) zero pulling velocity ($\hat{u}_p = 0$), and (3) zero current density ($\hat{j} = 0$). Figures 3(a, b) show the initial temperature and stream function distributions within the region from top ($\hat{x} = 3$) to bottom ($\hat{x} = 27$) under the micro (10^{-4} g) and unit gravity (g) conditions, respectively. The interface is identified by the zero temperature line. As displayed in Figs. 3(a, b), the stream function under the microgravity condition is of the order of 10^{-4} and that under the unit gravity condition is of the order of unity. The fluid motion under the microgravity condition is therefore negligible, the maximum stream function $\psi_{max} \approx 2 \times 10^{-4}$. Under the unit gravitational condition, the fluid circulates the following two vortices. The primary vortex, formed by the buoyancy force, rotates clockwise near the adiabatic hot region. The secondary vortex, formed by shear from the primary vortex, rotates counterclockwise just above the solid/liquid interface and below the primary vortex. The secondary vortex is much weaker ($\psi_{max} \approx -0.1$) than the primary vortex ($\psi_{max} \approx 2.0$). Although the flow strength has changed significantly with gravity, the temperature profile has remained the same because of low Prandtl number (Pr = 0.01613). As discussed by Brown (1986), a Grashof number of 10^5 is not large enough to alter the temperature field. At Gr > 10^6, the temperature profiles may change. This indicates that the gravity effect on the temperature distribution is negligible in the system studied here when the thermal and hydrodynamic steady state has been reached in the absence of external perturbations.

Figure 3(c) provides information on heat flux corresponding to the initial temperature fields as shown in Figs. 3(a, b) as well as the grid layout for these calculations. Heat enters the melt from the hot zone above the adiabatic region, passes through the solid–liquid interface, and is dissipated to the cold zone below the adiabatic region. The heat flux inside the ampoule is small in this case due to low conductivity of the ampoule material (quartz). Because of the relatively long adiabatic region, the heat flux vectors are parallel at the interface and preserve a flat interface shape.

6 Directional Solidification and Peltier Interface Demarcation

6.1 Directional Solidification Under Unit/Microgravity Conditions. To understand gravitational effects on directional solidification, numerical simulations have been performed by imposing a pulling velocity (u_p = 5 cm/h) upon the initial thermal hydrodynamic equilibrium temperature and velocity fields (Figs. 3(a, b)). The temperature and stream function contours at time t = 10 and 200 (s) are plotted in Figs. 4(a–d). A virtually flat interface ($\theta = 0$ line) is observed except

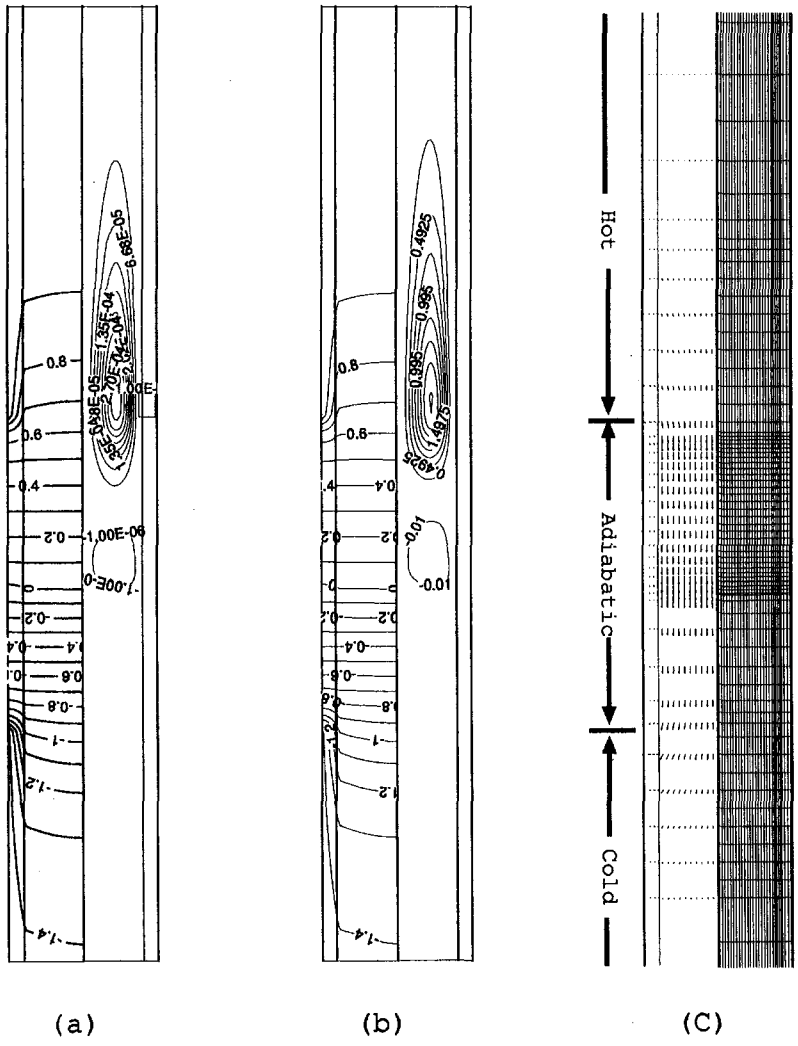

Fig. 3 Initial temperature and stream function for: (*a*) Gr = 10 × 10^{-4}g; (*b*) Gr = 10^5 × 1 g; and (*c*) heat flux and grid layout

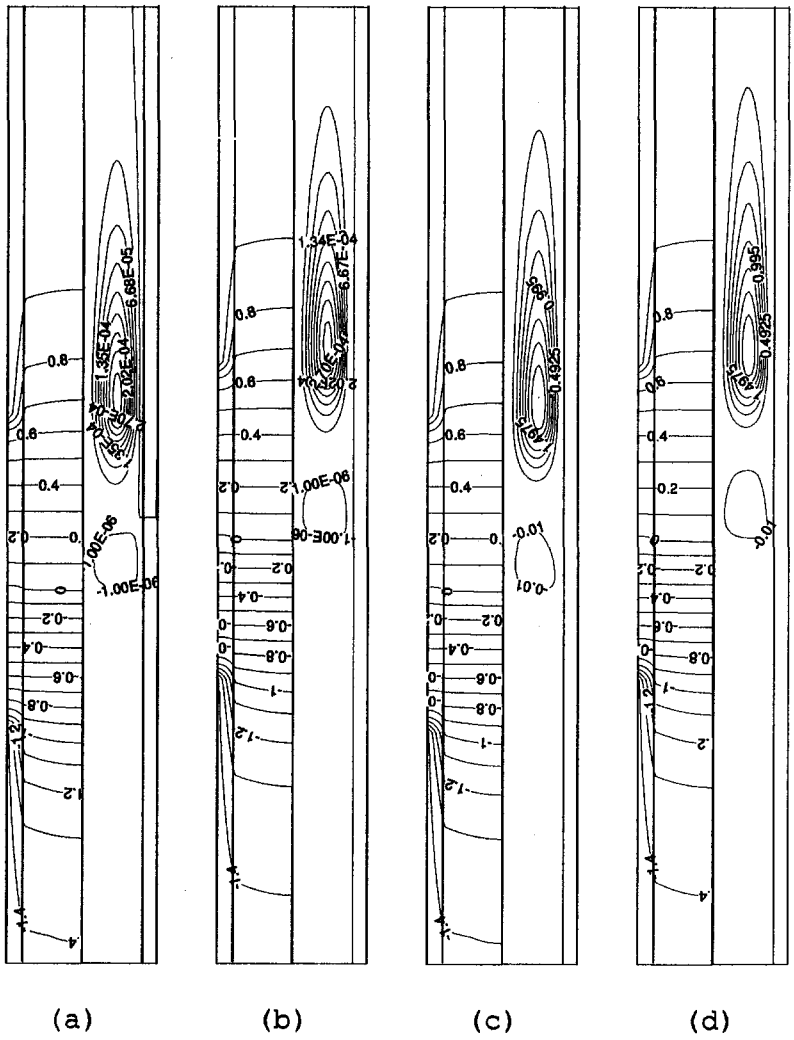

Fig. 4 Temperature and stream function during directional solidification with pulling velocity u_p = 13.9 μm/s (5 cm/h) for Gr = 10×10^{-4} g at time (*a*) t = 10 s and (*b*) t = 200 s; and for Gr = 10^5 (1 g) at time (*c*) t = 10 s and (*d*) t = 200 s

for a small curvature close to the ampoule wall. Although the temperature and stream function retain similar profiles at different times, a variation of the temperature gradient with time is observed by carefully examining the neighboring contour lines.

Further examination of the interface location and movement with time has been made in Figs. 5(*a*) and 5(*c*), where the solid and dashed lines represent the centerline interface location and its velocity under unit and microgravity conditions, respectively. The interface location, measured by x, decreases monotonically, indicating that solidification occurs as soon as the furnace is translated. During the initial translation ($t < 15$ s), the interface location under unit gravitational condition (Fig. 5(*a*)) is larger than that under microgravitational conditions (see also in Fig. 5(*b*)), indicating that less liquid has been solidified under unit-gravitational conditions. This can also be confirmed from the interface translation velocity in Fig. 5(*c*). A negative sign of the velocity represents interface movement toward the liquid side (solidification), and a positive sign represents the interface movement toward the solid side (melting). Due to buoyancy-induced convection, the solidification is slowed down in the beginning of translation. With continued translation, the interface position, x, under unit-gravity becomes closer to that under microgravity condition. At time t = 100 s, the interfaces for both cases move to almost the same location and progress at the same steady-state velocity as the moving furnace.

The transient behavior of the interface can be better understood from Eq. (21). In the absence of the Peltier effect, the interface movement is determined by the latent heat of the material and the heat flux difference at the interface between the solid and liquid sides. For the system studied (Fig. 1), directional solidification is accomplished by translating the furnace to change the temperature at the ampoule wall. The temperature change at the ampoule wall, in turn, affects the temperature distribution inside the Bismuth sample by conductive heat transfer in the microgravity environment. In the presence of a unit gravitational force, heat is transferred not only by conduction but also by convection due to buoyancy effects.

The buoyancy effects on heat transfer during directional solidification can be explained as follows. The initial thermal distribution and fluid motion are at steady state, as shown in Figs. 3(*a*, *b*). Due to the sudden onset of translation, the interface moves up, accompanying the solidification isotherm. The movement of the solidification interface compresses the secondary vortex near the solid/liquid interface and the fluid motion in the liquid is dominated by the primary vortex. The clockwise rotation of the fluid preferentially transports heat from the hot to the cold zone near the interface. Consequently, excess heat is accumulated near the interface, reducing the overall solidification rate.

In order to satisfy heat and momentum conservation, the primary vortex is weakened with time and a secondary vortex

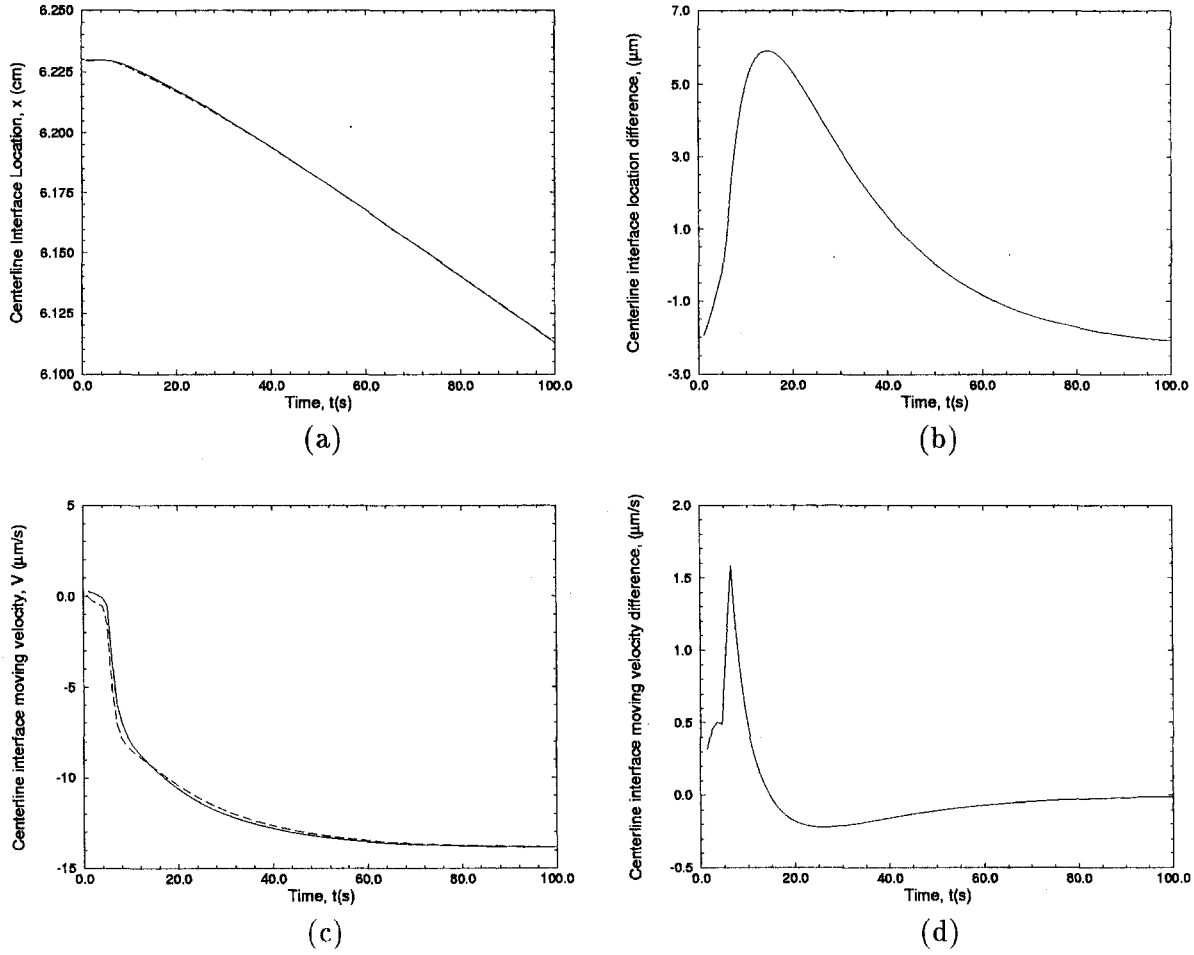

Fig. 5 Directional solidification with pulling velocity u_p = 13.9 μm/s (5 cm/h), (*a*) interface position, (*b*) difference of interface position between unity and microgravity conditions; (*c*) interface moving velocity, (*d*) difference of interface moving velocity between unity and microgravity conditions

near the interface is gradually reformed, rotating in a counterclockwise direction. In contrast to the primary flow, the secondary flow moves heat away from the region near the interface, and increases the solidification rate. Eventually, a new thermal/hydrodynamic equilibrium state is achieved and the solidification interface progresses at the same speed as the furnace movement, the new equilibrium state is called steady-state directional solidification.

Although the steady-state directional solidification is finally controlled by the pulling velocity (furnace translation velocity), the gravity-dependent convection does influence the solidification rate during the initial transient period (Fig. 5(*d*)). The Jackson–Hunt theory states that the solidification rate V_R of eutectic materials is correlated to the microstructure scale, e.g., lamellar (rod) spacing λ, by

$$\lambda^2 V_R = \text{const.} \tag{34}$$

From this correlation, it can be concluded that a lower growth rate in the unit-gravity case results in a coarser microstructure during the initial transient period. A progressively finer microstructure is formed as the growth rate increases. When the system reaches a new equilibrium, the steady-state microstructures formed under unit and microgravitational conditions have no significant difference. This discussion on the microstructure formation is based on the assumption that the minor species in Bi-related eutectic is sufficiently small, e.g., BiMn, and its appearance will not significantly affect the energy and momentum transport. Also the transport of solute (concentration) and its influence on the morphology have not been considered in this study.

6.2 Peltier Interface Demarcation During Directional Solidification. In the study of directional solidification, the Peltier effect is utilized to create a rapid thermal perturbation at the solid/liquid interface so as to mark the interface location and shape. Since an external electric current is involved in this process, heat and mass transfer during directional solidification is more complicated due to thermoelectric and magnetohydrodynamic effects. To understand the mechanism of the PID method, we have imposed an external electric current after steady-state directional solidification has been achieved at t = 100 s. Figure 6(*a*) shows the computational results of the centerline interface location before, during, and after a 240 second current pulse of $j_0 = +80$ A/cm^2. It is seen that the interface moves steadily with time before the pulsing ($t \leq 100$ s), and moves as a function of time during the initial 100 seconds of pulsing and gradually returns to steady state. To examine the gravitational effect, the difference of the centerline interface location between two cases is presented in Fig. 6(*b*). The change in the interface location due to the gravitational effect is on the order of 1 to 20 μm. Although this difference is small, it can change the morphological record significantly (velocity in Fig. 6(*c*), and velocity difference in Fig. 6(*d*)). As noted earlier, the velocity is correlated to the microstructure by the Jackson–Hunt theory. For the velocity difference of 10 percent observed in this case, the eutectic lamellar/rod spacing will

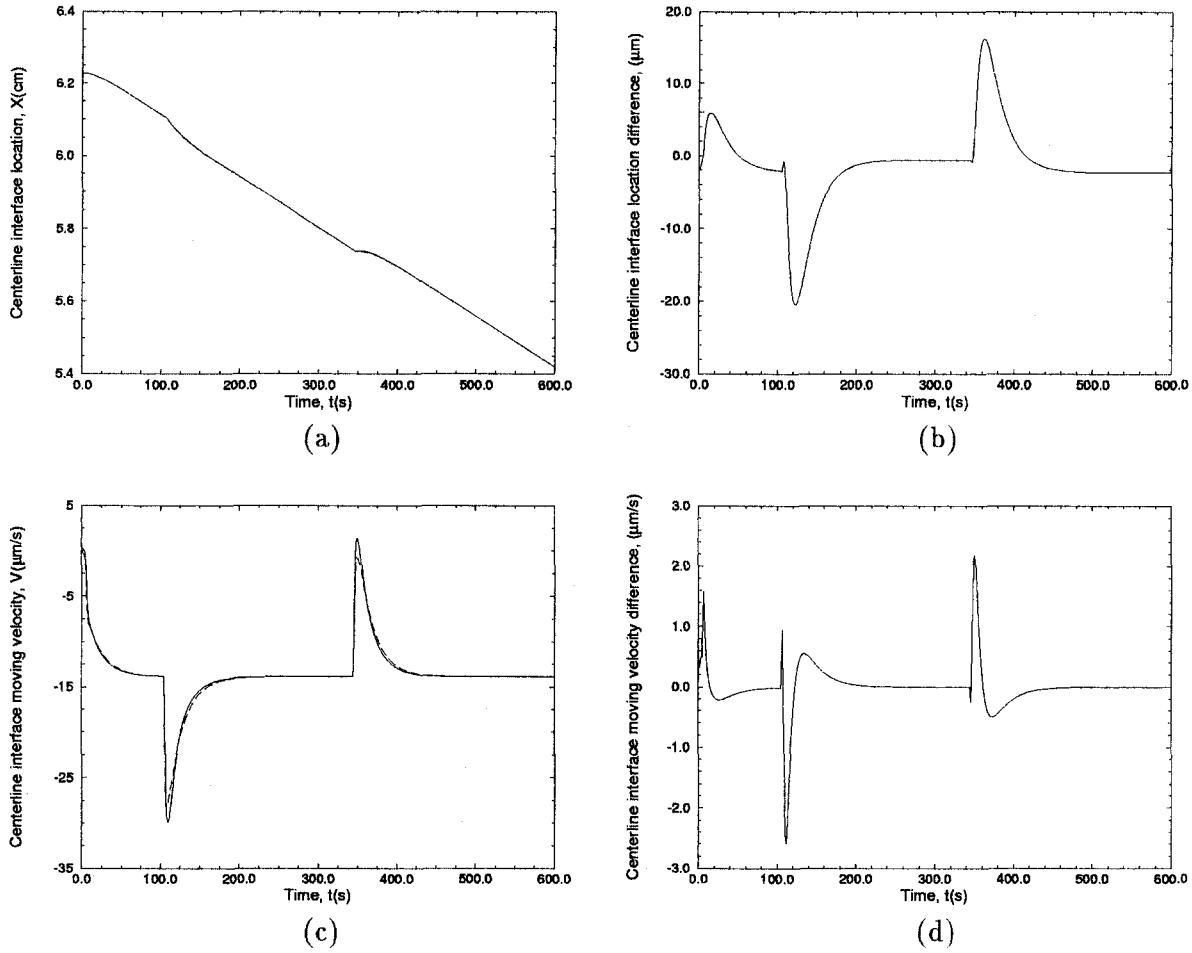

Fig. 6 Interface demarcation during directional solidification with current density $j_0 = +80$ A/cm^2 and pulling velocity $u_p = 13.9$ μm/s, (*a*) interface position, (*b*) difference of interface position between unity and microgravity conditions; (*c*) interface moving velocity, (*d*) difference of interface moving velocity between unity and microgravity conditions

change by about 5 percent, a 20 percent velocity difference will change the spacing by 10 percent.

It is also observed in Fig. 6(b) that the interface location during the pulse undergoes a transient process due to gravitational effects. This transient behavior can be explained by the thermoelectric and magnetohydrodynamic effects and their interaction during directional solidification. When an electric current is imposed from liquid to solid bismuth, the interface promptly moves up (interface location at the coordinate x decreases) due to the Peltier cooling. As a result of this interface movement, the heat flux difference between the liquid and solid near the interface is increased, and the longitudinal fluid motion is suppressed. Under this circumstance, the fluid motion is determined by a primary vortex due to gravitationally dependent buoyancy effects and Lorentz forces. Both buoyancy and Lorentz forces tend to drive the flow near the hot wall upward and take heat away from the interface so that solidification occurs and the interface moves up. With time, the primary vortex is weakened due to momentum transport to the interface and forms a secondary vortex. As previously explained, this secondary vortex leads to convective flows transporting heat from the hot to cold zone near the interface and results in a reduced amount of liquid bismuth solidified. This process continues until the mass, momentum, and heat transfer achieve a new balance and the interface progresses at a constant velocity (steady state growth). It is estimated from Figs. 6(a) and 6(c) that the new steady state is reached at $t = 240$ s with a current density of 80 A/cm^2.

Similar graphs for negative current pulsing are shown as Figs. 7(a–d). Due to the opposite current polarity, the history record of the morphology is different. The difference can be interpreted from the velocity change with time based on the Jackson–Hunt theory. By examining Figs. 6(a) and 6(c), for a positive pulse, the absolute velocity is increased promptly after pulsing. With continued pulsing, the velocity decreases. This reveals that a finer microstructure is observed followed by a coarse structure. By withdrawing the pulsing, the velocity can be suddenly reduced to zero and gradually recovered to the steady-state pulling velocity. Therefore a sharp region with very coarse structure followed by a gradually finer structure can be observed. For the negative pulsing (shown in Figs. 7(b) and 8), the solid bismuth is first melted due to the Peltier heating, and after a certain time (about 40 seconds) solidification is initiated as a coarse structure and evolves to the steady-state structure. With the pulsing off, a much finer structure is followed by a gradually coarser structure. The coarse structure continues for about 100 seconds, until a new equilibrium is obtained where the initial steady-state structure returns. The morphology patterns predicted here can provide experimentalists with useful information on interpreting microstructural results.

To gain an overall view of the thermal and hydrodynamic effects, we present the temperature and stream function contours during directional solidification with opposite polarity current pulsing in Figs. 8(a–c). Figure 8(a) is the temperature distribution and fluid motion after pulling about $t = 105$ s, and Figs. 8(b, c) are the results during current pulsing of ∓ 80 A/cm^2 at time t

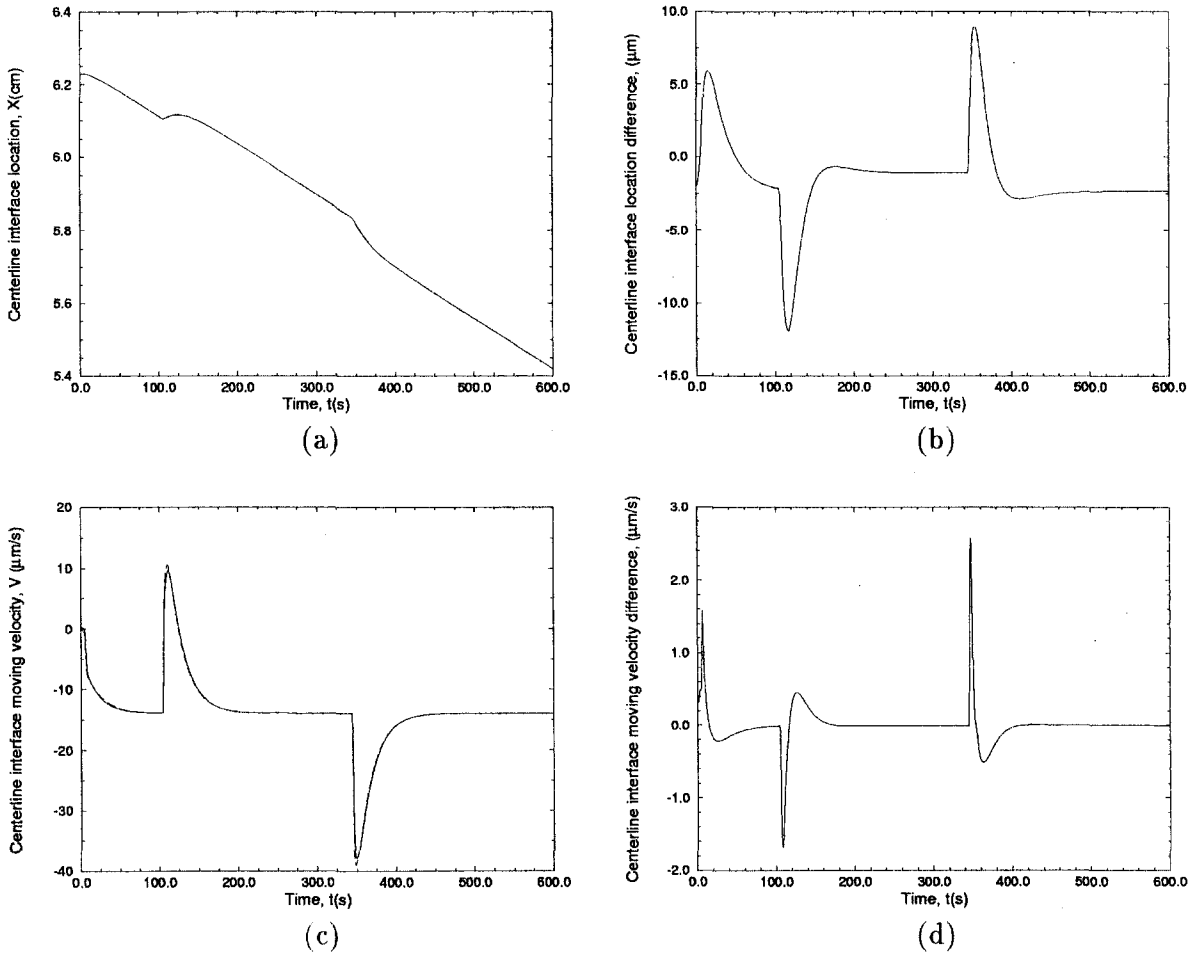

Fig. 7 Interface demarcation during directional solidification with current density $j_0 = -80$ A/cm^2 and pulling velocity $u_p = 13.9$ μm/s, (*a*) interface position, (*b*) difference of interface position between unity and microgravity conditions; (*c*) interface moving velocity, (*d*) difference of interface moving velocity between unity and microgravity conditions

= 345 s, respectively. It is seen that the flow patterns change little with pulsing after $t = 240$ s, maintaining two vortices. However, the extent of fluid movement has been changed due to the thermoelectric and magnetohydrodynamic effects. The numerical data show that at $t = 105$ s, the maximum and minimum values of the stream function are 1.9739 and −0.058, respectively. After current pulsing with electric polarity of −80 A/cm^2, the maximum value of the stream function is decreased to 1.909, and the minimum value is increased to −0.0434. By reversing current polarity, the maximum value of stream function is increased from 1.9739 to 2.0107, and the minimum is changed from −0.058 to −0.039. With respect to Eq. (18), the driving forces of fluid motion for a system with an electric field consist of buoyancy and Lorentz forces. The former, dependent on the temperature distribution and gravitational level, tends to maintain a two vortex structure as shown in Fig. 8(*a*). The latter, a function of radial distance $\hat{y}$ in the opposite direction of $\hat{j}$, tends to stretch the vortex structure in the radial direction. Thus the variations of stream function in Figs. 8(*b*, *c*) are attributed to the combined contribution of gravitational, thermoelectric, and magnetohydrodynamic effects.

7 Conclusions

A physics-based model is developed to study the gravitational (convection), thermoelectric (Peltier, Seebeck, Joule, and Thomson) and magnetohydrodynamic (Lorentz force) effects on directional solidification phenomena. It is applied to directional solidification in a Bridgman–Stockbarger system to study the effect of Peltier Interface Demarcation on interface movement under varying gravitational conditions.

An order of magnitude analysis has been performed to examine the importance and contributions of various governing parameters, in particular the thermoelectric and magnetohydrodynamic effects. For the system studied here, the maximum magnetic force induced by the electric current is of the same order of magnitude as that of the maximum gravitational force. These two forces are perpendicular to each other and cannot cancel each other. For the given bismuth material with imposed current density $j_0 = 80$ A/cm^2 across a 3-mm-dia cylinder, the dimensionless parameter representing the Joule heating, Re_m/N_J, is approximately 0.72, and the Thomson effect, N_T/Pr, is close to zero in the melt and approximately 1.06 in the solid. This indicates that the Thomson effect is negligible in comparison with Joule heating in the molten bismuth, while it is as important as Joule heating in the solid bismuth.

Numerical studies for directional solidification under varying gravity conditions reveal that the buoyancy-induced convection does not influence the temperature field significantly due to the low Grashof number; however, it does influence the fluid motion and the history of the interface movement. For a pulling velocity of 13.9 μm/s (5 cm/h), the maximum difference of the interface moving velocity is about 10 percent of the pulling velocity in the initial transient period. This difference is greatly diminished when the system reaches an equilibrium steady state.

When the PID technique is employed, the interface is disturbed due to the thermoelectric heating/cooling. In the pres-

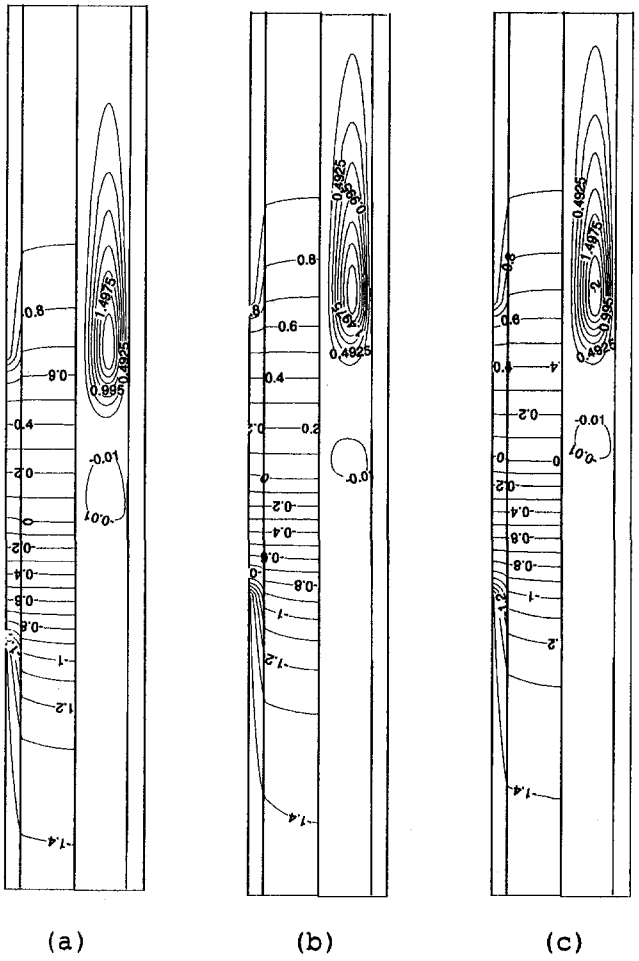

Fig. 8 Temperature and stream function: (*a*) before pulsing at time t = 104 s, (*b*) after negative current polarity pulsing at time t = 345 s, and (*c*) after positive current polarity pulsing at time t = 345 s

ence of gravity, the interface can be further disturbed and results in a maximum velocity change of 20 percent. For the BiMn eutectic, the composition of Mn (0.72 wt%) is sufficiently small that its influence on the energy and momentum balance can be neglected. Therefore the growth velocity of BiMn can be approximated by that predicted for Bi. Under this assumption, it is estimated from the Jackson–Hunt theory that the lamellar/rod spacing of BiMn eutectic can change as much as by 10 percent due to the gravitational effect.

The analysis based on the Jackson–Hunt theory also reveals that the morphology pattern varies with the current polarity. With a positive current pulse applied, a finer microstructure is formed, followed sequentially by a coarse structure. When the pulse is terminated, a sharp region with very coarse structure is followed by a gradually finer structure approaching the original steady state. With a negative current pulse, these morphological sequences are reversed. Thus, the morphology patterns predicted from numerical simulation can provide experimentalists useful information on interpreting microstructural results, as well as assistance in planning experiments.

Acknowledgments

Zheng and Larson acknowledge the sponsorship of this research by NASA (Grant #NCC8-100), and Zhang and Prasad acknowledge the support by AFOSR/DARPA MURI award to the Consortium for Crystal Growth Research at SUNY Stony Brook. Acknowledgments are also due to J. Iwan D. Alexander from University of Alabama Huntsville for helpful discussions.

References

Brown, R. A., 1986, "Interaction between convection, segregation and interface morphology," in: *Advanced Crystal Growth,* P. M. Dryburgh, B. Cockayne, and K. G. Barraclough, eds., Prentice-Hall, Englewood Cliffs, NJ, pp. 3–94.

Brush, L. W., Coriell, S. R., and McFadden, G. B., 1990, "Directional solidification of a planar interface in the presence of a time-dependent electric current," *Journal of Crystal Growth,* Vol. 102, pp. 725–742.

Favier, J. J., Garandet, J. P., Rouzaud, A., and Camel, D., 1994, "Mass transport phenomena during solidification in micro-gravity: Preliminary results of the first Mephisto flight experiment," *Journal of Crystal Growth,* Vol. 140, pp. 237–243.

Holmes, D. E., and Gatos, H. C., 1978, "Application of interface demarcation to multiphase system: In Sb-Sb Eutectic," *Journal of the Electrochemical Society,* Vol. 125, pp. 1873–1875.

Li, Q., Nguyen Thi, H., and Billia, B., 1996, "Quantitative analysis of the influence of Peltier interface demarcation on directional solidification," *Journal of Crystal Growth,* Vol. 167, pp. 277–284.

Lichtensteiger, M., Witt, A. F., and Gatos, H. C., 1971, "Modulation of dopant segregation by electric currents in Czochralski-type crystal growth," *Journal of the Electrochemical Society,* Vol. 118, pp. 1013–1015.

Panofsky, W. K. H., and Phillips, M., 1956, *Classical Electricity and Magnetism,* Addison-Wesley, Reading, MA, p. 115.

Patankar, S. V., 1980, *Numerical Heat Transfer and Fluid Flow,* Hemisphere, Washington, DC.

Pirich, R. G., and Larson, D. J., Jr., 1982, in: *Materials Processing in Reduced Gravity Environment of Space,* Rindone, G. E., ed., North-Holland, New York, p. 253.

Quenisset, J. M., and Naslain, R., 1981, "Effect of forced convection on eutectic growth," *Journal of Crystal Growth,* Vol. 54, p. 465.

Schaefer, R., and Glicksman, M., 1968, "Measurement of atomic kinetics of solidification using Peltier heating and cooling—I. Theory," *Acta Metallurgica,* Vol. 16, pp. 1009–1018.

Shercliff, J. A., 1979, "Thermoelectric magnetohydrodynamic," *Journal of Fluid Mechanics,* Vol. 91, pp. 231–251.

Silberstein, R. P., and Larson, D. J., Jr., 1987, "Spatial profile of thermoelectric effects during Peltier pulsing in Bi and Bi/MnBi eutectic," *Materials Research Society,* Symposium Vol. 87, pp. 29–138.

Wang, C. A., Witt, A. F., and Carruthers, J. R., 1984, "Analysis of crystal growth characteristics in a conventional vertical Bridgman configuration," *Journal of Crystal Growth,* Vol. 66, pp. 299–308.

Zhang, H., and Moallemi, M. K., 1995, "A multizone adaptive grid generation technique for simulation of moving and free boundary problems," *Numerical Heat Transfer,* Vol. B27, pp. 255–276.

Zhang, H., Prasad, V., and Moallemi, M. K., 1996, "A numerical algorithm using multi-zone grid generation for multiphase transport processes with moving and free boundaries," *Numerical Heat Transfer,* Vol. B29, pp. 399–421.

Zhang, H., Zheng, L. L., Prasad, V., and Larson, Jr., D. J., 1997, "An advanced numerical scheme for dynamic simulation of Bridgman crystal growth," *Proc. 32nd National Heat Transfer Conference,* ASME HTD-Vol. 347, pp. 281–291.

Zheng, L. L., and Larson, Jr., D. J., 1997a, "Thermoelectric effects on interface demarcation and directional solidification in bismuth," *Journal of Crystal Growth,* Vol. 180, pp. 293–304.

Zheng, L. L., and Larson, D. J., Jr., 1997b, "Experimental and numerical solidification of thermal and compositional transport during directional solidification in Bridgman Stockbarger system," *Journal of Crystal Growth,* in preparation.

The Effects of Transverse Acceleration-Induced Body Forces on the Capillary Limit of Helically Grooved Heat Pipes

S. K. Thomas
Assistant Professor.
Assoc. Mem. ASME
sthomas@cs.wright.edu

K. S. Klasing
Graduate Research Assistant.
Mem. ASME

Department of Mechanical and Materials Engineering,
Wright State University,
Dayton, OH 45435

K. L. Yerkes
Research Engineer,
AFRL/PRPG,
Air Force Research Laboratory,
Wright–Patterson AFB, OH 45433-7251

A helically grooved copper heat pipe with ethanol as the working fluid has been fabricated and tested on a centrifuge table. The heat pipe was bent to match the radius of curvature of the table so that uniform transverse (perpendicular to the axis of the heat pipe) body force fields could be applied along the entire length of the pipe. By varying the heat input (Q_{in} = 25 to 250 W) and centrifuge table velocity (radial acceleration $|\vec{a}_r|$ = 0 to 10g), information on dryout phenomena, circumferential temperature uniformity, heat lost to the environment, thermal resistance, and the capillary limit to heat transport was obtained. Due to the geometry of the helical grooves, the capillary limit increased by a factor of five when the radial acceleration increased from $|\vec{a}_r|$ = 0 to 6.0g. This important result was verified by a mathematical model of the heat pipe system, wherein the capillary limit to heat transport of each groove was calculated in terms of centrifuge table angular velocity, the geometry of the heat pipe and the grooves (including helix pitch), and temperature-dependent working fluid properties. In addition, a qualitative study was executed with a copper–ethanol heat pipe with straight axial grooves. This experimental study showed that the performance of the heat pipe with straight grooves was not improved when the radial acceleration was increased from $|\vec{a}_r|$ = 0 to 10.0g.

Introduction

Heat pipes have been proposed to be used aboard fighter aircraft such as the Navy F/A-18 to act as heat sinks for electronics packages that drive aileron or trailing edge flap actuators (Gernert et al., 1991; Yerkes and Hager, 1992). During combat, transient acceleration fields of up to 9g could be present on the aircraft. Therefore, knowledge of the thermal performance of heat pipes under elevated acceleration fields is of importance to designers of the electronics packages in need of cooling.

Yerkes and Beam (1992) analytically and experimentally studied a flexible copper–water arterial heat pipe in a transient heat flux and transient body force environment using a centrifuge table. The effects of transverse body forces on the liquid flow in the artery were analyzed by developing a relationship between the wicking height and the radial acceleration. With a constant heat input, the capillary limit of the heat pipe was reached as the radial acceleration increased above 8g. It was hypothesized that the transverse body force field partially deprimed the artery.

Yerkes and Hallinan (1995a, b) studied the effects of transient accelerations on an unheated meniscus in a capillary tube. A centrifuge table was used experimentally to examine the advancing or receding behavior of water and ethanol in the capillary tube. The analytical study involved the formulation of the transient nature of the acceleration field in the meniscus region and the dynamic behavior of the meniscus as a result of the temporal acceleration-induced body forces. The effects of the transverse body forces, the Bond number, and the capillary number on the motion of the meniscus were predicted and compared to the experimental results with excellent agreement.

Thomas and Yerkes (1997) determined the quasi-steady-state thermal resistance of a flexible copper–water heat pipe under transient acceleration fields with constant heat input using a horizontal centrifuge table. The performance of the heat pipe was examined in terms of the heat input, condenser temperature, radial acceleration, and sinusoidal acceleration frequency. In addition, the effects of the previous dryout history were noted. It was found that the thermal resistance of the heat pipe decreased with increasing acceleration frequency and condenser temperature, and increased with the heat input. The occurrence of dryout prior to changing the frequency tended to result in higher thermal resistances as compared to the case when dryout did not occur due to the inability of the artery to reprime fully.

The results of the previous studies have indicated a need for improved performance under transverse acceleration fields. In addition, a wick geometry amenable to analysis was sought to provide insight into the behavior of the working fluid within heat pipes under these conditions. Therefore, to address these points, a heat pipe with a helical groove wick structure was fabricated and tested. The objective of the present study was to determine experimentally the steady-state operating characteristics of a helically grooved copper–ethanol heat pipe when subjected to constant heat input and constant transverse (perpendicular to the axis of the heat pipe) body force fields. An iterative mathematical model to determine the capillary limit of helically grooved heat pipes for various operating temperatures and body force fields has been developed, which includes the effects of the geometry of the heat pipe and the grooves (including helix pitch) and temperature-dependent working fluid properties.

Experimental Setup

The purpose of the experiment was to examine the steady-state performance of a helically grooved copper–ethanol heat pipe under various heat inputs and transverse body force fields using a centrifuge table located at Wright-Patterson AFB (AFRL/PRPG). To ensure uniform radial acceleration fields

Contributed by the Heat Transfer Division and presented at the International Mechanical Engineering Congress & Exposition, Dallas, Texas, November 16–21, 1997. Manuscript received by the Heat Transfer Division September 3, 1997; revision received February 18, 1998. Keywords: Experimental, Heat Transfer, Heat Pipes, Liquid, Rotating. Associate Technical Editor: T. L. Bergman.

over the length of the heat pipe, the pipe was bent to match the 1.22 m radius of curvature of the centrifuge table. Physical information concerning the helically grooved heat pipe is given in Table 1 (Heat Pipe #1). It should be noted that the heat pipe container was weighed before and after the filling procedure. The weight of the working fluid inventory was 5.28×10^{-3} kg. Based on the properties of saturated ethanol at 20°C, the working fluid volume is 6.5 cm^3, which means that the heat pipe was overfilled by approximately 26 percent. The helix angle α was very small: Each groove rotated through an angle of 2.07 rad (120 arc deg) over the length of the pipe. The heat pipe was mounted to a platform, which overhung the edge of the horizontal centrifuge table. This allowed the heat pipe to be positioned such that the radius of curvature was equivalent to the outermost radius of the centrifuge table. Insulative mounting blocks were used to ensure that the heat pipe matched the prescribed radius as closely as possible. The horizontal centrifuge table was driven by a 20-hp dc motor. The acceleration field near the heat pipe was measured by a three-axis accelerometer. The acceleration field at the centerline of the heat pipe radius was calculated from these readings using a coordinate transformation.

Power was supplied to the heat pipe evaporator section by a precision power supply through power slip rings to the table. The input power was calculated using the current and voltage readings. While the current reading could be made directly using a precision ammeter, the voltage across the electric heater had to be measured on the rotating table because voltage drops were noted between the control room and the table, regardless of the size of wire used. Therefore, the voltage at the heater was obtained through the instrumentation slip ring assembly and read by a precision voltmeter. A pressure-sensitive nichrome heater tape with an aluminized backing was wound uniformly around the circumference of the evaporator section for heat input.

The calorimeter consisted of a length of $\frac{1}{8}$ in. OD copper tubing wound tightly around the condenser section. The size of the tubing was chosen to be small to minimize the effects of acceleration on the performance of the calorimeter. Thermal grease was used between the heat pipe and the calorimeter to decrease contact resistance. Type-T thermocouples were inserted through brass T-branch connectors into the coolant inlet and exit streams, and a rotameter and high-resolution digital flow meter were used to measure the mass flow rate of the coolant (ethylene glycol/water mixture). The mass flow rate was controlled using a high-pressure booster pump, which aided the low-pressure pump in the recirculating chiller. The temperature of the coolant was maintained at a constant setting by the recirculating chiller (T_{cw} = 20°C). Coolant was delivered to the centrifuge table via a double-pass hydraulic rotary coupling.

The rotameter and digital flow meter used to determine the mass flow rate of coolant through the calorimeter were calibrated by using a stop watch and precision scales. The mass flow rate was fixed during each experiment. Values of the spe-

Nomenclature

$\vec{a}$ = acceleration vector, m/s^2
a = adiabatic length near evaporator end cap, m
$\vec{A}$ = acceleration vector at any point in the helical groove, m/s^2
A_w = cross-sectional area of the wick = $\pi h(2r_v + h)$, m^2
b = adiabatic length near condenser end cap, m
b_{ij} = transformation matrix
Bo = Bond number = $\rho_l r_l w |\vec{A}_{res}|/2\sigma$
C_p = specific heat at constant pressure, J/(kg-K)
$\hat{e}$ = unit vector
D_o = tube outside diameter, m
D_v = vapor core diameter, m
f = acceleration frequency, Hz
$f_l \mathrm{Re}_l$ = drag coefficient
$\vec{F}_g$ = body force due to gravity, N
g = gravitational constant = 9.81 m/s^2
$\vec{h}$ = vector aligned with $\hat{e}_{y3}$
h = groove height, m
h_{fg} = heat of vaporization, J/kg
I = heater current, A
K = permeability = $2\epsilon r_l^2/(f_l \mathrm{Re}_l)$, m^2
L_a = adiabatic length, m
L_c = condenser length, m
L_e = evaporator length, m
L_g = groove length, m
L_t = total heat pipe length, m
m = mass, kg
$\dot{m}$ = mass flow rate, kg/s
N_g = number of grooves
p = helix pitch, m
P = pressure, N/m^2
Q = heat transfer rate, W
Q_{cap} = capillary limit heat transfer rate, W
Q_{in} = heat input at the evaporator, W
Q_t = heat transported, W
$\vec{r}$ = position vector to the helix from the (x_1, y_1, z_1) reference, m
r_c = capillary radius, m
r_h = radius of the helix = $r_v + h/2$, m
r_l = liquid hydraulic radius = $2wh/(2h + w)$, m
r_v = radius of the heat pipe vapor space, m
$\vec{R}$ = position vector to the centerline of the helix from the (x_1, y_1, z_1) reference, m
R = radius of curvature of the centerline of the helix, m
R_{th} = thermal resistance, K/W
R_{wire} = electrical resistance of heater lead wires, Ω
s = coordinate along the centerline of the helix, m
$\vec{t}$ = vector tangent to the helix
t = time, s
t_w = tube wall thickness, m
T_a = adiabatic temperature, K
T_{cec} = condenser end cap temperature, K
T_{cw} = cooling water temperature, K
T_{eec} = evaporator end cap temperature, K
T_{in} = calorimeter inlet temperature, K
T_{out} = calorimeter outlet temperature, K
V = heater voltage, V
$\vec{V}_l$ = liquid velocity vector, m/s
$V_{l,max}$ = liquid velocity in the adiabatic section = $Q_g/\rho_l w h h_{fg}$, m/s
w = groove width, m
x_1, y_1, z_1 = inertial coordinates at the center of the centrifuge table
x_2, y_2, z_2 = noninertial coordinates at the centerline of the helix
x_3, y_3, z_3 = noninertial coordinates in the helical groove
α = helix angle = $\tan^{-1}(p/2\pi r_h)$, rad
β = aspect ratio = w/h
Δ = uncertainty
ΔP = change in pressure, N/m^2
ϵ = porosity = whN_g/A_w
θ = s/R, rad
μ = absolute viscosity, kg/(m-s)
$\vec{\rho}$ = position vector to the helix from the (x_2, y_2, z_2) reference, m
ρ = density, kg/m^3
σ = surface tension, N/m
ϕ = angular parameter, rad
ϕ_0 = angle of the starting point of the helix, rad
$\vec{\omega}$ = angular velocity vector, rad/s

Subscripts

a = adiabatic
bf = body force
c = condenser
cap = capillary
e = evaporator
g = gravity or groove
l = liquid
max = maximum
r = radial
res = resultant
t = tangential or transported
v = vapor

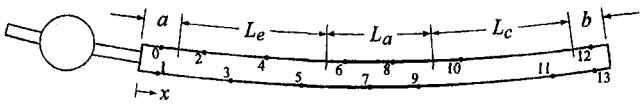

a = 25.4 mm	
L_e = 152 mm	
L_a = 101 mm	
L_c = 152 mm	
b = 25.4 mm	
L_t = 457 mm	

TC#	x (mm)	TC#	x (mm)
0,1	12.7	8	238.
2	55.8	9	259.
3	86.4	10	330.
4	116.	11	381.
5	147.	12,13	444.
6	198.	14	Coolant Outlet
7	218.	15	Coolant Inlet

Fig. 1 Thermocouple locations and relevant lengths

cific heat of ethylene glycol/water mixtures were obtained from ASHRAE (1977), which were in terms of percent ethylene glycol by weight and temperature. Measuring the specific gravity resulted in a value of 50 ± 5 percent ethylene glycol by weight. The average temperature between the calorimeter inlet and outlet was used as the temperature at which the specific heat was evaluated. The specific heat did not vary appreciably since it is a weak function of temperature.

Heat pipe temperatures were measured by Type-T surface-mount thermocouples, which were held in place using Kapton tape. All of the thermocouples were mounted directly to the surface of the heat pipe. Mounting locations for the thermocouples are shown in Fig. 1. A short unheated length next to the evaporator end cap was instrumented with two thermocouples specifically for the detection of dryout in the evaporator section. Temperature signals were conditioned and amplified on the centrifuge table. These signals were transferred off the table through the instrumentation slip ring assembly, which was completely separate from the power slip ring assembly to reduce electronic noise. Conditioning the temperature signals prior to leaving the centrifuge table eliminated difficulties associated with creating additional junctions within the slip ring assembly. Temperature and acceleration signals were collected using a personal computer and data logging software.

The thermocouples used in the present experiment were calibrated using a NIST traceable resistance temperature detector (RTD) and a low-deadband (±0.01°C) recirculating chiller. The uncertainty for the RTD was stated as ±0.005°C. The chiller temperature was set at eleven equally spaced values between 0.0 and 100.0°C, and readings were taken at each setting after the system had reached steady state. This procedure was repeated on three different days to reduce systematic errors. The combined data were used to generate polynomial best-fit curves of various orders. A regression analysis was used to determine the polynomial order that minimized the absolute errors between the raw data and the curve fit.

Since the heat pipe assembly was subjected to air velocities up to 11 m/s (25 mi/hr) due to the rotation of the table, efforts were made to reduce convective heat losses from the exterior of the heat pipe. A thin-walled aluminum box was fitted around the heat pipe and fastened to the centrifuge table, which allowed approximately 25 mm of ceramic wool insulation to be packed around the heat pipe. This insulation/box arrangement provided an effective barrier to convective losses from the heat pipe to the ambient.

The helically grooved copper–ethanol heat pipe was tested in the following manner. The recirculating chiller was turned on and allowed to reach the setpoint temperature. The centrifuge table was started from the remote control room at a slow constant rotational speed to prevent damage to the power and instrumentation slip rings. In this case, the radial acceleration remained less than $|\vec{a}_r| \leq 0.01\,g$. Power to the heater was applied, and the heat pipe was allowed to reach a steady-state condition, which was determined by monitoring various temperatures on the heat pipe until changes of less than 0.1°C over 2 min were noted. The centrifuge table velocity was then increased until the radial acceleration reached the next level ($|\vec{a}_r|$ = 0.0, 2.0, 4.0, 6.0, 8.0, 10.0g). Again, steady-state values were obtained at each acceleration setting. In all cases, the centrifuge table rotated in a clockwise direction as seen from above ($\omega_1 < 0$). After all data had been recorded, the power to the heater was removed, and the heat pipe was allowed to cool before the centrifuge table was shut down.

Uncertainty Analysis

Uncertainty estimates for the heat input, heat transported, and thermal resistance are given in this section. The heat input to the electric heater was calculated using the measured amperage and voltage. In addition, a correction was made for the losses due to the heat generated by the short length of wire leading to the heater:

$$Q_{in} = IV - I^2(R_{\text{wire}}) \tag{1}$$

The heat removed from the heat pipe by the calorimeter (transported heat) is given by

$$Q_t = \dot{m}C_p(T_{out} - T_{in}) \tag{2}$$

The thermal resistance of the heat pipe was defined as the ratio of the temperature drop across the heat pipe to the transported heat

$$R_{th} = \frac{T_{\text{eec}} - T_{\text{cec}}}{\dot{m}C_p(T_{out} - T_{in})} \tag{3}$$

Using the analysis given by Miller (1989), the maximum root-sum-square uncertainties for all of the measured and calculated values presented in this paper are given in Table 2.

Mathematical Modeling

The objective of the present analysis was to determine the effect of imposing a transverse body force field on a circular cross-sectional heat pipe with helical grooves with respect to the capillary limit. To determine the capillary limit, the total body force imposed on the liquid along the length of the helical grooves must be known. As shown in Fig. 2, the curved heat pipe was mounted to a centrifuge table at radius R. The angular velocity of the table resulted in an acceleration component directed toward the center of the table ($\vec{a}_r$). If the angular velocity of the centrifuge table changed with respect to time, a component of acceleration would be induced along a tangent to the heat pipe ($\vec{a}_t$). Since the liquid accelerated and moved in a curved path, a Coriolis acceleration component was also present. In addition to the body force due to gravity ($\vec{F}_g$), all of the above-mentioned acceleration components contributed to the total body force imposed on the fluid moving in the grooves.

To find the total body force on the liquid, an inertial reference frame (x_1, y_1, z_1) is placed at the center of the centrifuge table,

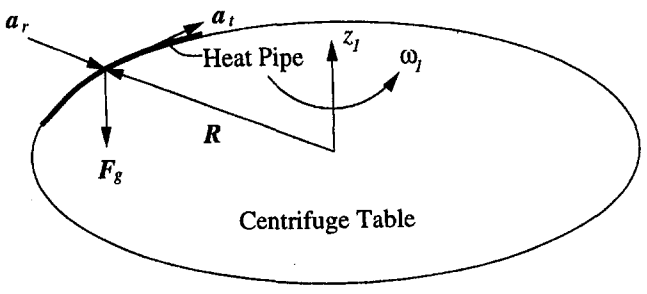

Fig. 2 Heat pipe mounted to the centrifuge table

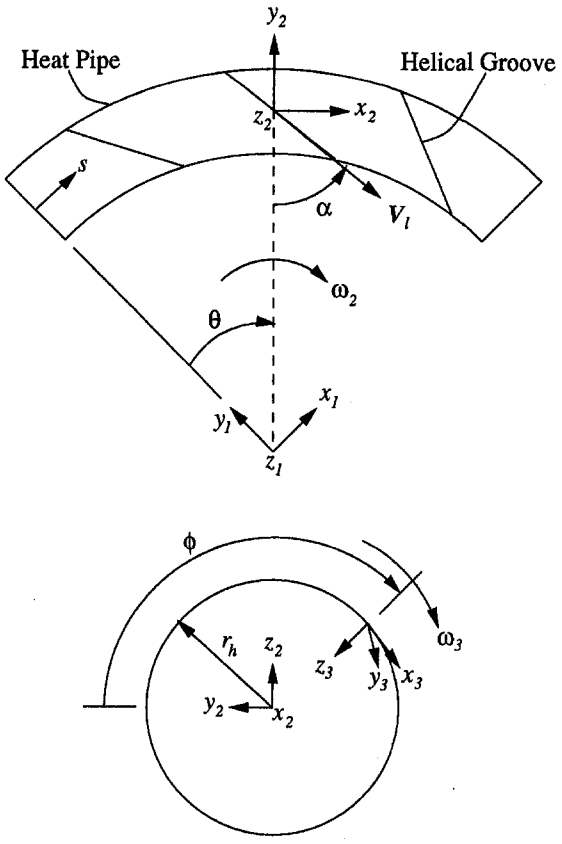

Fig. 3 Geometric considerations between the three coordinate systems: (*a*) top view of heat pipe mounted to the centrifuge table; (*b*) cross-sectional view of the heat pipe at a particular *s* location

with the z_1 direction oriented vertically [Fig. 3(a)]. A noninertial reference (x_2, y_2, z_2) is located at any point on the centerline of the helix. The (x_3, y_3, z_3) coordinate system is in the center of the helical groove at the same s location as the (x_2, y_2, z_2) system [Fig. 3(b)]. The x_3 unit vector is directed along the tangent to the helix, z_3 is directed toward the centerline, and y_3 is orthogonal to x_3 and z_3 (Fig. 4). With respect to the liquid flow within the helical grooves, the following assumptions are made:

1 The grooves are completely filled along the length of the heat pipe with no puddling or depletion.
2 There is no communication of liquid between the grooves.
3 The liquid velocity vector is directed along the unit vector $\hat{e}_{x_3}$ (tangent to the helical groove).
4 Condensation and evaporation are uniform along the lengths of the condenser and evaporator sections, respectively.
5 The liquid velocity may vary from one groove to another.

These assumptions result in the following liquid velocity profile along the length of a groove (Silverstein, 1992):

$$\vec{V}_l = \begin{cases} \left\{\left(\dfrac{s}{L_c}\right) V_{l,\max}\right\}\hat{e}_{x_3} & 0 \le s < L_c \\ \{V_{l,\max}\}\hat{e}_{x_3} & L_c \le s < L_c + L_a \\ \left\{\left(\dfrac{L_t - s}{L_e}\right) V_{l,\max}\right\}\hat{e}_{x_3} & L_c + L_a \le s < L_t \end{cases} \quad (4)$$

where $V_{l,\max}$ is the liquid velocity in the adiabatic section. Note that $V_{l,\max}$ is allowed to vary from one groove to another. The velocity of the liquid $\vec{V}_l$ shown in Fig. 3(a) results in an angular velocity $\vec{\omega}_2$ of the (x_2, y_2, z_2) reference about the z_1 axis. Since the helix angle α is constant, the angular velocity and acceleration are

$$\vec{\omega}_2 = \left\{-\frac{|\vec{V}_l| \sin\alpha}{R}\right\}\hat{e}_{z_1} \quad (5)$$

$$\frac{d\vec{\omega}_2}{dt} = \begin{cases} \left\{-\dfrac{V_{l,\max}^2 \sin\alpha}{2L_cR}\right\}\hat{e}_{z_1} & 0 \le s < L_c \\ 0 & L_c \le s < L_c + L_a \\ \left\{\dfrac{V_{l,\max}^2 \sin\alpha}{2L_eR}\right\}\hat{e}_{z_1} & L_c + L_a \le s < L_t \end{cases} \quad (6)$$

In addition to $\vec{\omega}_2$, the liquid motion results in an angular velocity $\vec{\omega}_3$ around the centerline of the helix, as shown in Fig. 3(b) due to the fluid path around the circumference of the heat pipe. The angular parameter ϕ is related to the arc length s by

$$\phi = \phi_0 + \frac{2\pi s}{p} \quad (7)$$

where ϕ_0 corresponds to the starting angle of the helix at s = 0. With this notation, the angular velocity and acceleration of the liquid around the x_2 axis are

$$\vec{\omega}_3 = \left\{\frac{2\pi|\vec{V}_l| \sin\alpha}{p}\right\}\hat{e}_{x_2} \quad (8)$$

$$\frac{d\vec{\omega}_3}{dt} = \begin{cases} \left\{\dfrac{\pi V_{l,\max}^2 \sin\alpha}{pL_c}\right\}\hat{e}_{x_2} & 0 \le s < L_c \\ 0 & L_c \le s < L_c + L_a \\ \left\{-\dfrac{\pi V_{l,\max}^2 \sin\alpha}{pL_e}\right\}\hat{e}_{x_2} & L_c + L_a \le s < L_t \end{cases} \quad (9)$$

The acceleration vector at point P on the helix with respect to the inertial reference (x_1, y_1, z_1) is given by (Shames, 1980)

$$\vec{A} = \frac{d^2\vec{r}}{dt^2} = \frac{d^2\vec{\rho}}{dt^2} + \frac{d^2\vec{R}}{dt^2} + 2\vec{\omega} \times \left(\frac{d\vec{\rho}}{dt}\right) + \left(\frac{d\vec{\omega}}{dt}\right) \times \vec{\rho} + \vec{\omega} \times (\vec{\omega} \times \vec{\rho}) \quad (10)$$

The length of the position vector $\vec{\rho}$ is constant, and rotates with angular velocity $\vec{\omega}_3$. Therefore,

$$\frac{d\vec{\rho}}{dt} = \vec{\omega}_3 \times \vec{\rho} \quad (11)$$

and

$$\frac{d^2\vec{\rho}}{dt^2} = \left(\frac{d\vec{\omega}_3}{dt}\right) \times \vec{\rho} + \vec{\omega}_3 \times \left(\frac{d\vec{\rho}}{dt}\right) \quad (12)$$

The length of the position vector $\vec{R}$ is also fixed and rotates with angular velocity $\vec{\omega} = (\vec{\omega}_1 + \vec{\omega}_2)$.

$$\frac{d\vec{R}}{dt} = (\vec{\omega}_1 + \vec{\omega}_2) \times \vec{R} \quad (13)$$

$$\frac{d^2\vec{R}}{dt^2} = \left[\frac{d}{dt}(\vec{\omega}_1 + \vec{\omega}_2)\right] \times \vec{R} + (\vec{\omega}_1 + \vec{\omega}_2) \times \left(\frac{d\vec{R}}{dt}\right) \quad (14)$$

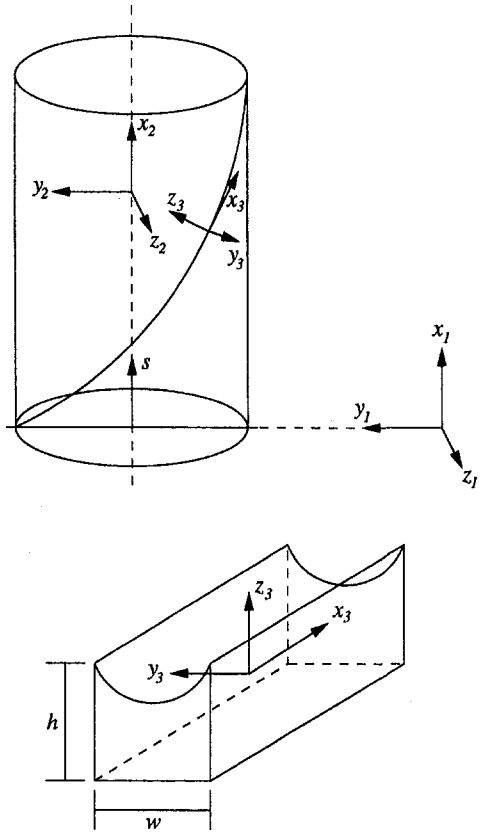

Fig. 4 Coordinate system situated in the helical groove

Combining these relations gives the acceleration vector at any point in the helical groove

$$\vec{A} = \left(\frac{d\vec{\omega}_3}{dt}\right) \times \vec{\rho} + \vec{\omega}_3 \times (\vec{\omega}_3 \times \vec{\rho}) + \left[\frac{d}{dt}(\vec{\omega}_1 + \vec{\omega}_2)\right] \times \vec{R} + (\vec{\omega}_1 + \vec{\omega}_2) \times [(\vec{\omega}_1 + \vec{\omega}_2) \times \dot{\vec{R}}] + 2(\vec{\omega}_1 + \vec{\omega}_2) \times (\vec{\omega}_3 \times \vec{\rho}) + \left[\frac{d}{dt}(\vec{\omega}_1 + \vec{\omega}_2)\right] \times \vec{\rho} + (\vec{\omega}_1 + \vec{\omega}_2) \times [(\vec{\omega}_1 + \vec{\omega}_2) \times \vec{\rho}] \quad (15)$$

The position vectors $\vec{R}$ and $\vec{\rho}$ are given by

$$\vec{R} = \{R \sin \theta\}\hat{e}_{x_1} + \{R \cos \theta\}\hat{e}_{y_1} \quad (16)$$

$$\vec{\rho} = \{r_h \cos \phi\}\hat{e}_{y_2} + \{r_h \sin \phi\}\hat{e}_{z_2} \quad (17)$$

Since $\vec{\rho}$, $\vec{\omega}_3$, and $d\vec{\omega}_3/dt$ are in terms of the (x_2, y_2, z_2) coordinate system, a transformation is needed between this coordinate reference and the (x_1, y_1, z_1) reference

$$\begin{Bmatrix} \hat{e}_{x_2} \\ \hat{e}_{y_2} \\ \hat{e}_{z_2} \end{Bmatrix} = \begin{vmatrix} \cos\theta & -\sin\theta & 0 \\ \sin\theta & \cos\theta & 0 \\ 0 & 0 & 1 \end{vmatrix} \begin{Bmatrix} \hat{e}_{x_1} \\ \hat{e}_{y_1} \\ \hat{e}_{z_1} \end{Bmatrix} \quad (18)$$

Using this transformation, $\vec{\rho}$, $\vec{\omega}_3$, and $d\vec{\omega}_3/dt$ are

$$\vec{\rho} = \{r_h \cos \phi \sin \theta\}\hat{e}_{x_1} + \{r_h \cos \phi \cos \theta\}\hat{e}_{y_1} + \{r_h \sin \phi\}\hat{e}_{z_1} \quad (19)$$

$$\vec{\omega}_3 = \left\{\frac{2\pi|\vec{V}_l|}{p} \sin \alpha \cos \theta\right\}\hat{e}_{x_1} + \left\{-\frac{2\pi|\vec{V}_l|}{p} \sin \alpha \sin \theta\right\}\hat{e}_{y_1} \quad (20)$$

$$\frac{d\vec{\omega}_3}{dt} = \begin{cases} \left\{\frac{B}{L_c} \cos \theta\right\}\hat{e}_{x_1} + \left\{-\frac{B}{L_c} \sin \theta\right\}\hat{e}_{y_1} & 0 \le s < L_c \\ 0 & L_c \le s < L_c + L_a \\ \left\{-\frac{B}{L_e} \cos \theta\right\}\hat{e}_{x_1} + \left\{\frac{B}{L_e} \sin \theta\right\}\hat{e}_{y_1} & L_c + L_a \le s < L_t \end{cases} \quad (21)$$

where $B = (\pi V_{l,\max}^2 \sin \alpha)/p$.

The components of the acceleration vector given in Eq. (15) can be found in terms of the (x_3, y_3, z_3) reference by using a coordinate transformation to relate the (x_1, y_1, z_1) and (x_3, y_3, z_3) coordinate systems

$$\begin{Bmatrix} \hat{e}_{x_3} \\ \hat{e}_{y_3} \\ \hat{e}_{z_3} \end{Bmatrix} = \begin{vmatrix} b_{11} & b_{12} & b_{13} \\ b_{21} & b_{22} & b_{23} \\ b_{31} & b_{32} & b_{33} \end{vmatrix} \begin{Bmatrix} \hat{e}_{x_1} \\ \hat{e}_{y_1} \\ \hat{e}_{z_1} \end{Bmatrix} \quad (22)$$

where b_{ij} is the transformation matrix made up of direction cosines between the coordinate systems. To determine the elements in the transformation matrix, the following geometric analysis is given. The position vector $\vec{r}$ can be written as

$$\vec{r} = \{(R + r_h \cos \phi) \sin \theta\}\hat{e}_{x_1} + \{(R + r_h \cos \phi) \cos \theta\}\hat{e}_{y_1} + \{r_h \sin \phi\}\hat{e}_{z_1} \quad (23)$$

The sign on the last term determines whether the helix twist is clockwise (+) or counterclockwise (−). The unit vector $\hat{e}_{x_3}$ is tangent to the helical groove, and is obtained by finding the derivative of the position vector $\vec{r}$ with respect to ϕ. The tangent vector is given by

$$\vec{t} = \left\{\left(\frac{p}{2\pi R}\right)(R + r_h \cos \phi) \cos \theta - r_h \sin \phi \sin \theta\right\}\hat{e}_{x_1} + \left\{-\left(\frac{p}{2\pi R}\right)(R + r_h \cos \phi) \sin \theta - r_h \sin \phi \cos \theta\right\}\hat{e}_{y_1} + \{r_h \cos \phi\}\hat{e}_{z_1} \quad (24)$$

The unit vector in the tangent direction is $\hat{e}_{x_3} = \vec{t}/|\vec{t}|$, where

$$|\vec{t}| = \sqrt{\left[\left(\frac{p}{2\pi R}\right)(R + r_h \cos \phi)\right]^2 + r_h^2} \quad (25)$$

$\hat{e}_{z_3}$ is directed from a point on the helical curve to the centerline of the helix at a given s:

$$\hat{e}_{z_3} = -\frac{\vec{\rho}}{|\vec{\rho}|} = \{-\cos \phi \sin \theta\}\hat{e}_{x_1} + \{-\cos \phi \cos \theta\}\hat{e}_{y_1} + \{-\sin \phi\}\hat{e}_{z_1} \quad (26)$$

The vector directed along $\hat{e}_{y_3}$ is orthogonal to the $\hat{e}_{z_3}$ and $\vec{t}$ vectors

$$\vec{h} = \hat{e}_{z_3} \times \vec{t}$$
$$= \left\{ -r_h \cos\theta - \left(\frac{p}{2\pi R}\right)(R + r_h \cos\phi)\sin\phi \sin\theta \right\} \hat{e}_{x_1}$$
$$+ \left\{ r_h \sin\theta - \left(\frac{p}{2\pi R}\right)(R + r_h \cos\phi)\sin\phi \cos\theta \right\} \hat{e}_{y_1}$$
$$+ \left\{ \left(\frac{p}{2\pi R}\right)(R + r_h \cos\phi)\cos\phi \right\} \hat{e}_{z_1} \quad (27)$$

where the unit vector is $\hat{e}_{y_3} = \vec{h}/|\vec{h}| = \vec{h}/|\vec{t}|$. The elements of the transformation matrix [Eq. (22)] are

$$b_{11} = \left\{ \left(\frac{p}{2\pi R}\right)(R + r_h \cos\phi)\cos\theta - r_h \sin\phi \sin\theta \right\} / |\vec{t}| \quad (28)$$

$$b_{12} = \left\{ -\left(\frac{p}{2\pi R}\right)(R + r_h \cos\phi)\sin\theta - r_h \sin\phi \cos\theta \right\} / |\vec{t}| \quad (29)$$

$$b_{13} = (r_h \cos\phi)/|\vec{t}| \quad (30)$$

$$b_{21} = \left\{ -r_h \cos\theta - \left(\frac{p}{2\pi R}\right) \times (R + r_h \cos\phi)\sin\phi \sin\theta \right\} / |\vec{t}| \quad (31)$$

$$b_{22} = \left\{ r_h \sin\theta - \left(\frac{p}{2\pi R}\right) \times (R + r_h \cos\phi)\sin\phi \cos\theta \right\} / |\vec{t}| \quad (32)$$

$$b_{23} = \left\{ \left(\frac{p}{2\pi R}\right)(R + r_h \cos\phi)\cos\phi \right\} / |\vec{t}| \quad (33)$$

$$b_{31} = -\cos\phi \sin\theta \quad (34)$$

$$b_{32} = -\cos\phi \cos\theta \quad (35)$$

$$b_{33} = -\sin\phi \quad (36)$$

For the limiting case of axial grooves, the above mathematical model remains valid. By taking the limit as $p \to \infty$, Eq. (7) becomes

$$\phi = \phi_0 \quad (37)$$

Also, the transformation matrix given by Eq. (22) becomes

$$b_{ij} = \begin{vmatrix} \cos\theta & -\sin\theta & 0 \\ -\sin\phi_0 \sin\theta & -\sin\phi_0 \cos\theta & \cos\phi_0 \\ -\cos\phi_0 \sin\theta & -\cos\phi_0 \cos\theta & -\sin\phi_0 \end{vmatrix} \quad (38)$$

A pressure balance within the heat pipe results in the following expression for the capillary limit (Faghri, 1994; Chi, 1976):

$$\Delta P_{\text{cap,max}} \geq \Delta P_v + \Delta P_l + \Delta P_{bf} \quad (39)$$

The maximum capillary pressure is

$$\Delta P_{\text{cap,max}} = \frac{2\sigma}{r_c} \quad (40)$$

where the capillary radius is equal to the helical groove width $r_c = w$. For a circular cross-sectional heat pipe with uniform heat input and output along the lengths of the evaporator and condenser, respectively, the pressure drop in the vapor is

$$\Delta P_v = \frac{4\mu_v Q_t}{\pi \rho_v h_{fg} r_v^4}(L_e + 2L_a + L_c) \quad (41)$$

The body forces imposed on the fluid within a particular groove may either aid or hinder the return of the fluid to the evaporator, depending on the groove pitch p and the angle of the starting point of the helix ϕ_0. However, even if the body force hinders the return of the fluid, each groove contributes to the heat transported Q_t. Therefore, the capillary limit equation [Eq. (39)] is first solved for the heat transported by each individual groove Q_g, and the results are summed to determine the total heat transport Q_t. Since the pressure drop in the vapor space is based on the total heat transport, Eq. (39) must be solved iteratively.

The body forces in the tangent direction due to acceleration [Eq. (15)] and gravity are integrated over the length of the groove to find the average pressure drop due to body forces

$$\Delta P_{bf} = -\rho_l \left(\int_0^{L_g} \hat{e}_{x_3} \cdot (-\vec{A} + \{-g\}\hat{e}_{z_1}) dx_3 \right)$$
$$= -\rho_l \sqrt{\left(\frac{2\pi r_h}{p}\right)^2 + 1} \left[\int_0^{L_t} \hat{e}_{x_3} \cdot (-\vec{A} + \{-g\}\hat{e}_{z_1}) ds \right] \quad (42)$$

where the length of a helical groove is given in terms of the s coordinate

$$L_g = s\sqrt{\left(\frac{2\pi r_h}{p}\right)^2 + 1} \quad (43)$$

The pressure drop in the liquid is given by (Faghri, 1994)

$$\Delta P_l = \int_0^{L_g} \frac{\mu_l \dot{m}_l}{\rho_l A_w K} dx_3$$
$$= \frac{\mu_l Q_g (f_l \text{Re}_l)(L_e + 2L_a + L_c)}{4\rho_l r_l^2 whh_{fg}} \sqrt{\left(\frac{2\pi r_h}{p}\right)^2 + 1} \quad (44)$$

The coefficient of drag within a rectangular groove is given by Shah and Bhatti (1987)

$$f_l \text{Re}_l = 24(1 - 1.3553\beta + 1.9467\beta^2 - 1.7012\beta^3 + 0.9564\beta^4 - 0.2537\beta^5) \quad (45)$$

where the range of the aspect ratio is $0 \leq \beta \leq 1$.

Combining these relations, the general expression for the maximum capillary limit for a single groove is

$$\frac{2\sigma}{w} \geq \frac{(L_e + 2L_a + L_c)}{h_{fg}}$$

$$\times \left\{ \frac{4\mu_v Q_t}{\pi \rho_v r_v^4} + \frac{\mu_l Q_g (f_l \mathrm{Re}_l)}{4\rho_l r_l^2 wh} \sqrt{\left(\frac{2\pi r_h}{p}\right)^2 + 1} \right\}$$

$$- \rho_l \sqrt{\left(\frac{2\pi r_h}{p}\right)^2 + 1} \left[\int_0^{L_t} \hat{e}_{x_3} \cdot (-\vec{A} + \{-g\}\hat{e}_{z_1}) ds \right] \quad (46)$$

This equation was solved for each individual groove. However, the total heat transported Q_t was not known *a priori*, so an iterative solution procedure was necessary:

1 Input an initial value for the heat transported $Q_t = Q_{t,i}$.
2 Starting with the groove at $\phi_0 = 0$, let the heat transported by that groove be $Q_g = \Delta Q_g$, where ΔQ_g is the step size.
3 Calculate the right- and left-hand sides of Eq. (46).
4 If the inequality holds, increment Q_g by ΔQ_g until the inequality no longer holds.
5 Repeat steps 2–4 for each groove.
6 The heat transported by the heat pipe is the sum of the heat transported by each groove:

$$Q_t = \sum_{j=1}^{N_g} (Q_g)_j$$

7 Use the value of Q_t found in step 6 as the input value in step 1.
8 Steps 1–7 are repeated until converged values for Q_g and Q_t are obtained.

The temperature dependence of the thermophysical properties was accounted for using the polynomial curve fits (evaluated at the adiabatic temperature) given by Faghri (1994). It should be noted that the circumferential heat transfer through the pipe wall was neglected in the present model.

As previously mentioned, an assumption imposed on this analysis is that there is no communication of liquid between the grooves. However, it is possible under some conditions that this assumption may no longer hold. If at any point along the helical groove the body force on the liquid due to the acceleration components $\vec{A}_{y_3}$ and $\vec{A}_{z_3}$ becomes significant with respect to the surface tension force, it is possible that fluid could be torn from the groove. To quantify the assumption of no communication of liquid between the grooves, the Bond number is used, which is defined as

$$\mathrm{Bo} = \frac{\rho_l r_l |\vec{A}_{\mathrm{res}}|}{2\sigma/w} = \frac{\text{Body force}}{\text{Surface tension force}} \quad (47)$$

where $\vec{A}_{\mathrm{res}}$ is the resultant acceleration vector between the y_3 and z_3 directions. If Bo < 1, it is assumed that the communication of liquid between grooves is negligible.

Results and Discussion

Experimental. The objective of this experiment was to gain a better understanding of the steady-state operating characteristics of a helically grooved copper–ethanol heat pipe in a transverse body force field. The heat input and radial acceleration were varied to find information on dryout phenomena, circumferential temperature uniformity, heat lost to the environment, thermal resistance, and the capillary limit.

Raw temperature and acceleration data versus time for a typical test run are presented in Fig. 5 for two different heat input settings. In Fig. 5(*a*), with a heat input of $Q_{in} = 20$ W, no dryout of the evaporator section was detected. As the radial acceleration was increased stepwise, the temperatures across the heat pipe did not vary significantly. In Fig. 5(*b*), however, with a heat input of $Q_{in} = 50$ W, partial dryout of the evaporator

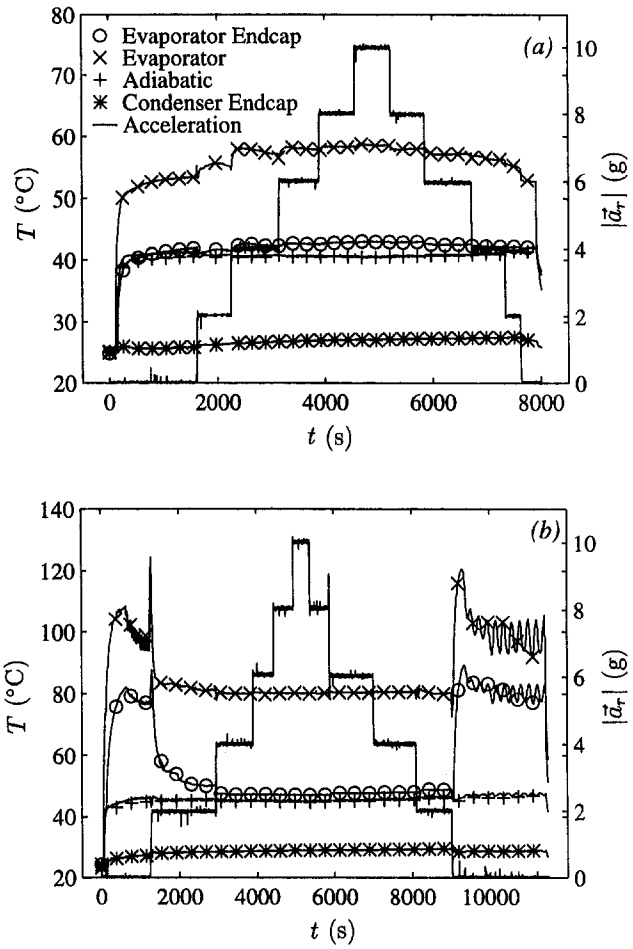

Fig. 5 Temperature and acceleration versus time for a typical test run (Heat Pipe #1): (*a*) Q_{in} = 20 W; (*b*) Q_{in} = 50 W

section was noted when $|\vec{a}_r| = 0.0g$. This can be seen in the dramatic increase of the evaporator end cap temperature above the adiabatic section temperature. Once the radial acceleration was increased to $|\vec{a}_r| = 2.0g$, the evaporator temperature decreased significantly, showing that the acceleration actually aided in the return of the working fluid back to the evaporator section. Dryout was also seen when the radial acceleration was decreased from $|\vec{a}_r| = 2.0$ to $0.0g$ at the end of the test in Fig. 5(*b*). In this case, regular fluctuations in the evaporator end cap temperature were seen. This indicated a pulsating rewetting phenomenon, where the liquid front advanced and receded within the evaporator section.

The circumferential temperature uniformity of the heat pipe was found using a series of thermocouples on the inboard and outboard sides, as shown in Fig. 1. The steady-state temperatures detected along the length of the heat pipe are shown in Fig. 6 for a radial acceleration of $|\vec{a}_r| = 10.0g$ and heat transport values of $Q_t = 35$, 71, and 107 W. While the temperatures within the evaporator section appear to vary from the inboard side to the outboard side of the heat pipe, this behavior was also found when the heat pipe was stationary. Therefore, this difference in the circumferential temperature distribution within the evaporator section is due to the proximity of the electric heater coil to the thermocouples. The inboard and outboard evaporator end cap temperatures were very close to those in the adiabatic section, indicating no partial dryout of the evaporator. Even at this acceleration, the temperature uniformity between the inboard and outboard sides of the heat pipe was excellent.

The heat transported was compared to the heat input for all the data collected. While a slight decrease in the heat transported

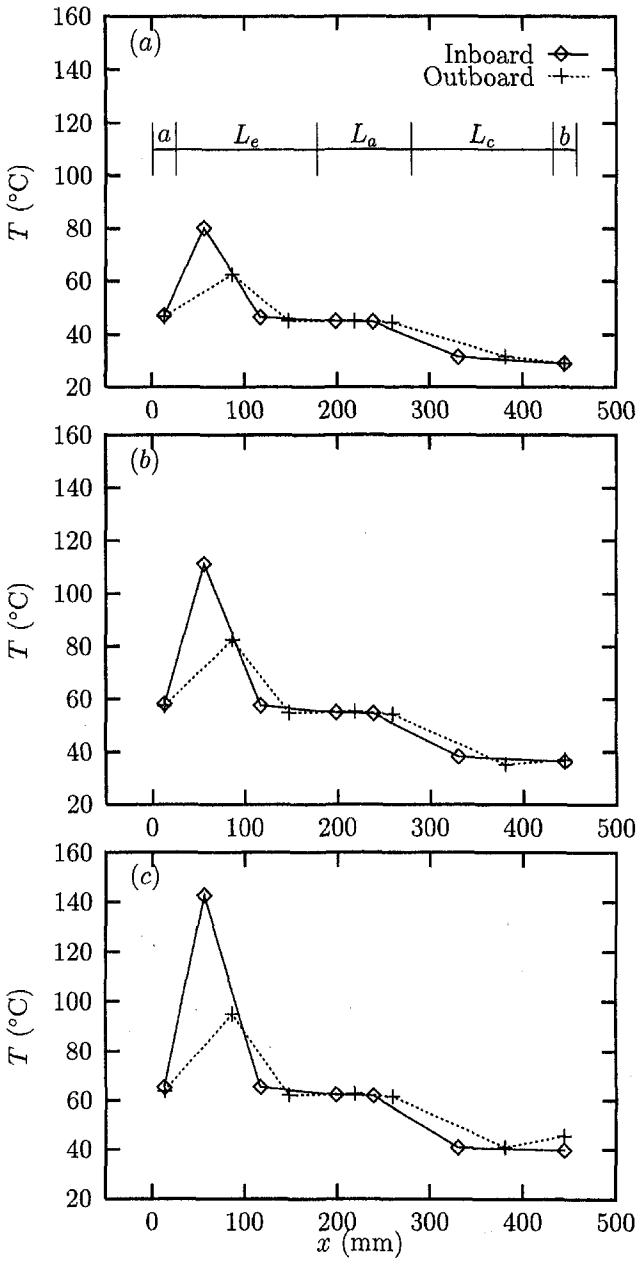

Fig. 6 Steady-state temperature distribution for $|\vec{a}_r|$ = 10.0*g* (Heat Pipe #1): (*a*) Q_t = 35 W; (*b*) Q_t = 71 W; (*c*) Q_t = 107 W

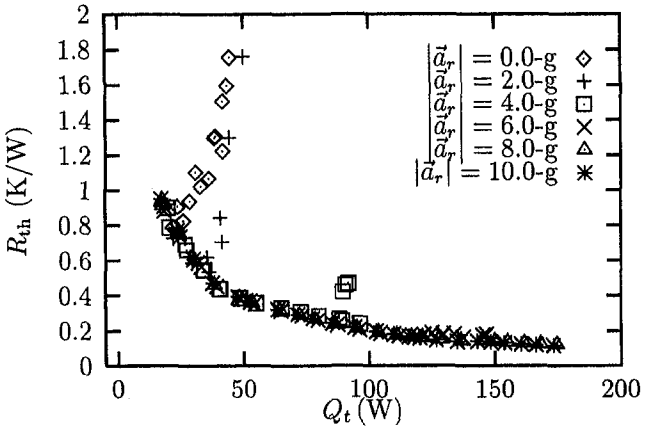

Fig. 7 Thermal resistance versus heat transported (Heat Pipe #1)

was noted for increasing radial acceleration rates (increasing table angular velocity), the decrease was seen to be only marginally significant compared to the uncertainty of the heat transported (Table 2). Therefore, the amount of heat lost due to external convection was quite small in comparison to that lost due to conduction through the mounting blocks.

Figure 7 shows the thermal resistance as a function of transported heat over the entire range of radial acceleration. In general, the thermal resistance decreased and then increased with transported heat when dryout commenced. When $|\vec{a}_r| = 0.0$ and $2.0g$, dryout resulted in a gradual increase in the thermal resistance, as shown in Fig. 7. In this case, the capillary limit was considered to be reached when the thermal resistance began to increase. For $|\vec{a}_r| \geq 4.0g$, dryout occurred suddenly, as shown in Fig. 8. In this figure, the heat input was changed from Q_{in} = 129 to 142 W, where the evaporator end cap and heater temperatures increased by 40°C in less than 2 minutes. After dryout was confirmed, the heat input was returned to Q_{in} = 129 W, at which time the heat pipe quickly reprimed and began to operate normally again. This runaway dryout behavior indicates an unstable operating condition near the capillary limit when under the influence of elevated transverse body force fields. While the capillary limit was reached for $|\vec{a}_r| = 0.0$, 2.0, 4.0 and $6.0g$, the capillary limit at 8.0 and $10.0g$ could not be determined due to reaching the maximum allowable amperage through the heater ($Q_{in,\max}$ = 250 W, $Q_{t,\max}$ = 175 W). The experimentally determined capillary limit values for $|\vec{a}_r| = 0.0$, 2.0, 4.0, and $6.0g$ are presented in the next section.

Numerical. A mathematical model that predicts the capillary limit of a helically grooved heat pipe subjected to a transverse body force field has been developed. The effects of temperature-dependent working fluid properties, the geometry of the heat pipe and the grooves (including helix pitch), and body force field strength were accounted for. To validate the present solution, the closed-form solution presented by Klasing et al. (1997) was used, wherein the capillary limit of a heat pipe under gravity with straight axial grooves as the wick structure was calculated. The geometric values given in Table 1 (Heat Pipe #1) were used in both models to calculate the capillary limit for adiabatic temperatures between 40 and 80°C. The solution of the capillary limit for a helically grooved heat pipe was iterative in nature, so a convergence check on ΔQ_g was required. The maximum percentage error for ΔQ_g = 0.1, 0.01, and 0.001 W was 7.65, 0.58, and 0.14, respectively, as compared to the closed-form solution. Therefore, in an effort to maintain a reasonable calculation time, ΔQ_g was chosen to be 0.01 W.

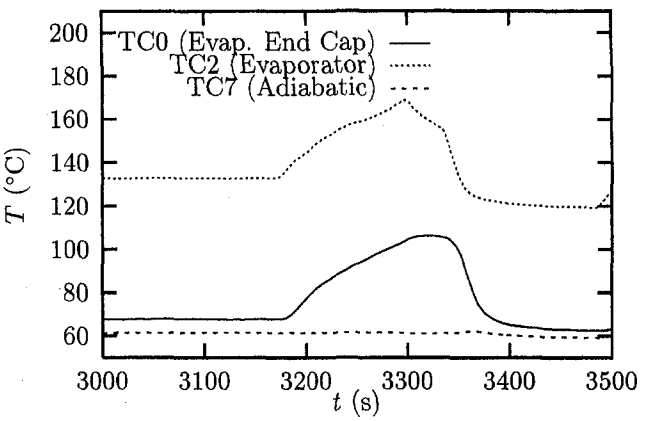

Fig. 8 Temperature versus time during an incident of dryout for $|\vec{a}_r|$ = 4.0*g*: Q_{in} increased from 129 W to 142 W at *t* = 3160 s, Q_{in} decreased from 142 W to 129 W at *t* = 3290 s (Heat Pipe #1)

Table 1 Heat pipe specifications

	Heat Pipe #1	Heat Pipe #2
Wick structure	Helical grooves	Axial grooves
Working fluid	Ethanol	Ethanol
Working fluid charge	6.5 cm^3	2.6 cm^3
Heat pipe length, L_t	457.2 mm	485.8 mm
Evaporator length, L_e	152.4 mm	139.7 mm
Adiabatic length, L_a	101.6 mm	168.3 mm
Condenser length, L_c	152.4 mm	149.2 mm
Tube outside diameter, D_o	15.88 mm	12.7 mm
Tube wall thickness, t_w	0.766 mm	0.52 mm
Vapor core diameter, D_v	13.46 mm	11.06 mm
Radius of curvature, R	1.22 m	1.22 m
Wall/wick materials	Copper	Copper
Helix pitch, p	139 cm CW	∞
Groove height, h	0.44 mm	0.30 mm
Groove width, w	0.47 mm	0.32 mm
Number of Grooves, N_g	50	60
Heater element	Nichrome heater tape	
Fill valve	Nupro B-4HW bellows valve	
Calorimeter	1/8 in. OD coiled copper tubing	

Table 2 Maximum uncertainties of measured and calculated values

Measured Values	
Mass flow rate	$\Delta\dot{m} = \pm 1.4 \times 10^{-4}$ kg/s
Calorimeter inlet temp.	$\Delta T_{\text{in}} = \pm 0.14$ K
Calorimeter outlet temp.	$\Delta T_{\text{out}} = \pm 0.14$ K
Evaporator end cap temp.	$\Delta T_{\text{eec}} = \pm 0.17$ K
Condenser end cap temp.	$\Delta T_{\text{cec}} = \pm 0.16$ K
Heater voltage	$\Delta V = \pm 2\%$ of reading
Heater current	$\Delta I = \pm 2\%$ of reading
Radial acceleration	$\Delta a_r = \pm$ 0.1-g
Electrical wire resistance	$\Delta R_{\text{wire}} = \pm 2.4 \times 10^{-3}\ \Omega$
Calculated Values	
Heat input	$\Delta Q_{\text{in}} = \pm 4\%$
Heat transported	$\Delta Q_t = \pm 14\%$
Thermal resistance	$\Delta R_{\text{th}} = \pm 14\%$
Capillary limit	$\Delta Q_{\text{cap}} = \pm 11\%$

Figure 9 shows the capillary limit of each helical groove versus the starting angle of the groove. When $|\vec{a}_r| = 0.0g$, the heat transported by the grooves has a peak in the upper right-hand quadrant, and a minimum in the lower left-hand quadrant. This was due to the presence of the body force due to gravity, which aided the liquid return in the grooves in the upper right-hand quadrant. As the resultant body force vector (gravity + acceleration due to rotation) increased in magnitude and changed in direction, the maximum heat transported by the grooves increased and shifted from the upper right-hand quadrant to the lower right-hand quadrant, as shown in Fig. 9(a). In addition, the increase in the resultant body force vector progressively deactivated the grooves where the body force acted in a direction unfavorable to the return of liquid back to the evaporator section. Faghri and Thomas (1989) showed that axial grooves are very sensitive to body force effects: A change in tilt angle from horizontal to -1 deg (unfavorable) resulted in a decrease in the capillary limit of a copper–water heat pipe from $Q_{in} = 700$ to less than 50 W in their study. In the present case, the benefits derived from the increase in the fluid flow rate through part of the grooves outweighed the loss of heat transport through those grooves that were hindered. For $|\vec{a}_r| \geq 4.0g$, the location of the grooves where the maximum heat transport occurred did not vary appreciably, since the body force due to the radial acceleration was significantly greater than that due to gravity [Fig. 9(b)].

Figure 10 shows the acceleration components due to rotation and gravity in the (x_3, y_3, z_3) coordinate system. The relative magnitudes of the acceleration in the x_3, y_3, and z_3 directions illustrate how the helical grooves contribute to the return of the fluid to the evaporator. Due to the curvature of the helical grooves, an acceleration component was induced in the x_3 direction. However, the magnitude of this acceleration component was relatively small due to the shallowness of the helix angle. The acceleration components in the y_3 and z_3 directions were significantly larger because their magnitude and direction were similar to that of $\vec{a}_r$. The acceleration for $\phi_0 = 0.0$ deg in Fig. 10(a) was less than zero along the entire length of the groove and $Q_{g,\text{cap}} < 0.01$ W (see Fig. 9). However, for the groove located at $\phi_0 = 180.0$ deg the acceleration in the x_3 direction was greater than zero along the groove length, which resulted in $Q_{g,\text{cap}} = 8.41$ W. When compared to Fig. 9(b), it can be seen that the positive acceleration components in the x_3 direction enhanced the capillary limit by increasing the rate of fluid return to the evaporator. In contrast, the negative acceleration components in the x_3 direction greatly hindered the return of working fluid to the evaporator.

The capillary limit versus radial acceleration is given in Fig. 11 for various adiabatic temperatures. Figure 11(a) shows the results of the present model, where the capillary limit of the heat pipe increased monotonically with adiabatic temperature and radial acceleration. Figure 11(b) shows a comparison of the experimentally and analytically obtained capillary limits. Since no attempt was made in the experiments to maintain a

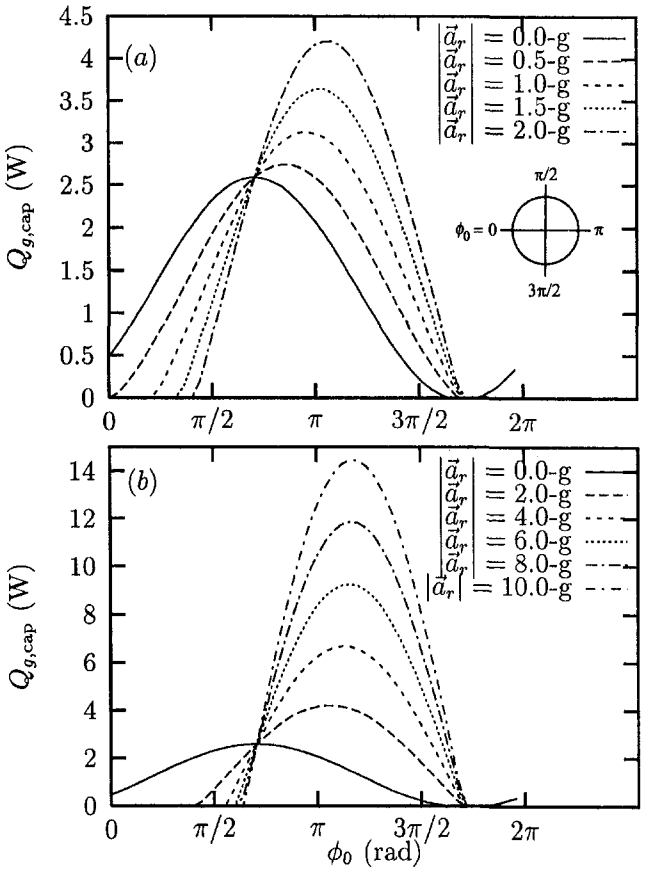

Fig. 9 Predicted values of the capillary limit per groove versus groove starting angle (T_a = 60°C, Heat Pipe #1): (a) 0 ≤ $|\vec{a}_r|$ ≤ 2.0g; (b) 0 ≤ $|\vec{a}_r|$ ≤ 10g

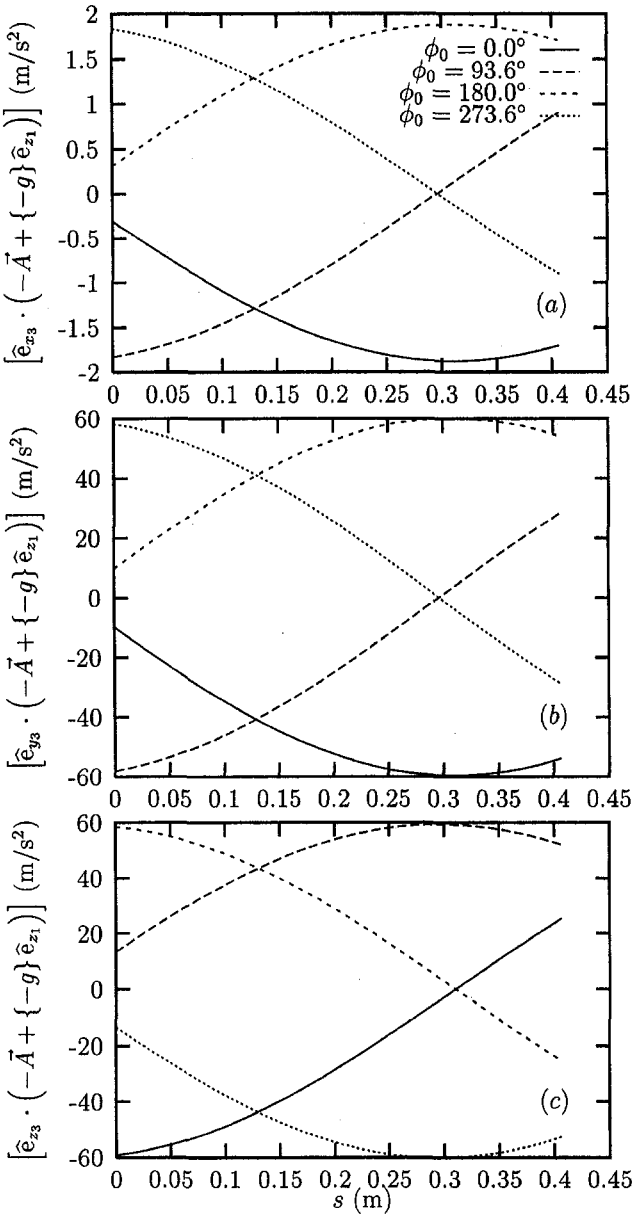

Fig. 10 Acceleration components due to rotation and gravity in the (x_3, y_3, z_3) coordinate system with $|\vec{a}_r| = 6.0g$ (Heat Pipe #1): (*a*) $\hat{e}_{x_3}$ direction; (*b*) $\hat{e}_{y_3}$ direction; (*c*) $\hat{e}_{z_3}$ direction

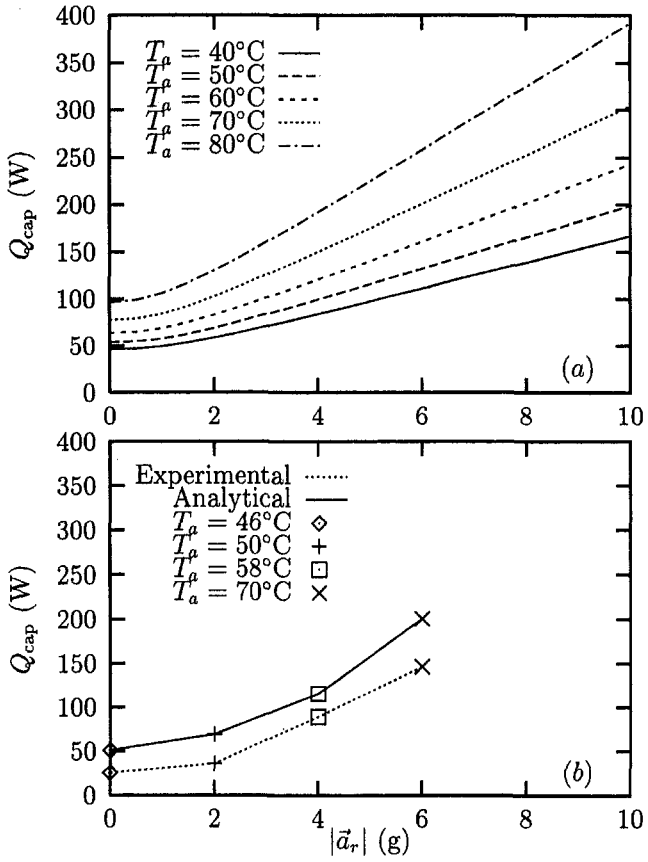

Fig. 11 Capillary limit versus radial acceleration (Heat Pipe #1): (*a*) present model; (*b*) comparison of present model and experimental results

constant adiabatic temperature, the model was evaluated at the same adiabatic temperatures as those seen in the experiments. Both curves in Fig. 11(*b*) have similar trends, but the mathematical model overpredicted the experimental capillary limit data by 27 to 50 percent. This overprediction is typical of the capillary limit analysis used in the present model (Richter and Gottschlich, 1994). However, since the trends between the analytical model and the experimental results are comparable, the present model can be very useful as a design tool to analyze various configurations. It should be noted that a fivefold increase in the capillary limit was achieved in the experiment by increasing the radial acceleration from $|\vec{a}_r| = 0$ to $6.0g$. While the direction of rotation of the heat pipe was clockwise as seen from above, this was found to have no effect on the performance of the heat pipe as determined by the analytical model.

Figure 12 shows the variation of the maximum heat transport of a helically grooved heat pipe with helical pitch. The heat transport results are normalized with the results of an identical heat pipe with straight axial grooves for comparison. The geometry of the heat pipe is the same as that given for Heat Pipe #1 in Table 1. A maximum value is observed at $p/L_t = 2$, where each helical groove rotates through an angle of $\phi = \pi$. Also shown in Fig. 12 is the operating point of Heat Pipe #1.

A heat pipe with straight axial grooves of similar dimensions (Heat Pipe #2 in Table 1) was also fabricated and tested for comparison with the results obtained from the helically grooved heat pipe. Figure 13 shows the inboard and outboard temperature distributions of the straight-grooved heat pipe for $|\vec{a}_r| = 0$ and $10g$ with a heat input of $Q_{in} = 25$ W. The evaporator end cap temperatures at this low heat input are significantly higher than the adiabatic temperatures for both radial accelera-

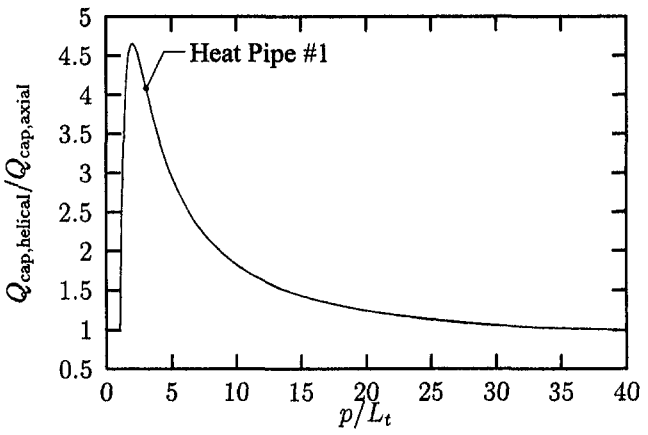

Fig. 12 Variation of the normalized capillary limit with helical pitch (Heat Pipe #1): $T_a = 70°C$, $|\vec{a}_r| = 10.0g$

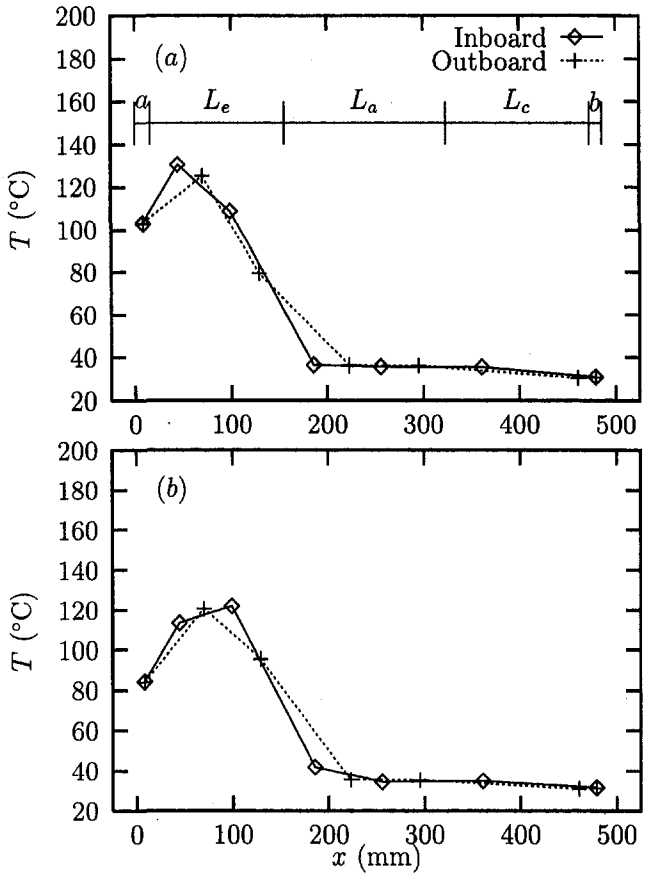

Fig. 13 Steady-state temperature distribution for Heat Pipe #2 at Q_{in} = 25 W: (a) $|\vec{a}_r|$ = 0.0g; (b) $|\vec{a}_r|$ = 10.0g

tion values, indicating dryout of the evaporator section. It can also be noticed that there is little difference in the temperature distributions between Figs. 13(*a*) and 13(*b*), indicating that higher transverse acceleration fields do not improve the movement of liquid back to the evaporator for a straight axially grooved heat pipe.

In regard to the assumption of no liquid communication between the grooves, the aforementioned Bond number analysis resulted in $Bo_{max} \leq 0.32$ over the range of parameters reported. Therefore, the assumption concerning no communication of liquid between the grooves appears to be valid.

Conclusions

The steady-state performance of a helically grooved copper–ethanol heat pipe has been examined experimentally as a function of heat input and transverse body force field strength. A mathematical model of the heat pipe system has been developed, which accounts for the effects of increased transverse body forces, the geometry of the heat pipe and the grooves (including helix pitch), and temperature-dependent working fluid properties. The following conclusions have been made concerning the results of the experimental and numerical analyses:

1 An increase in the transverse body force imposed on the heat pipe actually aided in the return of the working fluid back to the evaporator section. This resulted in a fivefold increase in the capillary limit when the radial acceleration was increased from $|\vec{a}_r| = 0$ to $6g$.
2 Even at the highest radial acceleration ($|\vec{a}_r| = 10g$), the temperature uniformity between the inboard and outboard sides of the heat pipe was excellent.
3 In general, the thermal resistance decreased and then increased with transported heat when dryout commenced. When $|\vec{a}_r| = 0.0$ and $2.0g$, dryout resulted in a gradual increase in the thermal resistance. For $|\vec{a}_r| \geq 4.0g$, dryout occurred suddenly, which indicates an unstable operating condition near the capillary limit when under the influence of elevated transverse body forces.
4 As the resultant body force vector increased in magnitude and changed in direction, the maximum heat transported by the grooves increased and shifted from the upper right-hand quadrant to the lower right-hand quadrant of the heat pipe circumference. In addition, the increase in the resultant body force vector progressively deactivated the grooves where the body force acted in a direction unfavorable to the return of liquid back to the evaporator section.
5 The mathematical model overpredicted the experimental capillary limit data by up to 50 percent, but since the trends between the analytical model and the experimental results were comparable, the present model can be very useful as a design tool to analyze various groove structure configurations.
6 The qualitative results from the straight axially grooved heat pipe (Heat Pipe #2) showed that the performance was not significantly improved over the range of transverse acceleration examined in the present study.

Acknowledgments

Funding for this work was provided by AFOSR Contract No. F49620-93-C-0063. The technical assistance of Mr. Don Reinmuller is noted and appreciated. The authors would like to acknowledge the valuable comments and suggestions made by the reviewers.

References

ASHRAE Handbook of Fundamentals, 1977, American Society of Heating, Refrigerating and Air-Conditioning Engineers, Inc., Atlanta, GA.

Chi, S., 1976, *Heat Pipe Theory and Practice: A Sourcebook,* Hemisphere Publ. Corp., New York.

Faghri, A., and Thomas, S., 1989, "Performance Characteristics of a Concentric Annular Heat Pipe: Part I—Experimental Prediction and Analysis of the Capillary Limit," ASME JOURNAL OF HEAT TRANSFER, Vol. 111, pp. 844–850.

Faghri, A., 1994, *Heat Pipe Science and Technology,* Taylor and Francis, Washington, DC.

Gernert, N., et al., 1991, "Flexible Heat Pipe Cold Plates for Aircraft Thermal Control," *Proc. Aerospace Technology Conference and Exposition,* SAE Paper No. 912105.

Klasing, K. S., Thomas, S. K., and Yerkes, K. L., 1997, "CAPLIM: A Visual Basic Program to Calculate the Capillary Limit of an Axially-Grooved Heat Pipe," *Proc. Intersociety Energy Conversion Engineering Conf.,* Vol. 2, Honolulu, HI, pp. 1514–1518.

Miller, R., 1989, *Flow Measurement Engineering Handbook,* 2nd ed., McGraw-Hill.

Richter, R., and Gottschlich, J. M., 1994, "Thermodynamic Aspects of Heat Pipe Operation," AIAA *J. Thermophysics Heat Transfer,* Vol. 8, No. 2, pp. 334–340.

Shah, R. K., and Bhatti, M. S., 1987, "Laminar Convective Heat Transfer in Ducts," in: *Handbook of Single-Phase Convective Heat Transfer,* Kakac, S., Shah, R. K., and Aung, W., eds., Wiley, New York.

Shames, I., 1980, *Engineering Mechanics,* 3rd ed., Prentice-Hall, New Jersey.

Silverstein, C., 1992, *Design and Technology of Heat Pipes for Cooling and Heat Exchange,* Taylor & Francis, Washington, DC.

Thomas, S., and Yerkes, K., 1997, "Quasi-Steady State Performance of a Heat Pipe Subjected to Transient Acceleration Loadings," AIAA *J. Thermophysics Heat Transfer,* Vol. 11, pp. 306–309.

Yerkes, K., and Beam, J., 1992, "Arterial Heat Pipe Performance in a Transient Heat Flux and Body Force Environment," *Proc. Aerospace Atlantic Conf.,* Dayton, OH, SAE Paper No. 921944.

Yerkes, K. L., and Hager, B., 1992, "Transient Response of Heat Pipes for Actuator Thermal Management," *Proc. Aerospace Atlantic Conf.,* Dayton, OH, SAE Paper No. 921024.

Yerkes, K., and Hallinan, K., 1995a, "Dynamic Behavior of an Unheated Meniscus Subjected to Transient Acceleration Field," AIAA *J. Thermophysics Heat Transfer,* Vol. 9, No. 2, pp. 322–328.

Yerkes, K., and Hallinan, K., 1995b, "Behavior of a Meniscus Subjected to Transient Accelerations for Increasing Capillary Numbers," AIAA *J. Thermophysics Heat Transfer,* Vol. 9, No. 3, pp. 543–549.

Capillary Performance of Evaporating Flow in Micro Grooves: An Analytical Approach for Very Small Tilt Angles

J. M. Ha
Research Associate.

G. P. Peterson
Tenneco Professor and
Executive Associate Dean.

Department of Mechanical Engineering,
Texas A&M University,
College Station, TX 77843-3123

The axial flow of an evaporating thin film through a V-shaped micro channel was investigated for the case of a grooved plate inclined with a very small tilt angle. For this problem, the addition of the gravity term caused by the tilt angle alters the form of the governing equation from linear to nonlinear. Because the effect of the tilt angle is very small, a perturbation method was applied to obtain a first order perturbation solution of $R = R_0 + \epsilon R_1$, where R_0 is the undisturbed solution of a horizontally placed plate, and R_1 is the disturbed solution caused by the tilt angle. A generalized graph of the nondimensional radius of curvature as a function of the nondimensionalized axial length was obtained. The perturbation parameter, ϵ, was expressed as a function of five nondimensional parameters. The results indicate that when the geometry is fixed, the effects of the Bond number and Capillary number are dominant. In addition, it was found that ϵ is inversely proportional to the square root of the Capillary number. This indicates that the perturbation method is applicable and accurate, even for the case of somewhat larger tilt angles (where the initial applicability of perturbation appears to be violated), if a sufficiently large heat flux is applied.

Introduction

The highest heat transfer coefficients typically occur when a pure substance or mixture undergoes a change of phase. In situations where this phase change process involves evaporating or condensing fluids, small capillary grooves are often used to increase the effective liquid-vapor interfacial area for evaporation or the effective solid-vapor surface area for condensation. These capillary grooves allow the liquid to coalesce and promote the flow of liquid either away from the condensing region or towards the evaporating region, decreasing the average film thickness. Using this technique, the size and thickness of the thin film region, the location and magnitude of the interline region, and the average heat transfer coefficient can all be significantly enhanced by controlling the number, cross-sectional shape, and length of the capillary grooves. The use of these techniques to improve the heat transfer coefficient is common in a number of applications, including conventional heat exchangers, chemical processing equipment, and nuclear reactors. More recently, however, increased interest in the use of phase change heat transfer processes for the thermal control of spacecraft and electronic components, either through traditional methods (Peterson and Ortega, 1990) or more innovative methods involving the use of micro heat pipe devices (Peterson, 1992), has resulted in the need for a better understanding of the liquid film behavior in these grooves.

As illustrated in Fig. 1, when a liquid contacts a flat surface, the extended meniscus is typically divided into the following three regions: the intrinsic meniscus region, dominated by the capillary forces; the evaporating thin film region, which has the combined effects of both capillarity and the disjoining pressure; and the adsorbed layer region, where the disjoining forces dominate, inhibiting evaporation. The junction of the evaporating thin film region and the adsorbed layer is referred to as the interline region, and it is here that a majority of the heat transfer occurs due to the thin film thickness.

The number, the length, and the shape of grooves can be easily controlled to enhance the heat transfer in the interline region, but the effect of variations in the size and shape of the extended meniscus formed in the capillary groove is still under investigation. A number of analytical and experimental investigations have been conducted to better understand the evaporating thin film formed on a flat plate (DasGupta et al., 1993; Mirzamoghadam and Catton, 1988a, 1988b; Potash and Wayner, 1972; Schoenberg and Wayner, 1992; Sujanani and Wayner, 1991; Wayner et al., 1976) or associated with capillary feeders (Ha and Peterson, 1996; Ma and Peterson, 1996; Peterson and Ma, 1996; Moosman and Homsy, 1980; Renk et al., 1978; Renk and Wayner, 1979a, 1979b). However, these are typically two-dimensional investigations that are helpful in understanding the evaporating flow up the groove wall, but are not directly applicable to small grooves. In order to better understand the flow field through these capillary grooves, the axial and cross-sectional flow characteristics occurring in the intrinsic meniscus must be investigated.

Stroes et al. (1992) carried out an experimental study of the evaporating flow through small grooves for the purpose of comparing the capillary forces in rectangular and triangular channels. Xu and Carey (1990) conducted a combined analytical and experimental investigation of the liquid behavior in micro grooves. Following the procedure outlined previously, Ha and Peterson (1994) conducted an analytical investigation of the axial intrinsic meniscus variation in V-shaped microgrooves. In this latter investigation, the axial dryout location was determined as a function of the input heat flux, the thermophysical properties of the system, and the geometric parameters of the grooves. The current investigation was undertaken in an effort to develop an analytical approach to predict the flow field and the axial wetted length or axial dryout location.

Theoretical Formulation

The current investigation considers thin liquid films flowing through V-shaped micro grooves, as illustrated in Figs. 2 and

Contributed by the Heat Transfer Division for publication in the JOURNAL OF HEAT TRANSFER. Manuscript received by the Heat Transfer Division July 8, 1996; revision received November 17, 1997. Keywords: Multiphase Flows, Thermocapillary Flows, Thin Film Flow. Associate Technical Editor: M. D. Kelleher.

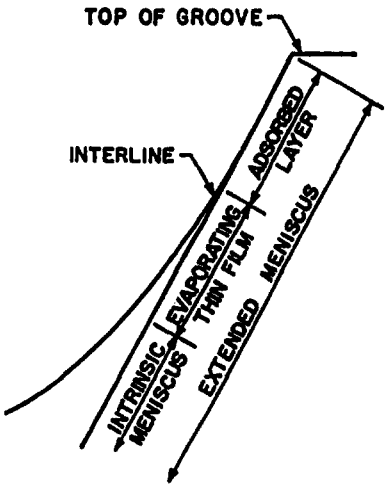

Fig. 1 Description of a meniscus

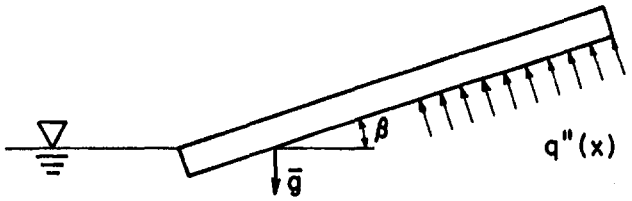

Fig. 2 Schematics of view side considered in the model

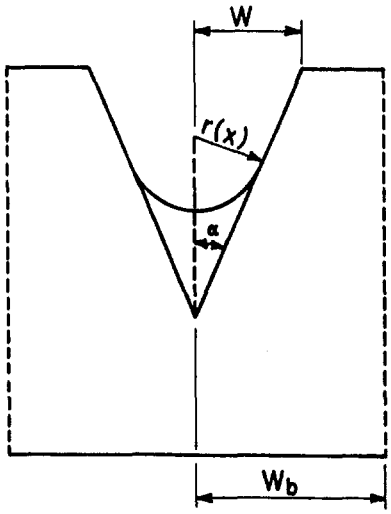

Fig. 3 Groove geometry

3. One end of the grooves (or in this case, the grooved plate) is immersed in a pool of liquid and is held stationary at a small inclination angle, while heat is applied to a portion of the underside of the plate. For small grooves and small inclination angles, the liquid will wick up the groove against the gravitational body force and against the frictional pressure gradients caused by continuous flow. For this situation, the capillary behavior will determine the axially wetted length and the dryout point. In the model presented here, an adiabatic region has been included between the point where the plate emerges from the liquid pool and the upper region of the plate to which a known uniform heat flux is applied, as shown in Fig. 2. The primary objective of this analysis is to identify the end point of the wetted region for a given uniform heat flux.

For grooves relying primarily on capillary pumping for the liquid flow, it is reasonable to assume that all the axial flow of the liquid occurs in the groove (i.e., no flow occurs over the flat portion between the grooves). For a very small groove, the capillary radius of the intrinsic meniscus can be treated as a constant at a given cross section. When heat is added to the plate, the radius of curvature at the interface of the intrinsic meniscus varies axially along the groove, and decreases gradually as the meniscus approaches the heated section. As the liquid recedes further and further towards the apex of the groove, the liquid film thins, finally reaching a minimum value. The wicking action or capillary pumping is the result of this decrease in the radius of curvature caused by the intrinsic meniscus receding into the groove.

At a given cross section, the liquid film is adsorbed at the groove wall, forming an extended thin film region above the intrinsic meniscus. The distribution of the thin film on the groove wall induces a large pressure gradient in the liquid. In this region, the film behavior is dominated by the dispersion forces. Since the resistance to flow in the evaporating thin film and adsorbed layer regions of the extended thin film is much larger than it is in the intrinsic meniscus region, the majority of the axial flow is confined to the intrinsic meniscus region.

Based on the above discussion, several simplifying assumptions can be made to determine the end of the axial wetted length or the axial dryout point. These are as follows: (1) the

Nomenclature

A = constant defined in Eq. (12)
B = constant defined in Eq. (12)
c_3 = constant in Eq. (8)
D = constant defined in Eq. (42)
g = gravitational acceleration
h_{fg} = latent heat of vaporization
K = parameter in Eq. (7)
P = pressure
$q''(x)$ = heat flux normal to the bottom of the plate at x
$r(x)$ = radius of curvature in the intrinsic meniscus at x
R = dimensionless radius of curvature defined in Eq. (16)
$\vec{V}$ = velocity vector of the fluid in Eq. (4)
w = half of the top groove width in Fig. 3
ω_b = half of the bottom width in Fig. 3
x = coordinate along the groove channel in the evaporating region
x' = coordinate along the groove channel in the adiabatic region
X = dimensionless length in the axial direction in Eq. (16)

Greek

α = half the vertex angle of the groove in Fig. 3
β = slope of the plate with respect to gravity in Fig. 2
Γ_c = mass flow rate per cross section in the x-direction in Eq. (7)
ϵ = perturbation parameter defined in Eq. (41)
ν = kinematic viscosity
ζ = dimensionless radius of curvature in Eq. (16)
ρ = density
σ = surface tension

Subscripts

j = junction of the intrinsic meniscus and the interline region
l = liquid
m = maximum length of axial or groove side direction
$m\beta 0$ = maximum value for $\beta = 0$
v = vapor
o = characteristic or reference

axial flow along the groove in the x-direction occurs primarily in the intrinsic meniscus region; (2) the radius of curvature of the intrinsic meniscus is constant at a given location, x, but the radius of curvature varies axially along the groove, and the capillary pressure gradient due to this decreasing radius drives the liquid flow in the x-direction; (3) the disjoining pressure gradient due to the variation of the film thickness along the z-direction drives the film flow up the groove wall; (4) evaporation occurs primarily in the thin film region, particularly near the interline and; (5) the vapor pressure is constant.

The liquid-vapor pressure difference across the interface can be expressed as

$$P_v - P_l = \frac{\sigma}{r} \tag{1}$$

by the Young–Laplace equation, where r is the mean radius of curvature given by

$$\frac{1}{r} = \frac{1}{r_1} + \frac{1}{r_2}. \tag{2}$$

At each point on the liquid-vapor interface, the surface has two principal radii of curvature, r_1 and r_2, in orthogonal planes normal to the surface. One of the radii, the axial radius r_2, approaches infinity when compared to the other comparatively small radius, r_1, of the intrinsic meniscus. Hence, the mean effective curvature can be expressed as

$$\frac{1}{r} \cong \frac{1}{r_1}. \tag{3}$$

Meanwhile, the general form of the force-momentum balance equation can be expressed as

$$\rho\left[\frac{\partial \vec{V}}{\partial t} + (\vec{V}\cdot\nabla)\vec{V}\right] = -\nabla P + \vec{F}_B + \mu\nabla^2\vec{V} \tag{4}$$

from which the axial flow along the groove can be determined. Because the flow rate is very small, the convective term in the governing equation can be neglected. For steady laminar flow, the force-momentum equation in the x-direction can be simplified to

$$\frac{dP_l}{dx} + \rho_l g \sin\beta + F_v = 0, \tag{5}$$

where β is the angle between the gravitational vector and a line normal to the grooved surface. The primary concern in the current work, to which Eq. 5 applies, is to identify the dryout point, not necessarily the velocity components of the liquid flow. Thus, the viscous term in this expression, F_v, is substituted for $\mu\nabla\vec{V}$ and can be related to the Fanning friction factor. Since the vapor pressure, P_v, is assumed to be constant, the liquid pressure gradient can be expressed in terms of the radius of curvature, or

$$\frac{dP_l}{dx} = -\frac{d}{dx}(P_v - P_l) = -\frac{d}{dx}\left(\frac{\sigma}{r(x)}\right). \tag{6}$$

Following the procedure originally proposed by Xu and Carey (1990), the form of Eq. (5) can be modified to

$$\frac{d}{dx}\left(\frac{\sigma}{r(x)}\right) = \frac{2K\nu_l}{c_3 r(x)^4}\Gamma_c + \rho_l g \sin\beta, \tag{7}$$

where

$$c_3 = 4\tan^2\alpha\left(\frac{1}{\tan\alpha} + \alpha - \frac{\pi}{2}\right)^3. \tag{8}$$

In the above expression, Γ_c, is the mass flow rate through the cross section of the groove, and the parameter K, originally determined by Ayyaswamy et al. (1974) is a function of the groove half angle, α, and the liquid contact angle. Note that Eq. (8) is valid for both the adiabatic or the evaporating regions.

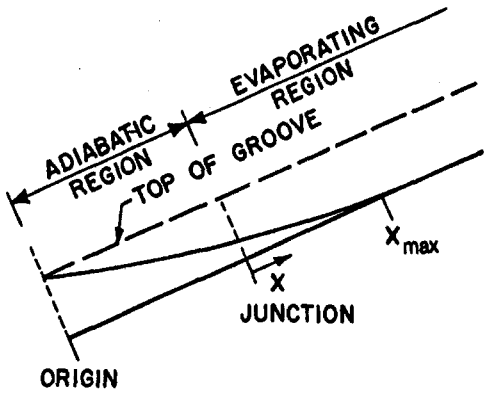

Fig. 4 Centerline film profile along the axial direction

Evaporating Region. If the liquid in the evaporating region is assumed to be saturated and the heat flux along the x-direction is given by $q''(x)$, the mass flow rate at a certain position, x, can be expressed as

$$\Gamma_c = \int_0^{\Gamma_c} d\Gamma_c = \frac{2\omega_b}{h_{fg}}\int_x^{x_{\max}} q''(x)dx, \tag{9}$$

where the value of $x_{\max}$ is the point farthest from the liquid pool at which the intrinsic meniscus could still be considered to exist. Note that mass flow rate is zero at the dryout point, $x_{\max}$, and, as shown in Fig. 4, is measured from the junction between the heated and adiabatic regions of the plate.

Initially, the case of the uniform heat flux will be considered. If $q''(x)$ is constant with respect to x, and represented by q''_b, the mass flow rate, Γ_c, in Eq. (9) at a position, x, can be expressed as

$$\Gamma_c = \int_0^{\Gamma_c} d\Gamma_c = \frac{2}{h_{fg}} q''_b\omega_b(x_{\max} - x). \tag{10}$$

Combining Eq. (7) with Eq. (10) yields

$$r(x)^2\frac{dr}{dx} = -A(x_{\max} - x) - Br(x)^4, \tag{11}$$

where

$$A = \frac{4K\nu_l q''_b\omega_b}{c_3\sigma h_{fg}} \quad \text{and} \quad B = \frac{\rho_l g\sin\beta}{\sigma}. \tag{12}$$

Equation (11) is the general equation of $r(x)$ for a uniform heat flux, and, as a nonlinear first order ordinary differential equation with respect to x, can be solved numerically. However, Eq. (11) has an exact solution for the case of $B = 0$, i.e., when the inclination angle is zero. The form of this solution is

$$r(x)^2\frac{dr}{dx} = -A(x_{\max} - x). \tag{13}$$

Using the method of separation of variables, the solution for $r(x)$ is given as follows:

$$r^3 = \tfrac{3}{2}A(x_{\max} - x)^2. \tag{14}$$

This equation for no tilt angle is expected to produce the longest axial wetted length. In the above solution, the boundary condition at the dryout point used (i.e., at $x = x_{\max}$) was $r = 0$. For the desired expression of $x_{\max}$, the boundary condition at the

junction can be used (i.e., at $x = 0$, $r = r_j$). The resulting expression for x_{max} with no inclination is given by

$$x_{m\beta 0} = \sqrt{\frac{2r_j}{3A}}\, r_j. \tag{15}$$

From the above result, it is apparent that if the radius at the junction, r_j, is known, the wetted length, and hence the dryout point, can be predicted in closed form. If this were not the case, the problem would become very difficult to solve numerically.

For the general case of $\beta \neq 0$ (i.e., the plate is at some tilt angle), Eq. (11) takes the form of a nonlinear differential equation with no analytical solution, that must be solved numerically. However, numerical computation only shows the final discrete results, and cannot give information about the relationship between the variables. Because it is useful to be able to predict the value of x_{max} in a closed form as a function of different variables, Eq. (11) can be approximated using perturbation methods to produce a closed form analytical solution.

For the case of very small inclination angles, Eq. (11) can be considered a weakly disturbed case of the problem with no inclination, making it suitable for solution by the perturbation method. As a first step, the variables can be nondimensionalized as

$$R = r/r_o, \quad \zeta = r_j/r_o, \quad X = x/x_{m\beta 0}. \tag{16}$$

Here, r_o and $x_{m\beta 0}$ are the characteristic lengths of the radius and axial axis, respectively; r_o is the radius at the origin $x' = 0$, which will be defined later, and $x_{m\beta 0}$ is x_{max} for the special case of $\beta = 0$. For this scaling situation, Eq. (11) assumes the following equivalent form:

$$R^2 \frac{dR}{dX} = \frac{x_{m\beta 0}^2}{r_o^3} A(X - X_{max}) - x_{m\beta 0} r_o B R^4. \tag{17}$$

The constant of the first term in the right-hand side can be simplified by Eqs. (15) and (16) as

$$\frac{x_{m\beta 0}^2}{r_o^3} A = \frac{2}{3}\zeta^3. \tag{18}$$

If the adiabatic region is not included, r_j is equal to r_o, and the above term takes a value of $\frac{2}{3}$. For the constant of the second term in Eq. (17), a new parameter, ϵ, can be introduced:

$$x_{m\beta 0} r_o B = \frac{\rho g}{\sigma}\sqrt{\frac{2r_j}{3A}}\, r_j r_o \sin\beta \equiv \epsilon. \tag{19}$$

If β is very small, the magnitude of ϵ can be as small as required but must be less than 1:

$$0 \leq \epsilon \leq 1. \tag{20}$$

Rewriting Eq. (17) with ϵ produces the following nonlinear expression:

$$R^2 \frac{dR}{dX} = \frac{2}{3}\zeta^3 (X - X_{max}) - \epsilon R^4. \tag{21}$$

The last term in the right-hand side, ϵR^4, can be treated as a source term, converting a nonlinear problem to a perturbed problem. Here, a regular perturbation method is applied. The solution of Eq. (21) can be approximated by adding small perturbations to the solution of the nonperturbed expression.

$$R = R_0 + \epsilon R_1 + \epsilon^2 R_2 + \epsilon^3 R_3 + \ldots \tag{22}$$

For simplicity, only the first order perturbation will be employed in the above power series of ϵ, or

$$R = R_0 + \epsilon R_1, \tag{23}$$

which will minimize the numerical uncertainty. Substituting the assumed form of the solution (Eq. (23)) into Eq. (21) produces the following:

$$(R_0 + \epsilon R_1)^2 (R_0' + \epsilon R_1') = \tfrac{2}{3}\zeta^3(X - X_{max}) - \epsilon(R_0 + \epsilon R_1)^4. \tag{24}$$

After manipulation, Eq. (24) can be arranged with respect to the order of ϵ as follows:

$$R_0^2 R_0' + 2\epsilon R_0 R_1 R_0' + \epsilon R_0^2 R_1' + \epsilon^2(\ldots) + \ldots = \tfrac{2}{3}\zeta^3(X - X_{max}) - \epsilon\{R_0^4 + \epsilon(\ldots) + \epsilon^2(\ldots) + \ldots\}. \tag{25}$$

Deleting the ϵ terms with order greater than two in the expansion process yields

$$R_0^2 R_0' + \epsilon(R_0^2 R_1' + 2R_0 R_1 R_0') = \tfrac{2}{3}\zeta^3(X - X_{max}) - \epsilon R_0^4. \tag{26}$$

Setting the coefficients of the powers of ϵ equal to each other yields the following two expressions:

$$R_0^2 R_0' = \tfrac{2}{3}\zeta^3(X - X_{max}) \tag{27}$$

$$R_0 R_1' + 2R_1 R_0' = -R_0^3. \tag{28}$$

The problem of solving the nonlinear first order differential equation has now been modified to that of solving two linear differential equations. Since $R = R_0 + \epsilon R_1 = 0$ at $X = X_{max}$, the boundary conditions for these two equations are

$$R_0 = 0 \quad \text{and} \quad R_1 = 0 \quad \text{at} \quad X = X_{max}. \tag{29}$$

Equation (27), the zeroth order equation that represents the undisturbed case of $\beta = 0$, has already been solved in Eq. (14), and in nondimensionalized form it is

$$R_0^3 = \zeta^3(X_{max} - X)^2. \tag{30}$$

If the solution of R_0 in Eq. (30) is substituted in Eq. (28), the first order perturbation equation, Eq. (28), can be solved as a typical first order, linear, nonhomogeneous ordinary differential equation, the solution of which has the following form:

$$R_1(X) = e^{-h(X)}\left[\int e^{h(X)}(-R_0^2)dX + c\right] \tag{31}$$

where

$$h(X) = \int \frac{2R_0'}{R_0} dX = 2\ln R_0. \tag{32}$$

Using the boundary condition given in Eq. (29) to determine the integration constant, c, in Eq. (31), the form of the solution for $R_1(X)$ is

$$R_1(X) = R_0^{-2}\int -R_0^4 dX = \tfrac{3}{11} R_0^2(X_{max} - X) = \tfrac{3}{11}\zeta^2(X_{max} - X)^{7/3}, \tag{33}$$

and the solution of Eq. (21) is the sum of the solutions to Eq. (30) and Eq. (33),

$$R(X) = R_0(X) + \epsilon R_1(X) = R_0\left\{1 + \frac{3\epsilon}{11} R_0(X_{max} - X)\right\} = \zeta(X_{max} - X)^{2/3}\left\{1 + \frac{3\epsilon}{11}\zeta(X_{max} - X)^{5/3}\right\}. \tag{34}$$

From the above result, the effect of a disturbance resulting from

a small tilt angle is clearly represented by the ϵ term added to the undisturbed term. With the boundary condition at $X = 0$, $R = r_j/r_o = \zeta$, Eq. (34) yields the desired expression for X_{max} in the implicit form

$$\left(1 + \frac{3\epsilon}{11}\zeta X_{max}^{5/3}\right)X_{max}^{2/3} = 1. \quad (35)$$

This equation indicates that the dryout point, X_{max}, is dependent upon ζ and ϵ. Returning to the original quantities, the final approximate expression of x_{max} for small angles of β is

$$\left\{1 + \epsilon \frac{3}{11 r_o r_j^{3/2}}\left(\frac{3A}{2}\right)^{5/6}(x_{max} - x)^{5/3}\right\}x_{max}^{2/3} = r_j\left(\frac{3A}{2}\right)^{-1/3}. \quad (36)$$

In order to apply Eq. (35) or (36), the effect of variations in ζ and ϵ must be understood along with the value of the radius at the junction, r_j, which can be found by analyzing the liquid flow behavior within the groove in the adiabatic region.

Adiabatic Region. In the adiabatic region, the axial mass flow rate at any position is constant and equal to the total mass flow rate evaporated over the entire length of the evaporating region. The mass flow rate per cross section in the x-direction, Γ_c, for uniform heat flux in the adiabatic region can be expressed as a function of x_{max} as follows:

$$\Gamma_c = \Gamma_j = \Gamma_o = \frac{2q_b''\omega_b}{h_{fg}}x_{max}. \quad (37)$$

Substituting this into the governing equation, Eq. (7), and rearranging yields

$$\frac{dr}{dx'} = -\frac{Ax_{max}}{r(x')^2} - Br(x')^2, \quad (38)$$

which must be solved numerically. Prior to solving, the numerical uncertainty was evaluated and found to be within acceptable levels. The assumption that the liquid of the meniscus completely fills the V-groove at the origin results in a boundary condition of the following form:

$$r(x) = r_o = \frac{w}{\cos\alpha} \quad \text{at} \quad x' = 0. \quad (39)$$

It is important to note where the location of the cross section where the above boundary condition can be applied: at the *b-b* cross section in Fig. 5, Eq. (39) it is applicable, but at the *a-a* cross-section, the liquid completely fills the groove, and the radius approaches infinity. The location of the *a-a* cross section is chosen in this work as the origin ($x' = 0$) and is defined as the point where the boundary condition given in Eq. (39) is applicable. In association with this boundary condition, the total wetted length may be modified for small tilt angles. The fluid will flow into the grooves due to the hydrostatic pressure, i.e., reflux flow. For this reason, it is necessary to modify the expression for x_{max} by adding an additional term to compensate for the hydrostatic pressure. From the geometry shown in Fig. 5, the additional term can be easily shown to take the form of $w/(\tan\alpha \tan\beta)$, making the total wetted length equal to $x_{max} + w/(\tan\alpha \tan\beta)$.

Results and Discussion

The radius of curvature at the junction, r_j, can be calculated from Eq. (38) with the boundary condition of Eq. (39), but the length of the adiabatic region must be known. To resolve this problem, an initial value of r_j less than $w/\cos\alpha$ is assumed

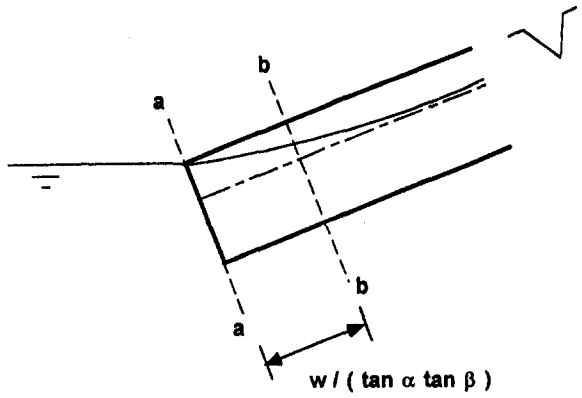

Fig. 5 Cross section of liquid-filled groove near the pool

as the first estimate to obtain an initial value of x_{max} using Eq. (36) for the case with an adiabatic region. This value is then substituted into Eq. (38) for the second value of r_j, which in turn results in a second value for x_{max}. This iterative procedure continues until r_j and x_{max} converge to within a predetermined allowable accuracy. After having converged the value of x_{max} or X_{max}, Eq. (34) can be used to obtain R.

While the above iterative method allows a value of r_j to be determined, the primary interest in this investigation focuses on the features of the evaporating region rather than the adiabatic region. As a result, for simplicity r_j is set equal to r_o, which implies there is no adiabatic region along the x-direction. For these conditions $\zeta = 1$ and Eq. (34) becomes

$$R(X) = (X_{max} - X)^{2/3}\left\{1 + \frac{3\epsilon}{11}(X_{max} - X)^{5/3}\right\}. \quad (40)$$

The variation of the radius of curvature with all the related variables is best illustrated by a case study. Consider a system comprised of saturated methanol at atmospheric pressure, in grooves with a cross section defined as $\omega = \omega_b = 0.19$ mm, $\alpha = 30$ deg, and $q_b'' = 5000$ W/m^2. Tilt angles of $\beta = 3$ deg and 5 deg correspond to $\epsilon = 0.269$ and 0.448, respectively. In Fig. 6, the universal dimensionless axial profile of the radius of curvature with respect to a dimensionless axial length is illustrated for the three values of ϵ, 0.0, 0.27, 0.45. As shown, as the value of ϵ increases, the location of the dryout point recedes, and, at the same position of X, the value of R gets smaller. Though ϵ approaches 0.45 (about half of the limit of ϵ), X_{max} recedes to only 0.987 of X_{max} for $\epsilon = 0$. Note that the nondimensionalized value of x or x_{max} is different for different q_b'', even though the dimensionless parameter X has the same values, because the axial position x was nondimensionalized by $x_{m\beta 0}$ in Eq. (15). For example, $\epsilon = 0.45$ has an X_{max} value of 0.987 that corresponds to $x_{max} = 5.96$ cm for $q_b'' = 5000$ W/m^2 and $\beta = 5$ deg, but $x_{max} = 2.98$ cm for $q_b'' = 20{,}000$ W/m^2 and $\beta = 10$ deg. At this point, a physically more meaningful explanation of the effect of ϵ can be presented by examining the dimen-

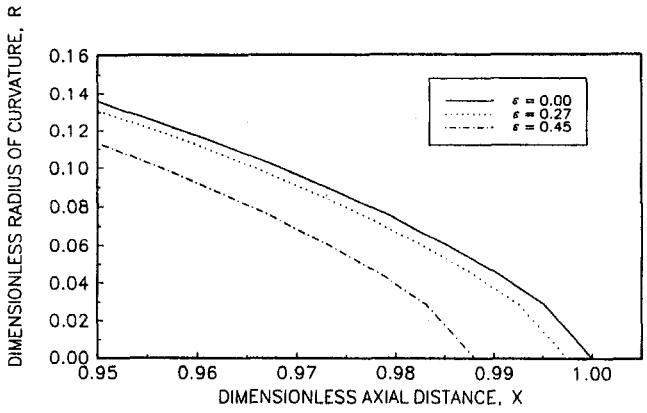

Fig. 6 Universal graph of R versus X with several values of ϵ

sionless parameters such as the Bond number, Bo (the ratio of gravitational and surface tension forces), and the capillary number, Ca (the ratio of viscous and surface tension forces) as follows:

$$\epsilon = \frac{\rho g}{\sigma}\sqrt{\frac{2r_j}{3A}}\, r_j r_o \sin\beta = 2\zeta\sqrt{\frac{\zeta}{3CaD}}\, Bo \sin\beta \quad (41)$$

where

$$Bo = \frac{\rho g r_o^2}{\sigma}, \quad Ca = \frac{\nu_l q_b''}{\sigma h_{fg}}, \quad D = \frac{8K\omega_b \cos\alpha}{c_3 w} \quad (42)$$

Because r_o, defined in Eq. (39), characterizes not only the groove width but also the groove depth, it is used as the reference length for the Bond number, Bo. In Eq. (41), ϵ is expressed by $\sin\beta$ and four dimensionless variables, ζ, Bo, Ca, and D, where $\sin\beta$ accounts for the inclination angle, ζ for the length of the adiabatic region, Bo for some of the fluid properties, Ca for the combined effect of the remaining fluid properties and the heat input, and D for the groove shape. If all the geometric conditions are fixed with $\zeta = 1$, then ϵ is dependent only on Bo and Ca.

The introduction of ϵ was, at first, motivated by a desire to determine the effect of small tilt angles. However, even for large title angles the value of ϵ may be small (as seen in Eq. (41)) if the capillary number, Ca, and/or the geometric parameter, D, are sufficiently large. As a result, this perturbation model can be applied, even for large tilt angles, if the heat input, q_b'', is large enough and the ratio of ω_b/w is suitable. For example, tilt angles of $\beta = 6$ deg and 10 deg (for methanol, $\omega = \omega_b = 0.19$ mm, $\alpha = 30$ deg) correspond to relatively small values 0.27 and 0.45 of ϵ for a heat flux of $q_b'' = 20{,}000$ W/m^2. Using these guidelines and recognizing the significance of the various terms and their effect on the validity of this approach allows it to be extended to cases that would not initially appear to be applicable.

Conclusion

A method for predicting the axial flow of evaporating thin films in V-shaped micro channels was developed for grooved plates inclined with very small tilt angles. The results indicate that for this situation the gravity term resulting from the tilt angle variation changes the form of the governing equation from linear to nonlinear. Because the effect of the tilt angle is very small, a perturbation method was applied to obtain a first order perturbation solution for $R = R_0 + \epsilon R_1$, where R_0 represents the undisturbed solution of a horizontal plate, and R_1 is the disturbed solution caused by the tilt angle. A generalized graph of the nondimensional radius of curvature with respect to the nondimensionalized axial length was obtained. The perturbation parameter introduced was expressed as a function of five nondimensional parameters. When the geometry was fixed, the effects of the Bond number and Capillary number were found to be dominant. The results indicate that ϵ is inversely proportional to the square root of the Capillary number. This implies that the validity of the perturbation method is appropriate, even for cases with a somewhat larger tilt angle (where the applicability of perturbation appears to be violated), if a sufficiently large heat flux is applied.

References

Ayyaswamy, P. S., Catton, I., and Edwards, D. K., 1974, "Capillary Flow in Triangular Grooves," *J. Applied Mechanics,* Vol. 41, pp. 332–336.

DasGupta, S., Schonberg, J. A., and Wayner, P. C., Jr., 1993, "Investigation of an Evaporating Extended Meniscus Based on the Augmented Young-Laplace Equation," ASME JOURNAL OF HEAT TRANSFER, Vol. 115, No. 1, pp. 201–214.

Ha, J. M., and Peterson, G. P., 1994, "Analytical Prediction of the Axial Dryout Point for Evaporating Liquids in Triangular Microgrooves," ASME JOURNAL OF HEAT TRANSFER, Vol. 116, No. 2, pp. 498–503.

Ha, J. M., and Peterson, G. P., 1996, "The Interline Heat Transfer of Evaporating Thin Films Along a Micro Grooved Surface," ASME JOURNAL OF HEAT TRANSFER, Vol. 118, pp. 747–755.

Ma, H. B., and Peterson, G. P., 1996, "Experimental Investigation of the Maximum Heat Transport in Triangular Grooves," ASME JOURNAL OF HEAT TRANSFER, Vol. 118, pp. 740–746.

Mirzamoghadam, A., and Catton, I., 1988a, "A Physical Model of the Evaporating Meniscus," ASME JOURNAL OF HEAT TRANSFER, Vol. 110, pp. 201–207.

Mirzamoghadam, A., and Catton, I., 1988b, "Holographic Interferometry Investigation of Enhanced Tube Meniscus Behavior," ASME JOURNAL OF HEAT TRANSFER, Vol. 110, pp. 208–213.

Moosman, S., and Homsy, G. M., 1980, "Evaporating Menisci of Wetting Fluids," *J. of Colloid and Interface Science,* Vol. 73, pp. 212–223.

Peterson, G. P., and Ortega, A., 1990, "Thermal Control of Electronic Equipment and Devices," *Advances in Heat Transfer,* Vol. 20, J. P. Hartnett and T. F. Irvine, eds., Pergamon Press, New York, NY, pp. 181–314.

Peterson, G. P., 1992, "An Overview of Micro Heat Pipe Research," Invited Review Article, *Applied Mechanics Review,* Vol. 45, No. 5, May, pp. 175–189.

Peterson, G. P., and Ma, H. B., 1996, "Theoretical Analysis of the Maximum Heat Transport in Triangular Grooves: A Study of Idealized Micro Heat Pipes," ASME JOURNAL OF HEAT TRANSFER, Vol. 118, pp. 731–739.

Potash, M., and Wayner, P. C., Jr., 1972, "Evaporation From a Two-Dimensional Extended Meniscus," *Int. J. Heat & Mass Transfer,* Vol. 15, pp. 1851–1863.

Renk, F., Wayner, P. C., Jr., and Homsy, G. M., 1978, "On the Transition Between a Wetting Film and a Capillary Meniscus," *J. of Colloid and Interface Science,* Vol. 67, pp. 408–414.

Renk, F. J., and Wayner, P. C., Jr., 1979a, "An Evaporating Ethanol Meniscus, Part I: Experimental Studies," ASME JOURNAL OF HEAT TRANSFER, Vol. 101, pp. 55–58.

Renk, F. J., and Wayner, P. C., Jr., 1979b, "An Evaporating Ethanol Meniscus, Part II: Analytical Studies," ASME JOURNAL OF HEAT TRANSFER, Vol. 101, pp. 59–62.

Schonberg, J. A., and Wayner, P. C., Jr., 1992, "Analytical Solution for the Integral Contact Line Evaporative Heat Sink," *AIAA J. of Thermophysical and Heat Transfer,* Vol. 6, No. 1, pp. 128–134.

Stroes, G., Rohloff, T., and Catton, I., 1992, "An Experimental Study of the Capillary Forces in Rectangular Channels Versus Triangular Channels," ASME HTD-Vol. 200, pp. 1–8.

Sujanani, M., and Wayner, P. C., Jr., 1991, "Spreading and Evaporative Processes in Thin Films," *J. Colloid and Interface Science,* Vol. 143, No. 2, pp. 472–488.

Wayner, P. C., Jr., Kao, Y. K., and LaCroix, L. V., 1976, "The Interline Heat-Transfer Coefficient of an Evaporating Wetting Film," *Int. J. Heat & Mass Transfer,* Vol. 19, pp. 487–492.

Xu, X., and Carey, V. P., 1990, "Film Evaporation From a Micro-Grooved Surface—An Approximate Heat Transfer Model and Its Comparison With Experimental Data," *AIAA J. of Thermophysical and Heat Transfer,* Vol. 4, No. 4, pp. 512–520.

A. R. Martin[1]
Doctoral Candidate,
Department of Mechanical Engineering,
University of Florida,
Gainesville, FL 32611
Assoc. Mem. ASME

C. Saltiel
President,
Synergetic Technologies, Inc.,
Delmar, NY 12054
Mem. ASME

W. Shyy
Professor and Chairman,
Department of Aerospace Engineering,
Mechanics, and Engineering Science,
University of Florida,
Gainesville, FL 32611
Mem. ASME

Heat Transfer Enhancement With Porous Inserts in Recirculating Flows

This investigation explores the use of porous inserts for heat transfer enhancement in recirculating flows, specifically flow over a backward-facing step. Numerical computations are performed for laminar flow with high porosity inserts, which are composed of small-diameter (150 μm) silicon carbide fibers aligned transverse to the streamwise flow. The inserts are varied in length and porosity in order to determine the most favorable combinations of maximum temperature reduction and head loss penalty. In general, the porous inserts reduce or eliminate the lower wall recirculation zone; however, in some cases the recirculation zone is lengthened if the inserts are short and extremely porous. Excellent heat transfer characteristics are shown within the inserts themselves due to the high-conductivity fiber material. Non-Darcy effects are shown to be important primarily as the porosity is increased. Deviation from local thermodynamic conditions between the inserts and the fluid is most apparent for the shortest inserts considered.

1 Introduction

The importance of heat transfer enhancement continues to grow due to the demands of energy efficiency and rising equipment costs. Durability is a vital issue for equipment operating under highly corrosive conditions, such as in coal-fired boilers or waste-to-energy incinerators, where losses to corrosion are magnified by excessive operating temperatures (Krause et al., 1977; Shreir, 1976; Thielsch and Cone, 1994). Since corrosion of metals is very sensitive to temperature (Shreir, 1976), even small increases in heat transfer rates can greatly lengthen equipment lifetime by reducing corrosion losses. A number of heat transfer augmentation devices are available to increase internal heat transfer and include roughened and extended surfaces, and swirl-flow devices (Bergles, 1985). Recent investigations have focused on the use of porous inserts in order to obtain heat transfer enhancement with a minimum of frictional losses. Huang and Vafai (1994) studied flow in a two-dimensional duct with intermittently placed porous blocks located on one of the walls, and in a related study, Vafai and Huang (1994) considered these blocks to be imbedded within the duct walls. Abu-Hijleh (1997) investigated flow over a backward-facing step where part of the downstream duct wall was porous.

While these studies demonstrate the possible gains in heat transfer with porous media, they do not address situations where the flow is inherently recirculating in the absence of the insert. Hendricks et al. (1991) experimentally investigated the use of brush inserts within a complex cooling passage for the mitigation of flow separation and augmentation of local heat transfer. The authors qualitatively showed that the inserts produced favorable changes in the flow field, but did not explore the effects of varying the insert length or porosity. In order to investigate the influence of these parameters on the flow field within a simple but well-studied geometry, we examine the flow over a backward-facing step, depicted in Fig. 1. This situation features one or more recirculation zones downstream of the inlet, depending on the Reynolds number. From a heat transfer perspective, the reduction or elimination of recirculation is highly desirable, as wall temperatures are typically very high in these regions. In lieu of smoothing out or extending the abrupt inlet region, one option is to partially fill the duct directly behind the step with a porous insert (see Fig. 1). The resistance to flow offered by the porous insert changes the streamwise velocity profile, which impacts the formation of recirculation zones beyond the insert. This flow resistance also may prevent the formation of recirculation zones within the porous region itself. In addition, if the porous insert is composed of a high-conductivity material with a large specific surface area, the removal of heat in these regions may be further enhanced by insert-wall conduction. Presuming that the porous medium consists of a uniform matrix, the porosity ϵ_f and the length a are key factors to the insert performance.

The objective of the present study is to explore the use of porous inserts for heat transfer enhancement in recirculating flows. Laminar flow over the backward-facing step shown in Fig. 1 is considered with a duct Reynolds number, Re_H, of 800 ($\mathrm{Re}_H = \rho UH/\mu$, where ρ is the fluid density, U is the average inlet velocity, H is the duct height, and μ is the fluid dynamic viscosity). The porous inserts consist of square arrays of fibers mounted transverse to the streamwise flow, with highly conducting silicon carbide (SiC) selected as the fiber material. Although the fiber arrays have porosities between 0.90 and 0.99, the small diameter of the fibers ($d = 150$ μm) relative to the duct dimensions results in a large interfacial surface area. A range of insert lengths, ranging from $0.10 \leq a/H \leq 0.25$, is considered for this problem. Non-Darcy effects are expected to be important in this application due to the combination of high porosity and large particle Reynolds numbers. Constant wall heat flux conditions are considered to emphasize the role of the porous insert in temperature reduction. Since there is a large discrepancy between the fluid and fiber array conductivity, local thermodynamic equilibrium (LTE) in the porous structure is not assumed.

2 Analysis

It is common to simplify the complex nature of flows in porous media by the volume averaging of the microscopic flow equations (Bejan, 1995). The volume average of any scalar or vector quantity Γ_k, associated with phase k, is defined as

[1] Current address: Division of Energy Processes, Department of Chemical Engineering and Technology, Royal Institute of Technology, S-100 40 Stockholm, Sweden.

Contributed by the Heat Transfer Division for publication in the JOURNAL OF HEAT TRANSFER. Manuscript received by the Heat Transfer Division September 8, 1997; revision received January 6, 1998. Keywords: Computational, Enhancement, Heat Transfer, Porous Media, Recirculating. Associate Technical Editor: R. W. Douglass.

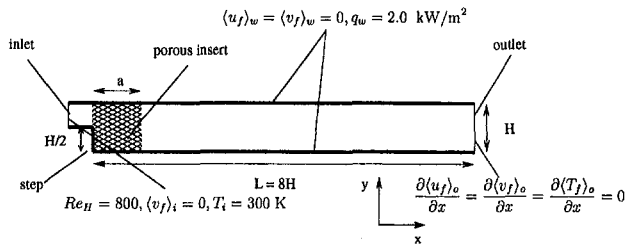

Fig. 1 Schematic of duct with backward-facing step

$$\langle\Gamma_k\rangle = \frac{1}{V}\int_V \Gamma_k dV \tag{1}$$

where V is the representative elementary volume (REV). (Γ_k is zero in regions not occupied by phase k.) The intrinsic volume average is defined as

$$\langle\Gamma_k\rangle^k = \frac{1}{V_k}\int_{V_k} \Gamma_k dV \tag{2}$$

and may be related to the total volume average by $\epsilon_k\langle\Gamma_k\rangle^k = \langle\Gamma_k\rangle$, where ϵ_k is the volume fraction of phase k. Within the fiber array, fluid phase f and solid phase s are present, while only the fluid phase exists downstream of the porous insert. For steady-state, incompressible flow with spatially uniform properties and volume fraction, the volume-averaged equations of continuity, momentum, and energy for the fluid phase are as follows (Amiri and Vafai, 1994; Bejan, 1995; Cheng, 1978):

$$\nabla\cdot\langle\mathbf{u}_f\rangle = 0 \tag{3}$$

$$\frac{\rho_f}{\epsilon_f^2}\langle\mathbf{u}_f\rangle\cdot\nabla\langle\mathbf{u}_f\rangle = -\nabla\langle p_f\rangle^f + \frac{\mu_f}{\epsilon_f}\nabla^2\langle\mathbf{u}_f\rangle - \mathbf{S}_f \tag{4}$$

$$\rho_f c_{p,f}\nabla\cdot\langle T_f\rangle^f\langle\mathbf{u}_f\rangle = \mathbf{k}_{ef}\epsilon_f\nabla^2\langle T_f\rangle^f + h_{fs}a_{fs}(\langle T_s\rangle^s - \langle T_f\rangle^f) \tag{5}$$

In these expressions, $\mathbf{S}_f$ is the interfacial momentum source term tensor, $\mathbf{k}_{ef}$ the effective fluid thermal conductivity tensor, h_{fs} the interfacial convection coefficient, and a_{fs} the specific surface area of the interface; the other variables are listed in the nomenclature. Outside the porous medium, $\epsilon_f = 1$, and the equations given above reduce to the Navier–Stokes form. Since the solid phase is stationary, only the energy equation needs to be considered within the porous medium:

$$0 = \mathbf{k}_{es}\epsilon_s\nabla^2\langle T_s\rangle^s - h_{fs}a_{fs}(\langle T_s\rangle^s - \langle T_f\rangle^f) \tag{6}$$

A discussion of the terms resulting from the volume-averaging procedure is presented below.

2.1 Momentum Source Term. In order to simplify the treatment of the momentum source term, $\mathbf{S}_f$, it is assumed that the microscopic flow field is periodic within each macroscopic cell. This simplification allows for $\mathbf{S}_f$ to be specified from the macroscopic variables alone. The Darcian Reynolds number, $\mathrm{Re}_{\sqrt{K}}$, is used as a criterion for determining the regime of macroscopic flow through the porous media:

$$\mathrm{Re}_{\sqrt{K}} = \frac{\rho U\sqrt{K}}{\mu} \tag{7}$$

where K is the Darcian or intrinsic permeability in a particular direction. Considering flow transverse to fiber arrays, Darcy flow holds when $\mathrm{Re}_{\sqrt{K}} \leq 1$, while non-Darcy effects exist beyond this point due to inertia and/or turbulence. Hence, the momentum source term in the x direction for the Darcy regime is

$$-S_x = \frac{\mu\langle u_f\rangle}{K_x} \tag{8}$$

The Darcian permeability for periodic fiber arrays has been studied by a number of researchers (Drummond and Tahir, 1984; Edwards et al., 1990; Eidsath et al., 1983; Ghaddar, 1995; Martin et al., 1997; Sangani and Acrivos, 1982); Åström et al. (1992) report the functional form of K_x as

$$K_x = \frac{C_x d^2}{32\epsilon_s} \tag{9}$$

where a closed-form solution for C_x is reported by Drummond and Tahir (1984) for square arrays:

$$C_x = \ln\left(\frac{1}{\epsilon_s}\right) - 1.4763 + \frac{2\epsilon_s - 0.7959\epsilon_s^2}{1 + 0.4892\epsilon_s - 1.6049\epsilon_s^2} \tag{10}$$

Non-Darcy resistance to flow is usually represented by the Forchheimer equation (Amiri and Vafai, 1994; Bear, 1988; Bejan, 1995),

$$-S_x = \frac{\mu\langle u_f\rangle}{K_x} + \frac{F\rho}{\sqrt{K_x}}\langle u_f\rangle\cdot|\langle u_f\rangle| \tag{11}$$

or the Ergun equation (Ergun, 1952),

Nomenclature

a = specific surface area; distance
A = first Ergun constant
B = second Ergun constant
C = permeability parameter
c_p = specific heat
d = fiber diameter
d_p = characteristic particle diameter
F = Forchheimer term
g = Nusselt number correlation constant
h = convective heat transfer coefficient
H = duct height
K, $\mathbf{K}$ = permeability scalar and tensor
k, $\mathbf{k}$ = thermal conductivity scalar and tensor
L = duct length
Nu = Nusselt number
p = pressure
q = heat flux
r = Nusselt number correlation constant
Re_d = particle Reynolds number
Re_H = duct Reynolds number
$\mathrm{Re}_{\sqrt{K}}$ = Darcian Reynolds number
$\mathbf{S}_f$ = interfacial momentum source term tensor
T = temperature
u = x velocity component
U = average velocity
$\mathbf{u}_f$ = velocity vector
V = representative elementary volume (REV)
v = y velocity component
α = kinetic energy coefficient
Γ = scalar or vector quantity
ϵ = volume fraction
η = nondimensional wall coordinate
μ = dynamic viscosity
ρ = density
Ψ = yaw angle

Subscripts and Superscripts

b = bulk
e = effective
f = fluid phase
fs = fluid–solid interface
h = homogeneous
i = inlet
k = phase
m = maximum
o = outlet
s = solid phase
w = wall
$*$ = nondimensional quantity

Table 1 Correlation values for Nu_x and values for Nu_y

ϵ_f	g	r	Nu_y
0.99	1.069	0.140	1.157
0.98	1.180	0.138	1.410
0.96	1.345	0.147	1.790
0.94	1.455	0.162	2.110
0.92	1.596	0.167	2.405
0.90	1.729	0.172	2.690

$$-S_x = A\frac{\epsilon_f^2}{(1-\epsilon_f)^3}\frac{\mu\langle u_f\rangle}{d_p^2} + B\frac{\epsilon_f}{(1-\epsilon_f)^3}\frac{\rho\langle u_f\rangle\cdot|\langle u_f\rangle|}{d_p} \quad (12)$$

In these equations, F is the Forchheimer term, A and B are the first and second Ergun coefficients, and d_p is the characteristic particle diameter. Martin et al. (1997) found these relations to be inadequate for flows in high-porosity cylinder arrays, and proposed the following equation as an alternative to the Forchheimer or Ergun relations:

$$-S_x = f'\frac{\rho\langle u_f\rangle\cdot|\langle u_f\rangle|}{\sqrt{K_x}} \quad (13)$$

where the modified friction factor f' is correlated for square arrays as

$$f' = 0.862\epsilon_f^{-0.555}\,\mathrm{Re}_{\sqrt{K_x}}^{-0.882} \quad (14)$$

The range of validity of Eq. (13) is $0.80 \le \epsilon_f \le 0.99$, and $1 < \mathrm{Re}_{\sqrt{K_x}} \le 300$.

When the flow is parallel to the fiber arrays it remains attached, so Darcy flow alone is considered:

$$-S_y = \frac{\mu\langle v_f\rangle}{K_y} \quad (15)$$

Similar to the transverse case, the Darcian permeability parallel to the fiber arrays is found from (Åström et al., 1992)

$$K_y = \frac{C_y d^2}{16\epsilon_s} \quad (16)$$

where (Drummond and Tahir, 1984)

$$C_y = \ln\left(\frac{1}{\epsilon_s}\right) - 1.476 + 2\epsilon_s - 0.5\epsilon_s^2 - \frac{0.05097\epsilon_s^4}{1+1.52\epsilon_s^2} \quad (17)$$

Both components of the momentum source term are zero in the pure fluid region.

2.2 Effective Conductivity and Energy Source Term. Since the fluid volume fraction is large in the porous medium, the effective conductivity of the fluid phase is taken as the actual fluid conductivity, or

$$k_{f,x} = k_{f,y} = k_f \quad (18)$$

The effective conductivity of the solid phase along the fiber axis is

$$k_{s,y} = k_s \quad (19)$$

while $k_{s,x} = 0$ since fibers are not interconnected. In regions outside the porous medium, k_f is taken as the conductivity.

The determination of the interfacial heat transfer coefficient, h_{fs}, is approximated from knowledge of the heat transfer coefficients transverse and longitudinal to the fiber array (microscopic heat transfer is also assumed to be periodic). Based on experimental results from yawed flows over long cylinders, the Nusselt number, $\mathrm{Nu} = h_{fs}d/k_f$, is taken to have the following form (Morgan, 1975):

$$\mathrm{Nu} = (\mathrm{Nu}_x^4\sin^2\Psi + \mathrm{Nu}_y^4\cos^2\Psi)^{1/4} \quad (20)$$

where Ψ is the yaw angle of the local velocity vector as measured from the fiber axis, and Nu_x and Nu_y are the Nusselt numbers transverse and parallel to the fiber array. Martin et al. (1997) correlated Nu_x to results obtained from microscopic modeling of flows in cylinder arrays:

$$\mathrm{Nu}_x = g\,\mathrm{Re}_d^r \quad (21)$$

where Re_d is the particle Reynolds number ($\rho\langle u_f\rangle d/\mu$) and g and r are constants listed in Table 1. Longitudinal to the fiber array, Nu_y is found via the equivalent annulus formulation presented by Sparrow et al. (1961), which is an accurate approximation for longitudinal flows in fiber arrays with high porosity. Values for Nu_y, listed in Table 1, are independent of Reynolds number since the longitudinal flow is attached. Finally, the interfacial surface area $a_{fs} = 4\epsilon_s/d$ for square arrays.

Table 2 Input parameters for porous insert analysis

Parameter	Value
ρ_f	1.23 kg/m^3
μ_f	1.79×10^{-5} N-s/m^2
$c_{p,f}$	1006 J/kg-K
k_f	0.025 W/m-°C
k_s	490 W/m-°C
T_i	300 K
H	0.025 m
L	0.2 m
Re_H	800
q_w	2.0 kW/m^2

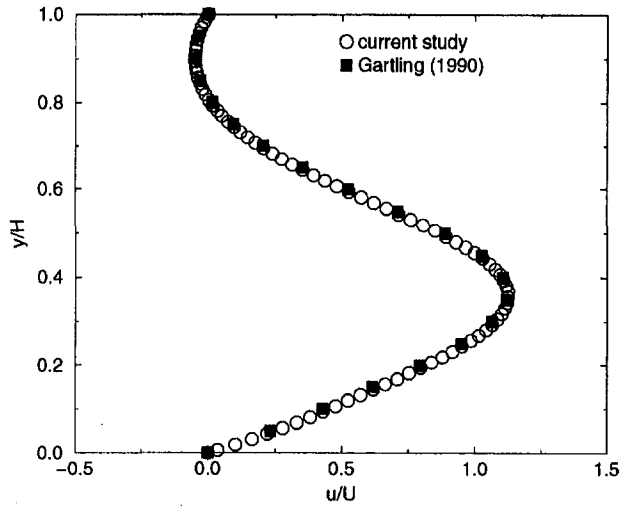

(a)

(b)

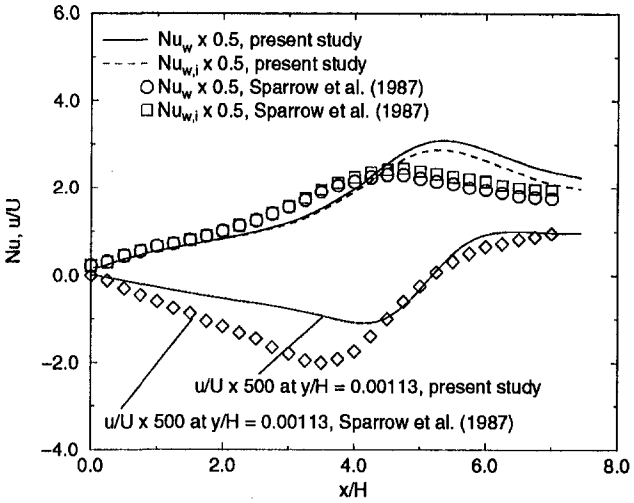

(c)

Fig. 2 Fluid flow and heat transfer in homogeneous duct: (*a*) transverse coordinate versus streamwise velocity component at $x/H = 7$, $Re_H = 800$; (*b*) streamline plot, $Re_H = 800$; (*c*) Nusselt number and near-wall velocity versus axial location, $Re_H = 600$.

2.3 Problem Description and Numerical Approach. A finite volume-based numerical procedure based on the SIMPLE algorithm (Patankar, 1980; Shyy, 1994) is used to solve the macroscopic equations, Eqs. (3)–(6), in a two-dimensional Cartesian coordinate system, with central differencing used to handle convective terms. The abrupt change in properties and source terms at the interface between the porous medium and the pure fluid is handled by computing the harmonic mean at this location, as described by Patankar (1980). Referring to

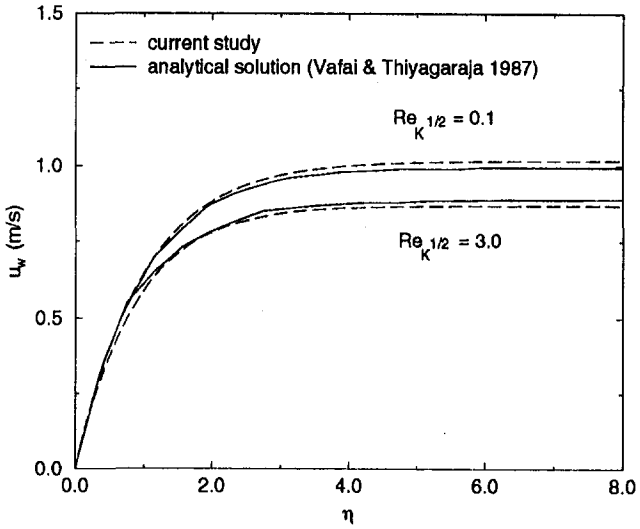

Fig. 3 Wall velocity versus nondimensional wall coordinate for fully developed porous medium flow

Fig. 1, the computational domain is divided into a 96 × 81 grid, with 20 cells located just behind the step along $x/H = 0.5$. No-slip and no-penetration boundary conditions are imposed at the solid walls, and the inlet velocity is parabolic (i.e., fully developed). At the outlet, the velocity is extrapolated in the streamwise direction, and global mass conservation is used after every iteration (see Shyy, 1994). The upper and lower walls are supplied a constant heat flux $q_w = 2.0$ kW/m^2, where both fluid and solid temperatures are taken as the wall temperature, T_w. Furthermore, it is assumed that the fiber array is in good thermal contact with the upper and lower walls, hence T_w is specified via

$$q_w = -(\epsilon_s k_s + \epsilon_f k_f) \left.\frac{\partial T_w}{\partial y}\right|_{y=0,H} \tag{22}$$

where contributions from both fluid and solid phases are included in the effective conductivity. The temperatures of the fluid and solid at the inlet and left wall are fixed at T_i, while the outlet is adiabatic. Physical properties of the fluid (air) and the fiber array (SiC) are taken at 300 K, and can be found from Incropera and Dewitt (1985) (refer to Table 2, which includes the input parameters). Computations are performed on a dedicated DEC 3000-600 workstation, with solution times of approximately four hours for the 96 × 81 grid.

A number of checks are performed in order to determine the validity of the model. For each combination of porosity and insert length, sufficient iterations are allowed so that the normalized residuals for each of the flow variables are less than 10^{-4}. In addition, grid dependency is explored by comparing the base grid results to solutions obtained from two refined grids, 191 × 81 and 96 × 161, for $\epsilon_f = 0.99$ and $a/H = 0.25$. No more than 2 percent difference is found between all three grid results, hence the coarsest grid is selected for the present study. Results are also compared to the investigation of Gartling (1990), who performed a detailed study of flow over a backward-facing step. Figure 2(*a*) shows the u velocity profile, normalized by the inlet velocity U, at a distance of $x/H = 7$ from the step. Excellent agreement can be seen, as results from the present study and Gartling (1990) are nearly indistinguishable. Streamlines are shown in Fig. 2(*b*) for this situation, showing a primary recirculation zone along the lower wall, and a secondary recirculation zone along the upper wall near the outlet.

In addition, the numerical study presented by Sparrow et al. (1987) has also been selected to validate the present model,

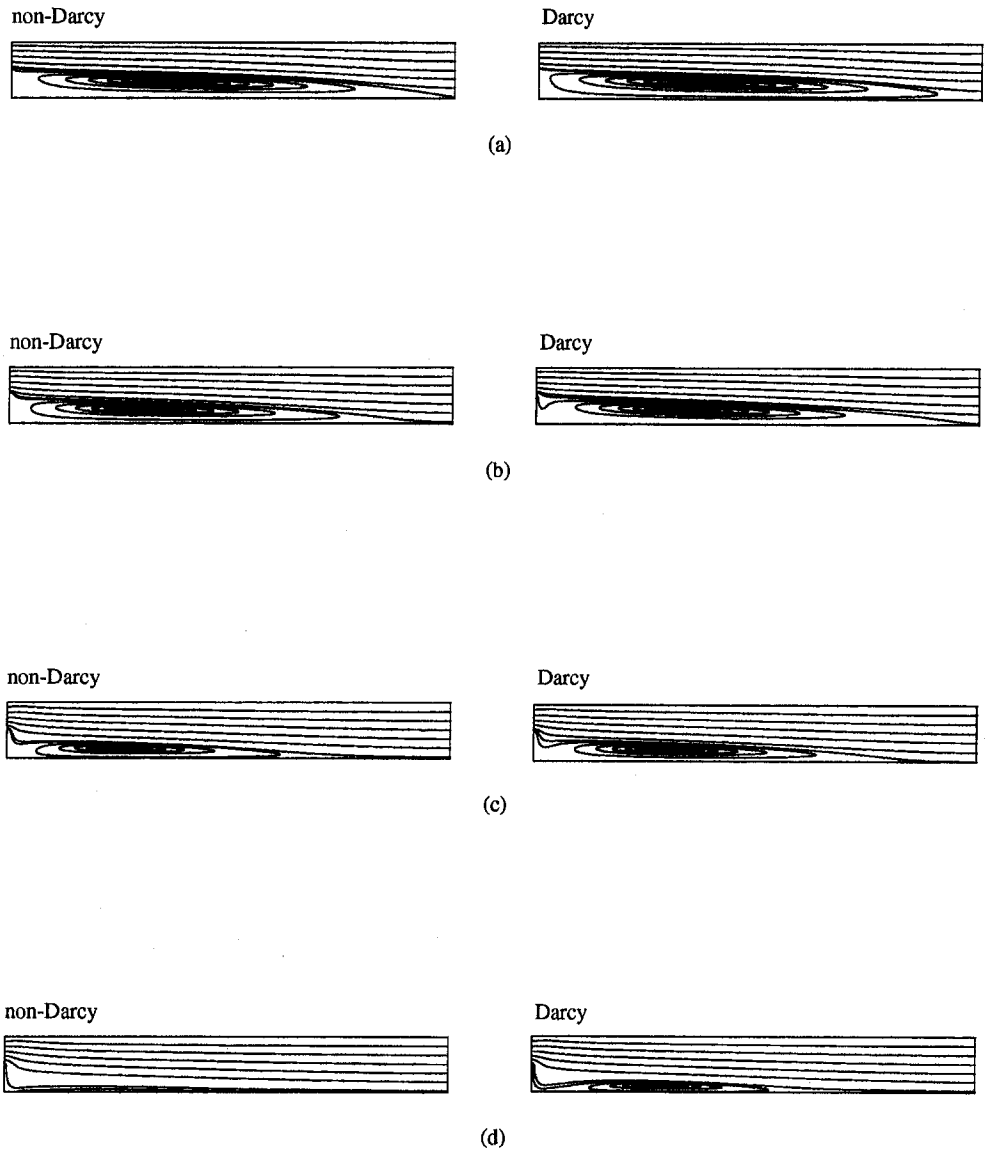

Fig. 4 Streamline plots, $\epsilon_f = 0.99$: (a) $a/H = 0.10$; (b) $a/H = 0.15$; (c) $a/H = 0.20$; (d) $a/H = 0.25$

with $\mathrm{Re_H} = 600$ (here, the lower wall is isothermal, and the upper wall and step are adiabatic). Figure 2(*c*) shows the development of the u velocity near the bottom wall and the lower wall Nusselt numbers downstream of the step, which are defined as follows:

$$\mathrm{Nu_w} = \frac{-\left.\frac{\partial T_w}{\partial y}\right|_{y=0} H}{T_w - T_b} \tag{23}$$

where T_b is the bulk temperature, and

$$\mathrm{Nu_{w,i}} = \frac{-\left.\frac{\partial T_w}{\partial y}\right|_{y=0} H}{T_w - T_i} \tag{24}$$

While the two solutions exhibit some quantitative discrepancies in the near-wall velocity profile, the location of the reattachment point compares well. The resolution of the results in the work of Sparrow et al. (1987) seems not to have reached a level as fine as the present one. With regard to heat transfer, good agreement is shown up to $x/H \approx 5$, after which the present study predicts higher Nusselt number values. This finding is due to a small recirculation zone, which was computed by the present model, but not shown to exist by Sparrow et al. (1987).

Finally, the porous medium flow equations were compared against the analytical solution reported by Vafai and Thiyagaraja (1987) for fully developed porous medium flow near a solid wall. The wall velocity, u_w, as a function of the dimensionless wall coordinate, η, is shown in Fig. 3 for non-Darcy and Darcy flow conditions. Here, the Forchheimer equation, Eq. (11), was considered for the momentum source term, as this formulation was employed by Vafai and Thiyagaraja (1987). The velocity distribution was found to match within about 2 percent of the analytical predictions.

3 Results—Fluid Flow

The qualitative impact of the fiber array inserts on the downstream flow is shown in Figs. 4 and 5 as a function of a/H and porosity. Referring to Fig. 4, the presence of even a high-porosity insert ($\epsilon_f = 0.99$) serves to change the nature of the flow field dramatically. With $a/H = 0.10$, the lower wall recirculation zone nearly fills the entire duct, which is in contrast to the shorter cell shown in the homogeneous case (see Fig. 2(*b*)). As a/H is

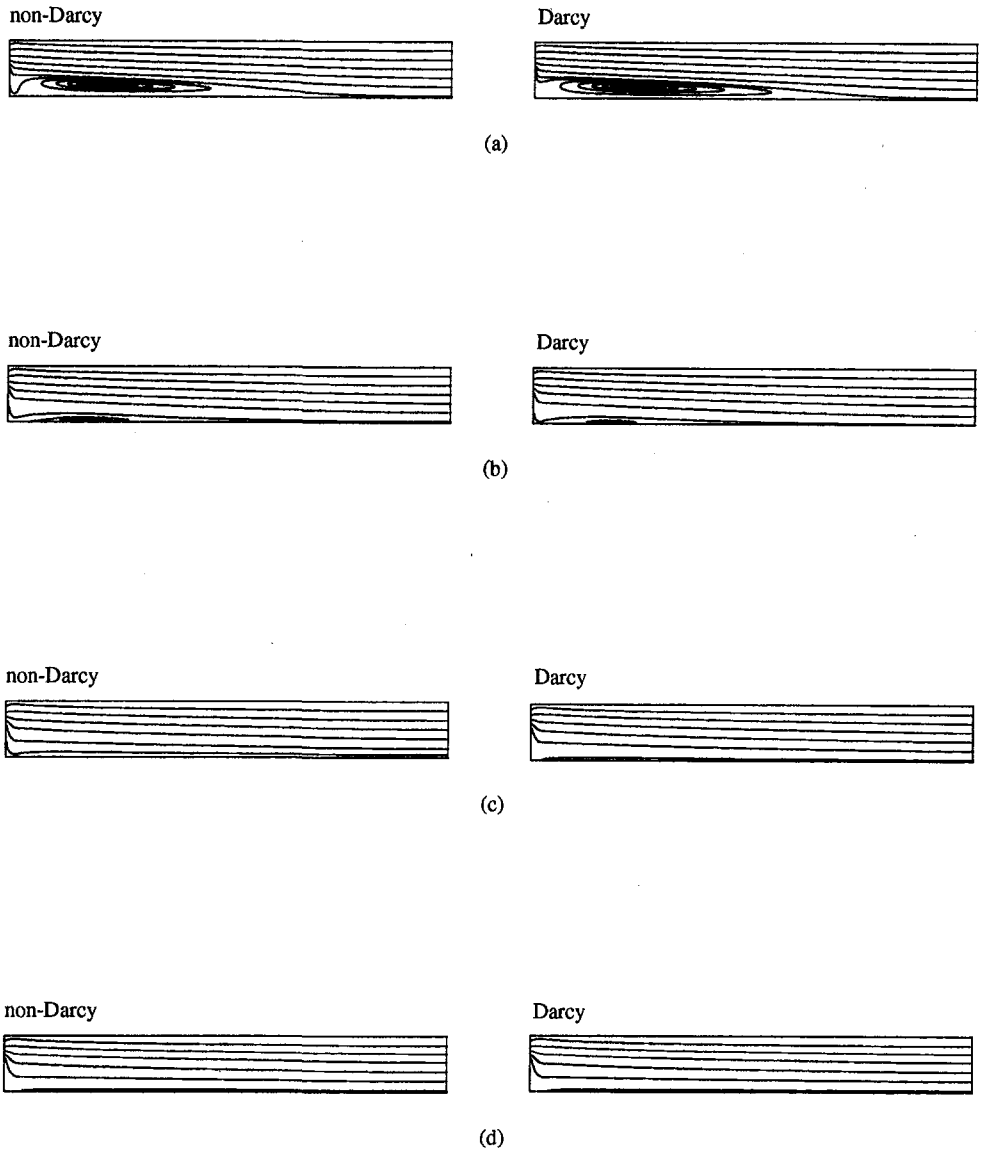

Fig. 5 Streamline plots, $\epsilon_f = 0.90$: (a) $a/H = 0.10$; (b) $a/H = 0.15$; (c) $a/H = 0.20$; (d) $a/H = 0.25$

increased, the recirculation zone is successively reduced in size and eventually disappears at the highest a/H value considered (0.25). In addition, the upper wall recirculation zone appears to have been eliminated when the fiber array insert is utilized. The general trends outlined above can be explained in terms of the local influence of the insert on the flow. As the flow moves from the inlet through the porous insert, the strong resistance to flow causes the streamwise velocity to flatten and spread across the entire duct. The velocity profile near the upper wall is affected first because of the proximity of the inlet, while the spreading of the flow toward the lower wall lags behind. This explains the lengthening of the recirculation zone for low a/H values followed by the elimination of this zone if a/H is large enough. Figure 5 illustrates the influence of a lower porosity on the downstream flow field ($\epsilon_f = 0.90$). As expected, the increased flow resistance causes the lower wall recirculation zone to decrease faster and thus disappear for a shorter segment. Again, the upper recirculation zone cannot be seen in this instance.

Another issue of importance is the influence of Darcy versus non-Darcy modeling assumptions. The previously described figures (Figs. 4 and 5) also feature streamlines for cases where Darcy flow is assumed to be valid regardless of Reynolds number. In general, the flow field is only weakly dependent on these modeling assumptions, as the non-Darcy assumption tends to compute a slightly shorter lower wall recirculation zone because of higher frictional losses. However, there is one notable exception to this trend for $a/H = 0.25$ and a porosity of 0.99 (Fig. 4(*d*)): Results from Darcy modeling show a small lower wall recirculation zone, which is not seen in the non-Darcy case. This particular combination of a/H and ϵ_f apparently lies near a transition condition, where the downstream flow field changes from recirculating to non-recirculating. As a consequence, the results show marked sensitivity to non-Darcy versus Darcy assumptions.

Quantitative effects of the porous inserts may be shown by examining the streamwise velocity profiles at various locations in the duct. Figures 6 and 7 illustrate the u velocity profiles at locations one-half and seven duct widths downstream of the step for $a/H = 0.10$ and 0.25. At $x/H = 0.5$ (Fig. 6), the flattening of the velocity profile can be seen more clearly with an increase in porosity and/or length of the porous insert. The lowest porosity case (0.90) shows a great deal of deviation from the homogeneous case regardless of the size of the insert. Slight differences can also be seen in Figs. 6 and 7 regarding the non-Darcy versus Darcy modeling assumptions, especially for higher porosities. At $x/H = 7$ (Fig. 7), the velocity profiles

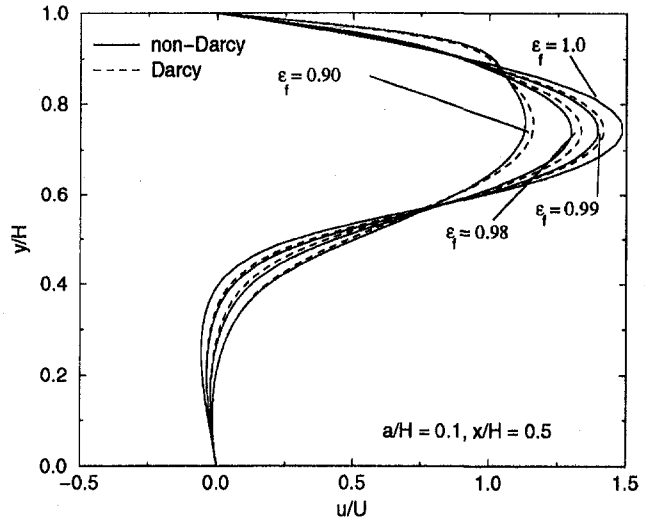

(a)

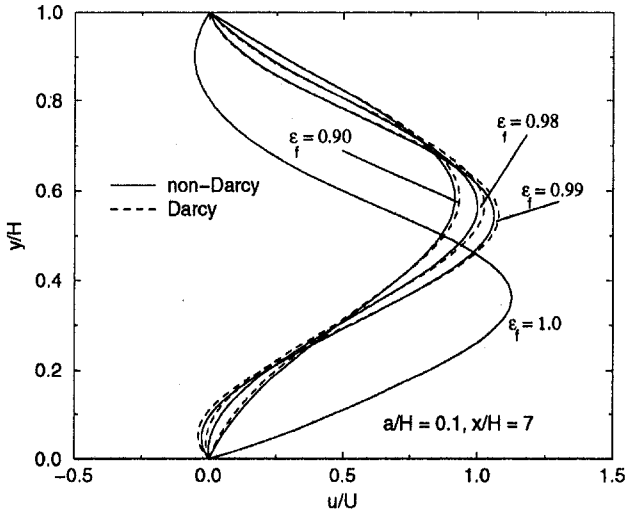

(a)

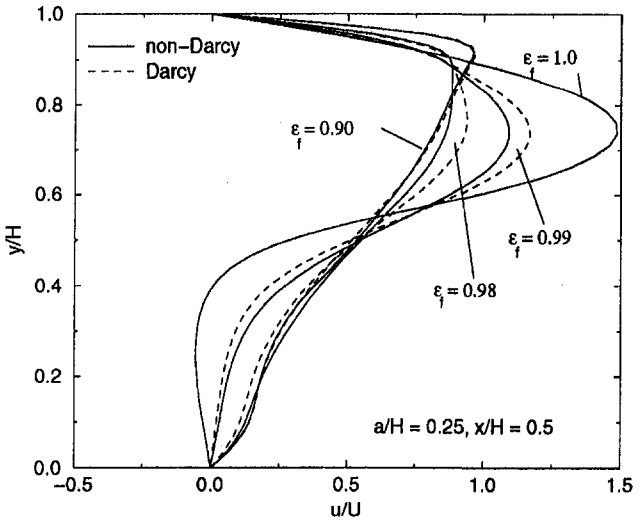

(b)

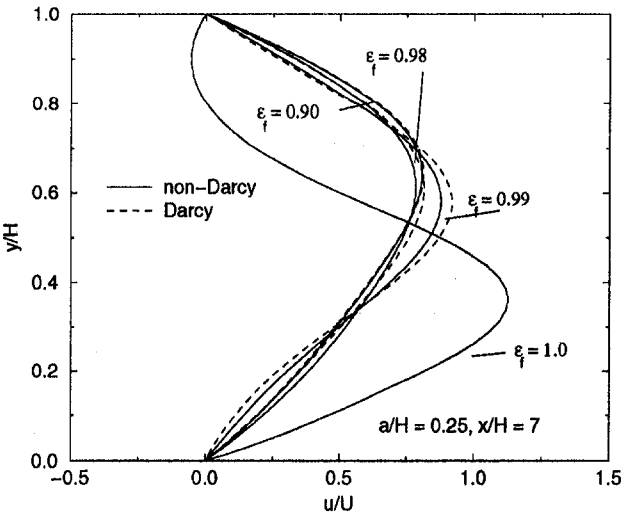

(b)

Fig. 6 Transverse coordinate versus streamwise velocity component at $x/H = 0.5$: (a) $a/H = 0.10$; (b) $a/H = 0.25$

Fig. 7 Transverse coordinate versus streamwise velocity component at $x/H = 7$: (a) $a/H = 0.10$; (b) $a/H = 0.25$

resulting from the porous insert differ greatly from the homogeneous case since the upper wall recirculation zone is no longer present. As the porosity is reduced and the insert length is expanded, the flow profile tends to approach a fully developed (parabolic) situation. Non-Darcy and Darcy results also show only slight variation. Results for $\epsilon_f = 0.92$, 0.94, and 0.96 typically lie close to $\epsilon_f = 0.90$ for a given a/H value (for sake of clarity, these cases are not depicted in the figures).

To evaluate the frictional losses resulting from the porous insert, the head loss, h_l, is calculated for the duct as follows (Fox and McDonald, 1992):

$$h_l = \left(\frac{\bar{p}_i}{\rho_f} + \alpha_i \frac{U_i^2}{2}\right) - \left(\frac{\bar{p}_o}{\rho_f} + \alpha_o \frac{U_o^2}{2}\right) \tag{25}$$

In this expression, $\bar{p}_i$ and $\bar{p}_o$ are the average inlet and outlet pressures, and α_i and α_o are the kinetic energy coefficients, defined as

$$\alpha_{i,o} = \frac{\int_{A_{i,o}} u^3 dA}{\left(\int_{A_{i,o}} u dA\right)^3} \tag{26}$$

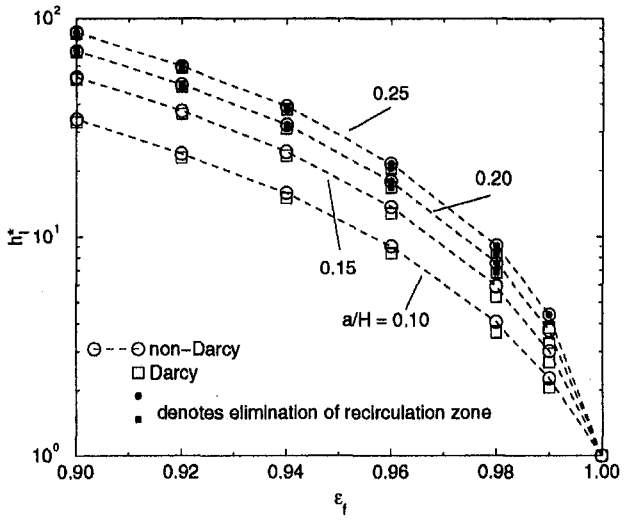

Fig. 8 Nondimensional duct head loss versus porosity

Figure 8 shows the duct head loss as a function of porosity for the various porous insert sizes (the head loss is divided by the homogeneous value to yield a dimensionless parameter, h_f^*). Frictional losses are seen to rise monotonically as the porosity is reduced, with a penalty roughly two orders of magnitude larger than the no-insert case when $\epsilon_f = 0.90$. Different combinations of a/H and ϵ_f can result in comparable head loss values, which is most evident at the high-porosity end. The minimum head loss value for elimination of the recirculation zone is about four times the homogeneous case, with $a/H = 0.25$ and $\epsilon_f = 0.99$. A comparison between the non-Darcy and Darcy modeling assumptions is also shown on the figure, with only slight differences shown.

4 Results—Heat Transfer

Heat transfer performance is shown in Fig. 9, which features the lower wall Nusselt number, Nu_w (Eq. (23)), as a function of axial location for the various configurations. For the homogeneous case, a local minimum is shown in Nu_w near the upstream edge of the recirculation zone; farther downstream, Nu_w reaches a local maximum value after reattachment. The addition of the porous insert causes significant changes in the character of Nu_w for a number of reasons. Since the insert has a large conductivity, differences between wall and bulk temperatures are small within this region, resulting in large Nu_w values. For the high-porosity case (Fig. 9(a)), the minimum value of Nu_w near the inlet decreases for $a/H = 0.10$ and 0.15 because of the extension of the lower wall recirculation zone. As a/H is increased, the recirculation zone is reduced in length and consequently the minimum value of Nu_w rises. With regard to the lowest porosity case (Fig. 8(b)), local minima can be seen near the inlet for $a/H = 0.10$ and 0.15, but not for higher a/H values since there is no recirculation for these cases. Slightly higher values of Nu_w can be seen in Fig. 9(c), which feature porosities corresponding to the maximum amount of temperature reduction (discussed subsequently). Regardless of the a/H and ϵ_f combination, the Nusselt number near the outlet asymptotically approaches the fully developed value of 4.12 (Bejan, 1995) when the porous insert is included; flattening of Nu_w at the outlet itself is due to the adiabatic boundary condition.

It is also of interest to quantify the values of maximum wall temperature with and without the porous insert. Figure 10 illustrates the nondimensionalized maximum wall temperature, T_m^*:

$$T_m^* = \frac{T_m}{T_{m,h}} \tag{27}$$

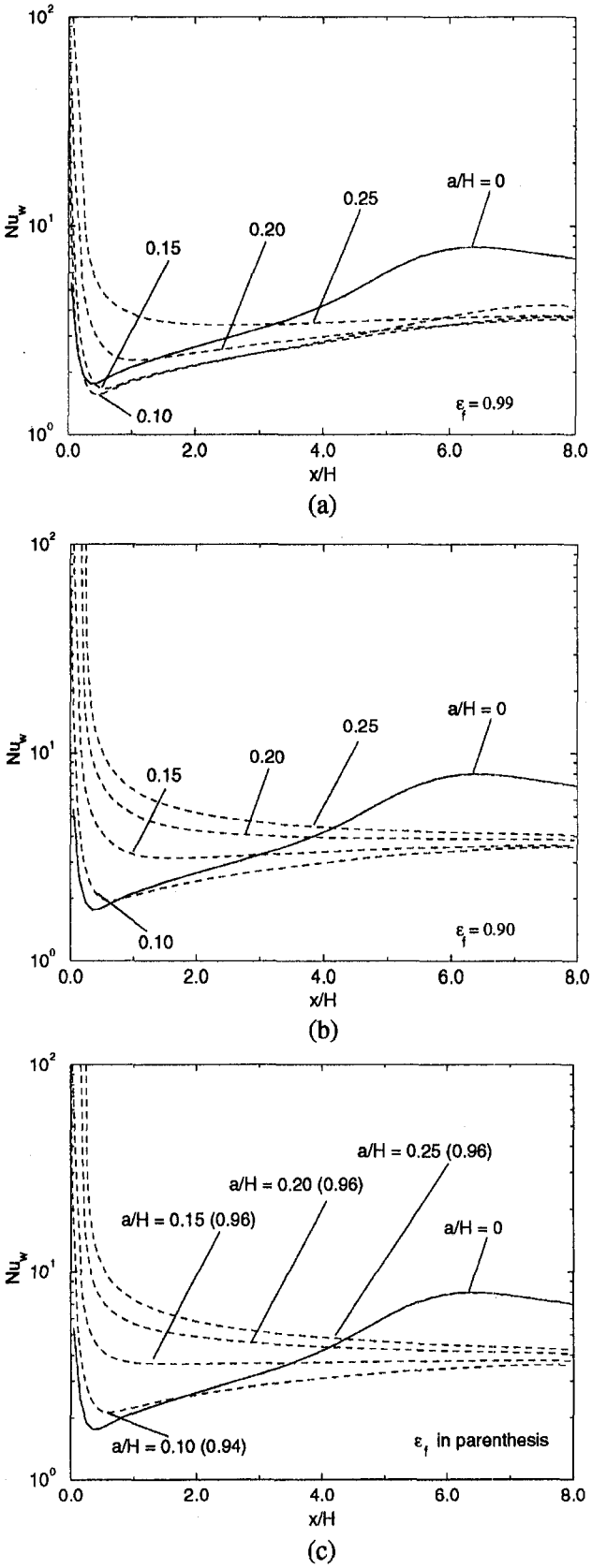

Fig. 9 Lower wall Nusselt number versus axial location (non-Darcy, non-LTE modeling assumptions): (*a*) $\epsilon_f = 0.99$; (*b*) $\epsilon_f = 0.90$; (*c*) ϵ_f selected for optimum temperature reduction

as a function of porosity ($T_{m,h}$ is the maximum wall temperature for the homogeneous case). As demonstrated in the Nusselt number findings, the porous inserts can have a detrimental im-

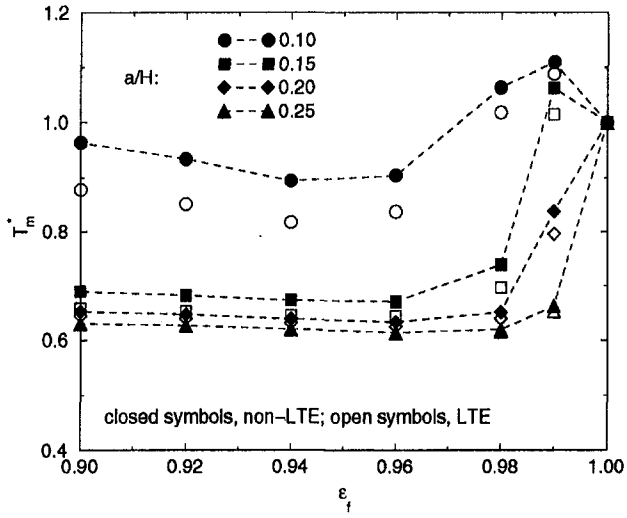

(a)

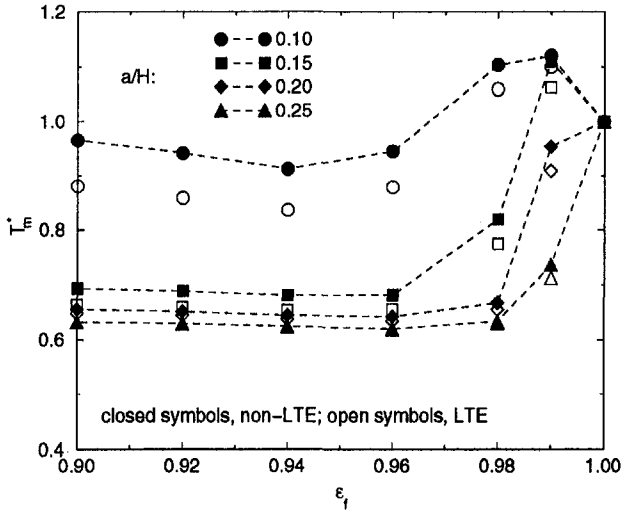

(b)

Fig. 10 Nondimensionalized maximum wall temperature versus porosity: (*a*) non-Darcy modeling assumption; (*b*) Darcy modeling assumption

pact; however, most cases show at least some reduction in wall temperature. The optimum value in temperature reduction with respect to ϵ_f is most apparent for the shorter inserts, with only slight sensitivity to porosity shown at the extreme a/H values. Nonequilibrium thermal conditions (denoted non-LTE) are shown to be important for high porosities and especially for small insert lengths. The value of T_m^* is consistently underpredicted by the LTE assumption, since this condition presumes infinite heat transfer between fluid and fibers. Comparing the non-Darcy versus Darcy flow assumptions, appreciable differences are seen primarily at the high-porosity end, where $\mathrm{Re}_{\sqrt{K}}$ is typically highest. Results shown in Fig. 10 can be combined with the head loss values shown in Fig. 8 in order to determine the most attractive combination of temperature reduction and frictional penalty. In general, the most equitable tradeoffs are favored for long, highly porous inserts, as opposed to those that are short and dense.

5 Conclusions

The use of fiber array inserts in recirculating flows has been shown to impact the downstream flow structure greatly, obviously affecting the degree of heat transfer. If the inserts are short and highly porous, the lower wall recirculation zone behind the step can be extended, resulting in poorer heat transfer performance with respect to the empty duct. On the other hand, with extension of the inserts and/or a decrease in porosity, the recirculation zone is either reduced in size or eliminated altogether. These trends illustrate the need for caution in designing porous inserts in order to prevent unwanted operating conditions from occurring. The most favorable condition of temperature reduction and head loss penalty is found for an insert of length $a/H = 0.25$ and a porosity of 0.99: The maximum wall temperature is reduced by over 30 percent, and the head loss is roughly four times higher than the no-fiber case. Beyond this porosity, only incremental wall temperature reductions are possible, accompanied by head losses that approach nearly two orders of magnitude. Non-Darcy effects are more influential at the high porosity end, and in one instance non-Darcy calculations show the disappearance of a recirculation zone, which is predicted by Darcy flow. The assumption of local thermodynamic equilibrium is valid only for long inserts, with significant differences appearing for shorter and more porous conditions. Results from this study illustrate the potential of porous inserts for heat transfer enhancement, suggesting the need for additional numerical and experimental investigations.

References

Abu-Hijleh, B., 1997, "Convection Heat Transfer From a Laminar Flow Over a 2-D Backward Facing Step With Asymmetric and Orthotropic Porous Floor Segments," *Numerical Heat Transfer, Part A,* Vol. 31, pp. 325–335.

Amiri, A., and Vafai, K., 1994, "Analysis of Dispersion Effects and Non-thermal Equilibrium, Non-Darcian, Variable Porosity Incompressible Flow Through Porous Media," *International Journal of Heat and Mass Transfer,* Vol. 37, No. 6, pp. 939–954.

Åström, B., Pipes, R., and Advani, S., 1992, "On Flow Through Aligned Fiber Beds and Its Application to Composites Processing," *Journal of Composite Materials,* Vol. 26, No. 9, pp. 1351–1373.

Bear, J., 1988, *Dynamics of Fluids in Porous Media,* Dover, New York.

Bejan, A., 1995, *Convective Heat Transfer,* 2nd ed., Wiley-Interscience, New York.

Bergles, A. E., 1985, "Techniques to Augment Heat Transfer," *Handbook of Heat Transfer Applications,* 2nd ed., J. P. Hartnett, W. M. Rosenhow, and E. N. Ganic, eds., McGraw-Hill, New York, pp. 3.1–3.80.

Cheng, P., 1978, "Heat Transfer in Geothermal Systems," *Advances in Heat Transfer,* Vol. 14, pp. 1–105.

Drummond, J., and Tahir, M., 1984, "Laminar Viscous Flow Through Regular Arrays of Parallel Solid Cylinders," *Journal of Multiphase Flow,* Vol. 10, No. 5, pp. 515–540.

Edwards, D. A., Shapiro, M., Bar-Yoseph, P., and Shapira, M., 1990, "The Influence of Reynolds Number Upon the Apparent Permeability of Spatially Periodic Arrays of Cylinders," *Physics of Fluids,* Vol. 2, No. 1, pp. 45–55.

Eidsath, A., Carbonell, R. G., Whitaker, S., and Herrmann, L. R., 1983, "Dispersion in Pulsed Systems—III: Comparison Between Theory and Experiments for Packed Beds," *Chemical Engineering Science,* Vol. 38, No. 11, pp. 1803–1816.

Ergun, S., 1952, "Fluid Flow Through Packed Columns," *Chemical Engineering Progress,* Vol. 48, No. 2, pp. 89–94.

Fox, R. W., and McDonald, A. T., 1992, *Introduction to Fluid Mechanics,* 4th ed., Wiley, New York.

Gartling, D. K., 1990, "A Test Problem for Outflow Boundary Conditions—Flow Over a Backward-Facing Step," *International Journal for Numerical Methods in Fluids,* Vol. 11, pp. 953–967.

Ghaddar, C. K., 1995, "On the Permeability of Unidirectional Fibrous Media: A Parallel Computational Approach," *Physics of Fluids,* Vol. 7, No. 11, pp. 2563–2586.

Hendricks, R. C., Braun, M. J., Canacci, V., and Mullen, R. L., 1991, "Simulation of Brush Insert for Leading-Edge-Passage Convective Heat Transfer," *Proc. Fourth International Symposium in Transport Phenomena,* Sydney.

Huang, P. C., and Vafai, K., 1994, "Analysis of Forced Convection Enhancement in a Channel Using Porous Blocks," *Journal of Thermophysics and Heat Transfer,* Vol. 8, No. 3, pp. 563–573.

Incropera, F., and DeWitt, D., 1985, *Fundamentals of Heat and Mass Transfer,* 2nd ed., Wiley, New York.

Krause, H. H., Vaughan, D. A., Cover, P. W., Boyd, W. K., and Oberacker, D. A., 1977, "Corrosion and Deposits From Combustion of Solid Waste," ASME *Journal of Engineering for Power,* Vol. 99, pp. 449–459.

Martin, A. R., Saltiel, C., and Shyy, W., 1997, "Frictional Losses and Convective Heat Transfer in Sparse, Periodic Cylinder Arrays in Cross Flow," *International Journal of Heat and Mass Transfer,* in press.

Morgan, R. V., 1975, "The Overall Convective Heat Transfer From Smooth Circular Cylinders," *Advances in Heat Transfer,* Vol. 11, pp. 199–263.

Patankar, S. V., 1980, *Numerical Heat Transfer and Fluid Flow,* Hemisphere, New York.

Sangani, A. S., and Acrivos, A., 1982, "Slow Flow Past Periodic Arrays of Cylinders With Application to Heat Transfer," *International Journal of Multiphase Flow,* Vol. 8, No. 3, pp. 193–206.

Shreir, L. L., 1976, *Corrosion,* Newnes-Butterworths, Boston.

Shyy, W., 1994, *Computational Modeling for Fluid Flow and Interfacial Transport,* Elsevier Science Publishers, Amsterdam.

Sparrow, E. M., Loeffler, A. L., and Hubbard, H. A., 1961, "Heat Transfer to Longitudinal Laminar Flow Between Cylinders," ASME JOURNAL OF HEAT TRANSFER, Vol. 83, pp. 415–422.

Sparrow, E. M., Kang, S. S., and Chuck, W., 1987, "Relation Between the Points of Flow Reattachment and Maximum Heat Transfer for Regions of Flow Separation," *International Journal of Heat and Mass Transfer,* Vol. 30, No. 7, pp. 1237–1246.

Thielsch, H., and Cone, F. M., 1994, "Corrosion in Recovery and Refuse-Fired Boilers," *Proc. 1994 International Joint Power Generation Conference,* Kansas City, MO.

Vafai, K., and Huang, P. C., 1994, "Analysis of Heat Transfer Regulation and Modification Employing Intermittently Emplaced Porous Cavities," ASME JOURNAL OF HEAT TRANSFER, Vol. 116, pp. 604–613.

Vafai, K., and Thiyagaraja, R., 1987, "Analysis of Flow and Heat Transfer at the Interface Region of a Porous Medium," *International Journal of Heat and Mass Transfer,* Vol. 30, No. 7, pp. 1391–1405.

Effects of Heat Exchanger Tube Parameters on Nucleate Pool Boiling Heat Transfer

Moon-Hyun Chun
Professor,
Department of Nuclear Engineering,
Korea Advanced Institute of
Science and Technology,
373-1, Kusong-Dong,
Yusong-Gu, Taejon 305-702, Korea
Fellow ASME

Myeong-Gie Kang
Professor,
Department of Mechanical
Engineering Education,
College of Education,
Andong National University,
388 Songchun-Dong,
Andong-City, Kyungbuk 760-749, Korea

In an effort to determine the combined effects of major parameters of heat exchanger tubes on the nucleate pool boiling heat transfer in the scaled in-containment refueling water storage tank (IRWST) of advanced light water reactors (ALWRs), a total of 1966 data points for q'' versus ΔT have been obtained using various combinations of tube diameters, surface roughness, and tube orientations. The experimental results show that: (1) increased surface roughness increases the heat transfer coefficient for both horizontal and vertical tubes, and the effect of surface roughness is more pronounced for the vertical tubes compared to the horizontal tubes, (2) the two heat transfer mechanisms, i.e., increased heat transfer due to liquid agitation by bubbles generated and reduced heat transfer by the formation of large vapor slugs and bubble coalescence, are different in two regions of low heat flux ($q'' \leq 50$ kW/m^2) and high heat flux ($q'' > 50$ kW/m^2) depending on the orientation of tubes and the degree of surface roughness, and (3) the heat transfer rate decreases as the tube diameter is increased for both horizontal and vertical tubes, but the effect of tube diameter on the nucleate pool boiling heat transfer for vertical tubes is greater than that for horizontal tubes. Two empirical heat transfer correlations for q'', one for horizontal tubes and the other for vertical tubes, are obtained in terms of surface roughness (ϵ) and tube diameter (D). In addition, a simple empirical correlation for nucleate pool boiling heat transfer coefficient (h_b) is obtained as a function of heat flux (q'') only.

Introduction

One of the key features of the passive safety systems employed in the advanced light water reactor (ALWR) designs such as the Westinghouse AP600 plant is the passive residual heat removal (PRHR) heat exchanger shown schematically in Fig. 1 (Corletti and Hochreiter, 1991). The PRHR system transfers decay heat from the reactor coolant system (RCS) to the containment by heating and boiling the water in the in-containment refueling water storage tank (IRWST) whenever the steam generators become unavailable for heat removal during normal operation, hot standby, heatup, or cooldown. The steam generated in the IRWST is condensed on the containment vessel and returned by gravity via the IRWST condensate return gutter (Westinghouse, 1992). The current version of ALWR requirements document requires the RCS temperature of 204.4°C (400°F) to be achieved in 72 hours, with or without reactor coolant pumps operating (MPR, 1991).

To determine the required heat transfer surface area as well as to evaluate the PRHR system performance during postulated accidents, an overall heat transfer coefficient applicable for the PRHR system is needed. Currently, the generalized PRHR boiling correlation developed by Corletti et al. (1990) is the only available correlation. However, the measured heat flux data obtained from the PRHR test facility, where the PRHR heat exchanger tubes are mounted vertically in a cylindrical tank, which has the prototypic height to preserve the buoyancy effects of the incontainment refueling water storage tank (IRWST), is one order of magnitude lower than conventional nucleate pool boiling heat transfer correlations summarized in Table 1. For example, the heat flux value calculated by the generalized PRHR boiling correlation of Corletti et al. (1990), $C_{sf} = 0.034$, is less than one-tenth of the value predicted by the Rohsenow correlation (1952), $C_{sf} = 0.013$.

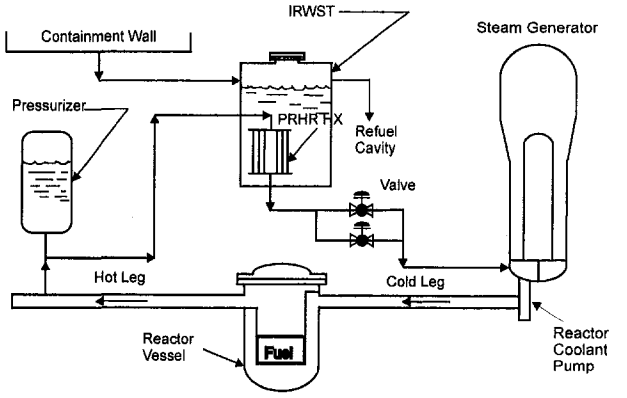

Fig. 1 Passive residual heat removal (PRHR) system for advanced light water reactors

Many workers in the past two generations have investigated the effects of the diameter (van Stralen and Sluyter, 1969; Cornwell et al., 1982; Cornwell and Houston, 1994), the orientation of heated surface (van Stralen and Sluyter, 1969; Jakob and Hawkins, 1957), and the surface roughness (Vachon et al., 1968; Chowdhury and Winterton, 1985; Nishikawa and Fujita, 1982; Cooper, 1984) on nucleate pool boiling heat transfer along with the effects of pressure and fluid properties. Earlier workers have generally found that a decrease in tube diameter and an increase in surface roughness give better heat transfer at a given superheat. Also, van Stralen and Sluyter (1969) have found that, in general, the heat flux on horizontal wires in pure liquids exceeds the value on vertical wires. However, there

Contributed by the Heat Transfer Division and presented at the 3rd ASME/JSME International Conference on Nuclear Engineering IV, New Orleans, Louisiana, March 10–13, 1996. Manuscript received by the Heat Transfer Division October 24, 1996; revision received February 23, 1998. Keywords: Boiling, Heat Exchangers, Phase-Change Phenomena. Associate Technical Editor: M. D. Kelleher.

Table 1 Conventional nucleate pool boiling heat transfer correlations and major parameters included

Author	Correlations	Key Parameters	Remarks
Rohsenow (1952)	$q'' = \mu_f h_{fg}\left[\frac{g(\rho_f-\rho_g)}{\sigma}\right]^{\frac{1}{2}}\left(\frac{c_{pf}\Delta T}{h_{fg}Pr_f^{s}C_{sf}}\right)^3$ (a) C_{sf} = coeff. of Eq.(a)	o Pressure o Fluid-heating surface combination	o C_{sf} = surface-fluid constant - It depends on both the surface and the fluid - Typical values ; 0.0025~0.015
Jakob and Hawkins (1957)	Horizontal : $h_b = 1042\Delta T^{1/3}$ (for $q'' < 16$ kw/m^2) (b) $h_b = 5.56\Delta T^3$ (for $16 < q'' < 240$ kw/m^2) (c) Vertical : $h_b = 537\Delta T^{1/7}$ (for $q'' < 3$ kw/m^2) (d) $h_b = 7.96\Delta T^3$ (for $3 < q'' < 63$ kw/m^2) (e)	o Surface orientation	o ΔT = (Heating Surface Temp. - Saturation Temp.) o h_b = in W/m^2-K o Fluid ; water o Pressure ; 0.1 MPa
Cornwell et al. (1982)	$Nu_b = C_{tb}Re_b^{2/3}$ (f) where, $Nu_b = \frac{h_b D}{k_f}$ and $Re_b = \frac{q''}{h_{fg}}\frac{D}{\mu_f}$ (tube boiling Reynolds (f) number) (C_{tb} = a constant dependent on the surface, fluid and pressure. 100 for water)	o Diameter	o Fluid ; water, refrigerants, and organics o Pressure ; $p < 0.1\ p_c$ o Tube diameter ; 6-32 mm o Surface ; commercial finish o Accuracy ; ±33 %
Cooper (1984)	Copper plate or Stainless Steel cylinders ; $h_b = 55p_R^{(0.12-0.2\log_{10}\varepsilon)}(-\log_{10}p_R)^{-0.55}M^{-0.5}q''^{\,0.67}$ (g) Copper cylinders ; $h_b = 93.5p_R^{(0.12-0.2\log_{10}\varepsilon)}(-\log_{10}p_R)^{-0.55}M^{-0.5}q''^{\,0.67}$ (h) p_R=reduced pressure, M=molecular weight; ε =surface roughness in microns	o Surface roughness o Liquid property	o Orientation ; horizontal
Cornwell and Houston (1994)	$Nu_b = CF(p)Re_b^{0.67}Pr^{0.4}$; $C = 9.7p_c$ (i) $F(p) = 1.8p_R^{0.17} + 4p_R^{1.2} + 10p_R^{10}$, $p_R = p/p_c$ (j)	o Diameter o General correlation	o Orientation ; horizontal o Fluid ; water, refrigerants, and organics o Pressure ; 0.001~0.8 p_c o Heat Flux ; 0.1~0.8 q_c'' o Diameter ; 8-50 mm o Surface ; machined or drawn
Corletti et al. (1990)	$q'' = \mu_f h_{fg}\left[\frac{g(\rho_f-\rho_g)}{\sigma}\right]^{\frac{1}{2}}\left(\frac{c_{pf}\Delta T}{h_{fg}Pr_f^{s}C_{sf}}\right)^3$ (k) C_{sf} = 0.034	o Pressure o Fluid-heating surface combination	o AP600 PRHR HX modeling o Three vertical tubes of 38.1 mm pitch o Fluid ; water at atmospheric pressure o Tube diameter ; 19.05 mm
Present Correlation	Horizontal : $q_H'' = 0.015\varepsilon^{0.084}\Delta T^{5.508}/D^{1.318}$ (5a) Vertical : $q_V'' = 0.024\varepsilon^{0.672}\Delta T^{4.862}/D^{1.656}$ (6a) Simple form : $h_b = 0.266\ (q'')^{0.812}$ (9)	o Diameter o Surface roughness o Surface orientation	o Fluid ; water o Pressure ; 0.1 MPa o Heat flux ; $0 < q'' < 160$ kW/m^2 o Tube diameter ; 9.7-25.4 mm o Surface roughness ; 15.1~60.9 nm o Accuracy ; +25 %, -25 %

seem to be some inconsistencies in their results. For example, Vachon's polished surface data (1968) suggest that a maximum in nucleate boiling heat transfer may be reached with a certain surface roughness for unidirectionally polished surface. In addition, according to Jakob and Hawkins nucleate boiling correlation (1957) the heat transfer coefficient of vertical heating surface is larger than that of horizontal heating surfaces, as opposed to the results of van Stralen and Sluyter (1969).

In an effort to investigate the potential areas for improvement of the thermal design of the PRHR system of ALWRs and to resolve the inconsistencies of the previous work by others, an experimental parametric study of a tubular heat exchanger has been performed under nucleate pool boiling conditions. That is, the present study is aimed at the determination of the combined effects of tube diameter, surface roughness, and tube orientation (horizontal and vertical) on the nucleate pool boiling heat trans-

Nomenclature

A = heat transfer area, m^2
C_p = specific heat, J/kg-K
C_1 = empirical constant between q'' and geometric parameters
C_2 = empirical constant to express surface roughness effect
C_3 = empirical constant to express wall superheat effect
C_4 = empirical constant to express tube diameter effect
C_5 = empirical constant between h_b and q''
C_6 = empirical constant to express heat flux effect
C_{sf} = empirical constant to express effects of liquid and heating surface combination in Rohsenow's correlation
C_{tb} = empirical constant to express surface roughness effect in Cornwell's correlation
D = tube outer diameter, m or mm
E = supplied voltage, V
h_b = boiling heat transfer coefficient, kW/m^2-K
h_{fg} = enthalpy of vaporization, J/kg
I = supplied current, A
k = thermal conductivity, W/m-K
L = tube length, m
Nu = Nusselt number
Pr = Prandtl number
p = liquid pressure, Pa
p_R = reduced pressure
q'' = heat flux, kW/m^2
q = total heat transfer, kW
Re = Reynolds number
T = temperature, K
ΔT = degree of superheat of the heating surface = $T_w - T_{sat}$, K
ϵ = average tube surface roughness in rms value, nm
μ = viscosity, kg/m-s
ρ = density, kg/m^3
σ = surface tension of liquid–vapor interface, N/m

Subscripts

b = boiling heat transfer
corr = correlation
exp = experiment
f = fluid
g = vapor
H = horizontal tube
sat = saturation state
t = tube
V = vertical tube
w = tube surface

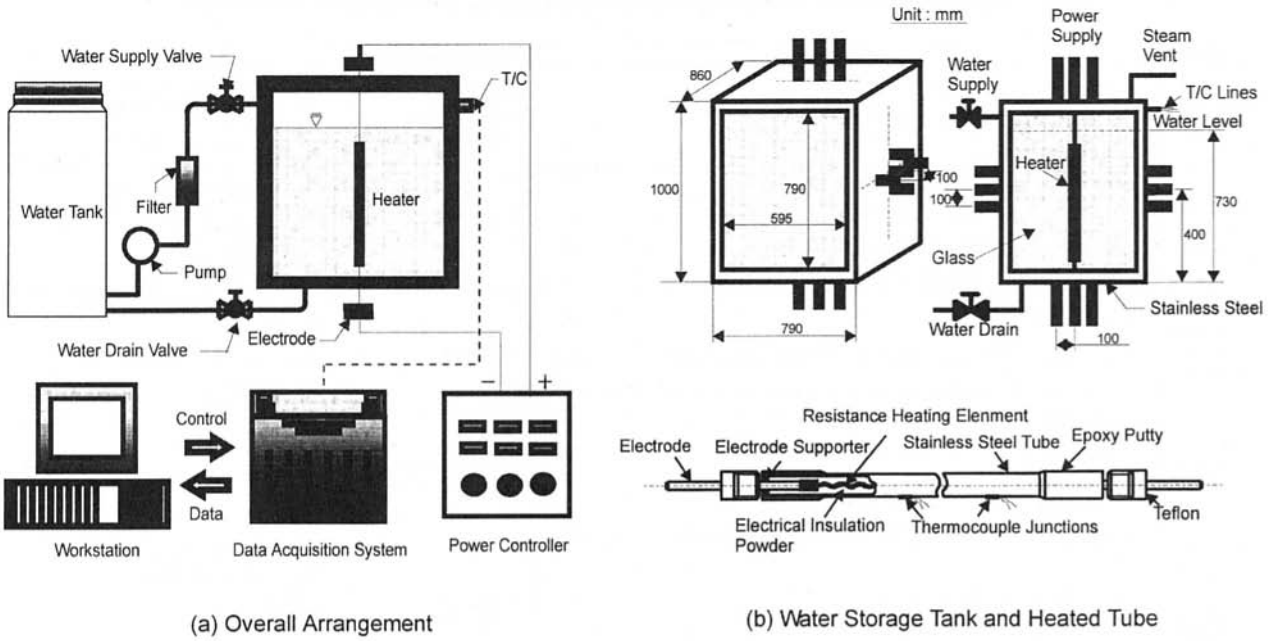

Fig. 2 Schematic diagram of experimental apparatus

fer. As a result, new empirical heat transfer correlations, one for horizontal heat exchanger tubes and the other for vertical heat exchanger tubes, in terms of major heat exchanger tube parameters and the tube wall superheat have been obtained. Because of the limited practical applicability of these correlations, however, a simple empirical correlation for nucleate pool boiling heat transfer coefficient h_b in terms of only q'' has also been presented here.

Experimental Apparatus and Procedure

A schematic view of the present experimental apparatus is shown in Fig. 2. The experimental apparatus essentially consists of a scaled ($\frac{1}{10}$th in length) IRWST (i.e., a water tank), three heat exchanger tubes shown in Fig. 2(b), water and power supply systems, and associated data acquisition system to measure the temperatures of tube surfaces and the water in the IRWST.

Two major scaling parameters for the AP600 PRHR system are (1) the heat flux on the tube surface and (2) the water volume of the tank (i.e., IRWST) per unit core decay power. The heat flux that corresponds to 2 percent of the core decay power is 101.2 kW/m^2, and the water volume per unit decay power is 0.05 m^3/kW. A comparison between the prototype (Corletti et al., 1990; van de Venne, 1992) of the IRWST and the scaled model is given in Table 2. The IRWST model (i.e., water tank) is made of stainless steel and has a rectangular cross section (790 × 860 mm) and a height of 1000 mm. This tank has a glass view port (595 × 790 mm), which permits viewing of the tubes and photographing. The heat exchanger tubes are simulated by resistance heaters made of stainless steel tubes whose heating length is 530.5 mm. To measure the surface temperatures of the heat exchanger, one of the three heat exchanger tubes was instrumented with five thermocouples outside the surface of the tube. The thermocouple tip (about 10 mm) has been bent at a 90 deg angle and brazed the bent tip on the tube wall. The thermocouple diameter is 1.5 mm. The first and the fifth thermocouples are placed at 115.25 mm from both ends of the heating element; the space between other thermocouples is 75 mm.

For vertical tube tests, the heat exchanger tubes are placed at 80 mm from the tank bottom and 290 mm from both sides. In horizontal tube tests, on the other hand, the tubes are situated at 400 mm from the tank bottom and 130 mm from both sides. The space between the heaters (i.e., pitch) is 100 mm for both cases and is not a major scaling factor for the present. There is no particular reason for using this spacing since the spacing between heaters is not used as a major test parameter in the present work.

To determine the combined effects of the major test parameters of the heat exchanger tube on the nucleate pool boiling heat transfer in the scaled IRWST, four different diameters (ranging from 9.7 mm to 25.4 mm), three different surface roughness (15.1, 26.2, and 60.9 nm in rms measured by the phase measuring interferometer as given in Table 3), and two different orientations of heat exchanger tubes (horizontal and vertical) are used to obtain the heat flux (q'') versus wall superheat ($\Delta T = T_w - T_{sat}$) data for various combinations of test parameters as summarized in Table 4. The three surface roughness of the heating tubes were obtained by polishing unidirectionally with three different grain size sand papers (#800, #2000, and #3000). The uncertainty (errors from measurement, instruments, and environmental conditions) in the heat flux, temperature, and surface roughness are estimated to be ±1.0 percent, ±1.0 percent, and ±5.0 nm, respectively.

The scaled tank is filled with water until the initial water level is reached at 730 mm. The water is then boiled for 30 minutes at saturation temperature to remove the air. The temper-

Table 2 Comparison between prototype (AP600 PRHRS) and experimental apparatus

Item	Prototype (P)	Scaled Model (M)	Ratio (M/P)
HX Tube Length, m	5.49	0.5305	1/10
Heat Transfer Area, m^2	382	0.0935	1/4000
Water Volume, m^3	1935	0.48375	1/4000
Power (2%), kWt	38660	9.665	1/4000
Heat Flux, kW/m^2	101.2	101.2	1/1
Water Volume per Unit Power, m^3/kW	0.05	0.05	1/1

Table 3 Values of tube surface roughness measured by phase measuring interferometer

Test Section (Sand Paper)	Grain Size, μm	rms Surface Roughness, nm		
		Circumferential	Axial	Average
# 800	31.75	70.3	51.5	60.9
# 2000	12.70	30.6	21.8	26.2
# 3000	8.47	17.2	13.0	15.1

Table 4 Test matrix and experimental q'' versus ΔT data for correlation development

Test	Heated Tube					Water Level (mm)	Heat Flux Range (kW/m²)	Number of Thermocouples		Number of Data
	Number of Tubes	Tube Orientation	D (mm)	ε (nm)	L (mm)			Water	Tube	
Nucleate Pool Boiling Heat Transfer Tests	1	H	19.05	60.9	530.5	730	0-160	5	5	373
	2	H	19.05	60.9	530.5	730	0-160	5	5	
	3	H	19.05	60.9	530.5	730	0-160	5	5	
	1	V	19.05	60.9	530.5	730	0-160	5	5	131
	1	H	19.05	26.2	530.5	730	0-160	5	5	121
	1	V	19.05	26.2	530.5	730	0-160	5	5	147
	1	H	19.05	15.1	530.5	730	0-160	5	5	85
	1	V	19.05	15.1	530.5	730	0-160	5	5	121
	1	H	9.7	60.9	300.0	730	0-80	5	3	90
	1	V	9.7	60.9	300.0	730	0-80	5	3	76
	1	H	9.7	15.1	300.0	730	0-80	5	3	63
	1	V	9.7	15.1	300.0	730	0-80	5	3	87
	1	H	14.0	60.9	300.0	730	0-90	5	3	116
	1	V	14.0	60.9	300.0	730	0-90	5	3	121
	1	H	25.4	60.9	300.0	730	0-110	5	3	148
	1	V	25.4	60.9	300.0	730	0-110	5	3	123
	1	H	25.4	15.1	300.0	730	0-110	5	3	80
	1	V	25.4	15.1	300.0	730	0-110	5	3	84

o q'' versus ΔT test data with Horizontal Tube (H) = 1076 points
o q'' versus ΔT test data with Vertical Tube (V) = 890 points
o Total Number of q'' versus ΔT test data = 1966 points

atures of the water and heater surfaces are measured while the heater power is set at constant value. However, once the water temperature is reached at saturation value (i.e., 100°C since all the tests are run at atmospheric pressure condition), the temperatures of the water and tube surfaces are measured when they are at steady state while controlling the heat flux on the tube surface with input power. In this manner a series of experiments has been performed for various combinations of test parameters.

The heat flux from the electrically heated tube surface is calculated from the measured values of the power input as follows:

$$q'' = \frac{q}{A} = \frac{EI}{\pi DL} = h_b(T_w - T_{sat}) = h_b\Delta T \qquad (1)$$

where E and I are the supplied voltage (in volt) and current (in ampere), and D and L are the outside diameter and the length of the heated tube, respectively. The tube surface temperature T_w used in Eq. (1), on the other hand, is the arithmetic average value of the temperatures measured by five thermocouples brazed on the tube surface.

Correlations of Experimental Data

As summarized in Table 4, a total of 1966 data (1076 with horizontal tubes and 890 with vertical tubes) has been obtained for heat flux (q'') versus wall superheat (ΔT) for various combinations of the diameter, surface roughness, and tube orientation. In Figs. 3–7 the experimental results for nucleate pool boiling heat transfer are plotted as the heat flux (q'') versus wall superheat (ΔT) using the diameter, the surface roughness, and the orientation of heated tubes as major test parameters.

A close review of the literature on the nucleate pool boiling heat transfer has revealed the following facts:

1 It is not realistic to obtain any general theoretical correlation for heat transfer coefficients in nucleate boiling. This is because the boiling occurs at nucleation sites, and the number of sites is very dependent upon: (a) the physical condition and preparation of the surface; and (b) how well the liquid wets the surface and how efficiently the liquid displaces air from the cavities (Whalley, 1987).

2 For a given fluid on a surface of given roughness, at constant pressure an empirical correlation may be developed in the following form (Cooper, 1984):

$$h_b \propto (q/A)^n \qquad (2)$$

3 Two practical approaches to developing nucleate boiling heat transfer correlation are possible: The first approach is to take account of both the effects of the surface roughness and the diameter of the heat exchanger tube. The second approach is to ignore both effects and develop a correlation that gives a typical boiling heat transfer coefficient at the particular heat flux for the fluid since the surface effects are often very difficult to define quantitatively.

Using the first and second approaches, simple correlations are sought in the following form:

$$q'' = C_1\epsilon^{C_2}\Delta T^{C_3}D^{C_4} \qquad (3)$$

$$h_b = C_5(q'')^{C_6} \qquad (4)$$

As a result, two empirical correlations, one for vertical tubes and the other for horizontal tubes, have been obtained using the present experimental data and the statistical analysis system (SAS) computer program (which uses the least-square methods as a regression technique) as follows:

$$q''_H = 0.015\epsilon^{0.084}\Delta T^{5.508}/D^{1.318} \quad \text{(for horizontal tubes)} \qquad (5a)$$

$$h_{bH} = 0.015\epsilon^{0.084}\Delta T^{4.508}/D^{1.318} \quad \text{(for horizontal tubes)} \qquad (5b)$$

$$q''_V = 0.024\epsilon^{0.672}\Delta T^{4.862}/D^{1.656} \quad \text{(for vertical tubes)} \qquad (6a)$$

$$h_{bV} = 0.024\epsilon^{0.672}\Delta T^{3.862}/D^{1.656} \quad \text{(for vertical tubes)} \qquad (6b)$$

From visual observations of boiling behavior and also from the analysis of the present experimental data, it has been confirmed that the effectiveness of two competing heat transfer mechanisms (i.e., increased heat transfer due to liquid agitation by bubbles generated and reduced heat transfer by the formation of large vapor slugs and bubble coalescence) is different in two regions of low heat fluxes and high heat fluxes depending on the degree of surface roughness and the tube orientation. Therefore, two empirical heat transfer correlations are derived for two different regions of heat flux to fit the present experimental data more closely and for convenience in discussion as follows:

For low heat flux region ($q'' \le 50$ kW/m²):

$$q''_H = 0.006\epsilon^{0.490}\Delta T^{5.116}/D^{1.318} \quad \text{(for horizontal tube)} \qquad (7a)$$

$$q''_V = 0.002\epsilon^{0.910}\Delta T^{5.600}/D^{1.656} \quad \text{(for vertical tube)} \qquad (7b)$$

For high heat flux region ($q'' > 50$ kW/m²):

$$q''_H = 0.054\epsilon^{0.086}\Delta T^{4.962}/D^{1.318} \quad \text{(for horizontal tube)} \qquad (8a)$$

$$q''_V = 0.031\epsilon^{0.640}\Delta T^{4.780}/D^{1.656} \quad \text{(for vertical tube)} \qquad (8b)$$

These correlations alone, however, may be of no use for general application unless the surface roughness ϵ(in nm) of the tubes in question is either given or a priori known. Therefore, using the second approach, another simple correlation has been obtained as follows:

$$h_b = 0.266(q'')^{0.812} \qquad (9)$$

In these equations, Eqs. (2)–(9), the dimensions for D, h, q'', ΔT, and ϵ are mm, kW/m²-K, kW/m², K, and nm (i.e., nanometer), respectively.

Predictions made by these correlations are shown by solid lines and compared with experimental data from Figs. 3–5. To show the degree of data spread, the mean and standard deviations of the error of the empirical equations represented by Eqs. (5)–(9) are given in Table 5.

Summary of Parametric Effects and Discussion

Figures 3(a) and 3(b) are q'' versus ΔT curves for a given tube diameter when the tube surface roughness is used as a major test parameter. In these figures the following observations can be made:

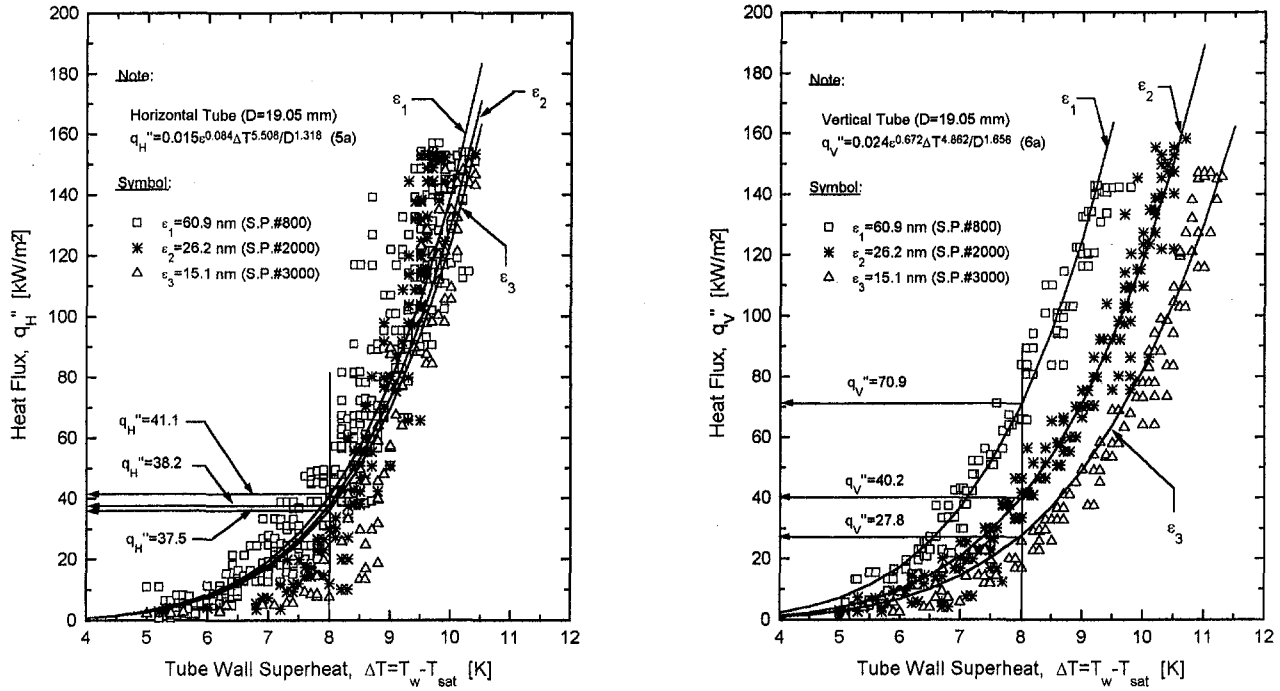

Fig. 3 Heat flux versus wall superheat for various surface roughness with different tube orientation

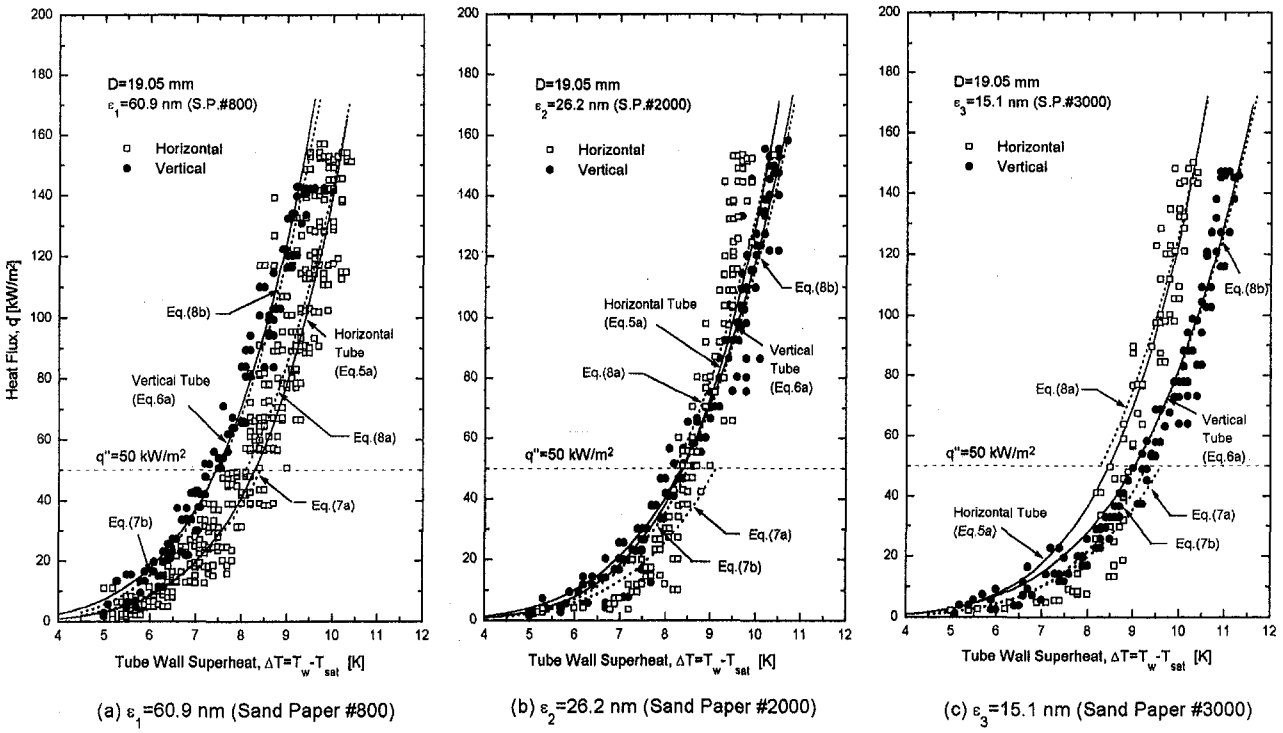

Fig. 4 Heat flux versus wall superheat for three different roughnesses with different tube orientation

1 Increased surface roughness gives better heat transfer at a given superheat for both horizontal and vertical tubes, which is in general agreement with previous investigators (Vachon et al., 1968; Chowdhury and Winterton, 1985; Nishikawa and Fujita, 1982; Cooper, 1984). As noted by earlier workers, the main reason for the increase of heat transfer in rough surface is because the rough surface usually has more cavities over a wide range of radius than the smooth surface has, while the nucleate boiling heat transfer coefficient depends on the nucleation site density.

2 Figure 3(a) shows that the effect of surface roughness on the nucleate boiling heat transfer for horizontal tubes is very small. For example, q_H'' increases only 9.6 percent (from 37.5 to 41.1 kW/m^2) when ϵ is increased by 300 percent (from 15.1 to 60.9 nm) according to Eq. (5a) at the given wall superheat (ΔT = 8 K) and the tube diameter (D = 19.05 mm). For

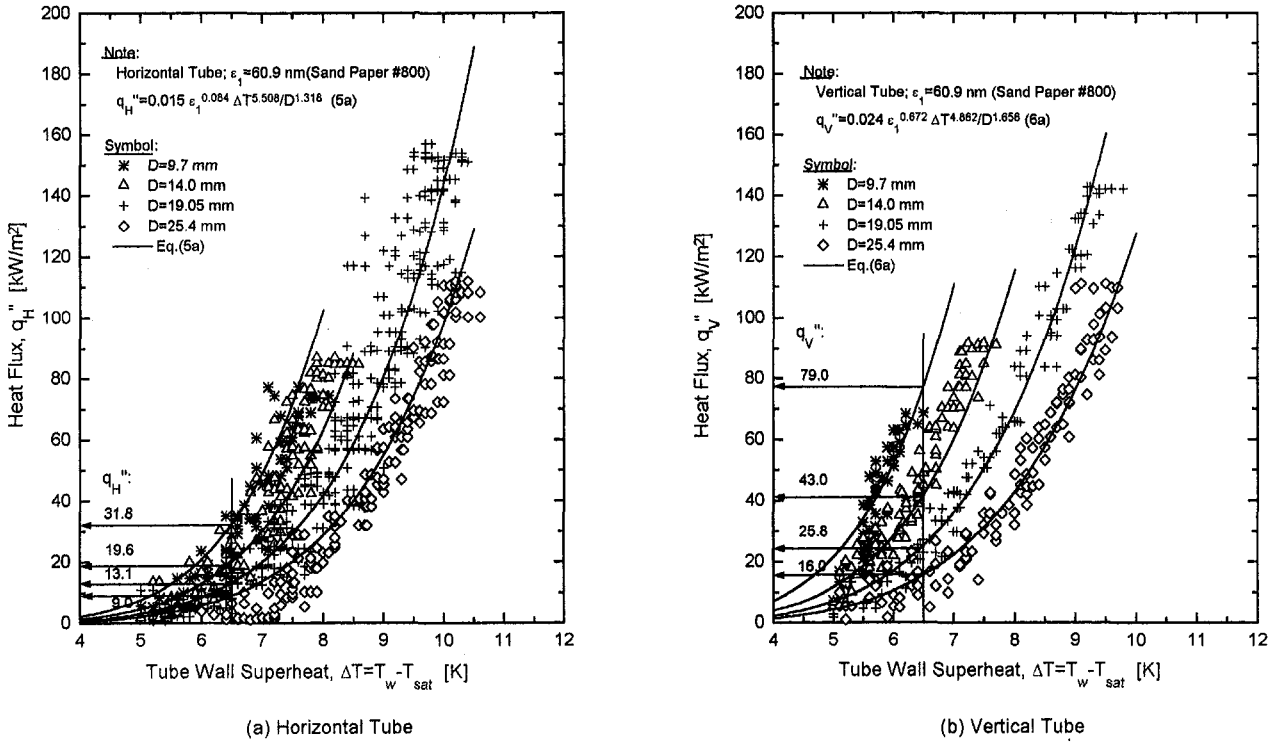

(a) Horizontal Tube (b) Vertical Tube

Fig. 5 Heat flux versus wall superheat for various tube diameters with different tube orientation

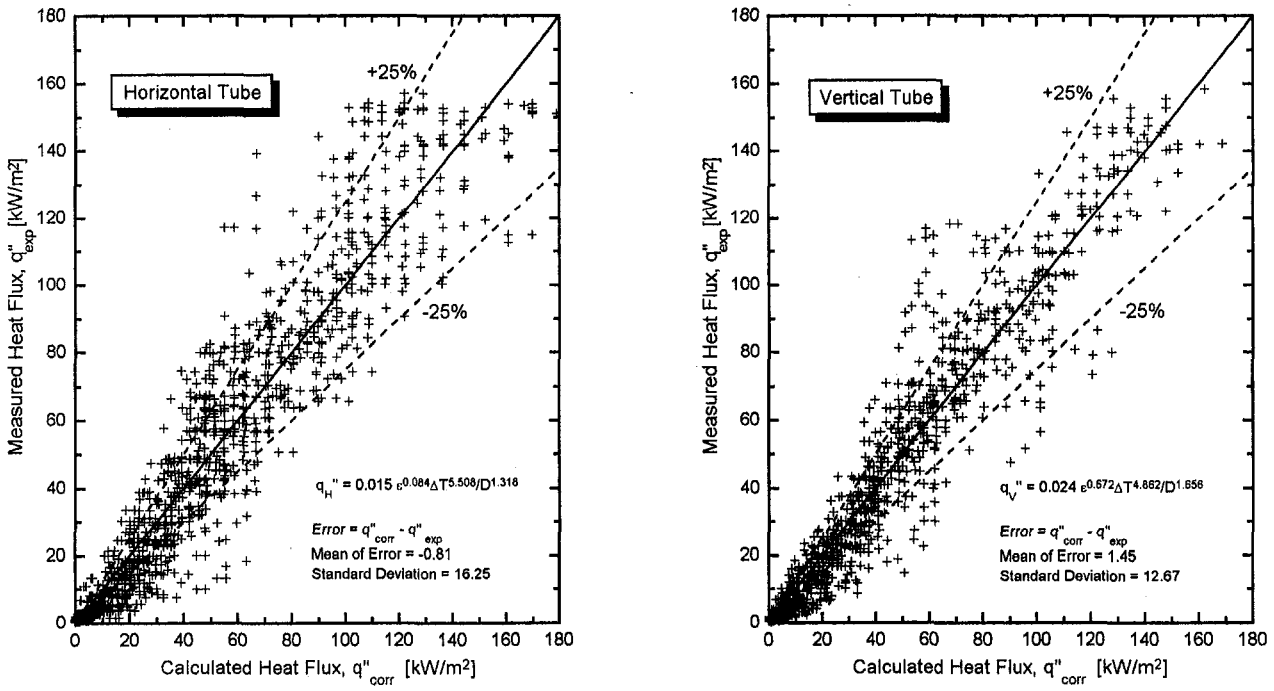

(a) Horizontal Tube (b) Vertical Tube

Fig. 6 Measured heat flux (q''_{exp}) versus calculated heat flux (q''_{corr}) for both horizontal and vertical tubes

vertical tubes, on the other hand, Fig. 3(*b*) shows that the effect of surface roughness on the nucleate boiling heat transfer is significantly larger than that for horizontal tubes. According to Eq. (6*a*), q''_V increases more than 150 percent (from 27.8 to 70.9 kW/m^2) under the same conditions used for horizontal tubes. In summary, Figs. 3(*a*) and 3(*b*) show that the vertical tubes are more sensitive to changes in roughness than are the horizontal tubes. The reason for this is partly because the number of bubble slug formation and the bubble residence time on the tube surface increase more rapidly for vertical tubes with rougher surfaces than for horizontal tubes and hence more sensitive to changes in roughness for vertical tubes. Another possible

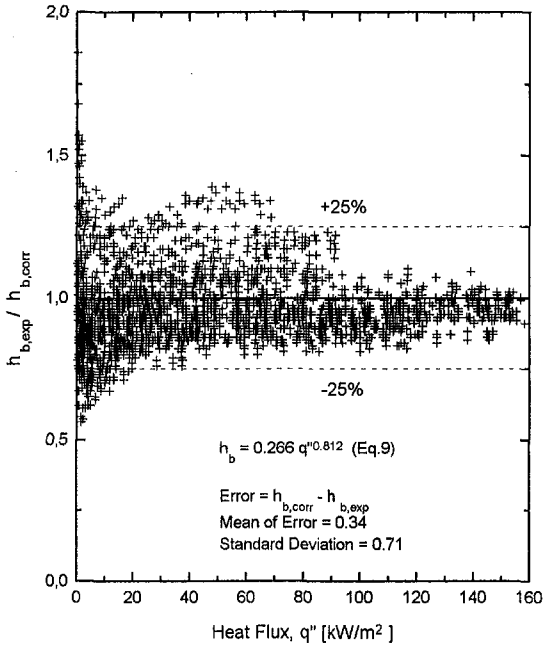

Fig. 7 Ratio of measured heat transfer coefficient ($h_{b,exp}$) to calculated heat transfer coefficient ($h_{b,corr}$) versus heat flux

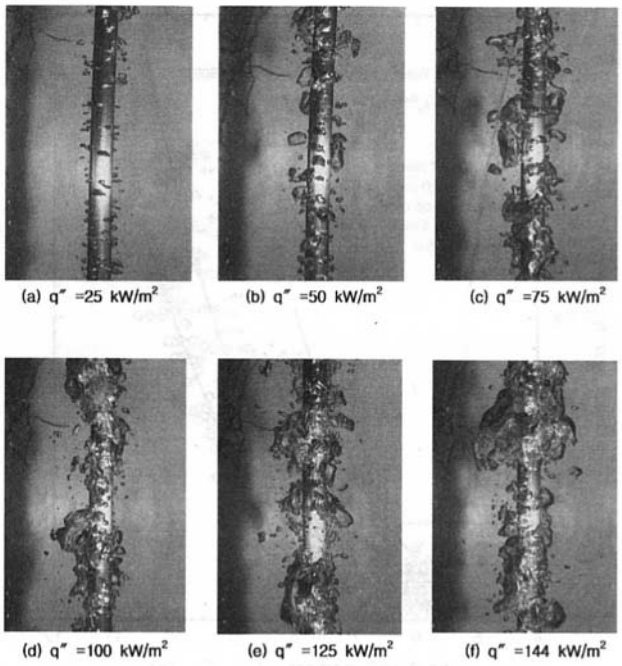

Photo 2 Bubble generation and coalescence on the vertical heated tube surface (D = 19.05 mm, ϵ = 60.9 nm) for various heat fluxes

explanation is that in vertical flow, there is stronger induced convective flow compared to the horizontal tubes, which could act to suppress boiling. Rougher surfaces would provide additional nucleation sites, which could counter the effects of the convective flow and hence show a greater sensitivity.

To examine the combined effects of tube orientation and surface roughness on nucleate pool boiling, q'' versus ΔT data obtained from the tests with horizontal and vertical tubes (for a given tube diameter D = 19.05 mm) are plotted in Fig. 4 for three different surface roughnesses. It is particularly interesting to note that the slope of q'' versus ΔT curve of the vertical tube becomes smaller than that of the horizontal tube as the surface roughness decreases from ϵ = 60.9 to ϵ = 15.1 nm. That is, when the surface roughness is ϵ = 26.2 nm, the slopes of two q'' versus ΔT curves shown in Fig. 4(b) shift and cross each other at about ΔT = 8.4 K and q'' = 50.0 kW/m^2. The reason for this may be attributable to the following phenomena:

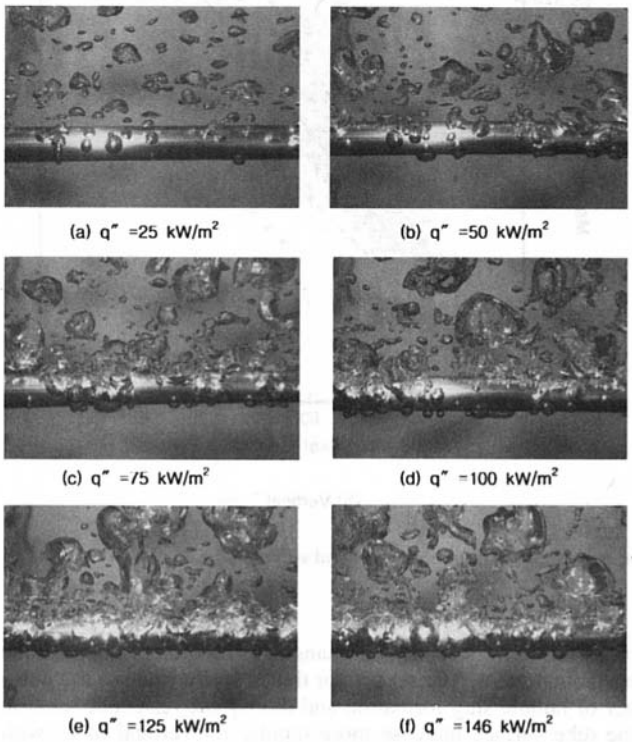

Photo 1 Bubble generation and coalescence on the horizontal heated tube surface (D = 19.05 mm, ϵ = 60.9 nm) for various heat fluxes

1 From visual observations (shown in Photos 1 and 2), the relationship between the combined effects of the orientation and the surface roughness of the tube and the heat transfer mechanisms in nucleate boiling region is first inferred as follows: There seem to be two competing effects on the nucleate boiling heat transfer. One is the effect of liquid agitation by bubbles generated on the surface, which increases heat transfer rate, and the other is the effect of bubble coalescence and the formation of large vapor slugs in the high heat flux region (e.g., $q'' > 50$ kW/m^2) in particular, which reduces heat transfer from the tube surface.

2 For vertical tubes, particularly in the high-heat-flux region ($q'' > 50$ kW/m^2), the coalescing bubbles originate from nuclei, which are distributed over the entire heating surface as noted by earlier workers (van Stralen and Sluyter, 1969). For horizontal tubes, on the other hand, bubble coalescence is generally limited to only part of the upper surface, while the lower half is almost entirely free from large bubbles or bubble coalescence. Therefore, the horizontal tube increases nucleate boiling heat transfer much more than the vertical tube, particularly in the high heat flux region and when the surface is smoother (e.g., $\epsilon < 26.2$ nm). For vertical tubes with smooth surface ($\epsilon < 26.2$ nm), the effect of reductions in the effective heat transfer area and in the number of active nucleation sites due to the bubble

Table 5 Mean and standard deviations of the error obtained by Eqs. (5a)–(6)

Equation Number	5a	6a	7a	7b	8a	8b	9
Mean of Error*	-0.81	1.45	0.13	-0.50	-2.26	-5.70	0.34
Standard Deviation of the Error	16.25	12.67	8.27	6.21	18.08	16.32	0.71

* Error = Calculated value - Measured value

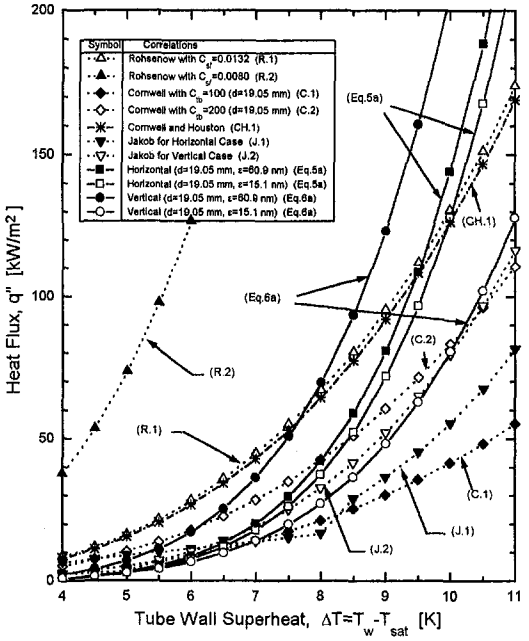

Fig. 8 Comparison of present correlation with typical existing correlations for q'' versus ΔT

coalescence and formation of large bubble slugs becomes more predominant than the liquid agitation effect and the net effect is the decrease in nucleate boiling heat transfer in comparison with horizontal tubes.

In essence, the effectiveness of the two heat transfer mechanisms, i.e., (1) increased heat transfer due to liquid agitation by bubbles generated, and (2) reduced heat transfer by the formation of large vapor slugs and bubble coalescence, is different in two regions of low heat flux and high heat flux depending on the orientation of the tube and the degree of surface roughness.

The effect of heat exchanger tube diameter on the nucleate boiling heat transfer for both horizontal and vertical tubes can be observed in Fig. 5, where q'' versus ΔT is plotted for four different tube diameters from D = 9.7 to D = 25.4 mm. The curves obtained by Eqs. (5) and (6) show that the heat transfer rate decreases as the tube diameter is increased for both horizontal and vertical tubes. This result is in general agreement with previous results obtained by others (van Stralen and Sluyter, 1969; Cornwell et al., 1982).

For a given surface roughness of the tube, the effect of tube diameter on the nucleate boiling heat transfer for vertical tubes is greater than that for horizontal tubes. For example, as shown in Fig. 5, when the tube diameter is decreased from 25.4 to 9.7 mm (~162 percent), q''_H increases from 9.0 to 31.8 kW/m^2 (~253 percent) whereas q''_V increases from 16.0 to 79.0 kW/m^2 (~394 percent). The reason for this is the number of bubble and bubble slug formed on the tube surfaces increases more rapidly as the tube diameter is increased for vertical tubes compared to the horizontal tubes.

A comparison between the measured heat flux q''_{exp} and the calculated heat flux q''_{corr} by Eqs. (5a) and (6a) for both horizontal and vertical tubes is shown in Fig. 6. This figure indicates that the scatter of the present experimental data is between +25 and −25 percent, with some exceptions, from the fitted curve of Eqs. (5a) and (6a). In Fig. 7, the ratio of measured to predicted heat transfer coefficients is plotted against the heat flux. This figure also shows that the scatter of the present data for both horizontal and vertical tubes ranges from +25 to −25 percent. The scatter of the present data is of similar size to that found in other existing pool boiling data. As noted by others (Cornwell and Houston, 1994), there seems to be some inherent randomness in pool boiling due to the uncertainties associated with nucleation site density, physical conditions of the tube surface, and others. This fact precludes greater accuracy of both theoretical and empirical correlations for heat transfer coefficients in nucleate boiling.

In Fig. 8, on the other hand, q'' versus ΔT curves obtained by typical existing correlations of Rohsenow (1952), Cornwell et al. (1982), Cornwell and Houston (1994), and Jakob and Hawkins (1957) are compared with the calculated values obtained by the present empirical correlations for water boiling on heated surfaces at atmospheric pressure. The wide scatter between the curves shown in Fig. 8 is mainly due to the difference in surface roughness ϵ and orientation of heated tubes. For example, in Rohsenow's correlation (1952) C_{sf} = 0.0132 is for mechanically polished stainless steel, whereas C_{sf} = 0.0080 is for ground and polished stainless steel. Also, in the correlation of Cornwell et al. (1982), C_{tb} = 100 and C_{tb} = 200 are for a very smooth surface and a very rough surface, respectively.

Finally, Eq. (6a), which represents a statistical mean value of the present experimental data for vertical tubes, is compared with the PRHR test data of Corletti et al. (1990, 1991) and Rohsenow's correlation (1952) in Fig. 9. From this figure it can be observed that the heat flux q'' for a given ΔT obtained by Corletti et al. (1990) is about one order of magnitude smaller than that of the present or Rohsenow's correlations. The main reason for this difference may be attributable to the difference in heat exchanger tube geometries. That is, when the tube length (L) and the tube pitch of the PRHR heat exchanger test tubes of Corletti et al. (1990) are compared with the present work, their tube length is about 10 times longer (i.e., L = 5486.4 mm) while their tube pitch (35.1 mm) is only 38 percent of the present work. When the heated tubes are extremely long and their pitches are very small, the vapor bubbles formed on the tube surface tend to remain on the same site longer, and cannot easily be removed. Also, when the vapors formed at the lower region of the tube surface are detached, they tend to coalesce into the bubbles at higher region of the tube surface and blanket the tube surface. Thus, for longer heated tubes with smaller pitches, the effect of bubble coalescence and the formation of large vapor slugs could be magnified, which could effectively

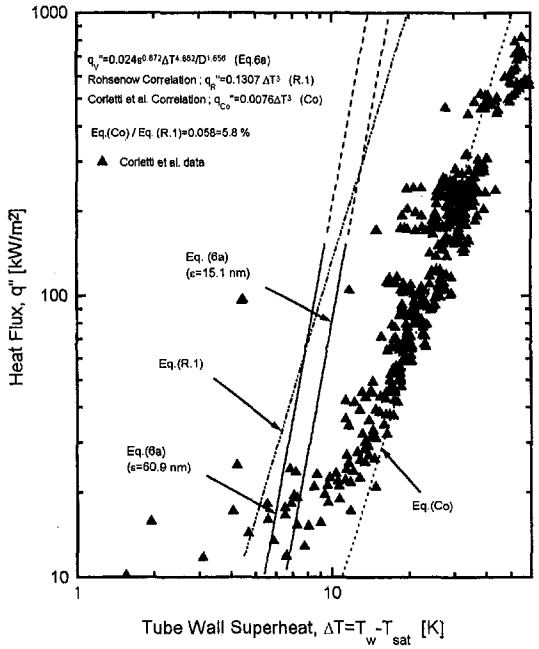

Fig. 9 Comparison of the present work with existing correlation and test data of Corletti et al. (1990)

reduce heat transfer from the tube surface. In addition, the larger vapor slugs formed on the tube surface decrease the number of active nucleation sites, which will also reduce the heat transfer rate. One possible explanation for the reduced boiling heat flux offered by Corletti and Hochreiter (1991) is the vertical orientation of the tubes, which prevents the tube from being in a fully developed nucleate boiling regime. As correctly pointed out by one of the reviewers of the present work, what has been found in the experiments of Corletti and Hochreiter (1991) is that the boiling is not true pool boiling but rather convective boiling. The length of the vertical tubes were 5.49 m (18 feet) and as such there is a strong natural convection flow, which is induced by the heat transfer and the effects of the boiling, which further enhances flow upward along the tubes. It is believed that the flow is so strong that it suppresses boiling such that the tube wall must reach a higher superheat to boil. This is shown in Fig. 9 of the present work. The present data agree reasonably well with the Rohsenow correlation but are a decade off from the test data of Corletti et al. (1990). In Fig. 9, one can see that if the correlations were shifted to the right to higher wall superheats, they would agree with the full-scale passive residual heat removal (PRHR) data and that the induced convection is suppressing the boiling action on the tubes.

Conclusions

An experimental parametric study of a tubular heat exchanger has been carried out under nucleate pool boiling conditions for an application to the thermal design of a passive residual heat removal system of advanced light water reactors. To determine the combined effects of major parameters of heat exchanger tubes on the nucleate pool boiling heat transfer in a scaled in-containment refueling water storage tank, a total of 1966 data (1076 with horizontal tubes and 890 with vertical tubes) for heat flux versus wall superheat has been obtained with various combinations of test parameters of tube diameter, surface roughness, and tube orientation. The main conclusions of the present experimental results are as follows:

1 Increased surface roughness increases heat transfer coefficient for both horizontal and vertical tubes. However, the effect of surface roughness on the nucleate boiling heat transfer for vertical tubes is significantly greater than that for horizontal tubes. The reason for this is partly because the liquid agitation effect of bubbles generated is more pronounced in vertical tubes with rough surface.

2 The effectiveness of the two heat transfer mechanisms, i.e., increased heat transfer due to liquid agitation by bubbles generated and reduced heat transfer by the formation of large vapor slugs and bubble coalescence, is different in two regions of low heat flux ($q'' \leq 50$ kW/m^2) and high heat flux ($q'' > 50$ kW/m^2) depending on the orientation of tubes and the degree of surface roughness.

3 The heat transfer rate decreases as the tube diameter is increased for both horizontal and vertical tubes. For a given surface roughness of the tube, the effect of tube diameter on the nucleate pool boiling heat transfer for vertical tubes is greater than that for horizontal tubes.

Two empirical heat transfer correlations for q'', one for horizontal tubes and the other for vertical tubes, are obtained in terms of surface roughness (ϵ) and tube diameter (D) as given by Eqs. (5) and (6). In addition, a simple empirical correlation, Eq. (9), for nucleate pool boiling heat transfer coefficient h_b is obtained as a function of heat flux (q'') only. The overall scatter of the present data ranges from +25 to −25 percent from the fitted curves of experimental correlations.

Acknowledgments

The authors gratefully acknowledge the financial support of the Korea Science and Engineering Foundation.

References

Westinghouse Electric Corp., 1992, AP600 Standard Safety Analysis Report prepared for U.S. Department of Energy, San Francisco Operations Office, DE-AC03-90SF18495.

Roy Chowdhury, S. K., and Winterton, R. H. S., 1985, "Surface Effects in Pool Boiling," *Int. J. Heat Mass Transfer,* Vol. 28, No. 10, pp. 1881–1889.

Cooper, M. G., 1984, "Heat Flow Rates in Saturated Nucleate Pool Boiling—A Wide Ranging Examination Using Reduced Properties," *Advances in Heat Transfer,* Vol. 16, Academic Press, Inc., pp. 157–239.

Corletti, M. M., Hochreiter, L. E., and Squarer, D., 1990, "AP600 Passive Residual Heat Removal Heat Exchanger Test," *ANS Trans.,* Vol. 62, pp. 669–671.

Corletti, M. M., and Hochreiter, L. E., 1991, "Advanced Light Water Reactor Passive Residual Heat Removal Heat Exchanger Test," *Proc. 1st JSME/ASME Joint International Conference on Nuclear Engineering,* Tokyo, Japan, pp. 381–387.

Cornwell, K., et al., 1982, "The Influence of Diameter on Nucleate Boiling Outside Tubes, *Proc. Seventh International Heat Transfer Conference,* München, Germany, Vol. 4, pp. 47–53.

Cornwell, K., and Houston, S. D., 1994, "Nucleate Pool Boiling on Horizontal Tubes: a Convection-Based Correlation," *Int. J. Heat Mass Transfer,* Vol. 37, Suppl. 1, pp. 303–309.

Jakob, M., and Hawkins, G. A., 1957, *Elements of Heat Transfer,* 3rd ed., Wiley International Edition, pp. 206–210.

Nishikawa, K., and Fujita, Y., 1982, "Effect of the Surface Roughness on the Nucleate Boiling Heat Transfer Over the Wide Range of Pressure," *Proc. Seventh International Heat Transfer Conference,* München, Germany, Vol. 4, pp. 61–66.

MPR Associates, Inc., 1991, "PWR Passive Plant Heat Removal Assessment," Joint EPRI-CRIEPI Advanced LWR Studies, NP-7080-M, Research Project 2660-51.

Rohsenow, W. M., 1952, "A Method of Correlating Heat-Transfer Data for Surface Boiling of Liquids," *Trans. ASME,* Vol. 74, pp. 969–976.

van Stralen, S. J. D., and Sluyter, W. M., 1969, "Investigations on the Critical Heat Flux of Pure Liquids and Mixtures Under Various Conditions," *Int. J. Heat Mass Transfer,* Vol. 12, pp. 1353–1384.

Vachon, R. I., et al., 1968, "Pool Boiling on Polished and Chemically Etched Stainless-Steel Surfaces," ASME JOURNAL OF HEAT TRANSFER, Vol. 90, pp. 231–238.

van de Venne, T., 1992, "Applications of Passive Safety Systems to Large PWRs," *Proc. ANP '92,* Tokyo, Japan, Paper No. 17.4.

Whalley, P. B., 1987, *Boiling, Condensation, and Gas-Liquid Flow,* Oxford University Press, pp. 124–135.

Heat Transfer Correlations for Liquid Film in the Evaporator of Enclosed, Gravity-Assisted Thermosyphons

M. S. El-Genk

H. H. Saber

Institute for Space and Nuclear Power Studies, Chemical and Nuclear Engineering, University of New Mexico, Albuquerque, NM 87131-1341
email: mgenk@unm.edu

Heat transfer correlations were developed for the liquid film region in the evaporator section of closed, two-phase, gravity-assisted thermosyphons in the following regimes: (a) laminar convection, at low heat fluxes, (b) combined convection, at intermediate heat fluxes, and (c) nucleate boiling, at high heat fluxes. These correlations were based on a data set consisting of a total of 305 points for ethanol, acetone, R-11, and R-113 working fluids, wall heat fluxes of 0.99–52.62 kW/m^2, working fluid filling ratios of 0.01–0.62, inner diameters of 6–37 mm, evaporator section lengths of 50–609.6 mm, and vapor temperatures of 261–352 K. The combined convection data were correlated by superimposing the correlations of laminar convection and nucleate boiling using a power law approach, to ensure smooth transition among the three heat transfer regimes. The three heat transfer correlations developed in this work are within ±15 percent of experimental data.

Introduction

The design optimization of closed, gravity-assisted, two-phase thermosyphons (GATPTs) depends on the use of reliable heat transfer correlations for the pool and the liquid film regions of the evaporator section. GATPTs are being used in many industrial applications, owing to their design and fabrication simplicity and effectiveness. They are lightweight, passive, and self-contained high-conductance thermal energy transport devices. When used in bundles, for example in gas/gas and gas/liquid heat exchangers, GATPTs offer excellent operation redundancy, where a failure of one or more thermosyphons does not impair the operation of the others. Thermosyphons are light because they operate with the evaporator section only partially filled with working fluid and are made of thin-walled, metallic containers. The thermal energy transport in GATPTs occurs by evaporation in the lower section (*evaporator*) and condensation in the upper section (*condenser*), taking advantage of the latent heat of vaporization of the working fluid. The condensed working fluid flows downward under the effect of gravity to the evaporator section, in the form of a thin, continuous liquid film (Fig. 1). The vapor generated in the evaporator section is the sum of that produced in two regions: (*a*) *the continuous liquid film,* which extends from the upper end of the evaporator section to the free surface of the liquid pool, and (*b*) the *liquid pool,* which resides at the bottom of the evaporator (Fig. 1).

During nominal operation, the sum of the liquid film length, L_f, and the liquid pool height, L_p, equals the total length of the evaporator section, L_e. The ratio of the initial liquid pool volume to the total volume of the evaporator section is referred to as the working fluid filling ratio, FR. During operation, the liquid pool height changes from its initial fill value, L_{pi}, depending on the operating heat flux and prevailing modes of heat transfer in the pool and in the film.

The heat transfer processes in the evaporator section of a GATPT are quite complex, owing to the many modes of heat transfer occurring in the pool and in the liquid film regions. Therefore, it is difficult to derive, from basic principles, heat transfer correlations, which incorporate the various processes taking place in each region. Only empirical and semi-empirical heat transfer correlations have been reported by various investigators for the liquid pool (Kusuda and Imura, 1973; Imura et al., 1979; Shiraishi et al., 1981; Ueda et al., 1988; Gro, 1990; Kaminaga et al., 1992; Jialun et al., 1992) and the continuous liquid film (Andros and Florschuetz, 1978; Semena and Kiselev, 1978; Andros, 1980; Shiraishi et al., 1981; Jialun et al., 1992) regions. Most of the reported correlations for the pool, however, have exhibited large discrepancies, in excess of 70 percent, with experimental data; the best correlations were within ±30 percent of the data. Such large discrepancies were attributed to improper sorting of the data among the different heat transfer regimes, and inappropriate selection of the dimensionless variables in the correlations.

Recently, El-Genk and Saber (1998) compiled a total of 731 heat transfer data points for uniformly heated liquid pools of water, ethanol, methanol, Dowtherm-A, R-11, and R-113 in small cylindrical enclosures of GATPTs (8–37 mm in diameter). They sorted and correlated the data in the various heat transfer regimes in the pool, namely: (*a*) *natural convection*, at low heat fluxes, (*b*) *combined convection*, at intermediate heat fluxes, and (*c*) *nucleate boiling heat transfer*, at high heat fluxes. These correlations were within ±15 percent of experimental data (El-Genk and Saber, 1998). The total power throughput of a GATPT, however, depends on the heat transfer coefficients in both the pool and liquid film regions. Therefore, to determine the heat transfer coefficient accurately in the evaporator section, reliable heat transfer correlations for the various modes of heat transfer in the liquid film and the liquid pool regions are needed. Determining the heat transfer coefficient for the former is important, because the evaporation rate of the working fluid from the falling liquid film is significantly higher than from the pool.

There are several heat transfer regimes that occur in the liquid film region in a GATPT, depending on the properties and vapor temperature of the working fluid and the wall heat flux in the evaporator section. These regimes are:

(*a*) *Partial wetting* occurs at very low wall heat flux and low wall temperature, whereby the liquid return from the con-

Contributed by the Heat Transfer Division and presented at the National Heat Transfer Conference, Baltimore, Maryland, August 8–12, 1997. Manuscript received by the Heat Transfer Division May 19, 1997; revision received January 5, 1998. Keywords: Boiling, Heat Pipes & Thermosyphons, Thin Film Flow. Associate Technical Editor: R. A. Nelson, Jr.

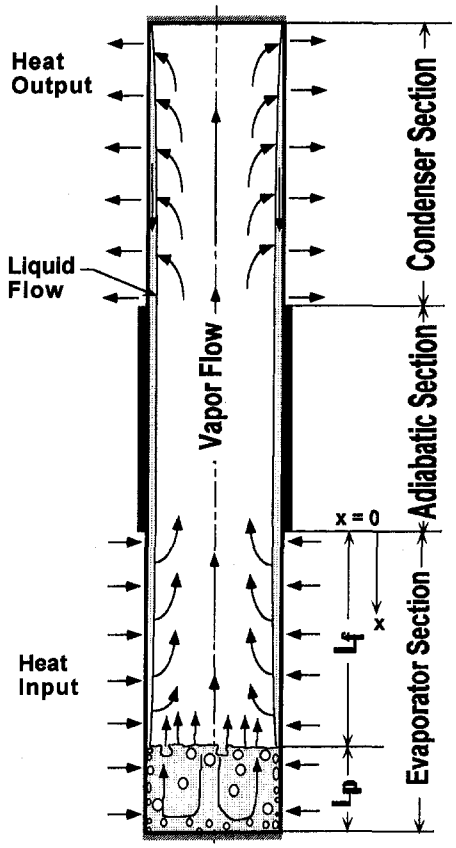

Fig. 1 A schematic of a closed gravity-assisted two-phase thermosyphon

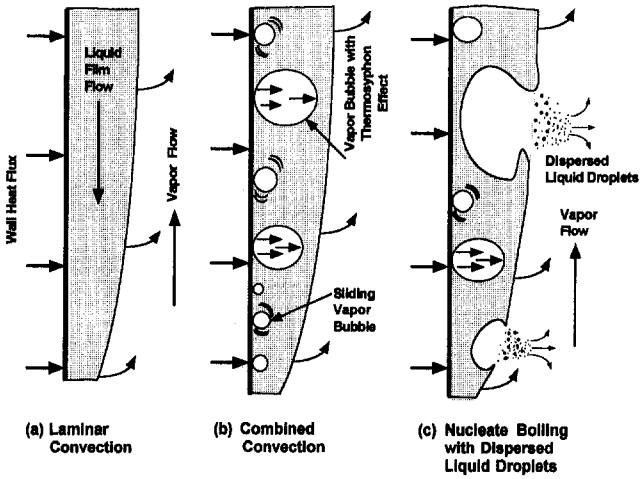

Fig. 2 A line diagram of the different heat transfer regimes of the liquid film in a GATPT

denser region is below the minimum wetting limit and thus is insufficient to establish a continuous liquid film in the portion of the evaporator wall above the liquid pool. The evaporation at the film's liquid–vapor interface depletes the liquid flow before it reaches the liquid pool, resulting in only partial wetting of the evaporator wall.

(*b*) *Evaporating falling liquid film,* which is typically laminar in GATPTs, occurs at low and intermediate heat fluxes where the wall superheat is below that required for incipient boiling (Fig. 2(*a*)). In this regime, the portion of the evaporator wall above the pool region is covered with a continuous liquid film having a progressively decreasing thickness with distance, x, from the top of the evaporator section.

(*c*) *Nucleate boiling* occurs at high heat fluxes, where the growing vapor bubbles at the wall burst at the liquid–vapor interface, dispersing tiny droplets of liquid into the vapor flow (Fig. 2(*c*)). Both bubble nucleation at the wall and entrainment of tiny liquid droplets in the vapor flow cause the effective heat transfer coefficient to be significantly higher than that for large pool nucleate boiling. Cerza and Sernas (1985, 1989) have observed that a bubble growing in a superheated falling liquid film continues to grow as it is swept downstream from its nucleation site, due to heat conduction through the liquid macrolayer beneath its base. The observed secondary nucleation in the liquid macrolayer and the splashing caused by bursting bubbles

Nomenclature

Cp = specific heat, J kg^{-1} K^{-1}
C_1 = coefficient = $(2(1 - FR)/(1 + FR))^{1/3}$, Eq. (1)
C_2 = coefficient = $1.5(1 - H_p^{2/3})/(1 - H_p)^{2/3}$, Eq. (2)
d = diameter, m
g = gravitational acceleration, m s^{-2}
FR = working fluid filling ratio = L_{pi}/L_e
H_p = dimensionless height = L_p/L_e
h = heat transfer coefficient, W m^{-2} K
h_{fg} = latent heat of vaporization, J kg^{-1}
k = thermal conductivity, W m^{-1} K^{-1}
K_p = dimensionless parameter = (Pl_m/σ), Eq. (7)
l_l = film thickness scale = $(\mu_l^2/g\rho_l(\rho_l - \rho_{pg}))^{1/3}$, m
l_m = bubble length scale = $(\sigma/(g(\rho_l - \rho_g))^{0.5}$, m
L = length or height, m
$N_{\mu f}$ = viscosity number = $(l_l/l_m)^{1.5}$ = $\mu_l/(\sigma g\sqrt{\sigma/g(\rho_l - \rho_g)})^{0.5}$
Nu_f = film Nusselt number based on l_l, $(h_f l_l/k_l)$
Nu_x = local film Nusselt number based on l_l, $(h_x l_l/k_l)$
Nu* = film Nusselt number based on l_m, $(h_{NB} l_m/k_l)$
P = pressure, Pa
P_a = standard atmospheric pressure = 1.013×10^5 Pa
Pr = Prandtl number = $(\mu Cp/k)$
Q^* = power throughput corresponding to the countercurrent flooding limit, W
q = heat flux, W m^{-2}
q_e = evaporator wall heat flux, W m^{-2}
q_e^* = transition heat flux to nucleate boiling, W m^{-2}
Re = film-averaged Reynolds number = $(4q_e L_f/\mu_l h_{fg})$
Re_g = vapor Reynolds number = $(q_e l_m/(\rho_g h_{fg} v_l))$
Re_x = film local Reynolds number = $(4q_e(L_e - x)/\mu_l h_{fg})$
T = temperature, K
x = distance measured from top of evaporator, m
μ = dynamic viscosity, N·s m^{-2}
ν = kinematic viscosity, m^2 s^{-1}
ρ = density, kg m^{-3}
σ = surface tension, N m^{-1}
η = dimensionless film parameter = $((q_e l_m/(\rho_g h_{fg} v_l))^2 K_P^2\ \mathrm{Re}_x/\mathrm{Pr}_l)$

Subscripts

e = evaporator section
g, v = vapor
f = liquid film
CC = combined convection
Ku = Kutateladze
l = liquid
NB = film nucleate boiling
LF = laminar liquid film
p = liquid pool
pi = initial pool
x = at a distance x from entrance of evaporator section

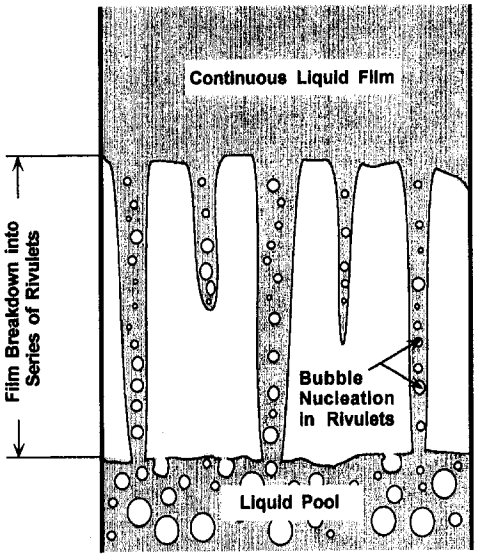

Fig. 3 Formation of liquid rivulets in the evaporator section of a GATPT, at high wall heat fluxes

also contributed to enhancing the nucleate boiling heat transfer in the falling liquid film.

(*d*) *Partial dryout* occurs at high heat fluxes when the rate of evaporation from the liquid film is very high, and the film is very thin. The local thinning of the liquid film, immediately above the pool region, results in a nonuniform azimuthal wall temperature and, hence, a difference in the local surface tension, which eventually breaks up the film into stable rivulets by the Marangoni effect. Some of these rivulets could also break up locally into isolated droplets (Fig. 3). Andros and Florschuetz (1978) and Andros (1980) reported that the width and spacing of the rivulets depend on the type of the working fluid and the wall heat flux. For Freon-113, they observed rivulets that were approximately 16 mm wide and had center-to-center spacing of 55 to 69 mm. For ethanol, however, which has a significantly higher surface tension, the liquid rivulets were slightly wider and had larger center-to-center spacing of 69 to 78 mm. The observations of Cerza and Sernas (1985, 1989) of the dryout in boiling falling liquid films were consistent with those of Andros (1980).

In practical applications, only film heat transfer regimes (*b*) and (*c*) are of interest to the design and operation of GATPTs. Regime (*a*) is encountered during the startup of thermosyphons or the operation at very low heat fluxes, while regime (*d*) should be avoided. In this regime, local film dryout could occur because of insufficient liquid flow, either due to a low initial filling ratio of the working fluid or because of reaching the countercurrent flooding limit (CCFL) at the exit of the evaporator (El-Genk and Saber, 1997a).

Only a few heat transfer correlations have been reported for the laminar convection and nucleate boiling regimes in the evaporating falling liquid film in GATPTs. Most reported correlations had exhibited large discrepancies with the data, in excess of ±30 percent (Shiraishi et al., 1981; Jialun et al., 1992). To the best of our knowledge, no correlations have been reported for combined convection heat transfer in the liquid film in GATPTs. In this regime, which falls between regimes (*a*) and (*c*), both laminar convection and nucleate boiling contribute to the film heat transfer (Fig. 2(*b*)).

This work compiled a total of 305 heat transfer data points from the literature for the liquid film region in GATPTs. These data were correlated in the applicable regimes, namely: (*a*) *film laminar convection,* at low heat fluxes, (*b*) *nucleate boiling*, at high heat fluxes, and (*c*) *combined convection*, at intermediate heat fluxes. A parametric analysis was performed to determine the prevailing heat transfer regime in the film region, as a function of the vapor temperature for a number of working fluids. Also, the values of the power throughput corresponding to the flooding limit at the exit of the evaporator (El-Genk and Saber, 1997a) were determined for the same working fluids as a function of the vapor temperature.

Reported Liquid Film Heat Transfer Correlations

This section reviews the heat transfer correlations reported by various investigators for the film region in the evaporator section of GATPTs. Shiraishi et al. (1981) have developed two correlations based on their own experimental data, one for laminar convection and the other for nucleate boiling. They based their correlations on measurements of the heat transfer coefficient at a single location, $x = 0.5\,L_f$. Their laminar convection correlation is the same as the inverse Nusselt condensation theory (Wallis, 1969), except for incorporating the coefficient, C_1, as:

$$\mathrm{Nu}_x = (4/3)^{1/3} C_1\,\mathrm{Re}^{-1/3}. \qquad (1)$$

Jialun et al. (1992) developed a laminar convection correlation for the average Nusselt number of the liquid film. The correlation is the same as that of Shiraishi et al. (1981), except for using the coefficient C_2:

$$\mathrm{Nu}_{LF} = (4/3)^{1/3} C_2\,\mathrm{Re}^{-1/3}. \qquad (2)$$

Equations (1) and (2) were within ±30 percent of the respective authors' own experimental data. No attempt was made to compare these correlations with the data of other investigators. The major differences between these two correlations are that: (*a*) Eq. (1) is for the local Nusselt number, while Eq. (2) is for the film average Nusselt number and (b) the dependencies of the coefficients C_1 and C_2 on the liquid pool height (or filling ratio) are not the same. The coefficients C_1 and C_2 start at 1.26 and 1.5, respectively, and approach zero at a filling ratio of unity. It is difficult, however, to predict the coefficient C_2 *a priori,* because it requires knowledge of the actual pool height in the evaporator section as a function of the wall heat flux.

Shiraishi et al. (1981) proposed using their correlation for the average nucleate boiling heat transfer coefficient in the pool region for the liquid film, when the evaporator heat flux $q_e \geq q_e^*$:

$$h_{NB} = 0.32\left(\frac{\rho_l^{0.65} k_l^{0.3} Cp_l^{0.7} g^{0.2}}{\rho_g^{0.25} h_{fg}^{0.4} \mu_l^{0.1}}\right)(P/P_a)^{0.23} q_e^{0.4}. \qquad (3a)$$

When compared with their own liquid pool data for ethanol, Eq. (3*a*) was consistently higher by more than 30 percent and lower than their pool data for R-113 by about 12 percent. Their water pool data, however, were more than 30 percent below Eq. (3*a*) at low heat transfer coefficients (<2000 W/m^2 K), but within ±10 percent of the data at high heat transfer coefficients (>4500 W/m^2 K).

Shiraishi et al. recommended using Eq. (1) to determine the heat transfer coefficient in the liquid film when $q_e < q_e^*$. The heat flux corresponding to the transition from laminar convection to nucleate boiling was determined from equating Eqs. (1) and (3*a*) as:

$$q_e^* = 2.87 C_1^{1.364}\left(\frac{h_{fg}\rho_l^{0.023}\rho_g^{0.34} g^{0.18} k_l^{0.955}}{\mu_l^{0.318} L_f^{0.455} Cp_l^{0.955}}\right)(P/Pa)^{0.31}. \qquad (3b)$$

For the film-averaged nucleate boiling heat transfer coefficient, Jialun et al. (1992) proposed the following correlation, based solely on their own experimental data:

Table 1 Compiled heat transfer database for uniformly heated liquid film in GATPTs

Regime	Reference	# Data points	Working fluid	L_e (mm)	d_i (mm)	T_v (K)	Filling ratio	q_e (kW/m^2)
Laminar Convection	Shiraishi et al. (1981)	2	R-113	280	37	305	0.5	1.85–2.58
	Andros (1980)	45	R-113	609.6, 304.8	27	301–307	0.0312–0.6208	0.99–3.04
	Shiraishi et al. (1981)	9	Ethanol	280	37	305, 318	0.5	1.71–4.81
Combined Convection	Shiraishi et al. (1981)	3	R-113	280	37	305	0.5	2.58–7.01
	Andros (1980)	61	R-113	609.6, 304.8	27	307–315	0.0312–0.6208	3.04–7.74
	Shiraishi et al. (1981)	8	Ethanol	280	37	305–318	0.5	4.81–17.20
Nucleate Boiling	Semena & Kiselev (1978)	7	R-113	50, 100, 350	6, 12, 18	281–317	0.15, 0.3	2–50
	Andros (1980)	111	R-113	609.6, 304.8	27	315–352	0.0312–0.6208	7.74–33.36
	Shiraishi et al. (1981)	4	R-113	280	37	305	0.5	7.01–31.42
	Semena & Kiselev (1978)	28	R-11	50, 100, 200	6, 12, 24	261–299	0.05, 0.2, 0.4	2–50
	Shiraishi et al. (1981)	7	Ethanol	280	37	305, 318	0.5	17.2–52.62
	Semena & Kiselev (1978)	9	Ethanol	50, 200	12, 18	301–332	0.1, 0.2	2–50
	Semena & Kiselev (1978)	11	Acetone	100, 350	7, 12	262–281	0.01, 0.2	2–50

$$h_{NB} = 0.0062C_2^{-1.2}\,\mathrm{Re}^{0.4}\,\mathrm{Pr}_l^{1.25}k_l(v_l^2/g)^{-1/3}\,. \quad (4)$$

When compared with the data of both Shiraishi et al. (1981) and Jialun et al. (1992), Eq. (4) predicted the data to within ±30 percent. Jialun et al. (1992) determined the value of the evaporator heat flux at the transition from laminar convection to nucleate boiling from equating Eqs. (2) and (4) as:

$$q_e^* = 291.9C_2^3(\mu_l h_{fg}/L_f)\,\mathrm{Pr}_l^{-1.7}\,. \quad (5)$$

It is worth noting that Eqs. (2), (4), and (5) cannot directly be applied, since they require a prior knowledge of the liquid pool height as a function of the wall heat flux, limiting their usefulness.

Xiang-Qun et al. (1992) performed experiments with a closed two-phase flow thermosyphon using water as the working fluid. However, since their data were for the overall average heat transfer coefficient in the evaporator section, including the film and the pool regions, they could not be compared with the correlations of other investigators nor used in the present work.

Semena and Kiselev (1978) performed a series of GATPT experiments. They investigated the effects of the working fluid filling ratio (0.01 to 0.4) and of the inner diameter (6–24 mm), length (50–350 mm), and orientation of the evaporator section, using Freon-11, 113, and 142, ethanol, and acetone as working fluids. They measured and correlated the data in the laminar convection and nucleate boiling regimes. Their laminar convection data were consistent with the inverse Nusselt theory for condensation. Their nucleate boiling correlation was similar to that of Kutateladze's (1959) for boiling in a large liquid pool, in that the Nusselt number increased with increasing wall heat flux raised to the power 0.7. No effort, however, was made to identify or correlate the combined convection data, in order to provide a smooth transition between the laminar convection and nucleate boiling regimes.

Present Heat Transfer Correlations

A total of 305 data points by a number of investigators were compiled and sorted in the different heat transfer regimes of the liquid film region in the evaporator section of GATPTs, based on the exponent of the wall heat flux (Table 1). The data that exhibited a dependence of the film Nusselt number on the wall heat flux raised to the (−1/3) power were classified in the laminar convection regime. The data for which the film Nusselt number increased with increasing wall heat flux raised to the power 0.67–0.7 were classified in the nucleate boiling regime. The data, for which the film Nusselt number increased with increasing wall heat flux raised to a power less than 0.67, were classified in the combined convection regime.

The data for the film laminar convection and nucleate boiling regimes were correlated separately using the appropriate dimensionless groups for each regime. In the intermediate regime of combined convection, the data were correlated by superimposing the present laminar convection and nucleate boiling correlations, using a power law approach. The developed correlations are presented and compared with experimental data next.

Laminar Convection Correlation

The liquid film laminar convection data (56 data points) for R-113 and ethanol (Table 1) were correlated and found to be consistent with the inverse of the Nusselt theory for filmwise condensation (Wallis, 1969). As shown in Table 1, Reynolds number for the laminar convection data was less than 200. For these data, the film local Nusselt number is proportional to the film local Reynolds number raised to the negative one third power as:

$$\mathrm{Nu}_x = (4/3)^{1/3}(\mathrm{Re}_x)^{-1/3}\,. \quad (6)$$

As shown in Fig. 4, this correlation is within ±15 percent of the experimental data for the different working fluids, evaporator lengths, and filling ratios of the working fluid (Table 1). The film heat transfer coefficient is quite high; even at Re < 200 (Fig. 4). For example, at a film Reynolds number $\mathrm{Re}_x = 3.2$ for ethanol at a vapor temperature of 305 K, the film local heat transfer coefficient at a distance $x = 70$ mm from the exit of the evaporator section is as much as 2286 W/m^2 K.

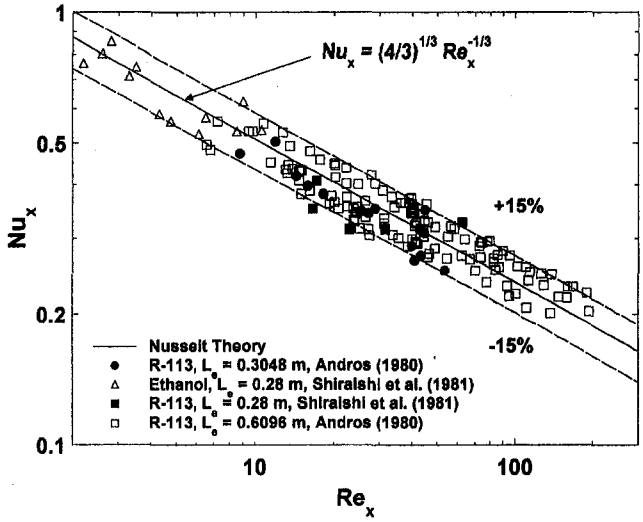

Fig. 4 Comparison of the correlation and data for liquid film laminar convection

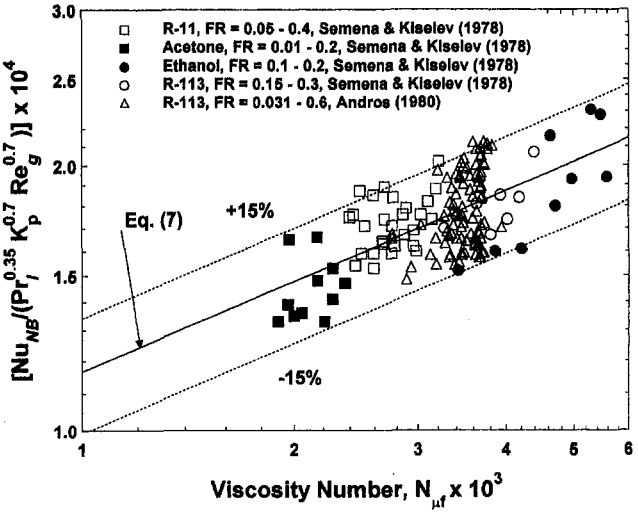

Fig. 5 Comparison of the correlation and data for liquid film nucleate boiling

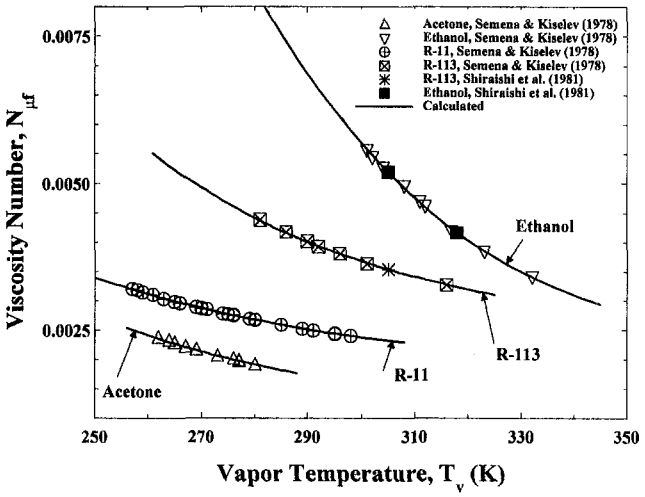

Fig. 7 Dependence of the viscosity number on vapor temperature of working fluids

Nucleate Boiling Correlation

The compiled nucleate boiling data for R-11, R-113, acetone, and ethanol (177 data points) are shown in Fig. 5 and listed in Table 1. The data were correlated as:

$$\mathrm{Nu}_{NB} = 1.155 \times 10^{-3} N_{\mu f}^{0.33} \mathrm{Pr}_l^{0.35} Kp^{0.7} (q_e l_m / (\rho_g h_{fg} \upsilon_l))^{0.7} . \quad (7)$$

As delineated in Fig. 5, this correlation is also within ±15 percent of most experimental data for Nf values from 1.9×10^{-3} to 5.6×10^{-3}. When the Nusselt number in Eq. (7) was divided by that of Kutateladze (1959) for nucleate boiling in large liquid pools:

$$\mathrm{Nu}_{Ku} = 6.95 \times 10^{-4} \mathrm{Pr}_l^{0.35} K_p^{0.7} (q_e l_m / (\rho_g h_{fg} \upsilon_l))^{0.7} , \quad (8)$$

the following relationship was obtained:

$$\mathrm{Nu}_{NB}^{*} / \mathrm{Nu}_{Ku}^{*} = 1.662 N_{\mu f}^{-0.337} . \quad (9)$$

Equation (9) and the experimental data indicate that for the range of values of the viscosity number in the present nucleate boiling data (Fig. 6), the Nusselt number ratio is significantly higher than unity, decreasing from 13.9 to 9.5 as $N_{\mu f}$ increases from 1.9×10^{-3} to 5.6×10^{-3}, respectively. These large Nusselt number values for the film nucleate boiling in GATPTs, compared with those for nucleate boiling in large pools (Kutateladze, 1959), are partially due to the dispersion of tiny liquid droplets in the vapor flow by bursting bubbles in the film Fig. 2(*c*). As the growing vapor bubbles in the liquid film reach the liquid–vapor interface, caps of thin liquid film surround them. With further growth of the bubbles, this liquid film becomes thinner due to the drainage of liquid due to shear. Eventually, the bubbles burst, dispersing tiny liquid droplets into the vapor flow stream (Cerza and Sernas, 1985, 1989). This entrainment mechanism, the conduction through the liquid macrolayer beneath the bubbles, the secondary nucleation in the macrolayer, and the mixing induced in the liquid film by sliding bubbles is responsible for the high nucleate boiling heat transfer (Eq. (9)), compared to that in a large pool (Kutateladze, 1959). El-Genk and Saber (1998) recently have shown that nucleate boiling in small, enclosed liquid pools (8 to 37 mm in diameter), such as those in the evaporator section of GATPTs, could be as much as 100–400 percent higher than in large pools.

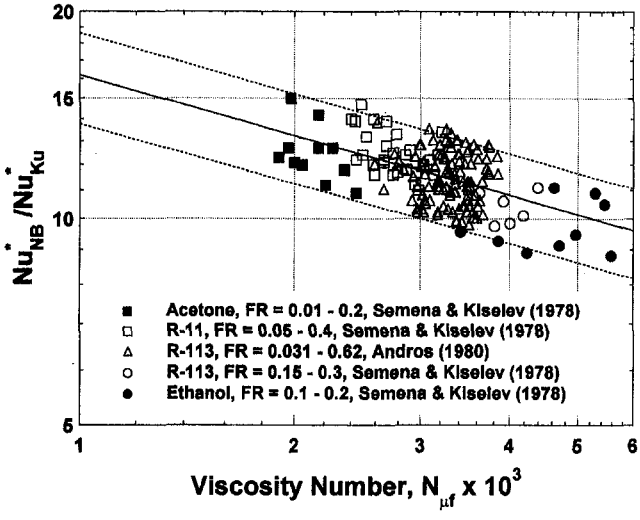

Fig. 6 Dependence of the film nucleate boiling Nusselt number on viscosity number of working fluids

In Eqs. (7) and (9), $N_{\mu f}$ is basically the ratio of the liquid shear stress to its surface tension, thus, the bursting of vapor bubbles, dispersing liquid droplets in the vapor flow, becomes more effective in enhancing the heat transfer coefficient as $N_{\mu f}$ increases (Fig. 5). As delineated in Fig. 7, decreasing the vapor temperature in GATPTs increases $N_{\mu f}$, and, hence the nucleate boiling heat transfers coefficient for the film (Eq. (7)). Except for acetone, Fig. 7 shows that, for the same vapor temperature, the viscosity number increases as the vapor pressure of the working fluid decreases. For example, at a vapor temperature of 285 K, the vapor pressures of R-11, R-113, and ethanol are 69.20 kPa, 24.04 kPa, and 2.93 kPa, respectively, and the corresponding values of the viscosity number are 2.59×10^{-3}, 4.20×10^{-3}, and 7.54×10^{-3}, respectively. Acetone, with a vapor pressure of 18.62 kPa at a vapor temperature of 285 K, had the lowest viscosity number of 1.814×10^{-3}.

Combined Convection Correlation

In the combined convection regime, both laminar convection and nucleate boiling (Fig. 2(*b*)) contribute to the heat transfer in the liquid film. In this regime, which occurs at intermediate heat fluxes, the dispersion of liquid droplets into the vapor flow is a minor contributor, compared to the contribution of nucleation and of the mixing induced by sliding bubbles at the wall. The growing bubbles at the wall function basically as microthermosyphons, transporting thermal energy from the wall by evaporation at the base and condensation at the top of the

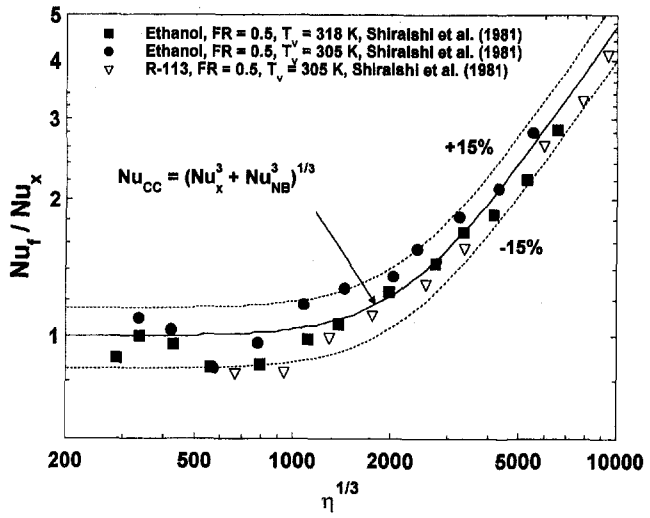

Fig. 8 Comparison of combined convection correlation with the data of Shiraishi et al. (1981)

bubbles, near the liquid film–vapor interface (Fig. 2(*b*)). Therefore, the combined convection data were correlated by superimposing the correlations of laminar convection (Eq. (6)) and nucleate boiling (Eq. (7)), using a power law approach. This approach has been applied successfully to single-phase convection in tubes, annuli, and rod-bundles (Churchill, 1977; Ruckenstein, 1978; El-Genk et al., 1990, 1993) as well as to the heat transfer in the liquid pool region of GATPTs (El-Genk and Saber, 1998).

The combined convection Nusselt number data (72 points) for the different working fluids were correlated as:

$$\mathrm{Nu}_{CC} = [\mathrm{Nu}_x^3 + \mathrm{Nu}_{NB}^3]^{1/3}. \qquad (10)$$

The exponents on the right-hand side of Eq. (10) were determined from the least-square fit of the heat transfer data in the combined convection regime (Table 1). As shown in Fig. 8, Eq. (10) provides a smooth and continuous transition among the three heat transfer regimes in the liquid film. Equation (10) is also in good agreement with most experimental data, to within ±15 percent.

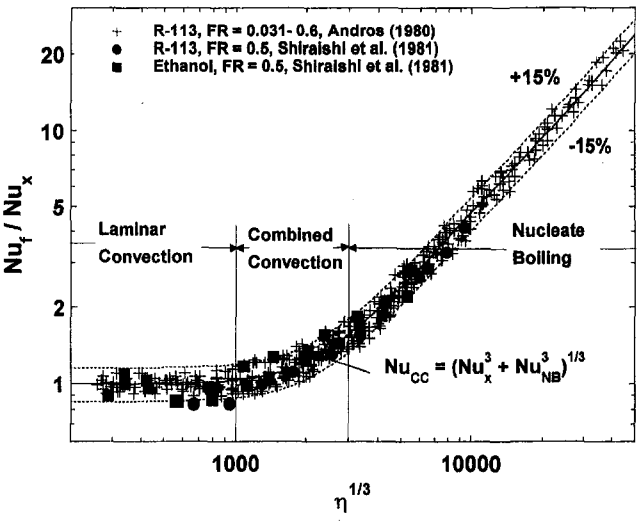

Fig. 9 Comparison of combined convection correlation with the data of different working fluids

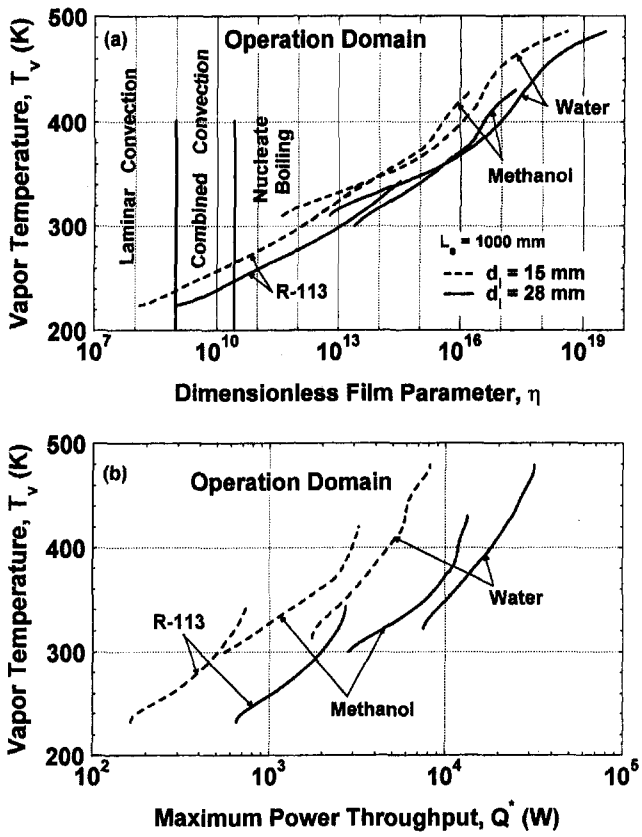

Fig. 10 Effect of vapor temperature on the operation domain of GATPTs for different working fluids

Figures 8 and 9 show that the various heat transfer regimes in the liquid film can be classified with the use of the following dimensionless film parameter:

$$\eta = (q_e l_m/(\rho_g h_{fg} \upsilon_l))^2 K_P^2 \,\mathrm{Re}_x/\mathrm{Pr}_l. \qquad (11)$$

This parameter depends on the properties of working fluid and the wall heat flux. In the laminar convection regime $\eta \leq 10^9$, in nucleate boiling regime $\eta \geq 2.7 \times 10^{10}$, and in the intermediate regime of combined convection $10^9 < \eta < 2.7 \times 10^{10}$.

Effect of Vapor Temperature on Film Heat Transfer and Flooding Limit

This section presents the results of an analysis that investigated the effects of vapor temperature and inner diameter on the power throughput at the flooding limit, Q^*, and the heat transfer regime in the liquid film region of the evaporator section of a GATPT. The working fluids considered in this analysis are water, methanol, and R-113. The total evaporator length is 1000 mm. The power throughput corresponding to the countercurrent flooding limit (CCFL) at the exit of the evaporator section was determined using the model of El-Genk and Saber (1997a). This model calculates the shear stress at the liquid–vapor (L–V) interface as the sum of the adiabatic and dynamic shear stresses. The dynamic shear stress accounts for the effect of evaporation/condensation at the L–V interface, which has been shown to affect the predictions of the CCFL strongly, particularly at high film Reynolds numbers (El-Genk and Saber, 1997a). The model predictions of the film Reynolds number at the CCFL for water and methanol were consistently in good agreement with the data to within ±10 percent.

In Figs. 10(*a*) and 10(*b*), the solid and broken curves represent the conditions corresponding to the CCFL in a GATPT having inner diameters of 28 mm and 15 mm, respectively. The

operation domains in these figures fall to the left of the curves. In Fig. 10(a), the different heat transfer regimes in the liquid film are classified based on the values of the film's dimensionless parameter (Fig. 9). Figures 10(a) and 10(b) indicate that the operation domain increases with increasing inner diameter of the GATPT, while the prevailing heat transfer regime in the liquid film depends on the values of the vapor temperature, the vapor pressure, and the inner diameter of the thermosyphon. For an example, at a vapor temperature of 300 K, the operation domain for a GATPT having an inner diameter of 15 mm and using R-113 as working fluid, extends to $\eta = 1.26 \times 10^{12}$, at which $Q^* = 507$ W. In this thermosyphon, the heat transfer regime in the liquid film could be either laminar convection, combined convection, or nucleate boiling, depending on the values of η and power throughput below 1.26×10^{12} and 507 W, respectively.

At the same vapor temperature of 300 K and inner diameter of 28 mm, the operation domain for methanol, which has lower vapor pressure than R-113, extends to $\eta = 2.49 \times 10^{13}$, at which Q^* is as high as 2810 W. For this working fluid, laminar convection, combined convection, and nucleate boiling heat transfer regimes could also occur in the liquid film region of the evaporator section, depending on the value of the power throughput below 2810 W, and the corresponding value of $\eta < 2.49 \times 10^{13}$.

Summary and Conclusions

Heat transfer correlations for the liquid film region in the evaporator section of GATPTs were developed for the following regimes: (a) laminar convection, at low wall heat fluxes, (b) combined convection, at intermediate wall heat fluxes, and (c) nucleate boiling, at high wall heat fluxes. These correlations were based on an experimental database consisting of a total of 305 heat transfer data points for ethanol, acetone, R-11, and R-113 working fluids (Table 1). These data were compiled and sorted into the different heat transfer regimes, based on the exponent of the wall heat flux that best correlated the film Nusselt number data.

The data in the liquid film laminar convection and nucleate boiling regimes were correlated separately, using the appropriate dimensionless groups in each regime. The laminar convection data and correlation (Eq. (6)) were consistent with the inverse Nusselt theory for filmwise condensation, where the film Nusselt number decreased with increasing wall heat flux raised to the $(-1/3)$ power. In the nucleate boiling regime, the combined contributions of bubble nucleation at the wall and dispersion of tiny liquid droplets into the vapor flow by bursting bubbles at the $L-V$ interface, caused the Nusselt number in this regime to be significantly higher than that for conventional nucleate boiling. The film nucleate boiling Nusselt number, which increased with increasing wall heat flux raised to the power of 0.7, was as much as 13.9 times that for pool boiling at a film viscosity number, $N_{\mu f} = 1.9 \times 10^{-3}$, decreasing to 9.5 at $N_{\mu f} = 5.6 \times 10^{-3}$. The viscosity number of the liquid film increased with decreasing vapor temperature of the working fluid.

The experimental data for the intermediate regime of combined convection, where both laminar convection and nucleate boiling contribute to the heat transfer in the liquid film, were correlated by superimposing the correlations for laminar convection (Eq. (6)) and nucleate boiling (Eq. (7)), using a power law approach. The combined convection correlation (Eq. (10)) provided smooth transition from laminar convection, at low wall heat fluxes, to nucleate boiling, at high wall heat fluxes. The three correlations developed in this work were in good agreement with most data, to within ± 15 percent.

The different heat transfer regimes in the liquid film were classified with the aid of a film dimensionless parameter (Eq. (11)) as follows: $\eta < 10^9$ for laminar convection, $10^9 < \eta < 2.7 \times 10^{10}$ for combined convection, and $\eta \geq 2.7 \times 10^{10}$ for nucleate boiling. These values of the film dimensionless parameter were used in conjunction with a model for predicting the CCFL to determine the useful operation domain and the possible heat transfer regimes that could occur in the liquid film, before reaching CCFL, as functions of the inner diameter and the type of working fluid. Results indicated that the operation domain for GATPTs increased with increasing inner diameter of GATPTs and increasing vapor temperature of the working fluid.

Acknowledgments

This research was funded partially by the University of New Mexico's Institute for Space Nuclear Power Studies and the Egyptian Authority for Scientific Missions, Cairo, Arab Republic of Egypt.

References

Andros, F. E., and L. W. Florschuetz, 1978, "The Two-Phase Closed Thermosyphon: An Experimental Study With Flow Visualization," *Two-Phase Transport and Reactor Safety*, T. N. Veziroglu and S. Kakac, eds., Hemisphere Publishing Corp., Washington DC, Vol. 4, pp. 1231–1267.

Andros, F. E., 1980, "Heat Transfer Characteristics of the Two-Phase Closed Thermosyphon (Wickless Heat Pipe) Including Direct Flow Observation," Ph.D. Dissertation, Arizona State University, Tempe, AZ.

Cerza, M., and V. Sernas, 1985, "A Bubble Growth Model for Nucleate Boiling in Thin, Falling, Superheated, Laminar Water Films," *Int. J. Heat Mass Trans.*, Vol. 28(7), pp. 1307–1316.

Cerza, M., and V. Sernas, 1989, "Boiling and Dryout in Falling Thin Films," *Proc. Nat. Heat Trans. Conf., Heat Transfer Measurements, Analysis, and Flow Visualization*, ASME HTD-Vol. 112, pp. 107– 108.

Churchill, S. W., 1977, "A Comprehensive Correlating Equation for Laminar, Assisting, Forced and Free Convection," *AIChE J.*, Vol. 23(10), pp. 10–16.

El-Genk, M. S., S. D. Bedrose, and D. V. Rao, 1990, "Forced and Combined Convection of Water in a Vertical Seven-Rod Bundle With $P/D = 1.38$," *Int. J. Heat Mass Trans.*, Vol. 33(6), pp. 1289–1297.

El-Genk, M. S., B. Su, and Z. Guo, 1993, "Experimental Studies of Forced, Combined, and Natural Convection of Water in Vertical Nine-Rod Bundles With a Square Lattice," *Int. J. Heat and Mass Trans.*, Vol. 36(9), pp. 2359–2374.

El-Genk, M. S., and H. Saber, 1997a, "Flooding Limit in Closed, Two-Phase Flow Thermosyphons," *Int. J. Heat and Mass Transfer*, Vol. 40(9), pp. 2147–2164.

El-Genk, M. S., and H. Saber, 1997b, "Performance Maps for Gravity Assisted Thermosyphons," *10th Int. Heat Pipe Conf.*, Stuttgart, Germany, Sept. 22–26.

El-Genk, M. S., and H. Saber, 1998, "Heat Transfer Correlations for Small, Uniformly Heated Liquid Pools," *Int. J. Heat and Mass Trans.*, Vol. 41(2), pp. 261–274.

Groß, U., 1990, "Pool Boiling Heat Transfer Inside a Two-Phase Thermosyphon—Correlation of Experimental Data," *Proc. 9th Int. Heat Trans. Conf.*, Jerusalem, Israel, Paper No. 1-Bo-10, pp. 57–62.

Imura, H., H. Kusuda, Jun-Ichi Ogata, T. Miyazaki, and N. Sakamoto, 1979, "Heat Transfer in Two-Phase Closed-Type Thermosyphons," *J. Heat Transfer Japanese Res.*, Vol. 8(2), pp. 41–53.

Jialun, H., Ma Tongze, and Z. Zhengfang, 1992, "Investigation of Boiling Liquid Pool Height of a Two-Phase Closed Thermosyphon," *Proc. 8th Int. Heat Pipe Conf.*, Beijing, China, Ma Tongze, ed., Inst. of Eng. Thermophysics, Chinese Academy of Sciences, pp. 154–159.

Kaminaga, F., Y. Okamoto, and T. Suzuki, 1992, "Study on Boiling Heat Transfer Correlation in a Closed Two-Phase Thermosyphon," *Proc. 8th Int. Heat Pipe Conf.*, Beijing, China, Ma Tongze, ed., Inst. of Eng. Thermophysics, Chinese Academy of Sciences, pp. 317–322.

Kusuda, H., and H. Imura, 1973, "Boiling Heat Transfer in an Open Thermosyphon," *Bulletin of JSME*, Vol. 16, pp. 1734–1740.

Kutateladze, S. S., 1959, *Heat Transfer in Condensation and Boiling*, AEC-tr-3770, p. 129.

Ruckenstein, E., 1978, "Interpolating Equations Between Two Limiting Cases for the Heat Transfer Coefficient," *AIChE Journal*, Vol. 24, pp. 940–941.

Semena, M. G., and Y. F. Kiselev , 1978, "Heat Exchange in the Heat Supply Zone of Two-Phase Thermosiphons for Small Degree of Filling," *Inz. Fiz. Zh.*, Vol. 35(4), pp. 600–605.

Shiraishi, M., K. Kikuchi, and T. Yamanishi, 1981, "Investigation of Heat Transfer Characteristics of a Two-Phase Closed Thermosyphon," *Proc. 4th Int. Heat Pipe Conf.*, London, UK, *Advances in Heat Pipe Technology*, D. A. Reay, ed., Pergamon Press, pp. 95–104.

Ueda, H., T. Miyashita, and Ping-hsu Chu, 1988, "Heat Transport Characteristics of a Closed Two-Phase Thermosyphon," *Trans. JSME*, Ser. B, Vol. 54(506), pp. 2848–2855.

Wallis, G. B., 1969, *One-Dimensional Two-Phase Flow*, McGraw-Hill, New York.

Xiang-Qun, C., Z. Zhengfang, and Ma Tongze, 1992, "Heat Transfer Correlation of the Evaporator Section in a Two-Phase Closed Thermosyphon," *Proc. 8th Int. Heat Pipe Conf.*, Beijing, China, Ma Tongze, ed., Institute of Engineering Thermophysics, Chinese Academy of Sciences, pp. 354–359.

APPENDIX

Example: Local film heat transfer coefficient for ethanol at 305 K

From Fig. (4) at $\mathrm{Re}_x = 3.2$, $\mathrm{Nu}_x = 0.7469$, $h_x = ?$

Properties of ethanol at 305 K:

$$k_l = 0.1678 \ \mathrm{W/m \cdot K}$$

$$\rho_l = 779.12 \ \mathrm{kg/m^3}$$

$$\rho_g = 0.414 \ \mathrm{kg/m^3}$$

$$\mu_l = 0.99 * 10^{-3} \ \mathrm{N \cdot S/m^2}$$

Since:

$$\mathrm{Nu}_x = \frac{h_x l_l}{k_l},$$

where l_l is the characteristic thickness of the evaporating falling liquid film:

$$l_l = \left(\frac{\mu_l^2}{g \rho_l (\rho_l - \rho_g)} \right)^{1/3}.$$

Then, at the operating temperature (305 K):

$$l_l = 5.48116 \times 10^{-5} \ \mathrm{m}$$

$$\therefore h_x = \frac{k_l \, \mathrm{Nu}_x}{l_l} = \frac{0.1678 * 0.7469}{5.48116 * 10^{-5}},$$

$$\therefore h_x = 2286.55 \ \frac{\mathrm{W}}{\mathrm{m^2 K}}.$$

Impact of Channel Geometry on Two-Phase Flow Heat Transfer Characteristics of Refrigerants in Microchannel Heat Exchangers

T. S. Ravigururajan
Department of Mechanical Engineering,
Wichita State University,
Wichita, KS 67260

Microchannel surfaces, often machined to 20 to 1000 μm in width and depth, are employed in high-heat-flux applications. However, a large number of variables control the two-phase flow heat transfer coefficient. The pressure, the surface heat flux, and the mass flux significantly affect the thermal transport. Experiments were conducted on a setup that was built for testing microchannel heat exchangers. The parameters considered in the study are power input: 20 to 300 W, volume flow rate: 35 to 300 ml/min, quality: 0 to 0.5, inlet subcooling: 5 to 15°C. The results indicate that the heat transfer coefficient and pressure drop are functions of the flow quality, the mass flux, and, of course, the heat flux and the related surface superheat. The heat transfer coefficient decreases from a value of 12,000 W/m²-K to 9000 W/m²-K at 80°C, when the wall superheat is increased from 10 to 80°C. The coefficient decreases by 30 percent when the exit vapor quality is increased from 0.01 to 0.65.

Introduction

High-energy lasers and micro-electromechanical devices use heat fluxes on the order of 20 W/cm² with temperature differences of 50 to 80°C. The heat-dissipation requirement in miniaturized electromechanical and electronic applications is expected to rise to 400 W/cm² by the turn of the century. Microscale heat transfer shows much promise toward achieving the twin goals of high heat flux and low wall–fluid temperature difference. A microchannel heat exchanger consists of channels with width and depth measuring several hundred microns (Fig. 1). Using microfabrication techniques such as chemical etching, diamond cutting, and other micromachining processes, one can form channels with width as small as 30 μm and depth of 60 μm (Tuckerman and Pease, 1981; Cuta et al., 1995). Over the last decade, several investigations have focused on microscale heat transfer characteristics. These include theoretical models on laminar flows in heat sinks (Keyes, 1987), performance studies on air-cooled, silicon heat sinks (Mahalingam and Andrews, 1987), and other related numerical models (Phillips, 1987; Nayak et al., 1987; Hwang et al., 1987). Studying single- and two-phase flows in microchannels, Choi et al. (1991), Pfahler et al. (1990), and Wu and Little (1984) observe that the single-phase flow and boiling characteristics that have been established for larger channels (diameter greater than 5 mm) may not be applicable to microchannel flows. They note that this is due to the presence of a thinner boundary layer, and, perhaps, a vastly different bubble-generating mechanism within a microchannel. Liquid velocity and subcooling, and channel geometry are found to have significant effects on single-phase and boiling heat transfer coefficients for flow of methanol in microchannels (Peng et al., 1994). They observe qualitatively that the heat transfer coefficient becomes independent of wall temperature beyond the transition region. However, they argue that because the transition is also a direct result of the liquid temperature rise through the microchannels, liquid velocity and subcooling are equally important in determining this transition. What is more important is their suggestion that nucleate boiling intensified in microchannel leading to smaller wall surface superheat than in "normal" channels. More recently, Bowers and Mudawar (1994) demonstrated heat transfer rates in excess of 200 W/cm² in minichannels (widths measuring 1 to 2 mm) with a much reduced pressure rise, specifically for very low flow rates.

The theoretical studies are focused on the single-phase regime in parallel channels for obvious reasons. These studies make several assumptions. These include several assumptions on steady state, flow incompressibility, and negligible radiation. Other assumptions that may be relevant to microchannels are identical fin-base temperature, uniform properties, and isotropic thermal conductivity.

The *objectives* of this work were: (1) to study the impact of mass flux, heat flux, and wall superheat on two-phase flow heat transfer coefficient for channels of different geometry for Refrigerant-124, (2) to investigate the relationship between the quality and the thermal performance, and (3) to study the impact of subcooled boiling in microchannel passages for parallel and diamond channels.

Experiment

Test Section. Preliminary work by Wegeng and Drost (1994) indicated that there could be significantly higher heat transfer coefficients in microchannel heat exchanger than that in conventional large-scale heat exchangers. It was also expected that two-phase heat transfer in microchannels may lead to significantly more efficient heat transfer, and that flow conditions and channel geometry might be important factors in microscale heat transfer. To investigate these possibilities, a test article was developed using a copper substrate in which the microchannels were cut by conventional machining and were 1000 μm deep by 270 μm wide. The metal test article consisted of a copper substrate and a stainless steel cover, as shown in Fig. 1. The stainless steel cover fitted over the microchannels

Contributed by the Heat Transfer Division for publication in the JOURNAL OF HEAT TRANSFER. Manuscript received by the Heat Transfer Division September 13, 1996; revision received February 23, 1998. Keywords: Augmentation and Enhancement, Boiling, Heat Exchangers. Associate Technical Editor: T. J. Rabas.

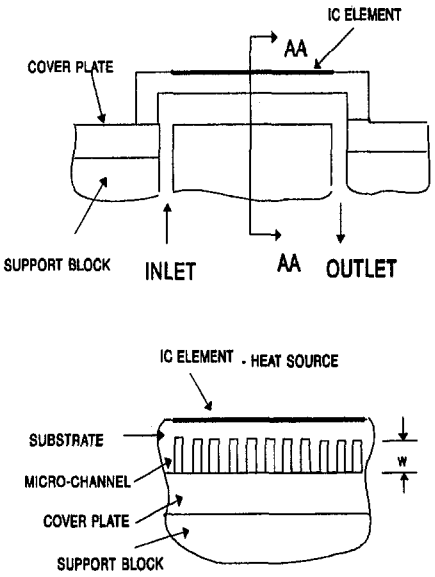

Fig. 1 Schematic of test section

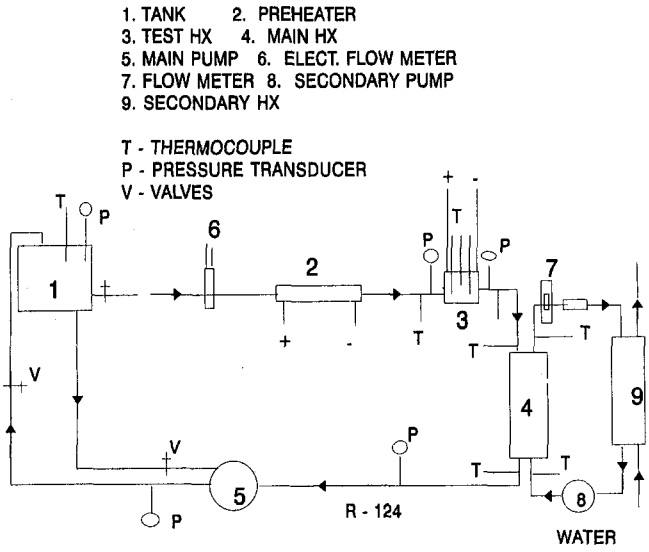

Fig. 2 Experimental test setup

to seal the channels at the top and to form the inlet and outlet headers. The two metal pieces were bolted together and sealed with an O-ring. The analytical expression of Tuckerman and Pease (1981) yielded an optimum channel size of about 2200 μm, while Bowers and Mudawar (1994) reported that channel width of less than 500 μm offers better heat transfer performance for refrigerant flows. In the present study, the channel size of 270 μm width and the depth of 1000 μm resulted in a hydraulic diameter of 425 μm.

A total of 54 microchannels, 2.052 cm long, were cut in the copper substrate. Including the inlet and outlet headers, the microchannel region of the test article was 2.25 cm by 2.42 cm overall. The test-section heater consisted of a thin titanium film sputter-deposited to a thickness of only a few thousand angstroms on the back side of the test article, covering the area of the microchannels. Cutting the test piece parallel to the tool axis formed the parallel channel, while the diamond-pattern channels were obtained by machining at an angle of 45 deg on either side of the central axis.

Experimental Loop. There were three sections to the experimental loop: the primary circulation section, the test-loop section, and the secondary heat-removal section (Fig. 2). The primary circulation section consisted of a surge tank, a metering valve, and a primary-loop circulation pump. This pressurized the system to specific operating pressures, and provided the driving pressure drop for the test loop. The test loop consisted of a 10 μm filter, a positive displacement flowmeter, a preheater, the test article, the shell side of shell-and-tube heat exchanger, and two metering valves to control the flow rate in the test-loop section.

The secondary section (heat removal) consisted of the tube side of the shell-and-tube heat exchanger, a circulation pump, a turbine flowmeter, and a cold water or ice bath for a heat sink. The instrumentation was designed to measure flow rate in the test loop and in the secondary loop, and fluid state (i.e., pressure and temperature) around the primary, test, and secondary loops. Thermocouples and pressure sensors were installed in the surge tank, at the inlet and outlet to the preheater, the test article, the shell-and-tube heat exchanger, and at other strategic locations in the test loop. More details on the test section fabrication and the experimental loop can be found in related references (Ravigururajan et al., 1996; Cuta et al., 1995).

Procedure. The working fluid, Refrigerant-124, filled the experimental rig as the loop was evacuated. The setup was run for about 10 minutes to stabilize the flow. The flow through the test section was controlled by simultaneous adjustment of valves in both the main and the bypass lines. Heat input to the preheater controlled the fluid temperature at the test-section inlet. This also controlled the degree of inlet subcooling. A cooling coil wrapped around the reservoir controlled the tank temperature (and the pressure).

Nomenclature

A = projected area, m^2
d = depth of channel, μm
I = current, amp
i = enthalpy, kJ/kg
h = heat transfer coefficient, W/m^2-K
L = length of channel, m
m = mass flow rate, kg/s
P = power, W
p = pressure, kPa
Δp = pressure difference, kPa
Pr = Prandtl number
q = heat transfer rate, W
q'' = heat flux, W/cm^2
T = temperature, K
ΔT = temperature difference, K
V = voltage, V
$\forall$ = volume flow rate, ml/min
ρ = density, kg/m^3
μ = dynamic viscosity, Pa·s

Subscripts

f = liquid
g = vapor
i = inlet
o = outlet
1ϕ = single-phase
2ϕ = two-phase

The valves were opened fully to achieve the maximum flow rate. The power input to the test section was adjusted from a minimum value of 20 W to 400 W. However, the power level was maintained to provide a wall superheat of 5 to 50°C depending on the flow rates. The experiments were repeated for different flow rates, which were obtained in steps of 25 ml/min. Data were collected for flow rates of 300 to 35 ml/min. Each run needed about 10 minutes (at high flow rates) to 20 minutes (at flow rates less than 100 ml/min) to reach steady state. Steady-state conditions were assumed to exist when temperature variations were within ±0.1°C over a 5 minute period.

Data Reduction. The energy balance between the power input and the energy absorbed by the test section was verified by performing single-phase tests. In single-phase flows, the inlet and outlet enthalpies were determined by measuring the fluid temperatures and pressures at both the inlet and the outlet. This energy was balanced by the energy input, that is, the power supply. The power input is calculated by the voltage across the gold bus and the current passing through it. An energy balance of less than ±5 percent was achieved. The energy absorbed by the working fluid is calculated by a simple energy balance as

$$q = m(i_{\text{out}} - i_{\text{in}}), \tag{1}$$

where

i_{out} = enthalpy at the outlet temperature
i_{in} = enthalpy at the inlet temperature.

The mass flow rate, m, is computed using the measured volume flow rate, $\forall$, and the density, ρ, which is calculated at the mean of the tank temperature and the inlet to the preheater temperature.

In two-phase (boiling) experiments, the outlet enthalpy, i_o, was calculated using the power input from the following expression:

$$i_o = i_i + P/m, \tag{2}$$

where i_i was the enthalpy at the test section inlet temperature.

The outlet enthalpy was compared with the saturated enthalpy at the outlet temperature to compute the vapor thermodynamic quality, x, from Eq. (3)

$$x = (i_o - i_{f,o})/(i_{g,o} - i_{f,o}), \tag{3}$$

where $i_{f,o}$ was the saturated liquid enthalpy at the test section outlet temperature and $i_{g,o}$ was the saturated vapor enthalpy at the same temperature. One should note that because the refrigerant entered the test section in a subcooled state, single-phase flow occurred within the initial section of the micro-channel heat exchanger. In this section, the heat transfer rate was equal to

$$q_{1\phi} = m(i_{f,o} - i_i) = h_{1\phi}A_{1\phi}(T_{\text{sur}} - T_m) \tag{4}$$

and

$$A_{1\phi} = m(i_{f,o} - i_i)A/P$$

The two-phase heat transfer and the heat transfer coefficient were similarly calculated from the following expression:

$$q_{2\phi} = m(i_o - i_{f,o}) = h_{2\phi}A_{2\phi}(T_{\text{sur}} - T_o) \tag{5}$$

and

$$A_{2\phi} = A - A_{1\phi}$$

Experimental Uncertainties. The microchannel heat exchanger (mHX) loop was built to facilitate experimentation over a wide range of parameters. The equipment, therefore, was selected to provide reliable and accurate data. The experimental uncertainties for the reduced data were based on the tolerances of individual components in the loop. The expected error due to the thermal resistance caused by the microchannel inner wall is 0.013°C/W, which was well within the experimental uncertainty.

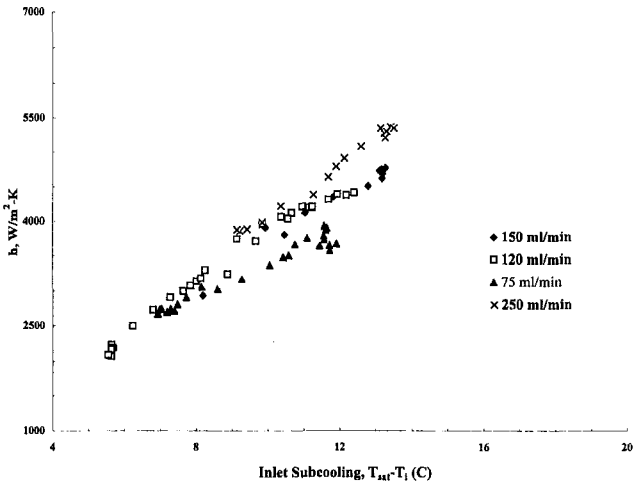

Fig. 3 Effect of inlet subcooling on heat transfer coefficient for parallel channel flows

The errors associated with the various equipment were: flow meter = 0.75 percent, pressure transducers = 0.4 percent of the scale, thermocouples (tank, HX inlet/outlet, secondary HX inlet/outlet, water inlet/outlet) = 0.2°C, resistance thermometers (surface temperature) = 0.1 percent, and the thermophysical properties = 2.5 percent. Based on the these tolerances and the method of Kline and McClintock (1953), the experimental uncertainties (on odds of 20 to 1) were estimated to be 3.8 percent for mass flow rate, 4.65 percent for Δp, 4.3 percent for heat absorbed by the refrigerant, and 9.2 percent for the heat transfer coefficient.

The heat loss from the test section to the surrounding atmosphere at 20°C was largely due to natural convection. The loss was found to be about 6.2 W when the power input was 200 W with a surface temperature of 40°C. Taking into account the radiation losses, the heat loss increased to 6.8 W, thus confirming the negligible loss due to radiation. Because of insulation, even at a higher surface temperature of 100°C, this loss was restricted to 7.1 W at a power input of 350 W. Therefore, the energy losses due to conduction and natural convection were minimal.

It is well known that temperature measurements can be made reliably and accurately. Because of this fact, the properties and energy balance calculations were based on temperature measurements. Use of pressure measurements was limited to pressure drop estimation. Also, the presence of noncondensable gases was minimized by maintaining the system pressure at 0.3 MPa or more. Studies have shown that limited release of noncondensable gases does not affect the two-phase flow characteristics (Tong et al., 1988). Consequently, the influence of any noncondensable gas on the results were neglected.

Results and Discussion

Subcooled Boiling. Subcooled boiling tests were performed on the diamond-channel mHX. The experiments were performed for an inlet subcooling, $(T_{\text{sat}} - T_i)$, of 5 to 15°C by controlling the power input to the preheater. The flow rate was varied from 75 to 250 ml/min and the heat flux was varied such that the exit fluid temperature was within the saturation temperature corresponding to the test-section exit pressure.

Figures 3–6 show the results of the subcooled boiling experiments. Inlet subcooling and the wall superheat, among other variables, are important characteristics that control subcooled

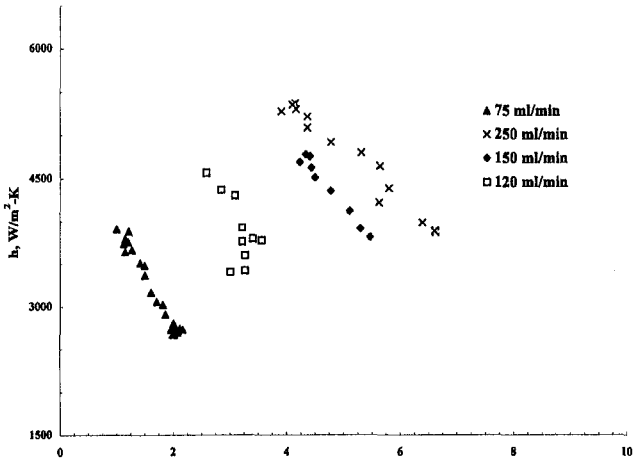

Fig. 4 Effect of wall superheat on heat transfer coefficient for parallel-channel flows

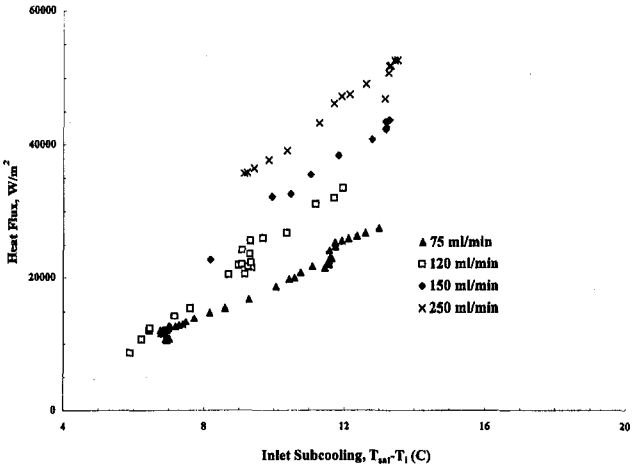

Fig. 5 Effect of inlet subcooling on heat flux for diamond-pattern channel flows

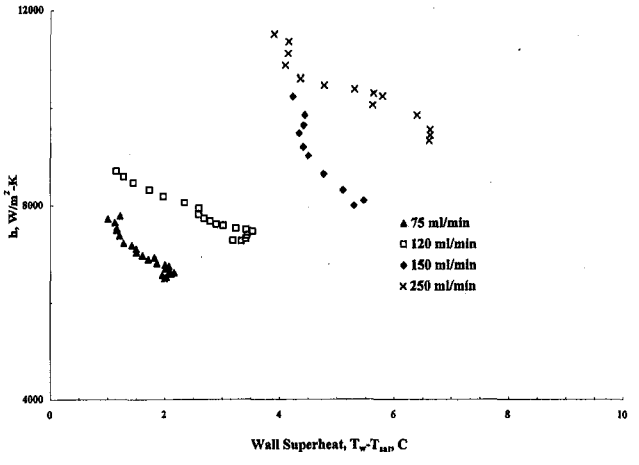

Fig. 6 Effect of wall superheat on heat transfer coefficient for diamond-pattern channel flows

boiling. Their effects on the heat transfer coefficient and the heat flux are illustrated in these figures. The dependency of heat transfer coefficient on the inlet subcooling is plotted for different flow rates in Fig. 3. The trend seen here is similar to that experienced in traditionally larger channels. The flow rate improves the heat transfer coefficient for inlet subcooling greater than 8°C. The difference is more pronounced as the subcooling is increased. The critical point occurs at higher values and shifts toward higher inlet subcooling as the flow rate is increased. Increasing wall superheat, on the other hand, decreases the heat transfer coefficient (Fig. 4). At a constant subcooling, higher heat transfer coefficient values are achieved for higher flow rates. The "h" value increases by more than 20 percent when the flow rate is increased from 150 ml/min to 250 ml/min at a subcooling level of 4°C. The enhancement is even higher at lower flow rates, as can be seen by the characteristics at 75 and 120 ml/min. At higher flow rate, the predominance of the convective transport during subcooling contributes to this higher heat transfer coefficient.

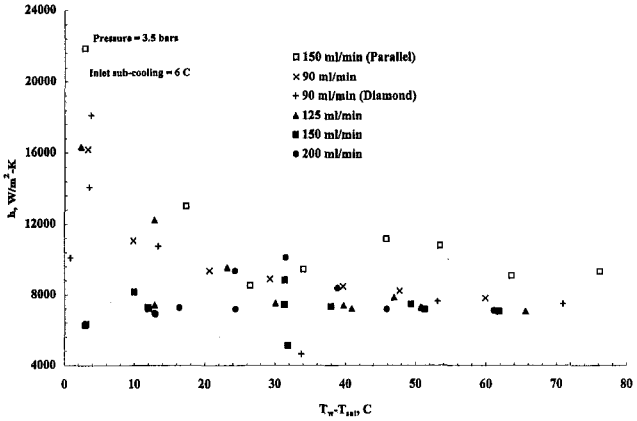

Fig. 7 Effect of wall superheat on heat transfer coefficient at different flow rates

The behavior of heat-flux characteristics with level of inlet subcooling is shown in Fig. 5 for different flow rates. The trends are similar to those obtained for the heat transfer coefficient characteristics. It is interesting to note the marked influence of the flow rate on the heat flux. The influence is greater as the subcooling is increased. Comparing the data for flow rates of 75 and 120 ml/min, the heat flux achieved is very close for subcooling of less than 8°C. The dependence of heat flux on the wall superheat is shown in Fig. 6. While the trends are similar to those seen in Fig. 4, one may notice the high heat flux achieved as the wall superheat is reduced. This observation is promising for applications that call for higher heat flux at low wall temperature differences, as in electronic components. These values are higher than what can be expected in saturated boiling in larger channels.

Saturated Flow Boiling. Following the subcooled boiling experiments, saturated boiling experiments were conducted with an average inlet subcooling of 5°C. The flow rates were varied from 35 ml/min to 300 ml/min. The preheater power supply was adjusted so as to maintain the desired inlet subcooling. Another parameter that is important in boiling heat transfer is the surface superheat. The surface superheat varied from 2°C to about 80°C. The results are plotted in Figs. 7–13.

The variation of heat transfer coefficient with respect to wall superheat is shown in Fig. 7. The heat transfer coefficient varied from high value of 18,000 W/m^2-K for a wall superheat of 4°C to about 7000 W/m^2-K for wall superheat greater than 40°C. The decrease is more pronounced within the wall superheat range of 0 to 20°C, followed by a steady decline. Figure 7 shows the data for four different volumetric flow rates. The peak heat transfer coefficient values decrease with increasing flow rates. For instance, at flow rates of 150 and 200 ml/min, the heat transfer coefficient is about 8000 W/m^2-K even for wall superheats of less than 5°C. The results for flow rates of 90 and 150 ml/min from an earlier study (Ravigururajan et

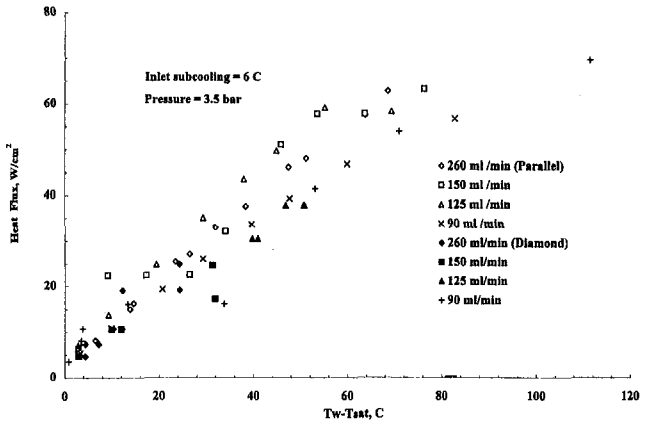

Fig. 8 Influence of wall superheat on heat flux at different flow rates

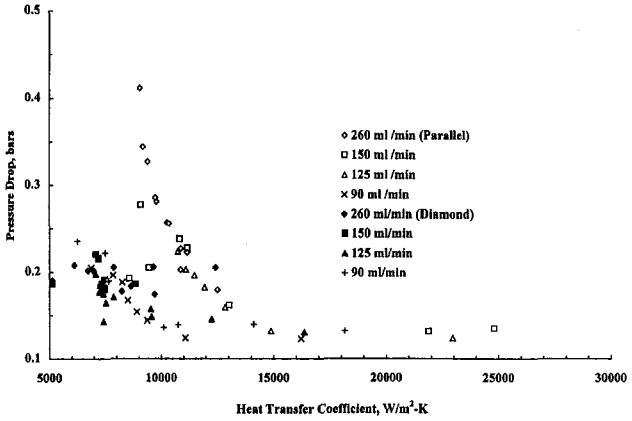

Fig. 11 Relationship between h and ΔP

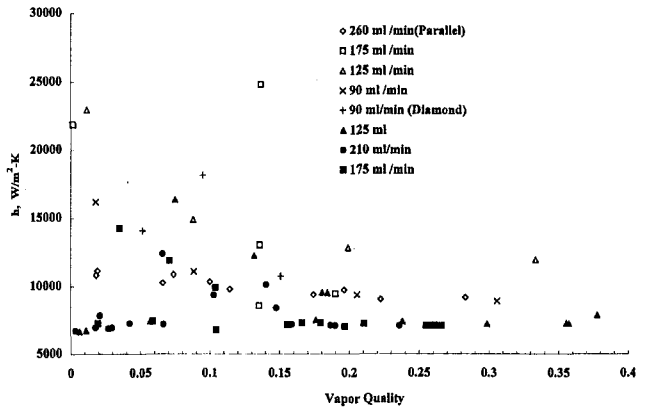

Fig. 9 Effect of vapor quality on heat transfer coefficient

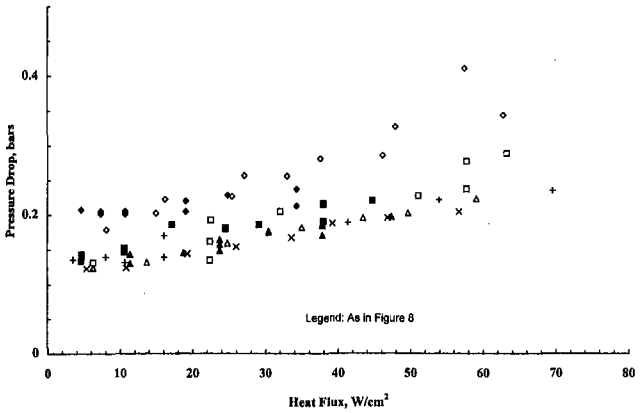

Fig. 12 Relationship between pressure drop and heat flux

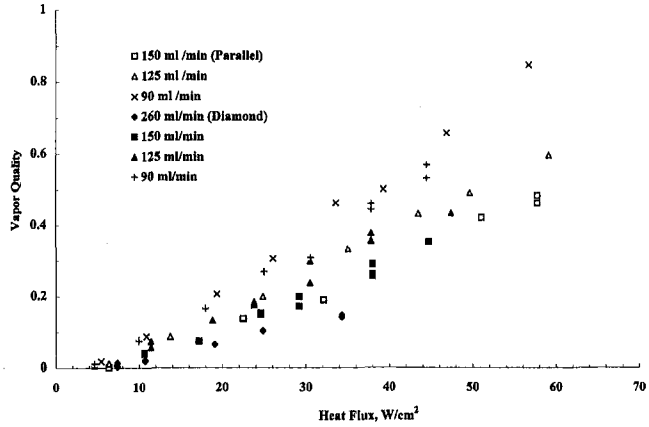

Fig. 10 Effect of heat flux on vapor quality

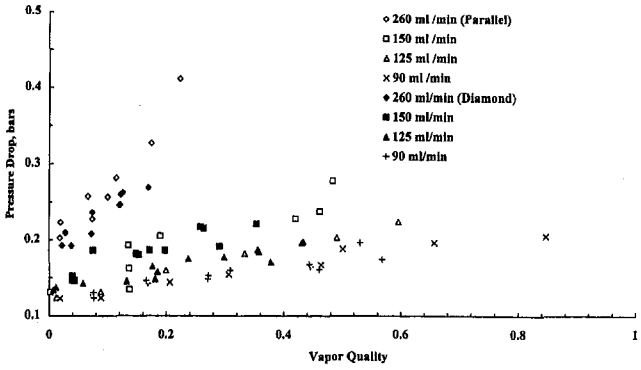

Fig. 13 Relationship between vapor quality and pressure drop

al., 1996) on a parallel-channel micro-heat exchanger are superimposed for comparison. As can be seen, the data for parallel channel flow are 20 percent higher than for the diamond channel at corresponding conditions. Also, in the parallel channel, the heat transfer coefficient is higher at 150 ml/min than at 90 ml/min, a trend opposite to that observed in the diamond channel. It is, however, clear that the heat transfer coefficients are higher for microchannel flow. For example, using Chen's correlation (1966), the heat transfer coefficient for refrigerants is about 3000 W/m^2-K at a wall superheat of 10°C. Thus, there is considerable enhancement in heat transfer that can be attributed to the thinner boundary layer and the narrow channel width.

In Fig. 8 the heat flux is plotted against the wall superheat. The figure shows the data for both the parallel and the diamond channel heat exchanger for different flow rates from 90 ml/min to 260 ml/min. The impact of flow rates on heat flux is minimal in diamond channel. In contrast, the flow rate has a more pronounced effect in the parallel channel. At a wall superheat of 50°C, a difference in heat flux of 25 percent can be noticed between flow rates of 90 ml/min to 150 ml/min. The difference that is noticeable in the nucleate boiling region decreases considerably when the wall superheat is increased to 70°C. The critical heat flux is higher by 20 percent in diamond channel at ml/min.

One of the important questions in flow boiling is the impact of quality on the heat transfer coefficient (Fig. 9). Both the heat transfer coefficient and the vapor quality are dependent functions. This form of the plot is provided to obtain the relationship between these two variables in a clearer manner. The heat transfer coefficient decreases with quality from a value of around 15,000 W/m^2-K at $x = 0.01$ to a value of 7000 W/m^2-K corresponding to a quality of 0.15. Similar decreases were noticed at other flow rates as well. This is different from the trend observed during the boiling process in large tubes. In large tubes, the heat transfer coefficient increases in the nucleate boiling region ($x < 0.3$) before decreasing in the film boiling regime. One reason for this steady decrease in heat transfer coefficient is possible choking of the channel width by the bubbles released from the surface. While no specific information is available on bubble dynamics in microchannels, in larger channels the bubble departure diameter ranges from 5 to 20 μm. The influence of inlet velocity on the heat transfer performance is not clear from this study. The heat transfer coefficient appears to increase in the flow rate range of 90 to 150 ml/min and then decrease for higher flow rates. One interesting observation is that, unlike in a parallel channel flow, the impact of quality on heat transfer coefficient is less severe at flow rates less than 150 ml/min. Perhaps, the alternate flow paths formed by the diamond pattern minimizes the possibility of choking. The results are preliminary at best and the reader is cautioned that this characteristic cannot be quantified from this limited study.

The variation of vapor quality with heat flux, on the other hand, shows some clear trends (Fig. 10). The quality increases as the flow rate is decreased at any particular heat flux. Conversely, at a quality of 0.2, the heat flux can be increased from 20 W/cm^2 at a volume flow rate of 90 ml/min to nearly 40 W/cm^2 at a flow rate of 150 ml/min. Although the figure may imply that larger heat fluxes can be achieved with higher flow rates, one cannot be sure of this observation. Much larger heat fluxes were not possible with the present experimental setup. As with the other plots, the data of the diamond channel are below those of parallel channel for similar flow rates. Consequently, much greater heat fluxes can be achieved with a diamond-channel micro heat exchanger than that is possible with a parallel-channel micro-heat exchanger.

As with any heat transfer enhancement, the pressure drop in microchannel flows is important for many applications. Often pressure drop changes differently than the heat transfer rates. The pressure drop data are plotted against the heat transfer coefficient at different flow rates (Fig. 11). This figure illustrates several characteristics that are of practical interest. First, the pressure drop is less severe in diamond-channel flow than in parallel channel flow. Second, the steep fall in pressure drop noticed in the parallel channel is absent in the diamond channel. Finally, the flow rate has less impact on the pressure drop variation in a diamond channel. The influence of flow rate on the pressure drop is weak when high heat fluxes are achieved with small ΔT superheat, which yields a large heat transfer coefficient. The limit on the heat transfer coefficient may therefore be due to the heat supplied to the surface. However, as the ΔT increases (decreasing "h") the pressure drop in the channels increases dramatically, especially at larger flow rates. The stronger dependence can be attributed to the two-phase acceleration caused by the increasing amount of vapor in the channel.

The relationship between the pressure drop and the heat flux is shown in Fig. 12. The influence of heat flux is negligible in the case of the diamond channel. In the parallel channel, the pressure drop increases slowly as the heat flux is increased. In addition, while the pressure drop increases with the increase in heat flux, the effect is more pronounced at higher flow rates. Two trends are visible from this plot: The ΔP increases with increasing heat flux and flow rate. The pressure drop in microchannels depends on the type of boiling process taking place within the channels. The pressure-drop behavior with the vapor quality is shown in Fig. 13. The pressure drop is high at larger flow rates even when the quality is low, perhaps mainly because of the large increase in vapor volume. The characteristics of both channel types are similar. The pressure drop increase is steeper at larger flow rates. Here again, more tests may be needed, encompassing each type of boiling regime, before any conclusions can be arrived at.

The boiling process in both the channels is indicated by the constant outlet fluid temperature for heat fluxes of greater than 40 W/cm^2. However, for a heat flux of less than 40 W/cm^2, in the subcooled region, significant differences in fluid outlet temperature can be noticed among various flow rates.

Inferences

Subcooled and saturated flow boiling experiments were conducted on a diamond-pattern microchannel heat exchanger. Based on the experiments and the data obtained at various flow rates, the following inferences can be made:

1. High heat flux may be achieved accompanied by small wall superheat in subcooled boiling.
2. Heat transfer coefficients are influenced by flow rates for inlet subcooling greater than 8°C.
3. The heat transfer coefficient is dependent on wall superheat. The value decreased dramatically to about 12,000 W/m^2-K corresponding to a wall superheat of 10°C, further decreasing to a value of about 9000 W/m^2-K at a wall superheat of 80°C.
4. The heat transfer coefficient decreases with quality from a value of around 11,000 W/m^2-K at $x = 0.01$ to a value of 8000 W/m^2-K corresponding to a quality of 0.65. This decreasing trend is noticed at different flow rates. For flow rates greater than 125 ml/min, the heat transfer coefficient remains constant in diamond-channel mHX.
5. The pressure drop decreases rapidly with an increasing heat transfer coefficient, decreases marginally when the heat flux is reduced, and increases with an increasing vapor quality.
6. Compared to the parallel channel mHX with corresponding channel depth and height, the diamond channel heat exchanger yields a lower heat transfer coefficient.

Acknowledgments

The author was supported by a Department of Energy Summer Fellowship through the AWU-NW division. He is grateful to Dr. M. K. Drost for his support and encouragement during his work at Pacific Northwest National Laboratory. Pacific Northwest National Laboratory is operated by Battelle Pacific, Inc., for the U.S. Department of Energy.

References

Bowers, M. B., and Mudawar, I., 1994, "High Heat Flux Boiling in Low Flow Rate, Low Pressure Drop Mini-channel and Micro-channel Heat Sinks," *Int. J. Heat Mass Transfer,* Vol. 37, No. 2, pp. 321–332.

Chen, J. C., 1966, "Correlation for Boiling Heat Transfer to Saturated Fluids in Convective Flow," *Ind. Eng., Chem., Proc. Design and Dev.,* Vol. 5, No. 3, pp. 322–339.

Choi, S. B., Barron, R. F., and Warrington, R. O., 1991, "Liquid Flow and Heat Transfer in Microtubes," *Micromechanical Sensors, Actuators, and Systems,* ASME DSC-Vol. 32, D. Choi et al., eds., pp. 123–128.

Cuta, J., Benett, W., McDonald, C. E., and Ravigururajan, T. S., 1995, "Fabrication and Performance Testing of Micro-Heat Exchangers," presented at the SPIE International Conference, Austin, TX.

Hwang, L. T., Turlik, I., and Reisman, A., 1987, "A Thermal Module for Advanced Packaging," *J. Electronic Materials,* Vol. 16, pp. 347–355.

Keyes, R. W., 1987, "Heat Transfer in Forced Convection Through Fins," *IEEE Transactions on Electronic Devices,* ED-31, pp. 1218–1221.

Kline, S. J., and McClintock, F. A., 1953, "Describing Uncertainties in Single-Sample Experiments," *Mechanical Engineering,* Vol. 75, Jan., pp. 3–8.

Mahalingam, M., and Andrews, J., 1987, "High Performance Air Cooling for Microelectronics," *Proc. Intl. Cooling Tech. for Electronic Equipment,* Honolulu, HI, 6028-625.

Nayak, D., Hwang, L. T., Turlik, I., and Reisman, A., 1987, "A High Performance Thermal Module for Computer Packaging," *J. Electronic Materials,* Vol. 16, pp. 357–364.

Peng, X. F., Wang, B. X., Peterson, G. P., and Ma, H. B., 1994, "Experimental Investigation of Heat Transfer in Flat Plates With Rectangular Micro-Channels," *Int. J. Heat Mass Transfer,* Vol. 38, No. 1, pp. 127–137.

Pfahler, J., Harley, H., Bau, H. H., and Zemel, J., 1990, "Liquid Flow and Heat Transfer in Micron and Submicron Channels," *J. Sensors and Actuators,* Vol. A21–23, pp. 431–434.

Phillips, R. J., 1987, "Micro-channel Heat Sinks," *The Lincoln Laboratory J.,* Vol. 1, pp. 31–48.

Ravigururajan, T. S., Cuta, J., McDonald, C. E., and Drost, M. K., 1996, "Effects of Heat Flux on Two-Phase Characteristics of Refrigerant Flows in a Micro-Channel Heat Exchanger," submitted to *J. Enhanced Heat Transfer.*

Tong, W., Simon, T. W., and Bar-Cohen, A., 1988, "Effect of Dissolved Gas on Boiling Incipience in Highly-Wetting Liquids," presented at the 5th Miami Int. Symp. on Multi-Phase Transport & Particulate Phenomena, Dec.

Tuckerman, D. B., and Pease, R. F. W., 1981, "High-Performance Heat Sinks for VLSI," *IEEE Electron Device Lett.,* EDL-2, pp. 126–129.

Wegeng, R. S., and Drost, M. K., 1994, "Developing New Miniature Energy Systems," *Mechanical Engineering,* Sept., pp. 82–85.

Wu, P. Y., and Little, W. A., 1984, "Measurement of the Heat Transfer Characteristics of Gas Flow in Fine Channel Heat Exchanger Used in Micro-miniature Refrigerators," *Cryogenics,* Vol. 24, pp. 415–423.

A Boundary/Finite Element Analysis of Magnetic Levitation Systems: Surface Deformation and Thermal Phenomena

S. P. Song
Graduate Research Assistant.

B. Q. Li[1]
Associate Professor.
Mem. ASME

School of Mechanical and Materials Engineering, Washington State University, Pullman, WA 99164

This paper describes a coupled boundary and finite element analysis of electromagnetic, free surface deformation and thermal problems in magnetic levitation systems under both normal and microgravity conditions. A computer code is developed, which involves the use of finite elements in the regions of interest and boundary elements in other regions for electromagnetic field calculations, along with an iterative and remeshing scheme for free surface deformation calculations. The code is tested against available analytical solutions and experimental measurements, and then applied to study the free surface deformation and temperature distribution in magnetically levitated droplets on earth and in microgravity. It is found that an accurate assessment of the thermal behavior of a droplet must be made along with its deformation, including the bulk movement, for magnetic levitation systems. In normal gravity, a magnetically levitated droplet assumes a conical shape with its apex pointing downward, and higher temperature occurs in the lower portion of the droplet. In microgravity, on the other hand, surface deformation is primarily attributed to the heating coils and the deformation is symmetric, with the droplet squeezed at the equator plane and bulged out along the axis of symmetry. Positioning coils give rise to a smaller deformation force and a lower Joule heating rate under normal operation conditions. The temperature profiles and free surface shapes induced by the positioning coils, though symmetric, are different from those induced by heating coils.

I Introduction

By Faraday's law of induction, eddy currents will be induced in an electrically conducting specimen when excited by an external alternating magnetic field. The interaction of the induced eddy currents and the total magnetic field, which is a combination of the self-induced and imposed magnetic fields, will result in electromagnetic forces or Lorentz forces in the specimen. If the external magnetic field is strong enough so as to balance the gravitational force, the specimen will be levitated by the magnetic field. Another phenomenon, perhaps a more familiar one, associated with magnetic induction, is the Joule heating effect, which comes from the self-interaction of the induced eddy currents in the specimen. Magnetic levitation, or more precisely magnetic levitation melting, is a processing technology for inductively heating or melting a conducting sample while suspended in an inert gas atmosphere or vacuum. The advantage of magnetic levitation is obvious. Without a container for melting, the potential contamination from container walls is eliminated, and thus it is possible to process materials of ultrahigh purity.

The first magnetic levitation processing system was invented in Germany more than half a century ago (Muck, 1923). There are many levitation systems in operation today. Much of the current research has been concerned with designing more advanced levitation systems and/or optimizing magnetic levitation conditions so as to support the largest possible load (Natarajan and El-Kaddah, 1995; Szekely et al., 1995). Recent studies have shown that it is now possible to levitate a copper sample of 1000 g magnetically under terrestrial conditions. This is in contrast with most levitation systems, which are only capable of supporting up to 50 g of liquid (Mestel, 1982; Szekely et al., 1995). Research activities in magnetic levitation have also contributed to the development of other similar or derivative electromagnetic processes widely used in industry including electromagnetic casting (Getzlev, 1971) and floating-zone single-crystal growth processes (Keller and Muhlbauer, 1981).

The concept of magnetic levitation has now been explored for space processing of materials and for measuring the thermal and physical properties of materials in microgravity, such as undercooled melts, which otherwise would be impossible under earthbound conditions. Studies suggest that with magnetic levitation (or more precisely positioning) in microgravity, it is possible to achieve a large undercooling by which materials of extremely high purity with very fine solidification microstructures can be obtained (Herlach, 1991; Herlach and Feuerbacher, 1991). Magnetic levitation in microgravity also offers a uniquely useful means to measure thermal and physical properties of materials (solid, liquid, or undercooled melts), such as surface tension, viscosity, conductivity, and heat capacity, without interference from the impurities originated from container walls (Herlach, 1991). For example, the surface tension and viscosity of a melt can be determined through detecting the frequency of surface oscillation of a melt blob and by measuring the decay of its surface deformation amplitude, respectively (Herlach, 1991; Egry et al., 1992; Szekely et al., 1995; Bayazitoglu et al., 1996). The needed free surface oscillation can be readily achieved in a magnetic levitation system in microgravity, for instance, by squeezing a melt drop by suddenly applying a pulse current.

There has been extensive work on magnetic levitation since the pioneer research on the subject was conducted by Okress et al. (1952). The published work has addressed issues ranging

[1] Corresponding author.

Contributed by the Heat Transfer Division for publication in the JOURNAL OF HEAT TRANSFER. Manuscript received by the Heat Transfer Division August 14, 1996; revision received January 30, 1998. Keywords: Liquid Metals, Materials Processing and Manufacturing Process, Microgravity Heat Transfer. Associate Technical Editor: A. S. Lavine.

from electrodynamics to transport phenomena involved in levitation systems using analytical, perturbation, and numerical methods. Rony (1969) studied magnetic levitation melting processes for metals and Mestel (1982) used an analytical approach to investigate the magnetically induced deformation and flow in an isothermal droplet. Bayazitoglu and co-workers (Suryanarayana and Bayazitoglu, 1991; Bayazitoglu and Sathuvalli, 1994, 1996; Sathuvalli and Bayazitoglu, 1993, 1994; Bayazitoglu et al., 1996) presented studies on the Joule heating, force distribution, and shape oscillations associated with magnetically levitated droplets. Lohofer (1989) solved a three-dimensional vector potential problem analytically and used the solution to study the power absorption and lifting force in a solid sphere in magnetic levitation systems. Numerical models, based on the mutual inductance method for surface deformation and the finite element method for turbulent flow, were developed recently (Zong et al., 1992, 1993). They analyzed both steady-state and unsteady-state fluid flow in levitation systems in microgravity, and provided a basic, lumped estimate of heat transfer in the liquid droplet. Their models were also used in further studies for developing a better understanding for the system design (Schwartz et al., 1992). All these studies, however, focused on the isothermal melt flow, and the detailed temperature effects were not considered. In a series of papers published recently, Li (1993, 1994a, b) has presented analytical models for the electrodynamic, fluid flow, and temperature distributions in an aluminum sphere in microgravity. Both the transient and steady-state conditions were considered. The analyses, however, were made by assuming that the deformation effect may be neglected, and thus are only applicable to levitation in a weak magnetic field.

While useful work has been done, many important issues remain unanswered. For example, to our best knowledge, there has not yet been any published research on how the free surface deformation would affect the Joule heating distribution and hence the temperature field in a droplet in magnetic levitation systems. While in general it is understood based on asymptotic analyses (Li, 1993) that either a higher applied current or a higher frequency would produce a higher temperature, the present study indicates that a more accurate assessment must include free surface deformation and sample position in the levitation potential well. The necessity of including magnetically induced free surface behavior in the analyses introduces nonlinearity and thus requires the use of numerical methods. Analyses of this type are of critical importance, especially in light of a high degree of temperature control required for carrying out most levitation experiments.

In this paper, a numerical analysis is described of free surface deformation and temperature field distribution in a conducting liquid droplet magnetically levitated under both normal and microgravity conditions. The analysis is carried out by applying a coupled boundary and finite element method, which is uniquely suited for this type of problems involving boundaries at infinity. By this method, finite elements are used to discretize the droplet region where information on electromagnetic field and temperature field distributions is needed, while boundary elements are applied in the free space outside the droplet region. The finite element and boundary element regions are then coupled through the interface boundary conditions. In developing the coupled boundary and finite element code, the LU decomposition, instead of direct matrix inversion, is used to facilitate the computation of interface flux distribution, and node data are

Nomenclature

a = radius of a sphere
A, A^* = tangential component of magnetic vector potential inside droplet, its complex conjugate
$\mathbf{A}$ = global unknown nodal vector of vector potential
$\mathbf{B}$, $\mathbf{B}^*$ = magnetic field, its complex conjugate
C = geometric coefficient resulting from boundary integral formulation
C_p = heat capacity
$E(\kappa)$ = elliptical integral of the second kind
f = force vector resulting from LU decomposition of BE matrix equations
$\mathbf{F}$ = force vector in BE formulation
$\bar{\mathbf{F}}$ = time-averaged Lorentz force
$\tilde{F}$ = global force vector of coupled BE–FE formulation
g = gravity constant
G = Green's function for free space
$\mathbf{H}$, $\mathbf{G}$ = global coefficient matrices of BE formulation
I = current (peak)
I_n = modified Bessel function of the first kind of order n
$j = \sqrt{-1}$
J = tangential component of current density
k = system parameter for electromagnetic field
K = thermal conductivity
$K(\kappa)$ = elliptical integral of the first kind
$\mathbf{K}$ = global coefficient matrix of FE formulation
$\tilde{\mathbf{K}}$ = global coefficient matrix of coupled BE–FE formulation
$\mathbf{M}$ = matrix resulting from LU decomposition of BE matrix equations
$\mathbf{N}$ = boundary flux coefficient matrix of FE formulation
$\mathbf{n}$ = outward normal
P_m, P_H = time-averaged magnetic pressure, pressure constant
P_l, P_l^1 = Legendre polynomials, associated Legendre polynomials of the first kind
$\mathbf{q}$ = global normal derivative vector of $\mathbf{A}$
$\mathbf{r}$, r = point vector and r coordinate
r_o = radial distance of a single coil in spherical coordinates
t = time
T, T_∞ = temperature, temperature of surroundings
$\mathbf{u}$ = free surface unknown vector
$\hat{z}$ = unit vector of z direction
z = z coordinate
z_c = center of mass along the z axis
α = subtended angle of the exciting coil for single sphere system
β = angle between the outnormal and x direction
ϵ = permittivity
ϵ_o = emissivity
$\partial\Omega^1$, $\partial\Omega^2$ = boundary of FE and BE computational domains
∇ = gradient operator
ϕ = shape function
$\hat{\phi}$ = unit vector in the azimuthal direction
γ = surface tension
κ = geometric parameter for elliptical functions
μ = magnetic permeability
ρ = density
θ = θ direction
σ = electrical conductivity
σ_o = Stefan–Boltzmann constant
ω = frequency
Ω_1, Ω_2 = FE and BE computational domains

Subscripts

I = boundary and finite element region interface
B = boundaries excluding the interface between the BE and FE regions
T = temperature
z = z component

Superscripts

* = complex conjugate
f = free surface
i = ith component
T = matrix transpose

appropriately arranged to preserve the skyline structure of the finite element discretization in order to improve the computational efficiency. The code is enhanced by an iterative scheme and remeshing capability for free surface calculations. The developed code is tested against available analytical solutions and experimental measurements, and is then applied to examine the free surface deformation and temperature field distribution in magnetically levitated droplets.

It should be pointed out that in carrying out the detailed numerical analyses, convection in the droplets has been neglected. Studies suggest that during magnetic levitation, a mild turbulent recirculating flow occurs in the liquid and is mainly attributed to the vortical nature of the Lorentz force, which is several orders of magnitude bigger than other forces, such as buoyancy and Marangoni forces, that may be present (Mestel, 1982; Li, 1994a). In terrestrial levitation systems, strong currents must be applied to support the sample weight, thereby inducing an internal turbulent flow. Likewise, in microgravity environments, strong currents intended for heating would also be responsible for a possible turbulent recirculating flow in the liquid droplets. These flows are thought to be in a mild or weak turbulence regime (Zong et al., 1993). The flow induced by the positioning coils alone in microgravity is often very weak because of the coil configuration and a relatively small current requirement (Zong et al., 1993). These convective flows will likely result in convective mixing in droplets and thus give rise to a more uniform temperature distribution than predicted by a conduction analysis only. While the flow is believed to play an undisputed role in redistributing the thermal energy in the droplets, several important points must be noted. First, there has been essentially no adequate turbulence model for this mildly turbulent flow in the droplets. This is further complicated by a lack of a reliable numerical algorithm by which turbulent flow and free surface deformation are simultaneously predicted with good confidence for a levitated droplet. Furthermore, in determining the thermal field distribution, the Joule heating plays a predominant role and its correct prediction is critically dependent upon the free surface geometry and droplet position but essentially independent of the flow under normal levitation conditions (Li, 1994a; Zhang et al., 1997). This is because, as in many other materials processing systems, the magnetic Reynolds number for levitation systems is small enough to warrant a decoupled calculation of the electromagnetic field from fluid flow (Mestel, 1982; Zong et al., 1992; Li, 1994a). Also, the major contribution to the deformation of droplet free surface comes from the induced electromagnetic forces. The fluid flow correction, to the best possible scenario, is below 10 percent (Schwartz and Szekely, 1995). In light of these, the thermal field is only modeled partially in our analyses. Nonetheless, the present analysis should capture the essential features of the free surface deformation and its effect on the thermal behavior of a magnetically levitated liquid droplet that so far have eluded analysis. The information provided in this study may also be used to provide basic guidelines for developing magnetic levitation systems or planning levitation experiments for both terrestrial and microgravity applications.

II Problem Statement

Without loss of generality, we consider a magnetic system as shown in Fig. 1. An electrically conducting sample is immersed in an alternating magnetic field generated by a set of current loops surrounding the sample. Because of induction, both Joule heating and Lorentz force will be generated in the sample. The former is responsible for melting the sample, while the latter levitates the sample and deforms the melt free surface. In this paper, we focus on the aspects of the electromagnetic, free surface deformation and thermal phenomena associated with the magnetically levitated melt samples.

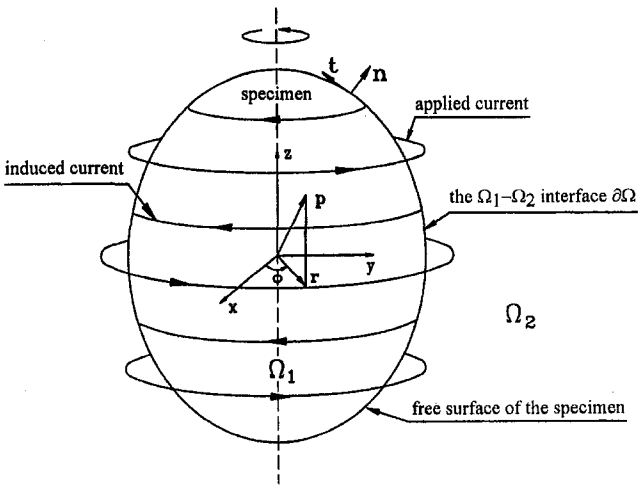

Fig. 1 Schematic representation of magnetic levitation system. The cylindrical coordinate system used for numerical analyses is also shown.

For the axisymmetric system shown in Fig. 1, the Maxwell equations may be simplified in terms of the tangential component of the magnetic vector potential A (Li, 1993),

$$\nabla^2 A - A/r = k^2 A - \mu J \tag{1}$$

where $k = \sqrt{j\mu\sigma\omega}$ is the system parameter and J the applied current density. Note that A and J are complex amplitudes of the corresponding variables written in phasor notation to represent the time harmonic variation of the electromagnetic field. Also, Eq. (1) applies to both the inside and outside of the sample. When applied to the outside region, which is free space, $k = 0$.

It is remarked that in writing Eq. (1), we have assumed that the displacement $\partial \mathbf{D}/\partial t$ may be neglected (Jackson, 1975). For induction systems such as magnetic levitation, the applied frequency is on the order of 10^6 Hz. For a good conductor such as metal, the electrical conductivity σ is on the order of 10^7 ($1/\Omega$-m or $C^2/N\text{-}m^2\text{-}s$). With these, $\omega\epsilon/\sigma \sim 10^{-12} \ll 1$, where $\epsilon = 8.854 \times 10^{-12}$ ($C^2/N\text{-}m^2$), therefore well justifying the approximation.

To solve the vector potential equation, physical constraints need to be imposed. Along the interface between the sample and the free space, the tangential component of the electric field and the normal component of the magnetic field must be continuous. Written in terms of the magnetic vector potential, these constraints become

$$A_o = A \tag{2}$$

$$\frac{1}{\mu_o}\frac{\partial A_o}{\partial n} = \frac{1}{\mu_i}\frac{\partial A}{\partial n} \tag{3}$$

where the subscripts i and o denote quantities inside and outside the sample. For a melt, $\mu_i = \mu_o = \mu$. To simplify the notation, the subscript i has been dropped from A and this hereinafter will hold true unless otherwise indicated.

Other electromagnetic field quantities may be calculated from A. For magnetic levitation systems, the time-averaged force and Joule heating power density distribution in a melt droplet are parameters of interest and can be calculated by the following equations (Zong et al., 1992; Li, 1993):

$$\bar{\mathbf{F}} = \frac{\omega}{2\pi}\int_0^{2\pi/\omega} \mathrm{Re}\,(Je^{j\omega t}\hat{\phi})\cdot\nabla\times(\mathrm{Re}\,(Ae^{j\omega t}\hat{\phi}))\,dt$$

$$= \frac{\omega\sigma}{2}\,\mathrm{Re}\,(jA^*\hat{\phi}\cdot\nabla\times(A\hat{\phi})) \tag{4}$$

$$Q = \frac{\omega}{2\pi\sigma}\int_0^{2\pi/\omega} \mathrm{Re}\,(Je^{j\omega t})\cdot \mathrm{Re}\,(Je^{j\omega t})dt$$

$$= \frac{J\cdot J^*}{2\sigma} = \frac{\sigma\omega^2 A^*\cdot A}{2} \tag{5}$$

The temperature distribution in a levitated specimen is governed by the heat conduction equation with internal heating provided by the induced Joule heating source,

$$\rho c_p \frac{\partial T}{\partial t} = \nabla\cdot(k\nabla T) + \frac{\sigma\omega^2 A\cdot A^*}{2} \tag{6}$$

Magnetic levitation is often carried out in a vacuum and hence the heat transfer between the chamber walls and the sample surface is by thermal radiation,

$$-K\frac{\partial T}{\partial n} = \sigma_o\epsilon_o(T^4 - T_\infty^4) \tag{7}$$

If the internal flow contribution may be neglected, the kinematic condition is automatically satisfied and the equilibrium surface shape is then defined by the balance of hydrostatic, magnetic, and surface tension forces. This balance condition is equivalent to requiring that the normal stress is continuous across the interface between the sample and its surroundings, i. e.,

$$\gamma\nabla_s\cdot\mathbf{n} = \rho g z + P_H + P_m \tag{8}$$

where $\nabla_s = \nabla - \mathbf{n}(\mathbf{n}\cdot\nabla)$ is the surface divergence operator (Weatherburn, 1972). In this equation, the magnetic effect comes into play through the time-averaged magnetic pressure, which is calculated from the known vector potential field (Jackson, 1975),

$$P_m = \frac{\mathbf{B}\cdot\mathbf{B}^*}{4\mu} = \frac{\nabla\times(A\hat{\phi})\cdot\nabla\times(A^*\hat{\phi})}{4\mu} \tag{9}$$

III Boundary and Finite Element Formulation

The numerical solution of the magnetic vector potential equation (Eq. (1)) often involves the discretization of the domain extending to infinity, even though the main interest here is the levitated sample itself. This would substantially increase the computational time and data storage requirement. To circumvent this problem, we developed a coupled boundary and finite element algorithm (Song and Li, 1995, 1996; Song, 1996) such that the finite element meshes are applied in the region occupied by the sample and the boundary elements are used to account for the outside region. A particular advantage of applying boundary elements in the outside region for the system under consideration is that the boundary condition at infinity can be directly formulated into the boundary integral equation. As a result, no discretization is required for the internal points, nor for the boundary at infinity, resulting in savings in both computational time and storage space. This feature can be particularly important for the present study in that the calculation of free surface deformation requires an iterative procedure by which the magnetic vector potential has to be updated each time the surface shape is changed.

Since the detailed description of the coupled boundary and finite element algorithm has been available elsewhere (Song, 1996; Song et al., 1997), only an outline is given below. For the sample region, the finite element formulation of the vector potential equation is constructed from Eq. (1) via the Weighted Residuals Method (WRM),

$$\int_{\partial\Omega_1} r\frac{\partial A}{\partial n}\phi d\Gamma - \int_{\Omega_1} r(\nabla A\cdot\nabla\phi + k^2 A\phi)d\Omega = 0 \tag{10}$$

where ϕ is the trial function. Following the Galerkin approximation and the standard finite element discretization procedure involving elemental calculations and assembly, the resultant equation may be rewritten in matrix form,

$$\mathbf{KA} + \mathbf{N_I q_I} = \mathbf{0} \tag{11}$$

To derive the boundary element formulation of the vector potential for the outside region, it is perhaps most convenient to make use of the vector Green's function approach and then take the tangential component of the final boundary integral form (Song, 1996; Song et al., 1997). Following this approach, one finally arrives at the needed boundary integral expression,

$$\frac{1}{2\pi}C(\mathbf{r}_i)A(\mathbf{r}_i) + \oint_{\partial\Omega_2} A(\mathbf{n}\cdot\nabla G)rd\Gamma$$

$$= \oint_{\partial\Omega_2} G(\mathbf{n}\cdot\nabla A)rd\Gamma + \int_{\Omega_2}\mu JGrd\Omega \tag{12}$$

Here, to simplify the notation, the subscript o has been dropped from A and J (see Eqs. (2) and (3)) and the same will apply to Eqs. (16) and (17). The geometric coefficient $C(\mathbf{r}_i)$ and the Green's function $G(\mathbf{r}_i, \mathbf{r})$ are calculated by the following equations,

$$C(\mathbf{r}_i) = \begin{cases} 1 & \text{when } \mathbf{r}_i \text{ lies inside domain } \Omega_2 \\ \dfrac{1}{2} & \text{when } \mathbf{r}_i \text{ lies on a smooth boundary } \partial\Omega_2 \\ (2\pi - \beta_1 - \beta_2)/2\pi & \text{when } \mathbf{r}_i \text{ lies on a nonsmooth boundary } \partial\Omega_2 \end{cases} \tag{13}$$

$$G(\mathbf{r}_i, \mathbf{r}) = \frac{1}{4\pi^2\sqrt{r_i r}}\left[\left(\frac{2}{\kappa} - \kappa\right)K(\kappa) - \frac{2}{\kappa}E(\kappa)\right] \tag{14}$$

$$\kappa^2 = \frac{4r_i r}{(r_i + r)^2 + (z_i - z)^2} \tag{15}$$

where β_1 and β_2 are the two angles between the normal of the two elements adjacent to a corner and the x axis (Song, 1996). It is noted that in deriving Eq. (12) the contribution from the boundary at infinity is calculated to be zero using the limiting approach described by Brebbia et al. (1984). Thus, the boundary formulation of the vector potential problem for this system involves only the variables along the interface between the boundary and finite element regions.

Now following the standard boundary element procedure to discretize the boundary of the free surface, which for the present case becomes the interface between the sample and free space, the boundary element equation for the vector potential may be written in terms of the matrix equation,

$$[\mathbf{H_I}, \mathbf{H_B}]\begin{pmatrix}\mathbf{A_I}\\ \mathbf{A_B}\end{pmatrix} + [\mathbf{G_I}, \mathbf{G_B}]\begin{pmatrix}\mathbf{q_I}\\ \mathbf{q_B}\end{pmatrix} = \begin{pmatrix}\mathbf{F_I}\\ \mathbf{F_B}\end{pmatrix} \tag{16}$$

where the quantities denoted by subscript B are related to the boundaries other than the interface, and they are zero for the present problem but included here for the sake of completeness.

The coupling of the boundary element and finite element formulations becomes relatively easy now. Starting with Eq. (16), the flux $\mathbf{q_I}$ at the interface is calculated first and then substituted into the finite element equation. In general, this would require the inversion of the matrix $\mathbf{G} = [\mathbf{G_I}, \mathbf{G_B}]$. To improve the efficiency of computation, a different approach is taken. By this approach, $\mathbf{q_I}$ is calculated by first applying the LU decomposition to partition $\mathbf{G}$, then solving for a related coefficient vector associated with each column of $\mathbf{H_I}$, e.g.,

$\mathbf{H}_I^i$, and finally multiplying the vector with the ith element of $\mathbf{A}_I$, e.g. $\mathbf{A}_I^i$. The procedure is repeated for $\mathbf{F} = (\mathbf{F}_I, \mathbf{F}_B)^T$. The results are added leading to an expression relating $\mathbf{q}_I$ to $\mathbf{A}_I$, that is,

$$\mathbf{q}_I = \mathbf{M}\mathbf{A}_I + \mathbf{f} \tag{17}$$

With this substituted into Eq. (11), making use of Eqs. (2) and (3) and performing needed algebraic operations, one has the final matrix equation for the magnetic vector potential

$$\tilde{\mathbf{K}}\mathbf{A} = \tilde{\mathbf{F}} \tag{18}$$

To preserve the skyline structure of the finite element stiffness matrix, the interface is treated as a macro-element during the matrix profile calculations. Furthermore, corner flux discontinuity associated with the boundary element formulation is accounted for using the double flux method, which, among others tested, is considered the best for the present analyses, taking into account both the accuracy and programming flexibility (Song, 1996).

With the vector potential known, the free surface shapes can be calculated. For levitation systems, the free surface shape problem described by Eq. (8) may be formulated more conveniently in a spherical coordinate system. After integrating along the surface of the droplet using the Weighted Residuals Method, the very same used for the finite element formulation, one has the integral form of the free surface shape condition,

$$\int_0^\pi \left\{ \frac{rr_\theta\phi_\theta + \phi(2r^2 + r_\theta^2)}{\sqrt{r^2 + r_\theta^2}} + \frac{r^2\phi}{\gamma}(P_H + \rho g r\cos\theta + P_m) \right\} \sin\theta d\theta = 0 \tag{19}$$

where $r = r(\theta)$ is the radial distance of the droplet, which defines the free surface shape, and r_θ the derivative of $r(\theta)$ with respect to θ. This equation must be solved along with the volume conservation constraint, which is used to determine the constant P_H,

$$\frac{2\pi}{3}\int_0^\pi r^3 \sin\theta d\theta = \text{Volume} \tag{20}$$

To complete the description of the surface deformation in levitation systems, the center of mass z_c, which defines the equilibrium position of the sample along the z axis of the levitation coils, must be determined as a part of the calculation since it is not known a priori,

$$\frac{\pi/2}{\text{Volume}}\int_0^\pi r^4 \cos\theta \sin\theta d\theta = z_c \tag{21}$$

Following the standard Galerkin finite element procedure, Eqs. (19), (20) and (21) can be discretized and written in matrix form similar to Eq. (18) but with the free surface nodes $\mathbf{u}$ as unknowns,

$$\mathbf{K}_f\mathbf{u} = \mathbf{F}_f \tag{22}$$

Note that the standard sparse stiffness matrix must also be modified to take into consideration the irregularities associated with the two constraints.

Finite element formulation of the thermal problem described by Eqs. (6) and (7) can be obtained by a procedure very similar to the above and has been well documented in many textbooks (Zinkiewicz and Taylor, 1989). It is thus omitted here.

IV Computational Procedure

The boundary and finite element code for the calculation of the vector potential, free surface deformation, and temperature field was developed following the descriptions presented above. An iterative computational procedure based on the simple successive substitution method was implemented. The procedure also requires the remeshing of the finite element region during iteration because of the change of the free surface shape. A mesh generator was developed based on the multiblock structure in combination with transmapping (Ida, 1986; HoLe, 1988) and was incorporated into the coupled boundary and finite element code. The calculation starts with an initial guess for free surface shape and iterates between the shape change and magnetic field calculations until convergence is met. Then the temperature distribution is calculated with the calculated free surface shape and Joule heating. The calculation also requires iterations to account for radiation boundary condition along the free surface. The whole iterative procedure for the free surface deformation and temperature calculation involves the following seven steps: (1) data input, (2) mesh generation, (3) calculation of magnetic vector potential $\mathbf{A}$, (4) calculation of free surface shape $\mathbf{u}$, (5) iteration between (2), (3), and (4) until convergence, (6) calculation of temperature, and (7) output of results. To increase the computational efficiency, steps (2), (3), and (4) are iterated in such a manner that $\mathbf{A}$ is updated only after a certain number of iterative steps for free surface calculation. For this type of problem, the nonlinearity comes from the free surface calculation but the computation of $\mathbf{A}$ is the most time-consuming part.

V Results and Discussion

With the boundary element and finite element code developed above, analyses can be carried out of electromagnetic field distribution, temperature distribution, and free surface deformation associated with liquid droplets suspended in magnetic levitation systems. In what follows, a selection of computed results is presented for levitated droplets under both normal and microgravity conditions and the results are compared with analytical solutions or experimental measurements wherever possible. A convergence criterion of relative error $< 1 \times 10^{-4}$ was set for all the calculations.

(A) Magnetic Levitation Under Earthbound Conditions. The coil configuration for magnetic levitation systems under terrestrial conditions is sketched in Fig. 2. The configuration is sometimes named a basket configuration because of the shape of the coil arrangement (Mestel, 1982; Natarajan and El-Kaddah, 1995). Two sets of coils are necessary. The lower

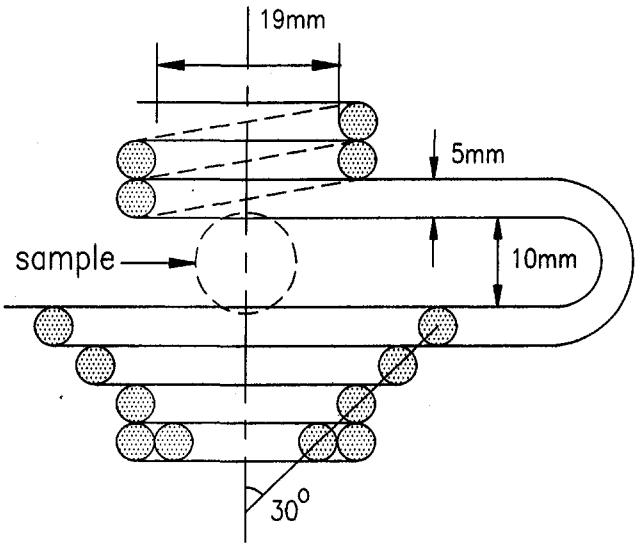

Fig. 2 The configuration and dimensions of coils used for magnetic levitation under terrestrial conditions

coils provide the needed Lorentz forces to support the load by counterbalancing the gravitational force, while the upper ones are designed to stabilize the load so that it will not be overthrown out of the current loops by the lower set of coils. These two sets of the coils form a potential well within which the sample will be confined at a designated location.

Analytical solutions may be obtained for the levitation coil setup described above. If the coils are considered coaxial, and the sample assumes a perfect sphericity, then the magnetic vector potential A, the time-averaged total Joule heating Q, the lifting forces F_z, and the temperature distribution T associated with the sample can all be calculated analytically. Since the details were documented in a recent publication (Li, 1993), only the final results of relevance to this study are given below, as they will serve to provide a check on our numerical development. Thus for a spherical sample levitated by a multiple coil system with N different coils, each having a different current at the same frequency, as shown in Fig. 2, the analytical solutions for the total power absorption and the lifting force are expressed as follows:

$$Q_{\text{tot}} = \frac{\pi}{2a\sigma} \sum_{i=1}^{N} \sum_{j=1}^{N} I_i I_j \sin \alpha_i \sin \alpha_j \sum_{n=1}^{\infty} P_n^1(\cos \alpha_i) \left(\frac{a}{r_{oi}}\right)^n \times \left\{ \frac{2n+1}{n(n+1)} \left(\frac{a}{r_{oj}}\right)^n P_n^1(\cos \alpha_j) \operatorname{Re}\left[\frac{kaI_{n+1/2}(ka)}{I_{n-1/2}(ka)}\right] \right\} \tag{23}$$

$$F_z = -\frac{\mu\pi}{2} \sum_{i=1}^{N} \sum_{j=1}^{N} I_i I_j \sin \alpha_i \sin \alpha_j \times \sum_{n=1}^{\infty} \frac{P_n^1(\cos \alpha_i) P_{n+1}^1(\cos \alpha_j)}{n+1} \left(\frac{a}{r_{oi}}\right)^n \left(\frac{a}{r_{oj}}\right)^{n+1} \times \left\{ 1 + (2n+1) \operatorname{Im}\left[\frac{I_{n+1/2}(k^*a)}{kaI_{n-1/2}(k^*a)}\right] \right\} \tag{24}$$

It is noted that a spherical coordinate system with its origin set at the center of the levitated sphere has been used for these equations (see the inset in Fig. 3), and this will hold true for Eqs. (25)–(31) as well.

For the lifting force, a simplified analytical expression has often been used. It was derived by treating the conducting sphere as an imaginary dipole in a magnetic field generated by the surrounding coils (Okress et al., 1952). For a single coil system, it becomes

$$F_z = \frac{3\pi^2 I_{\text{rms}}^2}{50} \left(1 - \frac{3}{4x} \frac{\sinh 2x - \sin 2x}{\sinh^2 x + \sin^2 x}\right) \times \frac{y}{(1+y^2)^4} \left(\frac{a}{\sqrt{r_o^2 - z^2}}\right)^3 \tag{25}$$

with $x = a\sqrt{\mu\omega\sigma/2}$, $I_{\text{rms}} = I\sqrt{2}$ and $y = z/\sqrt{r_o^2 - z^2}$. It is a simple matter to show that this equation is nothing but the first term of Eq. (24). This can be readily verified by setting $i = j = 1$ and substituting into Eq. (24) the following geometric and functional relations:

$$\cos \alpha = \frac{y}{\sqrt{1+y^2}} \tag{26}$$

$$1 + 3 \operatorname{Im}\left(\frac{I_{3/2}(k^*a)}{kaI_{1/2}(k^*a)}\right) = 1 - \frac{3}{4x} \frac{\sinh 2x - \sin 2x}{\sinh^2 x + \sin^2 x} \tag{27}$$

where use has been made of the relation, $I_{-1/2}(x) = \cosh(x) \times \sqrt{2/\pi x}$.

Figure 3 shows the results for lifting force computed by both Eqs. (24) and (25), along with the boundary/finite element

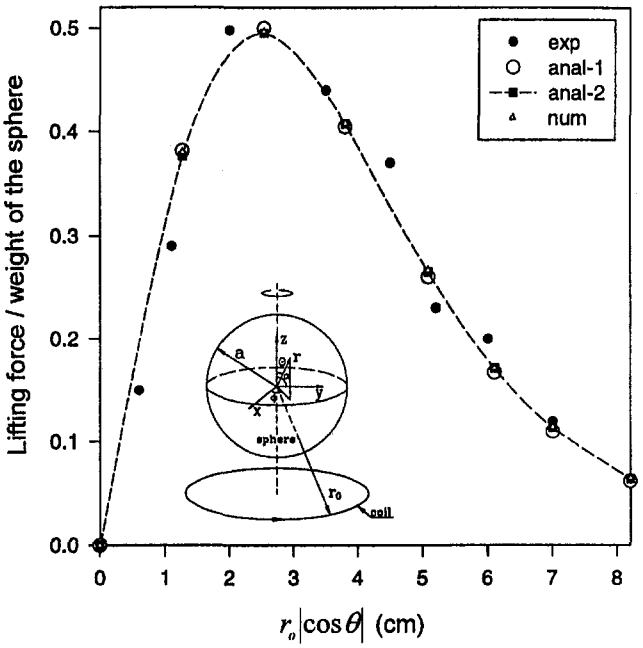

Fig. 3 Comparison of two analytical solutions (anal-1: Eq. (25) and anal-2: Eq. (24)), numerical solution and experimental measurements for lifting forces exerted on a 2.54-cm-dia bronze sphere by a single current loop. The inset shows the spherical coordinate system used for analytical solutions. Conditions for the calculations: $\sigma = 1.67 \times 10^7$ mho/m, $\rho = 7.2$ kg/m^3, I (peak) = 849 A, and frequency = 9600 Hz.

(BE/FE, hereafter) calculations and the experimental measurements made for a 2.54-cm-dia bronze sphere levitated in a single coil system. Clearly, the numerical results agree very well with the predictions from Eq. (24). In comparison, the simplified formula (Eq. (25)) gives a reasonably good approximation for the lifting force with a maximum error < 4 percent. Both the analytical and numerical results follow the experimental measurements within the experimental error margin (Okress et al., 1952). Numerical calculations were also compared with analytical solutions for the magnetic vector potential distribution for the system (Song and Li, 1996) and the comparison is just as gratifying. Further comparisons were also made for two coil systems where experimental measurements were available. These tests indicate that the numerical results agree very well with analytical solutions and also with the experimental measurements within the experimental error margin (Song, 1996). Two points may be concluded from these comparisons. First, Eq. (24) converges very rapidly and thus the first term can be used as a good approximation, when a/r_o is small as for the present case. Second, the BE/FE code developed may be used to predict the lifting force associated with a levitation system.

One of the objectives of this paper is to study the thermal phenomena in a levitated droplet. For a solid sphere levitated in a set of coaxial coils as shown in Fig. 2, the temperature distribution within the solid sphere may be obtained analytically with an additional assumption that the surface of the sphere is subject to a Newtonian cooling law. Following the procedures described by Li (1993), the temperature distribution may be predicted by

$$T(r,\theta) = \frac{\mu\omega}{16K} \sum_{i=1}^{N} \sum_{j=1}^{N} I_i I_j \sin \alpha_i \sin \alpha_j \times \sum_{l=0}^{\infty} \sum_{m=1}^{\infty} \sum_{n=1}^{\infty} \frac{2m+1}{m(m+1)} \frac{2n+1}{n(n+1)} \left(\frac{a}{r_{oi}}\right)^n \left(\frac{a}{r_{oj}}\right)^m \times P_m^1(\cos \alpha_i) P_n^1(\cos \alpha_j) P_l(\cos \theta) I_{lmn}(r) P_{lmn} \tag{28}$$

In this equation, P_{lmn} is a constant,

$$P_{lmn} = (-l(l+1) + m(m+1) + n(n+1)) \frac{(2s)!!}{(2s+1)!!} \times \frac{(2(s-l)-1)!!(2(s-m)-1)!!(2(s-n)-1)!!}{(2(s-l))!!(2(s-m))!!(2(s-n))!!}$$

$$2s = l + m + n = \text{Even}; \quad l \geq 0; \quad 0 \leq m - l \leq n \leq m + l \quad (29)$$

and $I_{lmn}(r)$ is a function of r,

$$I_{lmn}(r) = \frac{1}{a}\left\{\int_0^r \left(\frac{r'}{r}\right)^{l+1} \text{Re}\,[R_{mn}(r')]dr' + \int_r^a \left(\frac{r}{r'}\right)^{l} \text{Re}\,[R_{mn}(r')]dr' + \left(\frac{r}{a}\right)^{l} \frac{(l+1-ha)}{(ha+l)} \int_0^a \left(\frac{r'}{a}\right)^{l+1} \text{Re}\,[R_{mn}(r')]dr'\right\} \quad (30)$$

where $R_{mn}(r)$ involves a product of modified Bessel functions of different orders,

$$R_{mn}(r) = \frac{I_{m+1/2}(kr)I_{n+1/2}(k^*r)}{I_{m-1/2}(ka)I_{n-1/2}(k^*a)} \quad (31)$$

The temperature distributions calculated by the coupled boundary and finite element method described above appear in Fig. 4, along with those by the analytical solutions, for an aluminum sphere in a single coil system. Good agreement is apparent between the numerical and analytical solutions, thereby providing once again a validation of the numerical code developed.

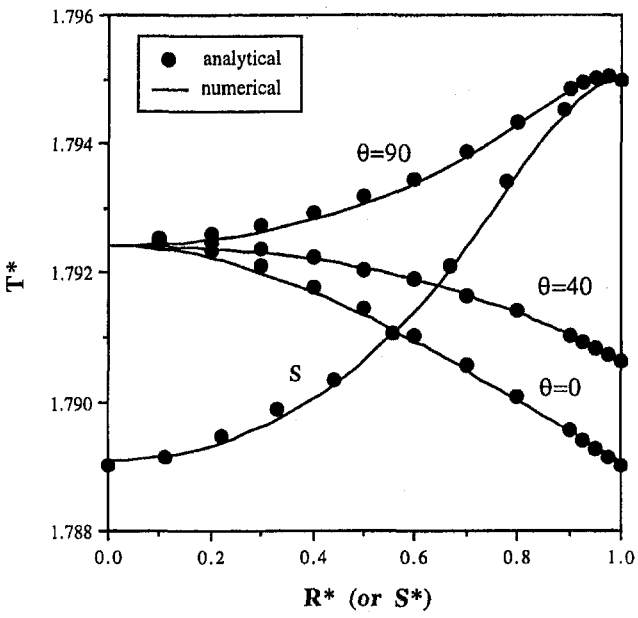

Fig. 4 Comparison of analytical and numerical solutions for radial and surface temperature distribution in a liquid aluminum sphere surrounded by a single current loop located at the equator plane. $T^* = T/(\mu\omega I^2/16aK)$ and $R^* = r/a$ are nondimensionalized temperature and radius, respectively. $s^* = s/(0.5\,\pi a)$ is the nondimensionalized surface distance measured from the pole to the equator. Data used for calculations: I (peak) = 300 A, frequency = 1.45×10^6 Hz, radius of sphere a = 6 mm, radius of coil loop r_o = 9 mm, subtended angle α = 90, and convective heat transfer coefficient hxK = 60.6 W/k-m^2. Other data are given in Table 1.

It should be stressed here that for this type of thermal problem, a careful distribution of finite element meshes is very important for computational accuracy. This is largely attributed to the fact that the Joule heating is distributed within a very small skin depth near the surface and follows an exponential decay inward from the surface. Through extensive numerical experiments, it is found that minimizing the error in the vector potential calculations is the key to improving the accuracy associated with thermal calculations. A small error in the vector potential calculations can result in a substantially bigger error in subsequent temperature prediction. Our tests against the analytical solutions with various mesh distributions and different types of elements showed that a four-node mesh with their size distribution following an increasing geometric progression at a ratio of 1.3 inward from surface, as illustrated in Fig. 5, is optimal for our problems. Tests were also carried out for the free surface calculations against available analytical solutions and gratifying agreement was also found (Song and Li, 1996).

With the tested code, the analyses were made to study the free surface deformation and thermal behavior of magnetically levitated droplets in normal gravity. Figure 5 illustrates a typical mesh distribution used for the present study. Of course, for specific problems, slight modification of this mesh was also made to obtain the best results. The parameters used for the calculations are given in Table 1. A typical calculation of the free surface shapes for a levitated droplet in a magnetic field required about 50 minutes CPU time on a DEC Workstation (Model 3000/300) and about a few seconds were needed for subsequent temperature calculations.

Figure 6 compares the free surface shapes of a liquid aluminum droplet with an initially spherical shape 5 mm in diameter for different applied currents. In both cases, the applied electromagnetic forces were able to support the droplet by balancing the gravitational force. The free surface deformation clearly reflects the equilibrium of the forces acting along the surface. Because of the magnetic field configuration, a stronger local Lorentz force and hence magnetic pressure exists along the surface of the droplet facing the lower set of coils through which currents flow in the same direction. This stronger pressure is required to balance a higher hydrostatic pressure. At the apex of the lower portion, the Lorentz force is zero and the hydrostatic pressure of a liquid blob is balanced primarily by surface tension. As a result of this, the liquid droplet tends to drip in this direction, causing a droplet to assume a conical shape as shown.

Comparison of the two droplet equilibrium shapes in Fig. 6 illustrates that a stronger applied current pushes the droplet up to a higher position in the potential well. This is as expected in that a higher current generates a bigger lifting force. However, as the liquid droplet moves up, the effect of the upper set of coils becomes more noticeable, thereby resulting in a flatter top surface. Numerical experiments show that this trend continues in the levitation potential with a further increase of the applied currents. For the levitation system under consideration, the minimum point, or zero lifting force point, in the potential well is located about 2 mm from the center of the nearest upper coil to the liquid droplet.

Analytical studies suggested that a stronger applied current will give a higher level of Joule heating and hence the higher maximum temperature (Li, 1993). In fact, for a system in which the currents are in phase, the temperature of a levitated sphere at a fixed position is proportional to the square of the applied current (Li, 1993; Song, 1996). For the levitation system under consideration, however, the story may be quite different. Figure 7 compares the temperature distributions in a liquid droplet with different applied currents. As the current is higher, the droplet is pushed farther away from the lower set of coils. While the Joule heating increases with the square of the applied current, it decreases rapidly with an increase in distance from the current source. In this particular system, increasing the distance from

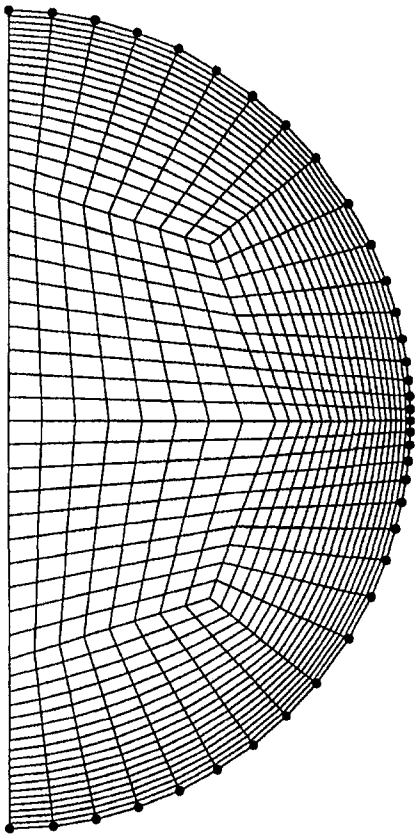

Fig. 5 A typical finite and boundary element mesh used for numerical calculations. Note that the boundary element mesh is greatly simplified and is coincident with the mesh of the interface between the boundary and finite element regions.

the lower set of coils means decreasing the distance toward the upper coils. Therefore, the effect from the lower coils is diminished, but is accompanied by an increasing effect from the upper coils. This, combined with the fact that the upper and lower coils have currents out of phase, changes the Joule heating induced in the droplet. Numerical calculations showed that the total Joule heating decreases when the droplet is moved away from the lower set of coils until closer to the upper coils and then increases when it gets closer to the upper coils (Song, 1996). For the results appearing in Fig. 7(*b*), the total Joule heating is lower even though the applied current is higher, thus resulting in an overall temperature decrease, in comparison with Fig. 7(*a*). Comparison of the two cases also indicates that the difference between the maximum and minimum temperatures

Table 1 Parameters for terrestrial levitation calculations

Parameters	Value	Units
Density of liquid Al alloy	2388	Kg/m^3
Electro-conductivity of liquid Al alloy	3.85×10^6	$(\Omega\text{–m})^{-1}$
Frequency	2.18×10^5	Hz
Applied current (peak)	339	A
Radius of initial sphere	5.0×10^{-3}	m
Thermal conductivity	135.9	W/mK
Environment temperature	298	K
Emissivity	0.3	
Surface tension of aluminum	0.915	N/m

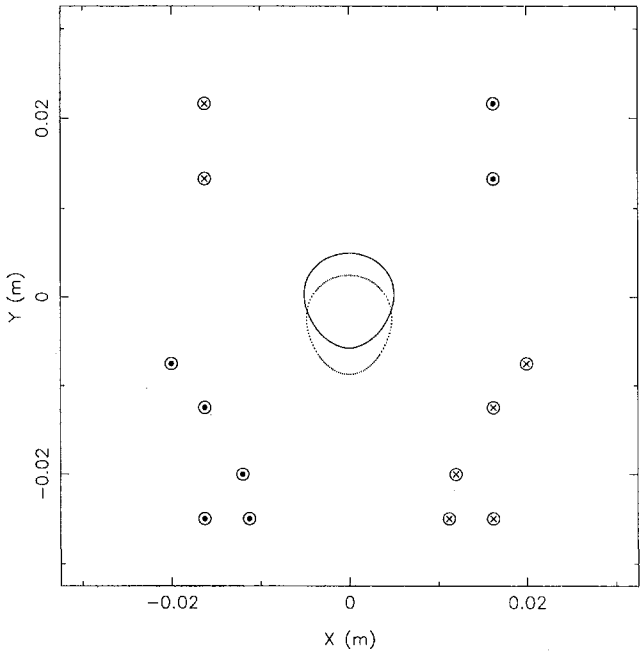

Fig. 6 Dependency of aluminum droplet shapes on applied currents under earthbound conditions: *I* (peak) = 441 A for the upper droplet and *I* (peak) = 339 A for the lower one

is also smaller in Fig. 7(*b*). Thus, an increase in the applied current may not necessarily bring up the temperature of the droplet, as intuitively expected, and indeed for this particular case under consideration, that may well result in an opposite effect. From numerical experiments, further increasing the current to push the droplet up to a point at which the total Joule heating is increased, a higher temperature level is possible; the surface deformation becomes different, however (Song, 1996). The local deformation of the liquid droplet also has an effect on the temperature distribution, though not as large as that described above. For the case in Fig. 7(*a*), the temperature was 30 K higher if the droplet was assumed spherical. These results clearly suggest that accurate thermal consideration must be made together with the droplet deformation and its position in a levitation system and that the developed BE/FE code can be a very useful tool for this purpose.

In induction heating, frequency is an important parameter and its effect on a levitated droplet in fact is not yet well understood. From Eq. (24), it is readily shown, with $I_{n+1/2}(x) \to e^x/\sqrt{x}$ as $x \to \infty$, that the lifting force may be approximated by the following expression when the electromagnetic skin depth is small, or k is very big:

$$F_z = -\frac{\mu\pi}{2}\sum_{i=1}^{N}\sum_{j=1}^{N} I_i I_j \sin\alpha_i \sin\alpha_j \times \sum_{n=1}^{\infty} \frac{P_n^1(\cos\alpha_i)P_{n+1}^1(\cos\alpha_j)}{n+1}\left(\frac{a}{r_{oi}}\right)^n\left(\frac{a}{r_{oj}}\right)^{n+1} \times \left\{1-\frac{2n+1}{a\sqrt{2\sigma\omega\mu}}\right\} \quad (32)$$

It is thus obvious that the lifting force goes up, and asymptotically approaches a constant, as the applied frequency increases. This suggests that a larger lifting force will be obtained for an exciting field with a higher frequency. Figure 8 shows the effect of applied frequency on the droplet shapes in the levitation system. The results are consistent with this equation in that a higher frequency provides a higher lifting force and thus the

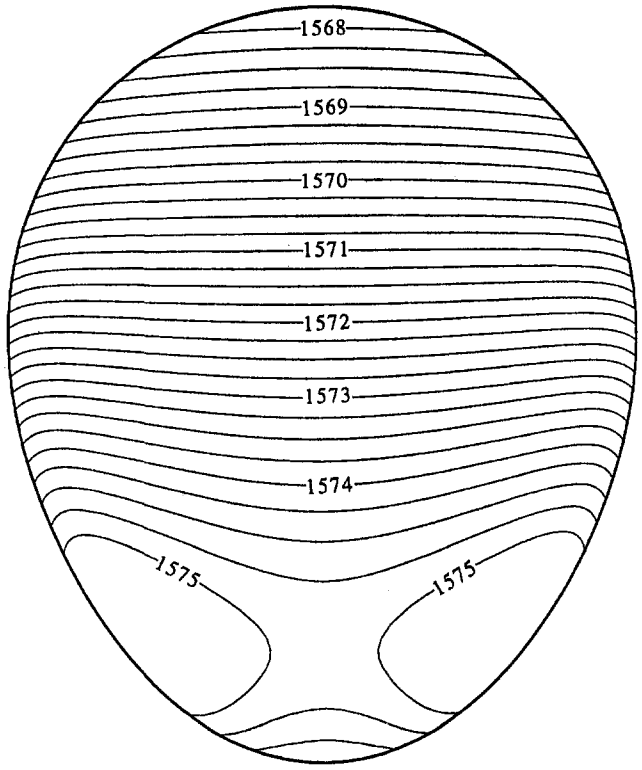

(a)

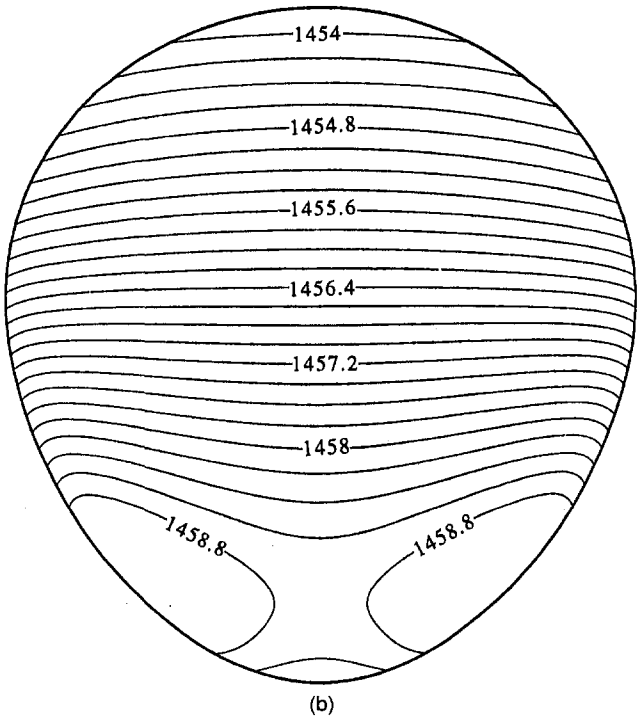

(b)

Fig. 7 The steady-state temperature distribution in the magnetically deformed aluminum droplets as a function of different applied currents: (*a*) *I* (peak) = 339 A and (*b*) *I* (peak) = 441 A. Temperature is in K.

droplet is pushed upward toward the stabilizing coils. There is only a slight change in the free surface shape, but the basic conical shape is maintained, reflecting the influence of the basket shape of coil sets.

For this particular system, the total time-averaged Joule heating and also the temperature level in a levitated sample increases with the square root of the applied frequency (Li, 1993). However, as pointed out earlier, there exists a drop in the Joule heating as the sample moves away from the lower coils, as a result of the current configuration. Comparison of Figs. 7 and 9 clearly indicates that the increase in the Joule heating resulting from a higher frequency was not enough to compensate for the decrease caused by a larger distance between the sample and the lower coils, thereby giving rise to a lower temperature level

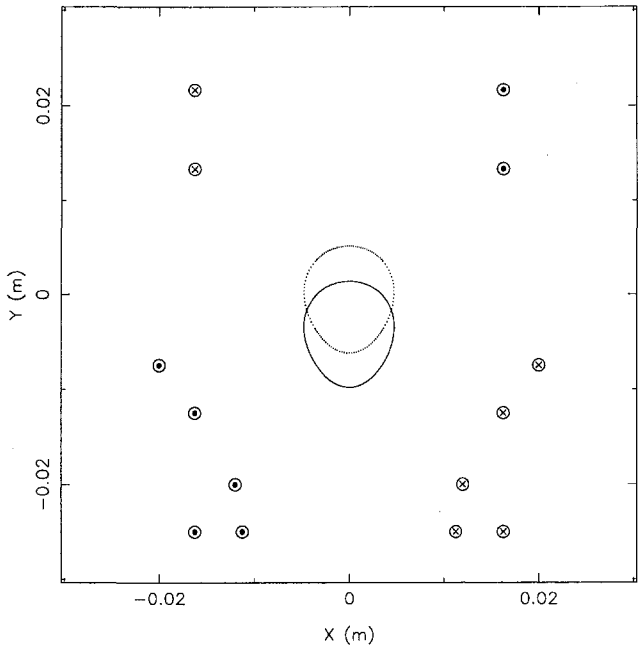

Fig. 8 Effect of applied frequency on the deformation of aluminum droplet shapes: The frequency = 436 kHz for the upper droplet, and 218 kHz for the lower droplet.

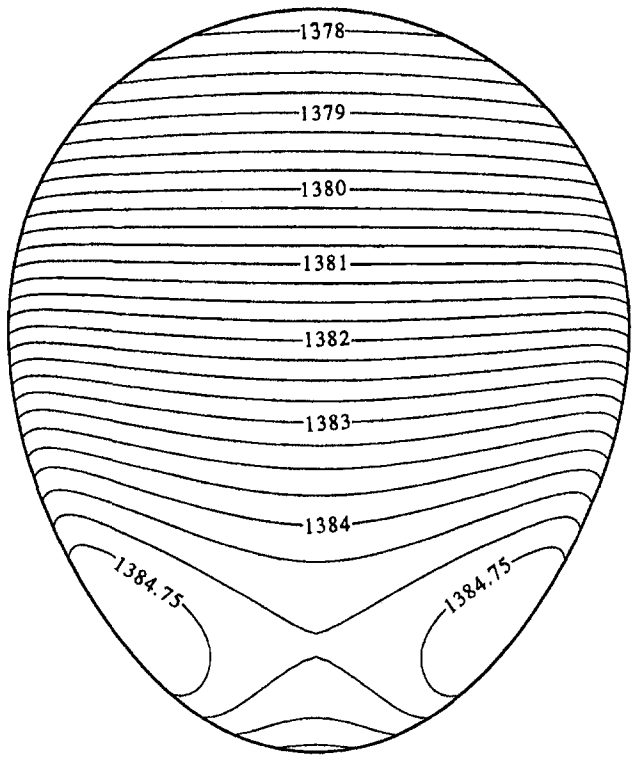

Fig. 9 Temperature distribution in liquid aluminum droplet magnetically levitated in normal gravity with an applied frequency of 436 kHz. Temperature is in K.

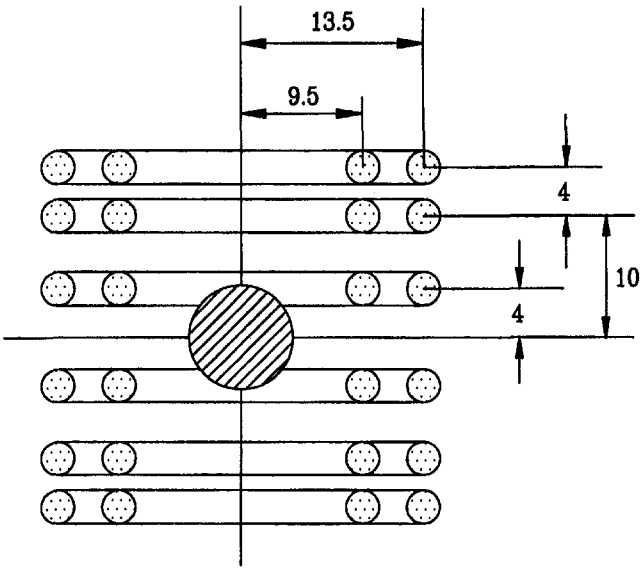

Fig. 10 Schematic representation of coil configuration used in TEMPUS system with dimensions in mm for magnetic levitation applications in microgravity

in the sample. It is also noted that because the sample is closer to the upper coils, the Joule heating distribution becomes more uniform; as a result of that, the temperature difference in the levitated droplet is smaller with a higher applied frequency.

(B) Levitation in Microgravity. While the basic formulas and the numerical model described above can be used with relatively little modification to study magnetic levitation in microgravity, some basic differences between the two types of levitation are worth noting. Figure 10 shows the coil design used in the TEMPUS device for microgravity applications. The device has been flown on the Space Shuttle and has been used to carry out some interesting studies on thermal property measurements and undercooling experiments (Szekely et al., 1995). The TEMPUS device uses two types of coaxial coil, all of the same diameter. This is an obvious modification. As the gravity in space is negligible as far as levitation is concerned, a strong upward force or lifting force becomes basically unneeded. Thus, the basket shape coil design is replaced by a set of coaxial coils. There are a total of twelve coils in the system, eight for positioning and four for heating. As for the eight positioning coils, there are four above and four below the equator plane of a sample to be levitated, and the currents flow in the opposite directions in the upper and lower coils. This coil configuration generates a quadrupole field and provides a positioning force to prevent the sample from drifting in space. There are additional four coils, symmetrically placed above and below the sample. These coils generate a dipole field and thus provide the needed heating or squeezing action for certain space experiments (Schwartz et al., 1992). Current conditions are also different. In general, lower current with a lower frequency is applied in the positioning coils and higher current with a higher frequency in the heating coils.

The boundary/finite element model was applied to study the free surface deformation and temperature distribution in a liquid metal droplet magnetically positioned in microgravity. The thermal and physical data used for the calculations presented below are given in Table 2, unless otherwise indicated. A typical calculation required 35 minutes for free surface shape prediction and additional several seconds for temperature distribution on a DEC Workstation (Model 3000/300).

Figure 11 plots the numerical, analytical, and experimental results of the vertical lifting force and total time-averaged Joule heating or power absorption produced by positioning coils only

Table 2 Parameters for microgravity levitation calculations

Parameters	Value	Units
Density of liquid silver	9,346	Kg/m^3
Electro-conductivity of liquid silver	6.0×10^6	$(\Omega\text{-m})^{-1}$
Frequency (positioning)	1.44×10^5	Hz
Applied current (peak, positioning)	140	A
Frequency (heating)	4.27×10^5	Hz
Applied current (peak, heating)	200	A
Radius of initial sphere	5.0×10^{-3}	m
Thermal conductivity of liquid silver	193.5	W/mK
Environment temperature	298	K
Emissivity	0.3	
Surface tension of silver	0.903	N/m

for a copper sphere. The analytical results were obtained using Eq. (23). Clearly, these results are in excellent agreement, validating once again the boundary and finite element model developed.

Figure 12 shows the numerically calculated result of free surface deformation of a silver droplet with an initial spherical diameter of 5 mm, magnetically positioned and heated by the TEMPUS device in microgravity. Apparently, the sample deformation is symmetric and mainly determined by the balance between the surface tension and the induced Lorentz force along the surface, as expected. The droplet is squeezed at the middle plane by a strong electromagnetic force generated there, and the liquid is pushed symmetrically both downward and upward away from the equator. This symmetric deformation of a droplet produced by the electromagnetic force represents a unique phenomenon in microgravity, which makes it possible to measure the surface tension and viscosities of highly reactive materials or undercooled melts; these measurements are otherwise impossible on Earth (Herlach, 1991; Egry et al., 1992; Bayazitoglu et al., 1996). The center of mass remains unchanged as a result of the absence of gravity effect. For this system, the squeezing force is mainly contributed by the heating coils and the positioning coils play only a minor role. These have been shown by numerical experiments and are also expected from the consider-

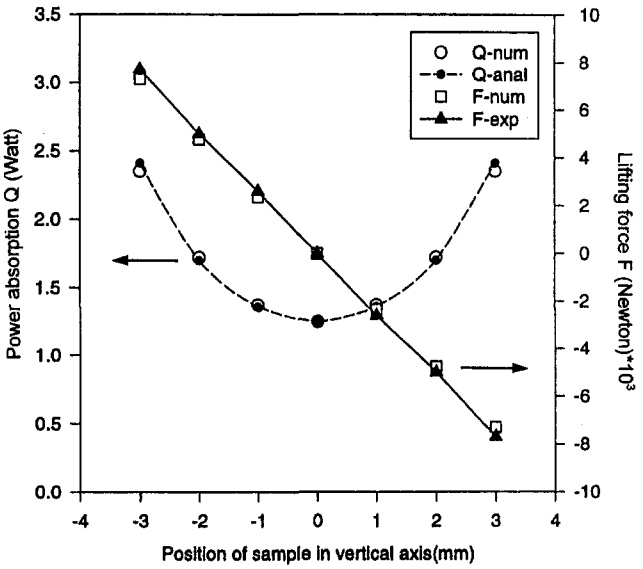

Fig. 11 Numerical, analytical, and experimental results of lifting force on and power absorption in a 10-mm-dia copper sphere (σ = 5.903 × 10^7 1/Ω-m) induced by TEMPUS positioning coils only according to the sample positions along the vertical axis

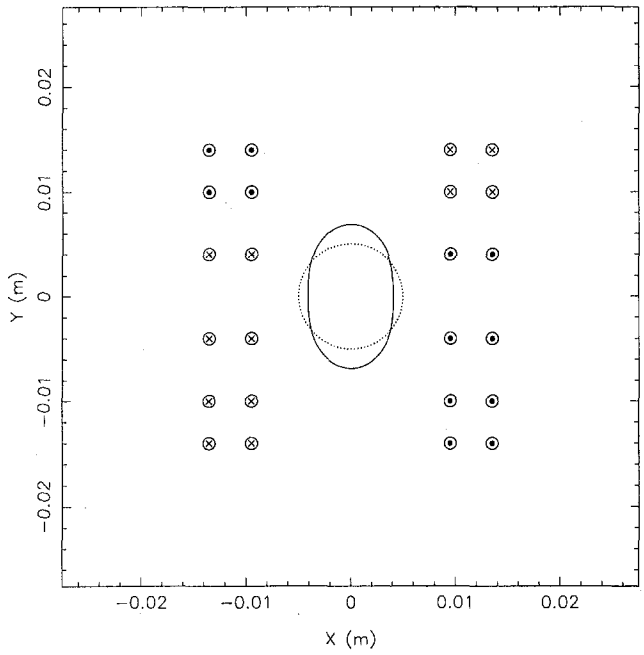

Fig. 12 Magnetically deformed free surface shape (solid curve) of a silver droplet in TEMPUS system under microgravity conditions. The deformation comes primarily from heating coils. The initial shape is plotted as a dotted line for comparison.

ation of the magnetic field configuration. As the heating coils have higher currents as well as higher frequency, they produce a higher Lorentz force. Also because the current direction of both the upper and lower heating coils is the same, their effects are additive and thus produce a force strongest at and weaker away from the equator plane, thereby pushing the liquid inward there. The positioning coils, on the other hand, have a lower current with a lower frequency, and in addition the current in the upper and lower positioning coils is out of a phase angle of 180. Thus they produce a weaker force field with a zero force at the equator and their effects on squeezing can be ignored in comparison with the heating coils.

It is noteworthy that for the system under consideration in which two different frequencies are applied, the total time-averaged Joule heating and time-averaged surface magnetic pressure for the temperature and surface deformation computations were obtained by slightly modifying Eqs. (5) and (9),

$$Q = \sum_{m=1}^{2}\sum_{m=1}^{2}\frac{1}{\sigma T_\omega}\int_0^{T_\omega}\mathrm{Re}\,(J(\omega_n)e^{j\omega_n t})\cdot\mathrm{Re}\,(J(\omega_m)e^{j\omega_m t})dt \quad (33)$$

$$P_m = \sum_{n=1}^{2}\sum_{m=1}^{2}\frac{1}{2\mu T_\omega}\int_0^{T_\omega}\mathrm{Re}\,(\nabla\times(A(\omega_n)e^{j\omega_n t}\hat{\phi}))\times\mathrm{Re}\,(\nabla\times(A(\omega_m)e^{j\omega_m t}\hat{\phi}))dt \quad (34)$$

where $T_\omega = 2\pi(\omega_1^{-1} + \omega_2^{-1})$.

The corresponding steady-state temperature distribution in the silver droplet is illustrated in Fig. 13. The dipole field effect of the heating coils is once again evident. The Joule heating reaches a maximum (Li, 1993) near the equator plane and decays rapidly both radially inward and along the surface toward the two poles. This type of heating is very similar to that produced if a single coil were placed at the equator plane of the droplet. Of course, a two coil system so placed in TEMPUS should provide a more uniform heating and thus a more uniform temperature distribution. The calculations also showed that while the thermal distribution is similar, a temperature of about 100 K higher would be predicted if the local deformation were neglected and the sample were assumed to be a perfect sphere. It is remarked here also that in real operation a sample is heated for a certain period of time and may not always reach a steady state; as such the temperature may not be as high as shown here. Nonetheless, our calculations show that the temperature profile during most of the transient stage is similar and the results presented here represent an upper limiting case (Song, 1996).

In contrast with the strong droplet deformation and heating effect of the heating coils, the positioning coils are designed mainly to keep the droplet from drifting in space. It is of interest to know what effect the positioning coils would have on a liquid droplet. Figure 14 shows the steady temperature and droplet deformation of the silver sample under the action of positioning coils only. Apparently, the positioning coils produce a barely noticeable departure from sphericity. However, the temperature distribution in the droplet is much different from that generated by the heating coils (cf. Fig. 13). It is much more uniform and demonstrates the quadrupole effect produced by the positioning coils. The maximum temperature occurs at two locations symmetric about the equator plane and the minimum temperature at the equator plane. The temperature level is much lower, in fact about 327 K below the melting point of the silver, indicating that the droplet is at a substantially large undercooling stage. This temperature change should not come as a surprise in that the positioning coils are out of a phase angle of 180 deg and

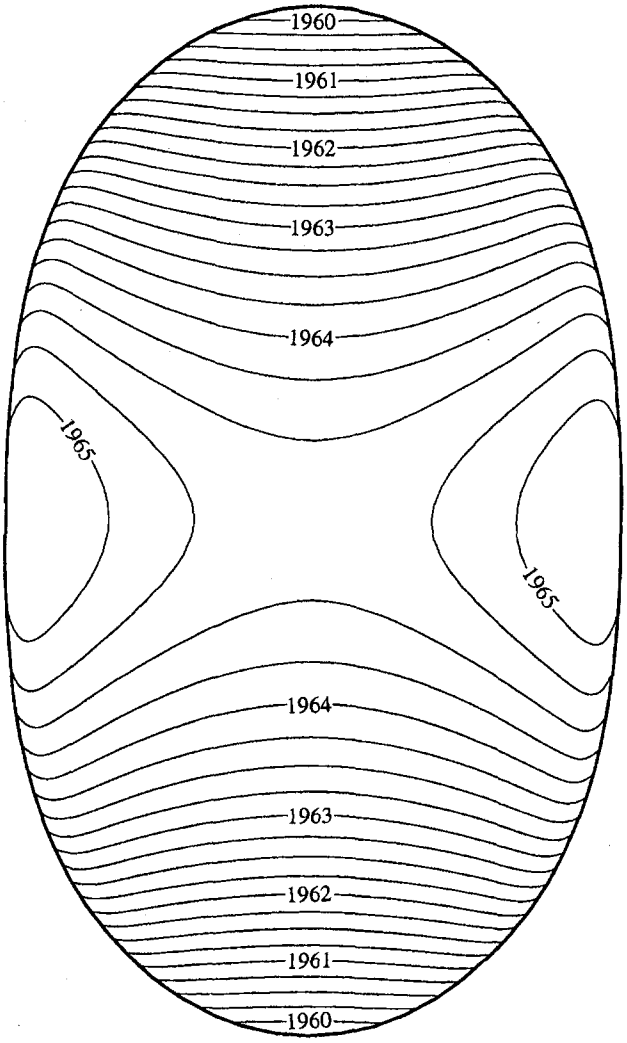

Fig. 13 The corresponding temperature distribution in the silver droplet calculated by the boundary and finite element model. The heating effect comes predominantly from heating coils and positioning coils assume only a minor role. Temperature is in K.

thus produce a canceling effect at the equator plane and hence a lower temperature.

To keep the silver droplet at a temperature higher than its melting point, a higher current must be applied in the positioning coils. This will result in a larger surface deformation of the droplet. The effect of a higher positioning current on the droplet deformation and temperature distribution appears in Fig. 15. It is seen that the positioning coils deform the droplet in a different manner from the heating coils in that the largest deformation occurs at the position around which the maximum temperature also occurs. The liquid is bulged out near the equator where the induced Lorentz force experiences a minimum and there the liquid is held up mainly by surface tension. The temperature contour is similar to that in Fig. 14, with a lowest temperature at the equator plane, and the temperature distribution is also very uniform. However, the difference between the maximum and minimum temperatures is slightly bigger.

VI Concluding Remarks

This paper has presented a coupled boundary and finite element analysis of electromagnetic, free surface deformation and thermal problems in magnetic levitation systems under both normal and microgravity conditions. For induction heating problems such as those encountered in magnetic levitation systems, the coupled boundary and finite element approach is perhaps the best choice. This is because by placing the finite elements in the regions of interest and boundary elements in other regions that extend to infinity, considerable computing time can be saved, especially when an iterative procedure, as is required for free surface calculation, is used. A computer code that combines the coupled boundary and finite element formulation as its core with an iterative procedure enhanced with automated remeshing capability was developed and tested against available analytical solutions as well as experimental measurements. With the tested computer code, numerical analysis was conducted of the free surface deformation and temperature distribution in magnetically levitated droplets on earth and in microgravity environment. Results showed that an accurate assessment of the temperature distribution in a magnetically levitated droplet must be made along with the effect of droplet deformation, including the bulk movement, for magnetic levitation systems. The induced Lorentz forces play an important role in free surface deformation. When magnetically levitated in normal gravity, a droplet assumes a conical shape with its apex pointing downward. The temperature distribution in the droplet is such that a higher spot occurs in the lower portion of the droplet facing the lower set of coils. For a magnetically positioned droplet in microgravity, on the other hand, surface deformation is caused primarily by the heating coils. Also the deformation is quite symmetric such that the droplet is squeezed at the equator plane and liquid bulges out at two poles. The positioning coils, however, generate only a very slight deformation. The Joule heating from the positioning coils is also much lower and in fact is not even enough to keep the silver sample above the melting point under normal operation conditions. In addition, the temperature profiles are different for heating and positioning coils. An increase of the current in positioning coils can result in a larger surface deformation but the droplet assumes a different equilibrium shape from that induced by the heating coils.

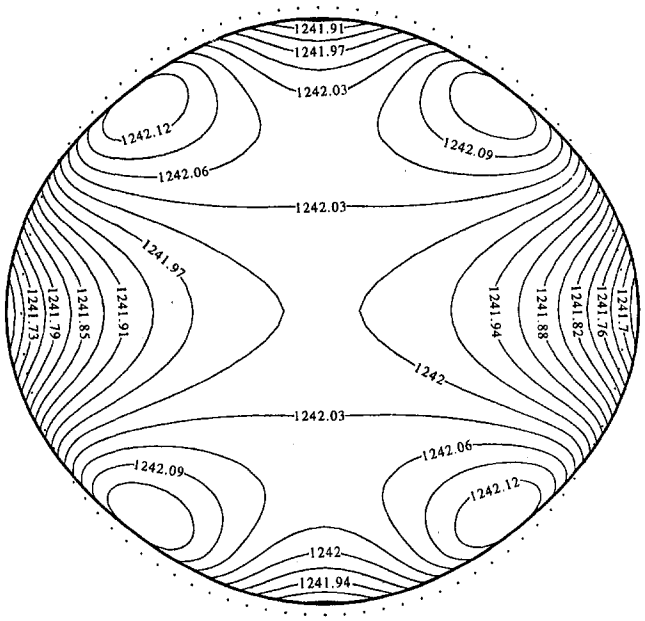

Fig. 15 Dependency of free surface deformation and temperature distribution in a silver droplet on the applied currents for positioning coils in TEMPUS system under microgravity conditions. Heating coils are turned off and the applied current for positioning is *I* (peak) = 270 A. The dotted line represents the original spherical shape. Temperature is in K.

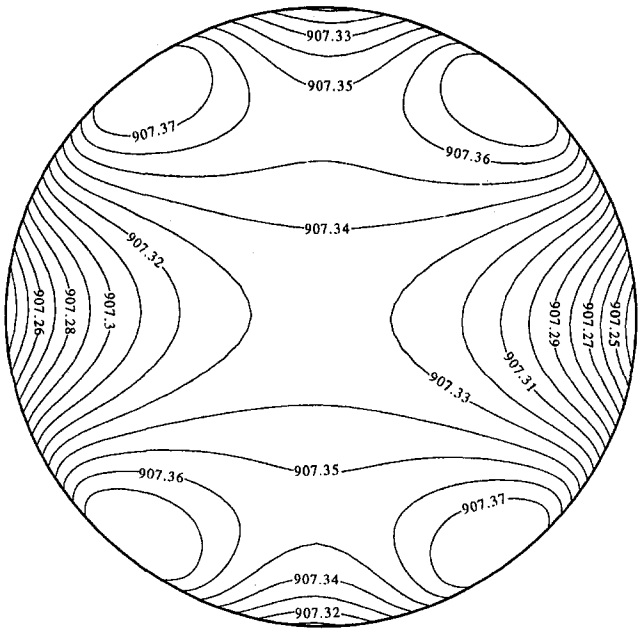

Fig. 14 Numerically computed surface deformation and corresponding temperature distribution in a silver droplet induced by positioning coils only in TEMPUS system under microgravity conditions. Temperature is in K.

Acknowledgments

The authors acknowledge the financial support of this work by the National Science Foundation (Grant No. NSF-CTS 9622275).

References

Bayazitoglu, Y., and Sathuvalli, U. B., 1994, "Eddy current heating in an electrically conducting sphere," *J. Materials Processing and Manuf. Sci.*, Vol. 3, pp. 117–141.

Bayazitoglu, Y., and Sathuvalli, U. B., 1996, "The Lorentz forces on an electrically conducting sphere in an alternating magnetic field," *IEEE Trans. on Magn.*, Vol. 32(2), pp. 386–400.

Bayazitoglu, Y., Sathuvalli, U. B., Suryanarayana, P. V. R., and Mitchell, G. F., 1996, "The Lorentz forces on an electrically conducting sphere in an alternating magnetic field," *Physics of Fluids*, Vol. 8(2), pp. 370–383.

Brebbia, C.A., Telles, J. C. F., and Wrobel, L.C., 1984, *Boundary Element Techniques: Theory and Applications in Engineering*, Springer-Verlag, New York.

Egry, I., Lohofer, G., Neuhaus, P., and Sauerland, S., 1992, "Surface tension measurements of liquid metals using levitation, microgravity and image processing," *Int. J. Thermophysics*, Vol. 13, pp. 65–74.

Getzlev, Z. N., 1971, "Casting in an electromagnetic field," *J. Metals*, No. 10, pp. 38–39.

Herlach, D. M., 1991, "Containerless Undercooling and Solidification of Pure Metals," *Annu. Rev. Mater. Sci.*, Vol. 21, pp. 23–44.

Herlach, D. M., and Feuerbacher, B., 1991, "Non-equilibrium Solidification of Undercooled Metallic Melts," *Advances in Space Research*, Vol. 11, No. 7, pp. 255.

Ida, N., 1986, "A mesh generator with automatic bandwidth reduction for 2-D and 3-D geometries," in: *Computational Electromagnetics*, Z. J. Cendes, ed., Elsevier Science, London, pp. 13–22.

HoLe, K., 1988, "Finite element mesh generation methods: a review and classification," *J. Computer-Aided Design*, Vol. 20, pp. 27–38.

Jackson, J. D., 1975, *Classical Electrodynamics*, Chaps. 2–6, Wiley, New York.

Keller, W., and Muhlbauer, A., 1981, *Floating-Zone Silicon*, Marcel Dekker, Inc., New York.

Li, B. Q., 1993, "The Magnetothermal Phenomena in Electromagnetic Levitation Processes," *Int. J. Engng Sci.*, Vol. 31, No. 2, pp. 201–220.

Li, B. Q., 1994a, "The Fluid Flow Aspects of Electromagnetic Levitation Processes," *Int. J. Engng Sci.*, Vol. 32, No. 1, pp. 45–67.

Li, B. Q., 1994b, "The Transient Magnetohydrodynamic Phenomena in Electromagnetic Levitation Processes," *Int. J. Engng Sci.*, Vol. 32, No. 8, pp. 1315–1336.

Lohofer, G., 1989, "Theory of an Electromagnetically Levitated Metal Sphere I: Absorbed Power," *SIAM J. Appl. Math.*, Vol. 49, No. 2, pp. 567–581.

Mestel, A. J., 1982, "Magnetic Levitation of Liquid Metals," *J. Fluid. Mech.*, Vol. 117, pp. 17–43.

Muck, O., 1923, German Patent No. 422004.

Natarajan, T. T., and El-Kaddah, N., 1995, "Calculation of the Electromagnetic Field and Melt Shape in Electromagnetic Confinement Systems: A Comparison Between Numerical Methods," in: *Materials Processing in the Computer Age II*, V. R. Voller, S. P. March, and N. El-Kaddah, eds., TMS/AIME, Warrendale, PA, pp. 255–265.

Okress, E. C., Wroughton, D. M., Comenetz, G., Brace, P. H., and Kelly, J. C. R., 1952, "Electromagnetic Levitation of Solid and Molten Metals," *J. Appl. Phy.*, Vol. 23, No. 5, pp. 545–552.

Rony, P. B., 1969, "The electromagnetic levitation melting of metals," *Trans. Vac. Met. Conf.*, American Vacuum Society, Boston, pp. 55–135.

Sathuvalli, U. B., and Bayazitoglu, Y., 1993, "Electromagnetic force calculations for a conical coil," *Met. Trans.*, Vol. 24B, pp. 737–748.

Sathuvalli, U. B., and Bayazitoglu, Y., 1994, "The Lorentz force on a sphere due to an axisymmetric non-homogeneous alternating magnetic field," ASME AMD-Vol. 194, pp. 293–305.

Schwartz, E., Szekely, J., Ilegbusi, O. J., Zong, J.-H., and Egry, I., 1992, "The Computation of the Electromagnetic Force Fields and Transport Phenomena in Levitated Metallic Droplets in the Microgravity Environment," in: *Magnetohydrodynamics in Process Metallurgy*, J. Szekely, J. W. Evans, K. Balzek, and N. El-Kaddah, eds., TMS/AIME, pp. 81–90.

Schwartz, E., and Szekely, J., 1995, "Mathematical Modelling: An Essential Component of the Design of Space Experiments," in: *Materials Processing in the Computer Age II*, V. R. Voller, S. P. March, and N. El-Kaddah, eds., TMS/AIME, Warrendale, PA, pp. 147–161.

Song, S. P., and Li, B. Q., 1995, "Coupled Boundary/Finite Element Solution of Thermal and Electrodynamic Problems in Materials Processing," in: *Materials Processing in the Computer Age II*, V. R. Voller, S. P. March, and N. El-Kaddah, eds., TMS/AIME, Warrendale, PA, pp. 243–254.

Song, S. P., 1996, "Coupled Finite Element and Boundary Element Method for the Solution of Scalar and Vector Potential Problems Involving Free Surface Deformation," M. S. Thesis, Louisiana State University, Baton Rouge, LA.

Song, S. P., and Li, B. Q., 1996, "Computation of Magnetically-Supported Free Surface by a Coupled Finite/Boundary Element Method," EPD Congress-96, G. W. Warren, ed., TMS/AIME, Warrendale, PA, pp. 725–736.

Song, S. P., Li, B. Q., and Khadadadi, J. A., 1998, "Coupled boundary and finite element solution of magnetothermal problems," *Int. J. Num. Meth. Heat and Fluid Flow*, Vol. 8, pp. 321–349.

Suryanarayana, P. V. R., and Bayazitoglu, Y., 1991, "Effect of Static Deformation and External Forces on the Oscillations of Levitated Droplets," *Phys. Fluids A*, Vol. 3, pp. 967–977.

Szekely, J., Schwartz, E., and Hyers, R., 1995, "Electromagnetic levitation—a useful tool in microgravity research," *J. of Metals*, Vol. 5, pp. 50–53.

Weatherburn, C. E., 1972, *Differential Geometry of Three Dimensions*, Cambridge University Press, London.

Zhang, X., Li, B. Q., and Pang, S. S., 1997, "A Perturbational Approach to Magnetothermal Problems of a Deformed Sphere in a Magnetic Field," *J. Eng. Math.*, Vol. 31, pp. 337–355.

Zienkiewicz, O. C., and Taylor, R. L., 1989, *The Finite Element Method*, 4th ed., McGraw-Hill, New York.

Zong, J. H., Li, B. Q., and Szekely, J., 1992, "The Electromagnetic and Hydrodynamic Phenomena in Magnetically-Levitated Molten Droplets—I. Steady State Behavior," *Acta Astronautica*, Vol. 26, No. 6, pp. 435–449.

Zong, J. H., Li, B. Q., and Szekely, J., 1993, "The Electromagnetic and Hydrodynamic Phenomena in Magnetically-Levitated Molten Droplets—II. Transient Behavior and Heat Transfer Considerations," *Acta Astronautica*, Vol. 29, No. 4, pp. 305–311.

Journal of Heat Transfer

Technical Notes

This section contains shorter technical papers. These shorter papers will be subjected to the same review process as that for full papers.

An Integral Method for the Compressible Laminar Boundary Layer

A. Pozzi[1] and L. Mazzei[2]

Introduction

One of the main drawbacks of integral methods, from the first method described by Pohlhausen (1921), through the well-known method of Thwaites (1949), the more accurate method of Jarre (1974), and up to more recent ones (Thomas and Amminger, 1988; Wherle, 1988), has been the quick degradation of their accuracy near separation.

The method presented here is able to achieve different degrees of accuracy for compressible boundary layers, even close to separation, and is easily generalized to unsteady flows. It is the extension to the compressible regime, where the strong interaction between the momentum and energy equations makes the task a nontrivial one, of the successful method for incompressible flows proposed by Pozzi and Teodori (1993).

Basic Equations

We start from the steady compressible two-dimensional laminar boundary layer equations in nondimensional form:

$$(\rho u)_{,x} + (\rho v)_{,y} = 0 \tag{1}$$

$$\rho(uu_{,x} + vu_{,y}) = \rho_e u_e u_{e,x} + (\mu u_{,y})_{,y} \tag{2}$$

$$\rho(uS_{,x} + vS_{,y}) = \frac{(\lambda S_{,y})_{,y}}{\mathrm{Pr}} + \frac{(\gamma - 1)(\mathrm{Pr} - 1)\mathrm{M}^2}{\mathrm{Pr}H_{ea}}(\mu u u_{,y})_{,y} \tag{3}$$

Here, the subscripts after the comma denote differentiation, the subscript e values at the outer edge of the boundary layer, u and v are, respectively, the x and y components of the velocity, ρ the density, μ the viscosity coefficient, λ the thermal conductivity, Pr the Prandtl number, M the Mach number, γ the specific heat ratio, H the total enthalpy, $S = (H/H_e) - 1$ and $H_{ea} = H_e/(C_pT_r)$, C_p being the specific heat at constant pressure, and T_r the reference temperature. All quantities here are implicitly regarded as nondimensionalized with respect to some reference state (i.e., free-stream conditions). The boundary conditions are $u(x, 0) = v(x, 0) = 0$ and $u(x, \infty) = u_e(x)$.

Before applying the integral method, we transform Eqs. (1)–(3) by taking the new independent variables $X = \int_0^x A^m dx$, $Y = \int_0^y A(\rho/\rho_s)\nu_s^{-1/2} dy$, and the new "velocity" components $U = u/A$ and $V = A^{-m}[UY_{,x} + \nu(\rho/\rho_s)\nu_s^{-1/2}]$. This is the Illingworth–Stewartson–Dorodnitzin transformation (Stewartson, 1964). Here, the subscript s denotes stagnation conditions, $A = a_e/a_s$, a being the speed of sound, ν is the kinematic viscosity and $m = (3\gamma - 1)/(\gamma - 1)$. The result is the "quasi-incompressible" form of Eqs. (1)–(3):

$$U_{,X} + V_{,Y} = 0 \tag{4}$$

$$UU_{,x} + VU_{,y} = U_{,YY} + (1 + S_w S^+)U_e U_{e,X} \tag{5}$$

$$US^+_{,X} + VS^+_{,Y} = \frac{S^+_{,YY}}{\mathrm{Pr}} + \frac{(\gamma - 1)(\mathrm{Pr} - 1)\mathrm{M}^2A^2}{2\,\mathrm{Pr}H_{ea}S_w}(U^2)_{,YY} \tag{6}$$

where the subscript w indicates the value of a quantity at the wall and $S^+ = S/S_w$.

These transformed equations are the basis for the application of the integral method, as described by Pozzi and Teodori (1993). Proceeding from there, we obtain four equations in the X coordinate only:

$$U_e\beta H_{,X} + 2HU_{e,X}(\alpha + 2\beta) + 2U_eH\beta_{,X} = 2U^+_{w,z} - 2\chi^+ HS_wU_{e,X} \tag{7}$$

$$H_{,X}U_e(\mathrm{M}/2 - \alpha^2/4) + H[U_{e,X}(2\mathrm{M} - \alpha^2/2) + U_e(\mathrm{M} - N)_{,X} + U_eD + S_wU_{e,X}P^+] = 1 \tag{8}$$

$$h\,\mathrm{Pr}(hU_ed) = -S^+_{w,z} \tag{9}$$

$$S_w(d_1 + d_2)(H_{,X}U_e + 2HU_{e,X}) + 2S_wHU_e(d_{1,X} + d_3) = \frac{2S_w}{\mathrm{Pr}} - \frac{(\gamma - 1)(\mathrm{Pr} - 1)\mathrm{M}^2A^2U_e^2}{\mathrm{Pr}H_{ea}} \tag{10}$$

where $h(x)$ is an unknown function, $z = Y/h(x)$ and $H = h^2$. The expressions for the other parameters are $\alpha = \int_0^\infty (1 - U^+)dz$, $\beta = \int_0^\infty U^+(1 - U^+)dz$, $\chi^+ = \int_0^\infty S^+ dz$ (related to the displacement and momentum thickness of the boundary layer as in Cohen and Reshotko, 1956), $N = \int_0^\infty z(1 - U^+)dz$, $\mathrm{M} = \int_0^\infty z[1 - (U^+)^2]dz$, $D = \int_0^\infty (1 - U^+)\int_0^z U^+_{,X}dzdz$, $P^+ = \int_0^\infty zS^+dz$, $d = \int_0^\infty S^+U^+dz$, $d_1 = \int_0^\infty zS^+U^+dz$, $d_2 = \int_0^\infty S^+\int_0^z U^+dzdz$, $d_3 = \int_0^\infty S^+\int_0^z U^+_{,X}dzdz$.

[1] Professor, Dipartimento di Progettazione Aeronautica, Facoltà di Ingegneria, Università degli Studi di Napoli "Federico II", Piazzale V. Tecchio 80, 80125 Napoli, Italy.

[2] Graduate Student, Division of Mechanics and Computation, William F. Durand Building, Stanford, CA 94305-4040; email: lmazzei@leland.stanford.edu; corresponding author.

Contributed by the Heat Transfer Division of The American Society of Mechanical Engineers. Manuscript received by the Heat Transfer Division August 16, 1996; revision received February 4, 1998. Keywords: Flow Separation, Forced Convection, Numerical Methods. Associate Technical Editor: R. D. Boyd.

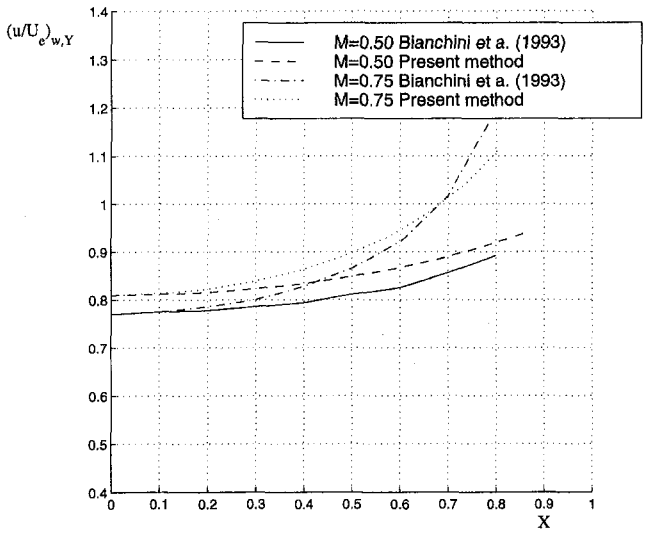

Fig. 1 Wall shear stress for plane stagnation flow

Solution Method

The solution of the ordinary differential equations derived in the preceding section proceeds as follows: First, U^+ and S^+ are expanded in a Taylor series up to a finite order and the remainder is approximated. The approximation of the velocity profile U^+ was discussed in detail by Pozzi and Teodori (1993); here, we need to introduce an additional unknown function $h_T(x)$ to account for the different thickness of the dynamic and thermal boundary layer. Hence, we define $z_T = Y/h_T$; and similarly to what was done for U^+, we express the enthalpy profile as

$$S^+ = 1 - Z_T^n + \sum_{r=1}^{n-1} q_r(Z_T^n - Z_T^r),$$

where n is the degree of the approximation, Z_T is the thermal counterpart of Z as defined for U^+ by Pozzi and Teodori (1993), and $r!\, q_r$ is the rth derivative of S^+ with respect to Z_T evaluated at the wall.

With these approximate profiles, we evaluate all the integral parameters (α, β, ...) previously defined and express all the derivatives of U^+ and S^+ in terms of the integral parameters. This results in a number of coupled ODEs depending on the order of the approximation, which can be solved using, for example, a Runge–Kutta method. Note that the numerical ODE solver is the only source of error on top of the approximation of the remainder in the Taylor series.

For more details on the handling of these equations, refer to the work of Pozzi and Teodori (1993), where all the main ideas are laid out. For the specific calculations and the details of the compressible case, contact the second author.

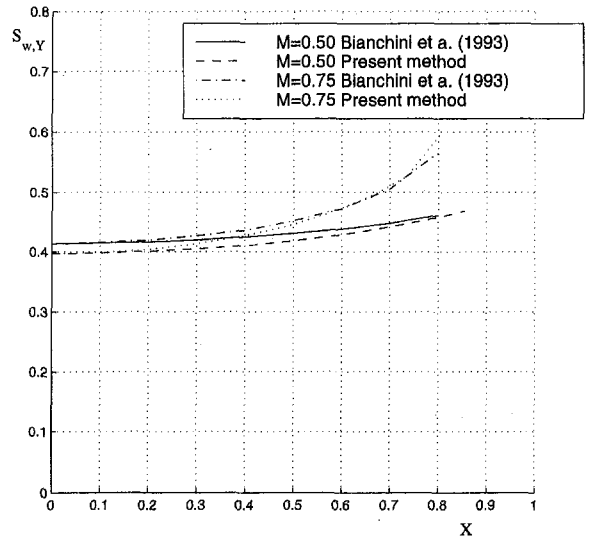

Fig. 2 Wall heat transfer for plane stagnation flow

Compressible Regime Results

We observe that the integral method applied to the transformed equations yields a result of the same order of accuracy as found in the incompressible case. Results from the first approximation are compared to data computed from the exact solution for plane stagnation flow (Bianchini et al., 1993). Figures 1 and 2 show, respectively, the evolution with X of $(u/U_e)_{w,Y}$ and $S_{w,Y}$ for two different Mach numbers. The error, of a few percent for the first approximation, is similar to the incompressible case, and the discrepancy is due mainly to the approximation of the initial conditions (see Pozzi and Teodori, 1993). Higher accuracy can be achieved in this case, too, by increasing the order of the approximation for the velocity and enthalpy profiles, resulting in a more accurate prediction of separation whenever it occurs.

References

Bianchini, A., Pozzi, A., and Teodori, A. R., 1993, "Some New Test Cases in Compressible Thermo-Fluid-Dynamics," *International Journal of Heat and Fluid Flow,* Vol. 14, No. 2, pp. 201–205.

Cohen, C. B., and Reshotko, E., 1956, "The Compressible Laminar Boundary Layer With Heat Transfer and Arbitrary Pressure Gradient," NACA Report 1294.

Jarre, G., 1974, "The Laminar Boundary Layer. A Representative Section Method," in: *Omaggio a Carlo Ferrari,* Levrotto, Torino, pp. 393–413.

Pohlhausen, E., 1921, "Der Wärmeaustausch zwischen festen Körpern und Flüssigkeiten mit kleiner Reibung und kleiner Wärmeleitung," *Zeitschrift für Angewandte Mathematik und Mechanik,* Vol. 1, No. 2, pp. 115–121.

Pozzi, A., and Teodori, A. R., 1993, "Separation Points in Laminar Flows," *Meccanica,* Vol. 28, No. 1, pp. 53–59.

Stewartson, K., 1964, *The Theory of Laminar Boundary Layers in Compressible Fluids,* Clarendon Press, Oxford.

Thomas, L. C., and Amminger, W. L., 1988, "A Practical One Parameter Integral Method for Laminar Incompressible Boundary Layer Flow With Transpiration," ASME *Journal of Applied Mechanics,* Vol. 55, No. 2, pp. 474–481.

Thwaites, B., 1949, "Approximate Calculation of the Laminar Boundary Layer," *Aeronautical Quarterly,* Vol. 1, Nov., pp. 245–280.

Wehrle, V. A., 1986, "Determination of the Separation Point in Laminar Boundary Layer Flows," *AIAA Journal,* Vol. 24, No. 10, pp. 1636–1641.

Unsteady Conjugate Heat Transfer in a Circular Duct With Convection From the Ambient and Periodically Varying Inlet Temperature

J. S. Travelho[1] and W. F. N. Santos[2]

Nomenclature

A = amplitude

a, a^* = duct radius, duct wall heat capacity =

[1] Senior Researcher, Universidade de Mogi das Cruzes, Departamento de Engenharia Mecânica, Mogi das Cruzes, SP 08780-911, Brazil; permanent address: LAC/INPE CP 515, São José dos Campos, SP, Brazil.

[2] Associate Researcher, Laboratório Associado de Combustão e Propulsão, Caixa Postal 01, Cachoeira Paulista, SP, 12630-000 Brazil.

Contributed by the Heat Transfer Division of THE AMERICAN SOCIETY OF MECHANICAL ENGINEERS. Manuscript received by the Heat Transfer Division January 9, 1997; revision received January 7, 1998. Keywords: Conduction, Conjugate Heat Transfer, Forced Convection. Associate Technical Editor: P. S. Ayyaswamy.

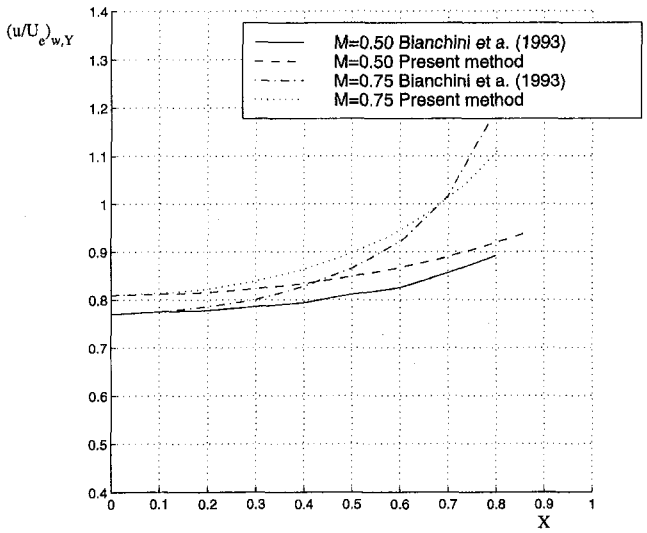

Fig. 1 Wall shear stress for plane stagnation flow

Solution Method

The solution of the ordinary differential equations derived in the preceding section proceeds as follows: First, U^+ and S^+ are expanded in a Taylor series up to a finite order and the remainder is approximated. The approximation of the velocity profile U^+ was discussed in detail by Pozzi and Teodori (1993); here, we need to introduce an additional unknown function $h_T(x)$ to account for the different thickness of the dynamic and thermal boundary layer. Hence, we define $z_T = Y/h_T$; and similarly to what was done for U^+, we express the enthalpy profile as

$$S^+ = 1 - Z_T^n + \sum_{r=1}^{n-1} q_r(Z_T^n - Z_T^r),$$

where n is the degree of the approximation, Z_T is the thermal counterpart of Z as defined for U^+ by Pozzi and Teodori (1993), and $r!\, q_r$ is the rth derivative of S^+ with respect to Z_T evaluated at the wall.

With these approximate profiles, we evaluate all the integral parameters (α, β, ...) previously defined and express all the derivatives of U^+ and S^+ in terms of the integral parameters. This results in a number of coupled ODEs depending on the order of the approximation, which can be solved using, for example, a Runge–Kutta method. Note that the numerical ODE solver is the only source of error on top of the approximation of the remainder in the Taylor series.

For more details on the handling of these equations, refer to the work of Pozzi and Teodori (1993), where all the main ideas are laid out. For the specific calculations and the details of the compressible case, contact the second author.

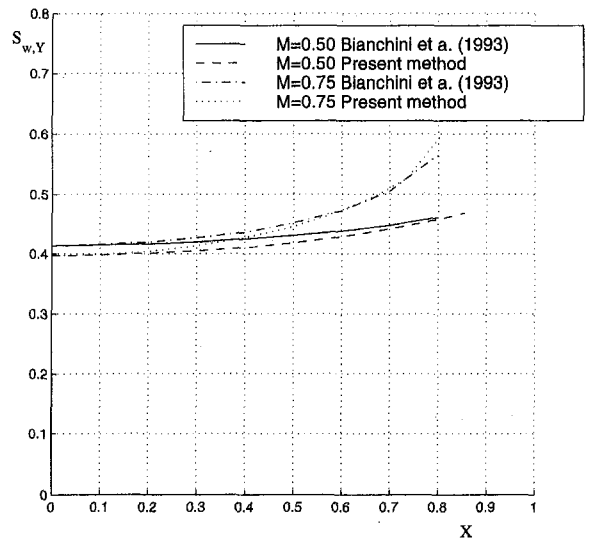

Fig. 2 Wall heat transfer for plane stagnation flow

Compressible Regime Results

We observe that the integral method applied to the transformed equations yields a result of the same order of accuracy as found in the incompressible case. Results from the first approximation are compared to data computed from the exact solution for plane stagnation flow (Bianchini et al., 1993). Figures 1 and 2 show, respectively, the evolution with X of $(u/U_e)_{w,Y}$ and $S_{w,Y}$ for two different Mach numbers. The error, of a few percent for the first approximation, is similar to the incompressible case, and the discrepancy is due mainly to the approximation of the initial conditions (see Pozzi and Teodori, 1993). Higher accuracy can be achieved in this case, too, by increasing the order of the approximation for the velocity and enthalpy profiles, resulting in a more accurate prediction of separation whenever it occurs.

References

Bianchini, A., Pozzi, A., and Teodori, A. R., 1993, "Some New Test Cases in Compressible Thermo-Fluid-Dynamics," *International Journal of Heat and Fluid Flow,* Vol. 14, No. 2, pp. 201–205.

Cohen, C. B., and Reshotko, E., 1956, "The Compressible Laminar Boundary Layer With Heat Transfer and Arbitrary Pressure Gradient," NACA Report 1294.

Jarre, G., 1974, "The Laminar Boundary Layer. A Representative Section Method," in: *Omaggio a Carlo Ferrari,* Levrotto, Torino, pp. 393–413.

Pohlhausen, E., 1921, "Der Wärmeaustausch zwischen festen Körpern und Flüssigkeiten mit kleiner Reibung und kleiner Wärmeleitung," *Zeitschrift für Angewandte Mathematik und Mechanik,* Vol. 1, No. 2, pp. 115–121.

Pozzi, A., and Teodori, A. R., 1993, "Separation Points in Laminar Flows," *Meccanica,* Vol. 28, No. 1, pp. 53–59.

Stewartson, K., 1964, *The Theory of Laminar Boundary Layers in Compressible Fluids,* Clarendon Press, Oxford.

Thomas, L. C., and Amminger, W. L., 1988, "A Practical One Parameter Integral Method for Laminar Incompressible Boundary Layer Flow With Transpiration," ASME *Journal of Applied Mechanics,* Vol. 55, No. 2, pp. 474–481.

Thwaites, B., 1949, "Approximate Calculation of the Laminar Boundary Layer," *Aeronautical Quarterly,* Vol. 1, Nov., pp. 245–280.

Wehrle, V. A., 1986, "Determination of the Separation Point in Laminar Boundary Layer Flows," *AIAA Journal,* Vol. 24, No. 10, pp. 1636–1641.

Unsteady Conjugate Heat Transfer in a Circular Duct With Convection From the Ambient and Periodically Varying Inlet Temperature

J. S. Travelho[1] and W. F. N. Santos[2]

Nomenclature

A = amplitude

a, a^* = duct radius, duct wall heat capacity =

[1] Senior Researcher, Universidade de Mogi das Cruzes, Departamento de Engenharia Mecânica, Mogi das Cruzes, SP 08780-911, Brazil; permanent address: LAC/INPE CP 515, São José dos Campos, SP, Brazil.

[2] Associate Researcher, Laboratório Associado de Combustão e Propulsão, Caixa Postal 01, Cachoeira Paulista, SP, 12630-000 Brazil.

Contributed by the Heat Transfer Division of THE AMERICAN SOCIETY OF MECHANICAL ENGINEERS. Manuscript received by the Heat Transfer Division January 9, 1997; revision received January 7, 1998. Keywords: Conduction, Conjugate Heat Transfer, Forced Convection. Associate Technical Editor: P. S. Ayyaswamy.

$\rho c_p a/\rho_w c_w l$

b^*, c^* = dimensionless parameters defined by Eq. (6)

c_p, c_w = fluid and wall specific heats at constant pressure

h = heat transfer coefficient

k = thermal conductivity of fluid

l = wall thickness

Nu_o = outside Nusselt number = ha/k

r, R = radial coordinate, dimensionless radial coordinate = r/a

s = Laplace transform parameter

t = time

$T(r, z, t)$ = fluid temperature

T_o, T = cycle mean temperature, reference temperature

U = mean velocity

$W(x)$ = function related to error function

z, Z = axial coordinate, dimensionless axial coordinate = $\alpha z/Ua^2$

α = thermal diffusivity of fluid

ΔT_o = amplitude of inlet oscillations

$\theta(R, Z, \tau)$ = dimensionless temperature = $(T(r, z, t) - T_o)\Delta T_o$

θ_∞ = dimensionless reference temperature = $(T_\infty - T_o)(1 + i)/\Delta T_o)$

ρ, ρ_w = fluid mass density, wall density

τ = dimensionless time = $\alpha t/a^2$

$\psi(Z)$ = dimensionless periodic part of ψ

ω = frequency of oscillations

Ω = dimensionless frequency of oscillations = $\omega a^2/\alpha$

$\sim$ = Laplace transform of

Introduction

The growing interest in transient heat transfer problems has been stimulated by the increasing need to understand the dynamic behavior of heat exchanger devices. This has led to an increased number of papers on thermal transients in tubes and ducts. Many of these investigations have attacked the problem of the transient heat transfer initiated by a timewise variation of wall temperature, wall heat flux, or internal heat generation. Thermal transients can also be imposed by timewise variation of the fluid temperature at the inlet. Nevertheless, available work on this subject is still limited.

Sparrow and DeFarias (1968) have analytically studied the transient conjugate problem of a slug flow inside a parallel plate duct with a periodically varying inlet temperature. The series solution presented by these authors results in a complex eigenvalue problem. A trial and error procedure was employed for the numerical evaluation of the real and imaginary parts of the eigenvalues. Their work was advanced by Cotta et al. (1987) by extending it to a circular duct, and by adopting the sign-count method for the determination of the complex eigenvalues. A theoretical and experimental study of laminar forced convection in the thermal entrance region of a parallel duct was presented by Kakaç et al. (1990). In their analysis, duct wall thermal capacity and convection from the ambient were accounted for, and the fluid inlet temperature was varied periodically with time. Their analytical solution was obtained through the generalized integral transform technique. Travelho and Santos (1991) solved the Sparrow and DeFarias problem (1968) by using Laplace transform. An important aspect of this solution is the absence of complex eigenvalues, which usually appear in problems of that type. Santos and Travelho (1993) advanced their analysis further by considering convection interaction with an ambient medium outside the parallel plate duct.

The present work is concerned with the analytical solution of the transient laminar forced convection in the thermal entrance region of a circular duct with an inlet temperature that varies periodically with time. Convection from the ambient medium is accounted for through a constant heat transfer coefficient. In this analysis, the effect of the duct wall heat capacity is taken into account and the slug flow model is assumed. A formal solution to this problem leads to a complex Sturm–Liouville problem, which is avoided here by applying the Laplace transform to the equations and the boundary conditions. Of particular interest is the determination of the amplitudes and phase lags for the wall temperature, fluid bulk temperature, and wall heat flux as function of the physical parameters of the problem.

Analysis

The problem considered here is that of a hydrodynamically developed laminar fluid flow inside a circular duct of radius a and wall thickness. The fluid temperature at the duct entrance varies periodically with time. Convective heat exchange from the ambient outside and the duct wall thermal capacity effects are considered, while axial conduction and viscous dissipation effects are neglected. It is assumed that the thermophysical properties of the wall and fluid are constant. Furthermore, a slug flow idealization of the actual velocity field will be utilized. Under these conditions, the temperature field is described by the energy equation in dimensionless form:

$$\frac{\partial\theta(R,Z,\tau)}{\partial\tau}+\frac{\partial\theta(R,Z,\tau)}{\partial Z}=\frac{1}{R}\frac{\partial}{\partial R}\left[R\frac{\partial\theta(R,Z,\tau)}{\partial R}\right] \quad (1a)$$

subject to:

$$\theta(R,0,\tau)=e^{i\Omega\tau} \quad \text{and} \quad \left.\frac{\partial\theta(R,Z,\tau)}{\partial R}\right|_{R=0}=0 \quad (1b,c)$$

$$-\left.\frac{\partial\theta(R,Z,\tau)}{\partial R}\right|_{R=1} = \frac{1}{a^*}\frac{\partial\theta(1,Z,\tau)}{\partial\tau}+\mathrm{Nu}_o[\theta(1,Z,\tau)-\theta_\infty] \quad (1d)$$

The boundary condition given by Eq. (1d) was obtained from the energy balance on the duct wall, by assuming a conjugated condition. The dimensionless parameter a^*, which appears in Eq. (1d), characterizes the effect of duct wall capacitance to heat transfer, and Nu_o, an indication of the effectiveness of heat transfer to the ambient.

Equation (1), subject to the conditions in (1b–d), can be split into two parts by using $\theta(R, Z, \tau) = \xi(R, Z) + \gamma(R, Z, \tau)$. In this way, $\xi(R, Z)$ is the solution of the following problem:

$$\frac{\partial\xi(R,Z)}{\partial Z}=\frac{1}{R}\frac{\partial}{\partial R}\left[R\frac{\partial\xi(R,Z)}{\partial R}\right] \quad \text{with} \quad \xi(R,0)=0 \quad (2a,b)$$

$$\left.\frac{\partial\xi(R,Z)}{\partial R}\right|_{R=0}=0 \quad \text{and}$$

$$\left.\frac{\partial\xi(R,Z)}{\partial R}\right|_{R=1}+\mathrm{Nu}_o[\xi(1,Z)-\theta_\infty]=0 \quad (2c,d)$$

and $\gamma(R, Z, \tau)$ satisfies the problem

$$\frac{\partial\gamma(R,Z,\tau)}{\partial\tau}+\frac{\partial\gamma(R,Z,\tau)}{\partial Z}=\frac{1}{R}\frac{\partial}{\partial R}\left[R\frac{\partial\gamma(R,Z,\tau)}{\partial R}\right] \quad (3a)$$

$$\gamma(R,0,\tau)=e^{i\Omega\tau} \quad \text{and} \quad \left.\frac{\partial\gamma(R,Z,\tau)}{\partial R}\right|_{R=0}=0 \quad (3b,c)$$

$$\left.\frac{\partial\gamma(R, Z, \tau)}{\partial R}\right|_{R=1} + \frac{1}{a^*}\frac{\partial\gamma(1, Z, \tau)}{\partial\tau}$$

$$+ \mathrm{Nu}_o\gamma(1, Z, \tau) = 0 \quad (3d)$$

The temperature function $\gamma(R, Z, \tau)$ is assumed to be of the form $\gamma(R, Z, \tau) = \psi(R, Z)e^{i\Omega(\tau - Z)}$. By introducing this assumption into problem (3), one obtains

$$\frac{\partial\psi(R, Z)}{\partial Z} = \frac{1}{R}\frac{\partial}{\partial R}\left[R\frac{\partial\psi(R, Z)}{\partial R}\right] \quad 0 \le R \le 1, Z \ge 0 \quad (4a)$$

$$\psi(R, 0) = 1 \quad \left.\frac{\partial\psi(R, Z)}{\partial R}\right|_{R=0} = 0 \quad \text{and}$$

$$\left.\frac{\partial\psi(R, Z)}{\partial R}\right|_{R=1} + c^*\psi(1, Z) = 0 \quad (4b, c, d)$$

The starred symbols are defined as follows:

$$c^* = \mathrm{Nu}_o + ib^*, \quad b^* = \frac{\Omega}{a^*} = \frac{\omega a\rho_w c_w l}{k} \quad (5a, b)$$

Method of Solution

A closed-form solution to the problem (2) and (4) can be obtained by the method of separation of variables, which leads to a characteristic-value problem. Both problems yield complex eigenvalues. The main difficulty associated with the analytical solution of these problems has been to evaluate the eigenvalues of the resulting complex transcendental equations. In order to avoid the need to obtain the complex eigenvalues, the present work solves problems (2) and (4) by using the Laplace transform technique. By taking the Laplace transformation with respect to the variable Z, Eqs. (2*a–d*) become

$$s\tilde{\xi}(R, s) = \frac{1}{R}\frac{\partial}{\partial R}\left[R\frac{\partial\tilde{\xi}(R, s)}{\partial R}\right] \quad (6a)$$

$$\left.\frac{\partial\tilde{\xi}(R, s)}{\partial R}\right|_{R=0} = 0 \quad \text{and}$$

$$\left.\frac{\partial\tilde{\xi}(R, s)}{\partial R}\right|_{R=1} + \mathrm{Nu}_o\left[\tilde{\xi}(1, s) - \frac{\theta_\infty}{s}\right] = 0 \quad (6b, c)$$

where $\tilde{\xi}(R, s)$ is defined as being $\tilde{\xi}(R, s) = \lim_{Z\to s}\xi(R, Z) = \int_0^\infty \xi(R, Z)e^{-sZ}dZ$, and s is the Laplace transform parameter.

The solution to problem (6) in the transformed plane is given by

$$\tilde{\xi}(R, s) = \frac{\mathrm{Nu}_o\theta_\infty}{s}\frac{I_0(\sqrt{s}\,R)}{\sqrt{s}\,I_1(\sqrt{s}) + \mathrm{Nu}_o I_0(\sqrt{s})} \quad (7)$$

where I_0 and I_1 are the modified Bessel functions of the first kind.

The main objective of this work is to determine the quantities of interest such as the wall temperature, the fluid bulk temperature, and the wall heat flux. As mentioned before, the solution to problem (1) is sought in the thermal entrance region. This situation occurs for small values of Z, corresponding to large values of s in the transformed plane. Therefore, after setting $R = 1$ in Eq. (7) and introducing the large argument expansions of the Bessel functions (two terms) of Eq. (7), as given by Abramowitz and Stegun (1964), and after expanding the resulting expression in terms of the conventional method of partial fractions, the inverse transform (see Santos and Travelho, 1993) is obtained from the table given by Roberts and Kaufmann (1966) as

$$\xi_w(Z) \equiv \xi(1, Z) = \theta_\infty\left\{1 - \frac{1}{(\eta_1 - \eta_2)}[\eta_1 e^{\eta_1^2 Z}\,\mathrm{erfc}\,(-\eta_1\sqrt{Z}) - \eta_2 e^{\eta_2^2 Z}\,\mathrm{erfc}\,(-\eta_2\sqrt{Z})]\right\} \quad (8)$$

where η_1 and η_2 are obtained by $\eta_2^1 = -\mathrm{Nu}_o/2 \pm [\mathrm{Nu}_o/2\,(\mathrm{Nu}_o/2 - 1)]^{1/2}$.

This expression becomes indeterminate for $\mathrm{Nu}_o = 2$. This indeterminacy arises due to the two-term approximation. It can be eliminated by using the L'Hospital's rule, resulting in

$$\xi_w(Z) = \theta_\infty\left[1 + 2\sqrt{\frac{Z}{\pi}} - (1 + 2Z)e^Z\,\mathrm{erfc}\,(\sqrt{Z})\right] \quad \text{for} \quad \mathrm{Nu}_o = 2 \quad (9)$$

The wall heat flux $\eta_h(Z)$ is given by $\xi_h = -\partial\xi(R, Z)/\partial R|_{R=1}$. From Eq. (2*d*), one obtains

$$\xi_h(Z) = -\frac{\mathrm{Nu}_o\theta_\infty}{(\eta_1 - \eta_2)}[\eta_1 e^{\eta_1^2 Z}\,\mathrm{erfc}\,(-\eta_1\sqrt{Z}) - \eta_2 e^{\eta_2^2 Z}\,\mathrm{erfc}\,(-\eta_2\sqrt{Z})] \quad \text{for } \mathrm{Nu}_o \ne 2 \quad (10a)$$

$$\xi_h(Z) = 2\theta_\infty\left[2\sqrt{\frac{Z}{\pi}} - (1 + 2Z)e^Z\,\mathrm{erfc}\,(\sqrt{Z})\right] \quad \text{for } \mathrm{Nu}_o = 2 \quad (10b)$$

The permanent fluid bulk temperature $\xi_b(Z)$ is obtained from its definition $\xi_b(Z) = 2\int_0^1 R\xi\,(R, Z)dR$. By applying the Laplace transform with respect to Z, and inserting $\tilde{\xi}(R, s)$ from Eq. (7), one obtains after a direct integration, the following equation

$$\tilde{\xi}_b(s) = \frac{2\theta_\infty\mathrm{Nu}_o}{s^{3/2}}\frac{I_1(\sqrt{s})}{\sqrt{s}I_1(\sqrt{s}) + \mathrm{Nu}_o I_o(\sqrt{s})} \quad (11)$$

The inverse transform of Eq. (11) is obtained by using a similar procedure used in Eq. (7). Therefore, for $\mathrm{Nu}_o \ne 2$

$$\xi_b(Z) = 2\theta_\infty\left\{2 + \frac{\mathrm{Nu}_o}{(\eta_1 - \eta_2)}\left[\frac{1}{\eta_1}e^{\eta_1^2 Z}\,\mathrm{erfc}\,(-\eta_1\sqrt{Z}) - \frac{1}{\eta_2}e^{\eta_2^2 Z}\,\mathrm{erfc}\,(-\eta_2\sqrt{Z})\right]\right\} \quad (12a)$$

$$\xi_b(Z) = 4\theta_\infty\left[1 - 2\sqrt{\frac{Z}{\pi}} + 2Ze^Z\,\mathrm{erfc}\,(\sqrt{Z})\right] \quad \text{for} \quad \mathrm{Nu}_o = 2 \quad (12b)$$

The reader should notice that the $\xi_w(Z)$, $\xi_h(Z)$, and $\xi_b(Z)$ are complex numbers due to the $(1 + i)$ factor in θ_∞. This means that the real and imaginary temperatures will behave in the same way, since the only expected difference will be in the transient part of solution.

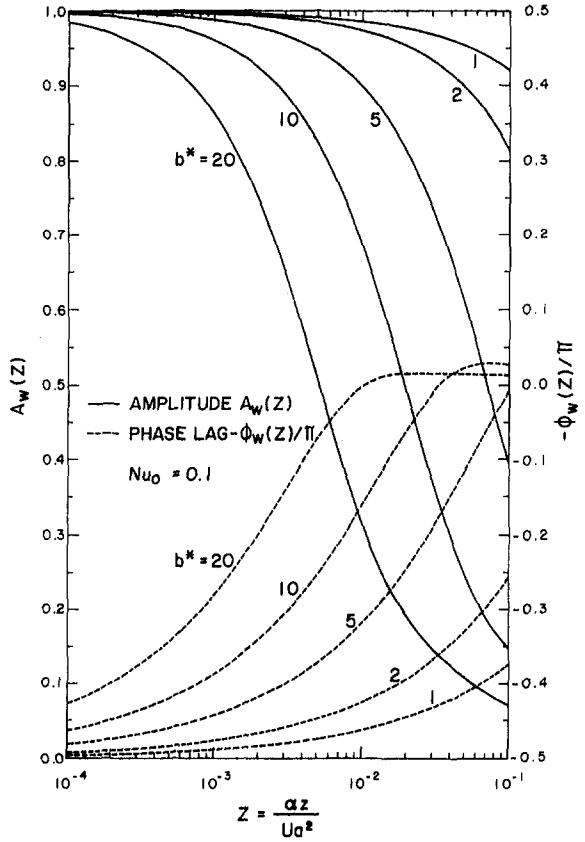

Fig. 1(*a*) Axial distributions of amplitudes and phase lags for dimensionless wall temperature for various values of b^* ($Nu_o = 0.1$)

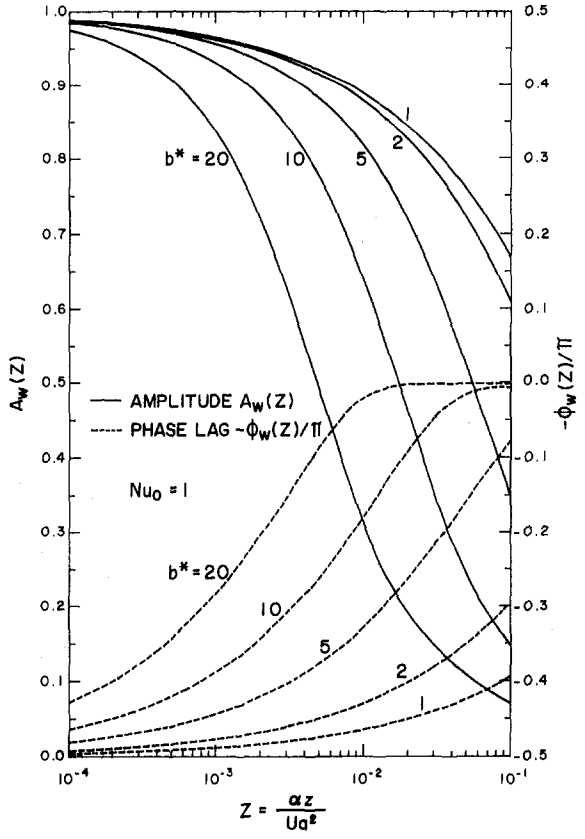

Fig. 1(*b*) Same with $Nu_o = 1$

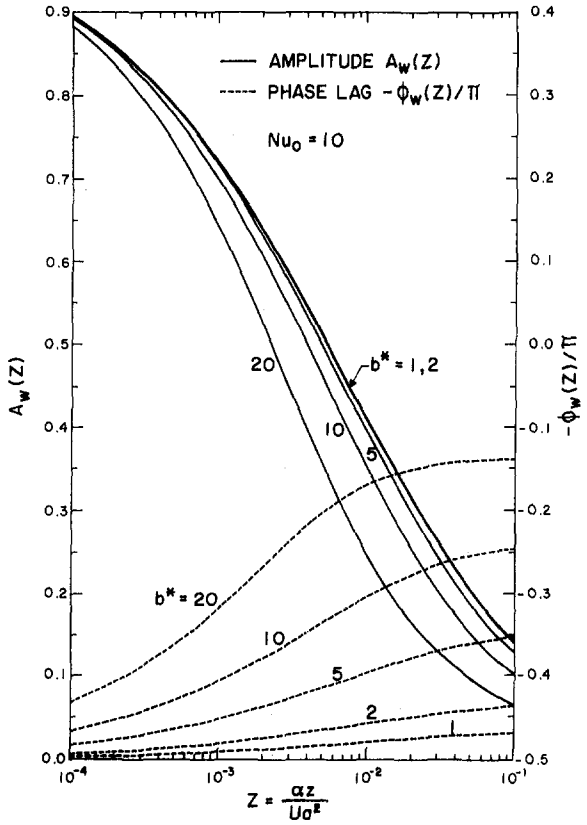

Fig. 1(*c*) Same with $Nu_o = 10$

Problem (4) can be solved by using a procedure similar to that used in problem (2). In this way, the periodic dimensionless wall temperature, wall heat flux, and fluid bulk temperature are given, respectively, by

$$\psi_w(Z) \equiv \psi(1, Z) = \frac{1}{(\lambda_1 - \lambda_2)} [\lambda_1 e^{\lambda_1^2 Z} \operatorname{erfc}(-\lambda \sqrt{Z}) - \lambda_2 e^{\lambda_2^2 Z} \operatorname{erfc}(-\lambda_2 \sqrt{Z})] \quad (13)$$

$$\psi_h(Z) \equiv -\left.\frac{\partial \psi(R, Z)}{\partial R}\right|_{R=1} = c^* \psi(1, Z) \quad (14)$$

$$\psi_b(Z) = -3 - \frac{2c^*}{(\lambda_1 - \lambda_2)} \left[\frac{1}{\lambda_1} e^{\lambda_1^2 Z} \operatorname{erfc}(-\lambda_1 \sqrt{Z}) - \frac{1}{\lambda_2} e^{\lambda_2^2 Z} \operatorname{erfc}(-\lambda_2 \sqrt{Z})\right] \quad (15)$$

where λ_1 and λ_2 are obtained by $\lambda_{1,2}^2 = -c^*/2 \pm [c^*/2\,(c^*/2 - 1)]^{1/2}$. The periodic parts of the interesting quantities obtained above can be presented in terms of amplitudes, $A(Z) = |\psi(Z)|$ and phase lags, $\phi(Z) = tg^{-1}[Im(\psi)/\mathrm{Re}(\psi)] - \Omega Z$.

Results and Discussion

The analytical solution indicates that the calculated quantities depend on the parameter b^*, which represents the ratio between the thermal capacity of the wall and the heat transfer by conduc-

tion across the fluid, and Nu_o, the effectiveness heat transfer to the ambient, and the axial coordinate Z. Amplitudes and phase lags of these quantities were evaluated for representative values of b^* and Nu_o over a range of possible values. For $Nu_o = 0$, the effect of external convection is eliminated and in this case, the insulated wall problem is recovered. If $b^* = 0$ ($a^* \to \infty$), the effect of heat capacity at the wall can be neglected, and therefore, one obtains the problem for time-varying inlet temperature without a participating wall.

Amplitudes and phase lags for dimensionless wall temperature, related to the parameters given above, are plotted as a function of the dimensionless axial coordinate in Figs. 1(a–c). As shown in these figures, the oscillations in the thermal entrance region are influenced by b^* and Nu_o. When Nu_o is small, i.e., when the external thermal resistance is larger, the oscillations in the thermal entrance region depend strongly on b^*. For larger values of b^*, the thermal wave has little penetration along the duct length, rapidly decaying with the axial distance. Therefore, oscillations in fluid temperature are damped within a short distance from the duct inlet. This is expected due to larger thermal capacitance of the wall. For small values of b^*, the thermal wave has a penetration more gradual along the duct because of smaller wall thermal capacitance, requiring a longer length for the same energy to be stored in the wall. For larger values of Nu_o, i.e., when the external thermal resistance is very low, the influence of b^* on the oscillations in the thermal entrance region is much smaller. Bulk temperature amplitudes and phase lags (not shown) present similar behavior to those shown for wall temperature. However, for the bulk temperature, the effects of both b^* and Nu_o are less pronounced. Bulk temperature amplitudes are less attenuated than those for the wall temperature.

The influences of b^* and Nu_o on the dimensionless wall heat flux amplitudes and phase lags were also investigated. For small values of Nu_o, the amplitudes for wall heat flux are larger for larger values of b^*. This is expected since due to a larger wall heat capacitance more heat is transferred to the wall. As Nu_o increases, i.e., when the external thermal resistance decreases, the amplitudes for wall heat flux increase independently of the wall thermal capacity.

Acknowledgments

This work was supported by FAPESP (Fundação de Amparo à Pesquisa do Estado de São Paulo), under contract No. 90/0076-3, to whom the authors express their appreciation.

References

Abramowitz, M., and Stegun, I. A., 1964, *Handbook of Mathematical Functions With Formulas, Graphs, and Mathematical Tables*, National Bureau of Standards Appl. Math. Ser. 55.

Cotta, R. M., Mikhailov, M. D., and Ozisik, M. N., 1987, "Transient Conjugated Forced Convection in Ducts With Periodically Varying Inlet Temperature," *Int. J. Heat Mass Transfer*, Vol. 30, pp. 2073-2082.

Kakaç, S., Li, W., and Cotta, R. M., 1990, "Unsteady Laminar Forced Convection in Duct With Periodic Variation of Inlet Temperature," ASME JOURNAL OF HEAT TRANSFER, Vol. 112, pp. 913–920.

Roberts, G. E., and Kaufmann, H., 1966, *Tables of Laplace Transforms*, W. B. Saunder, Philadelphia, PA.

Santos, W. F. N., and Travelho, J. S., 1993, "Transient Conjugated Forced Convection in a Parallel Plate Duct With Convection From the Ambient and Periodic Variation of Inlet Temperature," *Applied Scientific Research*, Vol. 51, pp. 625–638.

Sparrow, E. M., and DeFarias, F. N., 1968, "Unsteady Heat Transfer in Ducts With Time-Varying Inlet Temperature and Participating Walls," *Int. J. Heat Mass Transfer*, Vol. 11, pp. 837-853.

Travelho, J. S., and Santos, W. F. N., 1991, "Solution for Transient Conjugated Forced Convection in the Thermal Entrance Region of a Duct With Periodically Varying Inlet Temperature," ASME JOURNAL OF HEAT TRANSFER, Vol. 113, pp. 558–562.

Conjugate Heat Transfer for Developing Flow Over Multiple Discrete Thermal Sources Flush-Mounted on the Wall

J.-J. Hwang[1]

Nomenclature

De = duct hydraulic diameter = $2(WH)/(W + H)$
H = duct height
k_f = air conductivity
k_s = conductivity of the substrate material
L = heat source length
$\overline{Nu}$ = local Nusselt number
$\overline{Nu}_h$ = source-averaged Nusselt number
q_h = convective heat from the thermal source = $\int_0^L k_f (dT/dY)_{Y=0} W dX$
q_{in} = electronic power supplied by thermal foil
Re = Reynolds number = $U\,De/\nu$
S = spacing between discrete heat sources
T_o = air temperature at duct inlet, i.e., room temperature
T_w = local wall temperature
Tu = free-stream turbulence intensity = u'/U
U = average duct flow velocity
u' = streamwise velocity fluctuation
W = duct or source width, see Fig. 1
X, Y, Z = coordinate, see Fig. 1
ν = fluid kinematic viscosity

Introduction

Cooling of electronic equipment must be considered when designing such systems. Electronic chip and device temperatures must be maintained below a safe functional limit. Many cooling schemes are available for such tasks. One scheme that has received much attention is convection by naturally induced or forced flow. In addition, numerous studies have investigated the heat transfer from multiple heating devices mounted on an otherwise adiabatic wall to examine the capability of a convection scheme. Relevant works include Jaluria (1982, 1985a) and Park and Bergles (1987) for natural convection, along with Kraus and Bar-Cohen (1983) and McEntire and Webb (1990) for forced convection. However, printed circuit boards normally have a finite conductivity; such devices can influence heat transfer performances of each other through convection in the flow as well as conduction in the substrate. Therefore, the conjugate heat transfer related to electronic cooling has recently drawn much attention (Jaluria, 1985b). Ramadhyani et al. (1985) performed conjugate analysis of forced convection from small isothermal heat sources embedded in a large substrate for a hydrodynamically fully developed laminar channel flow. Incropera et al. (1986) experimentally and theoretically examined the problem of flush-mounted isothermal heat sources embedded in a wall of the horizontal channel with a hydrodynamically fully developed laminar or turbulent flow. The behavior of the surface

[1] Department of Mechanical Engineering, Chung-Hua University, Hsinchu, Taiwan 300.

Contributed by the Heat Transfer Division of THE AMERICAN SOCIETY OF MECHANICAL ENGINEERS. Manuscript received by the Heat Transfer Division April 14, 1997; revision received October 22, 1997. Keywords: Conjugate Heat Transfer, Electronic Equipment, Forced Convection. Associate Technical Editor: Y. Jaluria.

tion across the fluid, and Nu_o, the effectiveness heat transfer to the ambient, and the axial coordinate Z. Amplitudes and phase lags of these quantities were evaluated for representative values of b^* and Nu_o over a range of possible values. For $Nu_o = 0$, the effect of external convection is eliminated and in this case, the insulated wall problem is recovered. If $b^* = 0$ ($a^* \to \infty$), the effect of heat capacity at the wall can be neglected, and therefore, one obtains the problem for time-varying inlet temperature without a participating wall.

Amplitudes and phase lags for dimensionless wall temperature, related to the parameters given above, are plotted as a function of the dimensionless axial coordinate in Figs. 1(a–c). As shown in these figures, the oscillations in the thermal entrance region are influenced by b^* and Nu_o. When Nu_o is small, i.e., when the external thermal resistance is larger, the oscillations in the thermal entrance region depend strongly on b^*. For larger values of b^*, the thermal wave has little penetration along the duct length, rapidly decaying with the axial distance. Therefore, oscillations in fluid temperature are damped within a short distance from the duct inlet. This is expected due to larger thermal capacitance of the wall. For small values of b^*, the thermal wave has a penetration more gradual along the duct because of smaller wall thermal capacitance, requiring a longer length for the same energy to be stored in the wall. For larger values of Nu_o, i.e., when the external thermal resistance is very low, the influence of b^* on the oscillations in the thermal entrance region is much smaller. Bulk temperature amplitudes and phase lags (not shown) present similar behavior to those shown for wall temperature. However, for the bulk temperature, the effects of both b^* and Nu_o are less pronounced. Bulk temperature amplitudes are less attenuated than those for the wall temperature.

The influences of b^* and Nu_o on the dimensionless wall heat flux amplitudes and phase lags were also investigated. For small values of Nu_o, the amplitudes for wall heat flux are larger for larger values of b^*. This is expected since due to a larger wall heat capacitance more heat is transferred to the wall. As Nu_o increases, i.e., when the external thermal resistance decreases, the amplitudes for wall heat flux increase independently of the wall thermal capacity.

Acknowledgments

This work was supported by FAPESP (Fundação de Amparo à Pesquisa do Estado de São Paulo), under contract No. 90/0076-3, to whom the authors express their appreciation.

References

Abramowitz, M., and Stegun, I. A., 1964, *Handbook of Mathematical Functions With Formulas, Graphs, and Mathematical Tables*, National Bureau of Standards Appl. Math. Ser. 55.

Cotta, R. M., Mikhailov, M. D., and Ozisik, M. N., 1987, "Transient Conjugated Forced Convection in Ducts With Periodically Varying Inlet Temperature," *Int. J. Heat Mass Transfer*, Vol. 30, pp. 2073-2082.

Kakaç, S., Li, W., and Cotta, R. M., 1990, "Unsteady Laminar Forced Convection in Duct With Periodic Variation of Inlet Temperature," ASME JOURNAL OF HEAT TRANSFER, Vol. 112, pp. 913–920.

Roberts, G. E., and Kaufmann, H., 1966, *Tables of Laplace Transforms*, W. B. Saunder, Philadelphia, PA.

Santos, W. F. N., and Travelho, J. S., 1993, "Transient Conjugated Forced Convection in a Parallel Plate Duct With Convection From the Ambient and Periodic Variation of Inlet Temperature," *Applied Scientific Research*, Vol. 51, pp. 625–638.

Sparrow, E. M., and DeFarias, F. N., 1968, "Unsteady Heat Transfer in Ducts With Time-Varying Inlet Temperature and Participating Walls," *Int. J. Heat Mass Transfer*, Vol. 11, pp. 837-853.

Travelho, J. S., and Santos, W. F. N., 1991, "Solution for Transient Conjugated Forced Convection in the Thermal Entrance Region of a Duct With Periodically Varying Inlet Temperature," ASME JOURNAL OF HEAT TRANSFER, Vol. 113, pp. 558–562.

Conjugate Heat Transfer for Developing Flow Over Multiple Discrete Thermal Sources Flush-Mounted on the Wall

J.-J. Hwang[1]

Nomenclature

De = duct hydraulic diameter = $2(WH)/(W + H)$
H = duct height
k_f = air conductivity
k_s = conductivity of the substrate material
L = heat source length
$\overline{Nu}$ = local Nusselt number
$\overline{Nu}_h$ = source-averaged Nusselt number
q_h = convective heat from the thermal source = $\int_0^L k_f (dT/dY)_{Y=0} W dX$
q_{in} = electronic power supplied by thermal foil
Re = Reynolds number = $U\,De/\nu$
S = spacing between discrete heat sources
T_o = air temperature at duct inlet, i.e., room temperature
T_w = local wall temperature
Tu = free-stream turbulence intensity = u'/U
U = average duct flow velocity
u' = streamwise velocity fluctuation
W = duct or source width, see Fig. 1
X, Y, Z = coordinate, see Fig. 1
ν = fluid kinematic viscosity

Introduction

Cooling of electronic equipment must be considered when designing such systems. Electronic chip and device temperatures must be maintained below a safe functional limit. Many cooling schemes are available for such tasks. One scheme that has received much attention is convection by naturally induced or forced flow. In addition, numerous studies have investigated the heat transfer from multiple heating devices mounted on an otherwise adiabatic wall to examine the capability of a convection scheme. Relevant works include Jaluria (1982, 1985a) and Park and Bergles (1987) for natural convection, along with Kraus and Bar-Cohen (1983) and McEntire and Webb (1990) for forced convection. However, printed circuit boards normally have a finite conductivity; such devices can influence heat transfer performances of each other through convection in the flow as well as conduction in the substrate. Therefore, the conjugate heat transfer related to electronic cooling has recently drawn much attention (Jaluria, 1985b). Ramadhyani et al. (1985) performed conjugate analysis of forced convection from small isothermal heat sources embedded in a large substrate for a hydrodynamically fully developed laminar channel flow. Incropera et al. (1986) experimentally and theoretically examined the problem of flush-mounted isothermal heat sources embedded in a wall of the horizontal channel with a hydrodynamically fully developed laminar or turbulent flow. The behavior of the surface

[1] Department of Mechanical Engineering, Chung-Hua University, Hsinchu, Taiwan 300.

Contributed by the Heat Transfer Division of THE AMERICAN SOCIETY OF MECHANICAL ENGINEERS. Manuscript received by the Heat Transfer Division April 14, 1997; revision received October 22, 1997. Keywords: Conjugate Heat Transfer, Electronic Equipment, Forced Convection. Associate Technical Editor: Y. Jaluria.

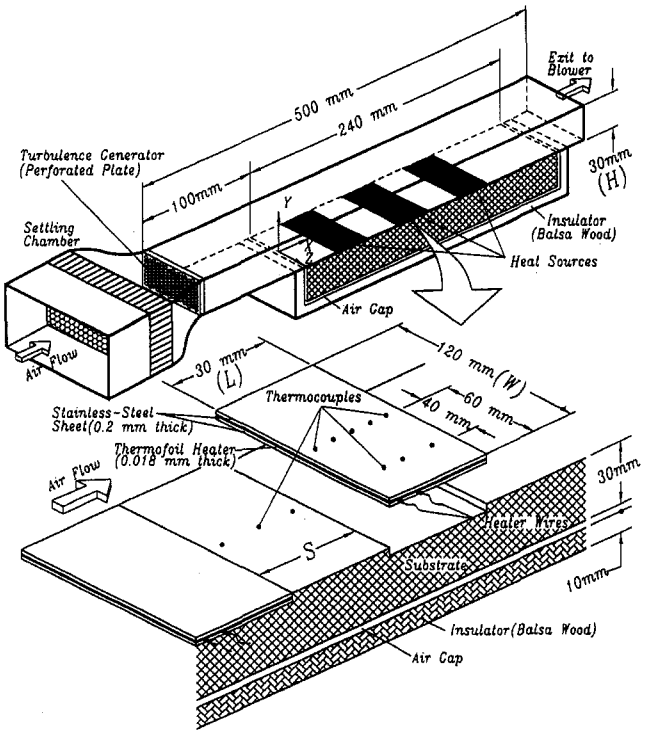

Fig. 1 Sketch of test section configuration and coordinate system

conductance on the heat-source surface has been well documented. Tewari and Jaluria (1990) experimentally examined the conjugate mixed convection from two thermal sources in tandem flush-mounted on a horizontal or vertical plate. Their results indicated that at a separation distance of more than three strip widths for both orientations, the two heat sources are essentially independent of each other, in terms of thermal effects. Culham et al. (1991) investigated the conjugate heat transfer from square flush-mounted heat sources by implementing an iterative scheme. The thermal boundary conditions were applied on the conduction solution based on the analytical solution of the boundary-layer energy equation. Anderson (1994) presented a novel means of decoupling the convective and conductive heat transfer in a conjugate-coupled problem. According to their results, when the Biot number exceeds one, the adiabatic heat transfer coefficient should be used to decouple the problem. If the Biot number is below one, the heat transfer coefficient based on the mean temperature can be used as the decoupler. Cole (1997) numerically analyzed the conjugate heat transfer from a small heated strip. That investigation also provided correlations for the modified Nusselt number in terms of the conjugate Peclet number and dimensionless substrate thickness.

In light of this discussion, the free-stream turbulence effect on the conjugate heat transfer on a discretely heated surface is relatively sparse, particularly with respect to experimental efforts, has seldom been mentioned, and requires further study. Therefore, this study investigates the conjugate heat transfer on a surface with several discrete thermal sources under different free-stream turbulence conditions. Three kinds of conductive substrates are tested herein: fiberglass board, bakelite plate, and aluminum plate. The free-stream turbulence intensity generated by different blockage ratios of perforated plates varies from 1.2 to 13.0 percent. Meanwhile, the air flow rate for each geometric configuration ranges from 1.2 to 2.5 m/s, yielding the nominal Reynolds number based on duct hydraulic diameter from 4800 to 11,200. In addition, laser holographic interferometry is employed to measure the convective heat flux, the local, and the average heat transfer coefficients. This technique is quite appropriate for the conjugate heat transfer problem since it allows one to determine the convective heat transfer directly from surfaces to the working fluid. Consequently, the conductive heat losses into the substrate can be quantified.

Experiments

Airflow-temperature distributions in the test duct are measured using real-time holographic interferometry. Hwang and Liou (1995) have thoroughly described the overall arrangement of the holographic interferometer, and the description is not repeated here. The airflow circuit consists of a settling chamber, a bell-like contraction, the test section, a flow meter, and a 5 hp centrifugal blower. The test channel, as depicted in Fig. 1, is 500 mm long and has a rectangular cross section of 120 mm (W) by 30 mm (H). The bottom duct wall is heated with three discrete heat sources, while the top wall is adiabatic. Two side walls are made of Plexiglas plate to provide optical access for laser holographic interferometry measurements. Each heat source consists of a thermofoil strip 0.018 mm thick, which is sandwiched between two sheets of stainless steel (0.2 mm thick). These heat sources are 30 mm long (L) and are mounted flush on the substrate with a fixed source spacing, i.e., S/L = 1.0. Three kinds of substrate (30 mm thick) are investigated: fiberglass board (k_s = 0.037 W/m-K), bakelite plate (k_s = 0.65 W/m-K), and aluminum plate (k_s = 164 W/m-K). The corresponding ratios of substrate-to-air conductivity are 1.37, 24.9, and 6320, respectively. High-conductivity epoxy is used at each of the above-mentioned interfaces to ensure good contact. The fact that the epoxy layer is extremely thin (0.13 mm thick or less) explains why the thermal resistance is estimated to be extremely small and, therefore, negligible. The test section is instrumented with 30 copper-constantan thermocouples distributed along the spanwise centerline (Z = 0) of the test plate (15 on the heat sources, and 15 on the unheated sections. An additional nine thermocouples along the lateral (Z/L = 0.33) of heat sources are used to verify the spanwise temperature uniformity. All the junction beads (about 0.25 mm in diameter) of the thermocouples are carefully embedded into the wall, and then ground flat to ensure that they are flush with the surfaces. The temperature signals are then transferred to a data acquisition unit (Yokogawa Da 100) and, finally, sent to a Pentium computer via a multi-I/O interface for further processing.

A turbulence generator (perforated plate) is placed 100 mm upstream from the test plate to promote the required turbulence intensities over the test plate. Both the turbulence intensity and the axial mean velocity are measured with a hot-wire anemometer with a normal I-type probe (Hwang, 1997). For the adiabatic

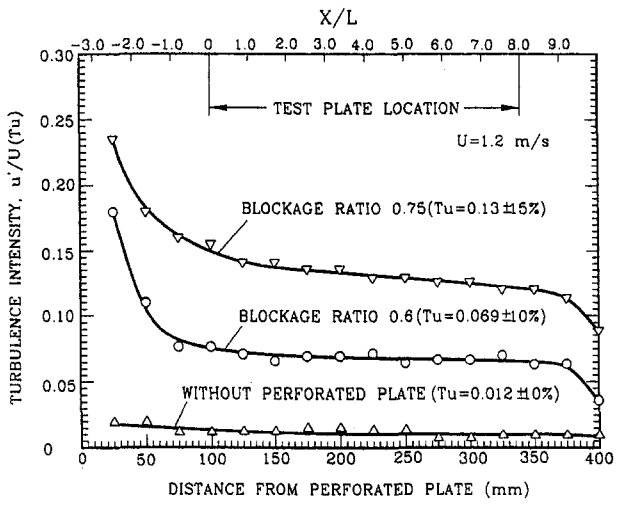

Fig. 2 Free-stream turbulence intensity distribution along the test section

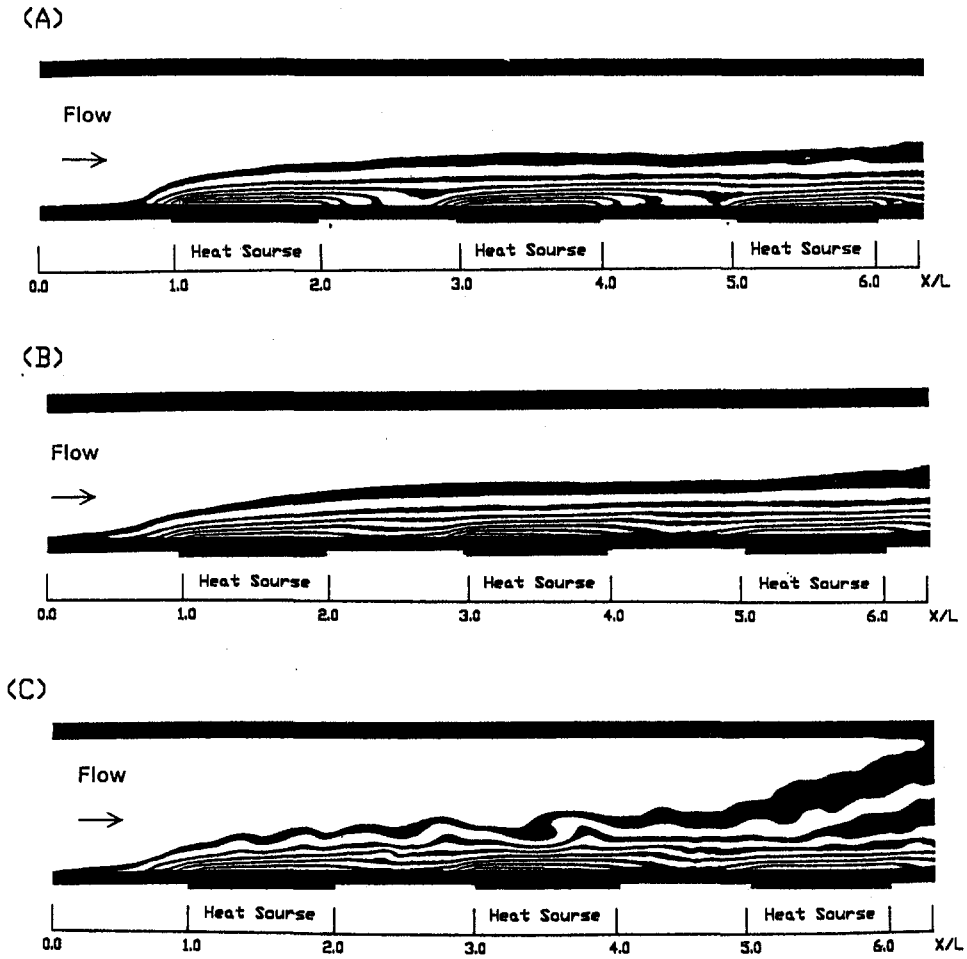

Fig. 3 Examples of holographic interferograms of flow over discrete heat sources: (*a*) $k_s/k_f = 1.37$ (fiberglass board), $Tu = 1.2$ percent, and $U = 1.2$ m/s; (*b*) $k_s/k_f = 24.9$ (bakelite board), $Tu = 1.2$ percent, and $U = 1.2$ m/s; (*c*) $k_s/k_f = 24.8$ (bakelite board), $Tu = 6.9$ percent, and $U = 1.2$ m/s

flow, Fig. 2 provides a characteristic example of the streamwise turbulence intensity distribution along the test section centerline. The data are averaged values and have a standard deviation of approximately 2.5 percent of the flow velocity. According to this figure, the turbulence intensity is characterized by average values between $0 \leq X/L \leq 8.0$, where the turbulence intensity is reasonably uniform. Those values are 0.13 ± 15, 0.069 ± 10, and 0.012 ± 10 percent, respectively, for the test section with upstream perforated plates having blockage ratios of 75, 60, and 0 percent (i.e., without a perforated plate).

The local Nusselt number is defined as $\mathrm{Nu} = -(dT/dY)_w \cdot Del(T_w - T_o)$, where the wall temperature gradient $(dT/dY)_w$ is determined by curve fitting, based on a least-squares method through the near-wall values of fluid temperature and fringe shift. The average Nusselt number on each discrete heat source is obtained by $\overline{\mathrm{Nu}}_h = \int_0^L [-(dT/dY)_w \cdot Del\,(T_w - T_o)]dX/L$. The maximum uncertainties of local and average Nusselt numbers are estimated according to the uncertainty estimation method of Kline and McClintock (1953) to be less than 8.9 and 9.6 percent, respectively.

Results

Figures 3(*a*, *b*) illustrate how substrate-to-air conductivity ratio (k_s/k_f) influences fluid-isotherm patterns. In the case of lower conductivity ratio $(k_s/k_f = 1.37)$, densely dome-shaped isotherms are observed near the surface of each heat source, indicating that the convective heat transfer from surfaces to coolant is extremely large and totally restricted in the heat-

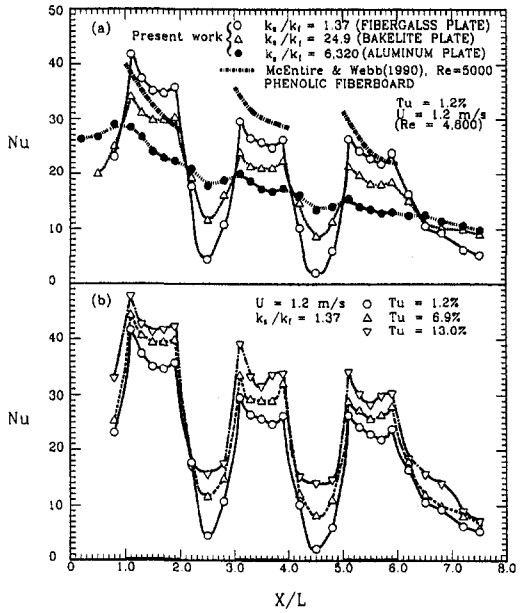

Fig. 4 (*a*) Effect of substrate-to-fluid conductivity ratio on the local Nusselt number distribution along the discrete-heat-source surface; (*b*) effect of free-stream turbulence on the local Nusselt number distribution along the discrete-heat-source surface

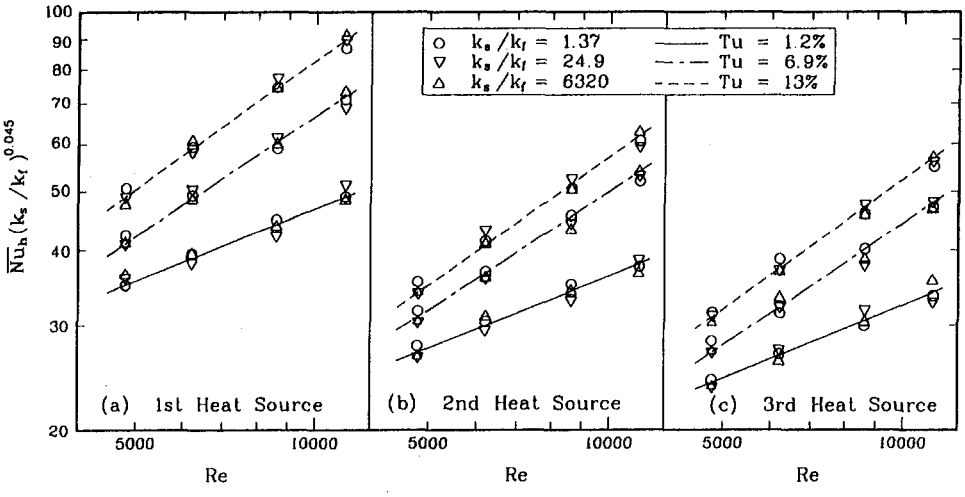

Fig. 5 Reynolds number dependence of the source-averaged Nusselt number

source region. In contrast, the fluid isotherms above the unheated sections are rather sparse and roughly perpendicular to the substrate wall. This finding implies that only a very small portion of electrically generated heat is conducted into this low-conductivity substrate initially by convection to cooling air from these unheated-section surfaces. As the substrate conductivity is increased to $k_s/k_f = 24.9$ (Fig. 3(b)), near each heat-source surface, the isotherms are less compact than those of the lower conductive substrate. Near the substrate surfaces of unheated sections ($2 \le X/L \le 3$ and $4 \le X/L \le 5$), however, relatively higher air temperature gradients are observed. Both of these facts indicate that, instead of direct convection from source surfaces to coolant, a fraction of electrically generated heat has been conducted into the higher conductivity substrate, which is subsequently convected to the coolant from the unheated-section surfaces. Figures 3(b, c) schematically depict how turbulence influences the thermal boundary layer generated by the discrete heat sources. An increasing turbulence intensity causes the thermal boundary layer to fluctuate significantly. This occurrence is attributed to the entrainment by cold turbulent eddies from the free stream toward the surface, which results in convective cooling of the heated surface by reducing the surface temperature. Comparing the isotherms at downstream ends ($X/L = 6.0$) of these two interferograms reveals that at higher turbulence-intensity conditions, the thermal energy has spread more rapidly from the near-wall region to the entire duct flow than that at lower turbulence-intensity conditions due to the stronger thermal mixing by a higher turbulence.

Figures 4(a, b) depict pictorially how k_s/k_f and Tu, respectively, influence the Nu distribution along the discretely heated surfaces. Around the heat sources, the local Nusselt number increases markedly near the beginning of each source, decreases downstream, increases to local maximum at the source end and, finally, dramatically declines to a local minimum in the middle of the unheated section. Similar but lower distributions are found as coolant flows over the next two heat sources due to the thermal-wake effect. For increasing k_s/k_f, the Nu distribution becomes even due to the spread in heat flux and/or surface temperature by board conduction. This figure also reveals that the local Nusselt number on the first source decreases with an increasing substrate conductivity. This fact merely reflects the preheating of the near-wall fluid due to upstream conduction and, thus, the thermal-wake effect (Choi et al., 1994; Sugavanam et al., 1995). Figure 4 compares our results with those of McEntire and Webb (1990) by using a conventional resistance heating/thermocouple technique. The Nusselt number was obtained for four discrete heat sources mounted on the Phenolic fiberboard. As Fig. 4(a) indicates, these two works correlate well with each other qualitatively. Quantitatively, the discrepancy is ascribed primarily to different substrate materials employed, or somewhat caused by unavoidable measuring errors by different techniques. Figure 4(b) illustrates how free-stream turbulence influences the local Nusselt number for a fixed throughflow velocity (U = 1.2 m/s) and substrate-to-fluid conductivity ratio ($k_s/k_f = 1.37$). This figure indicates that increasing the free-stream turbulence intensity can promote the local heat transfer coefficient.

Figures 5(a–c) respectively show the relationship between the Reynolds number and $\overline{Nu}_h (k_s/k_f)^{0.045}$ for the first, second, and third heat sources under various free-stream turbulence intensities. Also shown in this figure is the least-square curve fit of $\overline{Nu}_h$, a correlation of the form of $\overline{Nu}_h = a\,Re^b (k_s/k_f)^{-0.045}$, where a and b are constants and are listed in Table 1 for various free-stream turbulence intensities, as well as relative locations of the heat sources. The deviation of this equation is 9 percent for 90 percent for the experimental data in Fig. 5. Notably, the Reynolds-number dependence of $\overline{Nu}_h$ under the lowest free-stream turbulence ($Re^{0.4}$) differs markedly from that of the well-known average Nusselt number relation for a fully developed turbulent flow in a continuously heated circular duct (Dittus–Boelter correlation, $\sim Re^{0.8}$). This significant difference may be attributed to the relatively low Reynolds number range and the repeatedly redeveloping thermal boundary layer investigated herein. When the free-stream turbulence intensity is increased, the departure of the Reynolds-number dependence from 0.8 is reduced, indicating that the flow has approached a turbulence domination.

Table 2 displays the convective heat transfer ratio (q_h/q_{in}) of each heat source at various free-stream turbulence intensities and substrate conductivities. At a fixed substrate conductivity, even with one or two upstream heat sources, the value of q_h/q_{in} does not change by more than 10 percent. Varying the free-stream turbulence intensity remains nearly constant as well. Both these facts imply that the thermal wake, depending on the number of upstream heat sources as well as the free-stream

Table 1 Coefficients of source-averaged Nusselt number correlations

	$\overline{Nu}_h = a\,Re^b (k_s/k_f)^{-0.045}$					
Tu	1ST Heat Source		2ND Heat Source		3RD Heat Source	
	a	b	a	b	a	b
1.2 %	1.182	0.39	0.913	0.39	0.815	0.39
6.9 %	0.168	0.65	0.127	0.65	0.111	0.65
13.0 %	0.132	0.71	0.092	0.71	0.084	0.71

Table 2 Effects of free-stream turbulence on q_h/q_{in} for each thermal source

Tu	k_s/k_f = 1.37			k_s/k_f = 24.9			k_s/k_f = 6,320		
	1ST	2ND	3RD	1ST	2ND	3RD	1ST	2ND	3RD
1.2 %	0.87	0.83	0.84	0.63	0.62	0.65	0.45	0.43	0.42
6.9 %	0.85	0.83	0.81	0.64	0.66	0.61	0.45	0.44	0.43
13.0 %	0.84	0.80	0.82	0.61	0.60	0.62	0.44	0.42	0.42

turbulence intensity, negligibly influences q_h/q_{in}. Such a negligible influence is quite reasonable because an increase in fluid temperature adjacent to the strip due to the above-mentioned effects is accompanied by the corresponding increase in the strip surface temperature, which maintains the temperature gradients constant in the flow, near the heat source surface. The isotherm-patterns in Fig. 3 confirm this phenomenon. Therefore, we can conclude that the fraction q_h/q_{in} remains essentially unaltered as flow and thermal-fluid conditions are changed. This finding is very important in predicting $\overline{\mathrm{Nu}}_h$ for heat transfer problems that have significant conjugate coupling and highly nonuniform surface thermal boundary conditions. Regarding the effect of changing the substrate conductivity, the level of convective heat flux ratio decreases significantly with an increasing substrate conductivity due to a large fraction of heat spreading upstream or downstream in the substrate by conduction. In addition, the convection heat flux ratios (q_h/q_{in}) are 0.83 ± 4, 0.64 ± 5, and 0.43 ± 3 percent for the fiberglass, bakelite, and aluminum substrates, respectively.

Conclusions

This work investigates forced convection from discrete heat sources mounted flush on a conductive substrate in a rectangular duct. Of particular emphases are (a) the effects of free-stream turbulence (Tu = 1.2, 6.9, and 13.0 percent) and velocity (U = 1.2 to 2.5 m/s), and (b) the substrate conductivity (k_s/k_f = 1.37, 24.9, and 6,320) on the heat transfer characteristics in a conjugated-coupled sense. Most importantly, laser holographic interferometry successfully isolates the heat directly convected from the exposed surface of a source from the electrical heat dissipation, thereby facilitating the determination of conduction losses into the board. Experimental results in this work can also facilitate the prediction of heat transfer coefficient or surface temperature in the conjugate-coupling heat transfer problems relative to electronic cooling. According to those results, substrates of higher conductivity can spread more source heat flux by board conduction and, subsequently, smooth off the local heat transfer coefficient distributions along the discrete heated surfaces. In addition, both the local and the source-averaged Nusselt numbers decrease with increasing k_s/k_f. Moreover, elevating the level of free-stream turbulence can enhance the heat transfer by entraining the cold free-stream fluid near the wall region. The ratio of convective heat from the source surface to coolant and the total electronic heat input is nearly independent of the free-stream turbulence and the source location; however, it is significantly reduced by an increase in substrate conductivity. Finally, for the first time, correlations of source-averaged Nusselt number under various free-stream turbulence intensities are developed in terms of the flow Reynolds number and the substrate-to-fluid conductivity ratio.

Acknowledgments

The author would like to thank the National Science Council of the Republic of China for financially supporting this research under Contract No. NSC 85-2212-E-216-006.

References

Anderson, A. M., 1994, "Decoupling Convective and Conductive Heat Transfer Using the Adiabatic Heat Transfer Coefficient," ASME *Journal of Electronic Packaging,* Vol. 116, pp. 310–316.

Choi, C. Y., Kim, S. J., and Ortega, A., 1994, "Effects of Substrate Conductivity on Convection of Electronic Components," ASME *Journal of Electronic Packaging,* Vol. 116, pp. 198–205.

Cole, K. D., 1997, "Conjugate Heat Transfer From a Small Heated Strip," *Int. J. Heat Mass Transfer,* Vol. 40, pp. 2709–2719.

Culham, J. R., Lee, S., and Yovanovich, M. M., 1991, "The Effect of Common Design Parameters on the Thermal Performance of Microelectronic Equipment: Part II—Forced Convection," *ASME Heat Transfer in Electronic Equipment,* ASME HTD-Vol. 171, pp. 55–62.

Hwang, J. J., and Liou, T. M., 1995, "Heat Transfer in a Rectangular Channel With Perforated Turbulence Promoters Using Holographic Interferometry Measurement," *Int. J. Heat Mass Transfer,* Vol. 38, pp. 3197–3207.

Hwang, J. J., 1997, "Turbulent Heat Transfer and Fluid Flow in a Porous-Baffled Channel," AIAA *J. Thermophysics and Heat Transfer,* Vol. 11, pp. 429–436.

Incropera, P. F., Herby, J. S., Moffatt, D. F., and Ramadhyani, S., 1986, "Convective Heat Transfer From Discrete Heat Sources in a Rectangular Channel," *Int. J. Heat Mass Transfer,* Vol. 29, pp. 1051–1058.

Jaluria, Y., 1982, "Buoyancy-Induced Flow Due to Isolated Thermal Sources on a Vertical Surface," ASME JOURNAL OF HEAT TRANSFER, Vol. 104, pp. 223–227.

Jaluria, Y., 1985a, "Interaction of Nature Convection Wakes Arising From Thermal Sources on a Vertical Surface," ASME JOURNAL OF HEAT TRANSFER, Vol. 107, pp. 883–892.

Jaluria, Y., 1985b, "Natural Convection Cooling of Electronic Equipment," *Natural Convection, Fundamentals and Applications,* Kakac, S., Aung, W., and Viskanta, R., eds., pp. 961–987.

Kline, S. J., and McClintock, F. A., 1953, "Describing Uncertainties in Single-Sample Experiments," *Mechanical Engineering,* Jan., pp. 3–8.

Kraus, A. D., and Bar-Cohan, A., 1983, *Thermal Analysis and Control of Electronic Equipment,* Hemisphere, New York.

McEntire, A. B., and Webb, B. W., 1990, "Local Forced Convective Heat Transfer From Protruding and Flush-Mounted Two-Dimensional Discrete Heat Source," *Int. J. Heat Mass Transfer,* Vol. 33, pp. 1521–1533.

Park, K. A., and Bergles, A. E., 1987, "Natural Convection Heat Transfer Characteristics of Simulated Microelectronic Chips," ASME JOURNAL OF HEAT TRANSFER, Vol. 109, pp. 90–96.

Ramadhyani, S., Moffatt, D. F., and Incropera, P. F., 1985, "Conjugated Heat Transfer From Small Isothermal Heat Sources Embedded in a Large Substrate," *Int. J. Heat Mass Transfer,* Vol. 28, pp. 1945–1952.

Sugavanam, R., Ortega, A., and Choi, C. Y., 1995, "A Numerical Investigation of Conjugate Heat Transfer From a Flush Heat Source on a Conductive Board in Laminar Channel Flow," *Int. J. Heat Mass Transfer,* Vol. 38, pp. 2969–2984.

Tewari, S. S., and Jaluria, Y., 1990, "Mixed Convection Heat Transfer From Thermal Sources Mounted on Horizontal and Vertical Surfaces," ASME JOURNAL OF HEAT TRANSFER, Vol. 112, pp. 975–987.

A New Discrete Ordinates Quadrature Scheme for Three-Dimensional Radiative Heat Transfer

Ben-Wen Li,[1,2] Qiang Yao,[1] Xin-Yu Cao,[1] and Ke-Fa Cen[1]

Introduction

The choice of angular quadrature scheme plays an important role in the Discrete Ordinates Method. The quadrature scheme is chosen arbitrarily. However, in orthogonal coordinate systems, restrictions must be imposed on the direction set to preserve labeling and prevent biasing of any computed quantity. These restrictions include both symmetry under reflection and in 90 deg rotations of the coordinate axes (Carlson and Lathrop,

[1] Institute for Thermal Power Engineering, Zhejiang University, Hangzhou, Zhejiang 310027, China.

[2] E-mail: cws@sun.zju.edu.cn or heatli@hotmail.com.

Contributed by the Heat Transfer Division of THE AMERICAN SOCIETY OF MECHANICAL ENGINEERS. Manuscript received by the Heat Transfer Division September 12, 1997; revision received February 4, 1998. Keywords: Computational, Heat Transfer, Numerical Methods, Radiation, Three-Dimensional. Associate Technical Editor: M. P. Menguc.

Table 2 Effects of free-stream turbulence on q_h/q_{in} for each thermal source

Tu	k_s/k_f = 1.37			k_s/k_f = 24.9			k_s/k_f = 6,320		
	1ST	2ND	3RD	1ST	2ND	3RD	1ST	2ND	3RD
1.2 %	0.87	0.83	0.84	0.63	0.62	0.65	0.45	0.43	0.42
6.9 %	0.85	0.83	0.81	0.64	0.66	0.61	0.45	0.44	0.43
13.0 %	0.84	0.80	0.82	0.61	0.60	0.62	0.44	0.42	0.42

turbulence intensity, negligibly influences q_h/q_{in}. Such a negligible influence is quite reasonable because an increase in fluid temperature adjacent to the strip due to the above-mentioned effects is accompanied by the corresponding increase in the strip surface temperature, which maintains the temperature gradients constant in the flow, near the heat source surface. The isotherm-patterns in Fig. 3 confirm this phenomenon. Therefore, we can conclude that the fraction q_h/q_{in} remains essentially unaltered as flow and thermal-fluid conditions are changed. This finding is very important in predicting $\overline{\mathrm{Nu}}_h$ for heat transfer problems that have significant conjugate coupling and highly nonuniform surface thermal boundary conditions. Regarding the effect of changing the substrate conductivity, the level of convective heat flux ratio decreases significantly with an increasing substrate conductivity due to a large fraction of heat spreading upstream or downstream in the substrate by conduction. In addition, the convection heat flux ratios (q_h/q_{in}) are 0.83 ± 4, 0.64 ± 5, and 0.43 ± 3 percent for the fiberglass, bakelite, and aluminum substrates, respectively.

Conclusions

This work investigates forced convection from discrete heat sources mounted flush on a conductive substrate in a rectangular duct. Of particular emphases are (a) the effects of free-stream turbulence (Tu = 1.2, 6.9, and 13.0 percent) and velocity (U = 1.2 to 2.5 m/s), and (b) the substrate conductivity (k_s/k_f = 1.37, 24.9, and 6,320) on the heat transfer characteristics in a conjugated-coupled sense. Most importantly, laser holographic interferometry successfully isolates the heat directly convected from the exposed surface of a source from the electrical heat dissipation, thereby facilitating the determination of conduction losses into the board. Experimental results in this work can also facilitate the prediction of heat transfer coefficient or surface temperature in the conjugate-coupling heat transfer problems relative to electronic cooling. According to those results, substrates of higher conductivity can spread more source heat flux by board conduction and, subsequently, smooth off the local heat transfer coefficient distributions along the discrete heated surfaces. In addition, both the local and the source-averaged Nusselt numbers decrease with increasing k_s/k_f. Moreover, elevating the level of free-stream turbulence can enhance the heat transfer by entraining the cold free-stream fluid near the wall region. The ratio of convective heat from the source surface to coolant and the total electronic heat input is nearly independent of the free-stream turbulence and the source location; however, it is significantly reduced by an increase in substrate conductivity. Finally, for the first time, correlations of source-averaged Nusselt number under various free-stream turbulence intensities are developed in terms of the flow Reynolds number and the substrate-to-fluid conductivity ratio.

Acknowledgments

The author would like to thank the National Science Council of the Republic of China for financially supporting this research under Contract No. NSC 85-2212-E-216-006.

References

Anderson, A. M., 1994, "Decoupling Convective and Conductive Heat Transfer Using the Adiabatic Heat Transfer Coefficient," ASME *Journal of Electronic Packaging,* Vol. 116, pp. 310–316.

Choi, C. Y., Kim, S. J., and Ortega, A., 1994, "Effects of Substrate Conductivity on Convection of Electronic Components," ASME *Journal of Electronic Packaging,* Vol. 116, pp. 198–205.

Cole, K. D., 1997, "Conjugate Heat Transfer From a Small Heated Strip," *Int. J. Heat Mass Transfer,* Vol. 40, pp. 2709–2719.

Culham, J. R., Lee, S., and Yovanovich, M. M., 1991, "The Effect of Common Design Parameters on the Thermal Performance of Microelectronic Equipment: Part II—Forced Convection," *ASME Heat Transfer in Electronic Equipment,* ASME HTD-Vol. 171, pp. 55–62.

Hwang, J. J., and Liou, T. M., 1995, "Heat Transfer in a Rectangular Channel With Perforated Turbulence Promoters Using Holographic Interferometry Measurement," *Int. J. Heat Mass Transfer,* Vol. 38, pp. 3197–3207.

Hwang, J. J., 1997, "Turbulent Heat Transfer and Fluid Flow in a Porous-Baffled Channel," AIAA *J. Thermophysics and Heat Transfer,* Vol. 11, pp. 429–436.

Incropera, P. F., Herby, J. S., Moffatt, D. F., and Ramadhyani, S., 1986, "Convective Heat Transfer From Discrete Heat Sources in a Rectangular Channel," *Int. J. Heat Mass Transfer,* Vol. 29, pp. 1051–1058.

Jaluria, Y., 1982, "Buoyancy-Induced Flow Due to Isolated Thermal Sources on a Vertical Surface," ASME JOURNAL OF HEAT TRANSFER, Vol. 104, pp. 223–227.

Jaluria, Y., 1985a, "Interaction of Nature Convection Wakes Arising From Thermal Sources on a Vertical Surface," ASME JOURNAL OF HEAT TRANSFER, Vol. 107, pp. 883–892.

Jaluria, Y., 1985b, "Natural Convection Cooling of Electronic Equipment," *Natural Convection, Fundamentals and Applications,* Kakac, S., Aung, W., and Viskanta, R., eds., pp. 961–987.

Kline, S. J., and McClintock, F. A., 1953, "Describing Uncertainties in Single-Sample Experiments," *Mechanical Engineering,* Jan., pp. 3–8.

Kraus, A. D., and Bar-Cohan, A., 1983, *Thermal Analysis and Control of Electronic Equipment,* Hemisphere, New York.

McEntire, A. B., and Webb, B. W., 1990, "Local Forced Convective Heat Transfer From Protruding and Flush-Mounted Two-Dimensional Discrete Heat Source," *Int. J. Heat Mass Transfer,* Vol. 33, pp. 1521–1533.

Park, K. A., and Bergles, A. E., 1987, "Natural Convection Heat Transfer Characteristics of Simulated Microelectronic Chips," ASME JOURNAL OF HEAT TRANSFER, Vol. 109, pp. 90–96.

Ramadhyani, S., Moffatt, D. F., and Incropera, P. F., 1985, "Conjugated Heat Transfer From Small Isothermal Heat Sources Embedded in a Large Substrate," *Int. J. Heat Mass Transfer,* Vol. 28, pp. 1945–1952.

Sugavanam, R., Ortega, A., and Choi, C. Y., 1995, "A Numerical Investigation of Conjugate Heat Transfer From a Flush Heat Source on a Conductive Board in Laminar Channel Flow," *Int. J. Heat Mass Transfer,* Vol. 38, pp. 2969–2984.

Tewari, S. S., and Jaluria, Y., 1990, "Mixed Convection Heat Transfer From Thermal Sources Mounted on Horizontal and Vertical Surfaces," ASME JOURNAL OF HEAT TRANSFER, Vol. 112, pp. 975–987.

A New Discrete Ordinates Quadrature Scheme for Three-Dimensional Radiative Heat Transfer

Ben-Wen Li,[1,2] Qiang Yao,[1] Xin-Yu Cao,[1] and Ke-Fa Cen[1]

Introduction

The choice of angular quadrature scheme plays an important role in the Discrete Ordinates Method. The quadrature scheme is chosen arbitrarily. However, in orthogonal coordinate systems, restrictions must be imposed on the direction set to preserve labeling and prevent biasing of any computed quantity. These restrictions include both symmetry under reflection and in 90 deg rotations of the coordinate axes (Carlson and Lathrop,

[1] Institute for Thermal Power Engineering, Zhejiang University, Hangzhou, Zhejiang 310027, China.

[2] E-mail: cws@sun.zju.edu.cn or heatli@hotmail.com.

Contributed by the Heat Transfer Division of THE AMERICAN SOCIETY OF MECHANICAL ENGINEERS. Manuscript received by the Heat Transfer Division September 12, 1997; revision received February 4, 1998. Keywords: Computational, Heat Transfer, Numerical Methods, Radiation, Three-Dimensional. Associate Technical Editor: M. P. Menguc.

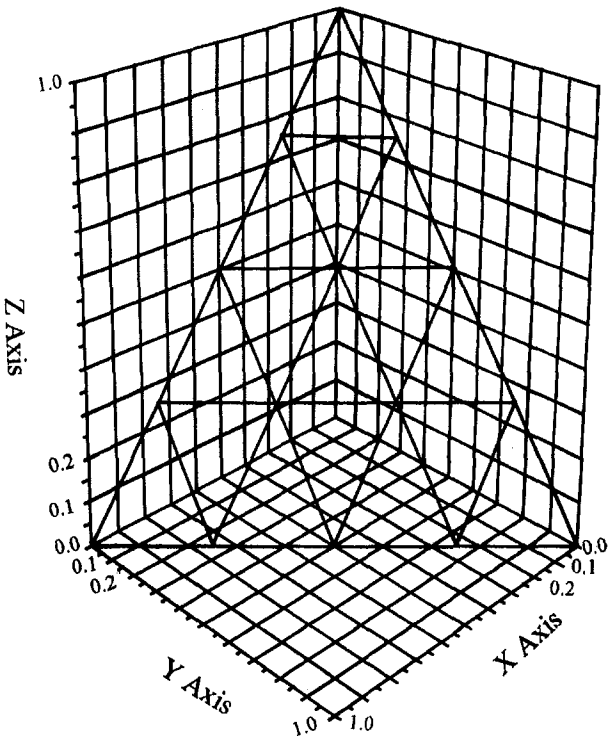

Fig. 1 Tessellation of basal equilateral triangle for the T_4 quadrature set

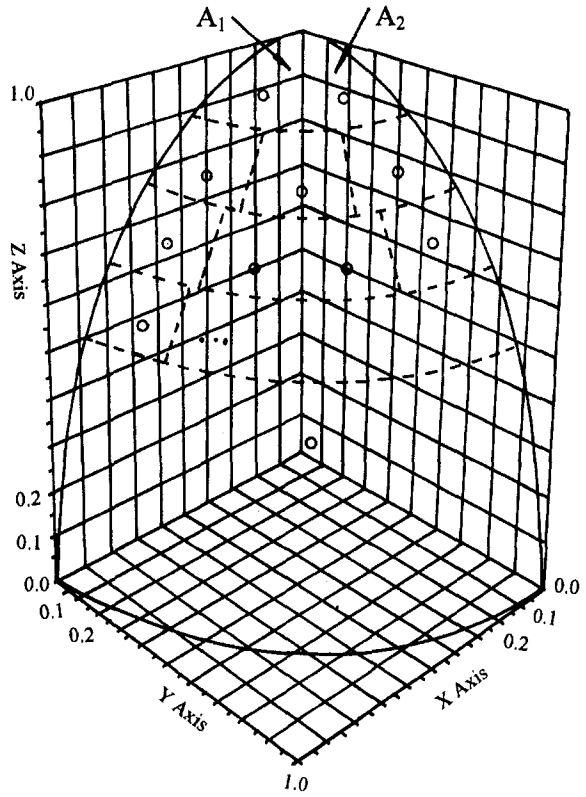

Fig. 3 Scheme of successive spherical rings arithmetic progression dividing

1968). Until now several kinds of quadrature schemes have been used (Fiveland, 1984, 1987; Jamaluddin and Smith, 1988a, b; etc.), and most of them were based on moment-matching criteria. Truelove (1987) further emphasized that the chosen quadrature scheme should also match the half-range first moment so as to improve the low-order discrete ordinate solutions of the transport equation.

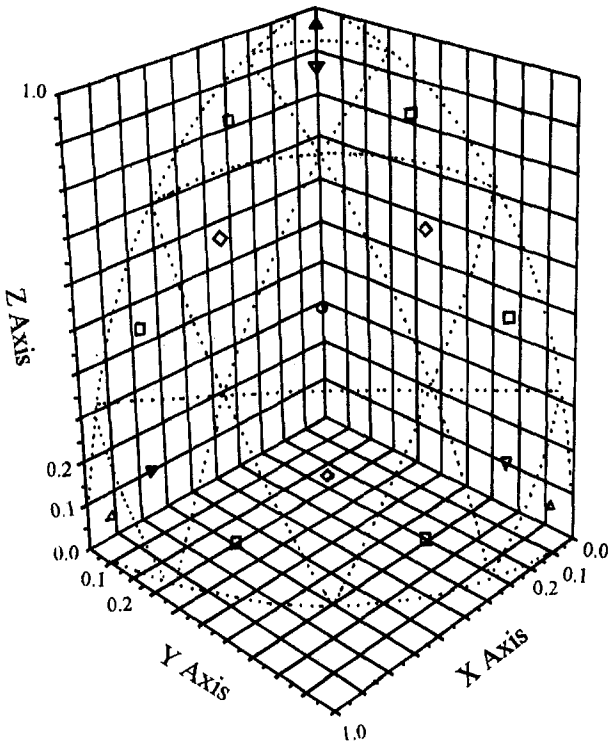

Fig. 2 Map of Fig. 1 onto the surface of the sphere resulting in the directions and spherical triangles (dotted lines) of the T_4 quadrature set

Among the several quadrature schemes proposed in the past, the T_N scheme of Thurgood et al. (1995) has some advantages over the conventional level symmetric sets as it is more accurate in computing the first-order moment with no upper limit of direction number. For more details regarding the T_N quadrature scheme, reference may be made to Thurgood et al. (1995).

The purpose of this note is to present a new angular quadrature scheme, the *S*pherical *R*ings *A*rithmetic *P*rogression ($SRAP_N$), which has a different arrangement of directions than the standard level symmetric sets or the T_N set. Similarly, the index N can be any integer greater than or equal to 2. For any fixed N, all directions have an equal solid angle, so the weights corresponding to areas on the surface of the unit sphere also have an equal value, thus ensuring that the $SRAP_N$ sets have positive weights for any N.

The T_N Quadrature Set

For the purpose of comparison with the newest quadrature set published in the latest reference, the construction procedure of T_N will be described briefly. For more details, together with the review of the quadrature characteristics, Thurgood et al. (1995) may be consulted.

The construction of a T_N quadrature set is carried out in three steps on an octant of unit sphere. First, the octant is mapped onto the basal equilateral triangle, which lies in the plane $x + y + z - 1 = 0$ with vertices at three points: (1, 0, 0), (0, 1, 0), and (0, 0, 1). The second step is to tessellate the basal triangle with smaller equilateral triangles, keeping the side length of the smaller triangles at $1/N$ times the side length of the basal triangle. Then each ray starting from the center of the sphere and passing through the centroids of the smaller triangles is defined as the direction associated with the smaller triangle. The third step is to map the assembly of equilateral triangles and centroids onto the surface of the unit sphere. Figure 1 shows the tessellation of the basal triangle for the T_4 quadrature set;

Table 1 Ordinates and weights for $SRAP_N$ and T_N quadrature sets ($N = 2 \sim 4$, one octant)

Direction	$SRAP_N$				T_N			
number	μ_m	η_m	ξ_m	ω_m	μ_m	η_m	ξ_m	ω_m
				N=2				
1	.8265136	.2154189	.5200672		.5773503	.5773503	.5773503	.5512855
				.3141593				
2	.8265136	.5200672	.2154189		.2357023	.2357022	.9428090	.3398372
3	.3083260	.2462096	.9188666		.2357023	.9428090	.2357022	.3398372
4	.3083260	.6726571	.6726571		.9428090	.2357022	.2357022	.3398372
5	.3083260	.9188666	.2462096					
				N=3				
1	.9047905	.3934405	.1629684		.9801961	.1400280	.1400280	.1113405
				.1745329				
2	.9047905	.1629684	.3934405		.1400280	.9801961	.1400280	.1113405
3	.6201532	.7577502	.2030386		.1400280	.1400280	.9801961	.1113405
4	.6201532	.5547116	.5547117		.8703883	.3481553	.3481553	.2061296
5	.6201532	.2030386	.7577502		.3481553	.8703883	.3481553	.2061296
6	.2255559	.9555107	.1900629		.3481553	.3481553	.8703883	.2061296
7	.2255559	.8100428	.5412533		.6963106	.6963106	.1740777	.2061296
8	.2255559	.5412533	.8100429		.1740777	.6963106	.6963106	.2061296
9	.2255559	.1900628	.9555107		.6963106	.1740777	.6963106	.2061296
				N=4				
1	.9391243	.1314814	.3174242		.5773503	.5773503	.5773503	.1552105
				.1121997				
2	.9391243	.3174242	.1314814		.9901475	.0990148	.0990148	.0526558
3	.7571031	.1690853	.6310349		.0990148	.0990148	.9901475	.0526558
4	.7571031	.4619496	.4619496		.0990148	.9901475	.0990148	.0526558
5	.7571031	.6310349	.1690853		.9428090	.2357022	.2357022	.0880364
6	.5047200	.1684182	.8466954		.2357023	.2357022	.9428090	.0880364
7	.5047200	.4796144	.7177937		.2357023	.9428090	.2357022	.0880364
8	.5047200	.7177937	.4796144		.8616404	.1230915	.4923660	.0995716
9	.5047200	.8466954	.1684181		.8616404	.4923660	.1230915	.0995716
10	.1802793	.1538714	.9715055		.1230915	.4923660	.8616404	.0995716
11	.1802793	.4465521	.8764078		.4923660	.1230915	.8616404	.0995716
12	.1802793	.6955212	.6955211		.4923660	.8616404	.1230915	.0995716
13	.1802793	.8764078	.4465521		.1230915	.8616404	.4923660	.0995716
14	.1802793	.9715055	.1538713		.6804138	.2721655	.6804138	.1320254
15					.2721665	.6804138	.6804138	.1320254
16					.6804138	.6804138	.2721655	.1320254

Fig. 2 shows the result of mapping Fig. 1 onto the surface of the sphere. The total direction number for T_N quadrature set is $(8 \times N^2)$. For the determination of the discrete directions and corresponding weights, sample calculations may be found from Thurgood et al. (1995).

The $SRAP_N$ Quadrature Set

Quadrature sets are usually constructed for an octant because of symmetry. Similar to the T_N quadrature set, the surface of the unit sphere is divided into contiguous regions. For each region, an associated direction is defined but different from the T_N quadrature set. The whole surface is divided in a manner such that each surface element on the octant has an equal elemental surface area, say $(\pi/2)/M$, where M is the total number of surface elements on the octant. Each ray direction starts from the center of the sphere, passes through the centroid of solid angle, and terminates at the surface of the element.

Focusing on the whole hemisphere rather than the octant, the whole hemispherical surface is divided into N spherical rings. Among them, the first spherical zone on the top of the sphere reduces to a crown; see Fig. 3 (only the octant is shown). Then from top to bottom, each ring is divided into different numbers of elements in such a way that the number of elements in the successive spherical rings constitutes an arithmetic progression with the first number 2 and one element added to every successive ring. As pointed out earlier, this procedure provides elements of equal surface areas having a value of $(\pi/2)/(2 + 3 + 4 + \ldots)$.

The determination of discrete directions is a geometric problem. Corresponding to each curved surface element, the location of the centroid $(\overline{x}_m, \overline{y}_m, \overline{z}_m)$ of the solid angle can be calculated through a series of integrations within the domain Ω_m

$$\begin{cases} \overline{x}_m = \dfrac{1}{V_m} \displaystyle\iiint_{\Omega_m} x dV \\ \overline{y}_m = \dfrac{1}{V_m} \displaystyle\iiint_{\Omega_m} y dV \\ \overline{z}_m = \dfrac{1}{V_m} \displaystyle\iiint_{\Omega_m} z dV \end{cases} \tag{1}$$

Table 2 Percent error in estimating $\int_{2\pi} \mu^a \eta^b \xi^c d\Omega$ for a variety of quadrature sets

Quadrature Set	NO.of Direction	Percent error in the moment (a,b,c)								
		(1,0,0)*	(3,0,0)*	(1.2.0)	(4,0,0)*	(2,2,0)	(5,0,0)*	(3,2,0)	(1,4,0)	(1,2,2)*
LSE_8[1]	80	1.70	-0.14	3.54	0	0	0.03	-0.47	5.52	5.61
LSO_8[1,2]	80	0	0	0	0	0	0.65	-1.29	-5.82	20.07
LSH_8[1]	80	0	0.22	-0.22	0	0	-0.19	1.02	-1.24	0.39
EWE_8[1]	80	1.49	-0.10	3.08	0	0	0.02	-0.35	4.68	5.17
EWO_8[1]	80	0	0	0	-0.19	0.28	0	0	-6.19	18.56
S_8[3]	80	2.07	-0.95	5.08	-1.82	2.73	-2.86	2.89	6.36	5.65
LSN_8[4]	80	0	0.82	-0.82	1.13	-1.70	1.07	0.33	2.01	-0.82
T_3	72	0.102	1.618	-1.413	3.236	-4.854	4.411	-3.969	3.515	-11.082
$SRAP_3$	72	1.606	-0.319	3.531	-0.309	0.010	-0.649	0.341	5.126	5.126
LSH_{10}[1]	120	0	0.17	-0.17	0.10	-0.15	0	0.52	0.21	-2.72
EWE_{10}[1]	120	1.02	-0.05	2.09	0	0	0.01	-0.16	3.17	3.36
EWO_{10}[1]	120	0	0	0	0.01	-0.01	0	0	-0.32	0.97
$SRAP_4$	112	1.000	0.058	1.937	0.223	-0.424	0.252	-0.329	3.070	3.070
T_4	128	0.131	0.470	-0.208	0.842	-1.264	1.159	-0.907	0.545	-1.067
$SRAP_5$	160	0.687	0.133	1.241	0.297	-0.430	0.398	-0.397	2.060	2.060
LSE_{12}[1]	168	0.97	-0.04	1.99	0	0	0.05	-0.14	3.05	3.06
S_{12}	168	1.44	-0.82	3.70	-1.71	2.57	-2.70	2.93	4.31	3.41
T_5	200	0.080	0.320	-0.160	0.625	-0.937	0.907	-0.854	0.484	-0.707
$SRAP_6$	216	0.504	0.139	0.870	0.279	-0.371	0.386	-0.356	1.483	1.483
$SRAP_7$	280	0.388	0.129	0.646	0.248	-0.312	0.347	-0.305	1.121	1.121
S_{16}	288	1.10	-0.65	2.84	-1.38	2.06	-2.16	2.37	3.30	2.43
T_6	288	0.054	0.218	-0.109	0.424	-0.637	0.613	-0.570	0.334	-0.519
$SRAP_8$	352	0.308	0.116	0.499	0.215	-0.263	0.302	-0.258	0.878	0.876
T_7	392	0.040	0.158	-0.079	0.308	-0.463	0.445	-0.416	0.241	-0.367
$SRAP_9$	432	0.250	0.102	0.397	0.186	-0.223	0.263	-0.220	0.707	0.703
T_8	512	0.030	0.120	-0.060	0.234	-0.352	0.338	-0.317	0.183	-0.276
Exact		π	$\pi/2$	$\pi/4$	$2\pi/5$	$2\pi/15$	$\pi/3$	$\pi/12$	$\pi/8$	$\pi/24$

1.Fiveland(1991)
2.Calson & Lathrop(1965)
3.Lee(1961)
4.Wakil & Sacadura(1992)
* Independent moments

After that, the direction cosine of m is

$$\begin{cases} \mu_m = \overline{x_m}/\sqrt{(\overline{x_m})^2 + (\overline{y_m})^2 + (\overline{z_m})^2} \\ \eta_m = \overline{y_m}/\sqrt{(\overline{x_m})^2 + (\overline{y_m})^2 + (\overline{z_m})^2} \\ \xi_m = \overline{z_m}/\sqrt{(\overline{x_m})^2 + (\overline{y_m})^2 + (\overline{z_m})^2} \end{cases} \quad (2)$$

The index N in the $SRAP_N$ quadrature is the number of rings (including the first crown on the top of sphere) and generally is recommended to be ≥ 2. The number of directions for $SRAP_N$ quadrature is $(2 + 3 + \ldots + (N + 1))$. For N from 2 to 4, the ordinates and weights of $SRAP_N$ and T_N quadrature sets are listed in Table 1.

Numerical Test of Double Moments

In order to check the accuracy of $SRAP_N$, a comparison between the T_N and $SRAP_N$ methods is made and double moments of the form $\int_{2\pi} \mu^a \eta^b \xi^c d\Omega$ are computed over a hemisphere. The results are listed in Table 2. Like the T_N quadrature set, all $SRAP_N$ quadrature sets have found to exactly satisfy the (0, 0, 0) moment and (2, 0, 0) moment (the diffusion condition), and therefore have not been reported here. In Table 2, the values accurate up to two places after the decimal are copied directly from Thurgood et al. (1995) while those accurate up to three decimal places (those of the T_N and $SRAP_N$ quadrature sets) are calculated by the authors.

Discussion and Conclusions

From the results listed in Table 2, it can be seen that the $SRAP_N$ quadrature set globally matches the double moment very well: It is more accurate than the others and compares well with the T_N set. The $SRAP_N$ set can also gives high accuracy for the half-range-fluxes ($\int_{2\pi} \mu d\Omega$, first-order moment) as pointed out by Truelove (1987). As is true for T_N quadrature set, the $SRAP_N$ set does not have a limit and thus can provide finer angular resolution by using higher order approximations in order to reduce the ray effect (Chai et al., 1993).

An alternate angular quadrature scheme $SRAP_N$ is constructed for the discrete ordinates method. From the construction of the T_N and $SRAP_N$ quadrature sets, the directions of T_N corresponding to smaller triangles pass through the centroids of each smaller triangle rather than those of solid angles associated with each spherical triangle; therefore, numerical errors may be produced. However, each direction of $SRAP_N$ quadrature set unbiasedly passes through the centroid of the solid angle associated with equally divided spherical surfaces. The accuracy of the $SRAP_N$ quadrature set can be improved if the spherical surface dividing method is more reasonable.

Acknowledgments

This work was financially supported by the National Postdoctoral Research Fund, China.

References

Carlson, B. G., and Lathrop, K. D., 1968, "Transport Theory–The Method of Discrete Ordinates," in: *Computing Methods in Reactor Physics*, H. Greenspan, C. N. Kelber, and D. Okrent, eds., Gordon and Breach, New York.

Chai, J. C., Lee, H. S., and Patankar, S. V., 1993, "Ray Effect and False Scattering in the Discrete Ordinates Method," *Numerical Heat Transfer*, Part B, Vol. 24, pp. 373–398.

Fiveland, W. A., 1984, "Discrete-Ordinates Solutions of the Radiative Transport Equation for Rectangular Enclosures," ASME JOURNAL OF HEAT TRANSFER, Vol. 106, pp. 699–706.

Fiveland, W. A., 1987, "Discrete-Ordinates Methods for Radiative Heat Transfer in Isotropically Scattering Media," ASME JOURNAL OF HEAT TRANSFER, Vol. 109, pp. 809–812.

Fiveland, W. A., 1991, "The Selection of Discrete Ordinate Quadrature Sets for Anisotropic Scattering," *Fundamentals of Radiation Heat Transfer*, ASME HTD-Vol. 160.

Jamaluddin, A. S., and Smith, P. J., 1988a, "Predicting Radiative Transfer in Rectangular Enclosures Using the Discrete Ordinates Method," *Combust. Sci. Tech.*, Vol. 59, pp. 321–340.

Jamaluddin, A. S., and Smith, P. J., 1988b, "Predicting Radiative Transfer in Axisymmetric Cylindrical Enclosures Using the Discrete Ordinates Method," *Combust. Sci. Tech.*, Vol. 62, pp. 173–181.

Lathrop, K. D., and Carlson, B. G., 1965, "Discrete Ordinates Angular Quadrature of the Neutron Transport Equation," LA-3168, Los Alamos Scientific Laboratory, NM.

Lee, C. E., 1961, "The Discrete Sn Approximation to Transport Theory," LA-2595, Los Alamos Scientific Laboratory, NM.

Thurgood, C. P., Pollard, A., and Becker, H. A., 1995, "The T_N Quadrature Set for the Discrete Ordinates Method," ASME Journal of Heat Transfer, Vol. 117, pp. 1068–1070.

Truelove, J. S., 1987, "Discrete-Ordinate Solutions of the Radiation Transport Equation," ASME Journal of Heat Transfer, Vol. 117, pp. 1068–1070.

Truelove, J. S., 1988, "Three-Dimensional Radiation in Absorbing-Emitting-Scattering Media Using the Discrete-Ordinates Approximation," *J. Quant. Spectrosc. Radiat. Transfer*, Vol. 39, No. 1, pp. 27–31.

Wakil, N. El., and Sacadura, J. F., 1992, "Some Improvements of the Discrete Ordinates Method for the Solution of the Radiative Transport Equation in Multidimensional Anisotropically Scattering Media," *Developments in Radiative Heat Transfer*, ASME HTD-Vol. 203.

Effects of Vibration on Ice Contact Melting Within Rectangular Enclosures

L. Quan,[1] Z. Zhang,[1] and M. Faghri[1]

Introduction

Contact melting has received considerable attention during the last two decades. Many studies have been published, for example, melting inside horizontal cylinders (Nicholas and Bayazitoglu, 1980; Bareiss and Beer, 1984; Sparrow and Geiger, 1986; Prasad and Sengupta, 1987); and melting in rectangular cavities (Moallemi et al., 1986; Hirata et al., 1991; Asako et al., 1994) were among the related investigations. A comprehensive review of natural convection melting was given by Viskanta (1985), and the scale analysis of contact melting was presented by Bejan (1992).

Vibration is one way to enhance convective heat transfer. For example, Lemlich (1955) reported an improvement in the heat transfer coefficient from wires vibrated in transverse modes at frequencies between 39 and 122 Hz. Natural convection melting under the influence of ultrasonic vibration within the rectangular enclosure was experimentally investigated by Choi and Hong (1991). To the best of the authors' knowledge, there is no other report available for melting under vibrating conditions and most analytical solutions do not apply when vibration is present.

The objective of the present study is to conduct experiments for ice contact melting under mechanical vibrations. The experiments are conducted within rectangular enclosures where isothermal conditions are maintained at the walls. The aspect ratios of the test cells (AR, height/width) are 0.4, 1.0, and 2.5, respectively. Stationary melting experiments are also conducted for comparison.

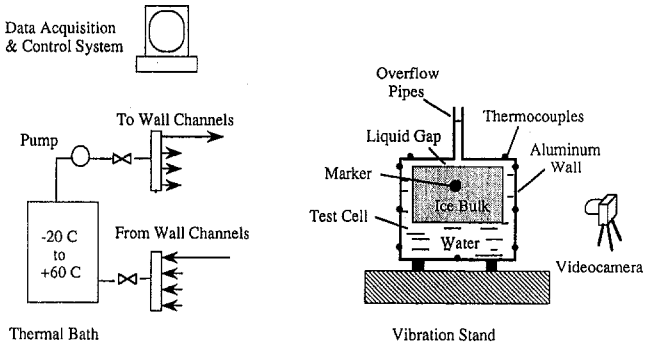

Fig. 1 Schematic view of the experimental setup

Experimental Setup and Procedure

The experimental apparatus consists of a thermal bath, a pump, test cells, vibration generators, and a data acquisition system. The schematic diagram is shown in Fig. 1. The four walls (top, bottom, and two sides) of the test cells are made of 10-mm-thick aluminum plates. The cross-sectional areas of three test cells are 52.2 mm × 130.5 mm, 82.5 mm × 82.5 mm, and 130.5 mm × 52.2 mm, respectively. The total volumes of the test cells are the same with depth of 152.5 mm.

Multipass, countercurrent channels are machined inside the aluminum walls of the test cells. The constant-temperature antifreeze solution is circulated through the channels by a pump to assure the uniform temperature distribution on the walls. The front and the back walls are made of two layers of Plexiglas separated by an air gap to facilitate the visual observation of the melting process. During the experiments, ice water is supplied to the test cell through the overflow pipes, which are mounted on the test cell walls to maintain the contact melting conditions, as shown in Fig. 1.

The temperature distributions at the inner surfaces of heating walls are measured by thermocouples. The temperature readings are obtained by an acquisition system that is accurate to within ±0.2°C. Although high-velocity constant-temperature coolant flow is circulated through the channels, the temperature measured at the contact surface is consistently lower than the bath temperature with a discrepancy of about 5 percent. The time-averaged wall temperature at the contact surface is used as the actual wall temperature. The instantaneous shape of the ice–water interface is videotaped and is input into the computer. Measured from the transferred computer image, the instantaneous volume of liquid region is calculated numerically to obtain the melted volume. The accuracy of the melted volume is evaluated by comparing the calculated value with the actual quantity of liquid accumulated at the end of each run.

Uncertainty Analysis

The methodology developed by Kline and McClintock (1953) is used to estimate the uncertainty. The difference be-

[1] Department of Mechanical Engineering and Applied Mechanics, University of Rhode Island, Kingston, RI 02881.

Contributed by the Heat Transfer Division of THE AMERICAN SOCIETY OF MECHANICAL ENGINEERS. Manuscript received by the Heat Transfer Division February 7, 1997; revision received February 23, 1998. Keywords: Natural Convection, Phase-Change Phenomena, Vibration. Associate Technical Editor: S. Ramadhyani.

References

Carlson, B. G., and Lathrop, K. D., 1968, "Transport Theory–The Method of Discrete Ordinates," in: *Computing Methods in Reactor Physics*, H. Greenspan, C. N. Kelber, and D. Okrent, eds., Gordon and Breach, New York.

Chai, J. C., Lee, H. S., and Patankar, S. V., 1993, "Ray Effect and False Scattering in the Discrete Ordinates Method," *Numerical Heat Transfer*, Part B, Vol. 24, pp. 373–398.

Fiveland, W. A., 1984, "Discrete-Ordinates Solutions of the Radiative Transport Equation for Rectangular Enclosures," ASME JOURNAL OF HEAT TRANSFER, Vol. 106, pp. 699–706.

Fiveland, W. A., 1987, "Discrete-Ordinates Methods for Radiative Heat Transfer in Isotropically Scattering Media," ASME JOURNAL OF HEAT TRANSFER, Vol. 109, pp. 809–812.

Fiveland, W. A., 1991, "The Selection of Discrete Ordinate Quadrature Sets for Anisotropic Scattering," *Fundamentals of Radiation Heat Transfer*, ASME HTD-Vol. 160.

Jamaluddin, A. S., and Smith, P. J., 1988a, "Predicting Radiative Transfer in Rectangular Enclosures Using the Discrete Ordinates Method," *Combust. Sci. Tech.*, Vol. 59, pp. 321–340.

Jamaluddin, A. S., and Smith, P. J., 1988b, "Predicting Radiative Transfer in Axisymmetric Cylindrical Enclosures Using the Discrete Ordinates Method," *Combust. Sci. Tech.*, Vol. 62, pp. 173–181.

Lathrop, K. D., and Carlson, B. G., 1965, "Discrete Ordinates Angular Quadrature of the Neutron Transport Equation," LA-3168, Los Alamos Scientific Laboratory, NM.

Lee, C. E., 1961, "The Discrete Sn Approximation to Transport Theory," LA-2595, Los Alamos Scientific Laboratory, NM.

Thurgood, C. P., Pollard, A., and Becker, H. A., 1995, "The T_N Quadrature Set for the Discrete Ordinates Method," ASME Journal of Heat Transfer, Vol. 117, pp. 1068–1070.

Truelove, J. S., 1987, "Discrete-Ordinate Solutions of the Radiation Transport Equation," ASME Journal of Heat Transfer, Vol. 117, pp. 1068–1070.

Truelove, J. S., 1988, "Three-Dimensional Radiation in Absorbing-Emitting-Scattering Media Using the Discrete-Ordinates Approximation," *J. Quant. Spectrosc. Radiat. Transfer*, Vol. 39, No. 1, pp. 27–31.

Wakil, N. El., and Sacadura, J. F., 1992, "Some Improvements of the Discrete Ordinates Method for the Solution of the Radiative Transport Equation in Multidimensional Anisotropically Scattering Media," *Developments in Radiative Heat Transfer*, ASME HTD-Vol. 203.

Effects of Vibration on Ice Contact Melting Within Rectangular Enclosures

L. Quan,[1] Z. Zhang,[1] and M. Faghri[1]

Introduction

Contact melting has received considerable attention during the last two decades. Many studies have been published, for example, melting inside horizontal cylinders (Nicholas and Bayazitoglu, 1980; Bareiss and Beer, 1984; Sparrow and Geiger, 1986; Prasad and Sengupta, 1987); and melting in rectangular cavities (Moallemi et al., 1986; Hirata et al., 1991; Asako et al., 1994) were among the related investigations. A comprehensive review of natural convection melting was given by Viskanta (1985), and the scale analysis of contact melting was presented by Bejan (1992).

Vibration is one way to enhance convective heat transfer. For example, Lemlich (1955) reported an improvement in the heat transfer coefficient from wires vibrated in transverse modes at frequencies between 39 and 122 Hz. Natural convection melting under the influence of ultrasonic vibration within the rectangular enclosure was experimentally investigated by Choi and Hong (1991). To the best of the authors' knowledge, there is no other report available for melting under vibrating conditions and most analytical solutions do not apply when vibration is present.

The objective of the present study is to conduct experiments for ice contact melting under mechanical vibrations. The experiments are conducted within rectangular enclosures where isothermal conditions are maintained at the walls. The aspect ratios of the test cells (AR, height/width) are 0.4, 1.0, and 2.5, respectively. Stationary melting experiments are also conducted for comparison.

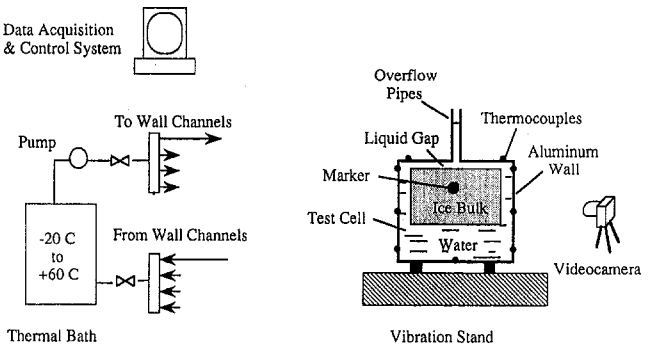

Fig. 1 Schematic view of the experimental setup

Experimental Setup and Procedure

The experimental apparatus consists of a thermal bath, a pump, test cells, vibration generators, and a data acquisition system. The schematic diagram is shown in Fig. 1. The four walls (top, bottom, and two sides) of the test cells are made of 10-mm-thick aluminum plates. The cross-sectional areas of three test cells are 52.2 mm × 130.5 mm, 82.5 mm × 82.5 mm, and 130.5 mm × 52.2 mm, respectively. The total volumes of the test cells are the same with depth of 152.5 mm.

Multipass, countercurrent channels are machined inside the aluminum walls of the test cells. The constant-temperature antifreeze solution is circulated through the channels by a pump to assure the uniform temperature distribution on the walls. The front and the back walls are made of two layers of Plexiglas separated by an air gap to facilitate the visual observation of the melting process. During the experiments, ice water is supplied to the test cell through the overflow pipes, which are mounted on the test cell walls to maintain the contact melting conditions, as shown in Fig. 1.

The temperature distributions at the inner surfaces of heating walls are measured by thermocouples. The temperature readings are obtained by an acquisition system that is accurate to within ±0.2°C. Although high-velocity constant-temperature coolant flow is circulated through the channels, the temperature measured at the contact surface is consistently lower than the bath temperature with a discrepancy of about 5 percent. The time-averaged wall temperature at the contact surface is used as the actual wall temperature. The instantaneous shape of the ice–water interface is videotaped and is input into the computer. Measured from the transferred computer image, the instantaneous volume of liquid region is calculated numerically to obtain the melted volume. The accuracy of the melted volume is evaluated by comparing the calculated value with the actual quantity of liquid accumulated at the end of each run.

Uncertainty Analysis

The methodology developed by Kline and McClintock (1953) is used to estimate the uncertainty. The difference be-

[1] Department of Mechanical Engineering and Applied Mechanics, University of Rhode Island, Kingston, RI 02881.

Contributed by the Heat Transfer Division of THE AMERICAN SOCIETY OF MECHANICAL ENGINEERS. Manuscript received by the Heat Transfer Division February 7, 1997; revision received February 23, 1998. Keywords: Natural Convection, Phase-Change Phenomena, Vibration. Associate Technical Editor: S. Ramadhyani.

tween the liquid volume fraction measured from the videotape image and that measured from draining the test cell at end of the experiment is less than 4 percent. As shown in Fig. 2, the slope of melted volume fraction versus Ste*Fo, where Ste is Stefan number and Fo is Fourier number, is weakly dependent on the wall temperature. For the experiments with the same nominal wall temperature, the differences in actual time-averaged measurements vary between 0.1 ~ 0.3°C. Therefore the contribution of the wall temperature difference to the overall uncertainty is small. The initial ice temperatures are controlled within −0.5 ~ −1.5°C. The uncertainty associated with initial ice temperature is negligible due to the large value of the latent heat of ice. The uncertainty in the melted volume fraction is shown with error bars in Fig. 2. The maximum uncertainty is estimated to be about 6 percent.

Results and Discussions

Effects of frequency and amplitude vibration on melted volume fraction with $AR = 1.0$ and nominal wall temperature of 10°C are shown in Fig. 2. The stationary experimental data by Hirata et al. (1991) is also plotted in this figure.

For the case of vertical vibration (wall temperature T_w = 9.3°C, frequency $f = 60$ Hz, amplitude $A = 0.23$ mm, acceleration $a = 3.3$ g), an enhancement of the overall melting rate as much as 115 percent is recorded. It is observed that the ice bulk oscillates slightly in the test cell. This relative motion between ice and water is induced by vibration due to their density differences. For the other two vertical vibrations ($f = 1.1$ Hz, T_w = 9.5°C and 0.55 Hz, T_w = 9.6°C, with the same amplitude A = 37.5 mm), the melting rates are increased moderately. The increment for the case of $f = 1.1$ Hz is slightly higher than that for $f = 0.55$ Hz. No relative motion of ice is observed in the above cases. The case of horizontal vibration (parallel to front Plexiglass wall), T_w = 9.4°C, $f = 1.67$ Hz, $A = 37.5$ mm, a = 0.42 g, has about 50 percent increase of melting rate as well. The relative slide motion of ice along the top surface of test cell is observed.

An additional experiment is conducted to estimate the kinetic energy input to the test cell filled with pure water under vibration ($f = 60$ Hz, $A = 0.23$ mm). After 4 minutes of vibration, the averaged water temperature in the well insulated test cell is measured as 0.30°C (±0.05°C) higher. This shows that the effect of direct kinetic energy input is negligible compared with the heat transfer enhancement due to vibration.

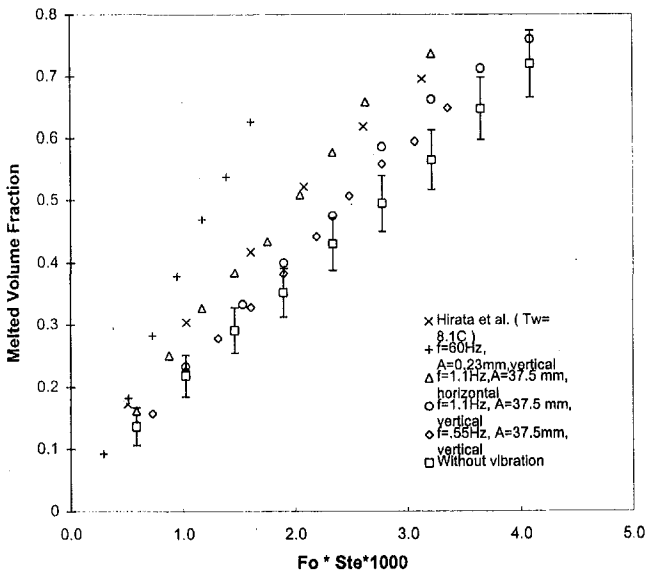

Fig. 2 Effects of frequency and amplitude (T_w near 10°C, AR = 1.0, Ste = 0.119, Gr = 1.8E + 6, AR = 2.21E + 8)

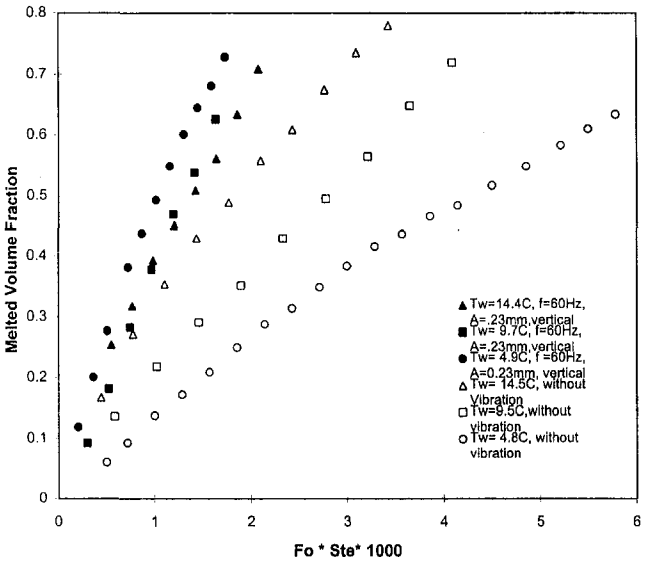

Fig. 3 Effects of wall temperature on melted volume fraction (AR = 1.0)

There are two melting processes, i.e., contact melting (which occurs at the top surface) and convective melting (natural convection and sedimentation induced convection). The effect of vibration on melting is twofold. It promotes the convective melting along the sides (vertical and bottom), as well as it increases contact melting on the top.

Effects of the wall temperature on the melted volume fraction for $AR = 1.0$ are shown in Fig. 3. For the stationary experiments, the result of melted volume fraction versus dimensionless time (Fo*Ste) with nominal T_w = 15°C has the highest value, while that with nominal T_w = 5°C has the lowest. It is known that water has density inversion at 3.98°C, and the natural convection at 5°C is weak due to both low thermal expansion coefficient and small temperature difference. In addition, the viscosity of water decreases significantly as a function of temperature between 0°C to 15°C. The rate of contact melting is inversely proportional to $\frac{1}{4}$ power of viscosity according to the analysis by Bejan (1992). Results of melted volume fraction versus Fo*Ste under vibrating conditions are different from stationary results. As seen in Fig. 3, the case of nominal T_w = 5°C has the highest melting value, while that with nominal T_w = 15°C has the lowest under the same vertical vibration condition (f = 60 Hz, A = 0.23 mm, a = 3.3 g). Natural convection is relatively weak at low wall temperatures. The effects of vibration on melting are shown more significantly when wall temperature is low.

Effects of aspect ratio on ice melting with nominal wall temperature of 10°C is shown in Fig. 4. The abscissa of Fig. 4 is the actual melting time. It is shown that for stationary experiments, the melting rates for AR = 0.4 and 2.5 are higher than that for AR = 1.0. The higher melting rates for both cases can be attributed to larger contact surface areas. Although the top contact surface area for aspect ratio of 2.5 is smaller, the total contact melting surface area is increased by the ice bulk inclination to the side wall(s). It is also noted that the test cell with AR = 1.0 has the smallest total heating area.

Vertical vibration ($f = 60$ Hz, $A = 0.23$ mm) increases melting rate significantly for all aspect ratios as shown in Fig. 4. The relative enhancement in melting for AR = 1.0 is about 115 percent, while for aspect ratio 0.4 and 2.5 the enhancement is about 140 percent and 170 percent, respectively. The higher melting enhancement for AR = 2.5 can be attributed to the sedimentation-driven convection for the low-pressure drag associated with its slender body shape. Slide motion of inclined ice bulk along the side wall can also contribute to higher melting

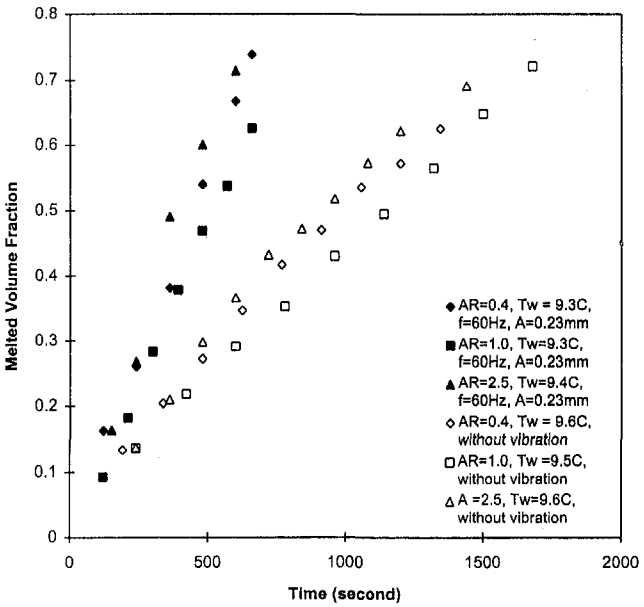

Fig. 4 Effects of aspect ratio at T_w near 10°C (AR = 1.0)

rates. In the case of $AR = 0.4$ where natural convection is the weakest, vibration enhanced convection contributes to the higher melting rate.

Conclusions

Ice contact melting experiments within rectangular enclosures are conducted under vibrating conditions. It is shown that vibration increases melting rates in all experiments. Aspect ratio is an important parameter in ice contact melting. Of the three aspect ratios, the results for $AR = 1.0$ have lower melting rates in stationary and vibrating conditions. The cases for $AR = 0.4$ and 2.5 also correspond to higher relative melting enhancement by vibration. Melting enhancement with horizontal vibration is greater than that with vertical vibration. Also, melting enhancement by vibration is more pronounced for low wall temperature cases.

Acknowledgments

This research was supported by the National Science Foundation, Grant No. CTS-9422629.

References

Asako, Y., Faghri, M., Charmchi, M., and Bahrami, P. A., 1994, "Numerical Solution for Melting of Unfixed Rectangular Phase-Change Material Under Low-Gravity Environment," *Numerical Heat Transfer,* Part A, Vol. 25, pp. 191–208.

Bareiss, M., and Beer, H., 1984, "An Analytical Solution of the Heat Transfer Process During Melting Inside a Horizontal Tube," *International Journal of Heat and Mass Transfer,* Vol. 27, pp. 739–746.

Bejan, A., 1992, "Lubrication by Close-Contact Melting," in: *Fundamental Issues in Small Scale Heat Transfer,* Y. Bayazitoglu and G. P. Peterson, eds., ASME HTD-Vol. 227, pp. 61–68.

Choi, K. J., and Hong, J. S., 1991, "Experimental Study of Enhanced Melting Process Under Ultrasonic Influence," *AIAA Journal of Thermophysics and Heat Transfer,* Vol. 5, No. 3, pp. 340–346.

Hirata, T., Makino, Y., and Kaneko, Y., 1991, "Analysis of Close-Contact Melting for Octadecane and Ice Inside Isothermally Heated Horizontal Rectangular Capsule," *International Journal of Heat and Mass Transfer,* Vol. 34, pp. 3097–3106.

Kline, S. J., and McClintock, F. A., 1953, "Describing Uncertainties in Single-Sample Experiments," *Mechanical Engineering,* Vol. 75, Jan., pp. 3–8.

Lemlich, R., 1955, "Effect of Vibration on Natural Convection Heat Transfer," *Industrial and Engineering Chemistry,* Vol. 47, pp. 1175–1180.

Moallemi, M. K., Webb, B. W., and Viskanta, R., 1986, "An Experimental and Analytical Study of Close-Contact Melting," ASME JOURNAL OF HEAT TRANSFER, Vol. 108, pp. 894–899.

Nicholas, D., and Bayazitoglu, Y., 1980, "Heat Transfer and Melting Front Within a Horizontal Cylinder," ASME *Journal of Solar Energy Engineering,* Vol. 102, pp. 229–232.

Prasad, A., and Sengupta, S., 1987, "Numerical Investigation of Melting Inside a Horizontal Cylinder Including the Effects of Natural Convection," ASME JOURNAL OF HEAT TRANSFER, Vol. 109, pp. 803–806.

Sparrow, E. M., and Geiger, G. A., 1986, "Melting in a Horizontal Tube With the Solid Either Constrained or Free to Fall Under Gravity," *International Journal of Heat and Mass Transfer,* Vol. 29, pp. 1007–1019.

Viskanta, R., 1985, "Natural Convection Melting and Solidification," in: *Natural Convection: Fundamentals and Applications,* S. Kakac, W. Aung, and R. Viskanta, eds., Hemisphere, Washington, DC.

Nonuniform Overall Heat Transfer Coefficients in Conventional Heat Exchanger Design Theory—Revisited

R. K. Shah [1,2] and D. P. Sekulić [1,3]

Nomenclature

A = heat transfer surface area, m^2
A_o = minimum free flow area on one side of an exchanger, m^2
C = fluid stream heat capacity rate = $\dot{m}c_p$, W/K
C^* = heat capacity rate ratio = $C_{\min}/C_{\max}$
c_p = specific heat of fluid at constant pressure, J/kgK
F = log-mean temperature difference correction factor
f = position function
h = heat transfer coefficient, W/m^2K [Btu/(hr ft^2°F) in Fig. 1]
$\dot{H}$ = enthalpy rate, W
$\dot{m}$ = fluid mass flow rate = $\rho u_m A_o$, kg/s
n = number of intervals in the Simpson method of integration
NTU = number of heat transfer units = $UA/C_{\min}$
$\dot{Q}$ = heat transfer rate, W
R = thermal resistance, K/W
R_h = heat capacity rate ratio = C_h/C_c
R_c = heat capacity rate ratio = C_c/C_h
T = temperature, °C (°F in Fig. 1)
U = overall heat transfer coefficient, W/m^2K
u_m = fluid mean axial velocity occurring at the minimum free flow area, m/s
Δ = denotes finite difference
ϵ = heat exchanger effectiveness = $(C_h/C_{\min})(T_{h,i} - T_{h,o})/(T_{h,i} - T_{c,i})$
η_o = total surface efficiency on one side of an extended surface exchanger
ξ = position coordinate(s)
κ = length effect correction factor defined by Eq. (14)
ρ = fluid density, kg/m^3

Subscripts

a = one end section of the heat exchanger

[1] Department of Mechanical Engineering, University of Kentucky, Lexington, KY 40506-0108.

[2] Present address: Delphi Harrison Thermal Systems, Lockport, NY 14094-1896.

[3] Permanent address: Karlja Petra I, 21413 Celarevo, Vojvodina/Serbia, Yugoslavia.

Contributed by the Heat Transfer Division of THE AMERICAN SOCIETY OF MECHANICAL ENGINEERS. Manuscript received by the Heat Transfer Division May 19, 1997; revision received December 12, 1997. Keywords: Heat Exchangers, Modeling & Scaling, Numerical Methods. Associate Technical Editor: J. R. Howell.

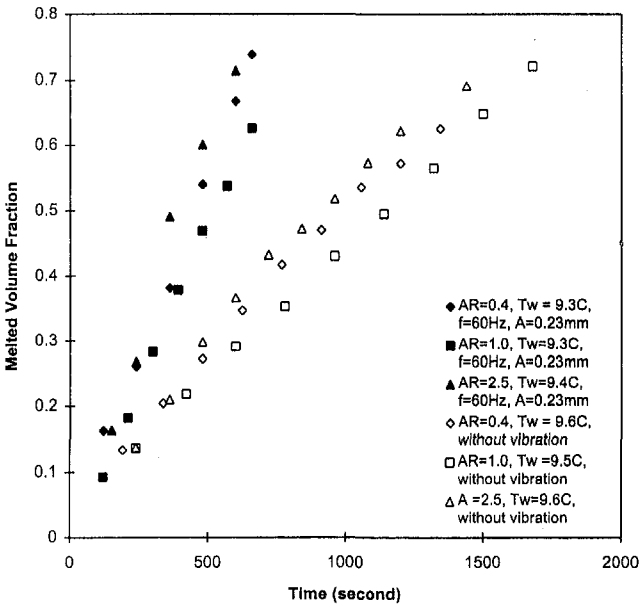

Fig. 4 Effects of aspect ratio at T_w near 10°C (AR = 1.0)

rates. In the case of $AR = 0.4$ where natural convection is the weakest, vibration enhanced convection contributes to the higher melting rate.

Conclusions

Ice contact melting experiments within rectangular enclosures are conducted under vibrating conditions. It is shown that vibration increases melting rates in all experiments. Aspect ratio is an important parameter in ice contact melting. Of the three aspect ratios, the results for $AR = 1.0$ have lower melting rates in stationary and vibrating conditions. The cases for $AR = 0.4$ and 2.5 also correspond to higher relative melting enhancement by vibration. Melting enhancement with horizontal vibration is greater than that with vertical vibration. Also, melting enhancement by vibration is more pronounced for low wall temperature cases.

Acknowledgments

This research was supported by the National Science Foundation, Grant No. CTS-9422629.

References

Asako, Y., Faghri, M., Charmchi, M., and Bahrami, P. A., 1994, "Numerical Solution for Melting of Unfixed Rectangular Phase-Change Material Under Low-Gravity Environment," *Numerical Heat Transfer,* Part A, Vol. 25, pp. 191–208.

Bareiss, M., and Beer, H., 1984, "An Analytical Solution of the Heat Transfer Process During Melting Inside a Horizontal Tube," *International Journal of Heat and Mass Transfer,* Vol. 27, pp. 739–746.

Bejan, A., 1992, "Lubrication by Close-Contact Melting," in: *Fundamental Issues in Small Scale Heat Transfer,* Y. Bayazitoglu and G. P. Peterson, eds., ASME HTD-Vol. 227, pp. 61–68.

Choi, K. J., and Hong, J. S., 1991, "Experimental Study of Enhanced Melting Process Under Ultrasonic Influence," *AIAA Journal of Thermophysics and Heat Transfer,* Vol. 5, No. 3, pp. 340–346.

Hirata, T., Makino, Y., and Kaneko, Y., 1991, "Analysis of Close-Contact Melting for Octadecane and Ice Inside Isothermally Heated Horizontal Rectangular Capsule," *International Journal of Heat and Mass Transfer,* Vol. 34, pp. 3097–3106.

Kline, S. J., and McClintock, F. A., 1953, "Describing Uncertainties in Single-Sample Experiments," *Mechanical Engineering,* Vol. 75, Jan., pp. 3–8.

Lemlich, R., 1955, "Effect of Vibration on Natural Convection Heat Transfer," *Industrial and Engineering Chemistry,* Vol. 47, pp. 1175–1180.

Moallemi, M. K., Webb, B. W., and Viskanta, R., 1986, "An Experimental and Analytical Study of Close-Contact Melting," ASME JOURNAL OF HEAT TRANSFER, Vol. 108, pp. 894–899.

Nicholas, D., and Bayazitoglu, Y., 1980, "Heat Transfer and Melting Front Within a Horizontal Cylinder," ASME *Journal of Solar Energy Engineering,* Vol. 102, pp. 229–232.

Prasad, A., and Sengupta, S., 1987, "Numerical Investigation of Melting Inside a Horizontal Cylinder Including the Effects of Natural Convection," ASME JOURNAL OF HEAT TRANSFER, Vol. 109, pp. 803–806.

Sparrow, E. M., and Geiger, G. A., 1986, "Melting in a Horizontal Tube With the Solid Either Constrained or Free to Fall Under Gravity," *International Journal of Heat and Mass Transfer,* Vol. 29, pp. 1007–1019.

Viskanta, R., 1985, "Natural Convection Melting and Solidification," in: *Natural Convection: Fundamentals and Applications,* S. Kakac, W. Aung, and R. Viskanta, eds., Hemisphere, Washington, DC.

Nonuniform Overall Heat Transfer Coefficients in Conventional Heat Exchanger Design Theory—Revisited

R. K. Shah [1,2] and D. P. Sekulić [1,3]

Nomenclature

A = heat transfer surface area, m^2
A_o = minimum free flow area on one side of an exchanger, m^2
C = fluid stream heat capacity rate = $\dot{m}c_p$, W/K
C^* = heat capacity rate ratio = $C_{\min}/C_{\max}$
c_p = specific heat of fluid at constant pressure, J/kgK
F = log-mean temperature difference correction factor
f = position function
h = heat transfer coefficient, W/m^2K [Btu/(hr ft^2°F) in Fig. 1]
$\dot{H}$ = enthalpy rate, W
$\dot{m}$ = fluid mass flow rate = $\rho u_m A_o$, kg/s
n = number of intervals in the Simpson method of integration
NTU = number of heat transfer units = $UA/C_{\min}$
$\dot{Q}$ = heat transfer rate, W
R = thermal resistance, K/W
R_h = heat capacity rate ratio = C_h/C_c
R_c = heat capacity rate ratio = C_c/C_h
T = temperature, °C (°F in Fig. 1)
U = overall heat transfer coefficient, W/m^2K
u_m = fluid mean axial velocity occurring at the minimum free flow area, m/s
Δ = denotes finite difference
ϵ = heat exchanger effectiveness = $(C_h/C_{\min})(T_{h,i} - T_{h,o})/(T_{h,i} - T_{c,i})$
η_o = total surface efficiency on one side of an extended surface exchanger
ξ = position coordinate(s)
κ = length effect correction factor defined by Eq. (14)
ρ = fluid density, kg/m^3

Subscripts

a = one end section of the heat exchanger

[1] Department of Mechanical Engineering, University of Kentucky, Lexington, KY 40506-0108.

[2] Present address: Delphi Harrison Thermal Systems, Lockport, NY 14094-1896.

[3] Permanent address: Karlja Petra I, 21413 Celarevo, Vojvodina/Serbia, Yugoslavia.

Contributed by the Heat Transfer Division of THE AMERICAN SOCIETY OF MECHANICAL ENGINEERS. Manuscript received by the Heat Transfer Division May 19, 1997; revision received December 12, 1997. Keywords: Heat Exchangers, Modeling & Scaling, Numerical Methods. Associate Technical Editor: J. R. Howell.

arith = arithmetic mean
b = other end section of the heat exchanger
c = cold fluid stream
corr = corrected value
exact = exact value
h = hot fluid stream
i = fluid stream inlet port
int = integral mean
j = refers either to the cold (c), hot (h), or $C_{\min}$, $C_{\max}$ fluid stream
ln = logarithmic mean
m = mean value
max = maximum value
min = minimum value
o = fluid stream outlet port
w = wall
1/2 = middle point in the sense defined by Eq. (17)

Superscripts

* = hypothetical value
$\breve{}$ = area-averaged value
$\tilde{}$ = temperature-range-averaged value
$\breve{\tilde{}}$ = position and temperature-range-averaged value

Introduction

In conventional methods of exchanger heat transfer analysis, it is idealized that the overall heat transfer coefficient U is constant and uniform throughout the exchanger and invariant with time (Kays and London, 1984). This coefficient is dependent upon a number of thermal resistances in series, and in particular, on heat transfer coefficients on both fluid sides. These individual heat transfer coefficients may vary with flow Reynolds number, heat transfer surface geometry, fluid thermophysical properties, entrance length effect due to developing thermal boundary layers, and other factors. In a viscous liquid exchanger, a tenfold variation in the heat transfer coefficient is possible when the flow pattern encompasses laminar, transition, and turbulent regions on one side. Thus, if an individual heat transfer coefficient were to vary across the exchanger surface area, it is highly likely that U will not remain constant and uniform in the exchanger.

The overall heat transfer coefficient nonuniformity effect has been investigated many times since 1933. Early studies presumed the overall heat transfer coefficient as an explicit function of temperature only, for example U as a linear function of the temperature (Colburn, 1933), or the mean overall heat transfer coefficient as a function of arithmetic mean or integral mean reference temperature (Larian, 1943). Various averaging procedures for determining mean overall heat transfer coefficient values have been a subject of a number of more recent studies. Hausen (1983), Roetzel (1969), and Peters (1970) proposed methods for calculating average overall heat transfer coefficients at two or three points in the heat exchanger, utilizing approximate methods of integration and taking the length effect into consideration. Most recent efforts by Roetzel (1974, 1988) and Roetzel and Spang (1993) further refined the inclusion of both temperature and length effects, and also considered variable heat capacity rates. An in-depth literature review on the subject is provided by Shah (1993) and hence is not elaborated here. The method of Roetzel has received even wider attention since it has been included in the most recent edition of the German *VDI-Wärmeatlas* (Roetzel and Spang, 1993).

The main objective of this note is to reconsider the applicability of Roetzel's method in situations where a highly nonlinear overall heat transfer coefficient is present. The attention will be paid only to nonuniformities in the overall heat transfer coefficient due to temperature and length effects.

Local and Mean Overall Heat Transfer Coefficients

In order to outline how to take into account the temperature and length effects, let us first formulate specific definitions of local and mean overall heat transfer coefficients. The local overall heat transfer coefficient U is defined as follows:

$$U = \frac{d\dot{Q}}{dA\Delta T} \tag{1}$$

where elemental surface area is dA and the temperature difference is $\Delta T = (T_h - T_c)$. When both the temperature and length effects are not negligible, Eq. (1) can be integrated to obtain the mean overall heat transfer coefficient that can be used in conventional heat exchanger design.

Traditionally, the mean overall heat transfer coefficient $U_m(T)$ is defined as

$$\frac{1}{U_m A} = \frac{1}{(\eta_o h_m A)_h} + R_w + \frac{1}{(\eta_o h_m A)_c} \tag{2}$$

Here fouling resistances and other resistances are not included for simplifying the discussion, but can be easily included if desired. In Eq. (2), h_m's are the mean heat transfer coefficients obtained from the experimental/empirical correlations, and hence represent the surface area average values. The experimental/empirical correlations are generally "constant fluid property" correlations. If the temperature variations and subsequent fluid property variations are not significant in the exchanger, the reference temperature T in $U_m(T)$ for fluid properties is the arithmetic mean of inlet and outlet fluid temperatures used on each fluid side for determining individual h_m's; and in some cases, this reference temperature is the log-mean average temperature or integral mean temperature. If the fluid property variations are significant on one or both fluid sides, this approach using the arithmetic mean temperature as a reference temperature is not adequate.

A more rigorous approach in defining the mean overall heat transfer coefficient is the area average used in the definition of NTU for the conventional ϵ-NTU method. The proof that the area average overall heat transfer coefficient is inherent to conventional heat exchanger theory is given next.

Area Average $\breve{U}$. For counterflow and parallel-flow heat exchangers, energy balances combined with the definitions of heat exchanger effectiveness and number of transfer units under the usual idealizations (Kays and London, 1984) lead to:

$$\mathrm{NTU} = \frac{1}{C_{\min}}\int_A U dA = \frac{1}{C_{\min}}\int_Q \frac{d\dot{Q}}{\Delta T} = \frac{\breve{U}A}{C_{\min}}$$
$$= \begin{cases} \dfrac{1}{1 - C^*} \ln\left(\dfrac{1 - C^*\epsilon}{1 - \epsilon}\right) & \text{counterflow} \\ -\dfrac{1}{1 + C^* \ln\left[1 - \epsilon(1 + \epsilon)\right]} & \text{parallel-flow} \end{cases} \tag{3}$$

where the second equality from the left comes from integrating Eq. (1).

It is easy to see that expressions given by Eq. (3) represent effectiveness–NTU expressions that can be independently derived for respective flow arrangements. Thus, it is obvious from Eq. (1) that the area average overall heat transfer coefficient is, indeed, given by

$$\breve{U} = \frac{1}{A}\int_A U dA \tag{4}$$

Note that Eq. (4) is obtained under the condition of constant heat capacity rates. This definition takes into account exactly both the temperature and length effects for counterflow and parallel-flow exchangers regardless of how large are the effects.

However, it may not be possible to have a closed-form expression of $U(A)$ for integration even for counterflow and parallel-flow. Also, no rigorous proof is available that Eq. (4) is exact for other exchanger flow arrangements (Roetzel, 1992).

Temperature Average $\tilde{U}$. If the local overall heat transfer coefficient is a function of temperature only such as for liquid turbulent flows, the following procedure for defining average overall heat transfer coefficient, denoted by $\tilde{U}$, can be performed for the counterflow arrangement. Combining Eq. (1) with the energy balance yields

$$dA = \left[\frac{1}{C_c} - \frac{1}{C_h}\right]^{-1} \frac{d(\Delta T)}{U\Delta T} \tag{5}$$

or, after integration

$$A = \left[\frac{1}{C_c} - \frac{1}{C_h}\right]^{-1} \int_{\Delta T_a}^{\Delta T_b} \frac{d(\ln \Delta T)}{U(T)} \tag{6}$$

where ΔT_a and ΔT_b represent temperature differences at end sections of the heat exchanger. For example, for a counterflow arrangement, $\Delta T_a = T_{h,i} - T_{c,o}$, and $\Delta T_b = T_{h,o} - T_{c,i}$. Hence, the temperature average overall heat transfer coefficient can be introduced by

$$A = \left[\frac{1}{C_c} - \frac{1}{C_h}\right]^{-1} \frac{1}{\tilde{U}} \int_{\Delta T_a}^{\Delta T_b} d(\ln \Delta T) \tag{7}$$

From Eqs. (6) and (7), the temperature average $\tilde{U}$ is found as follows (Roetzel, 1969):

$$\tilde{U} = (\ln \Delta T_b - \ln \Delta T_a)\left[\int_{\ln \Delta T_a}^{\ln \Delta T_b} \frac{d(\ln \Delta T)}{U(T)}\right]^{-1} \tag{8}$$

Exactly the same result can be obtained for the parallel-flow arrangement. Note that the $\tilde{U}$ of Eq. (4) and the $\tilde{U}$ of Eq. (8) are identical over the given temperature range for both counterflow and parallel-flow exchangers if U is a function of temperature only. Operationally, if the overall heat transfer coefficient is a function of the area only, Eq. (4) is preferred to evaluate the average U value; if the overall heat transfer coefficient is a function of temperature only, Eq. (8) is preferred to calculate the average U value. Note that the local overall heat transfer coefficient in Eq. (8) is a function of local temperatures only.

Position and Temperature Average $\bar{U}$. When both temperature and length effects are present, an average value of an overall heat transfer coefficient should include both position and temperature averaging. The theory for exact averaging in such a general case does not exist. Let us introduce an additional idealization that will allow utilization of the partial averaging procedures as presented above. We idealize local $U(T, \xi) = U_m(T)f(\xi)$, where $U_m(T)$ is a pure temperature function in the units of overall heat transfer coefficient as defined by Eq. (2), and $f(\xi)$ is a pure position function (ξ is a dimensionless flow length) (Roetzel, 1969; Peters, 1970). Hence, Eq. (1) reduces to

$$U_m(T)f(\xi) = \frac{d\dot{Q}}{dA\Delta T} \tag{9}$$

and after splitting variables, and integrating

$$\int_{\dot{Q}} \frac{d\dot{Q}}{U_m(T)\Delta T} = \int_A f(\xi)dA \tag{10}$$

The following are the key steps in the averaging procedure. First, note that Eq. (8) defines an average overall heat transfer coefficient if U depends on the temperature only. The overall heat transfer coefficient on the left-hand side of Eq. (10) also depends on the temperature only. Let us assume that the left-hand side of Eq. (10) can be written *by definition* in the form

$$\int_{\dot{Q}} \frac{d\dot{Q}}{U_m(T)\Delta T} = \frac{1}{\tilde{U}} \int_{\dot{Q}} \frac{d\dot{Q}}{\Delta T} \tag{11}$$

where $\tilde{U}$ is given by Eq. (8), since the left-hand side of Eq. (11) is averaged over temperature only as is Eq. (8). The integral on the right-hand side of Eq. (11) can be replaced *by definition* of the true mean temperature difference (MTD) as follows:

$$\int_{\dot{Q}} \frac{d\dot{Q}}{\Delta T} = \frac{\dot{Q}}{\Delta T_m} \tag{12}$$

The integral on the right-hand side of Eq. (10) can be transformed again *by definition* as follows:

$$\int_A f(\xi)dA = \frac{A}{A}\int_A f(\xi)dA = \kappa A \tag{13}$$

where a correction factor κ takes into account the length effect on the overall heat transfer coefficient

$$\kappa = \frac{1}{A}\int_A f(\xi)dA \tag{14}$$

Collecting results from Eqs. (10)–(14)

$$\dot{Q} = \kappa\tilde{U}A\Delta T_m = \bar{U}A\Delta T_m \tag{15}$$

where the overall heat transfer coefficient that takes into account both temperature and length effects is defined as follows:

$$\bar{U} = \kappa\tilde{U} \tag{16}$$

Various overall heat transfer coefficients discussed so far are summarized in Table 1.

A Step-by-Step Procedure to Determine $\bar{U}$

A step-by-step method to determine $\bar{U}$ for an exchanger is presented below based on the work of Roetzel and Spang (1993) and slightly modified in this work. In this method, not only are the variations in individual h's due to the temperature effect taken into account, but also the heat capacity rate is considered temperature dependent.

1 Hypothesize the given exchanger as a counterflow exchanger (if it is different from a counterflow exchanger), and determine individual heat transfer coefficients and enthalpy rates at three points in the exchanger: both ends and a third point within the exchanger designated with a subscript 1/2. This third point is determined by:

$$\Delta T^*_{1/2} = (\Delta T_a \Delta T_b)^{1/2} \tag{17}$$

2 In order to consider the temperature-dependent specific heats, compute the enthalpy rates $\dot{H}$ of the $C_{\max}$ fluid (with a subscript $j = C_{\max}$) at the third point (that with a 1/2 subscript) within the exchanger from the following equation using the known values at each exchanger end (designated by subscripts a and b).

$$\dot{H}_{j,1/2} = \dot{H}_{j,b} + (\dot{H}_{j,a} - \dot{H}_{j,b})\frac{\Delta T^*_{1/2} - \Delta T_b}{\Delta T_a - \Delta T_b} \tag{18}$$

where $\Delta T^*_{1/2}$ is given by Eq. (17). If $\Delta T_a = \Delta T_b$ (i.e., $C^* = 1$), the quotient in Eq. (18) becomes $\frac{1}{2}$. If the specific heat does not vary significantly, Eq. (18) could also be used for the $C_{\min}$ fluid (i.e., $j = C_{\max}$ or $C_{\min}$). However, when it varies significantly as in a cryogenic heat exchanger, the third point calculated for the $C_{\max}$ and $C_{\min}$ fluid separately by Eq. (18) will not be physically located close enough to each other (Venkatarath-

Table 1 Definitions of local and mean overall heat transfer coefficients

Symbol	Definition	Meaning	Comments
U	$U = \frac{d\dot{Q}}{dA\Delta T}$	Local heat flux per unit of local temperature difference.	This is the basic definition of the *local* overall heat transfer coefficient.
U_m	$\frac{1}{U_m A} = \frac{1}{(\eta_o h_m A)_h} + R_w + \frac{1}{(\eta_o h_m A)_c}$	Overall heat transfer coefficient defined using area average heat transfer coefficients on both sides.	Individual heat transfer coefficients should be evaluated at respective reference temperatures (usually arithmetic mean of inlet and outlet fluid temperatures on each fluid side).
$\check{U}$	$\check{U} = \frac{1}{A}\int_A U(A)\, dA$	Overall heat transfer coefficient averaged over: heat transfer surface area	Overall heat transfer coefficient is either a function of: (1) local position only (laminar gas flow), (2) temperature only (turbulent liquid flow), or (3) both local position and temperature (a general case). U(T) represents a position average overall heat transfer coefficient evaluated at a local temperature. Integration should be performed numerically and/or can be approximated with an evaluation at three points.
$\tilde{U}$	$\tilde{U} = (\ln\Delta T_b - \ln\Delta T_a)\left[\int_{\ln\Delta T_a}^{\ln\Delta T_b} \frac{d(\ln\Delta T)}{U(T)}\right]^{-1}$	temperature range	
$\bar{\bar{U}}$	$\bar{\bar{U}} = \kappa\, \tilde{U}$	local position range and temperature range.	

nam, 1996). In that case, compute the third point for the $C_{\min}$ fluid by the energy balance as follows:

$$(\dot{H}_i - \dot{H}_{1/2})_{C_{\max}} = (\dot{H}_{1/2} - \dot{H}_o)_{C_{\min}} \tag{19}$$

Subsequently, using the equation of state or tabular/graphic results, determine the temperature $T_{h,1/2}$ and $T_{c,1/2}$ corresponding to $\dot{H}_{h,1/2}$ and $\dot{H}_{c,1/2}$. Then:

$$\Delta T_{1/2} = T_{h,1/2} - T_{c,1/2} \tag{20}$$

3 The heat transfer coefficient $h_{j,1/2}$ on each fluid side at the third point is evaluated at the following corrected reference temperatures (Spang and Roetzel, 1992)

$$T_{h,1/2,\text{corr}} = T_{h,1/2} - \tfrac{3}{2}(T_{h,1/2} - T_{c,1/2})\frac{1 - F}{1 + R_h^{2/3}} \tag{21}$$

$$T_{c,1/2,\text{corr}} = T_{c,1/2} + \tfrac{3}{2}(T_{h,1/2} - T_{c,1/2})\frac{1 - F}{1 + R_c^{2/3}} \tag{22}$$

In Eqs. (21) and (22), F is the log-mean temperature difference correction factor, $R_h = C_h/C_c$ and $R_c = C_c/C_h$. Consequently, the proposed method can be applied for a wide range of flow arrangement configuration for which $F \neq 1$. The temperatures $T_{h,1/2,\text{corr}}$ and $T_{c,1/2,\text{corr}}$ are used only in the evaluation of fluid properties for the computation of $h_{h,1/2}$ and $h_{c,1/2}$ (Spang and Roetzel, 1992). The foregoing correction to the reference temperature $T_{j,1/2}$ results in the cold temperature being increased and the hot temperature being decreased. Calculate the overall conductance at the third point by:

$$\frac{1}{U_{1/2}A} = \frac{1}{(\eta_o h_{1/2} A)_h} + R_w + \frac{1}{(\eta_o h_{1/2} A)_c} \tag{23}$$

Note that η_o can be determined accurately at local temperatures.

4 Calculate the apparent overall heat transfer coefficient at this point.

$$U^*_{1/2}A = U_{1/2}A\,\frac{\Delta T_{1/2}}{\Delta T^*_{1/2}} \tag{24}$$

5 Knowing the heat transfer coefficient at each end of the exchanger evaluated at the respective actual temperatures, compute overall conductances according to Eq. (23) and find the mean overall conductance for the exchanger (taking into account the temperature dependency of the heat transfer coefficient and the heat capacities) from the following equation (Simpson's method of integration), (Roetzel, 1988):

$$\frac{1}{\tilde{U}A} = \frac{1}{6}\frac{1}{U_a A} + \frac{2}{3}\frac{1}{U^*_{1/2}A} + \frac{1}{6}\frac{1}{U_b A} \tag{25}$$

6 Finally, the true mean heat transfer coefficient that also takes into account the laminar flow entry length effect, as well as the temperature effect, is given by:

$$\bar{\bar{U}}A = \kappa \tilde{U}A \tag{26}$$

where the entry length effect factor $\kappa \leq 1$ is given by Roetzel and Spang (1993) or Shah (1993).

Comparative Analysis of Various Methods

In order to establish the error of averaging overall heat transfer coefficient, six different methods for evaluating the exchanger heat transfer area are applied to five different sets of input data for a specific example. In this example, the thermal resistance on one fluid side is controlling (i.e., very high compared to that for the other fluid side), and hence the variation in h on that side corresponds to the variation in overall U for the exchanger. The methods used are as follows: (1) the method summarized in this paper (later in the text referred to as the Roetzel method), (2) exact (numerical) method, (3) Colburn (1933) method (i.e., the logarithmic mean difference of the $U\Delta T$ product), (4) the arithmetic mean of the terminal U values, (5) the U value determined at the arithmetic mean of inlet and outlet temperatures of the $C_{\min}$ fluid stream, and finally (6) the U value determined at the log-mean average temperature (defined as the difference between the heat transfer surface wall *temperature* and the logarithmic mean *temperature difference*).

The five sets of data are generated based on the data provided in Example B of the Colburn's original paper (1933). The problem (of finding the heat transfer area needed to meet the specified performance) was originally defined as follows:

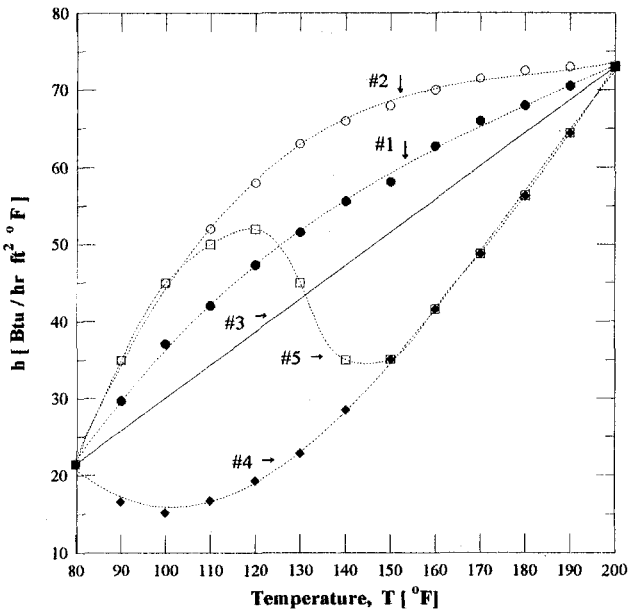

Fig. 1 Heat transfer coefficient on the liquid side versus local temperature. Data set #1 (data symbols: ●), Colburn (1933) example B; Data set #2 (data symbols: ○); Data set #3 (solid line) linear dependence; Data set #4 (data symbols: ♦); Data set #5 (data symbols □). Each data set is fitted by a polynomial curve fit, dotted lines. Note that all data in the figure are provided in the English units as given in the original Colburn paper (Colburn, 1933) [1 Btu/(hr ft² °F) = 5.678 W/(m²K), *T*(°F) = 1.8*T*(°C) + 32].

"Straw oil is to be heated from 80°F to 200°F, flowing at an average velocity of 3 feet per second through a standard 2-inch horizontal pipe. The oil has a mean specific heat of 0.47, a mean specific gravity of 0.85, and a mean thermal conductivity of 0.078 in English units. The viscosities of the oil are 18 and 4 centipoises at 80°F and 200°F, respectively, and a plot of viscosity vs. temperature on logarithmic paper may be considered a straight line. The outside and inside diameters of the pipe are 2.38 and 2.07 inches, respectively; the thermal conductivity of the pipe is 35 in English units. Since the oil side resistance is controlling, the heat transfer coefficient on the steam side will be assumed constant at 2150."

Using the data from this problem, Colburn (1933) showed that the local heat transfer coefficient on the oil side follows the temperature change nonlinearly (see Fig. 1, Colburn's data). This dependence, in turn, causes a nonlinear change in the overall heat transfer coefficient. The data for this problem are the first set of data used in our analysis. The other four sets were generated from the first one under the following assumptions. For the second set of data, it is assumed that a hypothetical fluid exchanges heat under the conditions of even more pronounced nonlinearity with respect to local temperatures, as given by the data set #2 in Fig. 1 (all other conditions the same). The third set of data assumes a linear dependence of the local heat transfer coefficient on the oil side but between the same terminal values as before. The fourth set of data (the data set #4, Fig. 1) corresponds to the mirror image of data set #2. Finally, the fifth set of data (the data set #5) assumes an "oscillatory" behavior. The data set #5 is selected arbitrarily to have the h terminal values as those for the data sets #2 and #4 and with a negative gradient in the central zone to find the impact of an oscillatory behavior on the surface area determination. To be able to perform the numerical integration, all data are fitted by polynomial and/or logarithmic curve fits.

The final results of the study are presented in Tables 2 and 3. Table 2 summarizes calculated errors introduced by various methods for the original Colburn problem. The exact value is determined by using the Simpson integration method with 200 intervals. For the sake of completeness, the results for various numbers of intervals of the Simpson method are included, as well as the result obtained by Colburn (1933) using graphic integration. It is interesting to note that a small number of intervals in the Simpson numerical procedure provide good accuracy.

Further observations in Table 2 are of interest. First, the Roetzel method causes the same overprediction as the well-known Colburn method for the problem analyzed. Use of the arithmetic mean value of the terminal U values provides the largest error. The evaluation of U at various reference temperatures as a rule underestimates the correct result. The good estimation obtained by using the arithmetic mean temperature as a reference temperature is an accident, rather than the rule, as it will be seen from Table 3.

Table 3 provides results for all five data sets and five averaging methods along with an exact method. All plus numbers indicate percent overestimation of the required surface areas compared to that by the exact numerical values, and all negative numbers indicate underestimation. Under the conditions of severe nonlinearities (data sets #2, 4, 5), *neither* method of averaging provides very accurate results. If the local heat transfer coefficient varies linearly, the best results are obtained by the

Table 2 Comparison of various averaging methods for the original Colburn problem

Method[1]	$(A-A_{exact})/A_{exact}$ x100 %
Roetzel method	+ 12
Exact (numerical)	0
Numerical (Simpson n=2)	+ 6
Numerical (Simpson n=4)	+ 1
Numerical (Simpson n=8)	0
Numerical (simplified)	+ 1
Graphical (Colburn)	+ 0.5
Colburn method	+ 12
Arithmetic mean U	+ 17
U @ $\bar{T}_{arith}$	- 1
U @ $(T_w - \Delta T_{ln})$	- 10

[1] Calculation has been performed with a logarithmic curve fit. U @ $\bar{T}_{arith}$ denotes U evaluated at the arithmetic average of liquid terminal temperatures; U @ $(T_w - \Delta T_{ln})$ denotes U evaluated at a log-mean average temperature defined as the difference between the wall temperature and logarithmic mean temperature difference. Simplified numerical calculation has been performed as follows: $A = (1/2)\Delta Q \sum [1/(U\Delta T)_a + 1/(U\Delta T)_b]_i$ where 12 increments (i) with the corresponding terminal values (a, b) of the $(U\Delta T)$ products have been used, Hewitt et al. (1994).

Table 3 Comparison of various methods for averaging *U*; the numerical values in the table represent $[(A - A_{exact})/A_{exact}] \times 100$, percent

Method[1]	Colburn Example Data Set #1[1]	Data Set #2[2]	Data Set #3[2]	Data Set #4[2]	Data Set #5[2]
Roetzel	+12	+19	+6	-16	+20
Exact	0	0	0	0	0
Colburn	+12	+25	+1	-31	-3
U_{arith}	+17	+31	+5	-28	+1
U @ $\bar{T}_{arith}$	-1	-7	4	+17	+26
U @ $(T_W - \Delta T_{ln})$	-10	-11	-9	-14	+24

[1] U_{arith} denotes arithmetic average of terminal values. Subsequent U values are determined at respective reference T values as described in Table 2.
[2] Calculations performed with a polynomial curve fit.

Colburn model. If the nonlinearities are pronounced, the three point method of Roetzel as presented in this paper is not always a better choice compared to the Colburn method. The surface area predicted by the Roetzel method can be considerably higher or lower compared to the exact numerical results.

In most shell-and-tube heat exchangers, the shell-side flow undergoes changes from crossflow to parallel-flow between and across baffle plates. Thus, the shell-side coefficient undergoes cyclic and not necessarily monotonic changes through the exchanger. In this regard, data set #5 was selected to demonstrate this influence on the surface area requirement. From the review of the results for a single data set #5 in Table 3, no general conclusions regarding which method of averaging U is the best can be drawn. However, it appears that the surface area predicted is quite accurate using the Colburn method, as was the case with data set #3. However, further study is needed to investigate the influence of the cyclic behavior of h or U on the surface area requirement for many multipass shell-and-tube heat exchangers.

Based on the findings of this work, it appears that none of the approximate methods considered here will accurately predict the exchanger surface area requirement when the variation of the heat transfer coefficient on one of the two-fluid sides is highly nonlinear and the corresponding thermal resistance is controlling. If the nature of variation in h is unknown, as in practical applications, the reliability of the approximate methods is even more questionable. The best approach is to conduct the numerical integration to take into consideration the actual variation of the heat transfer coefficient. In many applications, the heat transfer coefficient on one fluid side may not be controlling (i.e., the heat transfer coefficients on both sides may be of the same order of magnitude). In this case, the conclusions derived from the example of this paper are not necessarily applicable. Hence, the best solution is to conduct exact numerical integration to take into account the variations in the heat transfer coefficient on one or both fluid sides.

It should be emphasized that the most published correlations are not accurate to better than 10–15 percent, and also the variation in fluid properties and fouling factors may introduce additional uncertainties in h or U. Hence, even the "exact" numerical method may not have real validity. The approximate methods of overall heat transfer coefficient averaging may or may not have poor accuracy. In light of many commercial computer programs available for the design and analysis of heat exchangers that use some method of averaging U values, the results presented in this paper provide some guidelines on the averaging methods, particularly which ones should be avoided. However, unfortunately, none of the approximate methods came out superior to others in terms of accuracy and reliability.

Conclusions

The methods for incorporating the influence of nonuniformity in the overall heat transfer coefficient in conventional design procedures have been presented. Various definitions of mean overall heat transfer coefficients have been introduced (see Table 1) depending on the pertinent nonuniformity effect. The influences of the length effect (developing thermal boundary layer influence), the temperature effect (changes in thermophysical properties due to fluid temperature variations), and the combined effect have been included in the analysis by defining an area average mean overall heat transfer coefficient, a temperature average mean overall heat transfer coefficient and their combination. A step-by-step procedure is presented for evaluation of the mean overall heat transfer coefficient.

Five different methods of averaging U were compared to determine how they rank in accuracy in predicting exchanger surface area requirement for an example where the heat transfer coefficient on one fluid side was controlling; hence, the variations in h corresponded to the variations in U. For a significant nonlinear variation in h, none of the five methods yielded accurate results. The only plausible method in such a case is the numerical approach. The overall heat transfer coefficients using various reference temperatures in most cases underestimated the heat transfer surface and *should be avoided.*

References

Colburn, A. P., 1933, "Mean Temperature Difference and Heat Transfer Coefficient in Liquid Heat Exchangers," *Ind. Eng. Chem.*, Vol. 25, pp. 873–877.

Hausen, H., 1983, *Heat Transfer in Counterflow, Parallel Flow, and Cross Flow,* McGraw-Hill, New York.

Hewitt, G. F., Shires, G. L., and Bott, T. R., 1994, *Process Heat Transfer,* CRC Press, Boca Raton, FL.

Kays, W. M., and London, A. L., 1984, *Compact Heat Exchangers,* 3rd ed., McGraw-Hill, New York.

Larian, M. G., 1943, "Countercurrent Multitubular Heat Exchangers," *Ind. Eng. Chem.*, Vol. 35, pp. 840–844.

Peters, D. L., 1970, "Heat Exchanger Design With Transfer Coefficients Varying With Temperature or Length of Flow Path," *Wärme- und Stoffübertragung,* Vol. 3, pp. 220–226.

Roetzel, W., 1969, "Berücksichtigung veränderlicher Wärmeübergangskoeffizienten und Wärmekapazitäten by der Bemessung von Wärmeaustauschern," *Wärme- und Stoffübertragung,* Vol. 2, pp. 163–170.

Roetzel, W., 1974, "Heat Exchanger Design With Variable Heat Transfer Coefficients for Crossflow and Mixed Flow Arrangements," *Int. J. Heat Mass Transfer,* Vol. 17, pp. 1037–1049.

Roetzel, W., 1988, "Analytische Berechnung von Wärmeübertragern mit nachträglicher Berücksichtigung temperaturabhängiger Wärmekapazitäten," *Wärme- und Stoffübertragung,* Vol. 23, pp. 175–177.

Roetzel, W., and Spang, B., 1993, "Design of Heat Exchangers, Section Ca; Heat Transfer, Section Cb; Computed Heat Transfer Coefficients, Section Cc," in: *VDI-Wärmeatlas,* 6th ed., VDI-Verlag GmbH, Düsseldorf.

Roetzel, W., 1992, personal communication, Universität der Bundeswehr Hamburg, Institut für Thermodynamik, Hamburg, Germany.

Shah, R. K., 1993, "Nonuniform Heat Transfer Coefficients for Heat Exchanger Thermal Design," in: *Aerospace Heat Exchanger Technology,* R. K. Shah and A. Hashemi, eds., Elsevier, New York, pp. 417–445.

Spang, B., and Roetzel, W., 1992, "Test of Thermal Design Method Considering Variable Transfer Coefficients and Heat Capacities for Cross-Flow Arrangements," *Proc. 1st European Thermal Sciences and 3rd UK National Heat Transfer Conference,* IChEME Symp. Series No. 129, pp. 445–442.

Venkatarathnam, G., 1996, personal communication, Indian Institute of Technology, Madras, India.

Effect of Fouling on Temperature Measurement Error and a Solution

Y. I. Cho[1] and B.-G. Choi[1]

The objective of the present study was to investigate the effect of fouling on the accuracy of temperature measurement. When a thin scale layer is deposited on a temperature-measuring probe, the temperature reading can be in error by several degrees in spite of ±0.1 K resolution of the probe. This erroneous temperature reading can pose a serious problem in the evaluation of heat exchanger performance and in the operation of an automated process control system.

Nomenclature

A = heat transfer surface area
C_p = heat capacity

[1] Department of Mechanical Engineering and Mechanics, Drexel University, Philadelphia, PA 19104.

Contributed by the Heat Transfer Division of THE AMERICAN SOCIETY OF MECHANICAL ENGINEERS. Manuscript received by the Heat Transfer Division August 28, 1997; revision received January 9, 1998. Keywords: Fouling, Heat Transfer, Probes, Temperature, Thermocouples. Associate Technical Editor: M. S. Sohal.

Colburn model. If the nonlinearities are pronounced, the three point method of Roetzel as presented in this paper is not always a better choice compared to the Colburn method. The surface area predicted by the Roetzel method can be considerably higher or lower compared to the exact numerical results.

In most shell-and-tube heat exchangers, the shell-side flow undergoes changes from crossflow to parallel-flow between and across baffle plates. Thus, the shell-side coefficient undergoes cyclic and not necessarily monotonic changes through the exchanger. In this regard, data set #5 was selected to demonstrate this influence on the surface area requirement. From the review of the results for a single data set #5 in Table 3, no general conclusions regarding which method of averaging U is the best can be drawn. However, it appears that the surface area predicted is quite accurate using the Colburn method, as was the case with data set #3. However, further study is needed to investigate the influence of the cyclic behavior of h or U on the surface area requirement for many multipass shell-and-tube heat exchangers.

Based on the findings of this work, it appears that none of the approximate methods considered here will accurately predict the exchanger surface area requirement when the variation of the heat transfer coefficient on one of the two-fluid sides is highly nonlinear and the corresponding thermal resistance is controlling. If the nature of variation in h is unknown, as in practical applications, the reliability of the approximate methods is even more questionable. The best approach is to conduct the numerical integration to take into consideration the actual variation of the heat transfer coefficient. In many applications, the heat transfer coefficient on one fluid side may not be controlling (i.e., the heat transfer coefficients on both sides may be of the same order of magnitude). In this case, the conclusions derived from the example of this paper are not necessarily applicable. Hence, the best solution is to conduct exact numerical integration to take into account the variations in the heat transfer coefficient on one or both fluid sides.

It should be emphasized that the most published correlations are not accurate to better than 10–15 percent, and also the variation in fluid properties and fouling factors may introduce additional uncertainties in h or U. Hence, even the "exact" numerical method may not have real validity. The approximate methods of overall heat transfer coefficient averaging may or may not have poor accuracy. In light of many commercial computer programs available for the design and analysis of heat exchangers that use some method of averaging U values, the results presented in this paper provide some guidelines on the averaging methods, particularly which ones should be avoided. However, unfortunately, none of the approximate methods came out superior to others in terms of accuracy and reliability.

Conclusions

The methods for incorporating the influence of nonuniformity in the overall heat transfer coefficient in conventional design procedures have been presented. Various definitions of mean overall heat transfer coefficients have been introduced (see Table 1) depending on the pertinent nonuniformity effect. The influences of the length effect (developing thermal boundary layer influence), the temperature effect (changes in thermophysical properties due to fluid temperature variations), and the combined effect have been included in the analysis by defining an area average mean overall heat transfer coefficient, a temperature average mean overall heat transfer coefficient and their combination. A step-by-step procedure is presented for evaluation of the mean overall heat transfer coefficient.

Five different methods of averaging U were compared to determine how they rank in accuracy in predicting exchanger surface area requirement for an example where the heat transfer coefficient on one fluid side was controlling; hence, the variations in h corresponded to the variations in U. For a significant nonlinear variation in h, none of the five methods yielded accurate results. The only plausible method in such a case is the numerical approach. The overall heat transfer coefficients using various reference temperatures in most cases underestimated the heat transfer surface and *should be avoided.*

References

Colburn, A. P., 1933, "Mean Temperature Difference and Heat Transfer Coefficient in Liquid Heat Exchangers," *Ind. Eng. Chem.*, Vol. 25, pp. 873–877.

Hausen, H., 1983, *Heat Transfer in Counterflow, Parallel Flow, and Cross Flow,* McGraw-Hill, New York.

Hewitt, G. F., Shires, G. L., and Bott, T. R., 1994, *Process Heat Transfer,* CRC Press, Boca Raton, FL.

Kays, W. M., and London, A. L., 1984, *Compact Heat Exchangers,* 3rd ed., McGraw-Hill, New York.

Larian, M. G., 1943, "Countercurrent Multitubular Heat Exchangers," *Ind. Eng. Chem.*, Vol. 35, pp. 840–844.

Peters, D. L., 1970, "Heat Exchanger Design With Transfer Coefficients Varying With Temperature or Length of Flow Path," *Wärme- und Stoffübertragung,* Vol. 3, pp. 220–226.

Roetzel, W., 1969, "Berücksichtigung veränderlicher Wärmeübergangskoeffizienten und Wärmekapazitäten by der Bemessung von Wärmeaustauschern," *Wärme- und Stoffübertragung,* Vol. 2, pp. 163–170.

Roetzel, W., 1974, "Heat Exchanger Design With Variable Heat Transfer Coefficients for Crossflow and Mixed Flow Arrangements," *Int. J. Heat Mass Transfer,* Vol. 17, pp. 1037–1049.

Roetzel, W., 1988, "Analytische Berechnung von Wärmeübertragern mit nachträglicher Berücksichtigung temperaturabhängiger Wärmekapazitäten," *Wärme- und Stoffübertragung,* Vol. 23, pp. 175–177.

Roetzel, W., and Spang, B., 1993, "Design of Heat Exchangers, Section Ca; Heat Transfer, Section Cb; Computed Heat Transfer Coefficients, Section Cc," in: *VDI-Wärmeatlas,* 6th ed., VDI-Verlag GmbH, Düsseldorf.

Roetzel, W., 1992, personal communication, Universität der Bundeswehr Hamburg, Institut für Thermodynamik, Hamburg, Germany.

Shah, R. K., 1993, "Nonuniform Heat Transfer Coefficients for Heat Exchanger Thermal Design," in: *Aerospace Heat Exchanger Technology,* R. K. Shah and A. Hashemi, eds., Elsevier, New York, pp. 417–445.

Spang, B., and Roetzel, W., 1992, "Test of Thermal Design Method Considering Variable Transfer Coefficients and Heat Capacities for Cross-Flow Arrangements," *Proc. 1st European Thermal Sciences and 3rd UK National Heat Transfer Conference,* IChEME Symp. Series No. 129, pp. 445–442.

Venkatarathnam, G., 1996, personal communication, Indian Institute of Technology, Madras, India.

Effect of Fouling on Temperature Measurement Error and a Solution

Y. I. Cho[1] and B.-G. Choi[1]

The objective of the present study was to investigate the effect of fouling on the accuracy of temperature measurement. When a thin scale layer is deposited on a temperature-measuring probe, the temperature reading can be in error by several degrees in spite of ±0.1 K resolution of the probe. This erroneous temperature reading can pose a serious problem in the evaluation of heat exchanger performance and in the operation of an automated process control system.

Nomenclature

A = heat transfer surface area
C_p = heat capacity

[1] Department of Mechanical Engineering and Mechanics, Drexel University, Philadelphia, PA 19104.

Contributed by the Heat Transfer Division of THE AMERICAN SOCIETY OF MECHANICAL ENGINEERS. Manuscript received by the Heat Transfer Division August 28, 1997; revision received January 9, 1998. Keywords: Fouling, Heat Transfer, Probes, Temperature, Thermocouples. Associate Technical Editor: M. S. Sohal.

D_H = hydraulic diameter
D_s = inside shell diameter
$d_{t,o}$ = outside tube diameter
Q = heat transfer rate
R_f = fouling factor
$T_{c,\text{in}}$ = inlet temperature of cold water
$T_{c,\text{out}}$ = outlet temperature of cold water
ΔT_{LMTD} = log-mean-temperature-difference
U = overall heat transfer coefficient based on outside tube diameter

Introduction

It is well known that fouling causes performance degradation of heat exchangers (Taborek et al., 1972; Suitor et al., 1977; Bott, 1995). One of the most common techniques to monitor the performance degradation is to measure the inlet and outlet temperatures of cold and hot streams in the heat exchanger. However, the effect of thermocouple or thermister probe fouling on temperature measurements has not been carefully considered (ASTM, 1981; Kerlin and Shepard, 1982).

When hard water is used as a cooling stream in a heat exchanger, the water becomes locally supersaturated as it is heated inside the heat exchanger (Cowan and Weintritt, 1976). Thus, precipitation fouling occurs inside the heat exchanger.

Since the temperature of the water leaving the heat exchanger is substantially greater than the inlet water temperature, a temperature-measuring probe located immediately after the heat exchanger can experience a serious fouling problem. As water is heated and passes through the heat exchanger, a number of small particles of submicron to micron size are formed, as dissolved mineral ions precipitate due to temperature changes and flow disturbances inside the heat exchanger (Cowan and Weintritt, 1976; Fan, 1997). Thus, both precipitation and particulate fouling can occur on the surface of the temperature-measuring probe.

When one considers the flow around a temperature-measuring probe outside a heat exchanger, it is often an impingement type of flow. Thus, the surface of the probe becomes an ideal site for scale build-up. The objective of the present study was to investigate the effect of fouling on the use of a temperature-measuring probe. In particular, the fouling of thermocouple probes will be examined in the context of performance losses of a heat exchanger due to fouling.

Experimental Method

Figure 1 schematically shows the test facility, which consists of two reservoir tanks, two pumps, two flow meters, the primary heat transfer test section made of a concentric tube heat exchanger, and a plate-and-frame heat exchanger.

The primary heat transfer test section is made of two concentric copper tubes, i.e., a single-tube counterflow heat exchanger. The shell diameter (ID) was D_s = 0.01684 m and the tube diameter (OD) was $d_{t,o}$ = 0.01275 m, leading to a hydraulic diameter of D_H = 0.00409 m. The diameter of both the inlet and outlet connecting tubes was 0.0109 m. The location of the thermocouple probe relative to the outlet connecting tube is shown in Fig. 1. Of note is that the high velocity at the connecting tube (i.e., Re = 5710) ensured a good mixing for accurate outlet temperature measurement.

The thermocouple used in the present study was Omega Model TMTSS-125G-6 (grounded copper-constantan T type). The thermocouple junction was encased in a 304 stainless steel sheath with a stem diameter of 0.0032 m. Calibration was carried out at 273 and 373 K, confirming the manufacturer's claim of the resolution of ±0.1 K. Hot water discharged from the heat exchanger impinged on the tip of the thermocouple probe longitudinally. The temperature of the hot stream entering the concentric heat exchanger was maintained at approximately 367 K using a plate-and-frame heat exchanger where high-pressure steam provided by the Philadelphia city steam network was used.

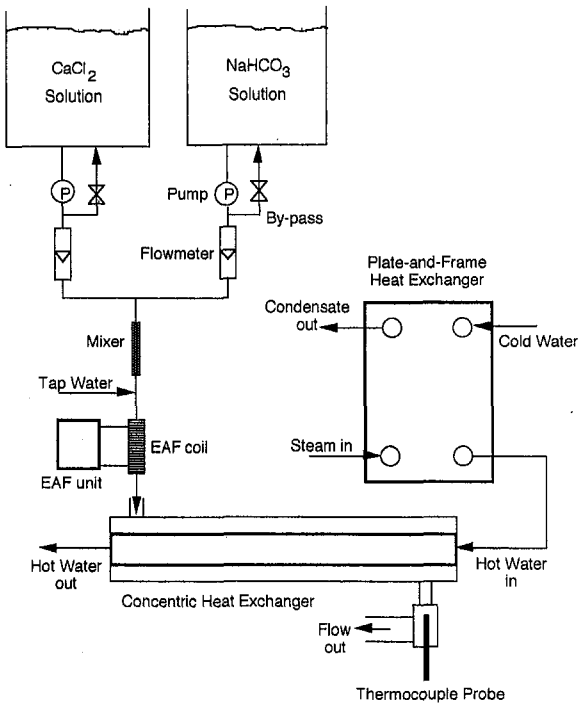

Fig. 1 Schematic diagram of the present test setup with a concentric tube heat exchanger as the primary test section. EAF coil for electronic anti-fouling treatment is used in a feed pipe to the heat exchanger.

Since the hardness of tap water available in Philadelphia is approximately 150 mg/L as $CaCO_3$, it is not suitable for fouling experiments. Therefore, hard water was prepared in our laboratory. The test solution was prepared by adding 0.01 M calcium chloride ($CaCl_2$) and 0.02 M sodium bicarbonate ($NaHCO_3$) to tap water such that the hardness of the test solution was equivalent to 1000 mg/L as $CaCO_3$. The resulting hard water caused severe scaling inside a pump, and one pump was lost on nearly every test due to the pump scaling. In order to avoid scaling in the pump, the calcium chloride and sodium bicarbonate solutions were prepared in two separate reservoir tanks and mixed using a static mixer as shown in Fig. 1.

The inlet temperature of the hard water was maintained at 302 K, whereas the outlet temperature was maintained at approximately 327 K. A flow rate of 2.7×10^{-5} m^3/s was used, resulting in a Reynolds number of 1870 inside the heat exchanger (i.e., in the shell side) and a Reynolds number of 5710 in the outlet connecting tube where the temperature-measuring probe was located. It is of note that the viscosity of the hard water was evaluated at a shell-side average temperature of 316 K and an outlet average temperature of 323 K in Reynolds number calculations. The velocities in the shell side and outlet connecting tube were 0.28 m/s and 0.29 m/s, respectively.

The overall heat transfer coefficient, U, was calculated using the log-mean-temperature-difference (LMTD) (Incropera and DeWitt, 1996), which was obtained from the four temperatures measured at both the inlet and outlet of the cold and hot streams. Fouling factor, R_f, was calculated using the usual definition:

$$Q = UA\Delta T_{\text{LMTD}} = \dot{m}_c C_p (T_{c,\text{out}} - T_{c,\text{in}}) \quad (1)$$

$$U = \frac{\dot{m}_c C_p (T_{c,\text{out}} - T_{c,\text{in}})}{A\Delta T_{\text{LMTD}}} \quad (2)$$

and

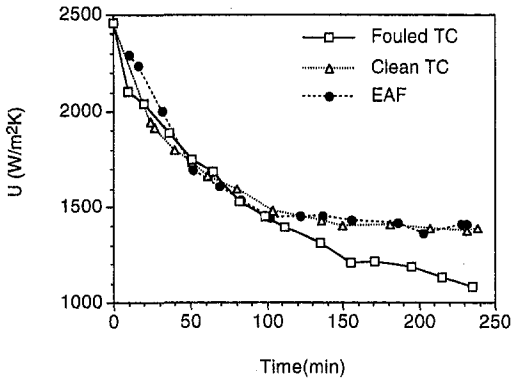

Fig. 2 Overall heat transfer coefficient versus time at a flow rate of 2.7 $\times$ 10^{-5} m^3/s for three different cases: with fouled thermocouple probe, with clean thermocouple probe, and with electronic anti-fouling (EAF) device

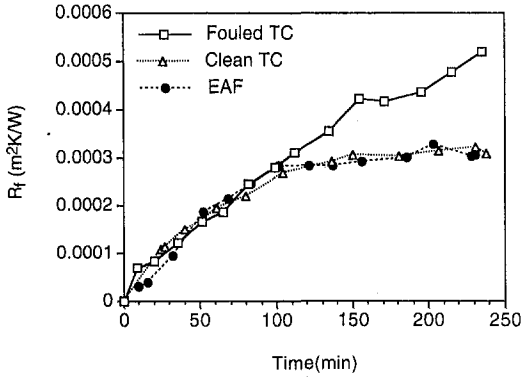

Fig. 3 Fouling factor versus time at a flow rate of 2.7 $\times$ 10^{-5} m^3/s for three different cases: with fouled thermocouple probe, with clean thermocouple probe, and with electronic anti-fouling (EAF) device

$$R_f = \frac{1}{U(t)} - \frac{1}{U_{\text{clean}}} \tag{3}$$

where U_{clean} is the overall heat transfer coefficient corresponding to the clean state, i.e., at $t = 0$. The errors estimated from the uncertainty analysis for Q, U, R_f, and A (heat transfer surface area) were 2.5, 3.0, 8.0, and 1.1 percent, respectively. In all test cases shown in the present paper, the heat balance between the cold and hot streams was within 5 percent.

Results and Discussion

Figure 2 presents the changes in the overall heat transfer coefficient, U, as a function of time for three different cases. The U value corresponding to the clean initial state was measured with tap water at a flow rate of 2.7 $\times$ 10^{-5} m^3/s, resulting in a value of 2460 W/m^2K. When the concentric heat exchanger was clean, the outlet temperature of the cold stream was 331 $\pm$ 0.1 K at a flow rate of 2.7 $\times$ 10^{-5} m^3/s.

As the heat exchanger continued to foul due to the use of the hard water, the outlet temperature measured with a "fouled" thermocouple probe decreased to 317.5 $\pm$ 0.1 K at the end of the 4 hour test, resulting in a U value of 1100 W/m^2K.

When the test was repeated and the thermocouple probe was manually cleaned every time we measured the outlet temperature, it decreased only to 320.2 $\pm$ 0.1 K at the end of the 4 hour test, rendering a U value of 1410 W/m^2K. The results shown in Fig. 2 clearly depict the effect of the thermocouple probe fouling on the estimation of the performance degradation of a heat exchanger. In other words, when one monitors a heat exchanger fouling with a fouled temperature-measuring probe, one significantly overestimates the fouling in the heat exchanger.

A fouled temperature-measuring probe gives a substantially lower temperature reading than a clean one. The error in the outlet temperature measurement depends on the magnitude of fouling on the surface of the probe. It can also cause an automated process control system to respond erroneously in such a way that further fouling can take place in both the heat exchanger and the probe.

Another identical test was carried out with an electronic anti-fouling (EAF) device. The outlet temperature was measured without cleaning the probe in this case. At the end of the 4 hour test the outlet temperature and the U value obtained with the EAF device were found to be exactly identical to the values obtained with the manually cleaned probe, as shown in Fig. 2.

Since the operating principle of the electronic anti-fouling device was introduced elsewhere (Fan, 1997; Fan and Cho, 1997a, 1997b; Cho et al., 1997a, 1997b), it will be described here only briefly. The EAF technology uses a square-wave current signal to create time-varying magnetic fields in a solenoid wrapped around a pipe. Subsequently, the time-varying magnetic field creates an induced electric field inside the pipe, a phenomenon that can be described by Faraday's law. The induced electric field, which oscillates with time, provides the necessary molecular agitation to charged mineral ions such that dissolved mineral ions such as calcium and bicarbonate collide and precipitate. Subsequently, the precipitation fouling is prevented on the surface of a temperature probe or heat exchanger.

Figure 3 shows the fouling factor calculated from the overall heat transfer coefficient as a function of time. The fouling factor obtained with the fouled temperature probe includes fouling in both the heat exchanger and temperature probe. The actual fouling that took place in the heat exchanger had to be significantly less, as demonstrated by the comparison with the case obtained with the manually cleaned temperature probe. In other words, fouling factors can be greatly overestimated if a temperature probe is fouled.

One may ask why fouling should affect temperature measurement under a steady-state condition. In order to illustrate the point, Fig. 4 shows a sketch of a typical thermocouple mounting. Since the fluid temperature is often substantially greater than the ambient temperature, heat flows from inside to outside through the probe sheath. When there is no scale deposit on the probe, the thermocouple junction temperature is equal to the fluid temperature. However, as the probe becomes surrounded by a scale layer, a temperature gradient across the scale layer due to heat flow is introduced. In other words, the junction temperature will be consistently lower than the fluid temperature. The temperature error due to the scale layer will depend primarily on the thickness and thermal conductivity of scale layer. In addition, for a heat exchanger located outdoors, the outside air temperature decreases in the winter, increasing the temperature difference between fluid and the outside air. Hence, the temperature error due to the scale layer will be larger in the winter than in the summer.

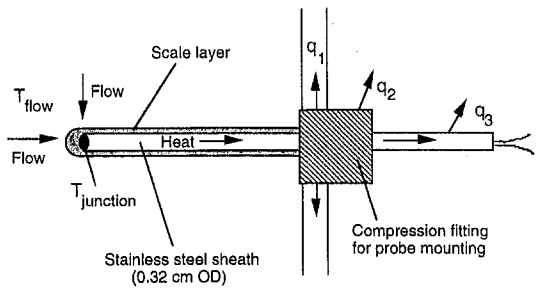

Fig. 4 Sketch of thermocouple probe mounting. Arrows indicate the direction of heat flow. q_1 = conduction heat loss throughout tube wall, q_2 = convective heat loss from fitting, and q_3 = convective heat loss from probe stem.

Conclusions

The present study was conducted in order to investigate the effect of fouling of a temperature-measuring probe on the accuracy of temperature measurement. When the temperature probe is fouled, the temperature reading can be in error by several degrees. Subsequently, this erroneous temperature measurement can overestimate the performance degradation of a heat exchanger caused by fouling.

A new electronic anti-fouling (EAF) device was found to prevent the fouling in a temperature probe. With the EAF device, the temperature measurement error caused by the probe-fouling can be avoided.

References

ASTM, 1981, *Manual on the Use of Thermocouples in Temperature Measurement,* STP 470B.

Bott, T. R., 1995, *The Fouling of Heat Exchangers,* Elsevier, Amsterdam, The Netherlands.

Cho, Y. I., Fan, C. F., and Choi, B. G., 1997a, "Theory of Electronic Anti-Fouling Technology to Control Precipitation Fouling in Heat Exchangers," *Int. Comm. Heat Mass Transfer,* Vol. 24, pp. 747–756.

Cho, Y. I., Choi, B. G., and Drazner, B. J., 1997b, "Use of Electronic Descaling Technology to Control Precipitation Fouling in Plate-and-Frame Heat Exchanger," in: *Compact Heat Exchangers for the Process Industries,* R. K. Shah, ed., Begell House, New York, pp. 267–273.

Cowan, J. C., and Weintritt, D. J. 1976, *Water-Formed Scale Deposits,* Gulf Publishing Company.

Fan, C. F., 1997, "A Study of Electronic Descaling Technology," Ph.D. thesis, Drexel University, Philadelphia, PA.

Fan, C. F., and Cho, Y. I., 1997a, "Microscopic Observation of Calcium Carbonate Particles: Validation of an Electronic Anti-Fouling Technology," *Int. Comm. Heat Mass Transfer,* Vol. 24, pp. 757–770.

Fan, C. F., and Cho, Y. I., 1997b, "A New Electronic Anti-Fouling Method to Control Fouling," *Proc. National Heat Transfer Conference,* Baltimore, MD, Vol. 12, pp. 183–188.

Incropera, F. P., and DeWitt, D. P., 1996, *Fundamentals of Heat and Mass Transfer,* 4th ed., Wiley, New York.

Kerlin, T. W., and Shepard, R. L., 1982, *Industrial Temperature Measurement,* Instrument Society of America.

Suitor, J. W., Marner, W. J., and Ritter, R. B., 1977, "The History and Status of Research in Fouling of Heat Exchangers in Cooling Water Service," *The Canadian J. of Chem. Eng.,* Vol. 55, pp. 374–380.

Taborek, J., Aoki, T., Ritter, R. B., Palen, J. W., and Knudsen, J. G., 1972, "Fouling: The Major Unresolved Problem in Heat Transfer," *Chemical Engineering Progress,* Vol. 68, pp. 59–67.

Application of an Equivalent Single-Tube Model for Predicting the Frequency-Response Characteristics of Multitube Two-Phase Condensing Flow Systems With Thermal and Flow Distribution Asymmetry

C. J. Kobus,[1] G. L. Wedekind,[2] and B. L. Bhatt[3]

Introduction

This paper is concerned with multiple, in-tube condensing flow systems involving complete condensation, the transient characteristics of which are important in a broad spectrum of energy transport and conversion processes. Sufficiently large flow excursions or oscillations could substantially affect the performance and control of the processes taking place, cause damage to mechanical equipment and components, and endanger the safety of such systems.

Most practical applications of in-tube condensation involve multiple-tube geometries, consisting of parallel channels connected to common headers. To the best knowledge of the authors, there do not appear to be any theoretical models or experimental data in the archival literature pertaining to the frequency-response characteristics of multitube condensing flow systems. Therefore, the model presented in this paper represents the results of merging a theoretical model capable of predicting the frequency-response characteristics of single-tube condensing flow systems (Bhatt and Wedekind, 1980) with a model capable of predicting the transient behavior of multitube systems (Wedekind and Bhatt, 1989).

Equivalent Single-Tube Model

Wedekind and Bhatt (1989) demonstrated a method of approximating an n-tube condensing flow system with an Equivalent Single-Tube Model (ESTM), based on the System Mean Void Fraction (SMVF) Model developed earlier. The concept of the ESTM is to obtain an equivalent single-tube system time constant, τ_s, which, in its generalized form for an n-tube system, is a weighted average of the time constants for each of the individual tubes. In the present model, the flow distribution and heat flux for each individual tube are allowed to be different; however, the tubes are of identical geometry. Thermodynamic properties of the two-phase mixture are assumed to be the same in each tube, and evaluated at a mean condensing pressure. The spatially averaged heat flux for each tube is assumed to be time-invariant.[4] Also, the inlet flow quality entering each tube is assumed to be the same and equal to unity; $x_{i,1} = x_{i,j} = 1$. Using the ESTM, based on the SMVF model, the frequency-response characteristics of the outlet liquid flow rate for an n-tube condensing flow system can be approximated utilizing the results from single-tube studies carried out earlier (Bhatt and Wedekind, 1980). Thus, the gain and phase shift characteristics, G_m and Φ_m, respectively, can be modeled in terms of the liquid-to-vapor density ratio, (ρ/ρ'), the equivalent system time constant, τ_s, and the angular frequency, ω; thus,

$$G_m = \left\{ \frac{1 + (\rho/\rho')^2(\omega\tau_s)^2}{[1 + (\omega\tau_s)^2]} \right\}^{1/2} \tag{1}$$

$$\Phi_m = \tan^{-1} \left\{ \frac{[(\rho/\rho') - 1](\omega\tau_s)}{1 + (\rho/\rho')(\omega\tau_s)^2} \right\} \tag{2}$$

where

$$\tau_s = \sum_{j=1}^{n} \gamma_j \tau_j = \tau_1 \sum_{j=1}^{n} \gamma_j \beta_j \tag{3}$$

The time constant for each individual tube, τ_j, involves the vapor density, ρ', the heat of vaporization, $(h' - h)$, and the spatially averaged heat flux, $\bar{f}_{q,j}$. It also involves the tube cross-sectional area, $A_{t,j}$, periphery, P_j, and the system mean void fraction, $\bar{\alpha}$; thus for tube 1:

$$\tau_1 = \frac{\rho'(h' - h)\bar{\alpha}A_{t,1}}{\bar{f}_{q,1}P_1} \tag{4}$$

where

[1] Graduate Assistant, Oakland University, Rochester, MI 48309: e-mail: cjkobus@oakland.edu; Mem. ASME.

[2] John F. Dodge Professor of Engineering, Oakland University, Rochester, MI 48309; e-mail: wedekind@oakland.edu; Mem. ASME.

[3] Professor and Associate Dean of Engineering and Computer Science, Oakland University, Rochester, MI 48309; e-mail: bhatt@oakland.edu; Mem. ASME.

Contributed by the Heat Transfer Division of THE AMERICAN SOCIETY OF MECHANICAL ENGINEERS. Manuscript received by the Heat Transfer Divison July 21, 1997; revision received February 17, 1998. Keywords: Condensation, Multiphase Flows, Transient and Unsteady Heat Transfer. Associate Technical Editor: M. Kaviany.

[4] The water flow rate was sufficiently high such that the heat transfer coefficient on the water side was greater than that on the refrigerant side; thus, the wall temperature of the copper tubing would be essentially constant. The small transients in the condensing temperature, due to small transients in the condensing pressure, would result in a near-time-invariant heat flux.

Conclusions

The present study was conducted in order to investigate the effect of fouling of a temperature-measuring probe on the accuracy of temperature measurement. When the temperature probe is fouled, the temperature reading can be in error by several degrees. Subsequently, this erroneous temperature measurement can overestimate the performance degradation of a heat exchanger caused by fouling.

A new electronic anti-fouling (EAF) device was found to prevent the fouling in a temperature probe. With the EAF device, the temperature measurement error caused by the probe-fouling can be avoided.

References

ASTM, 1981, *Manual on the Use of Thermocouples in Temperature Measurement,* STP 470B.

Bott, T. R., 1995, *The Fouling of Heat Exchangers,* Elsevier, Amsterdam, The Netherlands.

Cho, Y. I., Fan, C. F., and Choi, B. G., 1997a, "Theory of Electronic Anti-Fouling Technology to Control Precipitation Fouling in Heat Exchangers," *Int. Comm. Heat Mass Transfer,* Vol. 24, pp. 747–756.

Cho, Y. I., Choi, B. G., and Drazner, B. J., 1997b, "Use of Electronic Descaling Technology to Control Precipitation Fouling in Plate-and-Frame Heat Exchanger," in: *Compact Heat Exchangers for the Process Industries,* R. K. Shah, ed., Begell House, New York, pp. 267–273.

Cowan, J. C., and Weintritt, D. J. 1976, *Water-Formed Scale Deposits,* Gulf Publishing Company.

Fan, C. F., 1997, "A Study of Electronic Descaling Technology," Ph.D. thesis, Drexel University, Philadelphia, PA.

Fan, C. F., and Cho, Y. I., 1997a, "Microscopic Observation of Calcium Carbonate Particles: Validation of an Electronic Anti-Fouling Technology," *Int. Comm. Heat Mass Transfer,* Vol. 24, pp. 757–770.

Fan, C. F., and Cho, Y. I., 1997b, "A New Electronic Anti-Fouling Method to Control Fouling," *Proc. National Heat Transfer Conference,* Baltimore, MD, Vol. 12, pp. 183–188.

Incropera, F. P., and DeWitt, D. P., 1996, *Fundamentals of Heat and Mass Transfer,* 4th ed., Wiley, New York.

Kerlin, T. W., and Shepard, R. L., 1982, *Industrial Temperature Measurement,* Instrument Society of America.

Suitor, J. W., Marner, W. J., and Ritter, R. B., 1977, "The History and Status of Research in Fouling of Heat Exchangers in Cooling Water Service," *The Canadian J. of Chem. Eng.,* Vol. 55, pp. 374–380.

Taborek, J., Aoki, T., Ritter, R. B., Palen, J. W., and Knudsen, J. G., 1972, "Fouling: The Major Unresolved Problem in Heat Transfer," *Chemical Engineering Progress,* Vol. 68, pp. 59–67.

Application of an Equivalent Single-Tube Model for Predicting the Frequency-Response Characteristics of Multitube Two-Phase Condensing Flow Systems With Thermal and Flow Distribution Asymmetry

C. J. Kobus,[1] G. L. Wedekind,[2] and B. L. Bhatt[3]

Introduction

This paper is concerned with multiple, in-tube condensing flow systems involving complete condensation, the transient characteristics of which are important in a broad spectrum of energy transport and conversion processes. Sufficiently large flow excursions or oscillations could substantially affect the performance and control of the processes taking place, cause damage to mechanical equipment and components, and endanger the safety of such systems.

Most practical applications of in-tube condensation involve multiple-tube geometries, consisting of parallel channels connected to common headers. To the best knowledge of the authors, there do not appear to be any theoretical models or experimental data in the archival literature pertaining to the frequency-response characteristics of multitube condensing flow systems. Therefore, the model presented in this paper represents the results of merging a theoretical model capable of predicting the frequency-response characteristics of single-tube condensing flow systems (Bhatt and Wedekind, 1980) with a model capable of predicting the transient behavior of multitube systems (Wedekind and Bhatt, 1989).

Equivalent Single-Tube Model

Wedekind and Bhatt (1989) demonstrated a method of approximating an n-tube condensing flow system with an Equivalent Single-Tube Model (ESTM), based on the System Mean Void Fraction (SMVF) Model developed earlier. The concept of the ESTM is to obtain an equivalent single-tube system time constant, τ_s, which, in its generalized form for an n-tube system, is a weighted average of the time constants for each of the individual tubes. In the present model, the flow distribution and heat flux for each individual tube are allowed to be different; however, the tubes are of identical geometry. Thermodynamic properties of the two-phase mixture are assumed to be the same in each tube, and evaluated at a mean condensing pressure. The spatially averaged heat flux for each tube is assumed to be time-invariant.[4] Also, the inlet flow quality entering each tube is assumed to be the same and equal to unity; $x_{i,1} = x_{i,j} = 1$. Using the ESTM, based on the SMVF model, the frequency-response characteristics of the outlet liquid flow rate for an n-tube condensing flow system can be approximated utilizing the results from single-tube studies carried out earlier (Bhatt and Wedekind, 1980). Thus, the gain and phase shift characteristics, G_m and Φ_m, respectively, can be modeled in terms of the liquid-to-vapor density ratio, (ρ/ρ'), the equivalent system time constant, τ_s, and the angular frequency, ω; thus,

$$G_m = \left\{ \frac{1 + (\rho/\rho')^2(\omega\tau_s)^2}{[1 + (\omega\tau_s)^2]} \right\}^{1/2} \tag{1}$$

$$\Phi_m = \tan^{-1} \left\{ \frac{[(\rho/\rho') - 1](\omega\tau_s)}{1 + (\rho/\rho')(\omega\tau_s)^2} \right\} \tag{2}$$

where

$$\tau_s = \sum_{j=1}^{n} \gamma_j \tau_j = \tau_1 \sum_{j=1}^{n} \gamma_j \beta_j \tag{3}$$

The time constant for each individual tube, τ_j, involves the vapor density, ρ', the heat of vaporization, $(h' - h)$, and the spatially averaged heat flux, $\bar{f}_{q,j}$. It also involves the tube cross-sectional area, $A_{t,j}$, periphery, P_j, and the system mean void fraction, $\bar{\alpha}$; thus for tube 1:

$$\tau_1 = \frac{\rho'(h' - h)\bar{\alpha}A_{t,1}}{\bar{f}_{q,1}P_1} \tag{4}$$

where

[1] Graduate Assistant, Oakland University, Rochester, MI 48309: e-mail: cjkobus@oakland.edu; Mem. ASME.

[2] John F. Dodge Professor of Engineering, Oakland University, Rochester, MI 48309; e-mail: wedekind@oakland.edu; Mem. ASME.

[3] Professor and Associate Dean of Engineering and Computer Science, Oakland University, Rochester, MI 48309; e-mail: bhatt@oakland.edu; Mem. ASME.

Contributed by the Heat Transfer Division of THE AMERICAN SOCIETY OF MECHANICAL ENGINEERS. Manuscript received by the Heat Transfer Divison July 21, 1997; revision received February 17, 1998. Keywords: Condensation, Multiphase Flows, Transient and Unsteady Heat Transfer. Associate Technical Editor: M. Kaviany.

[4] The water flow rate was sufficiently high such that the heat transfer coefficient on the water side was greater than that on the refrigerant side; thus, the wall temperature of the copper tubing would be essentially constant. The small transients in the condensing temperature, due to small transients in the condensing pressure, would result in a near-time-invariant heat flux.

$$\bar{\alpha} = \frac{1}{(1-a)} + \frac{aLn(a)}{(1-a)^2}; \quad a = (\rho'/\rho)^{2/3} \tag{5}$$

$$\beta_j \equiv \tau_j/\tau_1 = \bar{f}_{q,1}/\bar{f}_{q,j} \tag{6}$$

$$\gamma_j \equiv m_{t,j}(z, t)_{z=0}/m_{t,i}(t) \tag{7}$$

The particular void fraction model used to determine the system mean void fraction, $\bar{\alpha}$, is that proposed by Zivi (1964), and was chosen for its simplicity and reasonable accuracy in determining the mean void fraction over the full range of flow quality,[5] $0 \le x \le 1$.

Physically, the flow distribution parameter, γ_j, is defined as the fraction of the total mass flow rate entering tube j. In general, $0 \le \gamma_j \le 1$, therefore, a flow distribution parameter $\gamma_j = 1/n$ represents flow distribution symmetry in an n-tube system. The parameter β_j is a thermal asymmetry parameter, and is defined as the heat flux[6] ratio between a reference tube (designated as tube 1) and the jth tube in the system. In general, $\beta_j \ge 0$; therefore, $\beta_j = 1$ represents thermal symmetry in the multitube system. In this phase of the model development, both the thermal and flow distribution asymmetry parameters are assumed to be known and independent of one another. Thus the reference to them as parameters.

Referring to Eqs. (3), (4), and (6), it should be pointed out that when thermal symmetry exists, the ESTM has no additional approximations for a multitube system than for a single-tube system (Bhatt and Wedekind, 1980) regardless of flow distribution asymmetry. When thermal asymmetry exists, the ESTM is an approximation; however, it seems reasonable that as the number of individual tubes increases, the approximation improves. Therefore, it may very well be that the two-tube system with significant thermal asymmetry represents a worst-case situation.

Comparison of Model Predictions With Experimental Data

The experimental apparatus used in the present research, including the geometry and dimensions of the two-tube condenser, is similar to the one used by Wedekind and Bhatt (1989); the details and experimental uncertainties described in that paper will not be repeated here. A feedback control loop, involving a pneumatically actuated regulating valve, an orifice flowmeter, a PID controller, and a sinusoidal function generator driving the set-point, provided the sinusoidal inlet vapor flow rate, and eliminated many of the experimental problems encountered in the earlier single-tube study (Bhatt and Wedekind, 1980). The major advantage of this technique is the ability to vary and increase the amplitude of the sinusoidal inlet vapor flow rate such that the amplitudes of the random fluctuations in the outlet liquid flow rate, inherent in two-phase flow, were small in comparison to that of the deterministic flow oscillations.

Since the inherent random fluctuations were observed to be present over the entire range of frequencies tested, the experimental uncertainties most significant to this study are related to discerning the amplitude and phase shift of the outlet liquid flow rate oscillations from the strip-chart traces, even though great care was taken to minimize the influence of the fluctuations. Therefore, the experimental data pertaining to the gain characteristics had an average maximum uncertainty[7] of ±10 percent, whereas the uncertainty associated with the phase shift characteristics was slightly higher at ±15 percent.

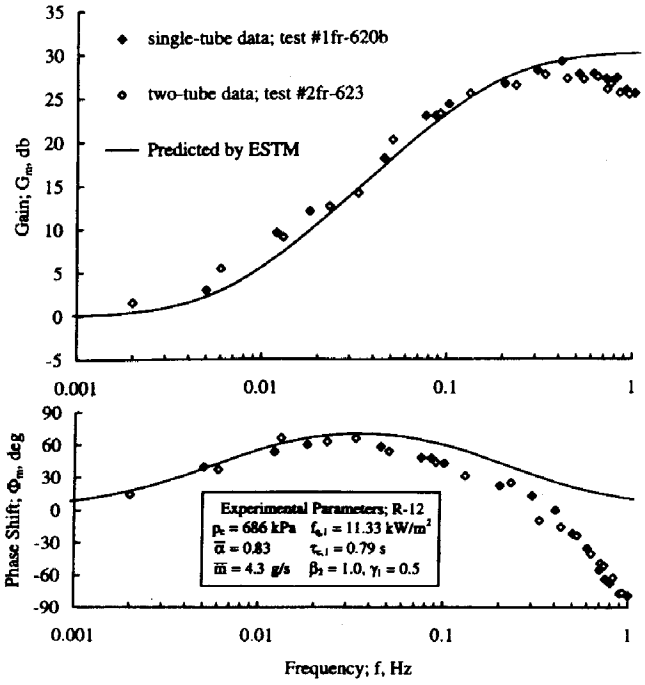

Fig. 1 Frequency-response characteristics of outlet liquid flow rate to sinusoidal inlet flow rate variation; comparison between single- and two-tube experimental data

The theoretical predictions of the Equivalent Single-Tube Model (ESTM) for the frequency-response characteristics of a two-tube condensing flow system are compared with experimental data for several different flow conditions. The initial frequency-response tests were carried out with a single-tube condenser, the results of which are depicted in Fig. 1. Then, as a means of model verification, the ESTM was used to design an equivalent test for a two-tube condenser that would yield the exact same frequency-response characteristics as that of the single-tube condenser (thus, $\tau_s = \tau_1$), even though the refrigerant flow rates in each of the two tubes were different than what they were for the single-tube condenser. The experimental results for the two-tube condenser are also plotted in Fig. 1. As can be seen from the graph, the measured frequency-response characteristics were virtually identical for both the single- and the two-tube condensers, just as the ESTM predicted.

The influence of thermal and flow distribution asymmetry for a two-tube condenser is depicted in Fig. 2 by comparing the previous set of experimental data where thermal and flow distribution symmetry was present ($\beta_2 = 1.0$, $\gamma_1 = 0.5$), with data involving significant thermal and flow distribution asymmetry between the two tubes ($\beta_2 = 2.6$, $\gamma_1 = 0.35$). The agreement between the experimental data and the ESTM is seen to be quite good for both the symmetric and asymmetric conditions, the predicted gain being even better than the predicted phase shift.

It is noted that the experimentally measured gain and phase shift appear to diverge some from the ESTM predictions at the higher frequencies. An analysis of the data indicates that the difference between the ESTM predictions and the measured frequency-response characteristics was not due to measurement uncertainties. Therefore, the difference must be the result of a physical mechanism not included in the present theoretical model. That physical mechanism is undoubtedly compressibility effects. Although inadequate experimental data were available back then, this gain and phase-shift attenuation at the higher frequencies were predicted in an earlier single-tube study by Bhatt and Wedekind (1980), where compressibility effects

[5] Comparisons have been made using other void fraction models to determine the mean void fraction, and the interested reader is referred to the earlier work of Wedekind and Bhatt (1977) for details.

[6] Since the condenser tubes were water-cooled and in concentric-tube configuration, the theoretical method utilized in this study for obtaining the effective point of complete condensation and the spatially averaged heat flux, $\bar{f}_q$, is described by Bhatt and Wedekind (1984).

[7] The maximum uncertainty varied with the frequency. The point of minimum uncertainty in the gain, ±1.5 db, occurred where the gain itself was at a maximum. The point of maximum uncertainty in the gain, ±4 db, occurred at the lowest frequencies, corresponding to the lowest values of gain where, in turn, the relative influence of the inherent random fluctuations on the deterministic transient was the highest.

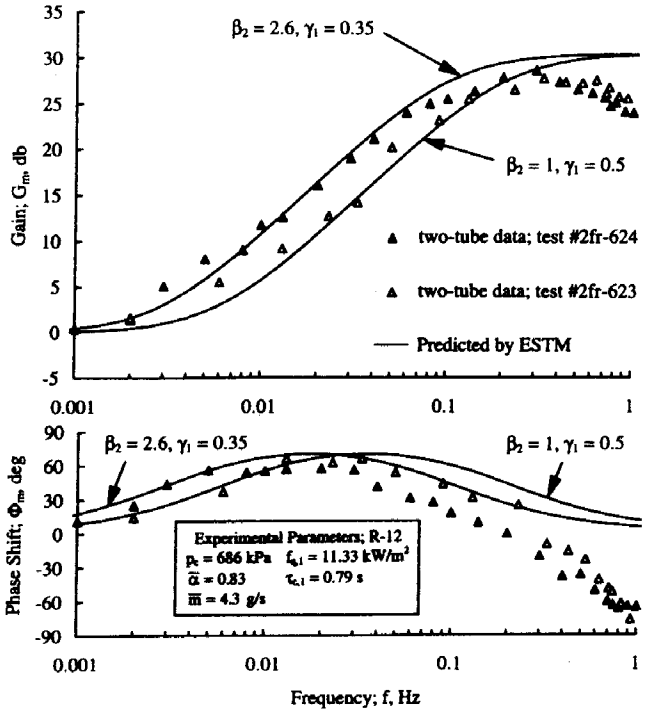

Fig. 2 Frequency-response of outlet liquid flow rate relative to sinusoidal inlet vapor flow rate variation for a two-tube condensing flow system; comparison with ESTM

were considered. Therefore, the gain and phase shift attenuation in the present experimental data at the higher frequencies in the two-tube system are evidence of the existence of some compressibility effects, even though an attempt was made to minimize them.

Summary and Conclusions

The degree of agreement between the experimental data and the ESTM predictions is quite good, especially when consideration is given to the complexity of the physical mechanisms involved, and the simplicity of the model, complete with its ability to handle any number of tubes, and to predict the effects of thermal and flow distribution asymmetry. There is some very sophisticated but, because of its complexity, not so "user-friendly" computer software available to design engineers who are working with two-phase condensing flow equipment. It is recognized that the utilization of this type of software may be both necessary and appropriate in some instances. The ESTM presented in this paper, however, offers the design engineer another tool, which, because of its simplicity, should have a place in the overall design and evaluation process for two-phase, in-tube condensing flow equipment. From a design perspective, the significant value of the ESTM is that it includes the primary physical mechanisms governing such complex frequency-response characteristics, yet is simple enough to be solved, and graphically demonstrated, on typical "spread-sheet" software.

Acknowledgments

The authors would like to acknowledge the National Science Foundation, Thermal Transport and Thermal Processing Program, Division of Chemical and Transport Systems, for its part in the support of this research under Grant No. CTS-9420853.

References

Bhatt, B. L., and Wedekind, G. L., 1980, "Transient and Frequency Response Characteristics of Two-Phase Condensing Flows: With and Without Compressibility," ASME JOURNAL OF HEAT TRANSFER, Vol. 102, pp. 495–500.

Bhatt, B. L., and Wedekind, G. L., 1984, "An Experimental and Theoretical Study Into the Determination of Condensing Length," *Basic Aspects of Two-Phase Flow and Heat Transfer, Proc. 22nd National Heat Transfer Conference*, Niagara Falls, New York, V. K. Dhur and V. E. Schrock, eds., ASME, pp. 179–183.

Wedekind, G. L., and Bhatt, B. L., 1977, "An Experimental and Theoretical Investigation Into Thermally Governed Transient Flow Surges in Two-Phase Condensing Flow," *Proc. Two-Phase Flow and Heat Transfer Symposium-Workshop*, Ft. Lauderdale, FL, Vol. 11, Oct., 1976, pp. 691–711; also, ASME JOURNAL OF HEAT TRANSFER, Vol. 99, pp. 561–567.

Wedekind, G. L., and Bhatt, B. L., 1989, "Modeling the Thermally Governed Transient Flow Surges Multitube Condensing Flow Systems With Thermal and Flow Distribution Asymmetry," ASME JOURNAL OF HEAT TRANSFER, Vol. 111, pp. 786–791.

Zivi, S. M., 1964, "Estimation of Steady-State Steam Void Fraction by Means of the Principle of Minimum Entropy Production," ASME JOURNAL OF HEAT TRANSFER, Vol. 86, p. 247.

Simplified and Accurate Mathematical Model for the Analysis of Heat and Moisture Transfer From Food Commodities

F. A. Ansari[1]

The present paper deals with a simple and accurate mathematical model for making reliable heat and mass transfer analyses from high-water–content solids when exposed to a cold air stream. Such physical situations are encountered in the refrigeration industry during air blast cooling of food commodities. The concept of enthalpy potential has been used to develop a simple linear surface boundary condition equation. This equation accounts for the cooling effect due to sensible convective heat transfer as well as the latent cooling effect due to produce desiccation. Investigations on ten fresh samples each of ripe tomato and cucumber established that there is a good agreement between the computed temperatures from the proposed model and the experimentally measured values.

Nomenclature

Bi = Biot number = $h \cdot x_0/k$
c_{pm} = specific heat of moist air, J/kg·K
h = surface film conductance, W/m^2·K
h_d = convective surface mass transfer coefficient, kg·/m^2·s
I = enthalpy of saturated air at the produce surface temperature, J/kg
I_{cm} = enthalpy of air at cooling medium temperature, J/kg
k = produce thermal conductivity, W/m·K
m = 0 for infinite slab, 1 for infinite cylinder, and 2 for sphere
Nu = Nusselt number = $h \cdot x_0/k_{air}$
Pr = Prandtl number = γ/α
q = rate of heat transfer, J/m^2·s
Re = Reynolds number = $v \cdot x_0/\gamma$
T = temperature, °C
T^+ = 0.0801 T
t = time, s
U = normalized temperature = $(T - T_{cm})/(T_i - T_{cm})$

[1] Professor, Mechanical Engineering Department, A. M. U., Aligarh—202 002, India.

Contributed by the Heat Transfer Division for publication in the JOURNAL OF HEAT TRANSFER. Manuscript received by the Heat Transfer Division August 6, 1997; revision received October 20, 1997. Keywords: Forced Convection, Mass Transfer, Refrigeration. Associate Technical Editor: Y. Jaluria.

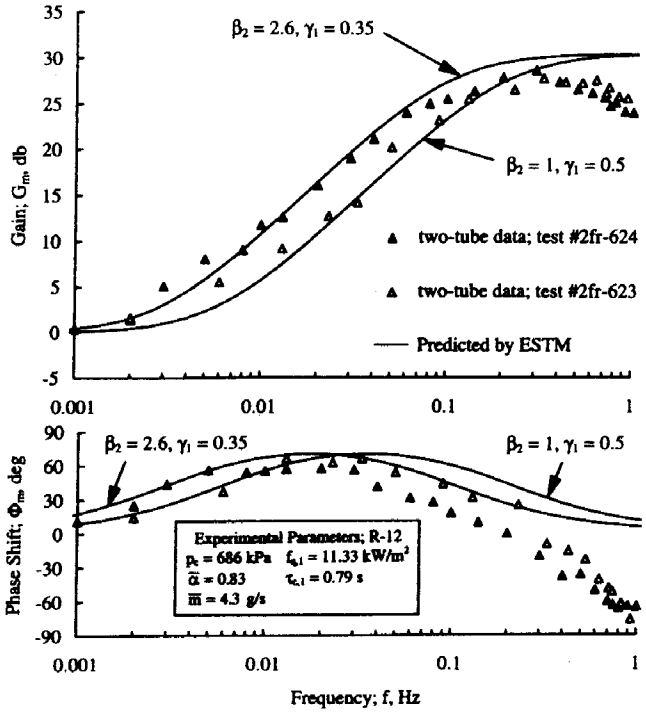

Fig. 2 Frequency-response of outlet liquid flow rate relative to sinusoidal inlet vapor flow rate variation for a two-tube condensing flow system; comparison with ESTM

were considered. Therefore, the gain and phase shift attenuation in the present experimental data at the higher frequencies in the two-tube system are evidence of the existence of some compressibility effects, even though an attempt was made to minimize them.

Summary and Conclusions

The degree of agreement between the experimental data and the ESTM predictions is quite good, especially when consideration is given to the complexity of the physical mechanisms involved, and the simplicity of the model, complete with its ability to handle any number of tubes, and to predict the effects of thermal and flow distribution asymmetry. There is some very sophisticated but, because of its complexity, not so "user-friendly" computer software available to design engineers who are working with two-phase condensing flow equipment. It is recognized that the utilization of this type of software may be both necessary and appropriate in some instances. The ESTM presented in this paper, however, offers the design engineer another tool, which, because of its simplicity, should have a place in the overall design and evaluation process for two-phase, in-tube condensing flow equipment. From a design perspective, the significant value of the ESTM is that it includes the primary physical mechanisms governing such complex frequency-response characteristics, yet is simple enough to be solved, and graphically demonstrated, on typical "spread-sheet" software.

Acknowledgments

The authors would like to acknowledge the National Science Foundation, Thermal Transport and Thermal Processing Program, Division of Chemical and Transport Systems, for its part in the support of this research under Grant No. CTS-9420853.

References

Bhatt, B. L., and Wedekind, G. L., 1980, "Transient and Frequency Response Characteristics of Two-Phase Condensing Flows: With and Without Compressibility," ASME JOURNAL OF HEAT TRANSFER, Vol. 102, pp. 495–500.

Bhatt, B. L., and Wedekind, G. L., 1984, "An Experimental and Theoretical Study Into the Determination of Condensing Length," *Basic Aspects of Two-Phase Flow and Heat Transfer, Proc. 22nd National Heat Transfer Conference*, Niagara Falls, New York, V. K. Dhur and V. E. Schrock, eds., ASME, pp. 179–183.

Wedekind, G. L., and Bhatt, B. L., 1977, "An Experimental and Theoretical Investigation Into Thermally Governed Transient Flow Surges in Two-Phase Condensing Flow," *Proc. Two-Phase Flow and Heat Transfer Symposium-Workshop*, Ft. Lauderdale, FL, Vol. 11, Oct., 1976, pp. 691–711; also, ASME JOURNAL OF HEAT TRANSFER, Vol. 99, pp. 561–567.

Wedekind, G. L., and Bhatt, B. L., 1989, "Modeling the Thermally Governed Transient Flow Surges Multitube Condensing Flow Systems With Thermal and Flow Distribution Asymmetry," ASME JOURNAL OF HEAT TRANSFER, Vol. 111, pp. 786–791.

Zivi, S. M., 1964, "Estimation of Steady-State Steam Void Fraction by Means of the Principle of Minimum Entropy Production," ASME JOURNAL OF HEAT TRANSFER, Vol. 86, p. 247.

Simplified and Accurate Mathematical Model for the Analysis of Heat and Moisture Transfer From Food Commodities

F. A. Ansari[1]

The present paper deals with a simple and accurate mathematical model for making reliable heat and mass transfer analyses from high-water–content solids when exposed to a cold air stream. Such physical situations are encountered in the refrigeration industry during air blast cooling of food commodities. The concept of enthalpy potential has been used to develop a simple linear surface boundary condition equation. This equation accounts for the cooling effect due to sensible convective heat transfer as well as the latent cooling effect due to produce desiccation. Investigations on ten fresh samples each of ripe tomato and cucumber established that there is a good agreement between the computed temperatures from the proposed model and the experimentally measured values.

Nomenclature

Bi = Biot number = $h \cdot x_0/k$
c_{pm} = specific heat of moist air, J/kg·K
h = surface film conductance, W/m^2·K
h_d = convective surface mass transfer coefficient, kg·/m^2·s
I = enthalpy of saturated air at the produce surface temperature, J/kg
I_{cm} = enthalpy of air at cooling medium temperature, J/kg
k = produce thermal conductivity, W/m·K
m = 0 for infinite slab, 1 for infinite cylinder, and 2 for sphere
Nu = Nusselt number = $h \cdot x_0/k_{air}$
Pr = Prandtl number = γ/α
q = rate of heat transfer, J/m^2·s
Re = Reynolds number = $v \cdot x_0/\gamma$
T = temperature, °C
T^+ = 0.0801 T
t = time, s
U = normalized temperature = $(T - T_{cm})/(T_i - T_{cm})$

[1] Professor, Mechanical Engineering Department, A. M. U., Aligarh—202 002, India.

Contributed by the Heat Transfer Division for publication in the JOURNAL OF HEAT TRANSFER. Manuscript received by the Heat Transfer Division August 6, 1997; revision received October 20, 1997. Keywords: Forced Convection, Mass Transfer, Refrigeration. Associate Technical Editor: Y. Jaluria.

X = normalized space coordinate = x/x_0
x = distance from the central plane, central axis or center, m
x_0 = half-thickness or radius, m
α = thermal diffusivity of the produce, m^2/s
γ = kinematic viscosity of air at mean temperature, m^2/s
ϕ = relative humidity of cold air, percent
τ = Fourier number = $\alpha \cdot t/x_0^2$

Subscripts and Superscripts

cm = cooling medium
i = initial
db = dry bulb
wb = wet bulb

Introduction

In the food preservation and processing industry, food commodities are cooled by a number of methods. In cold storage practice, the food is cooled quickly after harvesting or slaughtering and its temperature is reduced to the storage warehouse temperature. As reported earlier by the present author (Ansari, 1984), cold preservation is the best and least expensive method for preservation of food. The food, after precooling, is kept in the refrigerated warehouse to extend its high quality. During the cooling process, convective heat transfer occurs from the food surface. During air-blast cooling of exposed foods, desiccation provides additional cooling due to latent heat transfer. The author and his co-workers have thoroughly investigated and reported the validity of the available mathematical models for making heat and mass transfer analyses in such cases (Ansari, 1984; Ansari et al., 1984). During a long period of experimental and theoretical investigations, it was observed that both convective heat transfer and moisture transfer effects from the produce surface were significant up to the half-cooling time, defined as the time elapsed in reducing the temperature difference between the produce center and the cooling medium to half its initial value. After half-cooling time, the pure convection heat transfer model was found to calculate temperatures that were in better agreement with the measured values. On the basis of these observations, a calculation scheme was developed and reported (Ansari et al., 1984) that was a combination of the pure convection and simultaneous heat and mass transfer surface boundary condition equations available in the literature. In this scheme, temperature calculations were made with simultaneous heat and moisture transfer model up to the half-cooling time. During later stages of cooling, a pure convection model was used. Although this scheme of calculation was reported to predict temperatures that agreed quite satisfactorily with measured temperatures, it was devoid of sound mathematical logic. Mathematical models have been reported in the literature by many other investigators, who take into consideration the cooling effects of heat and moisture transfer (Dyner and Hesselschwerdt, 1964; Dincer, 1993; Dincer and Akaryildiz, 1993; Gaffney et al, 1985; Guemes et al., 1988; Hayakawa and Succar, 1982; Sastry et al., 1985). Both classical solutions (Arpaci, 1966; Carslaw and Jaeger, 1980; Dincer, 1993; Dincer and Akaryildiz, 1993) and numerical solutions (Ansari, 1984; Ansari et al., 1984, 1987; Gamal, 1992; Gaffney et al., 1985; Hayakawa and Succar, 1982) have been used to solve the mathematical models. Unfortunately, a better model is still not available in the literature. In the present work, the enthalpy-potential concept has been used to derive a simple linear surface boundary condition equation. The one-dimensional transient heat conduction equation is solved with the initial condition equation, center boundary condition equation, and the proposed boundary condition equation after normalizing the equation system. An optimized explicit finite-difference scheme is used. The computed temperatures have been compared graphically with the measured values for tomato and cucumber samples and are found to be in good agreement.

Table 1 Constants in the Nu–Re correlations defined by Eq. (9)

Constant	Infinite slab	Infinite cylinder	Sphere
p	0.0	0.0	0.1
q	0.664	0.260	0.30
r	0.5	0.6	0.5
s	0.333	−0.3	0.333

Mathematical Model

As reported in the literature (Ansari, 1984; Ansari et al., 1984), for infinite isotropic regular-shaped food produce initially at uniform temperature and exposed to symmetric cooling, the heat conduction phenomenon, initial condition, center boundary condition, surface boundary condition with pure convection heat transfer, and that with simultaneous heat and moisture transfer, are respectively represented by the following normalized equations:

$$\frac{\partial}{\partial X^m}\cdot\frac{\partial}{\partial X}\left(X^m\cdot\frac{\partial U}{\partial X}\right)=\frac{\partial U}{\partial \tau} \text{ for } \tau \geq 0,\ 0 \leq X \leq 1 \quad (1)$$

$$U = 1 \quad \text{for} \quad \tau = 0, \quad 0 \leq X \leq 1 \quad (2)$$

$$\frac{\partial U}{\partial X} = 0 \quad \text{for} \quad \tau > 0, \quad X = 0 \quad (3)$$

$$\frac{\partial U}{\partial X} = -\mathrm{Bi}\cdot U \quad \text{for} \quad \tau > 0, \quad X = 1 \quad (4)$$

$$\frac{\partial U}{\partial X} = -\mathrm{Bi}\cdot(C_1\cdot U^2 + C_2\cdot U + C_3) \text{ for } \tau > 0,\ X = 1 \quad (5)$$

$$C_1 = T_i^+ - T_{wb}^+ \quad (6)$$

$$C_2 = 0.3428 + T_{wb}^+ \quad (7)$$

$$C_3 = \frac{(1-\phi)}{C_1}\cdot(1.2977 - 0.6368T_{db}^+ + T_{db}^{+2}) - C_2\cdot U_{db} - C_1\cdot U_{db}^2 \quad (8)$$

Equations (5)–(8) are reported to be based on enthalpy potential (Badrinarayanan, 1976) and are nonlinear. These equations include the effects of convective heat transfer and moisture transfer from the produce surface. The temperature–time variations in the produce body are computed by solving the system of Eqs. (1)–(3) with appropriate surface boundary condition equation. In pure convection heat transfer, Eq. (4) is used, whereas in case of simultaneous heat and moisture transfers, Eqs. (5)–(8) are used. The requisite values of surface film conductance for solving this equation system are calculated from the Nu–Re correlations reported in the literature (Chapman, 1984; Ansari, 1986; Ansari et al., 1987) and are defined by the following equation;

$$\mathrm{Nu} = p + q\cdot\mathrm{Re}^r\cdot\mathrm{Pr}^s \quad (9)$$

The constants p, q, and exponents r, s, are different for different shapes and are given in Table 1.

Development of the Proposed Model

In case of simultaneous heat and mass transfer from the produce surface, the total heat transfer shall be a function of the enthalpy potential at the surface. It is represented by the following relationship (ASHRAE, 1981);

$$q = h_d \cdot (I - I_{cm}) \tag{10}$$

Surface film conductance and convective surface mass transfer coefficient are correlated by the following relationship (Stoecker and Jones, 1982);

$$h_d = \frac{h}{c_{pm}} \tag{11}$$

Combination of Eqs. (10) and (11) yields the rate of heat transfer of the produce surface in terms of enthalpy of saturated air at the surface temperature, which remains wet due to moisture diffusion from inside, and the enthalpy of cold air stream. The net rate of heat transfer shall be given as

$$q = \frac{h \cdot (I - I_{cm})}{c_{pm}} \tag{12}$$

The surface boundary condition equation may, therefore, be written as;

$$\frac{\partial T}{\partial x} = -\frac{h \cdot (I - I_{cm})}{k \cdot c_{pm}} \tag{13}$$

Using the thermodynamic property table of saturated air at atmospheric pressure reported in the literature (Stoecker and Jones, 1982), I/c_{pm} data for saturated air were generated. For simplifying the mathematical model, only the portion of the linearly varying data was chosen and this was regressed to get the following approximate correlation for saturated air at the wet produce surface:

$$\frac{I}{c_{pm}} = 2T + 9.47 \tag{14}$$

In the cold air blast ducts, the relative humidity is found to vary between 80 and 90 percent. For an average relative humidity of 85 percent, I for cold air stream was calculated from the temperature and humidity ratio of moist air (McQuiston and Parker, 1982), I_{cm}/c_{pm} data were generated and the linear portion of this data was regressed. It was found that the following approximation can be made in this case as well:

$$\frac{I_{cm}}{c_{pm}} = 2T_{cm} + 9.47 \tag{15}$$

Substitution of Eqs. (14) and (15) into Eq. (13) simplifies the surface boundary condition equation to the following form:

$$\frac{\partial T}{\partial x} = -2\frac{h}{k}(T - T_{cm}) \tag{16}$$

Application of nondimensionalization parameters reduces Eq. (16) to the following normalized form:

$$\frac{\partial U}{\partial X} = -2\mathrm{Bi} \cdot U \tag{17}$$

Experimental Procedure

The experimental setup along with the measurement procedure has been described by the author elsewhere (Ansari, 1995). It consisted of a closed circular duct with a 25 cm diameter, through which air was circulated by a centrifugal blower. Air was cooled by passing it over the evaporator coil of a vapor compression refrigeration system. The temperature inside the test section was maintained constant at any value between 6°C and 10°C with the help of air bypass fins. The cold air stream velocity was constant at 5.4 m/s. Copper-constantan thermocouples (28 SWG) were used to measure temperatures at the center of the food samples by a digital millivoltmeter with a resolution of 1 μV.

Table 2 Properties of food products under investigation

Produce	Mass density, ρ (kg/m^3)	Specific heat, c_p (J/kg·K)	Thermal conductivity, k (W/m·K)
Tomato	1016.9	3990.0	0.56
Cucumber	968.6	4060.0	0.55

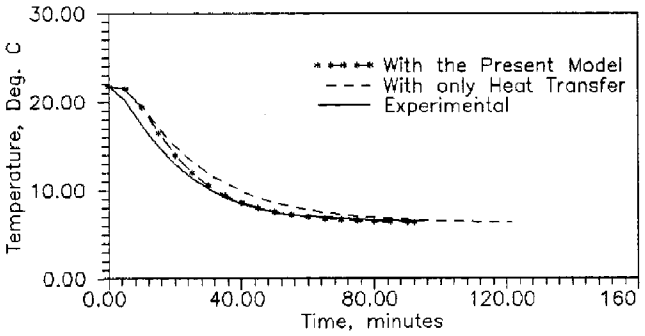

Fig. 1 Temperature–time variations for tomato sample

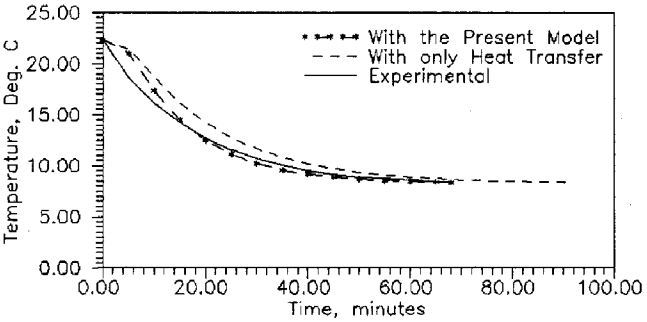

Fig. 2 Temperature–time variations for cucumber sample

Results and Discussion

Thorough investigations were made on 10 fresh samples each of tomato and cucumber. The thermophysical properties of these food products were taken from the literature (Gamal, 1992) and have been listed in Table 2. The values of surface film conductance, required for the solution of equation systems, were calculated from the measured air stream velocity by Eq. (9) and the thermophysical properties of air were also read from the literature (Chapman, 1984). The proposed Eq. (17) was solved numerically along with Eqs. (1)–(3). Comparative studies of a number of finite-difference schemes, made earlier by the author (Ansari, 1984) had revealed that a simple explicit scheme with $\Delta X = X/20$ yields accurate results and was used in the present investigations. Center and surface boundary condition equations were solved implicitly by four-point formulae, which are based on Lagrangian interpolation and are reported to have a small truncation error of the order of $(\Delta X)^3$ (Berezin and Zhidkov, 1965). The computed temperature–time variations at the center of all the food samples were compared with the measured temperatures reported in the literature (Gamal, 1992). In order to compare the present model with the other models available in the literature, computations were also made with pure convection surface boundary condition Eq. (4) as well as with the literature model of simultaneous heat and moisture transfer surface boundary condition Eqs. (5)–(8). It was observed that the computation results by the present surface boundary condition Eq. (17) are consistently in good agreement with the measured values. For one sample each of tomato and cucumber, plots are shown in Figs. 1 and 2. The temperatures

calculated by Eqs. (5)–(8) were almost the same as those by the proposed Eq. (17) and the difference was not visible on the plot. Due to this reason, these calculation results have not been shown on the graphs. Equations (5)–(8) are also reported to have been derived on the basis of enthalpy potential (Badrinarayanan, 1976). These are nonlinear and tedious to solve. Quite often, such cumbersome mathematical formulations happen to be more of academic interest and do not yield a comparable degree of accuracy, as many drastic simplifying assumptions are already made. These assumptions, in the present case, are: approximations of the food products with regular-shaped bodies, isotropicity, unidirectional heat transfer, initial uniform temperature distribution in the live respiring food samples, uniform cooling, etc. It was thought that one more simplifying assumption might not introduce too much error. The proposed linear Eq. (17) is very simple, its solution is easy, and it gives the same degree of accuracy. The overall good agreement between the computed temperatures from the present model and their measured values established that the effort is worthwhile. It may be emphasized that varying the slopes of the Eqs. (14) and (15) by up to 10 percent did not adversely affect the agreement between the computed and measured temperatures. This implies that the applications of the system of Eqs. (5)–(8) and other similar nonlinear and cumbersome mathematical models used by different investigators may hardly be justified. In view of all the plus points, discussed above, Eq. (17) developed in the present work is recommended for temperature calculations in food products exposed to a cold air stream.

Conclusions

On the basis of the present investigation by the author, it may be concluded that the proposed simultaneous heat and moisture transfer surface boundary condition equation is accurate and reliable. It incorporates the cooling effects due to convective heat transfer as well as due to moisture evaporation during desiccation of food. The derivation is based on the concept of enthalpy potential at the produce surface. The enthalpy versus temperature data for saturated air at the wet produce surface as well as those of unsaturated cold air stream were generated and regressed to get a linear correlation. This was then substituted in the enthalpy potential equation to get a simplified linear surface boundary condition equation. The mathematical model for infinite, isotropic regular-shaped bodies was solved by an optimized explicit finite-difference scheme. Investigations on ten samples each of tomato and cucumber established that the calculation results by the proposed model are in good agreement with the measured values. The model is recommended for making transient temperature–time calculations during air blast cooling of exposed food commodities and other hydrous materials.

References

Ansari, F. A., 1984, "Heat and Mass Transfer Analysis in Cold Preservation of Food," Ph.D. Thesis, University of Roorkee, Roorkee, India.

Ansari, F. A., Charan, V., and Varma, H. K., 1984, "Heat and Mass Transfer Analysis in Air Cooling of Spherical Food Products," *International Journal of Refrigeration,* Vol. 7(3), pp. 194–197.

Ansari, F. A., 1986, "An Empirical Method of Measuring Thermal Diffusivity and Surface Film Conductance," *American Society of Agricultural Engineers, Transaction,* Vol. 29(5), pp. 1492–1497.

Ansari, F. A., Mughis, A., and Ahmad, M., 1987, "Measurement of Thermophysical Properties of Mashed Potato," *Lebensm-Wiss. U-Technol.,* Switzerland, Vol. 20(6), pp. 267–270.

Ansari, F. A., 1995, "Thorough Heat and Mass Transfer Studies for Solid and Liquid Bodies Through Simple Experimentation," *Seminar on Fluid Mechanics Research,* Dhaka, Bangladesh, Dec. 27–28.

Arpaci, V. S., 1966, *Conduction Heat Transfer,* Addison-Wesley, Reading, MA.

ASHRAE, 1981, *Handbook of Fundamentals,* American Society of Heating, Refrigerating, and Air Conditioning Engineers, Inc., Atlanta, GA.

ASHRAE, 1989, *Handbook of Fundamentals,* American Society of Heating, Refrigerating, and Air Conditioning Engineers, Inc., Atlanta, GA.

Badrinarayan, K., 1976, "Heat and Mass Transfer Studies and Evaluation of Thermal Properties of Food Products," Ph.D. Thesis, Indian Institute of Technology, Madras, India.

Berezin, I. S., and Zhidkov, M. P., 1965, *Computing Methods,* Addison Wesley Publishing Co., Inc., Reading, MA, Vol. 1, p. 210.

Carslaw, H. S., and Jaeger, J. C., 1980, *Conduction of Heat in Solids,* 2nd ed., Oxford University Press, London.

Chapman, A. J., 1984, *Heat and Mass Transfer,* 4th ed., Macmillan Publishing Co.

Dincer, I., 1993, "An Exact Heat Transfer Analysis of Spherical Food Products," *International Journal of Energy Research,* Vol. 17(1), pp. 9–18.

Dincer, I., and Akaryildiz, E., 1993, "Transient Temperature Distributions Within Spherical Products With Internal Heat Generation and Transpiration: Experimental and Analytical Results," *International Journal of Heat and Mass Transfer,* Vol. 36, pp. 1998–2003.

Dyner, H., and Hesselschwerdt, A. L., Jr., 1964, "Time–Temperature Characteristics During Food Precooling," *ASHRAE Transactions,* Vol. 70, pp. 249–255.

Gaffney, J. J., Baird, C. D., and Chau, K. V., 1985, "Methods for Calculating Heat and Mass Transfer in Fruits and Vegetables Individually and in Bulk," *ASHRAE Transactions,* Vol. 91, pp. 333–352.

Gaffney, J. J., Baird, C. D., and Chau, K. V., 1985, "Influence of Air Flow Rate, Respiration, Evaporative Cooling, and Other Factors Affecting Weight Loss Calculations for Fruits and Vegetables," *ASHRAE Transactions,* Vol. 91, pp. 690–707.

Gamal, A. A., 1992, "Heat and Mass Transfer During Precooling of Food Products," M. Sc. Engineering Dissertation, Al-Fateh University, Tripoli, Libya.

Guemes, D. R., Pirovani, M. E., and di Pentima, J. H., 1988, "Heat Transfer Characteristics During Air Cooling of Strawberries," *International Journal of Refrigeration,* Vol. 12, pp. 169–173.

Hayakawa, K., and Succar, J., 1982, "Heat Transfer and Moisture Loss of Spherical Food Produce," *Journal of Food Science,* Vol. 47, pp. 595–605.

McQuiston, F. C., and Parker, J. D., 1982, *Heating, Ventilating, and Air Conditioning: Analysis and Design,* 2nd ed., Wiley, p. 15.

Sastry, S. K., Zuritz, C. A., and Anantheswaran, A., 1985, "Interaction Between Heat and Mass Transfer in Foods," *ASHRAE Transactions,* Vol. 91, pp. 353–370.

Stoecker, W. F., and Jones, J. W., 1982, *Refrigeration and Air Conditioning,* 2nd ed., McGraw-Hill.